transactions of the ASME

journal of heat transfer

Published Quarterly by
The American Society of
Mechanical Engineers
Volume 95 • Series C • Number 3
AUGUST 1973

TECHNICAL BRIEFS

(Contents continued on page 370)

EDITORIAL STAFF
Editor, **J. J. JAKLITSCH, JR.**
Production Editor,
MARINA EVDOCHENKO

HEAT TRANSFER DIVISION
Chairman, **L. H. BACK**
Secretary, **F. W. SCHMIDT**
Senior Technical Editor, **E. M. SPARROW**
Technical Editor, **L. H. BACK**
Technical Editor, **A. E. BERGLES**
Technical Editor, **R. B. KINNEY**
Technical Editor, **J. L. NOVOTNY**
Technical Editor, **R. SIEGEL**
Technical Editor, **R. L. WEBB**

POLICY BOARD, COMMUNICATIONS
Chairman and Vice-President
S. P. KEZIOS

Members-at-Large
R. E. ABBOTT
P. G. HODGE, JR.
J. W. HOLL
D. F. WILCOCK

Policy Board Representatives
Basic Engineering, **A. R. CATHERON**
General Engineering, **S. P. ROGACKI**
Industry, **W. B. MOEN**
Power, **G. P. COOPER**
Research, **G. C. WIEDERSUM, JR.**
Codes and Stds., **W. H. BYRNE**
Nom. Com. Rep.,
G. P. ESCHENBRENNER
Business Staff
345 E. 47th St.
New York, N. Y. 10017
212/752-6800
Mng. Dir., Com., **C. O. SANDERSON**

OFFICERS OF THE ASME
President, **D. C. DRUCKER**
Exec. Dir. & Sec'y, **ROGERS B. FINCH**
Treasurer, **HENRY N. MULLER, JR.**

EDITED and PUBLISHED quarterly at the offices of The American Society of Mechanical Engineers, United Engineering Center, 345 E. 47th St., New York, N. Y. 10017. Cable address, "Mechaneer," New York. Second-class postage paid at New York, N. Y., and at additional mailing offices.

CHANGES OF ADDRESS must be received at Society headquarters seven weeks before they are to be effective. Please send old label and new address.

PRICES: To members, $15.00, annually; to nonmembers, $30.00. Single copies, $10.00 each. Add $1.50 for postage to countries outside the United States and Canada.

STATEMENT from By-Laws. The Society shall not be responsible for statements or opinions advanced in papers or . . . printed in its publications (B13, Par. 4).

COPYRIGHT 1973 by The American Society of Mechanical Engineers. Reprints from this publication may be made on condition that full credit be given the TRANSACTIONS OF THE ASME, SERIES C—JOURNAL OF HEAT TRANSFER, and the author and date of publication stated.

INDEXED by the Engineering Index, Inc.

Downloaded 04 Feb 2011 to 194.85.80.107. Redistribution subject to ASME license or copyright; see http://www.asme.org/terms/Terms_Use.cfm

CONTENTS

(CONTINUED)

N. E. HARDWICK
Member, Technical Staff,
Bell Telephone Laboratories,
Greensboro, N. C.
Assoc. Mem. ASME

E. K. LEVY
Associate Professor,
Department of Mechanical Engineering
and Mechanics,
Lehigh University,
Bethlehem, Pa.
Assoc. Mem. ASME

Study of the Laminar Free-Convection Wake Above an Isothermal Vertical Plate

The steady, laminar, two-dimensional wake above a thin vertical isothermal heated plate cooled by free convection was investigated theoretically and experimentally. The system of partial differential equations governing the fluid motion and heat transfer in the vicinity of the plate and in the near wake region was formulated and solved using finite difference techniques. Using air, the temperature and velocity profiles in the wake region were measured experimentally using a laser holographic interferometer and a constant temperature hot wire anemometer.

Introduction

TECHNIQUES for evaluating free convection effects caused by arranging heated vertical plates in combinations of rows and columns are of importance to the electronics industry. For example, in many cases microelectronic components are mounted on substrates (or plates) that dissipate the energy they generate primarily by free convection. Electrical and space requirements dictate that these substrates be stacked close together leading to significant thermal interactions between them. When heated vertical plates are stacked in columns the wake of a plate interacts with the boundary layer of the plate above it. Such interaction could produce results significantly different from those obtained using the common, simplifying assumption of a continuous vertical wall (and neglecting the gap between top and bottom plates). Therefore, before a general analysis can be formulated for columns of plates, a sound theoretical and experimental understanding of the natural convection wake behind an isolated vertical plate is necessary.

The only work that could be found in the literature concerning the wake of a plate cooled by free convection was a paper by Yang [1][1] in which the velocity and temperature profiles in the *immediate neighborhood of the trailing edge were found using an* asymptotic series expansion and were continued into the wake region by an integral technique. For the case of laminar forced convection wakes behind flat plates (Blasius type conditions) without heat transfer, the classical solutions of Goldstein [2] and Tollmein [3] have been followed by the studies of Kuo [4], Imai [5], and Stewartson [6], and more recently Plotkin and Flugge-Lotz using numerical methods [7].

Engle [8], who used an integral method to analyze the natural convection in vertical channels subject to prescribed wall heat fluxes, extended his work to include boundary layer interactions between rows of staggered plates. Experimental work using the same configuration was reported by Sobel [9].

The objective of this investigation was to study the steady state laminar flow and heat transfer behavior in the near wake region behind a vertical isothermal plate cooled by free convection. The numerical and experimental results which have been obtained are presented in this paper.

Formulation of the Equations

In the usual natural convection analysis the general Navier-Stokes and energy equations are reduced to so-called "boundary layer" equations by means of order of magnitude arguments. For the case of the fluid properties adhering to the Boussinesq approximations having the basic assumptions that $\rho = \rho_0/[1 + \rho(T - T_\infty)]$ and that $\rho(T_w - T_\infty) \ll 1$, these equations are written:

$$\rho \left(u \frac{\partial u}{\partial x} + v \frac{\partial u}{\partial y} \right) = \beta \rho g (T - T_\infty) - \frac{\partial p'}{\partial x} + \mu \frac{\partial^2 u}{\partial y^2} \qquad (1)$$

$$\frac{\partial u}{\partial x} + \frac{\partial v}{\partial y} = 0 \qquad (2)$$

$$\rho c_p \left(u \frac{\partial T}{\partial x} + v \frac{\partial T}{\partial y} \right) = K \frac{\partial^2 T}{\partial y^2} \qquad (3)$$

However in the wake problem, because of the presence of large x derivatives as well as y derivatives in the vicinity of the trailing edge, such simplifications are not valid. The equations which must be solved in this case are the following:

---

[1] Numbers in brackets designate References at end of paper.

Contributed by the Heat Transfer Division and presented at the Winter Annual Meeting, New York, N. Y., November 26–30, 1972, of THE AMERICAN SOCIETY OF MECHANICAL ENGINEERS. Manuscript received by the Heat Transfer Division August 15, 1972; revised manuscript received November 10, 1972. Paper No. 72-WA/HT-41.

$$\rho\left(u\frac{\partial u}{\partial x}+v\frac{\partial u}{\partial y}\right)=\beta\rho g(T-T_\infty)-\frac{\partial p'}{\partial x}+\mu\left(\frac{\partial^2 u}{\partial x^2}+\frac{\partial^2 u}{\partial y^2}\right) \tag{4}$$

$$\rho\left(u\frac{\partial v}{\partial x}+v\frac{\partial v}{\partial y}\right)=-\frac{\partial p'}{\partial y}+\mu\left(\frac{\partial^2 v}{\partial x^2}+\frac{\partial^2 v}{\partial y^2}\right) \tag{5}$$

$$\frac{\partial u}{\partial x}+\frac{\partial v}{\partial y}=0 \tag{6}$$

$$\rho c_p\left(u\frac{\partial T}{\partial x}+v\frac{\partial T}{\partial y}\right)=K\left(\frac{\partial^2 T}{\partial x^2}+\frac{\partial^2 T}{\partial y^2}\right) \tag{7}$$

Note that equations (4), (5), and (7) are of the elliptic form and their solution requires that boundary conditions be specified on a closed boundary surrounding the region of interest. Equations (4) to (7) were solved in the "elliptic equation region" (see Fig. 1) which included the top portion of the plate to permit any influences of the wake to propagate upstream to the trailing edge. The boundary conditions for the elliptic equation region were generated by solving the parabolic set (1)–(3) over the entire plate-wake region. A similar procedure had been used [7] for a forced convection wake without heat transfer.

The upstream boundary of the elliptic region was located in a region of the plate that was far enough upstream of the trailing edge so that it was uninfluenced by the wake flow. Similarly the downstream boundary of the elliptic region was located far enough downstream of the trailing edge so that asymptotic wake conditions were reached.

Method of Solution

Equation sets (1)-(3) and (4)–(7) were both solved numerically using finite difference procedures. To accomplish this the fluid region was subdivided into a grid with each space point ($j\Delta X$, $k\Delta Y$) simply identified as a grid point (j, k).

Solution of the Parabolic Equations. Along the plate the finite difference forms of equations (1)–(3) were solved using the Liebmann (or Gauss-Seidel iteration) method subject to the boundary conditions listed in Fig. 1. This scheme was not suitable for extending the solution into the wake region. Therefore a wake solution for the finite difference form of the parabolic equations was obtained by starting at the top of the plate and marching in the downstream direction one row at a time. The formulations used here are described in detail in reference [10].

The resulting solutions for the plate and the wake were used to provide an initial iteration base for the subsequent solution of the elliptic region equations and to provide the necessary boundary conditions.

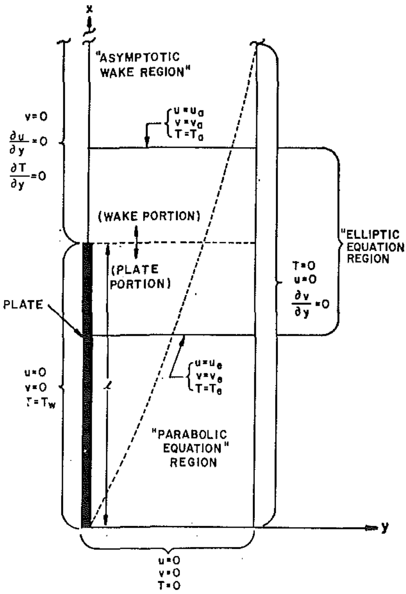

Fig. 1 Mathematical regions for natural convection flow

Solution of the Elliptic Region Equations. To facilitate the solution of the elliptic region equations, equation set (4)–(7) was rewritten in the conservative and unsteady form in terms of vorticity and stream function variables as shown in the following:

$$\frac{\partial\Omega}{\partial\tau}+\frac{\partial(U\Omega)}{\partial X}+\frac{\partial(V\Omega)}{\partial Y}=\frac{\partial^2\Omega}{\partial X^2}+\frac{\partial^2\Omega}{\partial Y^2}+\frac{\partial\theta}{\partial Y} \tag{8}$$

$$\frac{\partial^2\Psi}{\partial X^2}+\frac{\partial^2\Psi}{\partial Y^2}=\Omega \tag{9}$$

$$\frac{\partial\theta}{\partial\tau}+\frac{\partial(U\theta)}{\partial X}+\frac{\partial(V\theta)}{\partial Y}=\frac{1}{\Pr}\left(\frac{\partial^2\theta}{\partial X^2}+\frac{\partial^2\theta}{\partial Y^2}\right) \tag{10}$$

These changes were made so that the Dufort-Frankel method of solution [11–13] could be used. This scheme involves three time levels and results in truncation errors of second order in both time and space derivatives. Because the second differentials can be written in terms of three time levels the solution is stable for central differencing. The resulting finite difference equations are:

Nomenclature

c_p = constant pressure specific heat
g = acceleration of gravity
Gr = Grashof number, $g\beta l^3(T - T_\infty)/\nu^2$
j, k = grid point indices along X and Y-direction, respectively
K = thermal conductivity
l = height of vertical plate
n = number of time steps
p = pressure
p' = pressure perturbation ($p - p_\infty$)
Pr = Prandtl number, $\mu c_p/K$
T = temperature
u = x component of velocity
U = nondimensional x velocity (ul/ν)
U^* = $U\cdot(4\theta_w)^{-1/2}$
v = y component of velocity
V = nondimensional y velocity (vl/ν)
x = length coordinate measured parallel to the plate
X = nondimensional length coordinate (x/l)
y = length coordinate measured perpendicular to the plate
Y = nondimensional length coordinate (y/l)
Y^* = $(y/l)\cdot(\theta_w/4)^{1/4}$
β = fluid expansion coefficient
$\delta\tau$ = time-step
ϵ = emittance
θ = nondimensional temperature ($g\beta l^3(T - T_\infty)/\nu^2$)
θ_w = nondimensional plate temperature ($g\beta l^3(T_w - T_\infty)/\nu^2$)
μ = dynamic viscosity
ν = kinematic viscosity
ρ = fluid density
τ = time
Ψ = nondimensional stream function $\left(U = \frac{\partial\Psi}{\partial Y}, V = -\frac{\partial\Psi}{\partial X}\right)$
Ω = nondimensional vorticity variable $\left(\Omega = \frac{\partial U}{\partial Y} - \frac{\partial V}{\partial X}\right)$

Subscripts

j = node index in the X-direction
k = node index in the Y-direction
r = reference
w = plate
x = x-direction
y = y-direction
∞ = ambient conditions

$$\Omega^{n+1}{}_{j,k}\left(1+\frac{2\cdot\delta\tau}{\Delta X^2}+\frac{2\cdot\delta\tau}{\Delta Y^2}\right)=\Omega^{n-1}{}_{j,k}+\frac{\delta\tau}{\Delta X}\,(U^n{}_{j-1,k}\cdot\Omega^n{}_{j-1,k}$$

$$-U^n{}_{j+1,k}\cdot\Omega^n{}_{j+1,k})+\frac{\delta\tau}{\Delta Y}(V^n{}_{j,k-1}\cdot\Omega^n{}_{j,k-1}-V^n{}_{j,k+1}\cdot\Omega^n{}_{j,k+1})$$

$$+\frac{2\cdot\delta\tau}{(\Delta X)^2}\,(\Omega^n{}_{j+1,k}+\Omega^n{}_{j-1,k}-\Omega^{n-1}{}_{j,k})$$

$$+\frac{2\cdot\delta\tau}{(\Delta Y)^2}\,(\Omega^n{}_{j,k+1}+\Omega^n{}_{j,k-1}-\Omega^{n-1}{}_{j,k})$$

$$+\frac{\delta\tau}{\Delta Y}\,(\theta^n{}_{j,k+1}-\theta^n{}_{j,k-1})\quad(11)$$

$$\Psi_{j,k}$$

$$=\frac{-(\Delta Y)^2\cdot\Omega_{j,k}+\Psi_{j,k+1}+\Psi_{j,k-1}+\dfrac{(\Delta Y)^2}{(\Delta X)^2}\cdot(\Psi_{j+1,k}+\Psi_{j-1,k})}{\left(2+2\,\dfrac{(\Delta Y)^2}{(\Delta X)^2}\right)}\qquad(12)$$

$$\theta^{n+1}{}_{j,k}\left(1+\frac{2\cdot\delta\tau}{(\Delta X)^2\,\mathrm{Pr}}+\frac{2\cdot\delta\tau}{(\Delta Y)^2\,\mathrm{Pr}}\right)=\theta^{n-1}{}_{j,k}+\frac{\delta\tau}{\Delta X}\,(U^n{}_{j-1,k}\theta^n{}_{j-1,k}$$

$$-U^n{}_{j+1,k}\theta^n{}_{j+1,k})+\frac{\delta\tau}{\Delta Y}\,(V^n{}_{j,k-1}\cdot\theta^n{}_{j,k-1}-V^n{}_{j,k+1}\cdot\theta^n{}_{j,k+1})$$

$$+\frac{2\cdot\delta\tau}{\mathrm{Pr}\cdot(\Delta X)^2}\cdot(\theta^n{}_{j+1,k}+\theta^n{}_{j-1,k}-\theta^{n-1}{}_{j,k})$$

$$+\frac{2\cdot\delta\tau}{\mathrm{Pr}\cdot(\Delta Y)^2}\,(\theta^n{}_{j,k+1}+\theta^n{}_{j,k-1}-\theta^{n-1}{}_{j,k})\quad(13)$$

Since a first order time-dependent term is now included, these equations are now considered parabolic with respect to the time coordinates. However, because the solution is iterated until steady state is reached using the steady-state boundary conditions, the elliptic characteristics in the spatial variables are retained in the solution.

Convergence to steady state conditions required about 400–500 time steps in most cases. For a 50 × 20 grid this required approximately 90 min of computer time. (Splitting the grid size used to one-half the size had an insignificant effect on the results.)

The downstream boundary conditions as imposed by the numerical solution will not accurately reflect the conditions desired if they are applied before asymptotic conditions are reached. Therefore several computer runs were made in which the point of application was varied to see the effects. The downstream boundary was then positioned far enough downstream that the variables in the wake region of interest had negligible change when this position was moved further downstream.

Numerical Results

The velocity profiles obtained by solving the parabolic equations along the plate are considered first. These are plotted in Fig. 2 as the nondimensional x component of velocity versus the nondimensional distance Y at distances along the plate of x/l = 0.25, 0.5, and 1.0. ($X = x/l = 0$ corresponds to the leading edge of the plate and $X = 1.0$ to the trailing edge). The squares represent velocities taken from Ostrach's similarity solution [14] for $x/l = 0.5$.

Since the interim wake extension solutions suffer from infinite plate characteristics of the parabolic equations, the final wake solutions for the elliptic region are obtained using equation set (11)–(13). The nondimensional velocity profiles for six locations in the wake are given in Fig. 2. These curves indicate an abrupt change in the velocity in the vicinity of the trailing edge. The velocity along plate center line can be seen to increase from zero to a value greater than the velocity at any point parallel to the plate within one-tenth of the plate height into the wake. The reason for the rapid changes is the continuing presence of the buoyancy forces in conjunction with a free shear layer replacing the restrictive wall shear stresses that precede this region. Also included in Fig. 2 are the results of Yang's asymptotic series expansion and integral analyses for two locations in the wake. (All curves are for Gr = 3.07×10^6 and Pr = 0.72.)

The corresponding nondimensional temperature profiles in the wake and at the top of the plate are shown in Fig. 3. Again the solutions of Yang for two wake locations have been included.

The forms of the temperature and velocity profiles are different at different locations in the wake and universal solutions are not possible. However, some insight into how the velocity and temperature profiles vary with Grashof number can be gained by plotting the computed results in terms of the similarity variables taken from the standard plate boundary layer solutions [1, 14, 15]. The curves for the wake velocity profiles at $X = 1.05$ and 1.2 are shown in Fig. 4 for a range of Grashof numbers from 10^6 to 10^8. The corresponding temperature profiles plotted versus the plate solution similarity variable are shown in Fig. 5.

Experimental Investigation

The velocity and temperature profiles were checked experimentally to confirm the predicted flow and heat transfer patterns. A laser holographic interferometer was set up at Allentown Bell Laboratories to study the thermal wake development. This system was augmented by a DISA[2] constant temperature hot wire anemometer for measuring the velocity profiles in the wake and plate boundary layer.

Test Specimen. The isothermal plate used in the experiments consisted of a glass-insulated nichrome heater wire sandwiched between two 0.010 in. thick copper plates (see Fig. 6). Layers of nickel (50μ in. thick) and gold (140μ in. thick) were electroplated onto the copper plates. The outside gold layer was introduced to minimize thermal radiation ($\epsilon < 0.02$) and to prevent oxidation. The intermediate layer of nickel served as a barrier to the diffusion of copper into the porous gold layer. Temperature aging tests have shown that this metallizing system will not discolor after extended periods at 300 deg C.

The heater wire was imbedded in a Sylgard resin[3] approximately 0.020 in. thick that was pliable enough to compensate

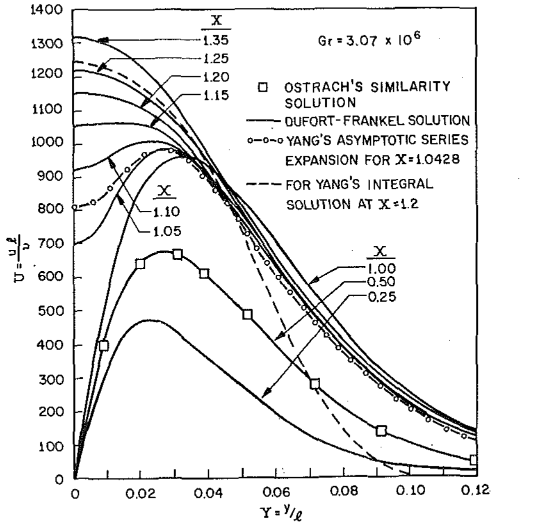

Fig. 2 ***X*-direction velocity profiles for plate solution and wake solution**

---

[2] DISA Elektronik A/S, Herlev, Denmark.

[3] Sylgard No. 182 potting and encapsulating resin, Dow Corning Corp., Midland, Mich.

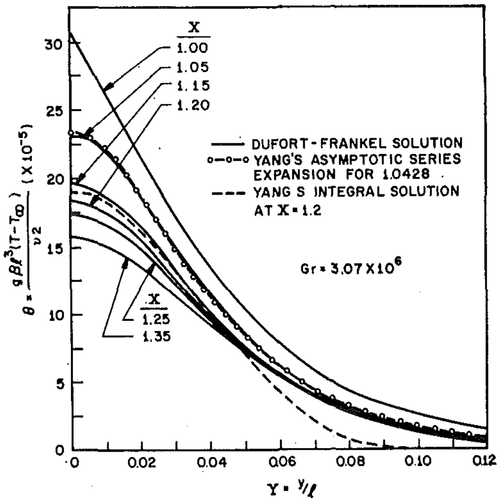

Fig. 3 Temperature profiles in the wake region

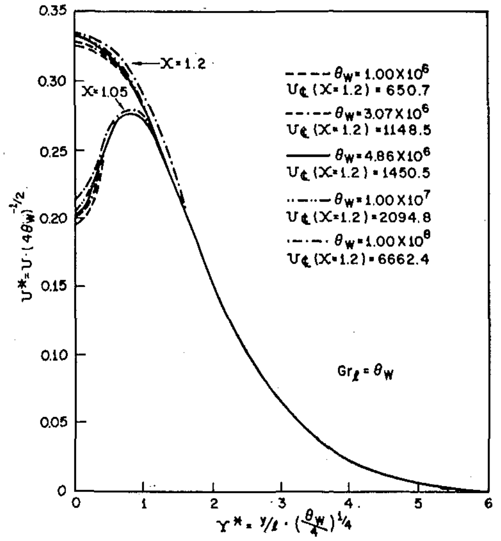

Fig. 4 Velocity profiles for a range of Grashof numbers plotted in terms of plate solution similarity variables

for thermal expansion at elevated temperatures without forming voids or warping excessively. An additional layer of Dow Corning RTV silicon rubber (~0.0025 in. thick) was applied to the inside of each plate to ensure adherence of the Sylgard resin to the plate and consequently to give good thermal contact to the gold plating layer. Small thermocouple wires (0.003 in. dia) were peened to the inside plate surface to monitor the plate temperature as well as to check the temperature variations over the plate. The thermocouples indicated that no significant temperature variations were present during test runs.

The plate was held by two thin plexiglass supports (1/8 in. wide) in a plexiglass shroud which was constructed to protect the convection flows from stray room currents.

Temperature Profiles. The isotherms in the boundary layer were obtained using the laser holographic interferometer system [10]. The principal difference between holographic interferometry and conventional interferometry is that the interference is between light beams which have occurred at different times instead of between two beams existing at the same time [16]. This is possible because the hologram plate positioned where the beams intersect is a diffraction grating that has the capability of reconstructing one of the laser beams when it is illuminated by the other beam [10, 16, 17].

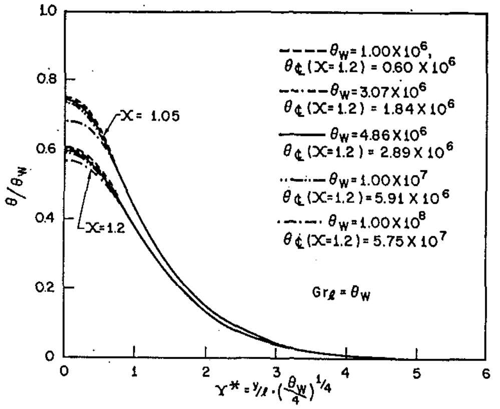

Fig. 5 Temperature profiles for a range of Grashof numbers plotted in terms of plate solution similarity variables

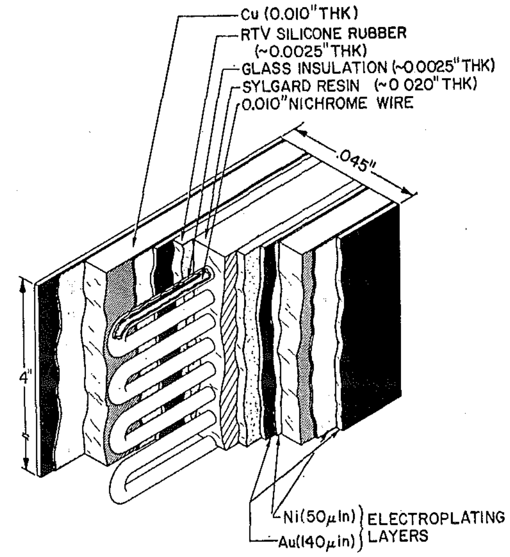

Fig. 6 Plate structure used for isothermal test specimen

Experimental data points taken from a 4 in. high plate with a temperature difference of 50 deg F (27.8 deg C) between the plate and the ambient air (this corresponds to Gr $= 3.07 \times 10^6$) are plotted in Fig. 7 along with the corresponding theoretical temperature profiles. The values obtained from the interferogram indicate that the measured temperatures are higher than predicted in the outer portions of the wake. In this region the temperatures seem to increase with distance in the downstream direction. This trend is in contrast to Yang's integral solutions [1] (plotted in Fig. 3) which show the temperature reaching ambient conditions at $Y \cong 0.10$ for $X = 1.20$ and in addition which predict temperatures greater than ambient at $Y = 0.10$ and $X = 1.0428$.

Measurement of Velocity Profiles. The velocity profiles were measured using a constant temperature hot wire anemometer system. To account for the affect of temperature variations in the flow field on the output of the anemometer and to calibrate the sensor for the low air velocities to be measured, an elaborate procedure was developed for direct calibration (see reference [10]). For Gr $= 3.07 \times 10^6$, the theoretical velocity profiles for the wake region are plotted in Fig. 8 along with the velocity profiles obtained using the hot wire anemometer.

Shown in Fig. 9 are plots of the measured and computed velocities along plate center line as functions of x for Gr $= 3.07 \times 10^6$. The experimental scatter in the velocity measurements at distances greater than $X = 1.6$ is attributed to the difficulty in alignment with the plate center line as well as to the larger velocity fluctuations that occurred in this region.

Another important characteristic of the trailing edge flow is seen by comparing the theoretical velocity profiles at the top of the plate obtained from the parabolic boundary layer equations (solid curve in Fig. 10) to those obtained from the elliptic equations (dashed curve in Fig. 10). The abrupt change to the free shear situation at the beginning of the wake has an upstream influence causing the velocity to increase in the vicinity of the plate near the trailing edge. To verify this experimentally, anemometer measurements (see data points in Fig. 10) were made using two plates of different heights.

Summary and Conclusions

The system of partial differential equations governing fluid motion and heat transfer along an isothermal vertical plate and in the wake above it was formulated in terms of finite difference equations and solved numerically. Numerical results were obtained for a Prandtl number of 0.72 and five different values of Grashof number ranging from 10^6 to 10^8.

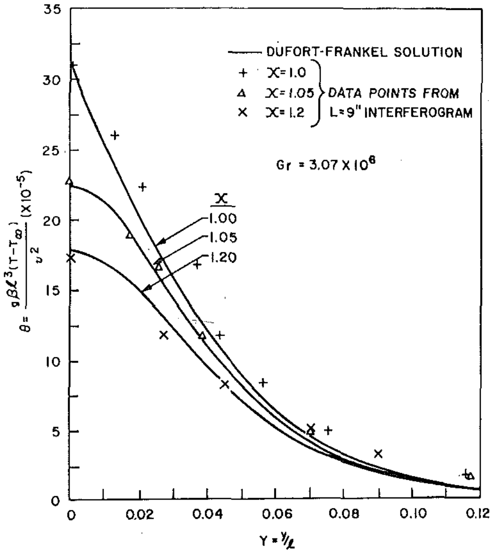

Fig. 7 Comparison between temperature profiles obtained from interferograms and analytical results — ΔT = 50 deg F (27.8 C)

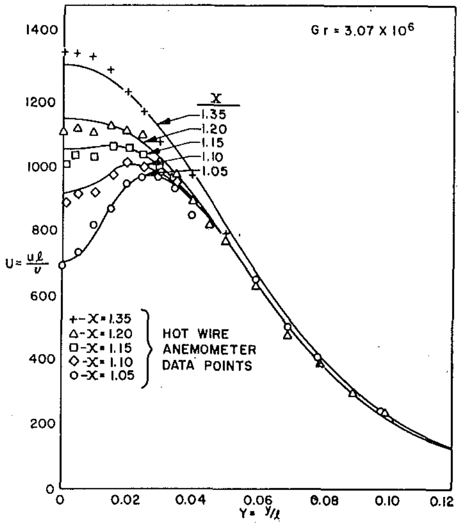

Fig. 8 Comparison between wake velocity profiles measured with hot wire anemometer and analytical results

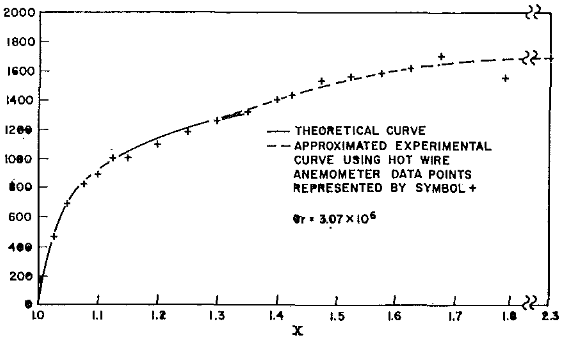

Fig. 9 Growth of center-line velocity, $U_{℄}$, in wake

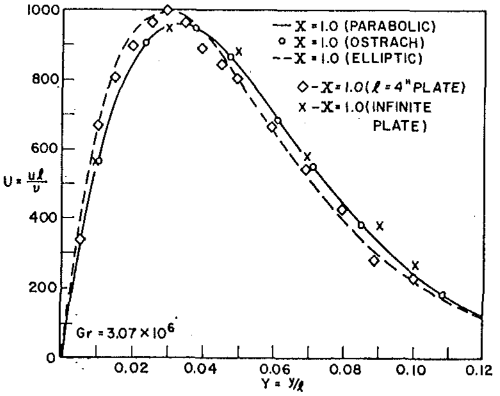

Fig. 10 Comparison between measured and calculated velocity profiles at top of plate

The theoretical and experimental results show a rapid transition from the free convection velocity and temperature profiles normally encountered along a plate to fully-developed wake conditions. The results also indicate that the influence of the wake is felt along the plate upstream of the trailing edge causing the velocity profiles near the top of the plate to be different from those usually obtained from the conventional parabolic boundary layer equations. Buoyancy forces in the wake cause the center-line velocity to continue to increase for significant distances downstream of the trailing edge.

The solutions obtained in this study are in a form amenable to coupling between the wake and boundary layers of neighboring plates. Therefore it forms the basis for a general solution that can be used to examine free convection from systems of vertical isothermal plates.

Acknowledgments

The authors would like to thank Bell Telephone Laboratories, Incorporated, and especially Dr. F. L. Howland and Dr. B. E. Nevis for their support, aid, and cooperation during this investigation. Helpful discussions were held with Dr. R. O'Regan concerning the holographic interferometer and Dr. A. Zinnes concerning theoretical aspects of his thesis that were related to this investigation. We also wish to acknowledge many stimulating discussions with Dr. J. A. Owczarek, Dr. A. H. Stenning, and Dr. G. T. McAllister of Lehigh University who were members of the doctoral committee.

References

1 Yang, K. T., "Laminar Free-Convection Wake Above a Heated Vertical Plate," *Journal of Applied Mechanics*, Vol. 31, TRANS. ASME, Series E, Vol. 86, Mar. 1964, pp. 131–138.

2 Goldstein, S., "Concerning Some Solutions of the Boundary Layer Equations in Hydrodynamics," *Proceedings of the Cambridge Philosophical Society*, Vol. 26, 1930, pp. 1–30.

3 Tollmein, W., "*Grenzschichten*," *Handbuch der Experimentalphysik*, Vol. IV, Part 1, 1931, p. 267.

4 Kuo, Y. H., "On the Flow of an Incompressible Fuid Past a Flat Plate at Moderate Reynolds Numbers," *Journal of Mathematics and Physics*, Vol. 32, 1953, pp. 83–101.

5 Imai, S., "On the Viscous Flow Near the Trailing Edge of a Flat Plate," *Proceedings of the Eleventh Congress of Applied Mechanics Munich*, H. Gortler ed., 1966, pp. 663–671.

6 Stewartson, K., "On the Flow Near the Trailing Edge of a Plate," *Proceedings of the Royal Society A*, Vol. 306, 1968, pp. 275–290.

7 Plotkin, A., and Flugge-Lotz, I., "A Numerical Solution for the Laminar Wake Behind a Finite Flat Plate," ASME Paper No. 68-WA/APM-20.

8 Engle, R. K., "The Development of Natural Convection on Vertical Flat Plates and in Vertical Channels," PhD Dissertation, New York University, New York, 1965.

9 Sobel, N., Landis, F., and Mueller, W. K., "Natural Convection Heat Transfer in Short Vertical Channels Including the Effects of Stagger," *Third International Heat Transfer Conference Proceedings*, American International Chemical Engineers, Chicago, 1966, pp. 121–125.

10 Hardwick, N. E., "Study of Free Convection Wake Above an Isothermal Vertical Plate," PhD Dissertation, Lehigh University, Bethlehem, Penn., 1972.

11 Dufort, E. C., and Frankel, S. P., "Stability Conditions in the Numerical Treatment of Parabolic Differential Equations," *Mathematical Tables and Other Aids to Computation*, Vol. 7, 1953, pp. 135–152.

12 Fromm, J., in *Methods in Computational Physics*, B Adler, S. Fernbach, and M. Rotenberg, eds., Vol. 3, Academic Press, New York, 1964, pp. 346–382.

13 Fromm, J. E., and Harlow, F. H., "Numerical Solutions of the Problem of Vortex Street Development," *Physics of Fluid*, Vol. 6, No. 7, July, 1963, pp. 975–982.

14 Ostrach, S., "An Analysis of Laminar Free Convection Flow and Heat Transfer About a Flat Plate Parallel to the Direction of the Generating Body Force," NACA TN 1111, Oct. 1951.

15 Schmidt, E., and Beckman, W., "Das Temperatur and Geschwindigkeitsfeld von-einer warme abgebenden Senkrechten Platte bei Naturlicher Konvektion," *Technische Mechanik Thermo-Dynamik*, Vol. 1, Oct. 1930, pp. 341–349; Nov. 1930, pp. 391–406.

16 Aung, W., and O'Regan, R., "Precise Measurement of Heat Transfer Using Holographic Interferometry," *Review of Scientific Instruments*, Vol. 42, No. 12, Dec. 1971, pp. 1755–1759.

17 Horman, M. H., "An Application of Wavefront Reconstruction to Interferometry," *Applied Optics*, Vol. 4, No. 3, Mar. 1965, pp. 333–336.

S. E. HAALAND

E. M. SPARROW
Mem. ASME

Fluid Mechanics Program,
University of Minnesota,
Minneapolis, Minn.

Stability of Buoyant Boundary Layers and Plumes, Taking Account of Nonparallelism of the Basic Flows

Consideration is given to the linear stability of buoyant boundary layers and plumes which belong to the class of flows for which (a) the streamwise velocity vanishes in the free stream and (b) the transverse velocity is inward-directed and has a finite value in the free stream. Disturbance equations for such flows are derived taking account of the fact that the basic flows depend upon the streamwise coordinate. The formulation is specialized to the case of the natural convection plume generated by a horizontal line source of heat. The existence of the so-called bottling effect is demonstrated, wherein the disturbance vorticity and temperature are contained within the boundary layer of the flow. The neutral stability curve exhibits both a minimum Grashof number and a lower branch, in contrast to the neutral curve for the conventional stability analysis, which does not exhibit these features. Consideration is given to the amplification of disturbances and to the frequencies which are the most amplified. Results are also presented for the limiting case of inviscid instability.

Introduction

Linear stability analysis for flows of the boundary-layer type is usually based on the Orr Sommerfeld (O-S) equation which is strictly valid for parallel flows. The fact that the basic flows depend upon the streamwise x coordinate is presumably accounted for by nondimensionalizing the disturbance equation by local values of a characteristic velocity and the boundary-layer thickness.

Pretsch [1][1] derived a more complete disturbance equation that, in addition to the terms found in the O-S equation, contained terms that take into account the x-dependence of the basic flow and that allow the disturbance amplitude to vary with x. Pretsch studied the class of flows in which the streamwise velocity has a given finite value in the free stream. By use of asymptotic analysis for large values of the wave number–Reynolds number product, he was able to show that for such flows the extra terms in the disturbance equation have a small effect on the stability characteristics and can, therefore, be neglected.

Recently, Haaland [2] investigated the linear stability of the class of flows in which (a) the streamwise velocity vanishes in the free stream and (b) the transverse velocity is inward-directed and has a finite value in the free stream. Such flows will hereafter be designated as class A flows. He showed that the usual approximation implied by the parallel-flow assumption, i.e., the neglect of the transverse convection of disturbance vorticity compared with the streamwise convection, is a nonuniform approximation for class A flows. It was also demonstrated that this transverse velocity term gives rise to the so-called bottling effect. That is, inclusion of this term results in the containment of the disturbance vorticity and temperature within the boundary layer. This means that class A stability problems which were previously defined on an unbounded domain can now be defined on a bounded domain. Moreover, for this class of flows, the wave number–Reynolds number product usually becomes so small that all the terms arising from the x-dependence of the basic flow have to be retained. By including these terms, while retaining the assumption of disturbances in the form of local plane waves, modified O-S equations (including temperature disturbances) were obtained. The modified O-S equations were solved for several flows, i.e., the similarity jet, the shear layer, and natural convection on inclined plates. In all cases it was found that the retention of the terms associated with the x-dependence of the basic flow had a strong effect on the neutral stability curve. See also Haaland [3] for further discussion of the stability analysis of class A flows.

In the present investigation, modified disturbance equations (including terms taking account of the x-dependence of the basic flow) will first be derived for buoyant boundary layers and plumes. These will then be specialized to the natural convection plume generated by a horizontal line source of heat, which belongs to class A flows. Since this flow is very unstable, it is a good example of

---

[1] Numbers in brackets designate References at end of paper.

Contributed by the Heat Transfer Division for publication (without presentation) in the Journal of Heat Transfer. Manuscript received by the Heat Transfer Division September 6, 1972. Paper No. 73-HT-G.

a case where the x-dependence of the basic flow is expected to have a large influence on the stability characteristics. For example, the neutral stability curve of Pera and Gebhart [4], based on the conventional linear stability model, does not exhibit a minimum Grashof number or a lower branch. On the other hand, the neutral curve corresponding to the more complete formulation displays both a minimum Grashof number and a lower branch.

The aforementioned bottling effect will be demonstrated for the plume. Among the numerical results, we will be concerned not only with neutral stability but also with amplification of disturbances and with those frequencies which are most greatly amplified. A computation is made of the degree of amplification experienced by a disturbance as it moves downstream. The numerical results to be presented here are primarily for a Prandtl number of 0.7, that is, for gases. The neutral curve for a Prandtl number of 6.7 (liquid water) has also been evaluated for purposes of comparison.

For very large Reynolds (or Grashof) numbers, the viscous terms in the disturbance equations become negligible. For the inviscid model, the disturbance equations for the velocity and temperature fields uncouple, and the terms resulting from the x-dependence of the basic flow drop out. Stability results for the inviscid case will be obtained and presented.

The only prior investigation of the linear stability of a plume that is known to the authors is that of Pera and Gebhart [4]. Further reference to their work will be made during the course of this paper.

Stability Analysis for Buoyant Boundary Layers

In this section, the disturbance equations for buoyant boundary-layer flows in general will be formulated, with account being taken of the terms which arise from the x-dependence of the basic flow. The formulation follows that of Haaland [2]. Let us consider flows for which the Boussinesq equations are valid (Landau and Lifshitz [5])

$$\frac{\partial \mathbf{V}}{\partial t} + \mathbf{V}\cdot\nabla\mathbf{V} = -\frac{1}{\rho}\nabla p - \mathbf{g}\beta_T(T - T_\infty) + \nu\nabla^2\mathbf{V}, \quad (1)$$

$$\nabla\cdot\mathbf{V} = 0, \quad (2)$$

$$\frac{\partial T}{\partial t} + \mathbf{V}\cdot\nabla T = a\nabla^2 T, \quad (3)$$

in which $\mathbf{V}$ is the velocity vector, p the reduced pressure (static pressure minus hydrostatic pressure), T the temperature, T_∞ the ambient fluid temperature (a constant), and $\mathbf{g}$ the gravity vector. The thermophysical properties, density ρ, thermal expansion coefficient β_T, kinematic viscosity ν, and thermal diffusivity a, are taken to be constants.

By taking the curl of (1), denoting the vorticity by $\mathbf{\Omega} = \nabla \times \mathbf{V}$, and using the continuity equation (2), one obtains the vorticity equation

$$\frac{\partial \mathbf{\Omega}}{\partial t} + \mathbf{V}\cdot\nabla\mathbf{\Omega} - \mathbf{\Omega}\cdot\nabla\mathbf{V} = \beta_T\mathbf{g} \times \nabla T + \nu\nabla^2\mathbf{\Omega}. \quad (4)$$

In the case of two-dimensional flows (x = streamwise coordinate, y = transverse coordinate), $\mathbf{V} = (\hat{U}, \hat{V}, 0)$, $\mathbf{\Omega} = (0, 0, \hat{\Omega})$, $T = \hat{T}$, and $\mathbf{g} = (g_x, g_y, 0)$, and with these, equation (4) reduces to

$$\frac{\partial \hat{\Omega}}{\partial t} + \hat{U}\frac{\partial \hat{\Omega}}{\partial x} + \hat{V}\frac{\partial \hat{\Omega}}{\partial y} = \beta_T\left(g_x\frac{\partial \hat{T}}{\partial y} - g_y\frac{\partial \hat{T}}{\partial x}\right) + \nu\nabla^2\hat{\Omega}. \quad (5)$$

Next, let $(U, V, 0)$, $(0, 0, \Omega)$, and T denote the basic flow solution which depends on x and y. Correspondingly, $(u, v, 0)$, $(0, 0, \omega)$, and τ denote two-dimensional disturbances which depend on x, y, t. When the sum of the basic flow and the disturbances are introduced into equation (5), there follows, after neglecting nonlinear terms in the disturbance quantities and subtracting out the vorticity equation for the basic flow,

$$\frac{\partial \omega}{\partial t} + U\frac{\partial \omega}{\partial x} + V\frac{\partial \omega}{\partial y} + u\frac{\partial \Omega}{\partial x} + v\frac{\partial \Omega}{\partial y} = \beta_T\left(g_x\frac{\partial \tau}{\partial y} - g_y\frac{\partial \tau}{\partial x}\right) + \nu\nabla^2\omega. \quad (6)$$

Consistent with the boundary-layer model for the basic flow, $\Omega = -\partial U/\partial y$, so that, by using the continuity equation, $\partial\Omega/\partial x = \partial^2 V/\partial y^2$. In addition, the continuity equation for the disturbance velocities is satisfied by a stream function ψ defined by $u = \partial\psi/\partial y$, $v = -\partial\psi/\partial x$. With the foregoing, equation (6) becomes

$$\frac{\partial \omega}{\partial t} + U\frac{\partial \omega}{\partial x} + \frac{\partial^2 U}{\partial y^2}\frac{\partial \psi}{\partial x} + V\frac{\partial \omega}{\partial y} + \frac{\partial^2 V}{\partial y^2}\frac{\partial \psi}{\partial y} = \beta_T\left(g_x\frac{\partial \tau}{\partial y} - g_y\frac{\partial \tau}{\partial x}\right) + \nu\nabla^2\omega, \quad (7)$$

where

$$\omega = -\left(\frac{\partial^2\psi}{\partial x^2} + \frac{\partial^2\psi}{\partial y^2}\right). \quad (8)$$

Furthermore, by starting with the energy equation (3) and proceeding along similar lines, the governing equation for the disturbance temperature can be derived as

$$\frac{\partial \tau}{\partial t} + U\frac{\partial \tau}{\partial x} - \frac{\partial T}{\partial y}\frac{\partial \psi}{\partial x} + V\frac{\partial \tau}{\partial y} + \frac{\partial T}{\partial x}\frac{\partial \psi}{\partial y} = a\nabla^2\tau. \quad (9)$$

Equations (7), (8), and (9) comprise a sixth-order system for the variables ψ, ω, and τ. The vorticity ω can easily be eliminated from these equations, but this step will not be taken since ω has greater physical significance that do the higher order derivatives of ψ.

Attention will now be directed to the last two terms that appear respectively on the left-hand sides of equations (7) and (9). These terms are due to the x-dependence of the basic flow and are commonly omitted in linear stability analyses by invoking the parallel-flow assumption. As seen from the continuity equation, $V = -\int^y (\partial U/\partial x)dy$ + constant; thus, the presence of a non-zero transverse velocity is a consequence of the x-dependence of the streamwise velocity. The terms $V(\partial\omega/\partial y)$ in (7) and $V(\partial\tau/\partial y)$ in (9) are transverse convection terms of disturbance vorticity and temperature, respectively. The term $(\partial^2 V/\partial y^2)(\partial\psi/\partial y)$ can be traced back to $u(\partial\Omega/\partial x)$, so this term represents streamwise convection of basic flow vorticity. The term $(\partial T/\partial x)(\partial\psi/\partial y)$ is due to streamwise convection of the basic temperature field.

The disturbances are assumed to be locally of the plane-wave type, that is

$$\{\psi, \omega, \tau\} = \{\varphi(y), \omega(y), \tau(y)\}e^{i(\alpha x - \beta t)} \quad (10)$$

in which α is the wave number and β is the circular frequency. Equation (10) is then substituted into the disturbance equations (7)–(9), but before stating the outcome, dimensionless variables and parameters will be introduced. The scales for the nondimensionalization are motivated by an examination of the form of the solution for the basic flow.

For boundary-layer flows which admit similarity solutions, one can, in general, write

$$U = U^*(x)\tilde{U}(\eta), \qquad V = \frac{U^*(x)}{R(x)}\tilde{V}(\eta),$$
$$T = T_\infty + [T^*(x) - T_\infty]\tilde{T}(\eta), \quad (11)$$

with

$$\eta = y/h(x), \qquad \mathrm{R}(x) = U^*h/\nu. \quad (12)$$

In the foregoing, R can be identified as a local Reynolds number based on the characteristic velocity U^* and the characteristic length h (proportional to the boundary-layer thickness); T^* is a characteristic temperature and η is the similarity variable. In cases where a global similarity solution does not exist, that is, where U, V, and T depend on R, equations (11) can still be employed locally provided that local similarity prevails.

Other nondimensional parameters that are pertinent to the analysis are the dimensionless wave number $\tilde{\alpha}$, the Strouhal number S, and the Grashof number G based on the length h. These are

$$\tilde{\alpha} = \alpha h, \qquad \mathrm{S} = \beta h/U^*, \qquad \mathrm{G} = g\beta_T(T^* - T_\infty)h^3/\nu^2. \quad (13)$$

In addition, the dimensionless counterparts of the disturbance amplitude functions φ, ω, τ are defined as

$$\tilde{\varphi} = \varphi/(U^*h), \qquad \tilde{\omega} = \omega/(U^*/h), \qquad \tilde{\tau} = \tau/(T^* - T_\infty). \quad (14)$$

Then, upon introducing equations (10) into (7)–(9) and subsequently forming dimensionless variables and parameters by using U^* as the velocity scale, h as the length scale, and the definitions contained in (11)–(14), one obtains after dropping the tilde

$$\omega'' - \alpha^2\omega = i\mathrm{R}[(\alpha U - \mathrm{S})\omega + \alpha U''\varphi] + V\omega' + V''\varphi' - (\mathrm{G}/\mathrm{R})[(g_x/g)\tau' - i(g_y/g)\alpha\tau], \quad (15)$$

$$\varphi'' - \alpha^2\varphi = -\omega, \quad (16)$$

$$\tau'' - \alpha^2\tau = i\,\mathrm{Pr}\,\mathrm{R}[(\alpha U - \mathrm{S})\tau - \alpha T'\varphi] + \mathrm{Pr}\,[V\tau' + (a_1T + a_2\eta T')\varphi'], \quad (17)$$

in which $\mathrm{Pr} = \nu/a$ is the Prandtl number,

$$a_1 = \frac{\mathrm{R}h}{T^* - T_\infty}\frac{d(T^* - T_\infty)}{dx}, \qquad a_2 = -\mathrm{R}\frac{dh}{dx}, \quad (18)$$

and the primes represent derivatives with respect to η.

Equations (15)–(17) represent the disturbance equations (for local plane-wave disturbances) for boundary-layer flows involving buoyancy. These equations take account of the explicit x-dependence of the basic flow and, therefore, constitute a modification of the traditional formulation which leads to the Orr–Sommerfeld equation. Subsequently, these equations will be specialized to the plume.

It is appropriate at this point to comment on the choice of space or time amplification for the disturbances (see also Haaland [3]). From the standpoint of experiment, space amplification appears more appropriate for boundary-layer flows (see, for example, Betchov and Criminale [6]). Therefore, the circular frequency β and its dimensionless counterpart, the Strouhal number S, are taken to be real, whereas the wave number α is taken as complex. On the neutral curve, both S and α are real and no choice has to be made about the type of amplification.

Governing Equations for the Plane Plume

The general formulation developed in the preceding section of the paper will now be specialized to the plume generated by a horizontal line source of heat. The coordinates are selected so that the streamwise coordinate x is vertically upward and the transverse coordinate y is horizontal. The basic flow solution for the plume is outlined in the Appendix, so that $\tilde{U}$, $\tilde{V}$, $\tilde{T}$ and their derivatives as required in the disturbance equations (15)–(17) are available (the tilde has been dropped in (15)–(17)).

For the aforementioned orientation of the coordinates, $g_x/g = -1$ and $g_y/g = 0$. Furthermore, according to equation (A6), R = G. In addition, use of the relationships given in the Appendix reduces equation (18) to $a_1 = -12/5$, $a_2 = -8/5$. As a result of these findings, the disturbance equations (15)–(17) become

$$\omega'' - \alpha^2\omega = i\mathrm{R}[(\alpha U - \mathrm{S})\omega + \alpha U''\varphi] + \tau' + V\omega' + V''\varphi', \quad (19)$$

$$\varphi'' - \alpha^2\varphi = -\omega, \quad (20)$$

$$\tau'' - \alpha^2\tau = i\,\mathrm{Pr}\,\mathrm{R}[(\alpha U - \mathrm{S})\tau - \alpha T'\varphi] + \mathrm{Pr}\,V\tau' - \mathrm{Pr}\,[(12/5)T + (8/5)\eta T']\varphi'. \quad (21)$$

The Reynolds number R and Strouhal number S can be specialized to the plume by introducing U^* and h from the Appendix into the defining equations (12) and (13). In addition, the commonly employed Grashof number Gr (based on x) is related to R by equation (A7).

From an examination of equations (19)–(21), and noting that U, V, and T are, respectively, even, odd, and even functions of η, it is seen that solutions are possible in which (a) φ and ω are even and τ is odd, (b) φ and ω are odd and τ is even. Of these two solution modes, the more interesting is that which is least stable. This ought to be the mode with the least constraint on the dependent variables, that is, when φ and ω are even and τ is odd. Accordingly, the boundary conditions are taken as

$$\varphi'(0) = \omega'(0) = \tau(0) = 0, \qquad \varphi(\infty) = \varphi'(\infty) = \tau(\infty) = 0. \quad (22)$$

The system consisting of equations (19)–(22) is homogeneous, so that $\varphi \equiv \omega \equiv \tau \equiv 0$ is a possible solution. In order to obtain a non-trivial solution, it is necessary to impose a normalizing condition. Since this fixes only the scale of the solution, any choice will suffice, for example

$$\omega(0) = 1. \quad (23)$$

Equations (22) and (23) represent 14 real conditions on the twelfth-order real system (19)–(21). Therefore, two of the four real parameters α_r, α_i, R, and S have to be eigenvalues. Since in the subsequent presentation of results we shall be interested in curves parameterized by α_i, the solutions will be carried out for fixed values of α (i.e., α_r and α_i) taking R and S to be the eigenvalues.

It is appropriate to examine the inviscid limit of the disturbance equations (19)–(21). As R approaches infinity, these equations reduce to

$$\varphi'' = [\alpha^2 + \alpha U''/(\alpha U - \mathrm{S})]\varphi, \quad (24)$$

$$\omega = -\alpha U''\varphi/(\alpha U - \mathrm{S}), \quad (25)$$

$$\tau = \alpha T'\varphi/(\alpha U - \mathrm{S}). \quad (26)$$

The formerly coupled system is now decoupled, and in addition the terms related to the x-dependence of the basic flow have dropped out. Once φ has been determined from equation (24), ω and τ follow directly from (25) and (26), respectively. As before, the even solution for φ is expected to be the least stable, so that the boundary conditions are chosen as

$$\varphi'(0) = \varphi(\infty) = 0, \qquad \varphi(0) = 1, \quad (27)$$

where the last member of (27) is a normalizing condition. Equation (24) is a fourth-order real system, for which six real conditions are specified by equation (27). Therefore, two of the three real parameters α_r, α_i, and S have to be eigenvalues. For the solutions, fixed values will be assigned to S, and α_r, α_i will be the eigenvalues.

The solution method to be employed here uses an analytical solution for large η in conjunction with numerical integration for intermediate and small η. The large-η solutions will be developed in the next section, where they will also be applied in demonstrating the bottling effect.

The Large-η Solutions and the Bottling Effect

As a first step in obtaining the large-η solutions of equations (19)–(21), it is necessary to have expressions for U, V, T and their derivatives that are valid for large values of η. On the basis of equations (A4), (A14), and (A15), one can write $F = F_\infty + F_1$,

$H = H_1$, and

$$U = U_1 = F_1', \tag{28a}$$

$$V = V_\infty + V_1 = V_\infty + [(8/5)\eta F_1' - (12/5)F_1] \tag{28b}$$

$$T = T_1 = H_1, \tag{28c}$$

where F_1 and H_1 are the first terms of exponentially decreasing expansions which involve known constants which depend on the Prandtl number, and $V_\infty = -(12/5)F_\infty$.

Large-η solutions for φ, ω, and τ can now be sought in a series of decreasing functions (i.e., successive approximations)

$$\varphi = A_1 + A_2 + \ldots, \qquad \omega = B_1 + B_2 + \ldots, \qquad \tau = C_1 + C_2 + \ldots. \tag{29}$$

After substitution of (28) and (29) into (19)–(21), terms of like order are collected. To the first order, one gets

$$LA_1 = -B_1, \qquad MB_1 = C_1', \qquad NC_1 = 0, \tag{30}$$

and to the second order

$$LA_2 = -B_2, \tag{31a}$$

$$MB_2 = C_2' + i\alpha \mathrm{R} U_1'' A_1 + V_1'' A_1' + i\alpha \mathrm{R} U_1 B_1 + V_1 B_1' \tag{31b}$$

$$NC_2 = -i\alpha \mathrm{R}\,\mathrm{Pr}\,T_1' A_1 - \mathrm{Pr}\,[(12/5)T_1 + (8/5)\eta T_1']A_1' + i\alpha \mathrm{R}\,\mathrm{Pr}\,U_1 C_1 + \mathrm{Pr}\,V_1 C_1', \tag{31c}$$

where the operators are defined by

$$L = D^2 - \alpha^2, \qquad M = D^2 - V_\infty D - (\alpha^2 - i\,\mathrm{S}\,\mathrm{R}), \tag{32}$$

$$N = D^2 - \mathrm{Pr}\,V_\infty D - (\alpha^2 - i\,\mathrm{S}\,\mathrm{R}\,\mathrm{Pr}), \qquad D = \partial/\partial\eta, \tag{33}$$

There are three independent solutions of equations (30) and (31) that vanish at infinity. These are designated by subscripts 1, 2, and 3. For the first set of solutions

$$\begin{aligned} \varphi_1 &= e^{-\alpha\eta} + e^{-\alpha\eta}\mathrm{O}[\max\,(e^{-|V_\infty|\eta}, e^{-\mathrm{Pr}|V_\infty|\eta})], \\ \omega_1 &= (b_1 + b_2\eta)e^{-(\alpha+|V_\infty|)\eta} + (b_3 + b_4\eta)e^{-(\alpha+\mathrm{Pr}|V_\infty|)\eta}, \\ \tau_1 &= (b_5 + b_6\eta)e^{-(\alpha+\mathrm{Pr}|V_\infty|)\eta}, \end{aligned} \tag{34}$$

for the second set

$$\varphi_2 = \frac{-e^{-\gamma\eta}}{\gamma^2 - \alpha^2}, \qquad \omega_2 = e^{-\gamma\eta}, \qquad \tau_2 = \mathrm{O}[e^{-(\gamma+\mathrm{Pr}|V_\infty|)\eta}], \tag{35}$$

and for the third set

$$\begin{aligned} \varphi_3 &= \frac{[\lambda/(\lambda^2 - \alpha^2)]e^{-\lambda\eta}}{(\lambda|V\infty| - i\,\mathrm{S}\,\mathrm{R})(\mathrm{Pr} - 1)}, \\ \omega_3 &= \frac{-\lambda e^{-\lambda\eta}}{(\lambda|V_\infty| - i\,\mathrm{S}\,\mathrm{R})(\mathrm{Pr} - 1)}, \qquad \tau_3 = e^{-\lambda\eta}, \end{aligned} \tag{36}$$

in which

$$\gamma = |V_\infty|/2 + \sqrt{V_\infty^2/4 + \alpha^2 - i\,\mathrm{S}\,\mathrm{R}}, \tag{37}$$

$$\lambda = |V_\infty|\,\mathrm{Pr}/2 + \sqrt{V_\infty^2\,\mathrm{Pr}^2/4 + \alpha^2 - i\,\mathrm{S}\,\mathrm{R}\,\mathrm{Pr}}. \tag{38}$$

The second and third sets of solutions and the leading term of φ_1 come from equations (30), whereas the other terms of the first set come from equations (31). The foregoing solutions degenerate for Pr = 1, and special solutions are required for this case. The $b_1, \ldots, b_6$ of equations (34) are abbreviations for rather lengthy expressions which contain the D_i, $|V_\infty|$, Pr, α, R, and S. It can be shown that the A_{n+1}/A_n, B_{n+1}/B_n, C_{n+1}/C_n of equation (29) decrease exponentially as η approaches infinity.

Consideration may now be given to a comparison of the relative rates at which the disturbance flow and the basic flow decay at large η. For the velocity and temperature fields of the basic flow

$$\Omega \sim \max\,(e^{-|V_\infty|\eta}, e^{-\mathrm{Pr}|V_\infty|\eta}), \qquad T \sim e^{-\mathrm{Pr}|V_\infty|\eta}, \tag{39}$$

whereas the large-η solutions for the disturbance flow are given by equations (34), (35), and (36). With respect to the exponents appearing in these equations, it is relevant to note that the real part of $\lambda > \mathrm{Pr}\,|V_\infty|$ and the real part of $\gamma > |V_\infty|$, provided that the real part of α^2 is positive (Haaland [2]). The comparison of decay rates has to be made separately for Pr > 1 and Pr < 1.[2]

When Pr > 1, exp $(-|V_\infty|\eta) >$ exp $(-\mathrm{Pr}\,|V_\infty|\eta)$. Then, as $\eta \rightarrow \infty$

$$\frac{\omega}{\Omega} \sim \frac{\max\,(e^{-\gamma\eta}, e^{-\lambda\eta}, e^{-(\alpha+|V_\infty|)\eta})}{e^{-|V_\infty|\eta}} \rightarrow 0, \tag{40a}$$

$$\frac{\tau}{T} \sim \frac{\max\,(e^{-\lambda\eta}, e^{-(\alpha+\mathrm{Pr}|V_\infty|)\eta}, e^{-(\gamma+\mathrm{Pr}|V_\infty|)\eta})}{e^{-\mathrm{Pr}|V_\infty|\eta}} \rightarrow 0. \tag{40b}$$

Equations (40*a*) and (40*b*) indicate that the disturbance vorticity ω decays faster than the basic flow vorticity and that the disturbance temperature τ decays faster than the basic flow temperature. That is, the disturbances are "bottled in" or contained within the respective boundary layers of the basic flow. It is readily shown that it is the transverse velocity terms $V(\partial\omega/\partial y)$ and $V(\partial\tau/\partial y)$ which are responsible for the bottling effect. If these terms were omitted, the bottling effect would not be exhibited by the solution.

When Pr < 1, exp $(-\mathrm{Pr}\,|V_\infty|\eta) >$ exp $(-|V_\infty|\eta)$. By proceeding as above, one finds

$$\frac{\omega}{\Omega} \text{ or } \frac{\omega}{T} \rightarrow 0, \qquad \frac{\tau}{\Omega} \text{ or } \frac{\tau}{T} \rightarrow 0, \tag{41}$$

so that the disturbances are, once again, bottled in by the inward-directed transverse velocity.

Solution of the Eigenvalue Problem

As was noted earlier, the solution method involves the use of the large-η solutions for φ, ω, and τ in conjunction with numerical integration of equations (19)–(21) at small and intermediate values of η. The details of the solution method are described by Haaland [2, 3], and therefore only an outline will be presented here.

The large-η solutions furnish the starting values for the numerical integration of (19)–(21), which proceeds inward from some large value of η $(=\eta^*)$ toward the centerline of the plume $(\eta = 0)$. Examination of the large-η solutions, equations (34)–(36), indicates that for given values of Pr, α, R, and S, numerical values of φ, ω, and τ can be obtained at η^*. With $\varphi_1(\eta^*)$, $\omega_1(\eta^*)$, and $\tau_1(\eta^*)$ (and their derivatives) as starting values, equations (19)–(21) are numerically integrated inward to $\eta = 0$. Then the integration is repeated using $\varphi_2(\eta^*)$, $\omega_2(\eta^*)$, and $\tau_2(\eta^*)$ as the starting values. Next the integration is carried out once again starting with $\varphi_3(\eta^*)$, $\omega_3(\eta^*)$, and $\tau_3(\eta^*)$.

The three solutions that are generated in this way are summed up, with each solution being multiplied by a constant. These constants are determined by applying equation (23) and two of the three boundary conditions at $\eta = 0$ as stated in equation (22). The remaining boundary condition in (22) is satisfied only when R and S are eigenvalues. The initial guesses for R and S are refined iteratively by applying the Newton–Raphson method to the unsatisfied boundary condition. Variational equations with respect to R and S are found by differentiation of (19)–(21). The solution of the variational equations with appropriate boundary conditions provides the values for the coefficients in the equations for the increments ΔR and ΔS.

Results and Discussion

The numerical solutions for the plume were, in the main, carried out for a Prandtl number of 0.7. This is the Prandtl number

---

[2] The Pr = 1 case yields the same general conclusions as the other cases.

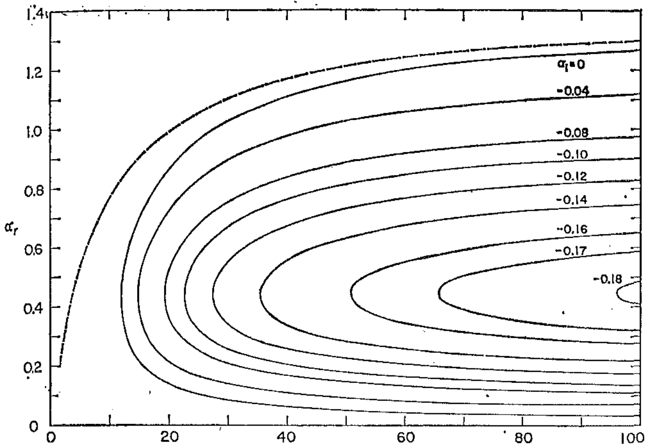

Fig. 1 Neutral stability and amplification contours; wave number–Reynolds number diagram (Pr = 0.7)

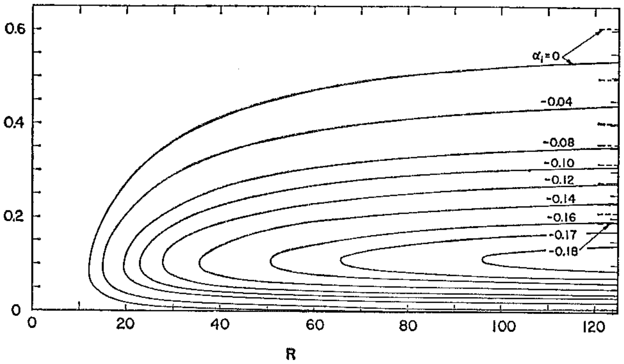

Fig. 2 Neutral stability and amplification contours; Strouhal number–Reynolds number diagram (Pr = 0.7)

of air and other gases. For comparison, some additional solutions were obtained for Pr = 6.7, which corresponds to liquid water. The primary presentation of results will be for Pr = 0.7, and the comparison of the results for the two Prandtl numbers will be made at the end.

The neutral stability curve and several amplification curves are presented in Fig. 1. In the figure, α_r, which is the real part of the wave number, is plotted against the Reynolds number R. The curves are parameterized by α_i, the imaginary part of the wave number, where $\alpha_i = 0$ corresponds to neutral stability and increasingly negative values of α_i correspond to greater amplification of the disturbance. In addition to the solid lines, which depict the present results, there is a dashed line which represents the neutral stability curve computed by Pera and Gebhart [4] on the basis of the conventional formulation in which terms due to the x-dependence of the basic flow are omitted. The abscissa variable R is related to the commonly encountered Grashof number Gr by

$$\mathrm{Gr} = g\beta_T(T^* - T_\infty)x^3/\nu^2 = \mathrm{R}^4/64, \tag{42}$$

where $T^* = T^*(x)$ is the temperature at the centerline of the plume.

Examination of the figure shows that the present neutral stability curve exhibits both upper and lower branches and a minimum (i.e., critical) Reynolds number R = 12 (Gr = 324).[3] On the other hand, the neutral stability curve from the analysis which omits the terms due to the x-dependent basic flow exhibits neither a minimum value nor a lower branch. Clearly, the accounting of the x-dependence of the basic flow has a profound effect on the neutral stability characteristics. Amplification curves are not presented by Pera and Gebhart, so that no appraisal can be made as to how the x-dependence affects the amplification characteristics.

Further examination of Fig. 1 indicates that the upper branches of all the curves tend to rise with increasing Reynolds number. The results of the inviscid solution, to be described later, show that for each α_i there is a limiting value of α_r as R approaches infinity. Therefore, if Fig. 1 were to be extended to larger Reynolds numbers, the upper branches of all the curves would tend to level off.

Although the α_r, R diagram is the most common vehicle for presentation of stability results, it has the drawback that α_r is not a readily measurable quantity. Furthermore, the α_r, R diagram gives no indication as to which disturbance frequencies are most strongly amplified. In recent papers, stability information has sometimes been presented using a dimensionless frequency which is equivalent to the Strouhal number defined by equation (13). The neutral curve and the amplification contours for the present problem are presented in an S, R diagram in Fig. 2. These curves are generally similar in shape to those of the just-discussed α_r, R diagram.

At the right-hand margin of Fig. 2 is an array of dash-line segments. These lines represent the R → ∞ limits for the upper branches of the S versus R curves and are obtained from the inviscid solutions. The α_i parameterization of the dash-line segments is in the same order as the parameterization of the S versus R curves. It is seen that at the largest R value of the figure, the upper branches are still substantially below their respective limits for R → ∞.

Although the Strouhal number contains the circular frequency β of the disturbances, it also contains the x-dependent quantities U^* and h. Consequently, the Strouhal number corresponding to a disturbance of fixed frequency β varies as the disturbance moves in the streamwise direction. It can easily be shown with the aid of equation (13) and of the Appendix that $\mathrm{S} \sim x^{1/6}$ or that $\mathrm{S} \sim \mathrm{R}^{1/3}$. Correspondingly, in Fig. 2, the path of a disturbance of fixed frequency moving in the streamwise direction would be a line $\mathrm{S} \sim \mathrm{R}^{1/3}$.

To facilitate a more informative examination of the role of frequency, it is advantageous to devise a presentation where the path of a disturbance of fixed frequency is more easily followed. To this end, we introduce a characteristic time t^* defined as

$$t^* = \nu\left(\frac{1}{g\beta_T}\,\frac{\rho c_p I}{Q}\right)^{2/3}, \tag{43}$$

where Q is the energy per unit time and unit length imparted to the fluid by the horizontal line source of heat. I is an integral defined by equation (A5), the value of which depends on the Prandtl number (e.g., for Pr = 0.7, I = 1.245). From equation (43) it is seen that t^* is a constant for a particular experiment. With the definition of t^*, it is readily shown that

$$\beta t^* = \mathrm{S}/\mathrm{R}^{1/3}. \tag{44}$$

This equation enables the S, R diagram to be rephrased as a diagram of βt^* versus R, the end result being shown in Fig. 3.

In this figure, the path of a disturbance of fixed frequency which moves in the streamwise direction is a horizontal line. The extent to which a disturbance is amplified can be gauged by examining the amplification curves that are cut by the horizontal line that corresponds to the frequency of the disturbance; the more negative the α_i, the greater is the amplification. On this basis, it is expected that the most amplified frequencies would lie in the range βt^* = 0.02 to 0.03.

The dashed lines shown in the figure correspond to frequencies f $(=\beta/2\pi)$ that pertain to the experimental conditions of Pera and Gebhart [4]. The experiments were performed in air at a heating rate Q of 58.6 Btu/hr-ft. These authors found that greatest amplification occurred at disturbance frequencies around 3 Hz, and as seen in Fig. 3, this is in excellent accord with the present

---

[3] At the low Grashof numbers in the neighborhood of the critical point, the basic flow boundary-layer model may be somewhat inaccurate.

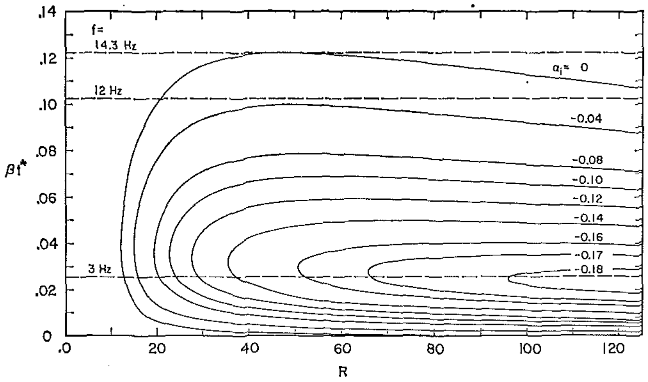

Fig. 3 Neutral stability and amplification contours; frequency–Reynolds number diagram (Pr = 0.7)

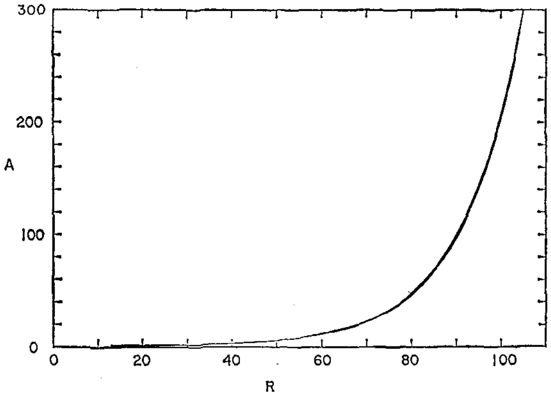

Fig. 4 Amplification of a disturbance of fixed frequency, $\beta t^* = 0.025$ (Pr = 0.7)

results. For frequencies greater than 12 Hz, Pera and Gebhart indicated that they were unable to detect amplified disturbances. Although Fig. 3 indicates that disturbances between 12 Hz and 14.3 Hz may be amplified, the extent of the amplification is so small that detection may not have been possible.

It is of interest to estimate the amplification experienced by a disturbance of fixed frequency as it moves in the streamwise direction. In view of the fact that the disturbance may encounter a range of α_i values, a logical generalization of the x-dependent factor in equation (10) is

$$\exp\left(i\int_{x_1}^{x}\alpha dx\right) = \exp\left(i\int_{x_1}^{x}\alpha_r dx\right)\exp\left(-\int_{x_1}^{x}\alpha_i dx\right) \tag{45}$$

where x_1 is the streamwise location at which amplification begins. The second exponential term on the right-hand side of equation (45) can be regarded as the x-dependent amplitude A of the disturbance (for example, Dring and Gebhart [7]; Jaffe, Okamura, and Smith [8]). In terms of the dimensionless variables relevant to the plume problem

$$A = \exp\left[-(5/12)\int_{R_1}^{R}\alpha_i d\mathrm{R}\right]. \tag{46}$$

The amplification factor A has been evaluated as a function of the Reynolds number R for the disturbance frequency $\beta t^* = 0.025$. As is seen in Fig. 3, this frequency lies in the band of most amplified frequencies. The variation of A with R ($\sim x^{3/5}$) is plotted in Fig. 4. The figure shows that the disturbance amplifies rather slowly at first, but then increases extremely rapidly. For example, at R = 100 (Gr = 1.6×10^6), the disturbance amplitude is about 300 times its initial amplitude.

The inviscid model represents the limit of the disturbance equations as R approaches infinity. Numerical results for the inviscid case were obtained by solving equation (24) for Pr = 0.7 and are shown in Fig. 5 as solid lines. The figure contains curves of α_r and α_i, respectively referred to the left- and right-hand ordinates, plotted as a function of the Strouhal number. The curve of α_i vs. S gives the R → ∞ limits of the α_i contours of Fig. 2, with the portion to the left of the maximum corresponding to the lower branches and the portion to the right of the maximum corresponding to the upper branches. The largest value of $-\alpha_i$ is about 0.2.

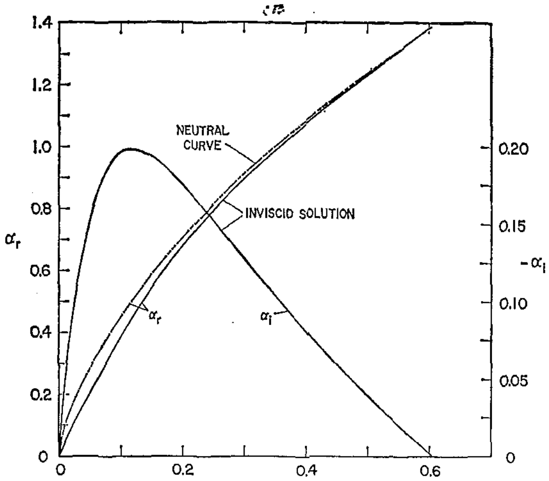

Fig. 5 Results from the inviscid model (Pr = 0.7)

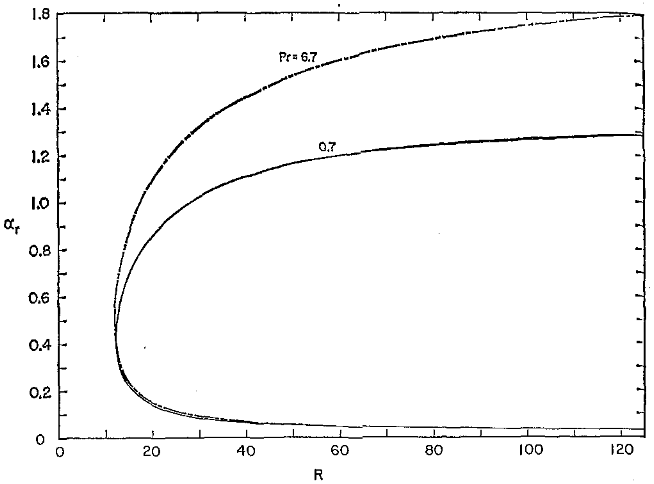

Fig. 6 Neutral stability curves for Pr = 0.7 and 6.7

In addition to the α_r results from the inviscid solution, Fig. 5 also contains the α_r versus S variation along the neutral curve. The two α_r curves are coincident at S = 0 and S = 0.605, where the lower and upper branches of the neutral stability curve approach R = ∞. However, the spread between the α_r curves is not large at most other S values, even though the local Reynolds number on the neutral curve may be small. From the α_r vs. S curve, one may evaluate the dimensionless wave speed $c = \mathrm{S}/\alpha_r$.

All of the results thus far presented have been for Pr = 0.7. In Fig. 6, a comparison is made of the neutral curves for Pr = 0.7 and Pr = 6.7. These Prandtl numbers correspond respectively to gases (in particular, air) and to liquid water. Both curves have the same general shape. In particular, each exhibits a minimum Reynolds number and a lower branch, thereby indicating that the findings of Fig. 1 are not confined to a specific Prandtl number. Although the upper branches of the two neutral curves are substantially different, the minimum Reynolds number and the lower branches are nearly coincident.

References

1 Pretsch, J., "Die Stabilität einer ebenen Laminarströmung bei Druckgefälle und Druckansteig," *Jahrb. deutscher Luftfahrtforschung*, Vol. 1, 1941, pp. 58–75.

2 Haaland, S. E., "Contributions to Linear Stability Theory of Nearly Parallel Flows," PhD thesis, Fluid Mechanics Program, University of Minnesota, Minneapolis, Minn., 1972.

3 Haaland, S. E., manuscript in preparation.

4 Pera, L., and Gebhart, B., "On the Stability of Laminar Plumes: Some Numerical Solutions and Experiments," *International Journal of Heat and Mass Transfer*, Vol. 14, 1971, pp. 975–984.

5 Landau, L. D., and Lifshitz, E. M., *Fluid Mechanics*, Pergamon, London, England, 1959.

6 Betchov, R., and Criminale, W. O., Jr., *Stability of Parallel Flows*, Academic, New York, N. Y., 1967.

7 Dring, R. P., and Gebhart, B., "A Theoretical Investigation of Disturbance Amplification in External Laminar Natural Convection," *Journal of Fluid Mechanics*, Vol. 34, 1968, pp. 551–564.

8 Jaffee, N. A., Okamura, T. T., and Smith, A. M. O., "Determination of Spatial Amplification Factors and Their Application to Predicting Transition," *AIAA Journal*, Vol. 8, 1970, pp. 301–308.

9 Gebhart, B., Pera, L., and Schorr, W., "Steady Laminar Natural Convection Plumes Above a Horizontal Line Heat Source," *International Journal of Heat and Mass Transfer*, Vol. 13, 1970, pp. 161–171.

APPENDIX

The Basic Flow Solution for the Plane Plume

The velocity and temperature fields for the plume can be expressed in the forms indicated in equations (11) and (12). In particular (for example, see Gebhart, Pera, and Schorr [9]),

$$U^*(x) = \left[\frac{4(g\beta_T)^2}{\nu}\left(\frac{Q}{\rho c_p I}\right)^2\right]^{1/5} x^{1/5}, \tag{A1}$$

$$T^*(x) - T_\infty = \left[\frac{1}{64\nu^2 g\beta_T}\left(\frac{Q}{\rho c_p I}\right)^4\right]^{1/5} x^{-3/5}, \tag{A2}$$

$$h(x) = \left[\frac{16\nu^3}{g\beta_T}\left(\frac{\rho c_p I}{Q}\right)\right]^{1/5} x^{2/5}, \tag{A3}$$

$$\tilde{U}(\eta) = F' \qquad \tilde{V}(\eta) = [(8/5)\eta F' - (12/5)F] \qquad \tilde{T}(\eta) = H \tag{A4}$$

in which F and H are functions of η. In the foregoing, Q is the energy per unit time and unit length imparted to the fluid by the horizontal line source and

$$I = 2\int_0^\infty F'H d\eta. \tag{A5}$$

The quantity $T^*(x)$ is the temperature at the centerline of the plume.

From an evaluation of the defining equations (12) and (13) for R and G using (A1)–(A3), it follows that

$$\mathrm{R} = \mathrm{G}. \tag{A6}$$

Furthermore, it is easily shown that the conventional Grashof number Gr is related to G and R by

$$2\sqrt{2}\,\mathrm{Gr}^{1/4} = \mathrm{R} = \mathrm{G}, \tag{A7}$$

where

$$\mathrm{Gr} = g\beta_T(T^* - T_\infty)x^3/\nu^2. \tag{A8}$$

The velocity and temperature functions F and H are obtained by solving the coupled system

$$F''' + (12/5)FF'' - (4/5)F'^2 + H = 0, \tag{A9}$$

$$H' + (12/5)\,\mathrm{Pr}\,FH = 0. \tag{A10}$$

subject to the boundary conditions

$$F(0) = F''(0) = 0, \qquad H(0) = 1, \qquad F'(\infty) = 0. \tag{A11}$$

The conditions $H'(0) = 0$ and $H(\infty) = 0$ are automatically satisfied by the solution. Once a solution of equations (A9) and (A10) is obtained, then the quantity I of equation (A5) can be evaluated.

For the numerical solutions, the condition $F' = 0$ at infinity is usually applied at a finite value of $\eta = \eta^*$. A more accurate condition which is equivalent to a first-order asymptotic solution of (A9) and (A10) can be derived as follows (Haaland [2]). From (A10), to first order

$$H = -H'/[(12/5)\,\mathrm{Pr}\,F_\infty]. \tag{A12}$$

Substitution of this into the first-order equivalent of (A9) gives

$$F''' + (12/5)F_\infty F'' - H'/[(12/5)\,\mathrm{Pr}\,F_\infty] = 0, \tag{A13}$$

which, after integration and substitution of the local value F instead of F_∞, becomes

$$F'' + (12/5)FF' - H/[(12/5)\,\mathrm{Pr}\,F] = 0. \tag{A13a}$$

This condition can be applied at a smaller value of η^* than the more inaccurate condition $F'(\eta^*) = 0$. Use of equation (A13*a*) permitted the use of the Newton–Raphson method (with full second-order convergence) in finding the missing starting value at $\eta = 0$.

Asymptotic solutions valid at large values of η can be developed as follows:

$$F(\eta) = F_\infty + D_1 \exp[-(12/5)F_\infty\eta] + D_2 \exp[-(12/5)\,\mathrm{Pr}\,F_\infty\eta], \tag{A14}$$

$$H = D_3 \exp[-(12/5)\,\mathrm{Pr}\,F_\infty\eta], \tag{A15}$$

where

$$D_3 = [(12/5)\,\mathrm{Pr}\,F_\infty]^3(1 - 1/\mathrm{Pr})D_2. \tag{A16}$$

The constants F_∞, D_1, D_2, and D_3 were evaluated by employing the numerical solutions of equations (A9) and (A10).

C. K. CHAN
Research Assistant.

C. L. TIEN
Professor.
Mem. ASME

Department of Mechanical Engineering,
University of California,
Berkeley, Calif.

Conductance of Packed Spheres in Vacuum

An analytical study is presented for the heat transfer through the solid phase of a packed bed of spheres bounded by two infinite plane surfaces of different temperatures. The prediction of the conductance is based on the constriction resistance for spheres in contact. Both exact and approximate equations are derived for solid, hollow, and coated spheres and for several regular packing patterns of different void fractions. Comparisons with the available experimental data indicate that the theory is satisfactory over a wide range of applied load and system parameters.

Introduction

THERMAL INSULATION has long been a subject of great importance in cryogenic applications [1, 2].[1] Evacuated multilayer insulation systems [3], though most effective thermally, have certain limitations in application. Besides the difficulty of installation around bodies of complex geometry and the highly anisotropic thermal behavior near penetrations, the thermal performance of such a system is extremely sensitive to compressive load. These factors result in a low predictability of the thermal performance of the multilayer insulation.

A new concept for high-performance insulation involves the use of packed hollow dielectric microspheres (20 to 200 μ in diameter) coated with low-emittance metallic films (about 400 Å thick). The space inside a microsphere is commonly filled with some residual gas at reduced pressures (microspheres supplied by 3M Co., Minneapolis, Minn., contain SO_2 at approximately 0.3 atm), but for all practical purposes it can be regarded as a vacuum. Packed spheres provide good mechanical strength to stand compressive loads as well as high constriction resistance against heat conduction. The use of hollow spheres reduces, in addition to weight, the system heat capacity, so that it consumes less cryogen and time in the cooldown process. The low-emittance coating shields against radiative transfer. Preliminary thermal tests [4] show that this new type of insulation is competitive thermally with multilayers; in addition, it is lightweight and easy to install and possesses many other advantages.

The major heat transfer mechanisms in packed spheres or powder insulation under the evacuated condition consist of the surface radiation transfer across the voids and the constricted conduction through the contact surface of packed particles. Extensive experimental results on heat transfer in powder insulations have been accumulated, and formulas for correlations and predictions have been proposed [1, 5–7]. These formulas are, however, mostly empirical in nature, due to complex geometry and radiation–conduction coupling. As part of a general fundamental research program on heat transfer through microsphere insulation, the present investigation is concerned with a theoretical analysis of conduction contributions. The specific objective is to establish an explicit functional relationship between the thermal conductance of packed spheres and fundamental system parameters such as the imposed thermal and load conditions, the geometric parameters (e.g., sphere diameter, shell thickness, packing configuration, etc.), and the thermal as well as mechanical properties of the constituent particles.

Analysis

Physical Model. Under the present considerations, heat can be conducted from one sphere to the other only through the contact interface. Thus from one sphere to another the conduction process is characterized by three series-connected thermal resistances, namely the macroscopic constriction resistance due to the contraction of conduction passages, the microscopic constriction resistance due to surface roughness at the contact area, and the film resistance due to surface contamination. In general, for spherical contact, the macroscopic constriction resistance is the predominant one, but the other two may become appreciable when the surface is rough and heavily oxidized. In the present analysis, only the macroscopic constriction resistance is considered.

Previous analysis [8] on macroscopic constriction resistance across spheres involves the replacement of the sphere by a conductor of infinite extent between two parallel planes with certain appropriate boundary conditions. The approximate analysis would not hold well for a hollow or coated sphere, especially when the thickness of the shell is of the same order of magnitude as the radius of the contact. A more fundamental analysis is presented here for the constriction resistance of spherical contacts involving three different types of spheres, namely solid, hollow, and composite (e.g., metal-coated).

Two basic assumptions are made in the present analysis. First, the radius of the circular contact area is given by the

---

[1] Numbers in brackets designate References at end of paper.

Contributed by the Heat Transfer Division of THE AMERICAN SOCIETY OF MECHANICAL ENGINEERS and presented at the ASME-AIChE Heat Transfer Conference, Atlanta, Ga., August 5–8, 1973. Manuscript received by the Heat Transfer Division September 21, 1972. Paper No. 73-HT-1

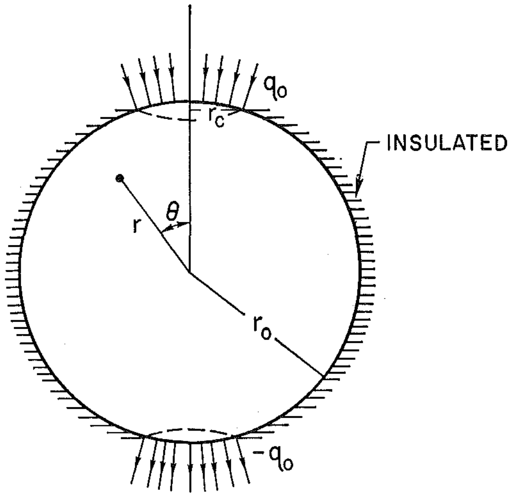

Fig. 1 Analytical model

Hertz relation for elastic contact of two smooth spheres of radius r_o pressed against each other under collinear force F:

$$r_c = \left[\frac{3}{4} \frac{1 - \mu^2}{E} F r_o \right]^{1/3} \tag{1}$$

where μ and E are Poisson's ratio and Young's modulus of the material, respectively. The relation is valid as long as the solids remain linearly elastic and $r_c \ll r_o$, r_o being the radius of the sphere. A similar analysis for hollow or coated spheres has not been developed, but for thick-walled spheres the above relation should be a good approximation. The second assumption is that the contact surface has a uniform heat flux and the rest of the surface is insulated. The reasons for assuming a uniform heat flux instead of a uniform temperature are: either condition represents only an idealization of the actual situation; the result for thermal-constriction resistance should be rather insensitive to either condition (more discussion on this later); and the uniform-heat-flux condition results in a much simpler analysis.

Constriction Resistance of a Single Sphere. The physical system under consideration is shown in Fig. 1. The temperature field inside the sphere must satisfy the steady-state heat conduction equation

$$\frac{\partial}{\partial r}\left(r^2 \frac{\partial T}{\partial r}\right) + \frac{1}{\sin\theta}\frac{\partial}{\partial \theta}\left(\sin\theta \frac{\partial T}{\partial \theta}\right) = 0 \tag{2}$$

as well as the boundary conditions at $r = r_o$

$$\begin{aligned} k_s \left(\frac{\partial T}{\partial r}\right)_{r_o} &= q_o \quad (0 \leq \theta \leq \theta_o) \\ &= 0 \qquad (\theta_o < \theta < \pi - \theta_o) \\ &= -q_o \quad (\pi - \theta_o \leq \theta \leq \pi) \end{aligned} \tag{3}$$

where $\theta_o = \sin^{-1}(r_c/r_o)$.

For hollow spheres, an additional boundary condition must be imposed at the inner surface ($r = r_i$). Since at cryogenic temperatures the radiant energy transfer within the inner space of the hollow sphere is much smaller than the conduction contribution, the inner surface can be regarded as adiabatic:

$$k_s \left(\frac{\partial T}{\partial r}\right)_{r_i} = 0 \qquad (\theta \text{ everywhere}) \tag{4}$$

For composite spheres, T_i (for $0 \leq r \leq r_i$) and T_o (for $r_i \leq r \leq r_o$) must satisfy

$$\frac{\partial}{\partial r}\left(r^2 \frac{\partial T_j}{\partial r}\right) + \frac{1}{\sin\theta}\frac{\partial}{\partial \theta}\left(\sin\theta \frac{\partial T_j}{\partial \theta}\right) = 0 \qquad (j = i, o) \tag{5}$$

$$\begin{aligned} k_{so} \left(\frac{\partial T_o}{\partial r}\right)_{r_o} &= q_o \qquad (0 \leq \theta \leq \theta_o) \\ &= 0 \qquad (\theta_o < \theta < \pi - \theta_o) \\ &= -q_o \quad (\pi - \theta_o \leq \theta \leq \pi) \end{aligned} \tag{6}$$

$$T_o = T_i \qquad (r = r_i, \theta \text{ everywhere}) \tag{7}$$

$$k_{so} \left(\frac{\partial T_o}{\partial r}\right)_{r_i} = k_{si} \left(\frac{\partial T_i}{\partial r}\right)_{r_i} \qquad (\theta \text{ everywhere}) \tag{8}$$

Nomenclature

A, A' = defined after equations (29) and (30), respectively
A_c = contact area
B_{2n-1}, B_{2n-1}' = defined after equations (27) and (28), respectively
C_o = arbitrary constant
C_1, C_2, C_3 = constants, equations (12), (13), and (14), respectively
D = sphere diameter
E = Young's modulus
F = contact force
F_v = vertical force
G, G' = defined after equations (32) and (33), respectively
k = conductance
k_s = solid conductivity
L = bed thickness
N_a = number of particles per unit area
N_t = number of particles per unit length
P = externally applied pressure
P_i = Legendre polynomial of degree i
q_o = heat flux
Q = total amount of heat through a sphere
r = radial coordinate
r_c = contact radius
r_i = inner radius
r_o = outer radius
R = constriction resistance
R' = modified constriction resistance
S_R, S_F, S_j, S_p, S_N = parameters, equations (20), (48), (49), (51), and (56), respectively
t = wall thickness
T = temperature
$\bar{T}$ = mean temperature
ΔT = temperature difference between the heat supply and removal regions
V_s = sphere volume
w = sphere weight
x = $\cos\theta$
x_o = $\cos\theta_o$
$\alpha_{2n-1}, \beta_{2n-1}$ = defined after equations (31) and (34), respectively
δ_s = solid fraction
θ = polar angle
θ_o = $\sin^{-1}(r_c/r_o)$
λ = k_{so}/k_{si}
μ = Poisson's ratio
ρ_s = mass density

Subscripts

$a, a'; b, b'; c, c'$ = pairs of heat supply and removal regions
i, ij = indices referring to the type of sphere and the packings; i = 1 for solid, 2 for hollow, and 3 for composite sphere; j = 1 for simple cubic, 2 for body-centered cubic, and 3 for face-centered cubic packing
i = inner
o = outer

By the method of separation of variables, solutions for the temperature in the solid, hollow, and composite spheres, respectively, are obtained as

$$T_1(r, \theta) = C_o + \sum_{n=1}^{\infty} C_1 r^n P_n(\cos \theta) \qquad (0 \leq r \leq r_o) \quad (9)$$

$$T_2(r, \theta) = C_o + \sum_{n=1}^{\infty} C_2 r^n \left[1 + \frac{n}{n+1}\left(\frac{r_i}{r}\right)^{2n+1}\right] P_n(\cos \theta) \qquad (r_i \leq r \leq r_o) \quad (10)$$

$$T_3(r, \theta) = C_o + \sum_{n=1}^{\infty} C_3 r^n \left[1 + \frac{n(\lambda - 1)}{n + \lambda(n+1)}\left(\frac{r_i}{r}\right)^{2n+1}\right] \times P_n(\cos \theta) \qquad (r_i \leq r \leq r_o) \quad (11)$$

where $\lambda = k_{so}/k_{si}$, P_i is the Legendre polynomial of degree i, C_o is an arbitrary constant, and C_1, C_2, and C_3 are constants determined by the outer boundary condition and the orthogonal properties of Legendre polynomials. These constants are zero when n is an even integer, but when n is odd, they are given as

$$C_1 = \frac{2n+1}{n}\left(\frac{q_o}{k_s r_o^{n-1}}\right)\int_{x_o}^{1} P_n(x)dx \quad (12)$$

$$C_2 = \frac{2n+1}{n}\left(\frac{q_o}{k_s r_o^{n-1}}\right)\left[\frac{1}{1 - (r_i/r_o)^{2n+1}}\right]\int_{x_o}^{1} P_n(x)dx \quad (13)$$

$$C_3 = \frac{2n+1}{n}\left(\frac{q_o}{k_{so} r_o^{n-1}}\right)\left[\frac{1}{1 - \dfrac{(\lambda-1)(n+1)}{n+\lambda(n+1)}\left(\dfrac{r_i}{r_o}\right)^{2n+1}}\right] \times \int_{x_o}^{1} P_n(x)dx \quad (14)$$

where $x_o = \cos \theta_o$. Equations (12)-(14) can be put into a more computable form when the following relation

$$\int_{x_o}^{1} P_n(x)dx = \frac{1}{2n+1}\left[P_{n-1}(x_o) - P_{n+1}(x_o)\right] \quad (15)$$

is used for the integral term.

By definition, the thermal resistance of the sphere is given by

$$R = (\bar{T}_a - \bar{T}_{a'})/Q \quad (16)$$

where $\bar{T}_a$ and $\bar{T}_{a'}$ are the respective mean temperatures of the two contact regions where heat is supplied and removed across the contact area A_c

$$\bar{T} = \int_{A_c} T(r_o, \theta)dA \Big/ \int_{A_c} dA \quad (17)$$

Q is the total amount of heat passing through the sphere, and for $r_c/r_o \ll 1$

$$Q \doteq q_o \pi r_c^2 \quad (18)$$

When the packing pattern of spheres is not simply cubic, there exist more than a pair of diametrically opposed contact regions. The calculation of mean temperatures is not simple, and a modified thermal resistance R' is introduced as

$$R' = [T(r_o, 0) - T(r_o, \pi)]/Q \quad (19)$$

The two thermal resistances can be related by a numerical factor S_R

$$R = S_R R' \quad (20)$$

where S_R depends on the contact radius and the wall thickness.

From the solutions given in equations (9), (10), and (11), closed-form expressions of R and R' can be established as in the following:

for solid spheres:

$$R_1 = A \sum_{n=1}^{\infty} B_{2n-1} \quad (21)$$

$$R_1' = A' \sum_{n=1}^{\infty} B_{2n-1}' \quad (22)$$

for hollow spheres:

$$R_2 = A \sum_{n=1}^{\infty} B_{2n-1}\alpha_{2n-1} \quad (23)$$

$$R_2' = A' \sum_{n=1}^{\infty} B_{2n-1}'\alpha_{2n-1} \quad (24)$$

for coated spheres:

$$R_3 = G \sum_{n=1}^{\infty} B_{2n-1}\beta_{2n-1} \quad (25)$$

$$R_3' = G' \sum_{n=1}^{\infty} B_{2n-1}'\beta_{2n-1} \quad (26)$$

where

$$B_{2n-1} = \frac{1}{(2n-1)(4n-1)}\left[P_{2n-2}(x_o) - P_{2n}(x_o)\right]^2 \quad (27)$$

$$B_{2n-1}' = \frac{1}{2n-1}\left[P_{2n-2}(x_o) - P_{2n}(x_o)\right] \quad (28)$$

$$A = \frac{2r_o}{\pi k_s r_c^2(1 - x_o)} \quad (29)$$

$$A' = \frac{2r_o}{\pi k_s r_c^2} \quad (30)$$

$$\alpha_{2n-1} = \frac{1 + [(2n-1)/2n](r_i/r_o)^{4n-1}}{1 - (r_i/r_o)^{4n-1}} \quad (31)$$

$$G = \frac{2r_o}{\pi k_{so} r_c^2(1 - x_o)} \quad (32)$$

$$G' = \frac{2r_o}{\pi k_{so} r_c^2} \quad (33)$$

$$\beta_{2n-1} = \frac{1 + [(\lambda-1)(2n-1)/(2n-1+2n\lambda)](r_i/r_o)^{4n-1}}{1 - [(\lambda-1)(2n)/(2n-1+2n\lambda)](r_i/r_o)^{4n-1}} \quad (34)$$

Conductance of Packed Spheres. The conductance of packed spheres depends on the packing pattern. For spheres of uniform size, the three basic regular arrangements are simple cubic, face-centered cubic, and body-centered cubic, Fig. 2. The void fraction of an actual bed (i.e., randomly packed spheres) is normally less than that of the simple cubic but greater than that of the other two close packing patterns. The regular packing patterns provide convenient physical models for analysis of the conduction transport in packed spheres. The analysis would illustrate the importance of various parameters in the actual bed, such as the porosity, the contact pattern, the applied load, and the physical properties of the sphere material. For a regular packing, each layer of the arrangement is isothermal normal to the direction of the heat flow, and each particle has an identical contact pattern with its neighboring particles, Fig. 2. Therefore the constriction resistance for each particle should be the same. The thermal resistance of a regular packed arrangement can thus be considered as a group of parallel resistances, each composed of a series of the resistances of a single particle. Hence the conductance of the medium is, by definition,

$$k_{ij} = \frac{N_a}{N_l}\frac{1}{R_{ij}} \quad (35)$$

where R_{ij} is the constriction resistance of a single particle. The

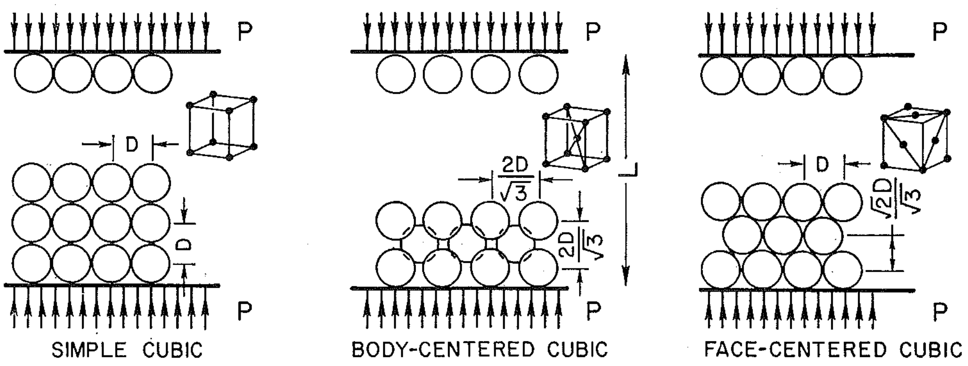

Fig. 2 Regularly packed spheres under compressive loads

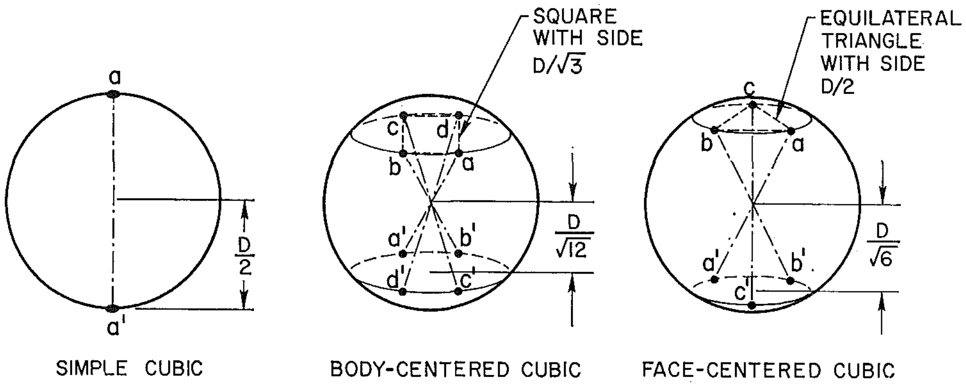

Fig. 3 Thermal-contact patterns of different regularly packed spheres

first subscript refers to the type of sphere ($i = 1$ for solid, $i = 2$ for hollow, and $i = 3$ for composite sphere), while the second subscript refers to the packing pattern ($j = 1$ for simple cubic, $j = 2$ for body-centered cubic, and $j = 3$ for face-centered cubic). N_l and N_a are the number of particles per unit length and per unit area, respectively.

Of all the physical contact points of a single particle, only those in contact with other particles of a layer above and below are of interest to the thermal analysis, because each layer of a regular arrangement is isothermal, Fig. 2. These thermal-contact regions can be grouped into pairs. Each pair is composed of a heat supply region on the upper hemisphere and a heat removal region on the lower hemisphere. These two regions are diametrically opposite to each other. For the simple cubic arrangement, there is only one pair of such contact areas. In this case R_{i1} is the same as R_i. In the case of face-centered cubic arrangement, by symmetry, the six thermal contact areas on a sphere can be grouped into three pairs: *a-a'*, *b-b'*, and *c-c'*, Fig. 3. The temperature difference and the heat flux will be the same for each pair. For simplification, R_{ij}' is to be determined. The temperature difference at each pair due to the total heat flux of all the pairs can be obtained from the result of a single pair by the method of superposition. For instance, in the case of a solid sphere, the temperature difference at *b-b'* and *c-c'* due to the heat flux at *a-a'* alone is the same and is equal to

$$(\Delta T)_{b\text{-}b'} = (\Delta T)_{c\text{-}c'} = 2 \sum_{n=1}^{\infty} C_1 r_o^n P_n(1/2) \tag{36}$$

The temperature difference at each pair due to the heat flux of all the pairs is

$$(\Delta T) = 2 \sum_{n=1}^{\infty} C_1 r_o^n [P_n(1) + 2P_n(1/2)] \tag{37}$$

Hence for solid spheres

$$R_{13}' = 1/3 A' \sum_{n=1}^{\infty} B_{2n-1}'[1 + 2P_{2n-1}(1/2)] \tag{38}$$

for hollow spheres

$$R_{23}' = 1/3 A' \sum_{n=1}^{\infty} B_{2n-1}'\alpha_{2n-1}[1 + 2P_{2n-1}(1/2)] \tag{39}$$

for coated spheres

$$R_{33}' = 1/3 G' \sum_{n=1}^{\infty} B_{2n-1}'\beta_{2n-1}[1 + 2P_{2n-1}(1/2)] \tag{40}$$

In the case of the body-centered cubic arrangement, there are four pairs of thermal contacts, Fig. 3. The corresponding equations for R_{i2}' for solid, hollow, and coated spheres are, respectively

$$R_{12}' = 1/4 A' \sum_{n=1}^{\infty} B_{2n-1}'[1 + P_{2n-1}(1/3)] \tag{41}$$

$$R_{22}' = 1/4 A' \sum_{n=1}^{\infty} B_{2n-1}'\alpha_{2n-1}[1 + P_{2n-1}(1/3)] \tag{42}$$

$$R_{32}' = 1/4 G' \sum_{n=1}^{\infty} B_{2n-1}'\beta_{2n-1}[1 + P_{2n-1}(1/3)] \tag{43}$$

Results and Discussion

For dielectric spheres with metal coating, the metal conductivity is three orders of magnitude higher than that of the dielectric. The expressions for R_3 and R_3' are reduced to those for hollow spheres. When the wall thickness t of a hollow sphere is small in comparison with its outer radius r_o, the two parameters r_c/r_o and t/r_o in equations (23) and (24) can be decoupled

$$R_2 = A\left(\frac{r_o}{t}\right)\sum_{n=1}^{\infty}\frac{B_{2n-1}}{2n} \tag{44}$$

$$R_2' = A'\left(\frac{r_o}{t}\right)\sum_{n=1}^{\infty}\frac{B_{2n-1}'}{2n} \tag{45}$$

Predicted values of the constriction resistance of a hollow sphere from equations (44) and (23) as well as the modified constriction resistance from equations (45) and (24) are shown in Figs. 4 and 5. The curve $t/r_o = 1$ corresponds to the case of a solid sphere. It should be noted that a thick-walled sphere ($t/r_o > 0.1$) has about the same resistance as a solid sphere. At reduced wall thickness, the resistance is inversely proportional to t, as indicated by equations (44) and (45). The result for $t/r_o = 1$ also reveals that the series $\left[(1 - x_o)^{-1}\sum_{n=1}^{\infty} B_{2n-1}\right]$ and $\sum_{n=1}^{\infty} B_{2n-1}'$ in equation (21) and (22) can be treated as a linear function of r_c/r_o, so the constriction resistance of a solid sphere can be expressed in the following explicit form:

$$R_1 = \frac{0.53}{k_s r_c} \qquad (r_c/r_o < 0.1) \tag{46}$$

$$R_1' = \frac{0.64}{k_s r_c} \qquad (r_c/r_o < 0.1) \tag{47}$$

If the constriction resistance of the sphere can be considered as twice the resistance of the circular contact area on a semi-infinite body [7, 8], then it is equal to $^1/_2 k_s r_c$ for an isothermal contact area and is equal to $0.54/k_s r_c$ when the heat flow on the area is constant. The resistances obtained with these two different boundary conditions for spherical particles differ by less than 20 percent, depending on the contact radius. However, for small r_c/r_o, as in most practical cases, the difference is much smaller [7]. The agreement between the present and the previous analysis is consistent with the assumption that the resistance of a solid sphere is insensitive to the precise details of the boundary conditions for small contact area.

For the special case of a thin-shell sphere, the heat flow can be considered to be one-dimensional, having two isothermal contact regions diametrically opposite to each other. It can easily be derived that in this case $R = (1/\pi t k_s) \ln [1/\tan (\theta_o/2)]$. A comparison between this simplified solution and the result of the two-dimensional constant-flux boundary analysis indicates that their difference is less than 5 percent for $(t/r_o) = 10^{-3}$ and r_c/r_o ranging from 10^{-3} to 10^{-2}. This agreement further confirms the validity of the constant-flux boundary assumption for hollow spheres.

It is of interest to see how the present analysis can predict the conductance of packed spheres from the fundamental system parameters. Two limiting cases of compressive forces are to be considered: (*a*) the system is under an externally applied load such that the contact force is independent of the force due to sphere weight and (*b*) the system is under no externally applied load so the contact force is mainly due to the sphere weight. For different packing patterns, the contact force F can be related to the vertical force F_v by a numerical factor S_F that expresses F_v in the direction of F. This vertical force can be the external load in case (*a*) or the weight of the spheres above the contact in case (*b*). Hence, for case (*a*)

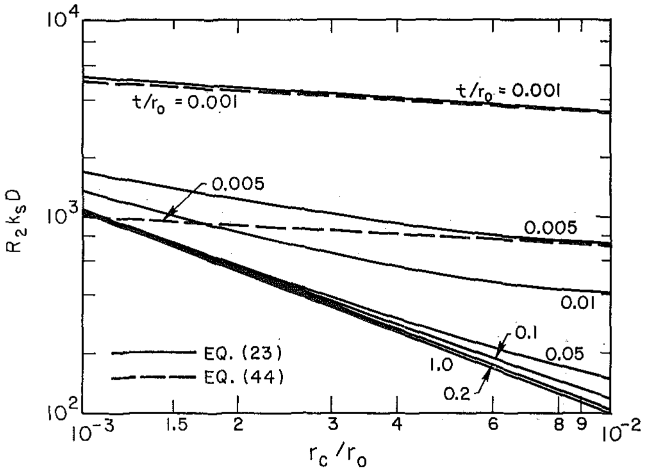

Fig. 4 Constriction resistance of a sphere

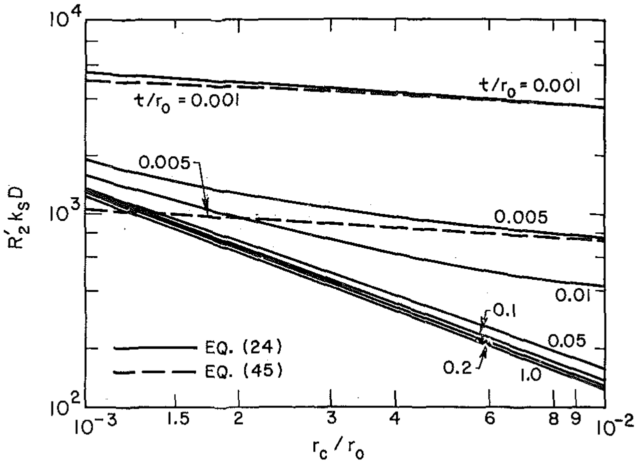

Fig. 5 Modified constriction resistance of a sphere

$$F = S_F \frac{P}{N_a} \tag{48}$$

To obtain an explicit form for the conductance of packed solid spheres, certain simplifications must be made for the constituent resistances R_{12}' and R_{13}'. Actual calculation of the resistance has shown that the second term $\left[2\sum_{n=1}^{\infty} B_{2n-1}'P_{2n-1}(^1/_2) \text{ or } \sum_{n=1}^{\infty} B_{2n-1}' P_{2n-1}(^1/_3)\right]$ in equation (38) or (41) is of the order of $(r_c/r_o)^2$, while the first term is of the order of r_c/r_o. Thus for small r_c/r_o,

$$R_{1j} = S_R S_j R_1' \tag{49}$$

where R_1' is given by equation (47). S_j is equal to 1, $^1/_4$, and $^1/_3$ for j equal to 1, 2, and 3, respectively. Values of S_R for solid and hollow sphere are presented in Table 1. From equation (35), there follows

$$k_{1j} = S_p k_s \left(\frac{1 - \mu^2}{E} P\right)^{1/3} \tag{50}$$

where S_p is a constant depending on the packing pattern only

$$S_p = \frac{1.56}{S_R S_j} (N_a/N_t)(0.75 S_F r_o/N_a)^{1/3} \tag{51}$$

Values of N_a, N_t, the solid fraction δ_S, S_j, S_F, S_p, and S_N (de-

Table 1 Values of S_R for hollow and solid spheres

t/r_0 r_c/r_0	0.001	0.005	0.01	0.05	0.1	0.2	1
0.001	0.9384	0.8726	0.8479	0.8230	0.8201	0.8191	0.8252
0.002	0.9549	0.8955	0.8569	0.8071	0.8030	0.7984	0.8193
0.004	0.9582	0.9263	0.8831	0.8171	0.8489	0.8447	0.8207
0.006	0.9569	0.9380	0.9081	0.8664	0.8532	0.8236	0.8334
0.008	0.9554	0.9431	0.9192	0.8732	0.8339	0.8395	0.8280
0.01	0.9538	0.9453	0.9256	0.8588	0.8372	0.8415	0.8331

Table 2 Basic parameters for different packing patterns

	Simple cubic	Body-centered cubic	Face-centered cubic
N_t	$\frac{1}{2r_o}$	$\frac{\sqrt{3}}{2r_o}$	$\frac{\sqrt{3}}{2\sqrt{2}r_o}$
N_a	$\frac{1}{4r_o^2}$	$\frac{3}{16r_o^2}$	$\frac{1}{2\sqrt{3}r_o^2}$
δ_s	0.524	0.680	0.74
S_j	1	$^1/_4$	$^1/_3$
S_F	1	$\frac{\sqrt{3}}{4}$	$\frac{1}{\sqrt{6}}$
S_p	1.36	1.96	2.72
S_N	0.452	0.713	1.02

fined later) for the three regular packing patterns are presented in Table 2.

Closed-form expressions such as equation (50) for hollow spheres are not available. However, the conductance can easily be obtained by realizing that it is related to the constriction resistance and thus to the contact radius r_c, which is expressed in terms of P and other system parameters, Fig. 6.

Sample calculations are carried out for aluminized and uncoated borosilicate glass spheres. Poisson's ratio and Young's modulus for glass are 0.22 and 5.51×10^{10} N/m², respectively. The thermal conductivity for aluminum at 200 deg K is 2.37 w/cm-deg K and the corresponding value for glass is 9.51×10^{-3} w/cm-deg K. The large difference between the two conductivities suggests that a composite sphere, for example an aluminum-coated (500-Å film) glass sphere of 100 μ dia can be treated as a hollow aluminum sphere with $t/r_o = 0.001$. The predicted values of the conductance of three different packed spheres under compressive load, as well as the experimental data of Cunnington and Tien [4] for a 50 percent (by weight) mixture of 44- to 135-μ aluminized spheres and uncoated spheres, are shown in Fig. 7. The conductance of the mixture is expected to be between the predicted values of the aluminized and the uncoated spheres. In view of the variations in sizes and the uncertainties of the porosity and the wall thickness of the spheres in the test, the predictions of the present analysis did correlate well with the experimental data.

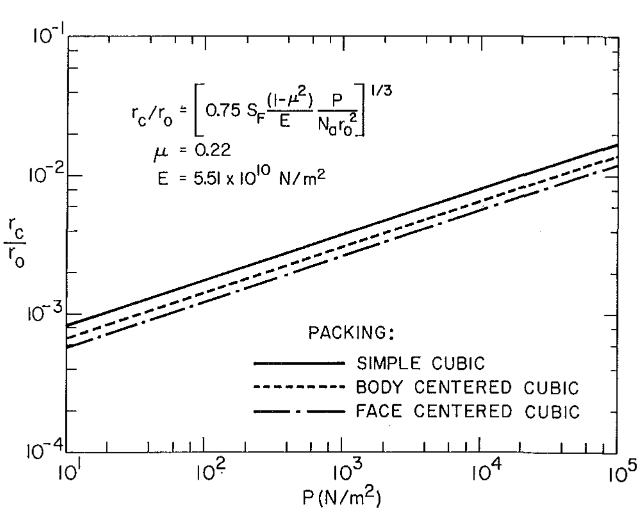

Fig. 6 Contact radius of borosilicate spheres under compressive loads

For the case of zero external load, the force on each contact is equal to the weight of the spheres above it. The contact resistance decreases with increasing depth from the uppermost surface. If the weight of each sphere is w, the series resistance of a bed of thickness L is

$$R_{\text{series}} = \frac{1.06 S_j}{k_s D} \left(\frac{4 r_o^2 E}{3(1-\mu^2) S_F w}\right)^{1/3} \sum_{n=1}^{LN_t} n^{-1/3} \tag{52}$$

The summation term can effectively be approximated by an integral, especially where LN_t is large. Considering N_a resistance in parallel, the conductance of the bed is

$$k_{ij} = S_N \left(\frac{(1-\mu^2)\rho_s V_s L}{E r_o^3}\right)^{1/3} k_s \tag{53}$$

where

$$S_N = 1.143 \left(\frac{S_F^{1/3}}{S_j}\right)\left(\frac{N_a}{N_t^{2/3}}\right) r_o^{4/3} \tag{54}$$

Although equation (53) has been derived assuming solid spheres, it can be applied for thick-walled spheres. The conductance for thin-walled spheres can also be predicted by following similar procedures as used in the case of compressive loading. The conductance of thick-walled borosilicate glass spheres predicted from equation (53) is shown in Fig. 8. An order-of-magnitude com-

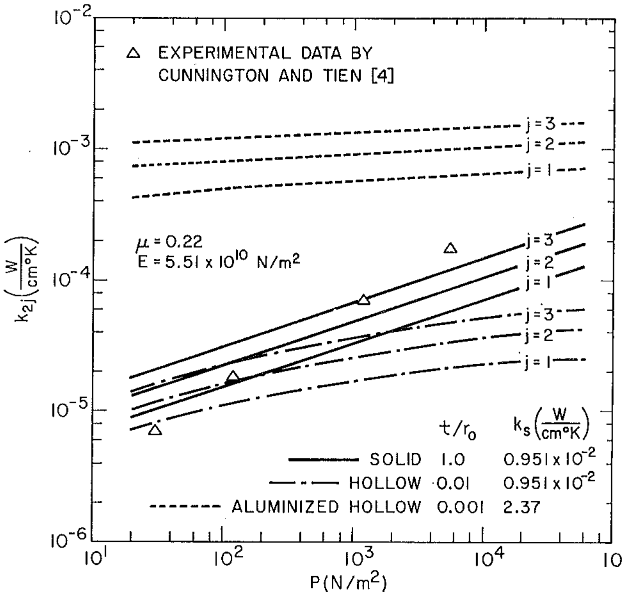

Fig. 7 Conductance of aluminized and uncoated glass spheres under compressive loads

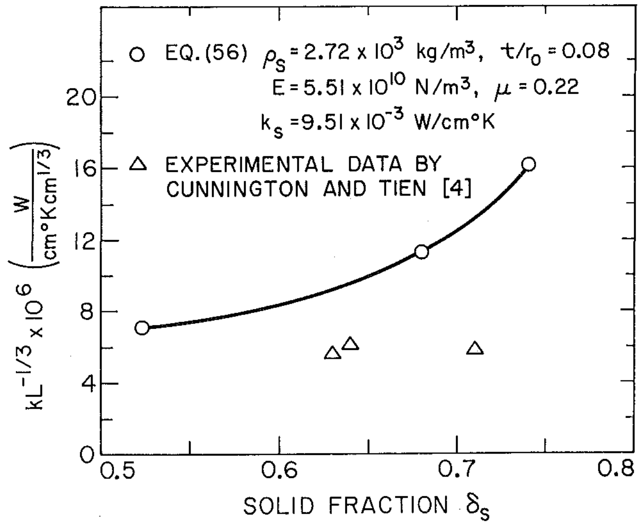

Fig. 8 Conductance of packed spheres under no external load

parison between the predicted values and the experimental data of aluminized spheres further establishes the reliability of the analysis.

Concluding Remarks

A method has been proposed to predict the conductance of different spheres in terms of the fundamental system parameters. It has been shown that the present proposal agrees well with available experimental data for the two extreme loading conditions. Two important points should be noted: first, the conductance in both loading cases depends on the thickness ratio t/r_o, but not on the sphere diameter; secondly, it is directly proportional to the conductivity of the material. Finally, it should be pointed out that the conductance derived in this paper will be a fundamental parameter for a complete analysis of heat transfer through evacuated microsphere insulation when both conduction and radiation are important.

References

1 Kaganer, M. G., *Thermal Insulation in Cryogenic Engineering*, Israel Program for Scientific Translations, Jerusalem, 1969.

2 Tien, C. L., and Cunnington, G. R., "Cryogenic Insulation Heat Transfer," in: *Advances in Heat Transfer*, Vol. 9, 1973, pp. 349–417.

3 Caren, R. P., and Cunnington, G. R., "Heat Transfer in Multilayer Insulation Systems," *Chem. Eng. Prog. Symp. Series*, Vol. 64, No. 87, 1968, pp. 67–81.

4 Cunnington, G. R., and Tien, C. L., "Heat Transfer in Microsphere Cryogenic Insulation," Paper No. C-1, Cryogenic Engineering Conference, Boulder, Colo., Aug. 1972.

5 Fulk, M. M., "Evacuated Powder Insulation for Low Temperatures," in: *Progress in Cryogenics*, Vol. 1, 1959, pp. 65–84.

6 Chen, J. C., and Churchill, S. W., "Radiant Heat Transfer in Packed Beds," *AIChE Journal*, Vol. 9, No. 1, 1963, pp. 35–41.

7 Luikov, A. V., Shashkov, A. G., Vasiliev, L. L., and Fraiman, Yu. E., "Thermal Conductivity of Porous Systems," *International Journal of Heat and Mass Transfer*, Vol. 11, 1968, pp. 117–140.

8 Yovanovich, M. M., "Thermal Contact Resistance Across Elastically Deformed Spheres," *Journal of Spacecraft and Rockets*, Vol. 4, No. 1, 1967, pp. 119–122.

G. HORVAY
Professor.
Fellow ASME

R. MANI[1]
Associate Professor.

M. A. VELUSWAMI
Graduate Research Assistant.

G. E. ZINSMEISTER
Associate Professor.
Mem. ASME

Department of Mechanical
and Aerospace Engineering,
University of Massachusetts,
Amherst, Mass.

Transient Heat Conduction in Laminated Composites

The layers are stacked parallel to the x axis. On the half-space $x \geqslant 0$ there is applied, at $x = 0$, a boundary temperature of y-periodicity conforming to the periodicity of the layered composite. The response is determined in the form of a normal mode expansion. A complex eigenvalue problem must be solved first, then the Fourier coefficients are determined from a biorthogonal expansion formula. The series converges to both the real and the imaginary parts of the prescribed input simultaneously. It is found that at low frequencies and not too small distances the static equivalent thermal constants k_{av}, $(\rho c)_{\text{av}}$ are applicable also in the non-static problem. This ceases to be true at high frequencies.

1 Introduction

A RIGOROUS SOLUTION to the problem of determining the temperature distribution in a composite (laminated) material subject to harmonic boundary excitation, where matrix and filler are stacked perpendicularly to the heat flow direction, Fig. 1(*a*), has long been available in the literature, see, e.g., [1, 2].[2] The solution has the advantage of enabling one to establish equivalent thermal properties in terms of which the problem of the laminated slab may be solved (in the case of reasonable boundaries[3]), as for a slab of homogeneous material of properties

$$k_{\text{av}} = \left[\frac{f}{k_F} + \frac{1-f}{k_M}\right]^{-1} \qquad (\rho c)_{\text{av}} = f(\rho c)_F + (1-f)(\rho c)_M$$

$$\varkappa_{\text{av}} = k_{\text{av}}/(\rho c)_{\text{av}} \qquad (1a)$$

Here k, (ρc), and $\varkappa$ denote conductivity, heat capacity, and diffusivity; $f/(1-f)$ represents the volumetric ratio of the F (filler) material to the M (matrix) material. The dual problem, Fig. 1(*b*), where the layers are lined up parallel to the heat propagation direction, does not seem to have been similarly considered. In the present paper we plan to make up for the deficiency. We determine the *thermal mode structure* of the temperature diffusion problem where the boundary temperature excitation is harmonic, of frequency ω (Dirichlet's problem). We again establish equivalent thermal parameters. In fact, we shall demonstrate that the appropriate low-frequency formulas are the familiar static ($\omega = 0$) formulas[4] (when higher mode shapes don't dominate the boundary temperature distribution[5]

$$k_{\text{av}} = fk_F + (1-f)k_M \qquad (\rho c)_{\text{av}} = f(\rho c)_F + (1-f)(\rho c)_M$$

$$\varkappa_{\text{av}} = k_{\text{av}}/(\rho c)_{\text{av}} \qquad (1b)$$

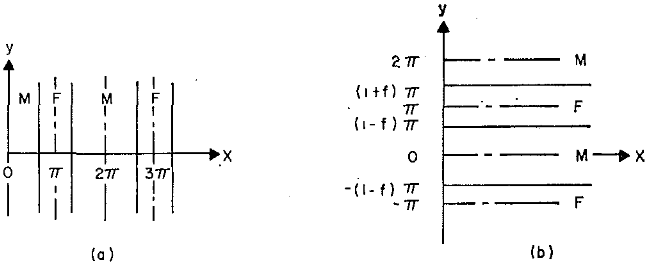

Fig. 1 Laminated material stacked (*a*) perpendicularly and (*b*) parallel to the direction of heat flow

In Fig. 1 and in the sequel we use, for convenience, a length scale whereby the stacking distance is assigned the value 2π. The problem presented by Fig. 1(*b*) is inherently more difficult than that presented by Fig. 1(*a*) (where invariably it is assumed that the boundary excitation has no y-variation). Fig. 1(*a*) represents a one-dimensional problem, whereas Fig. 1(*b*) represents a truly two-dimensional problem.

Referring to Fig. 1(*b*), we seek the solution

$$T = \begin{cases} T_M & 0 \leqslant y \leqslant (1-f)\pi \qquad (2a) \\ T_F & (1-f)\pi \leqslant y \leqslant \pi \qquad (2b) \end{cases}$$

---

[1] Presently with the Corporate Research and Development Center, General Electric Co., Schenectady, N. Y.

[2] Numbers in brackets designate References at end of paper.

[3] An unreasonable boundary would be one, for example, that encompasses a long narrow strip containing two layers of F and one layer of M material.

Contributed by the Heat Transfer Division for publication (without presentation) in the JOURNAL OF HEAT TRANSFER. Manuscript received by the Heat Transfer Division March 8, 1972. Paper No. 73-HT-R.

[4] The question of the range of validity of equivalent constants is raised with respect to elastic wave propagation in a layered medium, as in Fig. 1(*b*), in [3].

[5] When higher modes dominate, then the additional restriction to large distances must also be made.

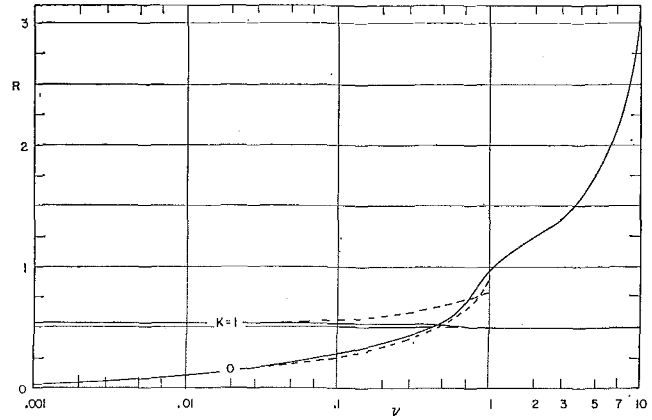

Fig. 2(a) Moduli R and phase angles θ of the roots z_0, z_1 of the eigenvalue equation (11) for $f = 1/3$, $a = 1/2$, $b = 5$; dashed lines: by power-series expansion to ν^1 terms (linear approximation); full lines: by numerical solution of eigenvalue equation; curves go with scale on left side unless otherwise indicated

$$T_M(x, y, t) = e^{-i\omega t}w_M(x, y) \qquad T_F(x, y, t) = e^{-i\omega t}w_F(x, y) \tag{2c}$$

of the temperature problem

$$y = 0, \pi: \quad \partial T/\partial y = 0 \tag{3a, b}$$

$$y = (1 - f)\pi: \quad T_M = T_F \qquad k_M \partial T_M/\partial y = k_F \partial T_F/\partial y \tag{3c, d}$$

$$x = \infty: \quad T = 0 \qquad x = 0: \quad T = e^{-i\omega t}\chi(y) \tag{3e, f}$$

(we assume that temperature boundary conditions are prescribed at $x = 0$; $\chi(y)$ represents the y-distribution of this boundary temperature), governed by the equation

$$\left(\nabla^2 - \frac{1}{\varkappa_j}\frac{\partial}{\partial t}\right) T = 0 \qquad j = M, F \tag{4}$$

or, equivalently, by

$$(\nabla^2 + ip_j)w_j = 0 \qquad p_j = \omega/\varkappa_j \tag{5a, b}$$

since we restrict ourselves to harmonic excitation.

In Section 2 we set up the complex eigenvalue equation (11). In Section 3 we establish the biorthogonal expansion formula (20). In Section 4 we relate our results for the zero-frequency case to the solution of Concus [4, 5]. In Section 5 we outline the solution of the eigenvalue equation (29) by Newton's iteration method in a form immediately adaptable to a digital computer.

In Sections 6 and 7 we establish a normal mode solution of the temperature distribution in the composite, expanded in powers of the frequency, and verify that on retaining only up to first-power terms in ω we may indeed use the static equivalent constants (1b) to describe the temperature behavior of the composite. But for higher frequencies this equivalence is no longer admissible.

In Section 8 we give some numerical examples and results. In Section 9 we summarize the mathematical highlights of the analysis and also comment on some practical uses that can be made of the results.

2 Complex Eigenvalue Equation

We seek solution of (5) in the form of product functions[6]

$$w_{Mk} = e^{-\lambda_k x}\varphi_k(y) \qquad w_{Fk} = e^{-\lambda_k x}\psi_k(y) \qquad \lambda = \lambda_r + i\lambda_i \tag{6a, b, c}$$

Placing (6) into (5) gives (prime denotes y-differentiation)

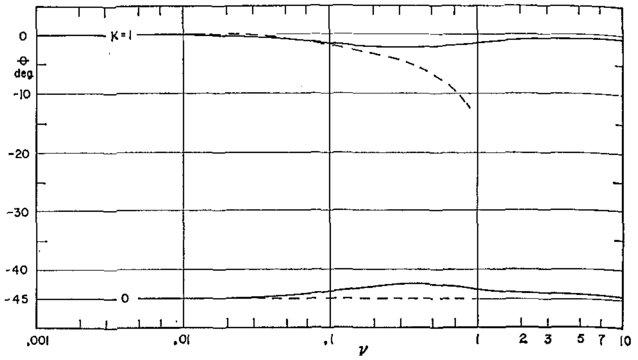

Fig. 2(b) Moduli R and phase angles θ of the roots z_0, z_1 of the eigenvalue equation (11) for $f = 1/3$, $a = 1/2$, $b = 5$; dashed lines: by power-series expansion to ν^1 terms (linear approximation); full lines: by numerical solution of eigenvalue equation; curves go with scale on left side unless otherwise indicated

$$\varphi_k'' + (\lambda_k^2 + ip_M)\varphi_k = 0 \qquad \psi_k'' + (\lambda_k^2 + ip_F)\psi_k = 0 \tag{7a, b}$$

subject by (3) to the boundary conditions

$$y = 0: \quad \varphi' = 0 \qquad y = \pi: \quad \psi' = 0 \tag{8a, b}$$

$$y = (1 - f)\pi: \quad \varphi = \psi \qquad k_M\varphi' = k_F\psi' \tag{8c, d}$$

Solution of (7) subject to (8a, b) is

$$\varphi_k = \mathfrak{A}_k \cos\frac{z_k}{1 - f}y \qquad \psi_k = \mathfrak{B}_k \cos\frac{z_k'}{1 - f}(\pi - y) \tag{9}$$

where

$$\lambda_k^2 = \frac{z_k^2}{(1 - f)^2} - ip_M = \frac{z_k'^2}{(1 - f)^2} - ip_F \tag{10}$$

Consistency with (8c, d) requires that the determinant of the coefficients $\mathfrak{A}$, $\mathfrak{B}$ vanish:[7]

$$0 = \begin{vmatrix} \cos z\pi & -\cos az'\pi \\ k_M\dfrac{z}{1 - f}\sin z\pi & k_F\dfrac{z'}{1 - f}\sin az'\pi \end{vmatrix}$$

$$= \left\{\frac{k_M}{f}\cos z\pi \cos az'\pi\right\}\Delta \tag{11a}$$

Here

$$\Delta = az \tan z\pi + bz' \tan (az'\pi) \tag{12a}$$

$$= \pi^{-1}(a\zeta \tan \zeta + b\zeta' \tan a\zeta') \tag{12b}$$

$$a = f/(1 - f) \qquad b = ak_F/k_M \qquad \zeta = z\pi \qquad \zeta' = z'\pi \tag{13a}$$

Furthermore

$$\mathfrak{B} = \cos \zeta/\cos a\zeta' \tag{13b}$$

and we may relate z_k' to z_k by (10), through the formula

$$z_k'^2 = z_k^2 + i\nu \qquad \nu = (1 - f)^2(p_F - p_M) \tag{14a, b}$$

ν is a new frequency parameter. For convenience, it also will be referred to as frequency.

It is readily noted that if z_k and z_k' satisfy the eigenvalue equation (11a), then so also do $-z_k$, $-z_k'$, but not the conjugates. $\bar{z}_k$ and $\bar{z}_k'$ satisfy the conjugate problem whereby in (7) ip_j is replaced by $-ip_j$.[8]

---

[6] This is not the only way, of course, to approach the problem. One may, for instance, seek a solution in the form of a Fourier integral and then convert this into a normal mode expansion, as is done in [6] in a different context. See also [10].

[7] We omit subscript k in (11)–(13), (23), (26), (28)–(35), (47)–(48), (56), and (69) for the sake of simpler writing, and place $\mathfrak{A}_k = 1$.

[8] This comment will be amplified in Section 9. Note that there is really only one independent set of eigenvalues, viz., z_k. But it is convenient to refer to z_k', related to z_k via (14a), also as an eigenvalue, and so also to ζ_k, ζ_k' related to the former via (13a), perhaps even to λ_k related to z_k, z_k' via (10).

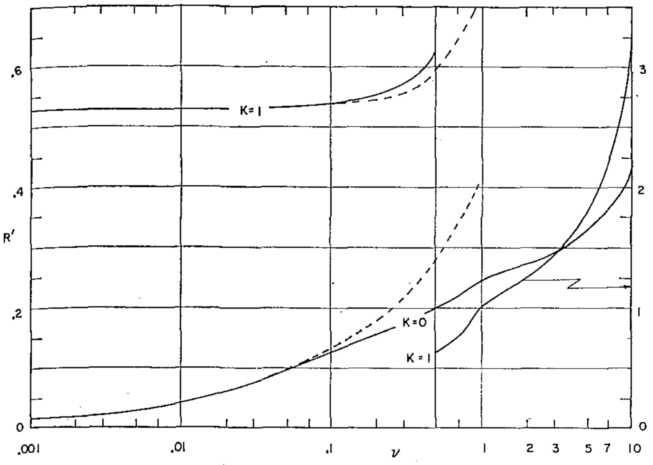

Fig. 3(a) Moduli R' and phase angles θ' of the roots z_0', z_1' of the eigenvalue equation (11) for $f = {}^1/_3$, $a = {}^1/_2$, $b = 5$; dashed lines: by linear approximation; full lines: by numerical solution of eigenvalue equation

In the limit of vanishing frequency the roots z_k, z_k' coalesce and become real, and so do the decay parameters λ_k:[9]

$$\nu = 0: \quad \lambda_k = \lambda_{kr} = z_k = z_k' \tag{15}$$

Since decay exists, z_k must be positive in the $\nu = 0$ limit. By continuity, z_k, z_k' must be chosen with a positive real part also for $\omega \neq 0$. From Figs. 2 and 3 it will be noted that the appropriate roots z_k are in the fourth quadrant; the roots z_k' are in the first quadrant.

We may rewrite the eigenvalue equation (11*a*) in the form

$$\pi\Delta = a\zeta \tan \zeta + b\zeta' \tan a\zeta' = 0 \tag{11b}$$

Observe that the vanishing of the factors $\cos \zeta$, $\cos a\zeta'$ in expression (11*a*) does not contribute eigenvalues, because they are offset by the corresponding denominators of $\tan \zeta$, $\tan a\zeta'$ in (12). Indeed, suppose that $\cos \zeta$ vanishes while $\cos a\zeta'$ does not. Then $\zeta = (n + \frac{1}{2})\pi$ (n = integer) and $\sin \zeta = 1$. Hence, omitting the factor k_M/f, (11*a*) becomes

$$a\zeta \cos a\zeta' = 0$$

which implies $\zeta = 0$ in contradiction to $\zeta = (n + \frac{1}{2})\pi$. When, on the other hand, both $\cos \zeta$ and $\cos a\zeta'$ vanish, then $\zeta = (n + \frac{1}{2})\pi$ and $a\zeta' = (m + \frac{1}{2})\pi$. Consequently, $a\zeta' - \zeta = (m - n)\pi$, whereas by (14) this difference must contain (for $\nu \neq 0$) an imaginary part.

3 Biorthogonal Expansion Formula

Let $z_0, z_1, z_2, \ldots$, be the sequence of fourth-quadrant complex eigenvalues of $\Delta = 0$, arranged according to ascending moduli (at $\nu = 0$), and (φ_0, ψ_0), (φ_1, ψ_1), . . ., the boundary temperature pairs associated with these eigenvalues. Introduce furthermore the boundary flux pairs

$$(\Phi_k, \Psi_k) = (k_M\varphi_k, k_F\psi_k) \tag{16}$$

We omitted the irrelevant $-\lambda_k e^{-\lambda_k x}$ factors on both sides of (16).

Multiplying (7*a*) by $k_M\varphi_l$ and subtracting the equation that results when the k and l indices are interchanged, there results

$$k_M(\varphi_l\varphi_k'' - \varphi_k\varphi_l'') + (\lambda_k^2 - \lambda_l^2)k_M\varphi_l\varphi_k = 0$$
$$0 \leqslant y \leqslant (1 - f)\pi \tag{17a}$$

Likewise

$$k_F(\psi_l\psi_k'' - \psi_k\psi_l'') + (\lambda_k^2 - \lambda_l^2)k_F\psi_l\psi_k = 0$$
$$(1 - f)\pi \leqslant y \leqslant \pi \tag{17b}$$

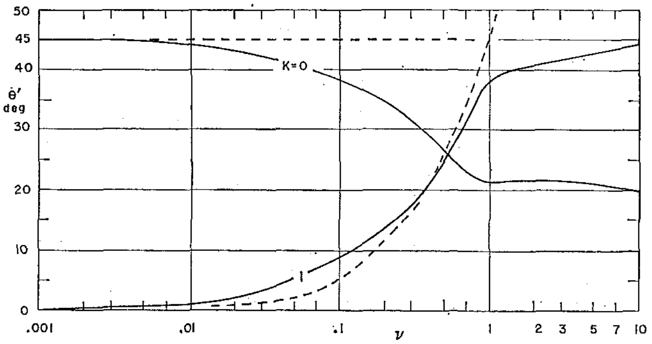

Fig. 3(b) Moduli R' and phase angles θ' of the roots z_0', z_1' of the eigenvalue equation (11) for $f = {}^1/_3$, $a = {}^1/_2$, $b = 5$; dashed lines: by linear approximation; full lines: by numerical solution of eigenvalue equation

It follows that

$$(\lambda_k^2 - \lambda_l^2)\left[\int_0^{(1-f)\pi} \Phi_l\varphi_k dy + \int_{(1-f)\pi}^{\pi} \Psi_l\psi_k dy\right]$$
$$= k_M\{\varphi_l\varphi_k' - \varphi_k\varphi_l'\}_{y=0} - k_F\{\psi_l\psi_k' - \psi_k\psi_l'\}_{y=\pi}$$
$$- \{k_M(\varphi_l\varphi_k' - \varphi_k\varphi_l') - k_F(\psi_l\psi_k' - \psi_k\psi_l')\}_{y=(1-f)\pi} \tag{18}$$

But the boundary terms vanish in the light of the boundary conditions (8). Hence, for the case of non-equality of eigenvalues λ_k, λ_l, biorthogonality of the function pairs follows:

$$k \neq l: \quad (\varphi_k, \psi_k) \perp (\Phi_l, \Psi_l) \tag{19}$$

The expansion formula for $w(x, y)$, where $w(0, y)$ is specified as $\chi(y)$, thus becomes

$$w(x, y) = \sum_0^\infty C_k e^{-\lambda_k x} \begin{cases} \varphi_k(y) & 0 \leqslant y \leqslant (1 - f)\pi \\ \psi_k(y) & (1 - f)\pi \leqslant y \leqslant \pi \end{cases} \tag{20a}$$

where

$$C_k = \frac{\displaystyle\int_0^{(1-f)\pi} \chi(y)\Phi_k(y)dy + \int_{(1-f)\pi}^{\pi} \chi(y)\Psi_k(y)dy}{\displaystyle\int_0^{(1-f)\pi} \varphi_k(y)\Phi_k(y)dy + \int_{(1-f)\pi}^{\pi} \psi_k(y)\Psi_k(y)dy} \tag{20b}$$

For the particular case of

$$w(0, y) = \chi(y) = 1 \tag{21}$$

with which we shall be mainly concerned, one finds, noting that by (9) and (13)

$$\varphi_k = \cos\frac{z_k y}{1 - f} \qquad \psi_k = \frac{\cos \zeta_k}{\cos a\zeta_k'} \cos\frac{z_k'(\pi - y)}{1 - f} \tag{22}$$

the expression

$$C_k = \frac{\displaystyle k_M\int_0^{(1-f)\pi} \varphi_k dy + k_F\int_{(1-f)\pi}^{\pi} \psi_k dy}{\displaystyle k_M\int_0^{(1-f)\pi} \varphi_k^2 dy + k_F\int_{(1-f)\pi}^{\pi} \psi_k^2 dy} \tag{23a}$$

$$= \frac{k_M \dfrac{1 - f}{z} \sin \zeta + k_F \dfrac{1 - f}{z'} \mathcal{B} \sin a\zeta'}{k_M \dfrac{1 - f}{4z}[2\zeta + \sin 2\zeta] + k_F \dfrac{1 - f}{4z'} \mathcal{B}^2[2a\zeta' + \sin 2a\zeta']} \tag{23b}$$

$$= \frac{4i\nu \sin \zeta}{i\nu \sin 2\zeta + 2(\zeta\zeta'^2/\pi^2)(1 + b \cos^2 \zeta/\cos^2 a\zeta')} \tag{23c}$$

In the last step we have also used (13*b*), (14), and (11*b*).

---

[9] We shall find it convenient to refer to λ as the decay parameter, λ_r as the decay constant, and λ_i as a phase-shift constant.

4 Concus' Zero-Frequency Solution

We write[10]

$$\zeta_k = z_k\pi = (x_k + iy_k)\pi = X_k + iY_k = R_k e^{i\theta_k}\pi$$
$$\zeta_k' = z_k'\pi = (x_k' + iy_k')\pi = X_k' + iY_k' = R_k' e^{i\theta_k'}\pi \tag{24}$$

At the frequency $\nu = 0$ all roots of the eigenvalue equation (11*b*) are real; the equation $\Delta = 0$ then acquires the form

$$\nu = 0: \qquad x = x': \qquad a \tan x\pi + b \tan ax\pi = 0 \tag{25}$$

This equation has been studied by Concus and Olander [4], and the roots have been tabulated by Concus [5] for a ranging from 0.001 to 1.000 and b ranging from 0.001 to 1000. If in any given problem a is assigned a value greater than one, we merely interchange the roles of F and M, and a is brought back into the $0 \leqslant a \leqslant 1$ range.

Of particular interest is the limiting case

$$f = \tfrac{1}{2} \qquad a = 1 \tag{26a}$$

where the roots

$$x_k = k/2 \qquad k = 0, 1, 2, \ldots \tag{26b}$$

are seen, by [4], to be independent of b. The solution (26*b*) of

$$a = 1: \quad \tan x\pi + b \tan x\pi = 0 \tag{26c}$$

by

$$2x_k = k = \text{odd integer} \tag{27a}$$

is not a contradiction, by virtue of the fact that the functional expression

$$\tan k\pi/2 = \pm\infty \tag{27b}$$

is double-valued.

5 Solution of the Eigenvalue Equation $\Delta = 0$

Let

$$\tilde{z} = \tilde{x} + i\tilde{y} = \tilde{R}e^{i\tilde{\theta}} \qquad \tilde{z}' = \tilde{x}' + i\tilde{y}' = \tilde{R}'e^{i\tilde{\theta}'} \tag{28}$$

be a truly approximate (i.e., non-exact) solution pair of

$$\Delta(z, z') = a\,\frac{x \sin 2x\pi - y \sinh 2y\pi + i(y \sin 2x\pi + x \sinh 2y\pi)}{\cos 2x\pi + \cosh 2y\pi}$$
$$+ b\,\frac{x' \sin 2ax'\pi - y' \sinh 2ay'\pi + i(y' \sin 2ax'\pi + x' \sinh 2ay'\pi)}{\cos 2ax'\pi + \cosh 2ay'\pi} = 0 \tag{29}$$

Then the residual

$$\tilde{\Delta} \equiv \Delta(\tilde{z}, \tilde{z}') \tag{30}$$

does not vanish. But let the departure ϵ fron the true value of z be small:

$$z = \tilde{z} + \epsilon \qquad |\epsilon/\tilde{z}|^2 \ll 1 \tag{31a}$$

Correspondingly,

$$z' = [(\tilde{z} + \epsilon)^2 + i\nu]^{1/2} \simeq \tilde{z}' + \epsilon\tilde{z}/\tilde{z}' \tag{31b}$$

Placing these into (11*b*), we find the first-order correction

$$\epsilon = -\tilde{\Delta}/\pi a\tilde{z}D(\tilde{z}, \tilde{z}') \tag{32}$$

$$D(z, z') = \frac{\tan z\pi}{z\pi} + b\,\frac{\tan az'\pi}{az'\pi} + \frac{2}{1 + \cos 2z\pi}$$
$$+ \frac{2b}{1 + \cos 2az'\pi} \tag{33}$$

Alternately, starting out with

$$z' = \tilde{z}' + \epsilon' \tag{34a}$$

we find

$$z \simeq \tilde{z} + \epsilon'\tilde{z}'/\tilde{z} \qquad \epsilon' = -\tilde{\Delta}/\pi a\tilde{z}'D(\tilde{z}, \tilde{z}') \tag{34b}$$

In accordance with Newton's method, the process is then iterated.

Moduli and phases of the roots z_0, z_0', z_1, and z_1' were calculated for low frequencies ($\nu < 0.1$) by the series expansion method of Section 6 in the linear approximation (i.e., terms up to ν^1 were retained); this is shown in dashed lines in Figs. 2 and 3. The curves obtained were extended to the right and provided first guesses for roots associated with $\nu > 0.1$. The ϵ or ϵ' scheme was used (programs EPS and EPSP, based on polar inputs of $\tilde{z}$, $\tilde{z}'$), whichever was found to be more promising. (In fact, for $k = 0$ the EPSP scheme turned out to be more favorable; for $k = 1$ usually EPS was preferable.) Invariably it was found that Newton's iteration scheme diverged, but the printouts gave successive values for x, y (also x', y') as the iterations progressed. By averaging the first two printouts, better initial estimates were obtained, and work then continued with programs EPSCAR or EPSPCAR using cartesian inputs but otherwise identical with EPS and EPSP. After about four or five such averagings, the result was within specified accuracy (five decimals for $\nu \leqslant 0.1$, four for $0.1 < \nu \leqslant 1.0$, three beyond $\nu = 1.0$). This was mainly the procedure for the z_0 root. In calculating z_1 the additional difficulty arose that the initial guess $\tilde{z}$ (or $\tilde{z}'$) had to be very accurate (accurate to three or more digits) before a consistent divergence scheme could be reached. (Consistent scheme: one where the first iteration gives results in the same quadrant as the initial guess and is within a factor of two of the initial guess.)

For high ν ($\nu \gtrsim 100$) and also for $k > 1$ the guessing game became quite laborious and further computation work was abandoned. (It is planned to reconsider the computational aspects more thoroughly in a later study, replacing at the same time the specified surface temperature distribution condition by the condition of specified heat flux [10].)

On the other hand, one must not expect the present method to be usable at very large ν, for we cannot with impunity place $\omega = \infty$ in (5), to wit, in

$$-i\varkappa_j\omega^{-1}\nabla^2 w + w = 0 \tag{35}$$

The equation must be properly treated as a *singular perturbation problem* in order to explore the nature of the solution near $\omega = \infty$. It is also planned to carry out this other study in the near future.

6 Low-Frequency Estimate of the Roots

Since the fundamental root λ_0 of $\Delta = 0$ (or, in the light of

$$\lambda_0^2 = z_0^2/(1 - f)^2 - ip_M \tag{36}$$

the root z_0 of $\Delta = 0$) dominates the behavior of the thermal wave at large distances x (irrespective of ω), it is desirable to provide an explicit formula for it. This we proceed to do in the low-frequency limit. Let

$$\zeta_0^2 = (z_0\pi)^2 = i\nu\pi^2\alpha_1 + \nu^2\pi^4\alpha_2 + i\nu^3\pi^6\alpha_3 + \nu^4\pi^8\alpha_4 + \ldots \tag{37a}$$

Then

$$\zeta_0'^2 = (z_0'\pi)^2 = (z_0^2 + i\nu)\pi^2 = i\nu\pi^2\beta_1 + \nu^2\pi^4\alpha_2 + i\nu^3\pi^6\alpha_3 + \ldots$$
$$\beta_1 = 1 + \alpha_1 \tag{37b}$$

---

[10] The present x, y symbols should not be confused with the symbols x, y of the coordinates in Fig. 1 and elsewhere.

On placing the $\zeta_0{}^2$, $\zeta_0{}'^2$ expressions into

$$\pi\Delta/a = \zeta \tan \zeta + (b/a)\zeta' \tan a\zeta' \qquad (38a)$$

$$= \zeta^2 + b\zeta'^2 + \frac{1}{3}(\zeta^4 + ba^2\zeta'^4) + \frac{2}{15}(\zeta^6 + ba^4\zeta'^6) + \ldots \qquad (38b)$$

and equating the coefficients of successive ν powers to zero,[11] one obtains, using the notations

$$k_M{}' = (1 - f)k_M \qquad k_F{}' = fk_F \qquad k_{\text{av}} = k_M{}' + k_F{}'$$
$$\tilde{k}_M = fk_M \qquad \tilde{k}_F = (1 - f)k_F \qquad \tilde{k} = \tilde{k}_M + \tilde{k}_F \qquad (39)$$

the results

$$\alpha_1 = -b/(1 + b) = -k_F{}'/k_{\text{av}} \qquad \beta_1 = 1/(1 + b) = k_M{}'/k_{\text{av}}$$
$$\alpha_2 = b(b + a^2)/3(1 + b)^3 = k_F{}'\tilde{k}_M\tilde{k}/3k_{\text{av}}{}^3$$

$$\alpha_3 = (2/45)b(a^2 + b)[3(1 + b)(a^2 - b) - 5b(a^2 - 1)]/$$
$$(1 + b)^5 = -(2/15)\alpha_1\alpha_2\Theta$$

$$\Theta = 5\,\frac{1 - a^2}{1 + b} + 3\left(\frac{a^2}{b} - 1\right) = 5\,\frac{1 - 2f}{1 - f}\,\frac{k_M}{k_{\text{av}}} + 3\left(\frac{\tilde{k}_M}{\tilde{k}_F} - 1\right) \qquad (40)$$

One therefore has, for the fundamental mode,

$$\lambda_0{}^2 = (\lambda_r + i\lambda_i)^2 = \lambda_r{}^2 - \lambda_i{}^2 + 2i\lambda_r\lambda_i = -ip_M + z_0{}^2/(1 - f)^2$$
$$= -ip_M + [i\nu\pi^2\alpha_1 + \nu^2\pi^4\alpha_2 + i\nu^3\pi^6\alpha_3 + \ldots]/(1 - f)^2\pi^2 \qquad (41a)$$

$$\simeq -i\omega\left[\frac{1}{\varkappa_M} + \frac{k_F{}'}{k_{\text{av}}}\left(\frac{1}{\varkappa_M} - \frac{1}{\varkappa_F}\right)\right] = -i\omega/\varkappa_{\text{av}} \qquad (41b)$$

$$\varkappa_{\text{av}} = k_{\text{av}}/(\rho c)_{\text{av}} \qquad (\rho c)_{\text{av}} = (1 - f)(\rho c)_M + f(\rho c)_F \qquad (42)$$

in accordance with (1b). Expression (41b) is appropriate in the ν^1 approximation.[12] Furthermore, because λ^2 is pure imaginary in the ν^1 approximation, also

$$\lambda_r = \lambda_i = (\omega/2\varkappa_{\text{av}})^{1/2} = |\lambda|/\sqrt{2} \qquad (43)$$

Since α_2 is positive, one obtains in the ν^2 approximation[13]

$$(\lambda_r/\lambda_i)^2 > 1 \qquad |2\lambda_r\lambda_i/\lambda^2| = 1 \qquad (44a, b)$$

while in the ν^3 approximation the imaginary part of λ^2 is increased (reduced) when $\alpha_3 \gtrless 0$. Thus

$$\alpha_3 \gtrless 0 \quad \text{implies} \quad |2\lambda_i\lambda_r/\lambda^2| \gtrless 1 \qquad (45a)$$

By expression (40c) the condition for $\alpha_3 \gtrless 0$ is

$$\Theta \gtrless 0: \quad \frac{1 - 2f}{f(1 - f)} \gtrless \frac{3}{2}\,\frac{k_F{}^2 - k_M{}^2}{k_Fk_M} \qquad (45b)$$

For the root $z_0{}^2$ itself, one has the estimate, to order ν^1,

$$|z_0|^2 = |\alpha_1\nu| = (1 - f)^2|p_F - p_M|k_F{}'/k_{\text{av}} \leqslant |p_F - p_M| \qquad (46a)$$

Therefore

$$|z_0|^2 < 0.1 \quad \text{when} \quad |p_F - p_M| < 0.1 \qquad (46b)$$

This represents a rough estimate of the range of validity of a first-power approximation.

For higher roots we write the three-term approximation

$$\zeta = z\pi = (x + i\nu g_1 + \nu^2 g_2)\pi = X + i\nu G_1 + \nu^2 G_2$$
$$\zeta' = z'\pi = (x' + i\nu h_1 + \nu^2 h_2)\pi = X' + i\nu H_1 + \nu^2 H_2 \qquad (47a, b)$$

By identifying the second expression with

$$\zeta' = \pi(z^2 + i\nu)^{1/2} = \zeta + \frac{i\nu\pi^2}{2\zeta} + \frac{\nu^2\pi^4}{8\zeta^3} \qquad (47c)$$

and using the notation (51), one finds

$$X' = X \qquad h_1\pi = H_1 = G_1 + \pi^2/2X = (g_1 + 1/2x)\pi$$
$$h_2\pi = H_2 = G_2 + G_1\pi^2/2X^2 + \pi^4/8X^3$$
$$= (g_2 + g_1/2x^2 + 1/8x^3)\pi$$
$$\tan \zeta = t + i\nu G_1(1 + t^2) + \nu^2(G_2 - tG_1{}^2)(1 + t^2)$$
$$\tan a\zeta' = t' + i\nu aH_1(1 + t'^2) + \nu^2(aH_2 - t'a^2H_1{}^2) \times (1 + t'^2) \qquad (48)$$

Placing these expressions into (38a) and equating the coefficients of successive ν powers to zero, one obtains (the first of (49) is the Concus equation, the roots x are tabulated in [4]):

$$[\ \ ]\nu^0 = 0: \quad at + bt' = 0 \qquad (49a)$$

$$[\ \ ]\nu^1 = 0: \quad G_1 = \frac{\pi^2}{2X^2}\,\frac{t - Xb(1 + t'^2)}{1 + t^2 + b(1 + t'^2)} \qquad (49b)$$

$$[\ \ ]\nu^2 = 0: \quad G_2 = \Bigg[X\left\{tG_1{}^2(1 + t^2) + baH_1{}^2t'(1 + t'^2)\right\} + G_1{}^2(1 + t^2) + bH_1{}^2(1 + t'^2) - \left(\frac{G_1\pi^2}{2X^2} + \frac{\pi^4}{8X^3}\right) \times \left\{(1 + t'^2)bX + \frac{b}{a}t'\right\}\Bigg]\Big/ X\{1 + t^2 + b(1 + t'^2)\} \qquad (49c)$$

7 Low-Frequency Expressions of the Expansion Coefficients

We restrict ourselves to the uniform boundary temperature $\chi(y) = 1$, as in (21). Then, expanding (23c) in powers of ν up to quadratic terms, we find, using (37),

$$C_0 = 1 + i\nu\pi^2\alpha_1\left(\frac{1}{6} + \frac{1}{3}\,\frac{a^2 + b}{1 + b}\right) + \nu^2\pi^4\Bigg[-\frac{a^4}{3}\alpha_1 + \left(\frac{1}{6} - \frac{1}{2}ba^2\right)\alpha_2 + \left\{\frac{1}{360} + a^2\left(\frac{1}{4} - \frac{11}{12}a^2\right)\right\}\alpha_1{}^2 - \frac{1 + b}{2}\alpha_3 - \left\{\frac{3}{4} + b\left(a^2 - \frac{1}{4}\right)\right\}\alpha_1\alpha_2 + \frac{1 + 9a^2 - 10a^4}{12}\alpha_1{}^3 - \left\{\frac{(1 - a^2)\alpha_1{}^2 - (1 + b)\alpha_2}{2}\right\}^2\Bigg] \qquad (50)$$

For $k \geqslant 1$ we use, in conjunction with expressions (47), the notations

$$s = \sin X \qquad c = \cos X \qquad t = \tan X \qquad c' = \cos aX$$
$$t' = \tan aX \qquad S = \sin 2X \qquad (51)$$

---

[11] The structure of these coefficient equations is

$\pi^2\nu^1$: $\{1 + b\}\alpha_1 + \{b\} = 0$
$\pi^4\nu^2$: $\{1 + b\}\alpha_2 + \{\ \ \}\alpha_1{}^2 = 0$
$\pi^6\nu^3$: $\{1 + b\}\alpha_3 + \{\ \ \}\alpha_2\alpha_1 + \{\ \ \}\alpha_1{}^3 = 0$
……

where $\{\ \ \}$ are real coefficients. It follows that all α_k are real. Therefore it also follows that, on reversing the sign of ν in (37a), one obtains the expression of $\bar{\zeta}^2$. The term $\nu^0\pi^0\alpha_0$, when incorporated into (37), leads to a ν^0 equation $\{1 + b\}\alpha_0 = 0$. Thus $\alpha_0 = 0$, and may be suppressed in (37) ab initio, as we have done.

[12] In the ν^2 approximation the equivalent diffusivity assumes a form $\varkappa_{\text{eq}} = \varkappa_{\text{av}}[1 + iF(\omega)]$ where the $\alpha_2\nu^2$ correction term gives rise to frequency-dependence.

[13] Equation (44b) follows from the fact that λ^2 is now of the form $\lambda^2 = iB\omega + A\omega^2$ ($B = -1/\varkappa_{\text{av}}$); hence $iB\omega = \lambda^2/(1 - iA\omega/B) \simeq \lambda^2(1 + iA\omega/B)$, and therefore $|B\omega| \equiv |2\lambda_i\lambda_r| \simeq |\lambda|^2$.

One obtains, to quadratic terms in ν (we omit subscript 1 of G, H)

$$C_k = \frac{2\pi^2 s}{X^3\{1 + bc^2/c'^2\}} \times \left[i\nu - \nu^2 \left\{ \frac{G}{t} - \frac{\frac{1}{2}\pi^2 S + X^2(G + 2H)(1 + bc^2/c'^2) + 2X^3 b(c^2/c'^2)(aHt' - Gt)}{X^3\{1 + bc^2/c'^2\}} \right\} \right] \quad (52)$$

A seeming indeterminacy arises when $c/c' = 0/0$. This happens when

$$X = m\pi/2 \qquad aX = n\pi/2 \qquad m \text{ and } n \text{ are odd integers} \quad (53a)$$

Then one arrives at the value

$$(c/c')^2 = c^2(1 + t'^2) = c^2\left[1 + \left(\frac{aX}{bX'}\tan X\right)^2\right]$$
$$= c^2 + (a/b)^2 s^2 = (k_M/k_F)^2 \quad (53b)$$

8 Examples

I $f = {}^1/_3$, $k_F/k_M = 10$; $a = {}^1/_2$, $b = 5$

Then

$$\alpha_1 = -0.8333 \qquad \alpha_2 = 0.0405 \qquad \alpha_3 = -0.0102$$
$$\Theta = -2.225$$

$$X_1 = 0.5290\pi = 1.663 = 95.2°$$
$$X_2 = 1.4710\pi = 4.622 = 264.8° \qquad X_3 = 2\pi$$
$$X_4 = 2.5290\pi = 7.942 = 95.2°$$
$$X_5 = 3.4710\pi = 10.91 = 264.8° \qquad X_6 = 4\pi$$
$$X_7 = 4.5290\pi = 14.24 = 95.2° \qquad G_1 = -0.396$$
$$H_1 = 2.573 \quad (54)$$

and to second-order terms in ν

$$C_0 = 1 - 3.775\nu i - 8.3945\nu^2 \qquad C_1 = 3.92\nu i + 8.45845\nu^2$$
$$C_2 = -0.184\nu i - 0.08543\nu^2$$
$$C_3 = 0 \qquad C_4 = 0.036\nu i + 0.00260\nu^2$$
$$C_5 = -0.0140\nu i - 0.00141\nu^2 \qquad C_6 = 0$$
$$C_7 = 0.0063\nu i + 0.00007\nu^2 \quad (55)$$

We find that

$$\sum_1^7 C_k = 3.774\nu i + 8.3743\nu^2 \quad (56a)$$

which indicates that the departure from one in C_0 is just cancelled out by the higher C_k. Thus

$$\sum_0^\infty C_k \simeq 1.0 = \chi(0) \quad (57)$$

as it should be.[14] In Figs. 2 and 3 we plot, versus ν, the linear approximation (in ν) to

$$R_k = |z_k| \qquad \theta_k = \arg z_k \qquad R_k' = |z_k'| \qquad \theta_k' = \arg z_k' \quad (58)$$

in dashed lines and the results based on Section 5 in full lines. Where the two curves coincide, full lines are drawn.

II $f = {}^1/_2$, $k_F/k_M = 10$; $a = 1$, $b = 10$

Then to ν^1 terms

$$\alpha_1 = -0.910 \qquad C_0 = 1 - 4.491\nu i \qquad X_k = \frac{k\pi}{2}$$
$$(c/c')^2 = 1/b^2 = 0.01 \quad (59a)$$

Hence

$$C_k = 0 \qquad k = 2, 4, 6, \ldots$$
$$C_1 = 4.63\nu i \qquad C_3 = -0.171\nu i \qquad C_5 = 0.037\nu i$$
$$C_7 = -0.0135\nu i \qquad C_9 = 0.0063\nu i \quad (59b)$$

and, to first-order terms,

$$\sum_1^9 C_k = 4.496\nu i \quad (60)$$

III $f = {}^2/_3$, $k_F.k_M = {}^{50}/_3$; $a = 2$, $b = {}^{100}/_3$

This example puts us outside of the range of Concus' tables. The eigenvalue equation now is

$$2\zeta \tan\zeta + \frac{100}{3}\zeta' \tan 2\zeta' = 0 \quad (61a)$$

Let

$$\hat{\zeta} = 2\zeta \qquad \hat{\zeta}' = 2\zeta' \quad (61b)$$

Then

$$\frac{1}{2}\hat{\zeta}' \tan\hat{\zeta}' + \frac{3}{100}\hat{\zeta}\tan\hat{\zeta}/2 = 0 \quad (61c)$$

Concus' tables are now applied with

$$\hat{a} = {}^1/_2 \qquad \hat{b} = 0.03 \quad X = \hat{X}/2 \quad (62)$$

One obtains to ν^1 terms

$$X_1 = 1.403 = 80.38° \qquad X_2 = 1.739 = 99.60° \qquad X_3 = \pi$$
$$X_4 = 4.55 = 260.8° \qquad X_5 = 4.880 = 279.6° \quad (63)$$

and we find to ν^1 terms

$$\alpha_1 = -0.970 \qquad C_0 = 1 - 5.06\nu i \qquad C_1 = 3.46\nu i$$
$$C_2 = 1.82\nu i \qquad C_3 = 0 \qquad C_4 = -0.116\nu i \qquad C_5 = 0.0824\nu i$$
$$\sum_0^5 C_k \simeq 1.0 \quad (64)$$

9 Summary

Mathematical Features. The salient mathematical feature of the two-media thermal wave problem is the biorthogonality of the expansion of a given excitation (be it real or complex) into complex eigenfunctions and the association of the latter with complex eigenvalues. In contrast, the seemingly more difficult stress problem [3] calls for a real eigenfunction expansion only. Another somewhat unexpected feature (if one judges by past experiences) is that the task of determining the zeroth eigenvalue is nontrivial and requires effort comparable to that required for the higher eigenvalues. A further interesting observation is that the modulus of an eigenvalue z_k does not necessarily increase monotonically with the frequency ν. For instance, in the range $0 \leqslant \nu \leqslant 1$ the modulus of the first eigenvalue varies from 0.528 to 0.500. Beyond $\nu = 1$ $|z_1|$ increases again. Still another surprising result is that while we labeled the eigenvalues as $z_0, z_1, z_2, \ldots$, in order of their ascending moduli at very low frequencies, this order does not necessarily maintain at higher frequencies. For instance, by Fig. 2(*a*), in the range $\nu \simeq 2.7$ to $\nu \simeq 20$ the root z_1 has a lower modulus than z_0. Nevertheless, it is proper to refer to the function pair $\varphi_0(y)$, $\psi_0(y)$ associated with z_0 as the funda-

---

[14] Note that Concus' tables are not quite accurate enough for our purpose. For instance, if we changed $X_1 = 0.5290$ to $X_1 = 0.52895$, then the ν^2 coefficient in C_1 would change to 8.3988.

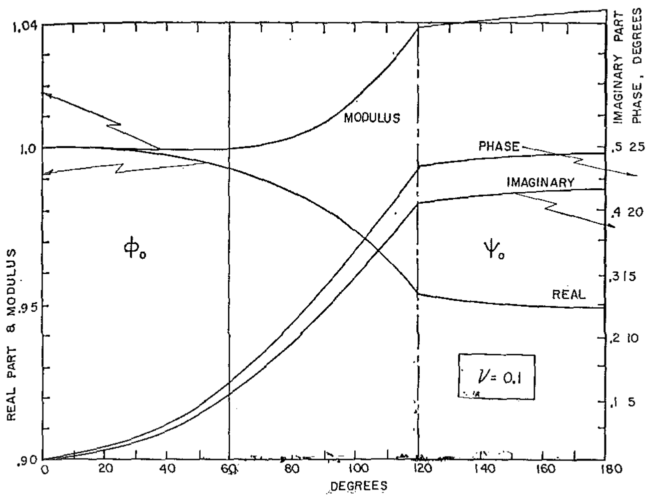

Fig. 4(a) Profile of the fundamental mode $\varphi_0(y)$, $\psi_0(y)$ for Example I: $f = {}^1/_3, a = {}^1/_2, b = 5; \nu = 0.10$

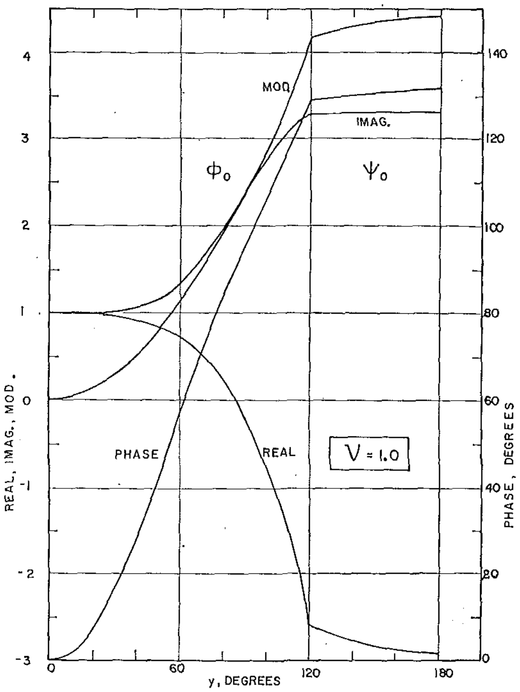

Fig. 4(b) Profile of the fundamental mode $\varphi_0(y)$, $\psi_0(y)$ for Example I: $f = {}^1/_3, a = {}^1/_2, b = 5; \nu = 1.0$

mental mode over the entire ν range. Indeed, it must be remembered that the physically important parameter is not z_k, but the decay constant λ_{kr}, (6c). And this, considered further below, behaves as expected, see Fig. 5.

Since in our numerical Example I, to which Figs. 2 and 3 pertain, $k_M/k_F = 0.1$ (our numerical results in this section will all refer to Example I), it follows from the definition (14b) that

$$\nu = -(1 - \varkappa_M/\varkappa_F)p_M(1 - f)^2 \tag{65}$$

is a negative quantity when $\varkappa_M/\varkappa_F < 1$, which is the case for

$$(\rho c)_M = (\rho c)_F \tag{66a}$$

For then

$$\varkappa_M/\varkappa_F = k_M/k_F \tag{66b}$$

as we now assume. We may retain all our previous results if instead of the temperature distribution (2c) we now contemplate

$$T = e^{i\Omega t}w(x, y) \tag{67}$$

i.e., we reverse the sign of the frequency,

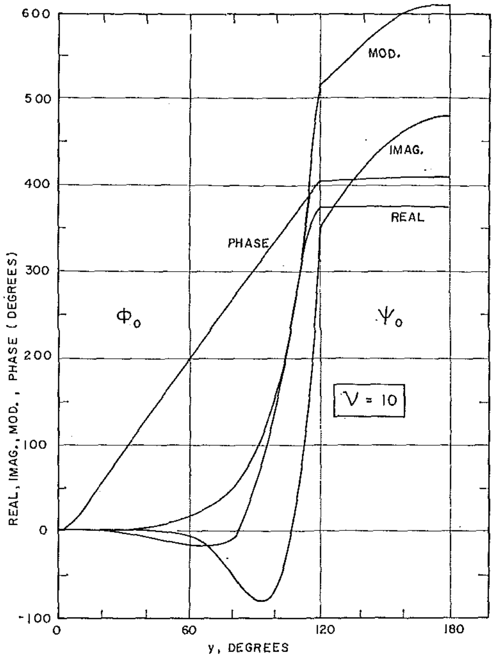

Fig. 4(c) Profile of the fundamental mode $\varphi_0(y)$, $\psi_0(y)$ for Example I: $f = {}^1/_3, a = {}^1/_2, b = 5; \nu = 10.0$

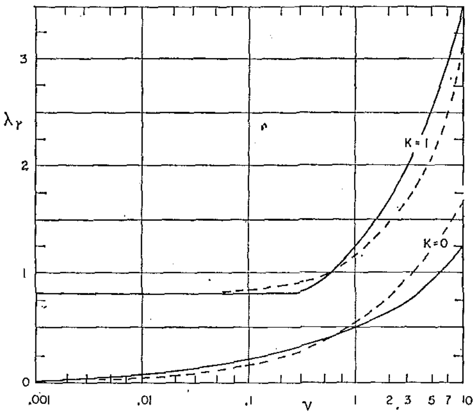

Fig. 5 Decay constants of fundamental mode and first mode for Example I: $f = {}^1/_3, a = {}^1/_2, b = 5$; dashed lines: linear approximation; full lines: on basis of rigorous solution in Fig. 2

$$\Omega = -\omega \tag{68a}$$

and correspondingly also introduce the frequency parameter

$$P = -p = \Omega/\varkappa \tag{68b}$$

For then

$$\nu = (1 - \varkappa_M/\varkappa_F)P_M(1 - f)^2 \tag{56b}$$

is a positive quantity.[15]

Physical Features. The imposed surface temperature profile $\chi(y)$ (which, in practice, is essentially constant over the width of several laminae) gradually distorts, as it propagates down the composite, into an assembly of nonuniform normal modes that die out at various rates. Fig. 4 plots, for the conditions of Example I at $\nu = 0.1$, 1.0, and 10.0, the most persistent mode, $\varphi_0(y)$, $\psi_0(y)$. Of greatest concern is the question: *is the rate of decay fast enough to prevent occurrence of significant thermal stresses* due to this nonuniformity and to preclude the risk of delamination? This entire aspect of the problem deserves further

---

[15] Alternatively, by the remark in the paragraph after (14), we could retain ν as a negative quantity and continue to use Figs. 2 and 3 drawn for positive ν by merely reversing the signs of θ, θ'.

exploration. (So also does a correlation with other related work in the composite area such as [7, 8].)

The decay constants λ_{0r}, λ_{1r} are plotted for the specifics of Example I in Fig. 5. Recalling (10), (60), and (65), one may write[16]

$$(1 - f)(\lambda_r + i\lambda_i) = [z^2 + iP_M(1 - f)^2]^{1/2}$$

$$= \left[x^2 - y^2 + i\left(2xy + \frac{\nu}{1 - \varkappa_M/\varkappa_F}\right)\right]^{1/2} = \text{say,}$$

$$[\xi + i\eta]^{1/2} = [(\sqrt{\xi^2 + \eta^2} + \xi)/2]^{1/2}$$

$$+ i(\operatorname{sgn} \eta)[(\sqrt{\xi^2 + \eta^2} - \xi)/2]^{1/2} \quad (69)$$

In particular, for

$$\nu = 0.1: \quad z_0 = 0.209977 - 0.200705i$$

$$= 0.290470 \, \underline{|-43.7067^\circ}$$

$$z_0' = 0.099939 + 0.078614i = 0.127153 \, \underline{|38.1891^\circ} \quad (70a)$$

one obtains

$$\xi + i\eta = 0.00381 + 0.0268i \qquad \lambda_0 = 0.1865 + 0.1620i \quad (70b,\, c)$$

Had we proceeded in the alternate way suggested by footnote 15, not adopting (67) but retaining the (2c) expression, and accordingly used

$$\bar{z}_0 = 0.209977 + 0.200705i \quad (71a)$$

appropriate for a negative ν, we would have found

$$\xi + i\eta = 0.00381 - 0.0268i \qquad \lambda_0 = 0.1865 - 0.1620i \quad (71b)$$

This reflects the fact that a switch from $e^{-i\omega t}$ to $e^{i\Omega t}$ leaves the decay rate unchanged but introduces a phase reversal.

Fig. 5 provides another important observation. The low-frequency approximation to λ_{0r} (dashed line) is above the rigorous value (full line) for $\nu > 0.4$. Thus, *use of the static values of the material properties gives an exaggerated estimate for the rate of decay when ν is not small enough.*

Acknowledgment

The authors are much indebted to the two referees of the paper for suggesting a number of improvements in the presentation.

References

1 Carslaw, H. S., and Jaeger, J. C., *Conduction of Heat in Solids*, Oxford, 1959.

2 Nahas, N. C., Griffis, C. L., and Couper, J. R., "Thermal Conductivity of Two-Phase Systems," University of Arkansas Experiment Station, Res. Rept. 5, 1964.

3 Sun, C.-T., Achenbach, J. D., and Herrmann, G., "Time-Harmonic Waves in a Stratified Medium Propagating in the Direction of the Layering," *Journal of Applied Mechanics*, Vol. 35, TRANS. ASME, Series E, Vol. 90, No. 2, June 1968, pp. 408–411.

4 Concus, P., and Olander, D. R., "Transient Diffusion in a Composite Slab," *International Journal of Heat and Mass Transfer*, Vol. 11, 1968, p. 610.

5 Concus, P., "Table of the Solutions of $a \tan \pi x = -b \tan a\pi x$," Lawrence Radiation Lab Report UCRL-17608, 1967.

6 Horvay, G., "Temperature Distribution in a Slab Moving From a Chamber at One Temperature to a Chamber at Another Temperature," JOURNAL OF HEAT TRANSFER, TRANS. ASME, Series C, Vol. 83, No. 4, Nov. 1961, pp. 391–402.

7 Peavy, B. A., "Analytical Studies of Probe Conduction Errors in Ground Temperature Measurements," *Journal of Research of NBS, Engineering & Instrumentation*, Vol. 72C, 1968, p. 243.

8 Coriell, S. R., and Jackson, J. L., "Bounds on Transport Coefficients of Two-Phase Materials," *Journal of Applied Physics*, Vol. 39, 1968, p. 4733.

9 Abramowitz, M., and Stegun, I. A., *Handbook of Mathematical Functions*, Dover, 1965.

10 Manaker, A. M., and Horvay, G., "Thermal Response in Laminated Composites," to be published.

---

[16] *The formula in the second line of (69) is stated on page 17 of [9].*

O. M. GRIFFIN
Ocean Technology Division,
Naval Research Laboratory,
Washington, D. C.
Mem. ASME

Heat, Mass, and Momentum Transfer During the Melting of Glacial Ice in Sea Water

The velocity, temperature, and concentration distributions near a melting surface of glacial, or pure, ice in saline water are determined for laminar flow conditions using integral techniques. Estimates are made of the relative thicknesses of the momentum, thermal, and mass diffusion boundary layers for a variety of the appropriate flow and thermal parameters. These findings are applied to the melting of glacial ice in sea water, but they also are applicable to other systems in which heat, mass, and momentum transfer occur simultaneously with phase transformation. The speed of sound at constant pressure in sea water is a function of temperature and salinity, and the variation of sound speed with changing environmental conditions plays an important role in underwater acoustic propagation. The results of the heat and mass transfer analyses are employed to determine the sound speed profiles within the temperature and salinity boundary layers near the melting glacial ice for free-stream water temperatures of 5 and 10 deg C.

Introduction

THE HEAT TRANSFER PROCESS near a melting flat surface has been investigated by Yen and Tien [1][1] and more recently by Pozvonkov, Shurgalskii, and Akselrod [2] under conditions of laminar flow and forced convection. The former study is concerned with an extension of the classical Leveque solution to the melting process, while the latter is a more refined application of the Karman–Pohlhausen integral method. It is instructive to apply the latter energy-balance type of integral solution to the transfer processes that simultaneously occur during the melting of an iceberg in sea water, and to estimate the rate of melting and the relative thicknesses of the momentum, temperature, and salinity boundary layers in a simple model situation. The results are applicable to the determination of the changes in sound speed near a melting iceberg, since the speed of sound in water at constant pressure is influenced by changes in temperature and salinity [3]. The present analysis also accounts for the subcooling of the solid below the melting temperature and the effect of this subcooling on the heat and mass transfer rates. The methods described here are applicable to other physical systems in which these transport processes occur simultaneously with phase transformation.

Problem Formulation

The melting problem is formulated by considering the boundary-layer equations [4] for simultaneous heat, mass, and momentum transfer. The phase transformation is assumed to occur under steady-state conditions, so that a coordinate system fixed to the melt interface is appropriate. This is a valid approximation for a large body such as an iceberg. The fluid phase is further assumed to be of constant density, and the assumption of a pure solid phase ensures that the results will be applicable to the melting of glacial ice. Physical properties that appear in the governing equations are considered to be constant for the system outlined in Fig. 1. The governing equations in the absence of a pressure gradient are:

continuity

$$\frac{\partial u}{\partial x} + \frac{\partial (v\xi)}{\partial y} = 0 \qquad (1)$$

momentum

$$u\frac{\partial u}{\partial x} + v\xi\frac{\partial u}{\partial y} = \frac{1}{\mathrm{Re}}\frac{\partial^2 u}{\partial y^2} \qquad (2)$$

energy

$$u\frac{\partial T}{\partial x} + v\xi\frac{\partial T}{\partial y} = \frac{1}{\mathrm{Re\,Pr}}\frac{\partial^2 T}{\partial y^2} \qquad (3)$$

mass diffusion

---

[1] Numbers in brackets designate References at end of paper.

Contributed by the Heat Transfer Division of THE AMERICAN SOCIETY OF MECHANICAL ENGINEERS and presented at the ASME-AIChE Heat Transfer Conference, Atlanta, Ga., August 5–8, 1973. Manuscript received by the Heat Transfer Division May 15, 1972. Paper No. 73-HT-3.

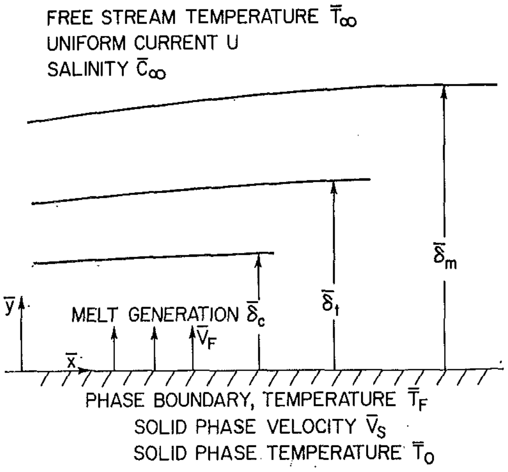

Fig. 1 Schematic diagram of the flow near the phase boundary between ice and flowing sea water, with coordinates fixed to the interface

$$u \frac{\partial C}{\partial x} + v\xi \frac{\partial C}{\partial y} = \frac{1}{\text{Re Sc}} \frac{\partial^2 C}{\partial y^2} \tag{4}$$

The absorption of latent heat during the melting results in a thermal energy balance between phases

$$\left.\frac{\partial T}{\partial y}\right|_{y=0^+} = \frac{\bar{M}}{(\bar{T}_\infty - \bar{T}_F)} \frac{\dot{\bar{m}} L}{\bar{K}_F} + \frac{\bar{K}_s(\bar{T}_F - \bar{T}_0)}{\bar{K}_F(\bar{T}_\infty - \bar{T}_F)} \left.\frac{\partial T_s}{\partial_y}\right|_{y=0^-} \tag{5}$$

where $\dot{\bar{m}}$ is the rate of melt generation per unit surface area. This energy balance along the interface reduces to

$$\left.\frac{\partial T}{\partial y}\right|_{y=0^+} = \text{Pe}\xi \left(\frac{1+B}{A}\right)$$

where the parameter B accounts for the heat conduction into the solid after the method of Griffin [5] or Roberts [6].[2] These equations are in nondimensional form and are related to the physical system by the transformation

$$x = \frac{\bar{x}}{L} \qquad y = \frac{\bar{y}}{L}$$

$$u = \frac{u}{U} \qquad v = \frac{\bar{v}}{\bar{v}_F} \qquad \xi = \frac{\bar{v}_F}{U}$$

$$T = \frac{\bar{T} - \bar{T}_F}{\bar{T}_\infty - \bar{T}_F} \qquad T_s = \frac{\bar{T} - \bar{T}_0}{\bar{T}_F - \bar{T}_0} \qquad C = \frac{\bar{C} - \bar{C}_F}{\bar{C}_\infty - \bar{C}_F}$$

$$A = \frac{\bar{c}_{pF}(\bar{T}_\infty - \bar{T}_F)}{\bar{M}} \qquad B = \frac{\bar{c}_{ps}(\bar{T}_F - \bar{T}_0)}{\bar{M}}$$

where the Schmidt number is denoted by $\text{Sc} = \bar{\nu}/\bar{\gamma}$, the Prandtl number by $\text{Pr} = \bar{\nu}/\bar{\alpha}$, and the Reynolds number by $\text{Re} = UL/\bar{\nu}$. The Peclet number is denoted by $\text{Pe} = UL/\bar{\alpha}$. The boundary conditions on the system are

$$\begin{array}{lllll} \bar{y} = 0 & \bar{u} = 0 & \bar{v} = \bar{v}_F(\bar{X}) & \bar{T} = \bar{T}_F & \bar{C} = \bar{C}_F \\ \bar{y} \to \infty & \bar{u} = U & & \bar{T} = \bar{T}_\infty & \bar{C} = \bar{C}_\infty \end{array}$$

and reduce in the nondimensional coordinates to

---

[2] The heat conduction into the solid is determined by assuming one-dimensional heat conduction in a medium moving with the steady-state velocity $\bar{V}_s$.

Nomenclature

a_i = coefficient of ith order appearing in the quartic temperature profiles
A = fluid-phase melting parameter, or Stefan number, $\bar{c}_{pF}(\bar{T}_\infty - \bar{T}_F)\bar{M}^{-1}$
b_i = coefficient of ith order appearing in the quartic velocity profile
B = solid-phase subcooling parameter, $\bar{c}_{ps}(\bar{T}_F - \bar{T}_0)\bar{M}^{-1}$
$\bar{c}_p$ = specific heat at constant pressure (J-kg^{-1} deg C^{-1})
c_i = coefficient of ith order appearing in the quartic concentration profiles
$\bar{C}, C$ = salinity or concentration (parts per thousand); normalized salinity or concentration
D = parameter defined in Table 1
F = parameter defined in Table 1
$\bar{h}$ = heat transfer coefficient (J-sec^{-1} m^{-2}-deg C^{-1})
$\bar{K}$ = thermal conductivity (J-sec^{-1} m^{-1}-deg C^{-1})
L = characteristic length scale in the streamwise, $\bar{x}$, direction (m)
Le = Lewis number for mass diffusion in the fluid phase, $\bar{\gamma}\bar{\alpha}^{-1}$
$\bar{M}$ = latent heat of fusion (J-kg^{-1})
Nu = Nusselt number, $\bar{h}\bar{x}k^{-1}$
Pe = Peclet number for the fluid phase, $UL\bar{\alpha}^{-1}$
Pr = Prandtl number for the fluid phase, $\bar{\nu}\bar{\alpha}^{-1}$
Re = Reynolds number for the fluid phase, $UL\bar{\nu}^{-1}$
Sc = Schmidt number for the fluid phase, $\bar{\nu}\bar{\gamma}^{-1}$
$\bar{S}$ = local speed of sound in water (m-sec^{-1})
$\bar{T}, T$ = local temperature (deg C); normalized temperature
$\bar{u}, u$ = local streamwise, $\bar{x}$, velocity (m-sec^{-1}); normalized velocity
U = free-stream velocity (m-sec^{-1})
$\bar{v}, v$ = local transverse, $\bar{y}$, velocity (m-sec^{-1}); normalized velocity
$\bar{x}, x$ = streamwise coordinate defined in Fig. 1 (m); normalized coordinate
$\bar{y}, y$ = transverse coordinate defined in Fig. 1 (m); normalized coordinate
$\bar{\alpha}$ = thermal diffusivity (m^2-sec^{-1})
$\bar{\gamma}$ = diffusion coefficient (m^2-sec^{-1})
$\bar{\delta}, \delta$ = boundary-layer thickness (m); normalized boundary-layer thickness
δ^{**} = characteristic integral scale defined in equations (10a)–(12a)
$\Delta_{1,2}$ = ratio of boundary-layer thicknesses defined by equations (13) and (14)
ζ = normalized coordinate defined in Table 1(c)
η = normalized coordinate defined in Table 1(a)
$\bar{\nu}$ = kinematic viscosity (m^2-sec^{-1})
ω = normalized coordinate defined in Table 1(b)
ξ = normalized rate of mass generation along the melt interface
$\bar{\rho}$ = mass density (kg-m^{-3})

Subscripts

F = fluid properties at the melt interface
S = solid properties at the melt interface
ref = reference quantity defined in the text
0 = conditions in the solid at large distances from the melt interface
∞ = conditions in the fluid phase at large distances from the interface
m = subscript relating to the momentum boundary layer
t = subscript relating to the thermal boundary layer
c = subscript relating to the mass diffusion boundary layer
$\bar{x}$ = local quantity, e.g., $\text{Re}_{\bar{x}} = \text{Re}\,\frac{\bar{x}}{L}$

$$\begin{array}{llllll} y = 0 & u = 0 & v = 1 & \xi = \bar{v}_F/U & T = 0 & C = 0 \\ y \rightarrow \infty & u = 1 & & & T = 1 & C = 1 \end{array}$$

The subcooling of the solid is denoted by the temperature difference $\bar{T}_F - \bar{T}_0$, the temperature of the solid phase far from the interface being equal to $\bar{T}_0$. The rate of fluid mass generation at the interface is related to the melting rate of the solid by the continuity equation

$$\bar{v}_F(\bar{x}) = \left(\frac{\bar{\rho}_s}{\bar{\rho}_F}\right) \bar{v}_s(\bar{x})$$

It should be noted that the melting rate $\bar{v}_s$ is generally a function of $\bar{x}$, as borne out in the analysis that follows. The results will be a useful approximation in that flow regime where the boundary-layer thicknesses (and the melting rate) vary slowly with displacement in the free-stream direction.

When equations (1)–(4) are integrated over the momentum (δ_m), thermal (δ_t), and mass diffusion (δ_c) boundary layers, these equations become

$$\{v(x, \delta_m) - 1\}\xi = -\int_0^{\delta_m} \frac{\partial u}{\partial x}\, dy \tag{6}$$

$$\frac{d}{dx}\left\{\delta_m \int_0^1 (1 - u)u d\omega\right\} - \xi = \frac{1}{\text{Re}} \left.\frac{\partial u}{\partial y}\right|_{y=0} \tag{7}$$

$$\frac{d}{dx}\left\{\delta_t \int_0^1 (1 - T)u d\eta\right\} - \xi = \frac{1}{\text{Re Pr}} \left.\frac{\partial T}{\partial y}\right|_{y=0} \tag{8}$$

$$\frac{d}{dx}\left\{\delta_c \int_0^1 (1 - C)u d\zeta\right\} - \xi = \frac{1}{\text{Re Sc}} \left.\frac{\partial C}{\partial y}\right|_{y=0} \tag{9}$$

when the boundary-layer thicknesses δ are each normalized by the length scale L. The assumptions of zero gradients for temperature, velocity, and concentration at the edges of the respective boundary layers are made. For the case of ice melting in sea water, the inequalities

$$\delta_m > \delta_t > \delta_c$$

are satisfied for large x by virtue of the relative magnitudes of the Prandtl and Schmidt numbers for water. These simultaneous integral equations can be simplified by making the approximation that the momentum, temperature, and concentration boundary layers bear a constant ratio to one another, or that the ratios

$$\frac{\delta_t}{\delta_m} = \Delta_1 \qquad \frac{\delta_c}{\delta_m} = \Delta_2$$

are independent of x. The integral equations given in the foregoing paragraph then reduce to

$$\delta_m{}^{**} \frac{d\delta_m}{dx} = \frac{1}{\text{Re}} \left.\frac{\partial u}{\partial y}\right|_{y=0} + \xi \tag{10}$$

$$\delta_t{}^{**} \frac{d\delta_t}{dx} = \frac{1}{\text{Re Pr}} \left.\frac{\partial T}{\partial y}\right|_{y=0} + \xi \tag{11}$$

$$\delta_c{}^{**} \frac{d\delta_c}{dx} = \frac{1}{\text{Re Sc}} \left.\frac{\partial C}{\partial y}\right|_{y=0} + \xi \tag{12}$$

where

$$\delta_m{}^{**} = \int_0^1 (1 - u)u d\omega \tag{10a}$$

$$\delta_t{}^{**} = \int_0^1 (1 - T)u d\eta \tag{11a}$$

$$\delta_c{}^{**} = \int_0^1 (1 - C)u d\zeta \tag{12a}$$

denote, respectively, the momentum ($\delta_m{}^{**}$), energy ($\delta_t{}^{**}$), and concentration ($\delta_c{}^{**}$) thicknesses. Equations (10) and (11) are similar in form to those presented by Posvonkov, et al. [2] for heat transfer only. The melting rate ξ, as yet undetermined, appears in each of equations (10)–(12).

These equations are solved by approximating the velocity, temperature, and concentration distributions with polynomial functions. A Pohlhausen quartic is chosen for each as follows:

$$T = a_0 + a_1\eta + a_2\eta^2 + a_3\eta^3 + a_4\eta^4 \qquad \eta = \frac{y}{\delta_t}$$

$$u = b_0 + b_1\omega + b_2\omega^2 + b_3\omega^3 + b_4\omega^4 \qquad \omega = \frac{y}{\delta_m}$$

$$C = c_0 + c_1\zeta + c_2\zeta^2 + c_3\zeta^3 + c_4\zeta^4 \qquad \zeta = \frac{y}{\delta_c}$$

The governing integral equations are each dependent on the melting rate ξ, and so the unknown coefficients in the three profiles are determined from the physical conditions listed in Table 1. The method of solution is similar to that of Griffin and Szewczyk [8] and Posvonkov, et al. [2], but is extended here to include heat, momentum, and mass transfer simultaneously with phase transformation in the flow. The temperature profile is dependent only on the thermal parameters A and B

$$T(\eta) = a_1(\eta - 3\eta^2 + 3\eta^3 - \eta^4) + (6\eta^2 - 8\eta^3 + 3\eta^4)$$

where

$$a_1 = \frac{3}{D}\left\{\sqrt{1 + \frac{4}{3}D} - 1\right\} \qquad D = \frac{A}{1 + B}$$

as listed in Table 1(a). The heat-balance and momentum equations evaluated at the melt interface lead to a solution for the velocity profile

$$u(\omega) = b_1(\omega - 3\omega^2 + 3\omega^3 - \omega^4) + (6\omega^2 - 8\omega^3 + 3\omega^4) \qquad \omega = \frac{y}{\delta_m}$$

where the matching condition at $y = 0$ and the solution for the unknown parameter b are outlined in Table 1(b).

A similar approach leads to the mass concentration or salinity profile

$$C(\zeta) = c_1(\zeta - 3\zeta^2 + 3\zeta^3 - \zeta^4) + (6\zeta^2 - 8\zeta^3 + 3\zeta^4) \qquad \zeta = \frac{y}{\delta_c}$$

as shown in Table 1(c). It should be noted that the matching conditions at $y = 0$ in Table 1(a–c) are determined by evaluating the momentum, energy, and mass diffusion equations (2)–(4) *in conjunction with* the interfacial energy balance (5) at $y = 0$.

The parameter Le is the Lewis number for mass diffusion, the ratio of Prandtl and Schmidt numbers. The parameters Δ_1 and Δ_2 are determined by dividing equations (11) and (12) by equation (10) upon the assumption that Δ_1 and Δ_2 are not functions of the space coordinates. The two results of these operations are

$$\Delta_1{}^2 = \left(\frac{\delta_m{}^{**}}{\delta_t{}^{**}}\right) \frac{\Delta_1 a_1(1 + D)}{\Delta_1 \text{ Pr } b_1 + a_1 D} \tag{13}$$

$$\Delta_2{}^2 = \left(\frac{\delta_m{}^{**}}{\delta_c}\right) \frac{\text{Le } \Delta_1 C_1 + a_1 D \Delta_2}{\text{Pr } \Delta_1 b_1 + a_1 D} \tag{14}$$

when the integrals in equations (10a)–(12a) and the unknown a_j, b_j, and c_j are evaluated as shown in Table 1.

The ratios Δ_1 and Δ_2 follow from equations (13) and (14) for specified values of the physical parameters. The thermal-boundary-layer solution to equation (11) is

Table 1 Quartic polynomials for approximating temperature, velocity, and concentration distributions

(a) Temperature	(b) Velocity	(c) Salinity
$T(x,y) = \sum_{j=0}^{4} a_j \eta^j$	$u(x,y) = \sum_{j=0}^{4} b_j \omega^j$	$C(x,y) = \sum_{j=0}^{4} c_j \zeta^j$
$\eta = \frac{y}{\delta_t}$	$\omega = \frac{y}{\delta_m}$	$\zeta = \frac{y}{\delta_c}$
Conditions	Conditions	Conditions
$y = 0$	$y = 0$	$y = 0$
$T = 0 \quad \left(\frac{\partial T}{\partial y}\right)^2 = \frac{1}{D}\frac{\partial^2 T}{\partial y^2}$	$u = 0 \quad \left(\frac{\partial T}{\partial y}\right)\left(\frac{\partial u}{\partial y}\right) = \frac{\mathrm{Pr}}{D}\frac{\partial^2 u}{\partial y^2}$	$C = 0 \quad \left(\frac{\partial T}{\partial y}\right)\left(\frac{\partial C}{\partial y}\right) = \frac{\mathrm{Le}}{D}\frac{\partial^2 C}{\partial y^2}$
$y = \delta_t \quad (\eta = 1)$	$y = \delta_m \quad (\omega = 1)$	$y = \delta_c \quad (\zeta = 1)$
$T = 1 \quad \frac{\partial T}{\partial y} = \frac{\partial^2 T}{\partial y^2} = 0$	$u = 1 \quad \frac{\partial u}{\partial y} = \frac{\partial^2 u}{\partial y^2} = 0$	$C = 1 \quad \frac{\partial C}{\partial y} = \frac{\partial^2 C}{\partial y^2} = 0$
Coefficients	Coefficients	Coefficients
$a_0 = 0$	$b_0 = 0$	$c_0 = 0$
$a_1 = \frac{3}{D}\left(\sqrt{1 + \frac{4}{3}D} - 1\right)$	$b_1 = \frac{6F}{1 + 3F}$	$c_1 = \frac{6H}{1 + 3H}$
$\frac{A}{D = 1 + B}$	$F = \frac{2\,\mathrm{Pr}\,\Delta_1}{a_1 D}$	$H = \frac{2\,\mathrm{Le}\,\Delta_1}{a_1 D\,\Delta_2}$
$a_2 = 6 - 3a_1$	$b_2 = 6 - 3b_1$	$c_2 = 6 - 3c_1$
$a_3 = -8 + 3a_1$	$b_3 = -8 + 3b_1$	$c_3 = -8 + 3c_1$
$a_4 = 3 - a_1$	$b_4 = 3 - b_1$	$c_4 = 3 - c_1$

$$\frac{\delta_t}{x} = \left\{\frac{2a_1}{\delta_t^{**}}\,\frac{(1 + D)}{\mathrm{Pe}_x}\right\}^{1/2} \tag{15}$$

after Pozvonkov, et al. [2], and the thicknesses of the momentum and mass diffusion boundary layers then follow from equations (13)–(15). The rate of melting follows from equations (5) and (15) and is

$$\xi\sqrt{\mathrm{Pe}_{\bar{x}}} = a_1 D\left\{\frac{\delta_t^{**}}{2a_1(1 + D)}\right\}^{1/2} \tag{16}$$

Likewise, the rate of heat transfer at the interface, or Nusselt number, is

$$\mathrm{Nu}_{\bar{x}} = \frac{\bar{h}\bar{x}}{\bar{K}_F} = \left\{\frac{a_1}{2(1 + D)}\,\delta_t^{**}\mathrm{Pe}_{\bar{x}}\right\}^{1/2} \tag{17}$$

The salinity or concentration $\bar{C}_F$ at the phase interface is not known a priori, but it can be determined from a mass balance on the dissolved species at the melt line $\bar{y} = 0$. This balance is, in general,

$$\dot{\bar{m}}_c = -\bar{\rho}\bar{\gamma}\left.\frac{\partial \bar{C}}{\partial \bar{y}}\right|_{\bar{y}=0} + \bar{C}_F(\dot{\bar{m}}_c + \dot{\bar{m}}) \tag{18}$$

where $\dot{\bar{m}}_c$ (kg/m²-sec) is the flux of dissolved species at the interface; $\dot{\bar{m}}$ (kg/m²-sec), the melting rate, is from equation (5); and $\bar{\rho}$ is the density of the mixture. Since the solid phase is impervious to the dissolved species ($\dot{\bar{m}}_c = 0$) during the melting of glacial ice, the foregoing equation reduces to

$$-\bar{C}_F\dot{\bar{m}} = -\bar{\rho}\bar{\gamma}\left.\frac{\partial \bar{C}}{\partial \bar{y}}\right|_{\bar{y}=0}$$

or, in the normalized system introduced earlier,

$$\frac{\left(\frac{\bar{C}_F}{\bar{C}_\infty}\right)}{1 - \left(\frac{\bar{C}_F}{\bar{C}_\infty}\right)} = \left(\frac{\bar{\rho}}{\bar{\rho}_F}\right)\left(\frac{\partial C}{\partial \zeta}\right)_{\zeta=0}\left(\frac{\delta_t}{\delta_c}\right)\frac{\mathrm{Le}}{a_1 D} \tag{19}$$

The concentration of dissolved species $\bar{C}_F$ is the result of a balance between the bulk motion and the rate of diffusion and is independent of space coordinates.

Solutions for Heat, Mass, and Momentum Transfer

The equations described in the preceding section were solved on a CDC 3800 computer for a range of values of the thermal and flow parameters. Computations for the ratio of the thermal and momentum boundary layers are illustrated in Fig. 2. These results indicate that the thermal boundary layer increases in thickness as the Stefan number A is increased,[3] but different subcooling conditions in the melting solid phase ($B = 0.0$, 0.2, and 0.5) have little effect on the thermal-boundary-layer thickness for $A \leqq 0.40$. A practical limit for A at standard conditions for water is $A \leqq 1.25$, which represents $\bar{T}_\infty - \bar{T}_F = 100$ deg C. The ratio of the mass-diffusion (salinity) and momentum-boundary-layer thicknesses is appreciably affected both by the fluid Stefan number A and the solid Stefan number B. The greater relative thickness of δ_c with increased A is due to the change in the rates of mass and momentum transport in the boundary layer as the temperature of the water is increased. The rate of mass transport approaches the momentum transport rate in the water as the temperature $\bar{T}_\infty$ is increased, since the kinematic viscosity $\bar{\nu}$ of the water drops sharply with rising temperature.

The change in the boundary-layer thickness ratio Δ_2 with the solid Stefan number B can be understood when reference is made to Fig. 3. Increased thermal transport to the solid decreases the rate of melting at the interface (for A constant) with a corresponding decrease in the thickness of the layer over which the dissolved species mix with the pure water generated at the boundary between phases. The increased rate of melting that accompanies increased Stefan number A (or greater thermal driving force $\bar{T}_\infty - \bar{T}_F$ is also evidenced by the results in Fig. 3. The

---

[3] G. S. H. Lock suggested in his rapport "Heat Transfer With Phase Transformation" at the Fourth International Heat Transfer Conference that the parameter A be named the Stefan number in honor of the scientist who pioneered the study of heat transfer in systems undergoing melting and solidification. The parameter B is a form of the Stefan number for the solid phase.

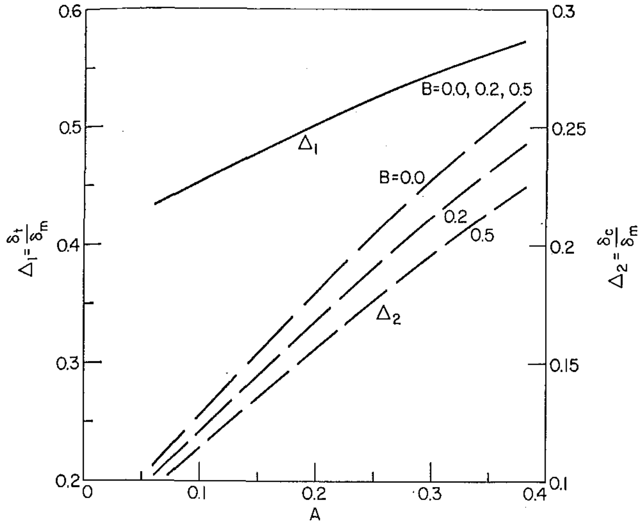

Fig. 2 The ratio of thermal and momentum boundary-layer thicknesses Δ_1 and mass diffusion and momentum boundary-layer thicknesses Δ_2 as a function of Stefan number *A*; three conditions of increased heat conduction into the solid are denoted by increasing values of the solid Stefan number *B*

concentration gradient at the melt interface is plotted in Fig. 4. The decreased value of the gradient $\partial C/\partial\zeta|_{\zeta=0}$ with increasing Stefan number *A* is a result of the thickening of the mass diffusion boundary layer δ_c with increased temperature differences $\bar{T}_\infty - \bar{T}_F$. Likewise, an increase in the solid Stefan number *B* results in a decrease in δ_c together with a corresponding increase in the concentration gradient near the melt interface, as indicated by the results plotted in Fig. 4.

Some representative results for heat, mass, and momentum transfer are summarized in Table 2. The momentum thickness δ_m^{**} is unaffected by changing thermal conditions, but noticeable increases can be seen in both the energy and concentration thicknesses as the Stefan number *A* is increased. The lower values of δ_t^{**} and δ_c^{**} that occur with increased subcooling of the solid result from the decreased melting rates that accompany the conduction of heat into the ice. The heat transfer coefficient at the melt interface (denoted by the Nusselt number Nu) is shown in relation to the equivalent Nusselt number for flow over a flat surface with no melting,

$$\mathrm{Nu}_{\bar{x},\mathrm{ref}}\,(\mathrm{Pr})^{-1/3} = 0.332(\mathrm{Re}_{\bar{x}})^{1/2} \tag{20}$$

The change in the Nusselt number with increasing Stefan number *A* has been described previously by Pozvonkov, et al. [2], for the case $B = 0.0$, and the increased heat transfer coefficient due to subcooling of the solid (for fixed *A*) is shown in Table 2 for the conditions given by $B = 0.20, 0.50$. The results for the Nusselt number at $B = 0.0$ also compare favorably with previous computations by Yen and Tien [1], who applied the classical Leveque solution for the thin thermal boundary layer to the problem of steady-state melting in forced flow. A recent communication by Yen and Tien [9] illustrates the good agreement between the two methods for $B = 0.0$.

Speed of Sound Near Melting Glacial Ice

Knowledge of the speed of sound as a function of environmental conditions is important in underwater acoustics for determining the refraction and propagation of sound in the ocean. It is possible to use the temperature and salinity profiles from the foregoing analysis to model the sound speed variation near melting glacial ice in sea water. This model situation offers insight into the physical processes that interact to produce changes in the sound speed in a polar environment. The speed of sound in sea water is a function of temperature, pressure, and salinity. Empirical equations have been developed over the years, using a mass of experimental data for widely varying conditions and seawater samples, to precisely relate the sound speed to those parameters that determine its variation in the sea.

The classical results of Del Grosso [3] are useful for determining the sound speed changes that occur in the thermal and mass diffusion boundary layers near melting ice in sea water. When pressure changes are absent, the equation for sound speed is

$$\begin{aligned} S = {} & 1448.6 + 4.618\bar{T} - 5.23 \times 10^{-2}\bar{T}^2 + 2.3 \times 10^{-4}\bar{T}^3 \\ & + 1.25(\bar{C} - 35.0) - 1.1 \times 10^{-2}(\bar{C} - 35.0)\bar{T} \\ & + 2.7 \times 10^{-8}(\bar{C} - 35.0)\bar{T}^4 \\ & \times - 2.0\ 10^{-7}(\bar{C} - 35.0)^4(1 + 0.577\bar{T} - 7.2 \times 10^{-3}\bar{T}^2) \end{aligned} \tag{21}$$

where the sound speed $\bar{S}$ is in the units of meters per second, the temperature $\bar{T}$ is in degrees Centigrade, and the salinity $\bar{C}$ is in

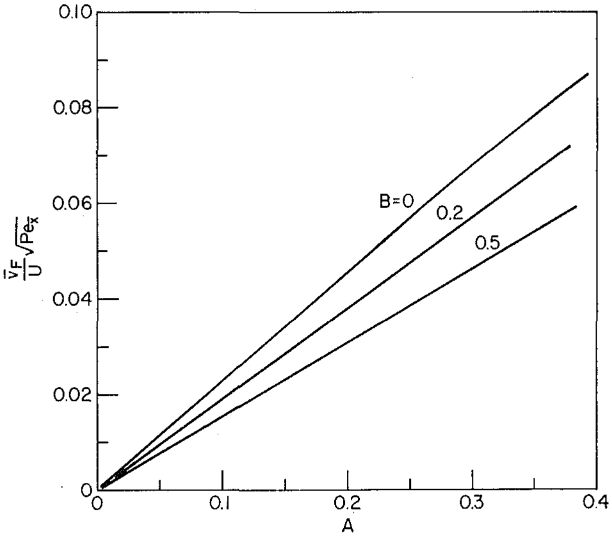

Fig. 3 The rate of melting at the phase interface $\xi\sqrt{Pe_{\bar{x}}}$ as a function of the Stefan number *A* for three conditions of solid subcooling denoted by the Stefan number *B*

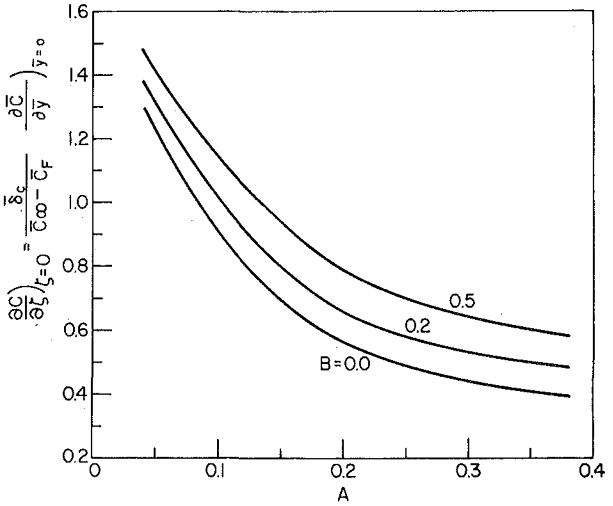

Fig. 4 The normalized concentration gradient $\partial C/\partial\zeta|_{\zeta=0}$, or rate of mass diffusion at the melt interface, as a function of the Stefan number *A* for three conditions of solid-phase subcooling

Table 2 Heat and mass transfer results

B	δ_m^{**}	δ_t^{**}	δ_c^{**}	$\frac{\delta_c}{\delta_m}$	$\frac{\delta_t}{\delta_m}$	$\frac{\mathrm{Nu}\bar{x}}{\mathrm{Nu},\bar{x}_{\mathrm{ref}}}$	$\frac{\bar{v}_F}{U}(\mathrm{Pe}\bar{x})^{1/2}$
			(A = 0.10, Pr = 10.27)				
0.00	0.117	0.0594	0.0217	0.133	0.449	0.938	0.0299
0.20	0.117	0.0592	0.0202	0.126	0.448	0.946	0.0192
0.50	0.117	0.0590	0.0188	0.120	0.447	0.955	0.0155
			(A = 0.20, Pr = 7.91)				
0.00	0.117	0.0652	0.0315	0.180	0.499	0.890	0.0452
0.20	0.117	0.0652	0.0291	0.169	0.499	0.904	0.0382
0.50	0.117	0.0648	0.0264	0.157	0.493	0.923	0.0312
			(A = 0.50, Pr = 4.30)				
0.00	0.118	0.0815	0.0557	0.309	0.629	0.782	0.109
0.20	0.118	0.0815	0.0519	0.289	0.629	0.812	0.094
0.50	0.118	0.0799	0.0474	0.266	0.620	0.837	0.078
			(A = 1.00, Pr = 2.32)				
0.00	0.118	0.1006	0.0837	0.480	0.797	0.650	0.200
0.20	0.118	0.1006	0.0795	0.452	0.797	0.686	0.175
0.50	0.118	0.0994	0.0741	0.419	0.781	0.730	0.149

parts per thousand (ppt). More recent correlations are now available [10] for sound speed in sea water as a function of temperature, pressure, and salinity.

Some results using equation (21) are plotted in Fig. 5 for water temperatures $\bar{T}_\infty$ of 5 and 10 deg C. For each case the salinity of the sea water far from the ice was taken as 35 ppt and the melting glacial ice was considered to be at the temperature 0 deg C. The ratio $\bar{C}_F/\bar{C}_\infty$ was determined from equation (19). The distance from the ice-phase boundary is normalized by the thermal boundary-layer thickness δ_t in the figure just mentioned, and the thickness ratios δ_c/δ_t and δ_t/δ_m are noted. When the water temperature is 10 deg C, the change in sound speed reaches 80 percent of the total change at $y = \delta_c = 0.30\,\delta_t$. At this point the salinity $\bar{C}$ = 35 ppt, and the temperature is 5.5 deg C. The change in sound speed appears to be confined to a layer near the phase interface where the temperature and salinity are rapidly changing with distance from the region of melting, as might be expected from the heat and mass transfer analysis.

Summary

Integral methods of solution have been used for the simultaneous calculation of the momentum, thermal, and mass diffusion boundary layers during the steady-state melting of pure (glacial) ice in sea water.

The results show that the principal driving forces for the simultaneous transport processes are the Stefan numbers for the fluid phase $A = \bar{c}_{pF}(\bar{T}_\infty - \bar{T}_F)\bar{M}^{-1}$ and solid phase $B = \bar{c}_{ps}(\bar{T}_F - \bar{T}_0)\bar{M}^{-1}$.

The momentum, energy, and mass diffusion equations for the fluid phase are interdependent due to the appearance of the melt velocity at the interface—or the rate of mass generation due to phase transformation—in each of the three equations. The mass diffusion equation is used to model the sea-water salinity distribution near the melting ice.

The effect of increased fluid Stefan number A is to increase the thermal boundary layer thickness, while the solid phase Stefan number B does not greatly affect the thermal boundary layer for $A < 0.50$. The rate of mass generation at the interface and the thickness of the mass diffusion boundary layer are both appreciably affected by the parameters A and B. The effect of larger Stefan number A is to increase both the mass diffusion boundary-layer thickness and the rate of mass generation. Increased subcooling of the solid decreases both the melting rate and the mass diffusion boundary-layer thickness when A is constant.

The results of the calculations have been used to model the effects of temperature and salinity on the speed of sound near melting ice in sea water. Sound speed profiles are presented for water temperatures of 5 and 10 deg C and for a free-stream salinity of 35 ppt. The results show that for both cases 80 percent of the change in sound speed occurs in the mass diffusion boundary layer.

Acknowledgment

The author wishes to thank the Naval Research Laboratory (NRL) for the support of this work. Further, the many helpful comments of R. A. Skop of NRL and Y. C. Yen of the U. S. Army Cold Regions Research and Engineering Laboratory are appreciated. One of the reviewers for the JOURNAL OF HEAT TRANSFER is to be thanked for pointing out an untenable assumption in the original mass transfer development.

References

1 Yen, Y. C., and Tien, C., "Laminar Heat Transfer Over a Melting Plate, the Modified Leveque Problem," *J. Geophy. Res.*, Vol. 68, No. 12, 1963, pp. 3673–3678.

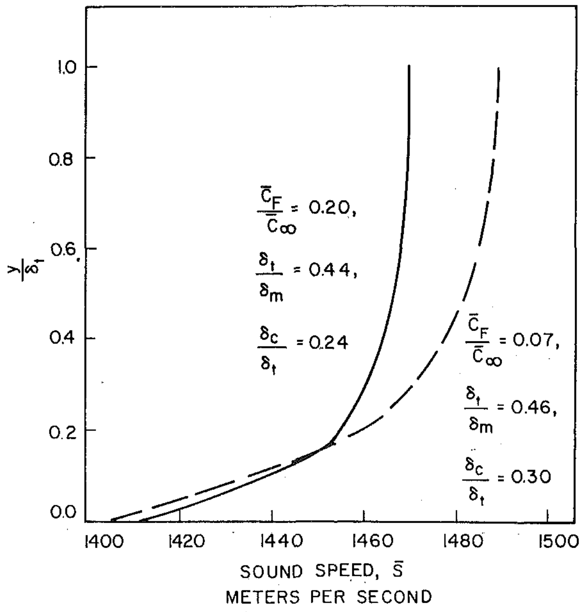

Fig. 5 The speed of sound in sea water $\bar{S}$ as a function of the normal distance from the melt interface for a free-stream salinity condition of 35 ppt and water temperatures of 5 deg C (solid line) and 10 deg C (dashed line); the solid temperature $\bar{T}_0$ = 0 deg C

2 Pozvonkov, F. M., Shurgalskii, E. F., and Axselrod, L. S., "Heat Transfer at a Melting Flat Surface Under Conditions of Forced Convection and Laminar Boundary Layer," *International Journal of Heat and Mass Transfer*, Vol. 13, 1970, pp. 957–962.

3 Del Grosso, V. A., "The Velocity of Sound in Sea Water at Zero Depth," Naval Research Laboratory Report 4002, 1952.

4 Bird, R. B., Stewart, W. E., and Lightfoot, E. N., *Transport Phenomena*, Chapter 19, Wiley, New York, 1960.

5 Griffin, O. M., "On the Melting of Solids to Non-Newtonian Fluids," *Chem. Engr. Sci.*, Vol. 25, 1970, pp. 109–117.

6 Roberts, A. L., "On the Melting of a Semi-Infinite Body Placed in a Warm Stream of Air," *J. Fluid Mech.*, Vol. 4, 1958, pp. 505–528.

7 Kays, W. M., *Convective Heat and Mass Transfer*, Chapters 10 and 14, McGraw-Hill, New York, 1966.

8 Griffin, O. M., and Szewczyk, A. A., "An Analytical and Experimental Study of the Melting of Bulk Solids on an Inclined Plane Heated Surface," in: *Heat Transfer 1970*, Vol. 1, Elsevier, Amsterdam, 1970.

9 Yen, Y. C., and Tien, C., "Heat Transfer at a Melting Flat Surface Under Conditions of Forced Convection and Laminar Boundary Layer," *International Journal of Heat and Mass Transfer*, Vol. 14, 1971, pp. 1875–1876.

10 Del Grosso, V. A., and Mader, C. W., "Speed of Sound in the Sea Water Samples," *J. Acous. Soc. Am.*, Vol. 53, No. 3, Part 2, pp. 961–974.

J. C. MUEHLBAUER
Department of Mechanical Engineering,
Clemson University,
Clemson, S. C.

J. D. HATCHER

D. W. LYONS
College of Industrial Management
and Textile Science,
Clemson University,
Clemson, S. C.

J. E. SUNDERLAND
Department of Mechanical and
Aerospace Engineering,
University of Massachusetts,
Amherst, Mass.

Transient Heat Transfer Analysis of Alloy Solidification

Approximate solutions are obtained for the temperature distribution and rate of phase change for the transient one-dimensional solidification of a finite slab of a binary alloy. The alloy is selected to avoid the eutectic composition so that solidification takes place over a range of temperatures. The slab is initially superheated and has a uniform temperature distribution. Solidification occurs after one surface is cooled by convection while the other surface is insulated. Temperature distributions are determined analytically and experimentally and are in reasonably good agreement.

Introduction

Transient heat transfer problems involving phase changes occur in areas such as solidification of castings, food processing, polymer production, welding, etc. Few exact solutions for the temperature distributions have been found for these problems due to inherent nonlinearities. An exact solution for the temperature distribution and phase change position of a melting or solidifying semi-infinite body was reported by Neumann [1].[1] The body was initially at a uniform temperature and the surface temperature was impulsively changed and held at a constant value so that a phase change occurred. For this problem the phase change position was proportional to the square root of time. Several investigators such as Weiner [2] and Citron [3] have studied the problem of multiple phase changes and obtained solutions similar to those found by Neumann.

Approximate solutions for this problem were reviewed by Muehlbauer and Sunderland [4]. The application of approximate solutions to the solidification of castings was reviewed in an excellent paper by Jones [5].

No closed-form exact solutions have been obtained when the freezing medium has finite thickness except for the case of zero superheat. Thus approximate methods must be used to describe the process analytically. One of the most useful techniques is the heat-balance integral method developed by Goodman [6, 7, 8]. Tien and Geiger [9] used the heat-balance integral method to obtain approximate solutions to the solidification of a binary eutectic. They used a time-dependent surface temperature. Cho and Sunderland [10] presented an exact solution for the temperature distribution and rate of phase change for a semi-infinite body where the phase change occurred over a range of temperatures. This solution assumed that the surface temperature was instantaneously changed and held at a constant temperature different from the phase change temperature range and the initial temperature. This exact solution and Goodman's integral techniques were used to determine the temperature distribution in a finite slab with a constant temperature at one face while the other face was insulated.

An experimental study for solidification has been presented by Bailey and Dula [11]. Their investigation indicated that the rate of freezing of finite slabs of water is similar to that found using Neumann's solution. Experimental studies related to solidification of metals have been reported by Bishop, et al. [12] and Bishop and Pellini [13]. No analytical comparisons were presented; however, excellent experimental data were presented for several alloys. Simurik [14] presented an experimental method for observing the freezing of castings. The method used a wax model and the phase change front was optically observed. Hills and Moore [15] used Goodman's integral method to study the solidification of lead and tin. They obtained good agreement between analytical and experimental results.

The current work is concerned with the transient one-dimensional solidification of a superheated finite slab of a binary alloy where the change of phase occurs over a range of temperatures. All physical properties of each phase are assumed to remain constant but may be different for different phases. One surface of

---

[1] Numbers in brackets designate References at end of paper.

Contributed by the Heat Transfer Division of The American Society of Mechanical Engineers and presented at the ASME-AIChE Heat Transfer Conference, Atlanta, Ga., August 5–8, 1973. Manuscript received by the Heat Transfer Division January 31, 1972. Paper No. 73-HT-4.

the slab is exposed to convection heat transfer, while the other surface is insulated.

Problem Statement

During the solidification process the slab may be composed of a liquid region of molten metal, a region that is both liquid and solid (two-phase or mushy region), and a solid region. These regions may exist singularly or simultaneously. Since they do not all exist throughout the entire solidification period (from pouring until the casting reaches ambient temperature), the solidification process is divided into smaller time intervals. If the cooling rate is sufficiently low that the two-phase and solidified regions do not occur all at the same time, the sequence of events that is likely to occur is shown in Fig. 1. In the first time interval or stage the surface temperature is lowered by convective cooling. The region of the slab influenced by the heat transfer lies between the cooled surface and a plane denoted by $P(t)$. This stage continues until the surface temperature drops to T_b, the liquidus temperature, at which time stage 2 is initiated. In stage 2 there exists a two-phase region and a liquid region that is only partially affected by surface cooling. However, if the cooling rate is very low, the entire liquid region may be influenced by surface cooling before the two-phase region forms. In such a case, stage 2 will not occur and the process will go from stage 1 directly to stage 3 where there is a two-phase and a liquid region. In stage 4 the entire region is two-phase. In stage 5 the solid and two-phase regions exist, and the final stage, stage 6, involves cooling of the solidified slab. The situation of very rapid cooling that would yield solid, two-phase, and liquid regions existing simultaneously is covered by Muehlbauer [16].

The temperature distribution for each stage is determined by first changing the variables and then using Goodman's [6] heat balance integral techniques. The energy liberated due to solidification in the two-phase region is treated as a pseudo specific heat, $\bar{C}p = \lambda/\Delta T$ as suggested by Paschkis [17], where ΔT is the difference between the solidus and liquidus temperatures. Similarly, a pseudo thermal diffusivity $\bar{\alpha}$ can be defined by

$$\bar{\alpha} = \frac{k}{\rho(Cp + \bar{C}p)}$$

so that the energy equation for the two-phase region becomes similar in form to that of the other regions.

A slab of thickness $2L$ with convection at the boundaries can be divided into a slab of thickness L with convection at one boundary and no heat flow at the other boundary because of the symmetry of the mathematical problem. The boundary conditions are thus

$$x = 0 \qquad \frac{\partial T}{\partial x} = \frac{T - T_A}{R_i}$$

and

$$x = L \qquad \frac{\partial T}{\partial x} = 0$$

Analytical

First Time Period. During this period the temperature at position $x = 0$ is reduced to T_b at time t_1, when the effect of surface cooling has penetrated to a position $x = P(t_1)$, where $P(t_1) < L$. This period is graphically represented in Fig. 1. The problem statement for the affected liquid region is:

$$\frac{\partial T_{L1}}{\partial t} = \alpha_L \frac{\partial^2 T_{L1}}{\partial x^2} \qquad 0 < x < P \qquad 0 < t < t_1 \tag{1}$$

$$x = P \qquad T_{L1} = T_0 \tag{a}$$

$$x = P \qquad \frac{\partial T_{L1}}{\partial x} = 0 \tag{b}$$

$$x = 0 \qquad \frac{\partial T_{L1}}{\partial x} = \frac{T_{L1} - T_A}{R_1} \tag{c}$$

$$t = 0 \qquad P = 0 \tag{d}$$

Using the heat balance integral technique with an assumed temperature profile in the affected liquid region of the form

$$T_{L1} = a + bx + cx^2 \tag{2}$$

the temperature profile is found to be

$$T_{L1} = T_0 - (T_0 - T_A)\frac{(P - x)^2}{P^2 + 2PR_1} \tag{3}$$

with the effective cooling distance $P(t)$ given by

$$P^2 + 4PR_1 - 8R_1^2 \ln\left(1 + \frac{P}{2R_1}\right) = 12\alpha_L t \tag{4}$$

This period ends when the temperature of the free slab surface reaches T_b. The time t_1 when this occurs is given by

$$t_1 = \frac{2}{3}\frac{R_1^2}{\alpha_L}\left\{\frac{1}{2}\left(\frac{T_0 - T_b}{T_b - T_a}\right)^2 + \left(\frac{T_0 - T_b}{T_b - T_a}\right) - \ln\left(1 + \frac{T_0 + T_b}{T_b - T_a}\right)\right\} \tag{5}$$

Second Time Period. During the second period there exists a mushy region and a liquid region. Part of the liquid region is not affected by the surface cooling until time t_2, when the effect of cooling reaches the position $x = L$. The mathematical statement of the problem using the illustration of Fig. 1 for the liquid region during stage 2 is

Nomenclature

a, b, c = temperature profile coefficients that may be functions of time
C_1 = integration constant in equation (20)
Cp = specific heat
$\bar{C}p$ = pseudo specific heat
h = heat transfer coefficient
k = thermal conductivity
K_L = thermal conductivity ratio, k_L/k_M
K_M = thermal conductivity ratio, k_M/k_S
L = slab length
P = distance of cooling penetration
R_i = ratio k/h
s = liquidus phase front position
t = time
t_i = time constant
T = temperature
T_{ji} = temperature variable
T_A = ambient temperature
T_b = liquidus temperature
T_0 = initial temperature
T_v = solidus temperature
v = solidus phase front position
x = distance from cooled surface
α = thermal diffusivity
$\bar{\alpha}$ = pseudo thermal diffusivity, $k/\rho \times (Cp + \bar{C}p)$
η = dimensionless variable, $x/2\sqrt{\bar{\alpha}(t - t_i)}$
λ = latent heat
ρ = density

Subscripts

j = L, M, S designate liquid, mushy, and solid regions, respectively
i = 1, 2, 3 . . . 6 designates time when used with t; designates time interval when used with other symbols.

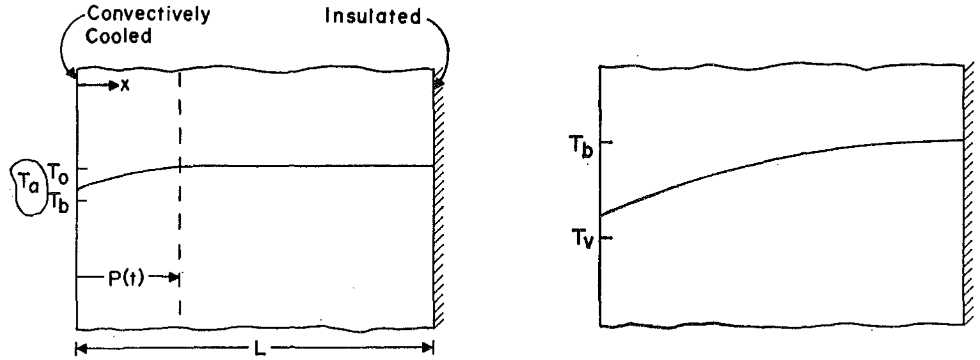

STAGE 1 $0<t<t_1$
Entire slab superheated

STAGE 4 $t_3<t<t_4$
Entire slab two phase

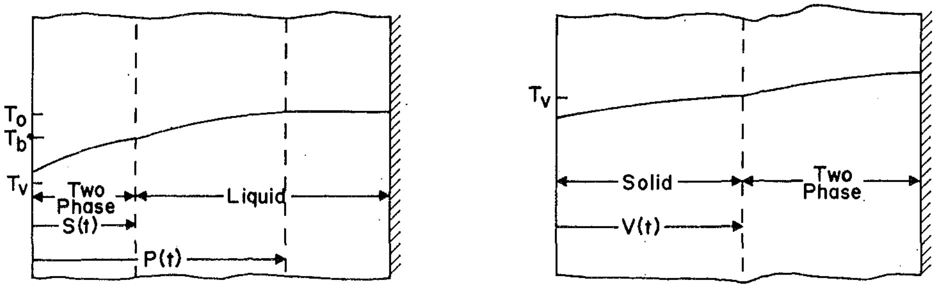

STAGE 2 $t_1<t<t_2$
Development of two phase region with P(t)<L

STAGE 5 $t_4<t<t_5$
Development of solid region

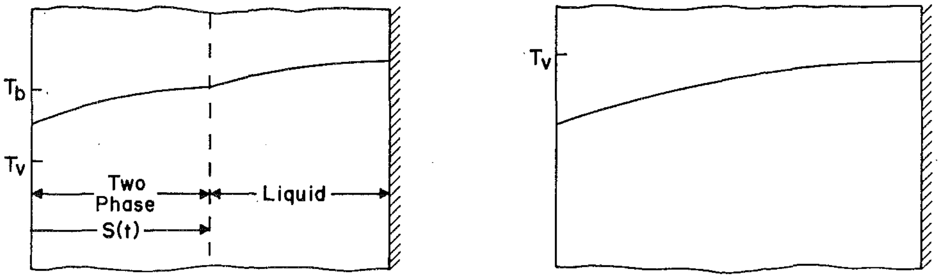

STAGE 3 $t_2<t<t_3$
Development of two phase region for time after P(t)=L but before initiation of solid region.

STAGE 6 $t_5<t<t_6$
Entire slab solidified

Fig. 1 Sequence of events that are likely to occur during solidification of a binary alloy with extended freezing range

$$\frac{\partial T_{L2}}{\partial t} = \alpha_L \frac{\partial^2 T_{L2}}{\partial x^2} \qquad s < x < P \qquad t_1 < t < t_2 \tag{6}$$

$$x = P \qquad T_{L2} = T_0 \tag{a}$$

$$x = P \qquad \frac{\partial T_{L2}}{\partial x} = 0 \tag{b}$$

$$x = s \qquad T_{L2} = T_b \tag{c}$$

$$x = s \qquad K_L \frac{\partial T_{L2}}{\partial x} = \frac{\partial T_{M2}}{\partial x} \tag{d}$$

$$t = t_1 \qquad T_{L2} = T_{L1} \tag{e}$$

$$t = t_1 \qquad s = 0 \tag{f}$$

Clearly the number of restraints (a)–(f) exceeds the number of constants of integration of equation (6); however, these equations will be used later to determine constants that appear in polynomial approximations of the temperature distributions.

For the mushy region during stage 2,

$$\frac{\partial T_{M2}}{\partial t} = \bar{\alpha} \frac{\partial^2 T_{M2}}{\partial x^2} \qquad 0 < x < s \qquad t_1 < t < t_2 \tag{7}$$

$$x = s \qquad T_{M2} = T_b \tag{a}$$

$$x = 0 \qquad \frac{\partial T_{M2}}{\partial x} = \frac{T_{M2} - T_A}{R_2} \tag{b}$$

and additional conditions are given by equations (6) (*d*)–(*f*).

The temperature profile for the liquid region is found using the heat balance integral technique to be

$$T_{L2} = T_0 - (T_0 - T_b)\cdot\left(\frac{P-x}{P-s}\right)^2 \tag{8}$$

The temperature profile for the mushy region is found by a change of variables

$$\eta = \frac{x}{2\sqrt{\bar{\alpha}(t-t_1)}} \tag{9}$$

in equation (7). From the transformed equation, the temperature profile for this region is found to be

$$T_{M2} = T_b - (T_b - T_A) \times \left\{\frac{\operatorname{erf}\left(\frac{s}{2\sqrt{\bar{\alpha}(t-t_1)}}\right) - \operatorname{erf}\left(\frac{x}{2\sqrt{\bar{\alpha}(t-t_1)}}\right)}{\frac{R_2}{\sqrt{\pi\bar{\alpha}(t-t_1)}} + \operatorname{erf}\left(\frac{s}{2\sqrt{\bar{\alpha}(t-t_1)}}\right)}\right\} \tag{10}$$

The effective cooling distance $P(t)$ is found by a heat balance on the liquidus phase front $s(t)$. This yields

$$P = s + 2K_L\left\{\frac{T_0 - T_b}{T_b - T_A}\right\} \times \left\{R_2 + \sqrt{\pi\bar{\alpha}(t-t_1)}\operatorname{erf}\frac{s}{2\sqrt{\bar{\alpha}(t-t_1)}}\right\}\exp\frac{s^2}{4\bar{\alpha}(t-t_1)} \tag{11}$$

The liquidus phase front is determined using a technique suggested by Goodman [6]. The boundary conditions $T_{L2} = T_b$ at $s(t)$ and $T_{M2} = T_b$ at $s(t)$ are differentiated with respect to time by the chain rule. The time-derivatives of the temperature profiles are replaced using the energy equations of the liquid and mushy regions. Making these substitutions and equating the results yields

$$\frac{\alpha_L}{P-s} = \frac{s}{2(t-t_1)} \tag{12}$$

Combining with equation (11) yields the following implicit expression for the liquidus phase front position:

$$\frac{sK_L}{\alpha_L(t-t_1)} = \frac{T_b - T_A}{T_0 - T_b} \times \left\{\frac{\exp\left\{-\frac{s^2}{4\bar{\alpha}(t-t_1)}\right\}}{R_2 + \sqrt{\pi\bar{\alpha}(t-t_1)}\operatorname{erf}\frac{s}{2\sqrt{\bar{\alpha}(t-t_1)}}}\right\} \tag{13}$$

This period ends when the effect of cooling spans the entire slab, i.e., $P(t) = L$, $t = t_2$. Time t_2 is found by placing $P(t) = L$ in equation (11) and solving in combination with equation (13).

Third Time Period. Liquid and mushy regions exist during the third period, which ends at t_3 when the liquidus phase front reaches the position $x = L$. With reference to Fig. 1 the problem can be described mathematically for the two regions. For the liquid region:

$$\frac{\partial T_{L3}}{\partial t} = \alpha_L\frac{\partial^2 T_{L3}}{\partial x^2} \qquad s < x < L \qquad t_2 < t < t_3 \tag{14}$$

$$x = L \qquad \partial T_{L3}/\partial x = 0 \tag{a}$$

$$x = s \qquad T_{L3} = T_b \tag{b}$$

$$x = s \qquad K_L\frac{\partial T_{L3}}{\partial x} = \frac{\partial T_{M3}}{\partial x} \tag{c}$$

$$t = t_2 \qquad T_{L3} = T_{L2} \tag{d}$$

$$t = t_2 \qquad s = s_2 \tag{e}$$

For the mushy region:

$$\frac{\partial T_{M3}}{\partial t} = \bar{\alpha}\frac{\partial^2 T_{M3}}{\partial x^2} \qquad 0 < x < s \qquad t_2 < t < t_3 \tag{15}$$

$$x = s \qquad T_{M3} = T_b \tag{a}$$

$$x = 0 \qquad \frac{\partial T_{M3}}{\partial x} = \frac{T_{M3} - T_A}{R_3} \tag{b}$$

$$t = t_2 \qquad T_{M3} = T_{M2} \tag{c}$$

and additional conditions are given by equations (14*c*) and (14*e*).

The mushy-region temperature distribution is the same as for the previous period, equation (10), except the time continues to t_3 and T_{M2} becomes T_{M3} and R_2 becomes R_3.

For the liquid region, the heat balance integral technique gives the temperature profile as

$$T_{L3} = T_b + \frac{(T_b - T_A)(2Lx - x^2 + s^2 - 2Ls)\exp\left\{-\frac{s^2}{4\bar{\alpha}(t-t_1)}\right\}}{2K_L(L-s)\left\{R_3 + \sqrt{\pi\bar{\alpha}(t-t_1)}\operatorname{erf}\frac{s}{\sqrt{2\,\bar{\alpha}(t-t_1)}}\right\}} \tag{16}$$

To determine an equation for the liquidus phase front position, the logarithm of an expression obtained from the boundary condition

$$x = s \qquad K_L\frac{\partial T_{L3}}{\partial x} = \frac{\partial T_{M3}}{\partial x} \tag{17}$$

is differentiated with respect to time. The resulting equation is then integrated from time t_2 to t by using the law of the mean. This yields

$$3\alpha_L(t-t_2) + (L-s)^2 - (L-s_2)^2 = (L-s)_{\xi_1}{}^2 \times \left\{\frac{s^2}{4\bar{\alpha}(t-t_1)} - \frac{s_2{}^2}{4\bar{\alpha}(t_2-t_1)} + \ln\left[\frac{R_3 + \sqrt{\pi\bar{\alpha}(t-t_1)}\operatorname{erf}\frac{s}{2\sqrt{\bar{\alpha}(t-t_1)}}}{R_3 + \sqrt{\pi\bar{\alpha}(t_2-t_1)}\operatorname{erf}\frac{s_2}{2\sqrt{\bar{\alpha}(t_2-t_1)}}}\right]\right\} \tag{18}$$

where $[L - s(t)]_{\xi_1}{}^2$ is $[L - s(t)]^2$ evaluated at time ξ_1 such that $t_2 \leq \xi_1 \leq t_3$. To evaluate $[L - s(t)]_{\xi_1}{}^2$, set $t = t_3$ and $s(t) = L$ in equation (18). However, the time t_3 is unknown and is determined from the fourth-time-period results.

Fourth Time Period. Throughout the fourth period, the slab exists in the mushy state, and the following equations apply:

$$\frac{\partial T_{M4}}{\partial t} = \bar{\alpha}\frac{\partial^2 T_{M4}}{\partial x^2} \qquad 0 < x < L \qquad t_3 < t < t_4 \tag{19}$$

$$x = L \qquad \frac{\partial T_{M4}}{\partial x} = 0 \tag{a}$$

$$x = 0 \qquad \frac{\partial T_{M4}}{\partial x} = \frac{T_{M4} - T_A}{R_4} \tag{b}$$

$$t = t_3 \qquad T_{M4} = T_{M3} \tag{c}$$

This period ends at time t_4 when the temperature at position $x = 0$ reaches T_v, which signifies the start of solid formation.

Following the heat balance integral technique up to the point of applying the initial condition produces a temperature profile of the form

$$T_{M4} = T_A + C_1(x^2 - 2Lx - 2LR_4) \exp \left\{ - \frac{3\bar{\alpha}(t - t_3)}{L^2 + 3LR_4} \right\} \tag{20}$$

At time t_3 the error-function form of T_{M3} does not satisfy the no-heat-flow boundary condition at position $x = L$. To avoid the difficulty of matching a polynomial profile and an error-function profile to satisfy the initial condition, the error-function form of T_{M3} is approximated at time t_3 with a polynomial T_M of the form

$$T_M = a + bx + cx^2 \tag{21}$$

subject to the conditions

$$x = L \qquad \frac{\partial T_M}{\partial x} = 0 \tag{22a}$$

$$x = L \qquad T_M = T_b \tag{22b}$$

$$x = 0 \qquad \frac{\partial T_M}{\partial x} + \frac{\partial T_{M3}}{\partial x} \tag{22c}$$

With the resulting polynomial approximation for T_M replacing T_{M3} in the initial condition $T_{M4} = T_{M3}$ at $t = t_3$, the constant C_1 in equation (20) is determined. The temperature profile is

$$T_{M4} = T_A + \frac{(T_b - T_A)(2LR_4 + 2Lx - x^2) \exp \left\{ - \dfrac{3\bar{\alpha}(t - t_3)}{L^2 + 3LR_4} \right\}}{2L \left\{ R_3 + \sqrt{\pi\bar{\alpha}(t_3 - t_1)} \operatorname{erf} \dfrac{L}{2\sqrt{\bar{\alpha}(t_3 - t_1)}} \right\}} \tag{23}$$

At time t_3 and position $x = L$, the temperature is T_b. This condition when applied to the temperature profile yields

$$\sqrt{\pi\bar{\alpha}(t_3 - t_1)} \operatorname{erf} \frac{L}{2\sqrt{\bar{\alpha}(t_3 - t_1)}} = \frac{L}{2} + R_4 - R_3 \tag{24}$$

which may be solved to obtain the time t_3, which is required also for the third-time-period solution. A combination of this equation and equation (23) gives the temperature profile as

$$T_{M4} = T_A + (T_b - T_A) \frac{(2LR_4 + 2Lx - x^2)}{L^2 + 2LR_4} \times \exp \left\{ - \frac{3\bar{\alpha}(t - t_3)}{L^2 + 3LR_4} \right\} \tag{25}$$

The fourth period ends when the temperature is T_v at position $x = 0$. When this condition is applied to the temperature profile, an expression for time t_4 is obtained

$$t_4 = t_3 + \frac{L^2 + 3LR_4}{3\bar{\alpha}} \ln \left\{ \frac{T_b - T_A}{T_v - T_A} \cdot \frac{2R_4}{L + 2R_4} \right\} \tag{26}$$

Fifth Time Period. A mushy region and a solid region exist during the fifth period as the solidus phase front moves from position $x = 0$ to position $x = L$. The problem statement for this period becomes the same as the third period if appropriate notational changes are made by replacing the mushy and liquid regions with solid and mushy regions, respectively. The temperature profile for the solid region becomes

$$T_{S5} = T_v - (T_v - T_A) \times \left\{ \frac{\operatorname{erf} \dfrac{v}{2\sqrt{\alpha_S(t - t_4)}} - \operatorname{erf} \dfrac{x}{2\sqrt{\alpha_S(t - t_4)}}}{\dfrac{R_5}{\sqrt{\pi\alpha_S(t - t_4)}} + \operatorname{erf} \dfrac{v}{2\sqrt{\alpha_S(t - t_4)}}} \right\} \tag{27}$$

and for the mushy region it is

$$T_{M5} = T_v + \frac{(T_v - T_A)(2Lx - x^2 + v^2 - 2Lv) \exp \left\{ - \dfrac{v^2}{4\alpha_S(t - t_4)} \right\}}{2K_M(L - v) \left\{ R_5 + \sqrt{\pi\alpha_S(t - t_4)} \operatorname{erf} \dfrac{v}{2\sqrt{\alpha_S(t - t_4)}} \right\}} \tag{28}$$

The solidus phase front position can be obtained from:

$$3\alpha_S(t - t_4) + (L - v)^2 - L^2 = (L - v)_{\xi_2}{}^2 \left\{ \frac{v^2}{4\alpha_S(t - t_4)} + \ln \left(1 + \frac{\sqrt{\pi\alpha_S(t - t_4)}}{R_5} \operatorname{erf} \frac{v}{2\sqrt{\alpha_S(t - t_4)}} \right) \right\} \tag{29}$$

where $[L - v(t)]_{\xi_2}{}^2$ is $[L - v(t)]^2$ evaluated at time ξ_2 such that $t_4 \leq \xi_2 \leq t_5$. To determine $[L - v(t)]_{\xi_2}{}^2$, set $t = t_5$ and $v(t) = L$ in equation (29). However, time t_5 is unknown and must be determined by the results of the sixth time period.

Sixth Time Period. During the sixth period the slab is cooled to ambient temperature. Equations (19) for the fourth period apply for this period if the necessary notational changes are made to replace the mushy region with a solid region. The temperature profile is given by

$$T_{S6} = T_A + (T_v - T_A) \frac{2LR_6 + 2Lx - x^2}{L^2 + 2LR_6} \exp \left\{ - \frac{3\alpha_S(t - t_5)}{L^2 + 3LR_6} \right\} \tag{30}$$

and the time t_5 can be determined from the graphical solution of

$$\sqrt{\pi\alpha_S(t_5 - t_4)} \operatorname{erf} \frac{L}{2\sqrt{\alpha_S(t_5 - t_4)}} = \frac{L}{2} + R_6 - R_5 \tag{31}$$

Experimental Investigation

To establish the usefulness of the analytical technique, temperature profiles were measured for the solidification of a superheated binary alloy. The alloy was cooled in a mold placed in a wind tunnel.

Alloy. A lead–tin alloy was chosen as the casting material because of its low but wide melting range. The two compositions used were 80–20 and 50–50 lead–tin (by weight). The properties required for the two alloys were obtained from several sources and are listed in the Appendix. The latent heat of fusion, mean specific heat as a liquid, and mean specific heat as a solid for the 50–50 alloy were obtained from Koerner [18]. The density as a function of temperature for the 50–50 alloy above 361 deg F was obtained from Koerner, and the remainder of data for both alloys was obtained from the ASM metals handbook. The thermal conductivity as a function of temperature for both alloys was obtained from a procedure suggested by Hsu [19]. This method develops property data as a volumetric function of each constituent of the alloy. Hsu has validated the expression for a liquid, but nothing is available for the solid mixture. Due to the lack of available data, this same method was used for the solid phase. The latent heat and the mean specific heats for liquid and solid for the 80–20 alloy were obtained, based on the method of Hsu.

Cooling Equipment. The mold was mounted flush with an inside wall of the wind tunnel shown in Fig. 2. Air was supplied to the

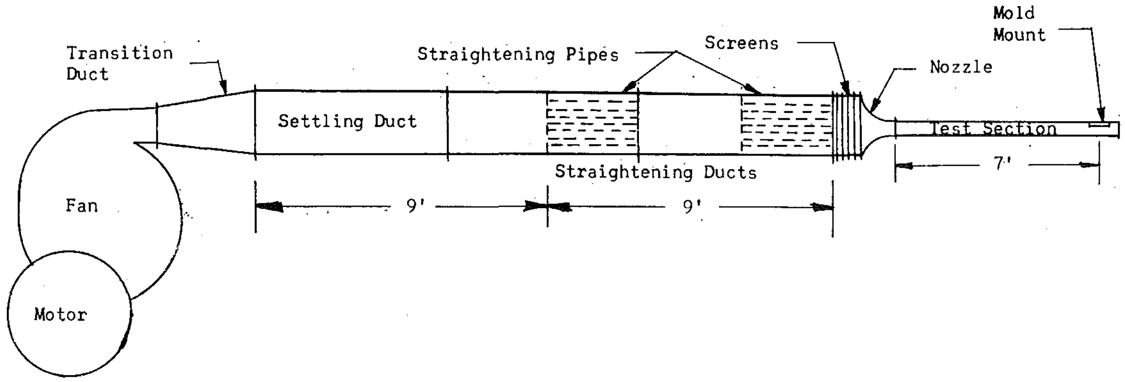

Fig. 2 Wind tunnel

test section through a nozzle constructed to the requirements specified by ASME [20]. With the addition of straightening ducts and screens, the turbulent eddies were reduced to a minimum. An accurate prediction of the convective heat transfer coefficient on the surface of the mold was obtained using a well-established equation given by Kays [21].

Mold. The sides of the mold, Fig. 3, were constructed from $^1/_4$-in. steel, and the base plate was made of aluminum. The top plate served as a cover and was put in place after the alloy was poured. During the tests the sides and top of the mold were covered with 8 in. of glass-wool insulation with a thermal conductivity of 0.0266 Btu/hr-ft-deg F at 80 deg F and 0.0433 Btu/hr-ft-deg F at 600 F. This minimized the heat loss and improved the one-dimensional solidification.

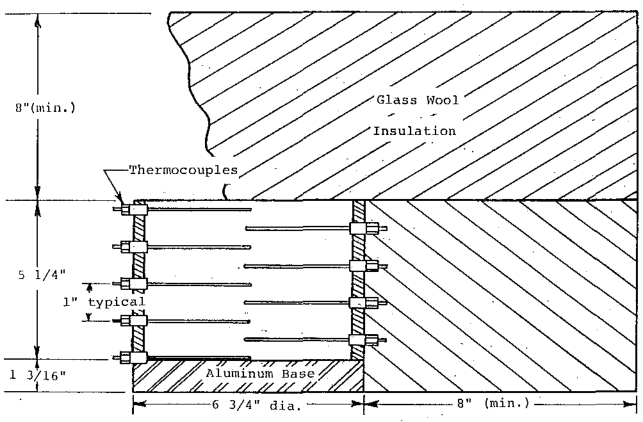

Fig. 3 Mold for alloy solidification

Temperature Measurement. The temperature measurements were obtained with $^1/_8$-in-OD ceramic-insulated grounded thermocouples. These thermocouples had a time response of 0.34 sec for recording 68.3 percent of a step temperature change in a water bath from 60 to 212 deg F. The emf output of these thermocouples was recorded using a multipoint recorder. The thermocouples were inserted through the side of the mold at $^1/_2$-in. intervals from the cold surface of the mold, and one thermocouple was placed just at the cold surface of the mold.

Procedure. The alloy was melted and the composition was varied by adding appropriate amounts of lead and tin. While the alloy was being melted, the mold was preheated. When the mold and alloy were at the desired uniform superheat temperature, the alloy was poured into the mold, and the top plate and top insulation were replaced. The wind tunnel was started and the thermocouple recording equipment was marked at zero time. Upon completion of a test, the solidified alloy was sectioned and analyzed to determine variation of composition in the vertical direction from the cooled surface of the mold.

Results and Discussion

The temperature distribution for a 50–50 lead–tin alloy that was initially superheated to 507 deg F is shown in Fig. 4. Fig. 5 shows the temperature distribution for an 80–20 lead–tin alloy that was initially superheated to 550 deg F.

The analytical and experimental results show reasonably good agreement. Some of the differences may result from experimental errors in location of the thermocouples, the influence of the thermocouples on the solidification of the alloy, inaccuracies in

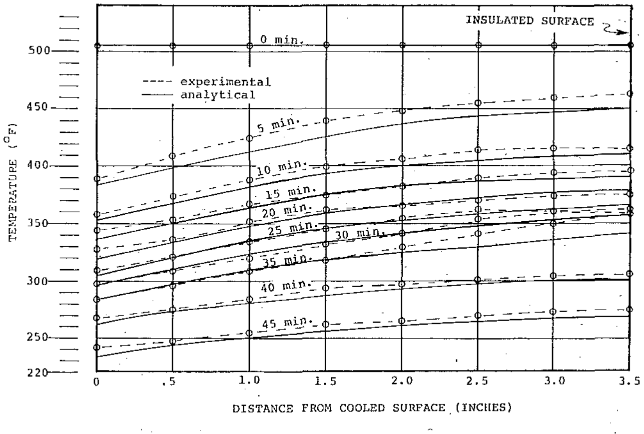

Fig. 4 Temperature profiles for solidification of 50–50 lead–tin alloy initally superheated to 507 deg F

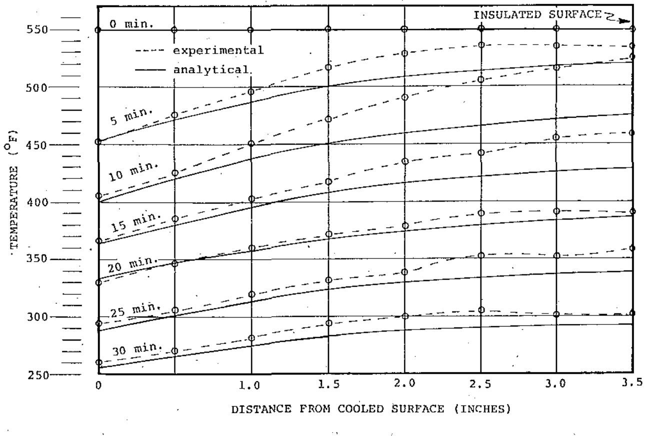

Fig. 5 Temperature profiles for solidification of 80–20 lead–tin alloy initially superheated to 550 deg F

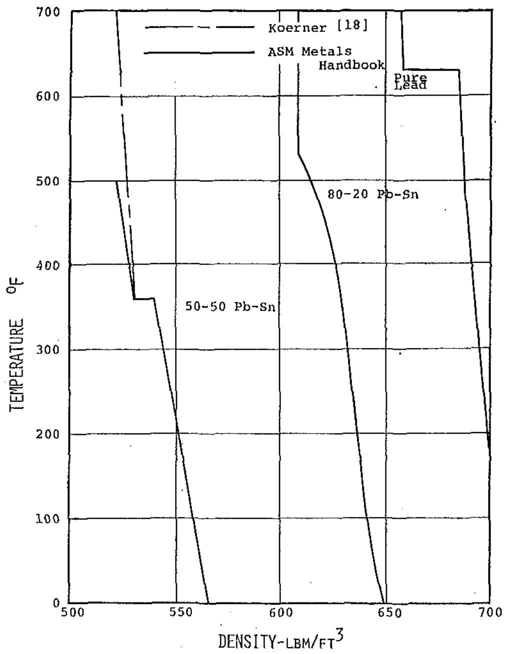

Fig. 6 Temperature versus density for lead–tin alloys

the analytical development, and composition changes in the alloy as solidification occurred. The casting was sectioned and a five percent variation in composition was measured. Another source of error resulted from the uncertainty in the property data, which was determined by the techniques previously discussed.

References

1 Neumann, F., in: *Die Partiellen Differentialgleichungen der Mathematischen Physik*, Vol. 2, 1912, p. 121.

2 Weiner, J. H., "Transient Heat Conduction in Multiphase Media," *British Journal of Applied Physics*, Vol. 6, 1955, p. 361.

3 Citron, J. S., "Heat Conduction in a Melting Slab," *Journal of Aerospace Science*, Vol. 27, 1960, p. 219.

4 Muehlbauer, J. C., and Sunderland, J. E., "Heat Conduction With Freezing or Melting," *Applied Mechanics Reviews*, Vol. 18, 1965, p. 951.

5 Jones, H., "A Comparison of Approximate Analytical Solutions of Freezing From a Plane Chill," *Journal of the Institute of Metals*, Vol. 97, 1969, p. 38.

6 Goodman, T. R., "The Heat-Balance Integral and Its Application to Problems Involving a Change of Phase," TRANS. ASME, Vol. 80, 1958, pp. 335–342.

7 Goodman, T. R., "The Heat-Balance Integral—Further Considerations and Refinements," JOURNAL OF HEAT TRANSFER, TRANS. ASME, Series C, Vol. 83, No. 1, Feb. 1961, pp. 83–86.

8 Goodman, T. R., "Application of Integral Methods to Transient Nonlinear Heat Transfer," *Advances in Heat Transfer*, Vol. 1, Irvine, T. F., and Hartnett, J. P., eds., 1964, p. 51.

9 Tien, R. H., and Geiger, G. E., "A Heat-Transfer Analysis of the Solidification of a Binary Eutectic System," JOURNAL OF HEAT TRANSFER, TRANS. ASME, Series C, Vol. 89, No. 3, Aug. 1967, pp. 230–234.

10 Cho, S. H., and Sunderland, J. E., "Heat-Conduction Problems With Melting or Freezing," JOURNAL OF HEAT TRANSFER, TRANS. ASME, Series C, Vol. 91, No. 3, Aug. 1969, pp. 421–426.

11 Bailey, J. A., and Dula, A., "An Acoustic Technique for Use in Some Solidification Studies," *Rev. Sci. Instruments*, Vol. 38, 1967, p. 535.

12 Bishop, H. F., Brandt, F. A., and Pellini, W. S., "Solidification of Steel Against Sand and Chill Walls," *Transactions of American Foundryman's Society*, Vol. 59, 1951, p. 435.

13 Bishop, H. F., and Pellini, W. S., "Solidification of Metals," *Foundry*, Vol. 80, 1952, p. 86.

14 Simurik, S., "Theory of Solidification and Method for Directly Following Its Progress," *Modern Castings*, Vol. 42, No. 4, 1962, p. 112.

15 Hills, A. W. D., and Moore, M. R., "Use of Integral-Profile Methods to Treat Heat Transfer During Solidification," in: *Heat and Mass Transfer in Process Metallurgy*, Institute of Mining and Metallurgy, London, 1967, p. 141.

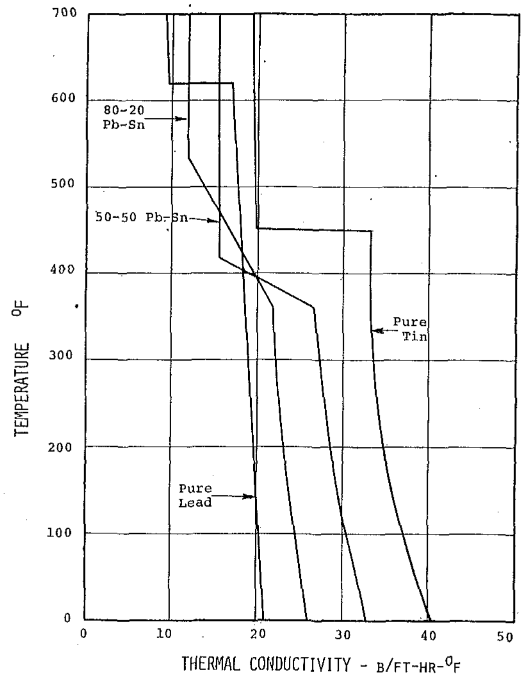

Fig. 7 Temperature versus thermal conductivity for various lead and tin combinations

16 Muehlbauer, J. C., "Transient, One-Dimensional Heat Transfer for Alloys During Solidification," PhD thesis, Clemson University, Clemson, S. C., 1968.

17 Paschkis, V., "Studies on the Solidification of Castings," *Transactions of American Foundryman's Society*, Vol. 53, 1945, p. 90.

18 Koerner, D. A., National Lead Co., personal communication, June, 1967.

19 Hsu, S. T., *Engineering Heat Transfer*, Van Nostrand, Princeton, N. J., 1963, p. 15.

20 ASME Power Test Codes, "Flow Measurements," Part 5, Chapter 4, ASME, New York, N. Y., 1949.

21 Kays, W. M., *Convective Heat and Mass Transfer*, McGraw-Hill, New York, 1966, p. 243.

22 Keenan, J. H., and Kaye, J., *Gas Tables*, Wiley, New York, 1948.

APPENDIX

Property Data. The property data used for the calculation of the analytical results for the 50–50 lead–tin alloy and 80–20 lead–tin alloy are presented herein. The following values for the 50–50 lead–tin mixture by weight were obtained from Koerner [18]:

Latent heat of fusion = 23 Btu/lb$_m$.
Mean specific heat as a liquid = 0.046 Btu/lb$_m$-deg F.
Mean specific heat as a solid = 0.051 Btu/lb$_m$-deg F.

The corresponding value for the 80–20 lead–tin mixture by weight were obtained based on Hsu [19]; the values used were:

Latent heat of fusion = 6.5 Btu/lb$_m$.
Mean specific heat as a liquid = 0.0393 Btu/lb$_m$-deg F.
Mean specific heat as a solid = 0.041 Btu/lb$_m$-deg F.

The density temperature data were obtained from the ASM metals handbook with certain portions supplied by Koerner [18]. These data are presented in Fig. 6. The values of thermal conductivity as a function of temperature for pure lead and tin, Fig. 7, are from Hsu [19]. The values of the thermal conductivity as a function of temperature for the two alloys were developed according to Hsu [19, p. 15]. The values were developed as the sum of the two components' thermal conductivities, each being adjusted by the volumetric percentage of the element in the mixture. Hsu [19] has shown this procedure to be valid for a liquid but has not validated the method for a solid. In the absence of data for a solid mixture, this method was used to obtain thermal-conductivity values for the solid mixture.

The air property data were obtained from the gas tables [22]. A velocity traverse of the boundary layer along the cooling plate indicated the velocity profile satisfied the $^1/_7$-power law for a turbulent-boundary-layer velocity profile.

The following are the physical conditions that existed for both sets of data presented in Figs. 4 and 5:

50–50 Pb–Sn

Initial temperature of alloy = 507 deg F.

Ambient temperature of air = 74 deg F.
Air dynamic pressure = 7.93 in. of H_2O.
Melting range of alloy = 361 deg F to 421 deg F.

80–20 Pb–Sn

Initial temperature of alloy = 550 deg F.
Ambient air temperature = 63 deg F.
Air dynamic pressure = 7.6 in. of H_2O.
Melting range of alloy = 361 deg F to 531 deg F.

M. H. HU
Research Assistant.

Y. P. CHANG
Professor.
Mem. ASME

Department of Mechanical Engineering,
State University of New York at Buffalo

Optimization of Finned Tubes for Heat Transfer in Laminar Flow[1]

The heat transfer of fully developed laminar flow in internally finned tubes is investigated analytically. If there is no heat generation in the fluid, the highest Nusselt number is obtained for the tube with 22 fins extended to about 80 percent of the tube radius. Its value is almost 20 times that for the finless tube. When there is heat generation at sufficiently large rate, the number of fins is reduced from 22 to 16 in order to obtain the highest Nusselt number.

Introduction

INTERNALLY FINNED TUBES have been employed for many years in compact heat exchangers [1, 2].[2] Most recently, the use of this type of tube has been considered in the design of gas-cooled nuclear reactors and jet engines of nuclear-powered aircraft. Various arrangements of internal fins have been investigated in the recent few years [3-5]. The continuous straight and spiral fins are the most common examples.

The apparent purpose of fins is to provide additional surface area for increasing the rate of heat transfer if a given temperature distribution is maintained at the surface, or for lowering the average surface temperature when heat is applied to the surface at a given rate and a given distribution. This statement, however, is rather loose, for the hydrodynamic aspect has not been considered. The presence of fins in a tube will alter the flow pattern and hence the flow friction. The flow may break down into vortices at edges and will slow down in troughs. If fins are continuous and straight, the former may be negligible, while the latter is important. For the same rate of mass flow, the larger the number of fins and their height, the higher will be the flow friction, and hence the pumping power. Therefore the investigation on heat transfer performance of finned tubes in turbulent flow is usually conducted under the condition of constant pumping power. For laminar flow, such a criterion is not needed, since the Nusselt number is independent of Reynolds number for fully developed velocity and temperature fields.

In spite of the importance of internally finned tubes in the design of compact heat exchangers, no results of analytical studies have been reported in the literature, and only limited experimental information is available. Fluid friction and heat transfer data for single-phase water flow in the turbulent regime were reported by Bergles, et al. [3, 4]. They found that the greatest increase in heat transfer was achieved with tubes having short spiral fins. On the basis of the nominal heat transfer area, the Nusselt number was found to be as high as 170 percent more than that for a smooth tube. Hilding and Coogan [5] tested turbulent air flow and found that straight fins of larger height give better heat transfer performance.

The analytical study of heat transfer in turbulent flow through a finned tube involves the production and suppression of turbulence, the mechanism of which has not yet been understood. In view of the damping effect of fins on the intensity of turbulence, straight fins will be more effective in improving the heat transfer performance for laminar flow than for turbulent flow. Taking into account the increase of solid–fluid contact area and the change of flow pattern, we can expect that a certain combination of the height and spacing of fins will give the highest improvement of heat transfer performance. This is the main purpose of the present study.

Since finned tubes have been considered for heat exchangers in nuclear-powered engines, the effect of heat generation in the fluid on the heat transfer coefficient will be studied with particular attention.

Statement of Problem

The problem to be investigated is concerned with the momentum and heat transfer in laminar flow of a single-phase fluid through an internally finned tube as shown schematically in Fig. 1. The fins are straight and continuous along the axis of the tube and are equally distributed around the wall. Properties of the fluid are assumed constant. The thickness of fins is neglected, for otherwise the problem would involve many aspects of the particular system to be chosen. The velocity and temperature are assumed to be fully developed. A constant and

---

[1] This study was supported in part by the National Science Foundation under grant GK-23688.

[2] Numbers in brackets designate References at end of paper.

Contributed by the Heat Transfer Division for publication (without presentation) in the JOURNAL OF HEAT TRANSFER. Manuscript received by the Heat Transfer Division May 23, 1972. Paper No. 73-HT-M.

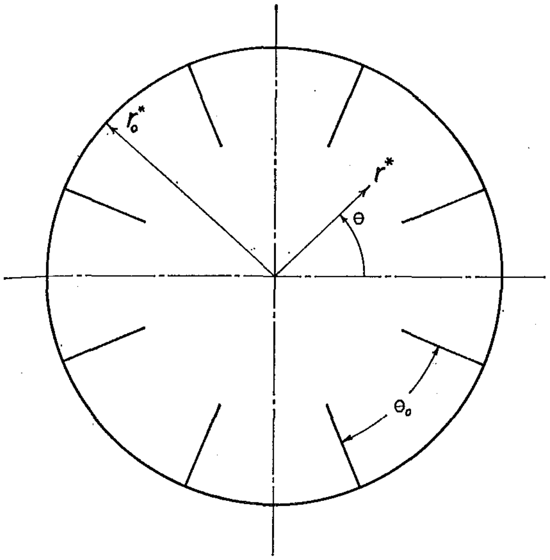

Fig. 1 Geometry of the internally finned tube

uniform heat flux is assumed to apply steadily over the cylindrical surface. A constant and uniform heat flux is also assumed at each fin. The last assumption is not quite realistic, but will simplify the analysis considerably, for otherwise we have to consider a specific system so that the heat conduction in the solid and the heat convection in the fluid can be analyzed simultaneously.

Under the foregoing conditions, the problem can be formulated for the channel of circular cross section as shown in Fig. 2. The momentum and energy equations are, for $0 < r^* < r_0^*$ and $|x^*| < \infty$,

$$\frac{1}{r^*}\frac{\partial}{\partial r^*}\left(r^*\frac{\partial u^*}{\partial r^*}\right)+\frac{1}{r^{*2}}\frac{\partial^2 u^*}{\partial \theta^2}=\frac{1}{\mu}\frac{dp^*}{dx^*} \tag{1}$$

$$\frac{1}{r^*}\frac{\partial}{\partial r^*}\left(r^*\frac{\partial T^*}{\partial r^*}\right)+\frac{1}{r^{*2}}\frac{\partial^2 T^*}{\partial \theta^2}=\frac{1}{\alpha}u^*\frac{\partial T^*}{\partial x^*}-\frac{Q^*}{k}-\Phi^* \tag{2}$$

where

$$\Phi^*=\frac{\mu}{k}\left[\left(\frac{\partial u^*}{\partial r^*}\right)^2+\left(\frac{1}{r^*}\frac{\partial u^*}{\partial \theta}\right)^2\right] \tag{3}$$

The boundary conditions are

$$u^*=0,\quad \frac{\partial T^*}{\partial r^*}=\frac{q_{w1}^*}{k}\qquad \text{for } r^*=r_0^*,\quad -\frac{\theta_0}{2}\le\theta\le\frac{\theta_0}{2} \tag{4}$$

$$u^*=0,\quad \frac{\partial T^*}{r^*\partial \theta}=\pm\frac{q_{w2}^*}{k}\qquad \text{for } r_1^*\le r^*\le r_0^*,\quad \theta=\pm\frac{\theta_0}{2} \tag{5}$$

$$\frac{\partial u^*}{\partial \theta}=0,\quad \frac{\partial T^*}{\partial \theta}=0\qquad \text{for } 0\le r^*\le r_1^*\quad \theta=\pm\frac{\theta_0}{2} \tag{6}$$

For the steady state in the temperature field to be established, the following condition is to be satisfied:

$$\frac{dT_b^*}{dx^*}=\left[\int_0^{\theta_0/2}(q_{w1}^*/k)d\theta+\int_{r_1^*}^{r_0^*}(q_{w2}^*/k)dr^* + \int_0^{\theta_0/2}\int_0^{r_0^*}\left(\frac{Q^*}{k}+\Phi^*\right)r^*dr^*d\theta\right]\Bigg/ \int_0^{\theta_0/2}\int_0^{r_0^*}\frac{u^*}{\alpha}r^*dr^*d\theta \tag{7}$$

Nomenclature

c_1 = constant parameter, $\frac{\rho c_p}{\mu}\left(\frac{r_0^{*3}}{q_0^*}\right)\left(\frac{dp^*}{dx^*}\right)\left(\frac{dT^*}{dx^*}\right)$, defined by (14)
c_2 = constant parameter, $\frac{1}{\mu}\left(\frac{r_0^{*3}}{q_0^*}\right)\left(\frac{dp^*}{dx^*}\right)^2$
c_p = specific heat at constant pressure
D_e^*, D_e = 4(cross-sectional area)/wetted perimeter, $D_e = D_e^*/r_0^*$
D_0^*, D_0 = diameter of finless tube, $D_0 = D_0^*/r_0^* = 2$
f = friction factor
G = Green's function defined by (19)
$\bar{G}$ = generalized Green's function defined by (25)
h = heat transfer coefficient
k = thermal conductivity
l^*, l = height of fin, $l = l^*/r_0^*$
m = number of fins
Nu = Nusselt number defined by (33)
p^* = pressure
Pr = Prandtl number
Q^* = rate of heat generation per unit volume
Q_s^* = rate of total heat transfer through solid–fluid interface
q_{w1}^* = heat flux at tube wall = $Q_s^*/2\pi r_0^* + 2\omega m l^*$, $\omega = q_{w2}^*/q_{w1}^*$
q_{w2}^* = heat flux at each side of fin = ωq_{w1}^*
q_0^* = $Q_s^*/\pi D_0^*$, reference heat flux
(r^*, θ, x^*) = cylindrical coordinates
r = r^*/r_0^*
r_0^* = radius of tube
r_1^* = $r_0^* - l^*$, $r_1 = r_1^*/r_0^*$
Re, Re$_0$ = Reynolds number, Re = $\rho u_m^* D_e^*/\mu$, Re$_0$ = $\rho u_m^* D_0^*/\mu$
T^* = temperature
T_m^* = averaged temperature over entire cross section
T = $(T^* - T_m^*)/(q_0^* r_0^*/k)$
T_b^* = bulk fluid temperature = $\int_0^{\theta_0/2}\int_0^1 u^*T^*r^*dr^*d\theta \Big/ \int_0^{\theta_0/2}\int_0^1 u^*r^*dr^*d\theta$
T_{sm}^* = averaged temperature over solid–fluid interface
u^* = velocity
u = dimensionless velocity = $u^*\Big/\left(-\frac{r_0^{*2}}{\mu}\frac{dp^*}{dx^*}\right)$
u_m = mean dimensionless velocity = $\int_0^{\theta_0/2}\int_0^1 u(r,\theta)rdrd\theta \Big/ \int_0^{\theta_0/2}\int_0^1 rdrd\theta$
u_{m0} = mean dimensionless velocity of finless tube
U = dimensionless velocity for $0 < r < r_1$ at $\theta = \pm\theta_0/2$
α = thermal diffusivity, $k/\rho c_p$
β_1 = q_{w1}^*/q_0^*, $\beta_2 = q_{w2}^*/q_0^*$
θ_0 = angle of circular sector, $\theta_0 = 2\pi/m$
λ = heat generation parameter = $r_0^*Q^*/q_0^*$
μ = viscosity
ρ = fluid density
Φ^* = dissipation function defined by (3)
Φ = dimensionless dissipation function = $\left(\frac{\partial u}{\partial r}\right)^2 + \left(\frac{1}{r}\frac{\partial u}{\partial \theta}\right)^2$

Equation (7) is obtained by integrating both sides of (2) over the cross section of the channel, and the following relation for fully developed temperature has been used:

$$\frac{dT^*}{dx^*} = \frac{dT_b^*}{dx^*} \tag{8}$$

By introducing the dimensionless quantities as defined in the Nomenclature and using (8), equations (1)-(7) take the form

$$\frac{1}{r}\frac{\partial}{\partial r}\left(r\frac{\partial u}{\partial r}\right) + \frac{1}{r^2}\frac{\partial^2 u}{\partial \theta^2} = -1 \tag{9}$$

$$\frac{1}{r}\frac{\partial}{\partial r}\left(r\frac{\partial T}{\partial r}\right) + \frac{1}{r^2}\frac{\partial^2 T}{\partial \theta^2} = -c_1 u - \lambda - c_2\Phi(r, \theta) \tag{10}$$

$$u = 0, \quad \frac{\partial T}{\partial r} = \beta_1 \qquad \text{for } r = 1, \quad -\frac{\theta_0}{2} \le \theta \le \frac{\theta_0}{2} \tag{11}$$

$$u = 0, \quad \frac{\partial T}{r\partial \theta} = \pm\beta_2 \qquad \text{for } r_1 \le r \le 1, \quad \theta = \pm\frac{\theta_0}{2} \tag{12}$$

$$\frac{\partial u}{\partial \theta} = 0, \quad \frac{\partial T}{\partial \theta} = 0 \qquad \text{for } 0 \le r \le r_1, \quad \theta = \pm\frac{\theta_0}{2} \tag{13}$$

where

$$c_1 = -\left[\int_0^{\theta_0/2} \beta_1 d\theta + \int_{r_1}^1 \beta_2 dr + \int_0^{\theta_0/2}\int_0^1 (\lambda + c_2\Phi) r dr d\theta\right] \Bigg/ \int_0^{\theta_0/2}\int_0^1 u r dr d\theta \tag{14}$$

Solution for Velocity

The boundary conditions on u, (11)-(13), are of the mixed type. In order to obtain the analytical solution for u, we can divide the circular sector into two regions by a circular arc of radius r_1. This approach will be quite lengthy, and therefore we do not use it. If, however, we let $U(r)$ denote the velocity for $\theta = \theta_0/2$ and $0 < r < r_1$, then the boundary condition over the contour of the circular sector is of the Dirichlet type. If $G(r, \theta|r', \theta')$ is the Green's function associated with the Dirichlet problem, we have

$$u(r, \theta) = \int_{-\theta_0/2}^{\theta_0/2}\int_0^1 G(r, \theta|r', \theta') r' dr' d\theta' - \int_0^{r_1} U(r')\left[\frac{\partial}{\partial \theta'} G\left(r, \theta|r', \frac{\theta_0}{2}\right) - \frac{\partial}{\partial \theta'} G\left(r, \theta|r', -\frac{\theta_0}{2}\right)\right]\frac{dr'}{r'} \tag{15}$$

Differentiating both sides of (15) with respect to θ, setting $\theta = \theta_0/2$, and using the boundary conditions (13) for u, we obtain

$$\int_0^{r_1} K(r|r')U(r')dr' - f(r) = 0 \tag{16}$$

where the kernel $K(r|r')$ and the function $f(r)$ are defined by

$$K(r|r') = \frac{2\pi}{m^2 r'}\left[\frac{\partial^2}{\partial\theta\partial\theta} G(r, \theta_0/2|r', \theta_0/2) - \frac{\partial^2}{\partial\theta\partial\theta} G(r, \theta_0/2|r', -\theta_0/2)\right] \tag{17}$$

$$f(r) = \frac{2\pi}{m^2}\int_{-\theta_0/2}^{\theta_0/2}\int_0^1 \frac{\partial}{\partial\theta} G(r, \theta_0/2|r', \theta') r' dr' d\theta' \tag{18}$$

Equation (16) is an integral equation in the form of a Fredholm equation of the first kind. Its solution will be discussed later.

The Green's function $G(r, \theta|r', \theta')$ can easily be constructed by the standard method of a partial eigenfunction expansion [6] for $r' < r$,

$$G(r, \theta|r', \theta') = \sum_{n=1}^{\infty} \frac{1}{n\pi} r'^{mn/2}(r^{-mn/2} - r^{mn/2}) \sin\frac{1}{2}mn \times \left(\theta + \frac{1}{2}\theta_0\right) \sin\frac{1}{2}mn\left(\theta' + \frac{1}{2}\theta_0\right) \tag{19a}$$

For $r' > r$ we simply exchange r and r'. The series in (19a) can be rewritten in closed form as

$$\begin{aligned} G(r, \theta|r', \theta') = \frac{1}{4\pi}\Bigg\{ &-\ln\left[r^m + r'^m - 2r^{m/2}r'^{m/2}\cos\frac{m}{2}(\theta - \theta')\right] \\ &+ \ln\left[1 + r^m r'^m - 2r^{m/2}r'^{m/2}\cos\frac{m}{2}(\theta - \theta')\right] \\ &+ \ln\left[r^m + r'^m - 2r^{m/2}r'^{m/2}\cos\frac{m}{2}(\theta_0 + \theta + \theta')\right] \\ &- \ln\left[1 + r^m r'^m - 2r^{m/2}r'^{m/2}\cos\frac{m}{2}(\theta_0 + \theta + \theta')\right]\Bigg\} \end{aligned} \tag{19b}$$

We substitute (19b) and (19a) into (17) and (18), respectively, to obtain

$$K(r|r') = \frac{(rr')^{m/2}}{r'}\left[\frac{r^m + r'^m}{(r^m - r'^m)^2} - \frac{1 + r^m r'^m}{(1 - r^m r'^m)^2}\right] \tag{20}$$

$$f(r) = -\frac{16}{m}\sum_{n=1}^{\infty}\frac{r^2 - r^{m(2n-1)/2}}{m^2(2n-1)^2 - 16} \tag{21}$$

Now the problem is to solve (16). We wish to use a simple, though approximate, method whose accuracy will be discussed later. We divide the radial length $(0, r_1)$ into N intervals. Let $i = 1, 2, 3, \ldots, N$ be the primary nodal points and $j = 1, 2, 3, \ldots, N$ the secondary nodal points. We assume that $U(r_i)$ remains constant within each interval. Then (16) can be written as a set of algebraic equations

$$\sum_{j=1}^{N} U_j(r_j)\int_{\Delta r_j} K(r_i, r')dr' = f_i(r_i)$$

or, in matrix notation,

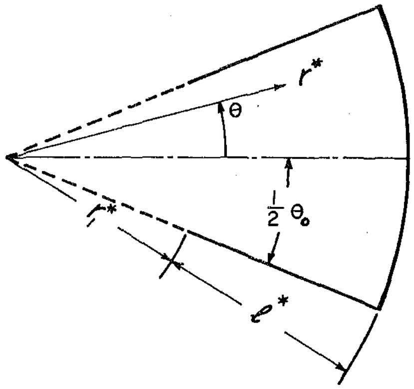

Fig. 2 Geometry of a circular sector of the tube

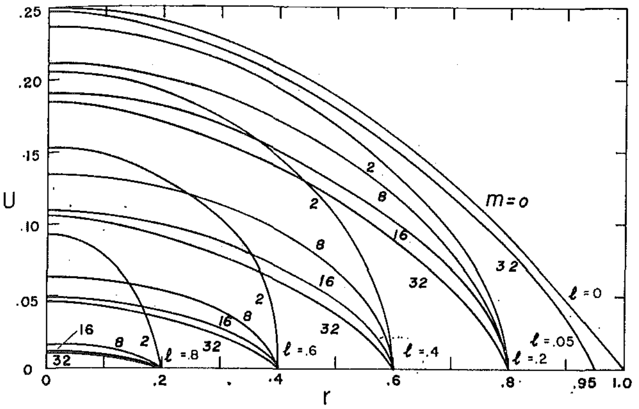

Fig. 3 Dimensionless velocity distributions at $0 < r < r_1$ and $\theta = \pm\theta_0/2$ for various values of m and l

$$|A_{ij}||U_j| = |f_i| \tag{22}$$

where the matrix elements are given by

$$\begin{aligned}A_{ij} &= \int_{\Delta r_j} K(r_i, r')dr' \\ &= \frac{2}{m}(r_i r_{j+1/2})^{m/2}\left(\frac{1}{r_i^m - r_{j+1/2}^m} - \frac{1}{1 - r_i^m r_{j+1/2}^m}\right) \\ &\quad - \frac{2}{m}(r_i r_{j-1/2})^{m/2}\left(\frac{1}{r_i^m - r_{j-1/2}^m} - \frac{1}{1 - r_i^m r_{j-1/2}^m}\right)\end{aligned} \tag{23}$$

with

$$r_{j+1/2} = r_j + \frac{\Delta r_j}{2}, \qquad r_{j-1/2} = r_j - \frac{\Delta r_j}{2}$$

Calculated results from (22) are shown in Fig. 3 for a wide range of values of the spacing and height of fins, which are characterized by the parameters m and l, respectively.

Substituting (19) into (15) gives the velocity distribution

$$\begin{aligned}u(r, \theta) &= \frac{1}{2\pi}\int_0^{r_1} M(r, r', \theta)U(r')dr' \\ &\quad + \frac{1}{2\pi}\sum_{n=1}^{\infty}\frac{32}{(2n-1)[m^2(2n-1)^2 - 16]} \\ &\quad \times [r^2 - r^{(n-1/2)m}]\sin\left[m\left(n - \frac{1}{2}\right)\left(\theta + \frac{1}{2}\theta_0\right)\right]\end{aligned} \tag{24}$$

where

$$\begin{aligned}M(r, r', \theta) &= m\left(\frac{1}{r'}\right)\left(r^{m/2}r'^{m/2}\cos\frac{m}{2}\theta\right) \\ &\quad \times \left\{\frac{1}{r^m + r'^m - 2r^{m/2}r'^{m/2}\sin\frac{m}{2}\theta}\right. \\ &\quad - \frac{1}{1 + r^m r'^m - 2r^{m/2}r'^{m/2}\sin\frac{m}{2}\theta} \\ &\quad + \frac{1}{r^m + r'^m + 2r^{m/2}r'^{m/2}\sin\frac{m}{2}\theta} \\ &\quad \left. - \frac{1}{1 + r^m r'^m + 2r^{m/2}r'^{m/2}\sin\frac{m}{2}\theta}\right\}\end{aligned}$$

Some calculated results from (24) for various values of m and l are shown in Fig. 4.

Solution for Temperature

We wish to solve (10) for $T(r, \theta)$ satisfying conditions (11)–(13) by the use of a generalized Green's function. By the method of partial eigenfunction expansion and the use of the well-known symmetry condition [7, 8], this function can be constructed as

$$\bar{G}(r, \theta|r', \theta') = -\frac{3m}{4\pi} + \frac{m}{2\pi}(r^2 + r'^2) - g(r, \theta|r', \theta') \tag{25}$$

where

$$\begin{aligned}g(r, \theta|r', \theta') \equiv \frac{1}{4\pi}\{&\ln[r^{2m} + r'^{2m} - 2r^m r'^m\cos m(\theta - \theta')] \\ &+ \ln[1 + r^{2m}r'^{2m} - 2r^m r'^m\cos m(\theta - \theta')] \\ &+ \ln[r^{2m} + r'^{2m} - 2r^m r'^m\cos m(\theta + \theta')] \\ &+ \ln[1 + r^{2m}r'^{2m} - 2r^m r'^m\cos m(\theta + \theta')]\}\end{aligned} \tag{26}$$

The solution of (10) is then determined up to an additive constant,

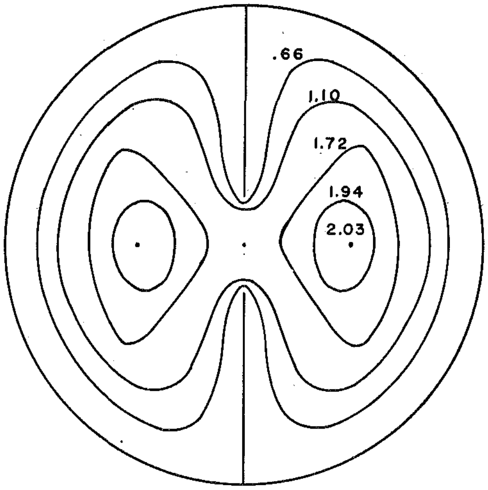

Fig. 4(a) Equi-velocity lines u/u_m for $l = 0.8$ and $m = 2$

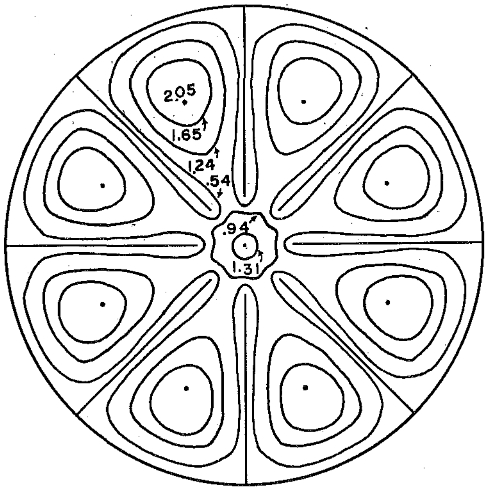

Fig. 4(b) Equi-velocity lines u/u_m for $l = 0.8$ and $m = 8$

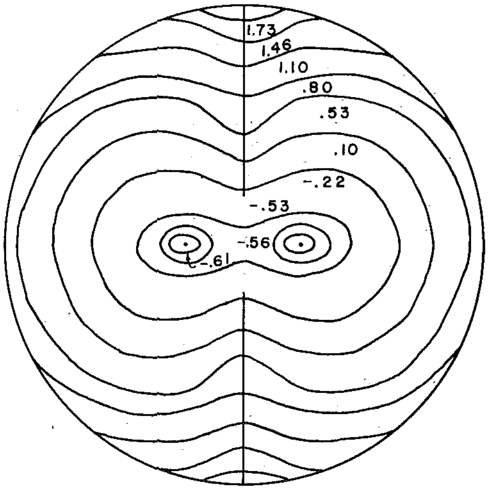

Fig. 5(*a*) Isotherms $(T - T_b)/(T_{sm} - T_b)$ for $l = 0.8$ and $m = 2$

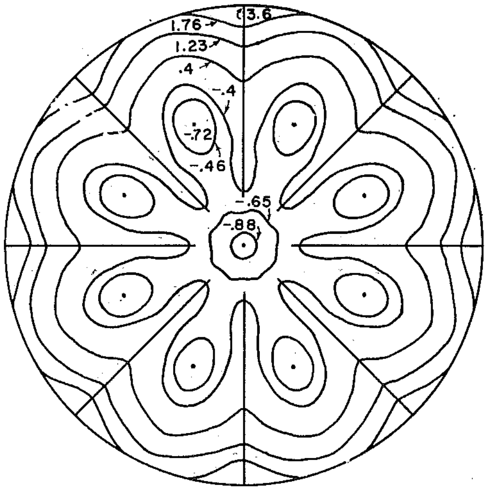

Fig. 5(*b*) Isotherms $(T - T_b)/(T_{sm} - T_b)$ for $l = 0.8$ and $m = 8$

$$T(r,\theta) = C + \int_0^{\theta_0/2} \overline{\mathrm{G}}(r,\theta|1,\theta')\frac{\partial T}{\partial r'}(1,\theta')d\theta' + \int_{r_1}^{1} \overline{\mathrm{G}}\left(r,\theta|r',\frac{1}{2}\theta_0\right)\frac{\partial T}{\partial \theta'}\left(r',\frac{1}{2}\theta_0\right)\frac{dr'}{r'} + \int_0^{\theta_0/2}\int_0^1 [c_1u + \lambda + c_2\Phi]\overline{\mathrm{G}}(r,\theta|r',\theta')r'dr'd\theta' \quad (27)$$

Substituting (25) into (27) and using condition (14), we obtain

$$T(r,\theta) = C + \frac{1}{2}\beta_1 + \frac{1}{6}\frac{m}{\pi}(1 - r_1^3)\beta_2 - \beta_2\int_{r_1}^{1} g\left((r,\theta|r',\frac{1}{2}\theta_0\right)dr' + \int_0^{\theta_0/2}\int_0^1 (c_1u + \lambda + c_2\Phi) \times \left[\frac{m}{2\pi}r'^2 - g(r,\theta|r',\theta')\right]r'dr'd\theta' \quad (28)$$

The constant C is determined by

$$\int_0^{\theta_0/2}\int_0^1 T(r,\theta)rdrd\theta = 0 \quad (29)$$

Now we can calculate $T(r,\theta)$ from (28). If the tube wall and fins are very thin and are of the same material and same thickness, and if the heat is applied electrically, then we can assume that $\beta_2 = \beta_1/2$, since heat is transferred to the fluid from both sides of the fin. Some calculated results from (28) are shown in Figs. 5(*a*) and 5(*b*).

Friction and Heat Transfer Coefficients

For fully developed flow, the friction coefficient is obtained by the balance of frictional and pressure forces as

$$f = -\frac{dp^*/dx^*}{\rho u_m^{*2}/2}\frac{D_e^*}{4} \quad (30)$$

If we follow the usual practice of defining the Reynolds number on the basis of the hydraulic diameter D_e^*, we obtain

$$f\,\mathrm{Re} = \frac{D_e^2}{2u_m} = \frac{2}{u_m[1 + m(1 - r_1)/\pi]^2} \quad (31)$$

Some calculated results of (31) are shown by dotted lines in Fig. 6. However, a better correlation for the friction factor is obtained if we write

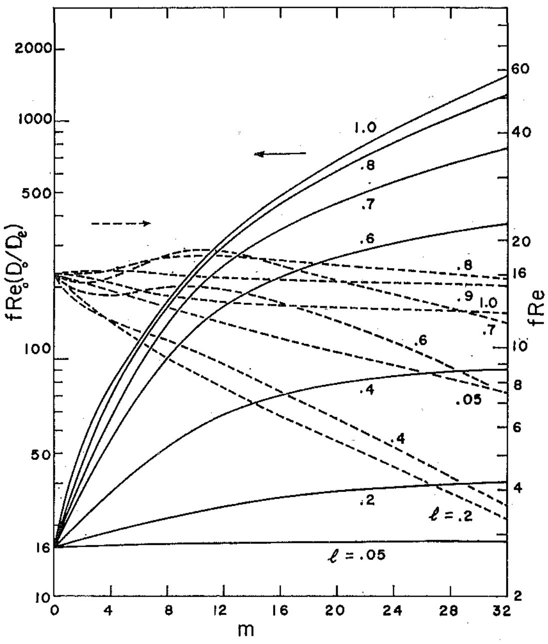

Fig. 6 Friction factor

$$f\,\mathrm{Re}_0\frac{D_0}{D_e} = \frac{D_0^2}{2u_m} \quad (32)$$

as shown by solid lines in Fig. 6.

Now we consider the heat transfer performance of finned and finless tubes. It has been shown in [4, 5] that the hydraulic diameter is not suitable for correlating data of heat transfer in finned tubes.

We define the heat transfer coefficient and the Nusselt number for finned as well as finless tubes as:

$$h = \frac{Q_s^*}{\pi D_0^*(T_{sm}^* - T_b^*)}, \qquad \mathrm{Nu} = \frac{hD_0^*}{k} \quad (33)$$

where Q_s^* is the rate of heat transfer at the interface of the solid and fluid, T_{sm}^* is the temperature averaged over the interface, and T_b^* is the bulk temperature of the fluid. Reasons underlying the definitions (33) are: they reduce to those of finless tubes; the finned tube replaces a finless tube of the same nominal diameter, which alone describes the compactness of a heat exchanger; for a given prescribed temperature of the solid surface, h (and hence Nu) dictates the rate of heat transfer, or conversely for a given rate of heat transfer it determines the average temperature difference between the fluid and the solid surface, an important factor in the design of heat exchangers. Some calculated results of Nu without and with heat generation are shown in Figs. 7 and 8.

Limiting Cases: Finless and Full-Fin Tubes

Since the velocity distribution was calculated numerically by a method that has not been used by other investigators, we consider two special cases whose results are well known: finless and full-fin tubes. For finless tubes, (24) and (28) reduce to

$$u(r) = \frac{1}{4}(1 - r^2)$$

$$T(r) = \left(r^2 - \frac{r^4}{4} - \frac{5}{12}\right)\beta_1 + \left(\frac{r^2}{4} - \frac{r^4}{8} - \frac{1}{12}\right)\lambda + c_2\left(4r^2 - 2r^4 - \frac{4}{3}\right)u_{m0}{}^2$$

and (31) and (33) become

$$f\,\mathrm{Re} = 2/u_{m0} \tag{34}$$

$$\mathrm{Nu} = D_0\beta_1\bigg/\left(\frac{11}{24}\beta_1 + \frac{\lambda}{16} + c_2 u_{m0}{}^2\right) \tag{35}$$

since $u_{m0} = 1/8$, $D_0 = 2$, these yield the well-known results of f Re $= 16$ and Nu $= 48/11$ in the absence of heat generation and dissipation. For full-fin tubes, i.e., $l = 1$, (24) and (28) for $c_2 = 0$ reduce to

$$u(r, \theta) = \frac{1}{2\pi}\sum_{n=1,3,5}^{\infty} -(-1)^{(n+1)/2}\frac{32}{n(m^2n^2 - 16)} \times (r^2 - r^{mn/2})\cos\frac{1}{2}mn\theta \tag{36}$$

$$\begin{aligned} T(r, \theta) = {} & C + \left(\frac{3}{8} - \frac{1}{4}r^2\right)\lambda + \frac{1}{2}\beta_1 + \beta_2\left(\frac{m}{\pi}\right)\left(\frac{7}{6} - r\right) \\ & + \beta_2\frac{2}{\pi}\sum_{n=1}^{\infty}(-1)^n\left(mr - \frac{1}{n}r^{mn}\right)\frac{\cos mn\,\theta}{m^2n^2 - 1} \\ & + c_1\frac{8}{\pi^2}\sum_{k=1,3,5}^{\infty}\frac{1}{k^2(mk + 4)}\left\{\frac{1}{3mk + 24} + \frac{4}{mk - 4}\left[\frac{1}{16}(1 - r^4) - \frac{4}{(mk + 4)^2}(1 - r^{(mk/2)+2})\right]\right\} \\ & + c_1\frac{32}{m\pi^2}\sum_{k=1,3,5}^{\infty}\sum_{n=1}^{\infty}(-1)^n\frac{1}{n(m^2k^2 - 16)(k^2 - 4n^2)} \\ & \left\{\frac{2mn}{m^2n^2 - 16}r^4 + \frac{8mn}{(mk + 2mn + 4)(mk - 2mn + 4)}r^{(mk/2)+2} \right. \\ & \left. - 4\left[\frac{2}{m^2n^2 - 16} - \frac{mk + 4}{(mk + 2mn + 4)(mk - 2mn + 4)}\right]r^{mn}\right\} \cos mn\theta \end{aligned} \tag{37}$$

Equation (36) is identical with that reported by Eckert, Irvine, and Yen [9], and hence the friction coefficient is as shown in Fig. 9. Equation (37), however, is different in form from that in [9]. Calculated values of the Nusselt number, as defined by (33), from the temperature distribution given by (28) with $r_1 = 0$, $\lambda = c_2 = 0$, and $\beta_2 = \beta_1$ are also shown in Fig. 9. The Nusselt number Nu defined in this paper is related to the Nusselt number Nu_E used in [9] by

$$\mathrm{Nu} = (1 + m/\pi)^2\mathrm{Nu}_E \tag{38}$$

In Fig. 9 are shown the results of Nu from (38) calculated by reading the values of Nu_E from Fig. 3 of [9]. It is seen that they agree well qualitatively, but not quite so well quantitatively, with a maximum error of about 9.6 percent. This error is probably due to the fact that the series solution of equation (13) in [9] was truncated somewhat earlier in their calculation. Of course we could also calculate Nu through the use of series (37), but the definite integral in (28) was used for the present calculation to yield accurate results.

Discussion and Optimum Fins

Before we discuss the results shown in Figs. 3–9, a few remarks are in order on the approximate numerical technique that was used in obtaining the matrix (22). The accuracy of this method has been discussed in [10] with regard to the use of fundamental

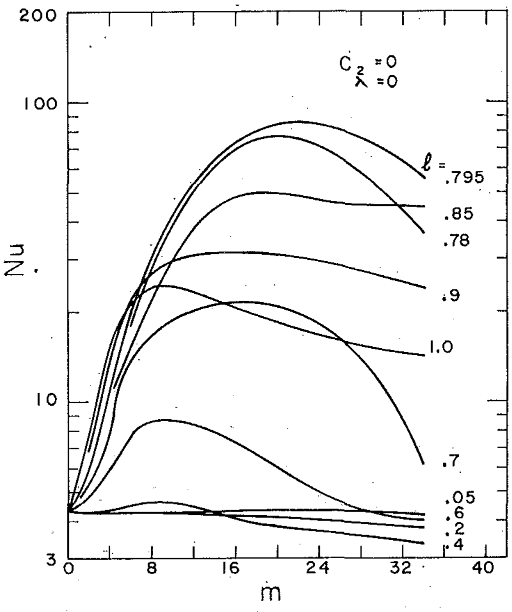

Fig. 7 Nusselt number on the basis of nominal diameter

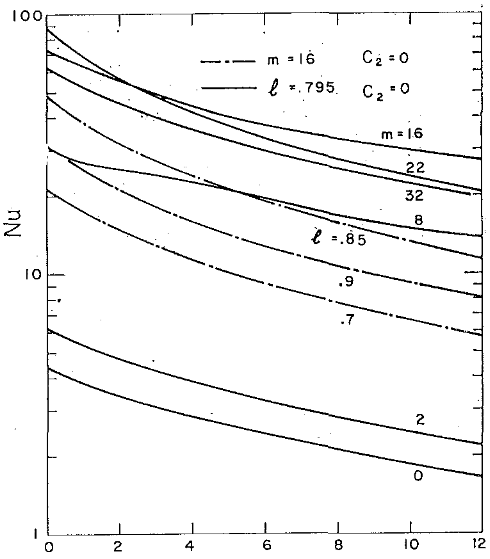

Fig. 8 Effect of heat generation to Nusselt number

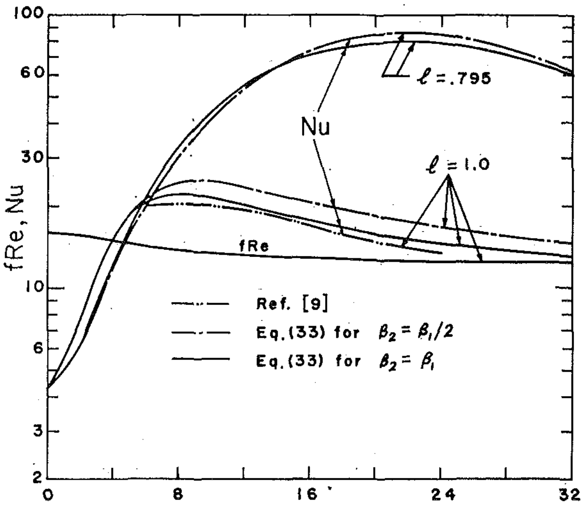

Fig. 9 Friction factor and Nusselt number for full-fin tubes

Green's functions (i.e., those in an infinite region), of incomplete Green's functions (i.e., those satisfying homogeneous boundary conditions only over a part of the surface), and of Green's functions (i.e., those satisfying homogeneous boundary conditions over all the surface). For a piecewise-smooth surface, the less the incompleteness of the Green's function, the more accurate is the result obtained by this approximate technique. Therefore, excellent results for u can be obtained by this technique for the present problem.

As shown in Fig. 4(a) for $m = 2$ and $l = 0.8$, the equi-velocity lines form two symmetric loops with the highest value in loop eyes. This is in contrast to the flow pattern of concentric loops for finless tubes. Two types of loops occur in Fig. 4(b) for $m = 8$ and $l = 0.8$: one at the center that may be referred to as the primary loop, while those between fins are secondary loops. For this combination of m and l, the highest velocity occurs in the eyes of secondary loops. If l is kept at the value of 0.8, the increase of m tends to shift secondary-loop eyes toward the tube wall, but the highest velocity is shifted from the secondary to the primary loop. Loops of isotherms of these two cases are shown in Figs. 5(a) and 5(b). For the case of $l = 0.8$ and $m = 2$, the lowest temperature occurs in the two eyes. For $l = 0.8$ and $m = 8$, the lowest temperature takes place along the tube axis. For either case, the highest temperature is at the base of each fin. It was found, but not shown here, that a further increase of l and m shifts the location of highest temperature along the fin toward the tip. If, however, there is heat generation at a large rate in the fluid, the highest temperature occurs at the tube wall near the fin base.

The dependence of Nusselt number upon the parameters l and m is quite complicated as shown in Fig. 7. For a given value of l, the maximum Nusselt number occurs at a certain value of m but not at the highest value of m. For a given value of $m < 8$ the Nusselt number goes through first a minimum and then increases with increasing l. For a given value of $8 < m < 30$, the Nusselt number not only goes through a minimum but also a maximum as l increases. Short fins of any number and long fins of very large number may cause a decrease in Nusselt number to below the value of a finless tube. The optimum value of Nusselt number is found as 86.82 at $l = 0.795$ and $m = 22$.

The increase of Nusselt number with fin height l is of great interest, as shown in Fig. 7. For instance, with 20 fins, the increase of l from 0.2 to 0.4 decreases the Nusselt number by 6.17 percent, though the solid-liquid contact area is increased by 54.3 percent; increasing l from 0.6 to 0.8 increases the Nusselt number by a factor of 12.8 while the solid-liquid contact area is increased only by 26.6 percent. To understand this surprising change of Nu with respect l and m, we have to look into the detailed velocity and temperature distributions in the primary and secondary loops. For short fins ($l < 0.32$), no secondary loop is found in either the velocity or the temperature field; the highest velocity is along the tube axis, and the highest temperature is around the fin base where the fluid is nearly stagnant. As l increases, secondary loops of both temperature and velocity begin to appear. When l is increased to about 0.8, the high-velocity flow in the primary loop joins force with the flow in the secondary loop in heat convection.

As $l \rightarrow 1$, the primary loop will begin to vanish, and the highest temperature will occur at a region around fin tips where the fluid is almost stagnant. Consequently the heat transfer coefficient drops drastically from the optimal value of 86.82 to that of the full-finned tube, 17.98.

We have also examined the effects of dissipation and heat generation on the Nusselt number on the basis of the same total heat transfer rate. It is found that the effect of dissipation is insignificant for all cases, and therefore it is not shown in any figure. However, the increase of the rate of heat generation decreases the Nusselt number appreciably. For $\lambda > 2.4$, the optimum value of m changes from 22 to 16, as can be seen in Fig. 8. Thus if the rate of heat generation in the fluid is so large that $\lambda > 2.4$, the tube with 16 fins extended to about 80 percent of the tube radius gives the highest heat transfer coefficient.

Calculations have also been made for finned tubes with $\beta_2 = \beta_1$, and it was found that the Nusselt number as shown in Fig. 9 does not change appreciably from that with $\beta_2 = \beta_1/2$. In other words, the Nusselt number is not quite sensitive to the selection of values of β_2.

From the above discussions, the following conclusions can be drawn: (a) the installation of internal fins in tubes improves the heat transfer performance more effectively for laminar flow than for turbulent flow and (b) the Nusselt number for laminar flow in the optimized finned tube can surpass that of many cases for turbulent flow in a finless tube such as [11]: $Pr < 10$ and $Re \leq 10^4$; $Pr \leq 1$, and $Re \leq 3 \times 10^4$; $Pr < 0.03$ and $Re < 10^6$. More discussions on (33) and Fig. 7 can be found in [12].

References

1 Kays, W. M., and London, A. L., *Compact Heat Exchangers*, 2nd Ed., McGraw-Hill, New York, 1964.

2 Fraas, A. P., and Qzisik, M. N., *Heat Exchanger Design*, Wiley, New York, 1965.

3 Bergles, A. E., "Survey and Evaluation of Techniques to Augment Convective Heat and Mass Transfer," in: *Progress in Heat and Mass Transfer*, Vol. 1, Pergamon Press, Elmsford, N. Y., 1969, pp. 331–424.

4 Bergles, A. E., Brown, G. S., Jr., and Snider, W. D., "Heat-Transfer Performance of Internally Finned Tubes," ASME Paper No. 71-HT-31.

5 Hilding, W. E., and Coogan, C. H., Jr., "Heat Transfer and Pressure Loss Measurements in Internally Finned Tubes," in: *Symposium on Air-cooled Heat Exchangers*, ASME, New York, 1964, pp. 57–85.

6 Stakgold, I., *Boundary Value Problems of Mathematical Physics*, Vol. 2, Macmillan, London, 1967.

7 Chang, Y. P., "Heat Conduction in Isotropic and Anisotropic Solids," mimeographed notes, Department of Mechanical Engineering, State University of New York at Buffalo, 1970–1972.

8 Sobolev, S. L., *Partial Differential Equations of Mathematical Physics*, Pergamon Press, Elmsford, N. Y., 1964.

9 Eckert, E. R. G., Irvine, T. F., Jr., and Yen, J. T., "Local Laminar Heat Transfer in Wedge-Shaped Passages," TRANS. ASME, Vol. 80, 1958, pp. 1433–1438.

10 Chang, Y. P., Kang, C. S., and Chen, D. J., "The Use of Fundamental Green's Functions for the Solution of Problems of Heat Conduction in Anisotropic Media," to appear in *International Journal of Heat and Mass Transfer*.

11 Kays, W. M., *Convective Heat and Mass Transfer*, McGraw-Hill, New York, 1966.

12 Hu, M. H., "Flow and Thermal Analysis for Mechanically Enhanced Heat Transfer Tubes," PhD dissertation, Department of Mechanical Engineering, State University of New York at Buffalo, June 1973.

B. L. MARSH
Member, Technical Staff,
Bell Laboratories,
Whippany, N. J.

F. A. COSTELLO
Associate Professor,
Department of Mechanical and
Aerospace Engineering,
University of Delaware,
Newark, Del.

Stochastic Optimization of Convective-Fin Design

In the design of convective fins, stochastic variations in fin dimensions have traditionally been handled by the use of safety factors. Often this process results in a multiplication of safety factors and thus an overly expensive design. This paper presents a probabilistic approach that not only analyzes the probability of system failure but also uses this analysis to synthesize the optimal design. Four methods of varying accuracy and difficulty are described and compared. The method based on the RMS approximation for the variances appears to be most useful for design purposes.

Introduction

At present, allowance for stochastic variations in material properties and dimensions in engineering designs is based upon the use of safety factors. The magnitude of the safety factors is based on experience with past failures. One of the shortcomings of this practice is that there is a multiplication of safety factors throughout the design, so the final design is too costly. This problem has been recognized, and several authors have attempted to rectify the situation. Shigley [1],[1] for example, has suggested the use of probability distribution functions for the mechanical properties of materials. Haugen [2] has developed relationships between the probability of system failure in terms of the probability of component failure. Several recent publications [3-5] deal with particular heat transfer applications.

The present paper takes the probabilistic approach a step further. Not only is the probability of system failure analyzed, but the failure analysis is used to devise the optimal design. The result is a synthesis of the optimal design rather than just an analysis of an existing design.

The system considered herein is a reasonably simple system: the convective fin of rectangular cross section. This problem is chosen because of the commercial importance of fin design, but also because the problem exhibits a nonlinear relationship between the dependent and independent variables that is characteristic of more complicated problems. It is hoped, therefore, that some of the findings reported herein concerning the relative merits of exact and approximate methods for predicting the probability of failure are applicable to more complex problems. Another advantage of the fin problem is that there are only two independent variables, so the results can conveniently be portrayed.

Theoretical Development

Of the many uncertainties associated with fin design, including the uncertainty or variability of thermal conductivity and convective heat transfer coefficient, the ones considered in this paper are those associated with the physical dimensions of the fin: the length and thickness. The problem to be solved can therefore be developed as follows: The heat transfer rate per unit length on one side of the fin is [6]

$$Q = (hkt)^{1/2}(T_0 - T_a) \tanh (hL^2/kt)^{1/2} \tag{1}$$

or, in dimensionless form,

$$q = \tau^{1/2} \tanh (\lambda/\tau^{1/2}) \tag{2}$$

A stochastic dimensionless length

$$\lambda \equiv \lambda_0(1 + \delta_\lambda) = hL/k \tag{3}$$

is introduced where λ_0 is the mean value of λ and δ_λ is a random variable assumed to be distributed parabolically according to the equation

$$f(\sigma_{\delta\lambda}, \delta_\lambda) = \frac{3}{4(5^{1/2}\sigma_{\delta\lambda})}\left(1 - \frac{{\delta_\lambda}^2}{5{\sigma_{\delta\lambda}}^2}\right), \; -5^{1/2}\sigma_{\delta\lambda} \leq \delta_\lambda \leq 5^{1/2}\sigma_{\delta\lambda} \tag{4}$$

$$= 0, \quad \text{elsewhere}$$

with mean of zero and variance ${\sigma_{\delta\lambda}}^2$. Similarly, a stochastic dimensionless thickness

$$\tau \equiv \tau_0(1 + \delta_\tau) = ht/k \tag{5}$$

is introduced with probability density function $f(\sigma_{\delta\tau}, \delta_\tau)$. These

---

[1] Numbers in brackets designate References at end of paper.

Contributed by the Heat Transfer Division for publication (without presentation) in the Journal of Heat Transfer. Manuscript received by the Heat Transfer Division October 26, 1972. Paper No. 73-HT-O.

Table 1 Accuracy of typical simulations at a single λ_0, τ_0

N	P	v_T	Percentage error in v_T
exact evaluation	0.9362	0.0014071	—
10	1.0000	0.0013173	6.382
100	0.9600	0.0013722	2.480
1000	0.9400	0.0014014	0.405
5000	0.9356	0.0014080	0.064
10,000	0.9361	0.0014073	0.014

evaluation at:
$q_r = 0.08$
$\lambda_0 = 0.1437$
$\tau_0 = 0.009169$
$\sigma_{\delta\lambda} = 0.1$
$\sigma_{\delta\tau} = 0.1$

parabolic probability distribution functions are more representative of the true distribution functions of λ and τ than the frequently chosen normal or Gaussian probability distribution function, since the normal distribution function indicates there is a finite probability that λ or τ become negative or extremely large. The parabolic distribution does not allow this when realistic values of $\sigma_{\delta\lambda}$ and $\sigma_{\delta\tau}$ are used.

The average total cost per fin produced can be approximated by an equation of the form

$$C_p = c_1\lambda_0\tau_0 + c_2 \tag{6}$$

where c_1 is the cost per unit volume of fin material and c_2 is the fixed cost per fin, including fabrication, tubing, etc. Since some fins may be rejected because they do not meet the heat transfer requirement, the cost per acceptable fin is then

$$C_a' = \frac{c_1\lambda_0\tau_0}{P(q \geq q_r)} + \frac{c_2}{P(q \geq q_r)} \tag{7}$$

where $P(q \geq q_r)$ is the probability that the design meets or exceeds the q requirement q_r. The optimization problem here considers both the cost of rejecting unsatisfactory fins and the cost of conservative design. The variation of the second term with respect to λ_0 and τ_0 is usually small, so we can simply optimize $C_a \equiv C'_a - c_2/P$. Minimizing this cost is equivalent to minimizing the total volume of material per acceptable fin,

$$v_T = \frac{\lambda_0\tau_0}{P(q \geq q_r)} \tag{8}$$

The minimum value of v_T for given q_r, $\sigma_{\delta\lambda}$, and $\sigma_{\delta\tau}$ may be found by searching over λ_0 and τ_0. Since an algebraic expression for $P(q \geq q_r)$ cannot be obtained, the search offers considerable difficulty. Various methods for evaluating P and hence v_T are described in the following section. The methods differ in accuracy and degree of difficulty.

Determination of the Cumulative Distribution Function for q

By Simulation. The simplest method of obtaining P is by digital simulation. Given q_r, λ_0, τ_0, $\sigma_{\delta\lambda}$, and $\sigma_{\delta\tau}$, a random number generator provides properly distributed values of δ_λ and δ_τ that are used in equation (2) to obtain q. This is repeated N times; the number of times n that $q \geq q_r$ yields

$$P = \frac{n}{N} \tag{9}$$

While easy to program on a computer, the method is not practical for this problem. If N is too small, P is not accurate enough for the optimization process. For very large N, a high degree of accuracy may be obtained, but running times on the computer become prohibitively long. Table 1 shows some representative simulations at a single λ_0, τ_0 point for various values of N and compares the results to a more accurate method that is introduced next.

By Integration. Another method is to develop P by integrating the joint probability distribution function $f_{\lambda,\tau}(\lambda, \tau)$ over the appropriate limits, thus obtaining

$$P(q \geq q_r) = 1 - \iint f_{\lambda,\tau}(\lambda, \tau)d\lambda d\tau \equiv 1 - F \tag{10}$$

Nomenclature

$a = \tanh \alpha/\alpha$
C_a = average material cost per acceptable fin
C_p = average production cost per fin
c_1 = cost per unit volume of fin material
c_2 = fixed cost per fin
$f(\sigma, \delta)$ = probability distribution function defined by equation (4)
f_λ = probability distribution function defined by equation (11)
$f_{\lambda,\tau}$ = joint probability distribution function for λ and τ
f_τ = probability distribution function for τ
F = cumulative probability distribution function for q
h = heat transfer coefficient
k = thermal conductivity
n = number of successful fins in simulation
N = number of trials in simulation
L = fin length
P = probability that heat transfer requirement is met = $P(q \geq q_r)$
q = stochastic dimensionless heat transfer rate = $Q/[k(T_0 - T_a)]$
q_r = dimensionless heat transfer rate requirement
q_{00} = mean value of q
q_1 = mean value of q at $\lambda_{\min}$, $\tau_{\max}$
q_2 = mean value of q at $\lambda_{\max}$, $\tau_{\min}$
Q = heat transfer rate
S = safety factor
t = fin thickness
T_a = ambient temperature
T_0 = fin root temperature
v_T = average volume per acceptable fin = $\lambda_0\tau_0/P$
v_{Tx} = average volume per acceptable fin evaluated by exact calculation of P
$\alpha = \lambda_0/\tau_0^{1/2}$
δ_λ = stochastic variation in λ
δ_τ = stochastic variation in τ
$\Delta_\lambda = \operatorname{sech}^2 \alpha$
$\Delta_\tau = \tanh \alpha/(2\alpha) - \operatorname{sech}^2 \alpha/2$
λ = stochastic dimensionless length = hL/k
λ_0 = mean value of λ
σ_q = standard deviation of q
$\sigma_{\delta\lambda}$ = standard deviation of variation of δ_λ
$\sigma_{\delta\tau}$ = standard deviation of variation of δ_τ
σ_λ = standard deviation of λ
σ_τ = standard deviation of τ
Σ = variance parameter defined by equation (21)
τ = stochastic dimensionless thickness = ht/k
τ_0 = mean value of τ

Subscripts

max = upper limit of random variable in probability distribution function
min = lower limit of random variable in probability distribution function
00 = evaluation at $\delta_\lambda = \delta_\tau = 0$

Superscripts

* = optimal value
$\bar{\ }$ = root mean square

Table 2 Definition of expressions for $P(q \geq q_r)$

Case	Region	τ limits	λ limits	Integral	$P(q \geq q_r)$
$q_1 < q_2$	I. $q_r \leq q_1$	$\tau_{\min}$ to $\tau(q_r, \lambda_{\min})$	$\lambda_{\min}$ to $\lambda(q_r, \tau)$	F_I	$1 - F_I$
	II. $q_1 \leq q_r \leq q_2$	$\tau_{\min}$ to $\tau_{\max}$	$\lambda(q_1, \tau)$ to $\lambda(q_r, \tau)$	F_{II}	$1 - F_I - F_{II}$
	III. $q_2 \leq q_r$	$\tau(q_r, \lambda_{\max})$ to $\tau_{\max}$	$\lambda(q_r, \tau)$ to $\lambda_{\max}$	P_{III}	P_{III}
$q_1 = q_2$	I. $q_r \leq q_1$	$\tau_{\min}$ to $\tau(q_r, \lambda_{\min})$	$\lambda_{\min}$ to $\lambda(q_r, \tau)$	F_I	$1 - F_I$
	II. $q_1 \leq q_r$	$\tau(q_r, \lambda_{\max})$ to $\tau_{\max}$	$\lambda(q_r, \tau)$ to $\lambda_{\max}$	P_{II}	P_{II}
$q_2 < q_1$	I. $q_r \leq q_2$	$\tau_{\min}$ to $\tau(q_r, \lambda_{\min})$	$\lambda_{\min}$ to $\lambda(q_r, \tau)$	F_I	$1 - F_I$
	II. $q_2 \leq q_r \leq q_1$	$\tau(\lambda, q_2)$ to $\tau(\lambda, q_r)$	$\lambda_{\min}$ to $\lambda_{\max}$	F_{II}	$1 - F_I - F_{II}$
	III. $q_1 \leq q_r$	$\tau(q_r, \lambda_{\max})$ to $\tau_{\max}$	$\lambda(q_r, \tau)$ to $\lambda_{\max}$	P_{III}	P_{III}

where the integration limits encompass all λ and τ for which $q < q_r$. For λ and τ statistically independent, $f_{\lambda,\tau}(\lambda, \tau) = f_\lambda(\lambda) f_\tau(\tau)$. From equation (4), by the substitution $\sigma_\lambda = \lambda_0 \sigma_{\delta\lambda}$ and the coordinate transformation implied by letting $f_\lambda d\lambda = f(\sigma_{\delta\lambda}, \delta_\lambda) d\delta_\lambda$

$$f_\lambda = \frac{3}{4(5^{1/2}\sigma_\lambda)} \left[1 - \frac{(\lambda - \lambda_0)^2}{5\sigma_\lambda^2}\right], \quad 0 \leq \lambda_0 - 5^{1/2} \times \sigma_\lambda \leq \lambda \leq \lambda_0 + 5^{1/2}\sigma_\lambda \tag{11}$$

$$= 0, \quad \text{elsewhere.}$$

A similar expression can be written for f_τ. The only difficulty in evaluating the integral is determining the limits of integration. The region over which the integration occurs is the intersection of the rectangle $\tau_{\min} \leq \tau \leq \tau_{\max}$, $\lambda_{\min} \leq \lambda \leq \lambda_{\max}$ and the semi-infinite region $q \leq q_r$. Because $q = q_r$ is a line of negative slope, the outline of this intersection will be either a three-sided figure in various orientations or a four-sided figure, depending on which side of $\lambda_{\max}$, $\tau_{\min}$ and $\lambda_{\min}$, $\tau_{\max}$ the line $q = q_r$ falls. In either case $q = q_r$ forms one side of the figure. If we let

$$q_1 = \tau_{\max}^{1/2} \tanh (\lambda_{\min}/\tau_{\max}^{1/2}) \tag{12}$$

and

$$q_2 = \tau_{\min}^{1/2} \tanh (\lambda_{\max}/\tau_{\min}^{1/2}) \tag{13}$$

and constant q lines are plotted for q_1 and q_2, the various cases are evident. The cases are listed in Table 2 along with the corresponding integration limits, values of F_i as evaluated from equation (10), and expressions for $P(q \geq q_r)$. In the table, functional forms such as $\tau(q_r, \lambda_{\min})$ imply that τ is to be determined according to equation (2) with $q = q_r$ and $\lambda = \lambda_{\min}$.

These integrals may be evaluated numerically to a high degree of accuracy, and the results are exact in the sense that no assumptions have been made concerning the form of the distribution function for q. The results of this exact solution will be compared to the approximate solutions to be derived next.

By Two-Dimensional Taylor's Series. The exact solution requires rather long computation times (but not as long as the digital simulation). A root-mean-square approximation might be used based on a Taylor's series expansion for q [3], so that

$$q = q_{00} + \frac{\partial q}{\partial \delta_\lambda} \delta_\lambda + \frac{\partial q}{\partial \delta_\tau} \delta_\tau \tag{14}$$

and

$$\sigma_q^2 = \overline{q - q_{00}} = \left(\frac{\partial q}{\partial \delta_\lambda}\right)_{00}^2 \sigma_{\delta\lambda}^2 + \left(\frac{\partial q}{\partial \delta_\tau}\right)_{00}^2 \sigma_{\delta\tau}^2 \tag{15}$$

The subscript *00* implies that the function is evaluated at $\delta_\lambda = \delta_\tau = 0$. Now, if $\alpha = \lambda_0/\tau_0^{1/2}$

$$\left(\frac{\partial q}{\partial \delta_\lambda}\right)_{00} = \lambda_0 \operatorname{sech}^2 \alpha \equiv \lambda_0 \Delta_\lambda \tag{16}$$

$$\left(\frac{\partial q}{\partial \delta_\tau}\right)_{00} = (\tau_0^{1/2}/2) \tanh \alpha - (\lambda_0/2) \operatorname{sech}^2 \alpha \equiv \lambda_0 \Delta_\tau \tag{17}$$

$$q_{00} = \tau_0^{1/2} \tanh \alpha \equiv a\lambda \tag{18}$$

Under this linear approximation, since λ and τ are independent random variables, q is parabolically distributed; therefore, an algebraic expression for $P(q \geq q_r)$ can be derived. For the parabolic distribution analogous to equation (11),

for $q_r < q_{00} + 5^{1/2}\sigma_q$

$$P(q \geq q_r) = 0$$

for $q_{00} - 5^{1/2}\sigma_q \leq q_r \leq q_{00} + 5^{1/2}\sigma_q$

$$P(q \geq q_r) = \int_{q_r}^{q_{00} + 5^{1/2}\sigma_q} \frac{3}{4(5^{1/2}\sigma_q)} \left[1 - \frac{(q - q_{00})^2}{5\sigma_q^2}\right] dq$$

or

$$P(q \geq q_r) = \frac{3}{20(5^{1/2})} \left(\frac{q_r - q_{00}}{\sigma_q}\right)^3 - \frac{3}{4(5^{1/2})} \left(\frac{q_r - q_{00}}{\sigma_q}\right) + \frac{1}{2}$$

for $q_r < q_{00} - 5^{1/2}\sigma_q$

$$P(q \geq q_r) = 1.0 \tag{19}$$

With this algebraic expression for $P(q \geq q_r)$, a two-dimensional search over λ_0 and τ_0 for given $\sigma_{\delta\lambda}$, $\sigma_{\delta\tau}$, and q_r can easily be conducted to find the minimum v_T.

By One-Dimensional Taylor's Series. The foregoing two-dimensional, root-mean-square (2D RMS) method is simpler than the exact solution but is still somewhat awkward since the optimization is over two variables. Jakob [6] shows that for an optimal deterministic fin

$$\alpha = 1.4192 \tag{20}$$

If this is assumed true for the stochastic case at all times, then Δ_λ, Δ_τ, and a are constant. The problem now involves a one-dimensional search over λ_0 (or τ_0) to find the minimum v_T.

The optimal values of λ_0/q_r, τ_0/q_r^2, and v_T/q_r^3 are found to be functions of Σ only, where

$$\Sigma = (\Delta_\lambda^2 \sigma_{\delta\lambda}^2 + \Delta_\tau^2 \sigma_{\delta\tau}^2)^{1/2} \tag{21}$$

Numerical Results

Computations were performed with each of the above methods for numerous values of q_r, $\sigma_{\delta\lambda}$, and $\sigma_{\delta\tau}$ to minimize v_T; optimal values of λ_0 ($\equiv \lambda_0^*$) and τ_0 ($\equiv \tau_0^*$) were obtained.

Although according to the one-dimensional, root-mean-square method (1D RMS), λ_0^*/q_r, τ_0^*/q_r^2, and v_T^*/q_r^3 are functions of Σ only, this is not true in the exact and 2D RMS methods. The results suggest, however, that for practical purposes λ_0^*/q_r, τ_0^*/q_r^2, and v_T^*/q_r^3 are functions of $\sigma_{\delta\lambda}$ and $\sigma_{\delta\tau}$ only. Table 3 shows some results indicating this for several values of q_r.

The 2D RMS method provides a good approximation to the exact results for λ_0^*/q_r with the maximum percentage of error in the results in Fig. 1 being approximately 1.34 percent. The 1D RMS method is a poor approximation to the exact solution for λ_0^*/q_r (Fig. 2). The error is a result of the assumption that $\lambda_0/\tau_0^{1/2}$ is constant. Nonetheless, the maximum error is 12.54

Table 3 Lack of dependence of λ_0^*/q_r, τ_0^*/q_r^2, and v_{Tx}^*/q_r^3 on q_r

q_r	$\sigma_{\delta\lambda}$	$\sigma_{\delta\tau}$	λ_0^*/q_r	τ_0^*/q_r^2	v_{Tx}^*/q_r^3
0.02	0.1	0.1	1.7959	1.4326	2.7483
0.04	0.1	0.1	1.7960	1.4326	2.7483
0.06	0.1	0.1	1.7960	1.4326	2.7483
0.08	0.1	0.1	1.7960	1.4326	2.7483
0.02	0.1	0	1.9452	1.2641	2.5271
0.08	0.1	0	1.9455	1.2640	2.5271
0.02	0	0.1	1.5941	1.5426	2.5271
0.08	0	0.1	1.5966	1.5403	2.5271

percent. The maximum error in τ_0^*/q_r^2 for the 2D RMS method is approximately 1.90 percent (Fig. 3). In Fig. 4 the maximum error for the 1D RMS method is seen to be 13.62 percent.

Fig. 5 shows v_{Tx}^*/q_r^3 as a function of $\sigma_{\delta\lambda}$ and $\sigma_{\delta\tau}$, where v_{Tx} is v_T evaluated at λ_0^* and τ_0^* using the exact computation for P. The values of λ_0^* and τ_0^* are, however, found by minimizing v_T using the various approximation schemes. The maximum error in the given data for v_{Tx}^*/q_r^3 is 0.94 percent for the 2D RMS method and 3.66 percent for the 1D RMS method.

For the 1D RMS method, λ_0^*/q_r and τ_0^*/q_r^2 can be shown as functions of Σ alone (Fig. 6).

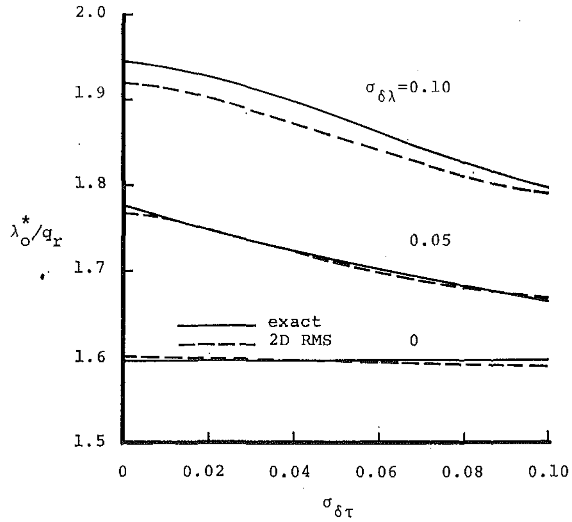

Fig. 1 Optimal λ_0/q_r determined by exact and 2D RMS methods

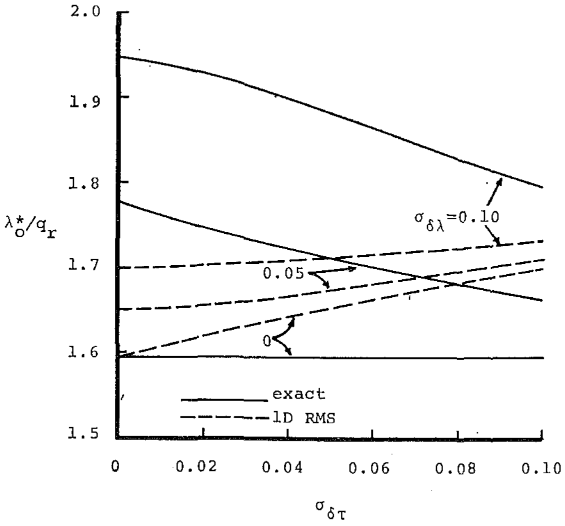

Fig. 2 Optimal λ_0/q_r determined by exact and 1D RMS methods

Computation times for the four methods are compared in Table 4, which shows estimated relative timings for each method. These values are for comparative purposes only; actual timings, relative or absolute, are highly dependent on the type of computer, search algorithm, initial values, etc.

The stochastic optimization approach given previously is superior to a safety-factor approach, but for the convenience and comfort of designers familiar with safety factors, the optimal safety factor is

$$S^* = \tau_0^{*1/2} \tanh (\lambda_0^*/\tau_0^{*1/2})/q_r \qquad (22)$$

The numerator is the nominal value of q for λ_0^* and τ_0^*, and q_r is the design or required value of q. Fig. 7 shows S^* as a function of $\sigma_{\delta\lambda}$ and $\sigma_{\delta\tau}$ for the 2D RMS and 1D RMS methods, respectively, with exact results included. These values of S do not determine the optimal fin, however, since there are two design variables, λ_0 and τ_0. However, if the designer used $\lambda_0^*/\tau_0^{*1/2} = 1.4192$, which is consistent with the 1D RMS approximation, S^* is a function of Σ only, as shown in Fig. 6. This relationship can be correlated by the linear equation

$$S^* = 1 + 2\Sigma \qquad (23)$$

The utility of this last equation is shown in Table 5. It is desired to design an optimal fin given $q_r = 0.08$, $\sigma_{\delta\lambda} = 0.1$, and $\sigma_{\delta\tau} = 0.1$. An exact solution is given, along with an optimal safety-factor solution found by using equations (20) and (23). Finally, a solution is given with a more conservative safety factor, in which the designer has decided, in this example, to design the fin for a value of q_r that is 30 percent higher than the normally required value.

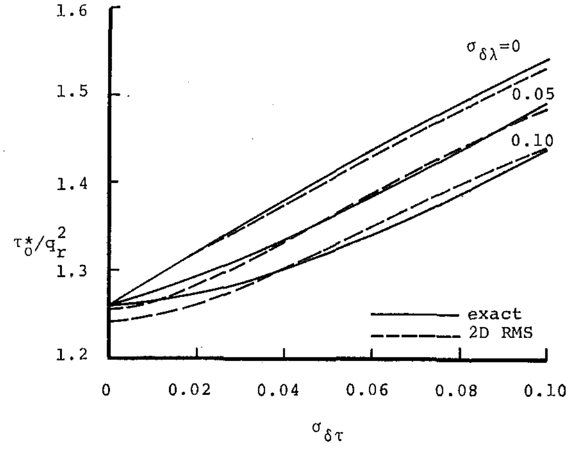

Fig. 3 Optimal τ_0/q_r^2 determined by exact and 2D RMS methods

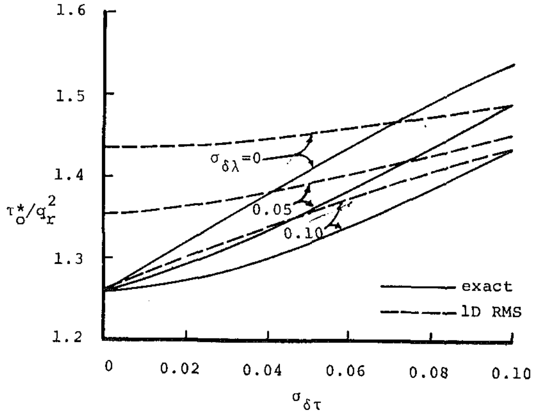

Fig. 4 Optimal τ_0/q_r^2 determined by exact and 1D RMS methods

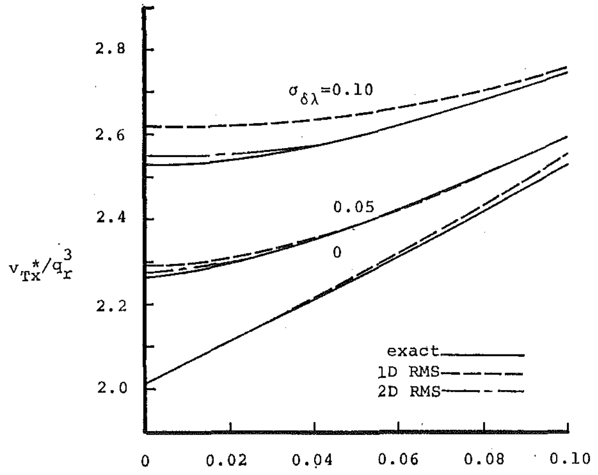

Fig. 5 Optimal v_T/q_r^3

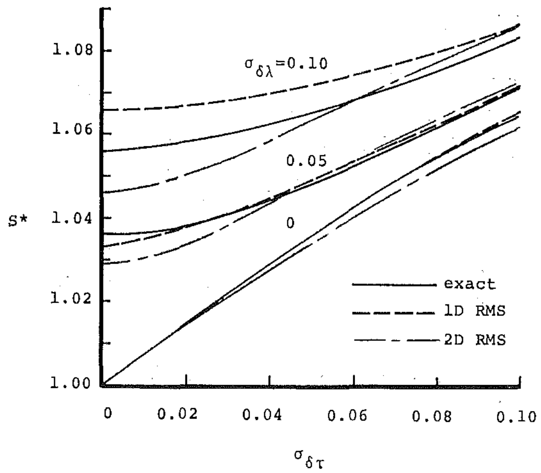

Fig. 7 Optimal safety factor

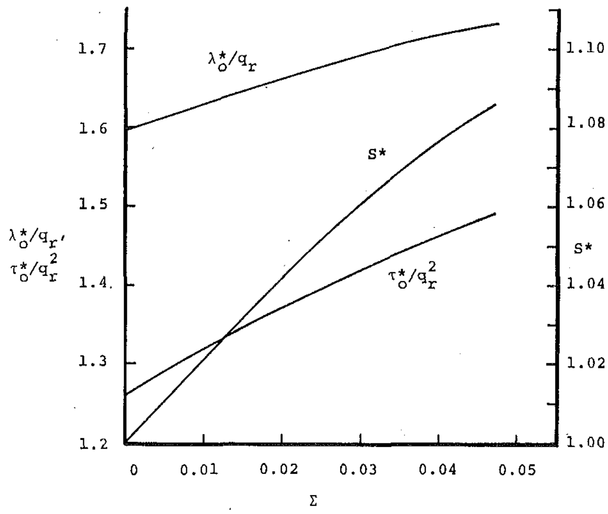

Fig. 6 λ_0^*/q_r, τ_0^*/q_r^2, and S^* versus Σ

Table 4 Comparison of computation times

Optimization method	Estimated relative computation time
simulation	39,656
"exact" by integration	8292
2D RMS	25
1D RMS	1

Table 5 Comparison of exact, optimal safety-factor, and arbitrary safety-factor solutions

Safety factor S	λ_0	τ_0	P	v_{Tx}	v_{Tx}/q_r^3	Percentage excess in v_{Tx}/q_r^3
optimal	0.144	0.00917	0.936	0.00141	2.75	–
$1 + 2\Sigma$	0.140	0.00968	0.954	0.00142	2.77	0.71
1.3	0.166	0.0137	1.000	0.00227	4.43	61.2

Conclusion

Four methods of determining the optimal fin design have been discussed. The two-dimensional method, based on the linearization of q to determine its variance, provides results close to the exact solution. Since in this problem $\lambda_0^*/\tau_0^{*1/2}$ remains relatively constant, a one-dimensional method may also be applied to determine the optimal safety factor. In other problems a similar multidimensional analysis could be conducted in search of groupings of variables that are almost constant so that a similar reduction in dimensionality could be effected.

All methods provide an optimal safety factor, but equation (23) gives S^* as a function of Σ alone. Although only an approximation, the use of this safety factor with equation (20) is convenient for designers and provides them with a rational and nearly optimal selection of the fin dimensions.

Although the fin problem is not representative of all problems in engineering, the results of this investigation are at least encouraging with regard to the use of linearization schemes for stochastic optimization and design.

Acknowledgment

This research was supported by the Office of Sea Grant Programs, National Oceanic and Atmospheric Administration, through grant GH-109.

References

1 Shigley, J. E., *Mechanical Engineering Design*, McGraw-Hill, New York, 1962.

2 Haugen, E. B., *Probabilistic Approaches to Design*, Wiley, New York, 1968.

3 Costello, F. A., "Limits of Validity of RMS Approximation for Satellite-Temperature Variances," JOURNAL OF HEAT TRANSFER, TRANS. ASME, Series C, Vol. 90, No. 4, Nov. 1968, pp. 487–488.

4 Hung, H. M., "Heat Transfer of Thin Fins With Stochastic Root Temperature," JOURNAL OF HEAT TRANSFER, TRANS. ASME, Series C, Vol. 91, No. 1, Feb. 1969, pp. 129–134.

5 Samuels, J. C., "Heat Conduction in Solids with Random External Temperatures and/or Random Internal Heat Generation," *International Journal of Heat and Mass Transfer*, Vol. 9, 1966. pp. 301–314.

6 Jakob, M., *Heat Transfer*, Vol. I, Wiley, New York, 1949.

A. F. EMERY
Professor,
Department of Mechanical Engineering,
University of Washington,
Seattle, Wash.
Consultant,
Sandia Laboratories,
Livermore, Calif.

The Use of Singularity Programming in Finite-Difference and Finite-Element Computations of Temperature

This report contains a description of a numerical technique designed to overcome the difficulties associated with the usual solution of two-dimensional discretized thermal problems when there are singularities arising from point sources or discontinuous boundary conditions. The method is here applied to both the finite-difference and the finite-element approach by incorporating in the numerical computations the known analytical form of the singularities.

§1 Introduction

THE USUAL numerical method of solving linear two-dimensional field problems with singularities, such as those arising from point sources or from sharp boundary corners, is to refine the mesh, but this can be done only at the expense of increased computing effort, and frequently it is not possible to know when the mesh has been sufficiently refined.

A more promising approach is to superimpose a closed-form analytical solution and a numerical solution in the vicinity of the singularity. This can be done in both the finite-difference and the finite-element methods of solving the field equations. Motz [1][1] presented one of the first demonstrations of this technique in solving a Poisson equation for a sharp reentrant corner by finite differences, and this approach was later extended by Woods [2] to classical linear elastic problems. Morley [3] and Fix [4] have applied the technique to elastostatic eigenvalue problems solved by the Rayleigh-Ritz technique. Fix has shown that only if the singular solution is adjoined to the polynomial function used in the numerical solution is the normal accuracy of the finite-difference operator achieved. Emery and Segedin [5–8] have used superposition in conjunction with finite-difference methods to solve several fracture-mechanics problems. The use of superposition with finite-element algorithms is typified by the solutions of Wait and Mitchell [9] to Motz's original problem. Yamamoto [10, 11] has utilized the method for the solution of fracture-mechanics and stress-concentration problems. Pian and Tong [12] have used the technique in their hybrid finite-element model for fracture analysis. Gallagher [13] gives a review of the different superposition models available. In this paper we would like to demonstrate the applicability of superimposing analytical solutions to thermal problems and to illustrate how the method can be incorporated into the usual finite-difference and finite-element computer codes. The superposition technique used herein was termed singularity programming in [14] and should not be confused with the usual superposition method where a singular solution or a Green's function is adjoined to a second solution, whose values are then adjusted such that the combined solution achieves the correct boundary conditions. In singularity programming, the singular solutions are used to generate an effective (or pseudo) spatially varying heat source, which is usually only considered close to the point of the singularity.

In §2 and §3 the finite-difference and finite-element approaches are outlined. In §4 they are applied to problems of point sources of heat. The solution is found for a range of mesh sizes, and it is shown that with singularity programming, striking accuracy can be obtained with a coarse mesh. In §5 a discontinuous boundary condition is treated for which the singularity functions are known.

In §6 the method is applied to thermal singularities caused by a boundary corner. In contrast to the previous sections where the singularity function was known completely, here the form of the singularity is known, but not its strength. Further effort is thus required to evaluate these singularity strengths K. Usually there are several singularity functions that must be considered, and it may be that the evaluation of the several K's does not yield consistent values. It has been found that by including extra singularity functions consistency can be obtained. In this sense, the technique is adaptive in that the need for higher order singularity functions can be detected. In §7, singularity programming is applied to a problem involving an instantaneous plane source.

---

[1] Numbers in brackets designate References at end of paper.

Contributed by the Heat Transfer Division for publication (without presentation) in the JOURNAL OF HEAT TRANSFER. Manuscript received by the Heat Transfer Division September 13, 1972. Paper No. 73-HT-K.

§2 Finite Difference Singularity Programming

Consider a region R with the bounding surface ∂R and let the variable T satisfy the field equation of conservation of energy[2]

$$k\nabla^2 T + Q + q = 0 \tag{1}$$

where Q represents distributed heat sources and q represents point sources of heat and the boundary condition on ∂R

$$\beta T = g \tag{2}$$

Replacing the derivatives in equations (1) and (2) by finite-difference expressions of the form

$$\frac{\partial^2 T}{\partial x^2} = \frac{T(x + \Delta x) - 2T(x) + T(x - \Delta x)}{\Delta x^2} + 2\frac{\partial^4 T}{\partial x^4}\frac{\Delta x^2}{4!} + \ldots$$

and ignoring the error terms will yield good approximations except near "singular points." A singular point is defined as any point in $R + \partial R$ for which T or a derivative of T in the Taylor series expansion for T becomes infinite or large in such a way that the corresponding error term in the finite-difference equations cannot be ignored. Such singularities can be found at point sources of heat, or at abrupt changes in boundary conditions or abrupt changes in direction of the boundary tangent as at re-entrant corners. Here nearness is characterized not by the physical distance x but by the distance in terms of the number of nodal points, for if $\Delta x \to 0$ the error term will tend toward zero for any nodal point not at the singularity.

Hence it is usual to treat singular problems by reducing the mesh spacing Δx in order to keep the error terms negligible. While this remedy can be effective if the troublesome derivative is large, it is inadequate if the derivative becomes infinite at the nodal point in question, and in any case the price to be paid for this is a mesh size so small that the computational effort required can become prohibitive.

The essence of singularity programming is to assume that T can be decomposed into two parts:

$$T = \bar{T} + \sum_{p=1}^{P}\sum_{i=1}^{N_p} K_i^P S_i^P = \bar{T} + \sum_{j=1}^{N} K_j S_j = \bar{T} + K_i S_i \tag{3}$$

where P is the number of singular points in $R + \partial R$, N_p is the number of singular functions to be considered at each singular point, N is the product $P \times N_p$, and in the last form of equation (3) the Einstein summation convention is used. $\bar{T}$ is "smooth" in the sense that the finite-difference approximations involving $\bar{T}$ have acceptable accuracy. The S_i, termed singularity functions, are assumed to satisfy the homogeneous form of the equations for T, namely when point heat sources are absent,

$$\begin{aligned} \nabla^2 S_i &= 0 \text{ in } R \\ \beta S_i &= 0 \text{ on } \partial R \text{ near the singularity} \end{aligned} \tag{4a}$$

or to satisfy only the field equation when point sources are present

$$K_i \nabla^2 S_i + \frac{q_i}{k} = 0 \tag{4b}$$

In the former case the K_i depend upon the boundary conditions that cause the singularity, while in the latter case the K_i are known through the magnitude of q_i. Birkhoff [15] gives the derivation of several singularity functions for the Poisson equation. Generally speaking, S_i is found by solving $\nabla^2 S_i = 0$ in polar coordinates, i.e., $S_i = r^n\,(A \cos n\theta + B \sin n\theta)$, with A, B, and n adjusted to satisfy $\beta S_i = 0$ in ∂R near the singularity.

If we denote the finite approximation to ∇^2 and β as $\Diamond$ and B, it follows that

$$\Diamond T = \Diamond \bar{T} + K_i \Diamond S_i$$

Since $\bar{T}$ is smooth, $\Diamond \bar{T}$ is a good approximation to $\nabla^2 \bar{T}$, and we have

$$\begin{aligned} \Diamond T &= \nabla^2 \bar{T} + K_i \Diamond S_i \\ &= \nabla^2 T - K_i \nabla^2 S_i + K_i \Diamond S_i \end{aligned} \tag{5}$$

or

$$\Diamond T = K_i \Diamond S_i - Q/k$$

Correspondingly we find upon assuming that $B\bar{T} = \beta \bar{T}$

$$\begin{aligned} BT &= \beta T + K_i(BS_i - \beta S_i) \\ &= g + K_i(B - \beta)S_i \end{aligned} \tag{6}$$

It is thus apparent that the presence of singularities can be taken into account by adding the pseudo heat sources $K_i \Diamond S_i$ and the pseudo boundary conditions $K_i(B - \beta)S_i$ to the actual heat sources Q and boundary conditions g and solving the set of equations (5) and (6). The solution then proceeds by taking the standard finite-difference program and adding to each nodal point the pseudo source term and to each boundary nodal point the temperature or flux pseudo boundary contribution $K_i(B - \beta)S_i$. In evaluating these terms, $\Diamond$ and B are the operators used by the program. For example, if ∇^2 is modeled by $\{T(i, j + 1) - 2T(i, j) + T(i, j - 1)\}/\Delta x^2 + \{T(i + 1, j) - 2T(i, j) + T(i - 1, j)\}/\Delta y^2$, then $\Diamond S_i$ would be evaluated by substituting S_i for T in the preceding formula. It is usual to neglect all $\Diamond S_i$ whose values are less than 1 percent of $\Diamond S_i$ in the immediate vicinity of the singularity. Likewise, most problems in which the boundary is a large number of nodal points away from the singularity will have a negligible contribution to g.

For problems where both K_i and S_i are known, this is all that is needed.

When the singularity strength is unknown, K_i can most conveniently be found by first solving two subsidiary solutions in the following way:

1 Solve for T^0 from

$$\begin{aligned} \Diamond T^0 + Q/k &= 0 \\ BT^0 &= g \end{aligned} \tag{7}$$

which corresponds to the usual finite-difference solution ignoring singularities

2 Solve for T^1 from

$$\Diamond T_i^1 = \Diamond S_i \qquad BT_1^1 = (B - \beta)S_i \tag{8}$$

The solution of equations (5) and (6) is then written in the form

$$T = T^0 + K_i T_1^1 \tag{9}$$

3 In order to evaluate K_i, we now collocate by insisting that the energy equation (1) hold at points on the boundary at which we have hitherto required only satisfaction of the boundary conditions.[3] If $\Diamond^*$ is the finite-difference form of ∇^2 on the boundary, we have

$$\Diamond^* T = K_i \Diamond^* S_i - Q/k$$

or

$$\Diamond^* T^0 = K_i(\Diamond^* S - \Diamond^* T_i^1) - Q/k \tag{10}$$

4 Equation (10), when applied to the requisite number of boundary points, will yield sets of algebraic equations for K_i. It is best to use points on the boundary near the singularity to determine K_i, for at points far from the singularity, S_i becomes

---

[2] Although the derivation is for constant thermal properties, the extension to variable properties is easily carried out.

[3] One of the simplest ways to detect the presence of a singularity is to check the satisfaction of the energy equation at boundary points (normally this check is not made since the energy equation is usually not applied at a boundary point). Even weak singularities will usually display gross errors near the singular point.

smooth and $(\Diamond - \nabla^2)S_i$ approaches zero quite rapidly. Because of truncation errors, the use of points for which $\Diamond{}^*T^0 + Q/k$ and $\Diamond{}^*S_i - \Diamond{}^*T_i{}^1$ are small often leads to ill-conditioned equations and consequently erratic values of K_i (see [14] for examples). When using several boundary points to determine K_i, if the values are equal we say that K_i is consistent and that the solution has been found. However, if the values are not equal, either the nodal spacing is too coarse or some important singularities have been neglected (see §4 in the following).

5 If there are multiple singularities, each singular point gives rise to values of K_i, say $K_i{}^A$ and $K_i{}^B$. However, when using boundary points near singularity A, the truncation error will adversely affect the values of $K_i{}^B$. The best procedure is to evaluate $K_i{}^A$ using points near A and $K_i{}^B$ using points near B, which corresponds to $(\Diamond - \nabla^2)S_i$ being equal to zero at points far from the singularity. This can always be achieved by refining the mesh sufficiently. Otherwise it is best to regard the terms in $K_i{}^B$ as known perturbations in the equations for A and vice versa, and continually correct until convergence has been achieved.

§3 Finite-Element Singularity Programming

The appropriate integral to minimize for steady thermal problems [16] is

$$I = \frac{1}{2}\int_R \left\{ k\left[\left(\frac{\partial T}{\partial x}\right)^2 + \left(\frac{\partial T}{\partial y}\right)^2\right] - QT \right\} dA + \int_R q_n T ds \tag{11}$$

where q_n is the outwardly directed heat flux on the boundary of any element that does not have a prescribed boundary temperature.

We subdivide R into elemental areas and let the temperature be expressed in polynomial form by the basis functions

$$T = \alpha_0 + \alpha_1 x + \alpha_2 y + \ldots + K_i S_i \tag{12}$$

or

$$T = \langle f\rangle\{\alpha\} + \langle S\rangle\{K\} \tag{13}$$

where $\langle f\rangle$ is a row vector whose components are functions of x and y and $\{\alpha\}$ is a column vector of coefficients; $\langle S\rangle$ is a row vector whose components are singularity functions and $\{K\}$ is a column vector of singularity strengths. If the temperatures and the singularity functions at the nodal points are denoted by $\hat{T}$ and $\hat{S}$, respectively, we have

$$\{\hat{T}\} - [\hat{S}]\{K\} = [A]\{\alpha\} \tag{14}$$

where $[A]$ is a square matrix whose rows are $\langle f\rangle$ evaluated at the nodal points and $[\hat{S}]$ is a matrix (not necessarily square) whose rows are $\langle S\rangle$ evaluated at the nodal points. Solving for $\{\alpha\}$ we have

$$\{\alpha\} = [A]^{-1}\{\hat{T}\} - [A]^{-1}[\hat{S}]\{K\} \tag{15}$$

or

$$T = \langle f\rangle[A]^{-1}\{\hat{T}\} - \langle f\rangle[A]^{-1}[\hat{S}]\{K\} + \langle S\rangle\{K\} \tag{16}$$

If we define

$$\begin{aligned}
\bar{M} &= [A^{-1}]^T\{k_x\langle f_x\rangle^T\langle f_x\rangle + k_y\langle f_y\rangle^T\langle f_y\rangle\}[A^{-1}] \\
\bar{N} &= [A^{-1}]^T\{k_x\langle f_x\rangle^T\langle S_x\rangle + k_y\langle f_y\rangle^T\langle S_y\rangle\}[A^{-1}] \\
\bar{P} &= k_x\langle S_x\rangle^T\langle S_x\rangle + k_y\langle S_y\rangle^T\langle S_y\rangle \\
\bar{R} &= Q\langle f\rangle \\
\bar{O} &= Q\langle S\rangle \\
A &= [A^{-1}]
\end{aligned} \tag{17}$$

where $\langle f_x\rangle = \langle \partial f/\partial x\rangle$, superscript T denotes transpose, and M, N, P, R, and O are the integrals of $\bar{M}$ et seq. over the elemental area, we find for constant k_x and k_y

$$\begin{aligned}
I = \frac{1}{2}[\{\hat{T}\}^T\{M\{\hat{T}\} + (N - M\hat{S})\{K\}\} \\
+ \{K\}^T\{(N - \hat{S}^T M)\{\hat{T}\} + (P - N^T\hat{S} - \hat{S}^T N + \hat{S}^T M\hat{S})\{K\}\} \\
+ 2RA\{\hat{T}\} - 2RA\hat{S}\{K\} + 2O\{K\}]
\end{aligned} \tag{18}$$

[Differentiating with respect to T_i and K_i, we find the linear equations for the element to be

$$\frac{\partial I}{\partial T_i} = M\{\hat{T}\} + \underline{(N - M\hat{S})\{K\}} + A^T R^T = 0 \tag{19}$$

$$\begin{aligned}
\frac{\partial I}{\partial K_i} = \underline{(N^T - \hat{S}^T M^T)\{\hat{T}\}} + \underline{(P - N^T\hat{S} - \hat{S}^T N + \hat{S}^T M\hat{S})}\{K\} \\
- \underline{\hat{S}^T A^T R^T} + \underline{O^T} = 0
\end{aligned} \tag{20}$$

Here M is the usual thermal-conductance matrix [16] and $A^T R^T$ is the usual thermal source term; the underlined terms are the additional terms due to singularity programming.

Singularity programming is implemented by taking a standard finite-element thermal analyzer and adding the underlined terms. In general these terms are added only to the conductance matrices of the elements near the singularity. Some testing must be done to determine how far the influence of the singularity extends, and thus how many elements must include these terms, but normally the distance is not large. Inasmuch as S must be evaluated in each element (for example if $S = r^n \cos n\theta$, r is measured from the point of the singularity to the nodal point of the element, and thus S is not independent of an element's spatial position or orientation) and the integrating routines for N, P, and O must be rather carefully formulated in order to achieve a satisfactory accuracy, as well as the fact that the inclusion of S in very many elements effectively expands the band width of the matrix, it is best if the singular terms are added only to elements close to the singularity where the effect of singularity programming is most noticeable.

The polynomial portion of T is determined by the type of element used: bilinear for three-node triangles, bicubic for four-node quadrilaterals or six-node triangles, etc. Inasmuch as one of the primary aims of singularity programming is to yield improved accuracy in the simplest manner, the bilinear polynomial $\alpha_0 + \alpha_1 x + \alpha_2 y$ was chosen. The choice was dictated by the observation that almost all existing finite-element thermal analyzers are based upon bilinear polynomials and by previous tests of the bicubic and hybrid models [16] indicating that only the six-node triangle was better. However, the difficulty of automatic mesh generation for the six-node triangle discouraged its use. Furthermore, if singularity programming is valid, then the singular function should account for all of the ill-behaved part of T and the polynomial basis should need to treat only the smooth part of T, and for this the bilinear form should suffice.

In general, equations (19) and (20) are sufficient to define the solution, and when the element contributions are combined and the flux boundary integral included, if necessary, equation (11), the solution to the set of equations will yield T and $\{K\}$.

§4a The Point-Source Problem—Known Value of *K*

Consider a square region $(-{}^1/_2 < x < {}^1/_2, -{}^1/_2 < y < {}^1/_2)$ with zero boundary temperature and with a steady line source of heat of strength $K = 1.0$ Btu/hr-ft located at the center $x = y = 0$. The singular solution S is given by

$$S = \frac{-1}{2\pi k}\ln(r/R) \quad (r^2 = x^2 + y^2) \quad \text{and} \quad R = \text{reference length} \tag{21}$$

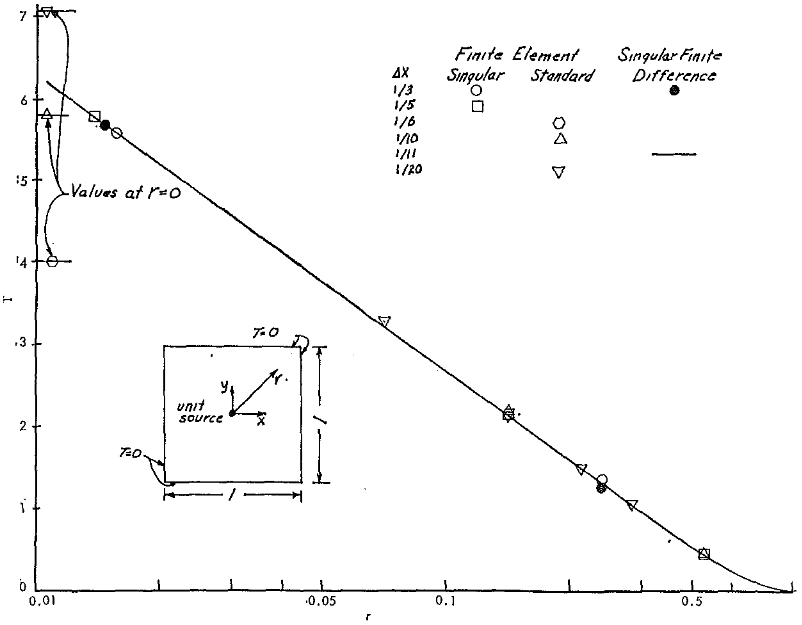

Fig. 1 Comparison of temperature along the diagonal

To establish the element thermal-stiffness matrix, a source of heat of strength $1/\pi\epsilon^2$ was uniformly distributed over a circle of radius ϵ centered at $x = y = 0$. The stiffness matrix was formed and then ϵ was allowed to approach zero. Fig. 1 compares the temperatures on the diagonal obtained by the standard finite element, singular finite element, and singular finite difference. It is obvious that the singular techniques using a mesh spacing of $\Delta x = \Delta y = {}^1/_3$ are as accurate as nonsingular methods using $\Delta x = \Delta y = {}^1/_{20}$. And of course near the singularity even the finest regular mesh cannot retain any reasonable accuracy, as evidenced by the temperatures computed at the source as indicated by the limiting lines on the figure. The values of T shown for points on the diagonal that are within the singular element enclosing the point source were estimated by interpolating the smooth part of T and adding S. In fact, one of the major shortcomings of the standard procedure is its inability to provide for any reasonably accurate interpolation near the source.

§4b The Two-Point Source Problem—*K* Known

When two point sources of unit strength, S_1 and S_2, are placed at $x = -0.125$, $y = 0$ and at $x = 0.125$, $y = 0$ respectively, see Fig. 2, the singular functions are again known, but now we must consider the interaction between the two singularities. Fig. 2 compares the standard finite-element and the singular finite-element solutions, and the superiority of the singular element with $\Delta x = \Delta y = {}^1/_3$ is apparent. The success of the singular element is due to its ability to extract from the numerical solution the singular part. The dashed curve in Fig. 2 shows the smooth part of the solution (i.e., $T - K_iS_i = \bar{T}$) for $\Delta x = {}^1/_{11}$, and its smoothness is readily observable.

In computing this solution with finite differences by imaging about the line $x = 0.0$, care must be taken to consider the effect of S_2 by including the term $\Diamond S_2$ in the region $-0.5 \leq x \leq 0.0$, in addition to $\Diamond S_1$. Table 1 gives a comparison of the temperature at $x = 0$, $y = 0$ when $\Diamond S_2$ is and is not considered. Apparently, for $\Delta x = {}^1/_{11}$ where the singular points are separated by about six mesh increments, the second singularity no longer contributes to the pseudo heat source term because $(\Diamond - \nabla^2)S_2$ has sufficiently approached zero.

Table 1 *T* at x = 0 and y = 0

	$\Delta x = \Delta y = {}^1/_3$	$\Delta x = \Delta y = {}^1/_{11}$
$\bar{T}$ $(\Diamond S_2 = 0)$	−0.199	−0.179
$\bar{T}$ $(\Diamond S_2 \neq 0)$	−0.187	−0.177
T $(\Diamond S_2 = 0)$	0.132	0.155
T $(\Diamond S_2 \neq 0)$	0.144	0.157

§5 Discontinuous Boundary Conditions—*K* Known

Consider the rectangular region shown in Fig. 3(*b*). The temperature is prescribed to be zero for $0 \leq x \leq 0.25$ and $0.75 \leq x \leq 1.0$ and unity for $0.25 \leq x \leq 0.75$. Because of the discontinuous change in temperature at $x = 0.25$ and 0.75, there is a singularity in the heat flux at these points. The appropriate singular function is

$$S = \frac{\theta_1 - \theta_2}{\pi} \tag{22}$$

with the corresponding heat flux on $y = 0$ of

$$q_y = \frac{1}{\pi}\left(\frac{\cos\theta_1}{r_1} - \frac{\cos\theta_2}{r_2}\right) \tag{23}$$

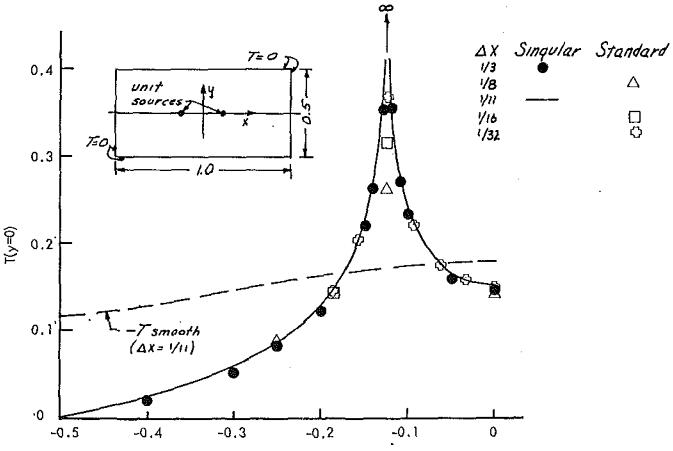

Fig. 2 Comparison of the temperatures along $y = 0$ predicted by singular and standard finite-element procedures

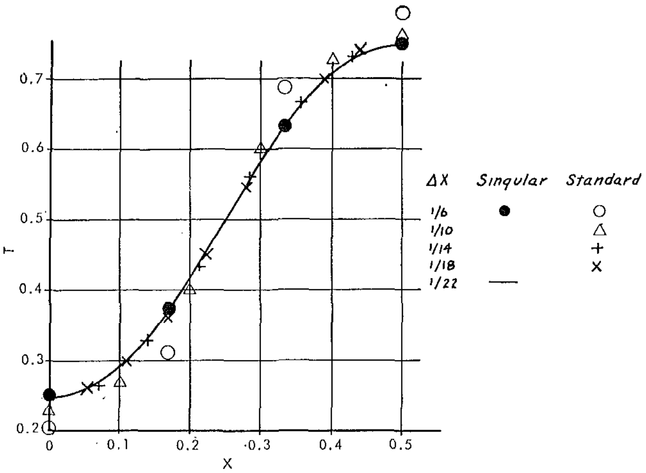

Fig. 3(a) Temperatures on the lower surface calculated by singular and standard finite-difference procedures

Because the usual finite-difference procedure assumes that the value of a function at a nodal point represents the average value over the region $-\Delta x/2 \leq x \leq \Delta x/2$, the singular point was placed at the center of a mesh interval. The computations were made by assuming that the insulated lower surfaces was a plane of symmetry. Consequently it was necessary to introduce the images of the singular points 1 and 2 in the calculations. Figure 3(*a*) is a comparison of the temperatures calculated on the lower surface by the standard finite-difference and singular finite-difference procedures. Acceptable accuracy is obtained by the standard technique only for $\Delta x < {}^1/_{14}$, even though the singularity is far removed from this plane, whereas $\Delta x = {}^1/_6$ suffices for the singular procedure. The heat flux on the upper surface $y = 0$, $0 \leq x \leq 0.25$ is compared in Fig. 3(*b*). As expected, even the use of $\Delta x = {}^1/_{22}$ with the standard procedure is not adequate, while $\Delta x = {}^1/_6$ with the singular approach is quite satisfactory. The heat flux for the singular procedure is calculated according to

$$q = q_{\text{smooth}} + q_{\text{sing.}} = k\left\{\Delta T_{\text{smooth}} + \frac{\partial T_{\text{sing.}}}{\partial y}\right\}$$

$$= k\left\{\Delta(T - T_{\text{sing.}}) + \frac{\partial T_{\text{sing.}}}{\partial y}\right\} \quad (24)$$

where Δ is the finite-difference form of $\partial/\partial y$ and $\partial T_{\text{sing.}}/\partial y$ is determined analytically.

§6 Interrupted Heat Flux—*K* Unknown

Consider the rectangular area shown in Fig. 4 where the flow of heat from the left boundary to the lower is impeded by an insulated splitter plate extending from $x = 0$ to $x = 0.5$. The general form of the singularity function is

$$S = r^n(A \cos n\theta + B \sin n\theta)$$

where A, B, and n determined from the boundary conditions near the singularity for the configuration of Fig. 4, namely $q_y = 0$ on $\theta = \pi$ and $-\pi$, are

$$n = \frac{m\pi}{\alpha} \; (m = 1, 2, 3, \ldots) \text{ where } \alpha \text{ is the included angle}$$

$$(2\pi \text{ in this case})$$

and

$$A = B\,\frac{\sin m\pi}{\cos m\pi}$$

In this case there are at least two operative singular functions

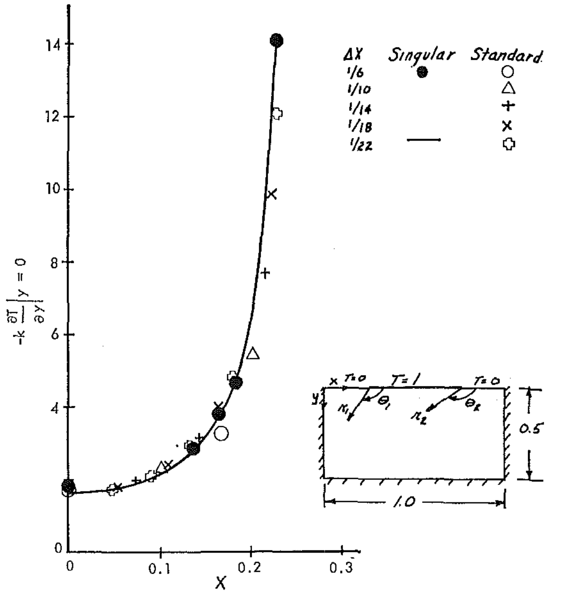

Fig. 3(*b*) Heat flux on the upper surface calculated by standard and singular finite-difference procedures

$n = {}^1/_2$ and $n = {}^3/_2$ that give rise to infinite terms in the finite-difference expressions for $\partial^2T/\partial x^2$ and $\partial^2T/\partial y^2$. Consequently, there are two values of K_i to be determined.

§6a Finite-Difference Singularity Programming

Using the singular finite-difference technique with only S_1 ($n_1 = {}^1/_2$) and applying equation (10) at the nodal point at the tip of the splitter and at the next two nodal points on the splitter, see Fig. 4, we find the results of Table 2. We note that: (*a*) K_1 varies significantly from point to point; (*b*) K_1 evaluated at the tip varies as Δx is diminished. This type of variation, namely point to point and with Δx, suggests that the next singularity function with $n_2 = {}^3/_2$ must be considered. By including K_2S_2 and solving the set of simultaneous equations at P and Q, P and R, and Q and R, we find the average K_1, K_2 and their standard deviations given in Table 3. By including K_2 we note that the values of $\bar{K}_1$ agree to within 0.1 percent and that the standard deviation is less than ${}^1/_2$ percent. This type of consistency is taken to be indicative of a satisfactory solution. Furthermore, a mesh of $\Delta = {}^1/_8$ is seen to be quite as good as $\Delta = {}^1/_{20}$. The values of K_2 do not appear to be as consistent, showing a deviation of about 15 percent. This order of variation is not unusual and appears to be related to the greater sensitivity of the numerics to strong singularities ($n = {}^1/_2$) than to the lesser ones ($n = {}^3/_2$). The importance of evaluating K_2 lies not with its own value but with its effect upon the consistency of K_1. Table 4 lists the con-

Table 2 Evaluation of K_1 when K_2 is neglected

Δx =	$K_1(P)$	$K_1(Q)$	$K_1(R)$
${}^1/_8$	1.1567	1.1023	1.0108
${}^1/_{12}$	1.1490	1.1132	1.0688
${}^1/_{16}$	1.1453	1.1187	1.0835
${}^1/_{20}$	1.1432	1.1219	1.0920

Table 3 Simultaneous evaluation of K_1 and K_2

Δx	$\bar{K}_1$	$\sigma(K_1)$	$\bar{K}_2$	$\sigma(K_2)$
${}^1/_8$	1.1325	0.0012	−0.492	0.013
${}^1/_{12}$	1.1326	0.0016	−0.431	0.075
${}^1/_{16}$	1.1334	0.0029	−0.429	0.063
${}^1/_{20}$	1.1338	0.0018	−0.442	0.050

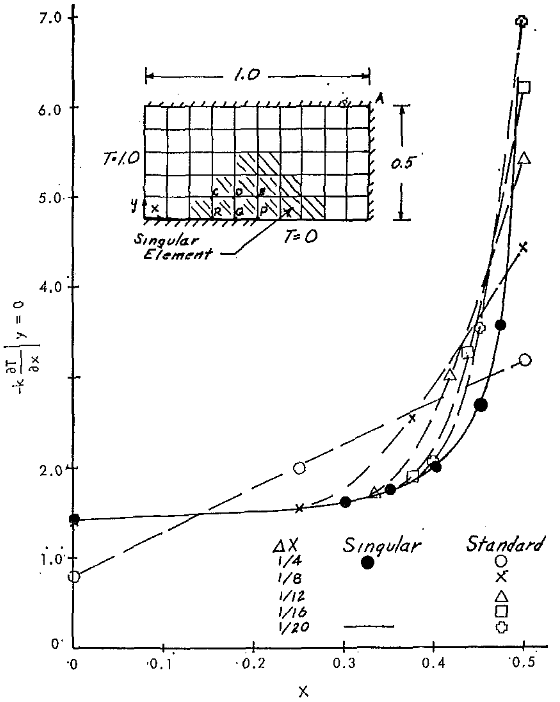

Fig. 4(a) Comparison of singular and standard finite-difference values of heat flux along the splitter plate

Table 4 Temperature at point A

Δx	T_0	K_1T^1	K_2T^2	$T_A\ (= T^0 + K_1T^1 + K_2T^2)$
$^1/_8$	0.1735	0.0073	0.0007	0.1815
$^1/_{12}$	0.1784	0.0038	0.0003	0.1824
$^1/_{16}$	0.1801	0.0025	0.0001	0.1827
$^1/_{20}$	0.1809	0.0018	0.0001	0.1827

tribution of T^0, K_1T^1, and K_2T^2 to the temperature at point A of Fig. 4. The contribution of K_2T^2 even with the coarse grid of $\Delta x = \Delta y = {}^1/_8$ is only 0.4 percent of T_A and less than 10 percent of the effect of K_1T^1. Consequently the 15 percent variation in K_2 is not incommensurate with a variation of 0.5 percent in K_1.

§6b Finite-Element Singularity Programming

The splitter-plate problem was also solved using the finite-element method with square elements. In this case the number of elements that included the singular effect was varied. Fig. 4 illustrates the case where 12 elements included the singularity functions. Other cases were generated by expanding or contracting the singular-element region in a nearly circular pattern. Table 5 lists the values of K_1, K_2, and T_A and compares them to the finite-difference singularity programming results. In these finite-element calculations the values of K_1 and K_2 appear to be more dependent upon the number of singular elements than upon the total number of elements. Even when all of the elements are singular, the finite-element results for K_1 and K_2 are significantly different from the finite-difference results, although the values of T_A are not. This is caused by a compensation between the effects of K_1T^1 and K_2T^2 that tends to adjust K_1 to offset any errors in K_2T^2. The errors in K_1 and K_2 apparently stem from the finite-element formulation. For square elements (obtained by adjoining four triangles and condensing out the central point), the boundary points on the splitter plate have the equations (Fig. 4)

$$\tfrac{3}{2}T_Q - \tfrac{1}{4}(T_P + T_R) - \tfrac{1}{4}T_C - \tfrac{1}{2}T_D - \tfrac{1}{4}T_E = 0 \qquad (25)$$

which, by use of the Taylor series expansion, may be written as

$$-\Delta y \left.\frac{\partial T}{\partial y}\right|_Q - (\Delta y)^2 \nabla^2 T\Big|_Q + \ldots = 0 \qquad (26)$$

Thus to an accuracy of $(\Delta y)^2$, the finite-element algorithm satisfies neither the field equation $\nabla^2 T = 0$ nor the boundary condition $\partial T/\partial y = 0$, but rather a weighted sum of both. As a consequence of this combined boundary condition, the singularity strength is not accurately evaluated.

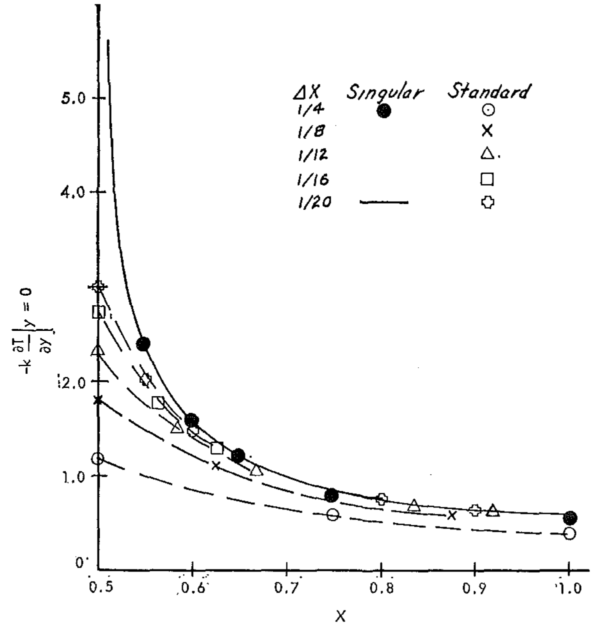

Fig. 4(b) Comparison of singular and standard finite-difference values of the vertical heat flux

§6c Comparison of Singular and Nonsingular Techniques

Regardless of the small error in K_1 produced by the singular finite-element technique, the resulting answers are significantly better than any normal finite-element or finite-difference method, as shown in Table 6. Figs. 4(a) and 4(b) give a comparison of the singular finite-difference and usual finite-difference values for

Table 5

		Finite element				Finite difference		
Δx	Number of singular elements	$K_1\ (K_2 = 0)$	K_1	K_2	T_A	K_1	K_2	T_A
$^1/_2$	2 (all elements singular)	1.285	1.285	0.091	0.170			
$^1/_4$	2	1.277	1.276	0.067	0.179			
	6	1.234	1.234	−0.032	0.179			
	8 (all)	1.224	1.224	−0.045	0.178			
$^1/_8$	2	1.275	1.275	−0.056	0.182	1.1325	−0.492	0.1815
	6	1.232	1.232	−0.048	0.182			
	12	1.212	1.212	−0.077	0.181			
	18	1.203	1.203	−0.086	0.181			
	32 (all)	1.195	1.195	−0.094	0.181			

Table 6 Comparison of values of T_A by different methods

Δy	1st-order triangular element (16)	2nd-order triangular element (16)	1st-order quadrilateral element	1st-order finite difference	2nd-order finite difference	Singular finite element	Singular finite difference
$^1/_2$	0.1429		0.1176			0.170	
$^1/_4$	0.1591	0.1737	0.1579	0.083	0.133		
$^1/_6$	0.1659	0.1771	0.1674				
$^1/_8$	0.1697	0.1784	0.1717	0.151	0.174	0.181	0.1815
$^1/_{10}$	0.1721		0.1741				
$^1/_{12}$	0.1738		0.1756	0.166	0.178		0.1824
$^1/_{16}$	0.1759		0.1775	0.173	0.180		0.1827
$^1/_{20}$	0.1772			0.176	0.181		0.1827
$^1/_{24}$	0.1781						
$^1/_{32}$	0.1793						

the heat flux along the splitter plate and on the line $y = 0$, $x > 0.5$. The singular heat fluxes were calculated as in §5. For both figures there is a substantial error in the finite-difference results even for the finest mesh ($\Delta = {}^1/_{20}$) at points closer than 0.1 to the singular point. In both cases the singular results for $\Delta = {}^1/_4$ differed by less than 0.001 from the singular results for $\Delta = {}^1/_{20}$.

Fig. 5 compares the heat flux along the splitter computed by the standard and singular finite-element methods with the singular finite-difference results.

§7 Transient Singularities

Although it is conceptually possible to include in the singular finite-element method transient singular problems—such as a transient point source—the numeric difficulties are so great that the method loses much of its appeal. In general, transient singular solutions are not available in analytic form, or if they are, they are so complex that the necessary spatial integrations are nearly impossible to perform. Inasmuch as the intent of singularity programming is to reduce computation times, and since transient singularities are not necessarily singular for all times (viz. the instantaneous point source), these problems are best treated by either singular finite-difference techniques for which no spatial integrations are necessary or by standard discretization techniques. If we define ∇ to be the finite-difference approximation to $\partial/\partial t$, the singular finite-difference procedure gives

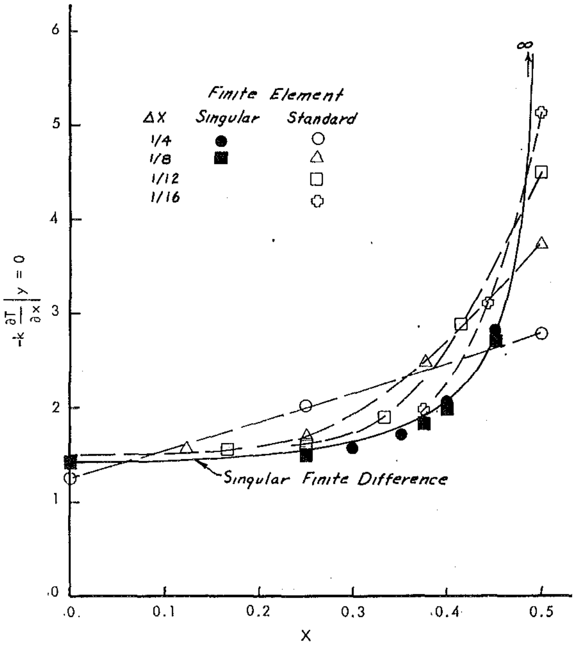

Fig. 5 Comparison of singular finite-difference and standard and singular finite-element values of heat flux along the splitter plate

$$\nabla T - \Diamond T = K(\nabla S - \Diamond S) \tag{29}$$

where ∇ can be any desired time discretization; it is chosen here as the Crank–Nicholson differencing [16].

Consider the region shown in Fig. 6 where a plane source of heat is located in the center. At the point P, located at $x = {}^{10}/_{11}$, the temperature should be approximately that near a plane source in an infinite region, namely

$$T_{\text{ref}} = \frac{Q}{2\sqrt{\pi\kappa t}} \exp\left[-(x_p - x_s)^2/4\kappa t\right] \tag{30}$$

where x_s is the location of the source. Fig. 6 is a comparison of the results obtained by standard and singular finite-difference techniques. A base time step Δt_0 was taken to be the usual explicit stability limit [16].

$$\Delta t_0 = \Delta x^2/4\kappa \tag{31}$$

Time steps of 2, 4, 8, and 16 Δt_0 with the singular finite-difference procedure gave values of T_p that were identical to each other and to T_{ref} to within 10^{-5}. On the other hand, the standard finite-difference procedure with time steps as small as $\Delta t_0/16$ showed reasonable accuracy only for $\kappa t > 0.01$.

Furthermore, since time increments less than $\Delta t_0/8$ gave nearly equal values of T_p for $\kappa t > 0.001$, there is no possibility of improving the standard technique by further reductions in time step unless the spatial mesh is simultaneously refined.

§8 Conclusions

It has been demonstrated that both singular finite-element and finite-difference algorithms are powerful tools for yielding striking improvements in accuracy and reductions in computing time for

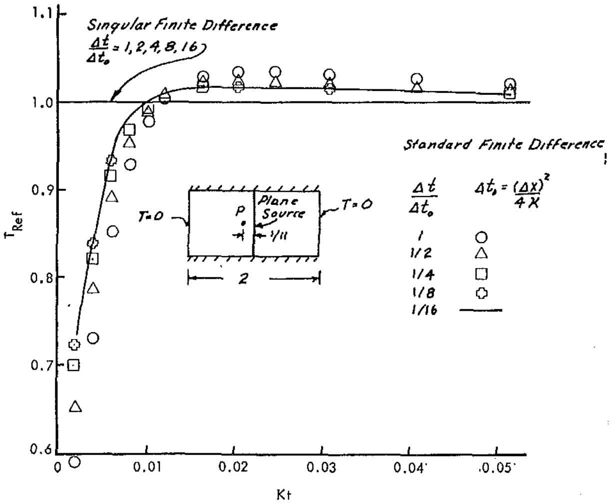

Fig. 6 Normalized temperature at point P due to a unit plane source of heat

problems that contain points of singularity. Although the singular finite-element algorithm tends to give slightly inaccurate values of the singularity strength K, the overall accuracy of the method and the ease with which the singular strength K is automatically computed compared to the need for choosing the boundary points in the singular finite-difference method renders it the logical choice for implementation.

One of the major attractions of either approach is the ease with which they are implemented. In finite-difference methods, one need only add a pseudo source term to the true source term. For the finite-element method, subroutines to evaluate the extra matrix terms are all that are needed. Thus existing computer codes can be easily modified.

References

1 Motz, H., "The Treatment of Singularities of Partial Differential Equations by Relaxation Methods," *Quart. Appl. Math.*, Vol. 4, No. 4, Jan. 1947, p. 371.

2 Woods, L. C., "The Relaxation Treatment of Singular Points in Poisson's Equation," *Quart. J. Mech. Appl. Math.*, Vol. 6, Part 2, 1953, p. 163.

3 Morley, L. S. D., "A Modification of the Rayleigh-Ritz Method for Stress Concentration Problems in Elastostatics," *J. Mech. Phys. Sol.*, Vol. 77, 1969, p. 73.

4 Fix, G., "Higher-Order Rayleigh-Ritz Approximations," *J. Math. Mech.*, Vol. 18, Jan. 1969, p. 645.

5 Emery, A. F., and Segedin, C. M., "Numerical Computation of Plane Stress Intensity Factors for Symmetrical Loads," Report SCL-DC-67-130, Sandia Laboratory, Livermore, Calif., 1968.

6 Emery, A. F., "Numerical Computations of the Plane Stress Intensity Factors for Hollow Cylinders Under Torsion, Flexure and Pressure," Report SCL-DR-69-59, Sandia Laboratory, Livermore, Calif., 1969.

7 Emery, A. F., and Segedin, C. M., "The Evaluation of the Stress Intensity Factors for Cracks Subjected to Tension, Torsion, and Flexure by an Efficient Numerical Technique," *Journal of Basic Engineering*, TRANS. ASME, Series D, Vol. 94, No. 2, June 1972, pp. 387–392.

8 Segedin, C. M., and Emery, A. F., "The Use of Singularity Programming for Plane Elastic Problems," *Proc. 3rd Australasian Conference on Solid Mechanics*, Auckland, N. Z., 1971.

9 Wait, R., and Mitchell, A. R., "Corner Singularities in Elliptic Problems by Finite Element Methods," *J. Comp. Phy.*, Vol. 8, Aug. 1971, p. 45.

10 Yamamoto, Y., "Finite Element Approaches with the Aid of Analytical Solutions," *Recent Advances in Matrix Methods of Structural Analysis and Design*, Gallagher, R. H., et al., eds., University of Alabama Press, 1971.

11 Yamamoto, Y., and Tokuda, N., "Stress Intensity Factors in Plate Structures Calculated by the Finite Element Method," *J. Soc. Naval Arch. of Japan*, Vol. 130, Dec. 1971.

12 Pian, T. H. H., and Tong, P., "Finite Element Methods in Continuum Mechanics," in: *Advances in Applied Mechanics*, Vol. 12, Academic, New York, N. Y., 1972.

13 Gallagher, R. H., "Survey and Evaluation of the Finite Element Method in Fracture Mechanics Analysis," First International Conference on Structural Mechanics in Reactor Technology, Berlin, Germany, 1971.

14 Emery, A. F., and Segedin, C. M., "Singularity Programming—A Numerical Technique for Determining the Effect of Singularities in Finite Difference Solutions, Illustrated by Application to Plane Elastic Problems," to be published in *International Journal for Numerical Methods in Engineering.*

15 Birkhoff, G., "Angular Singularities of Elliptic Problems," *J. Approx. Theory*, Vol. 6, 1972, p. 215.

16 Emery, A. F., and Carson, W. W., "An Evaluation of the Use of the Finite-Element Method in the Computation of Temperature," JOURNAL OF HEAT TRANSFER, TRANS. ASME, Series C, Vol. 93, No. 2, May 1971, pp. 136–146.

Heat or Mass Transfer in Laminar Flow in Conduits With Constriction

J. C. F. CHOW
K. SODA
Department of Energy Engineering,
University of Illinois at Chicago Circle,
Chicago, Ill.

Analytical solutions are obtained on the effects of boundary constriction on heat or mass transfer at the entrance region in a well-developed steady laminar flow in symmetric and axisymmetric conduits subjected to uniform wall temperature or mass concentration. The solutions are limited to the fluids of constant properties with negligible viscous dissipation, moderate Reynolds number, and large Peclet or Schmidt number, and the spread of the wall constriction is large compared to the mean width or radius of the conduits. It is found that both the bulk temperature and heat transfer rate at the wall are oscillatory in nature, and their amplitudes decrease drastically as the fluid moves away from the entrance. Near thermal entry length, the bulk fluid temperature approaches its mean value with vanishing oscillation, but the heat transfer rate at the wall stays oscillatory in nature due to the irregularity of the wall. The thermal entry length changes very little from the corresponding straight-wall conduits. These results are also true for the mass transfer.

Introduction

Analysis of forced convection and mass transfer in laminar flow inside a conduit has been the subject of extensive study since the publication of Graetz's paper in 1855 [1].[1] Until now, little analytical work has been done on the effect of irregular surface upon the nature of heat and mass transfer in a conduit, due to the lack of hydrodynamic data [2]. Recently, Chow, et al. [3, 4], have obtained hydrodynamic solutions on steady laminar flow with moderate Reynolds numbers in conduits with irregular surfaces, where the spread of roughness is large compared with the mean radius of the conduit. These results are of considerable interest, especially for blood flow in arteries with stenoses and for membrane oxygenators using parallel plates with wavy surfaces. The hydrodynamic solutions are used here to obtain temperature and mass concentration distribution and heat and mass fluxes from the wall in the entrance region for a fluid with constant fluid properties and negligible viscous dissipation subjected to uniform wall temperature and mass concentration for symmetric parallel plates and axisymmetric tubes with arbitrary wall variation. We are able to obtain the solution using Green's functions. Numerical results are presented for the bulk fluid temperature and the Nusselt number for the conduits with sinusoidal wall variations and are compared with those of the conduits with straight walls.

Formulation of the Problem

Consider a Newtonian fluid of constant fluid properties flowing steadily in a conduit. The boundary of the conduit is given by

$$\eta(x) = 1 + \epsilon g(x),\ \epsilon = \frac{a}{y_0'},\ x = \frac{x'}{\lambda} \tag{1}$$

where x', y', a, and λ are, respectively, the longitudinal and transverse (or radial) axes of the conduit, the height of the wall constriction, and the characteristic length along the x' axis over which the significant changes in fluid quantities occur; $g(x)$ describes the wall variation relative to the mean half-width (or radius) y_0'. At $x' = x_0'$, the wall temperature and mass concentration are suddenly changed from $T' = T_0'$ to $T' = T_w'$ and $C' = C_0'$ to $C' = C_w'$, respectively, and maintained there for the remaining conduits. The equation governing the heat transfer is the same as that for the mass transfer with negligible viscous dissipation. Thus, in the following, we shall consider the equation governing the heat transfer only, which is also applicable to the mass transfer problem by replacing the temperature T' by the mass concentration C' and the Prandtl number ν/α by the Schmidt number ν/D. The symbols ν, α, and D are, respectively, kinematic viscosity, thermal diffusivity, and mass diffusivity.

The steady nondimensional energy equation governing the temperature field for constant fluid properties and large Peclet number in plane symmetric and axisymmetric conduits is

---

[1] Numbers in brackets designate References at end of paper.

Contributed by the Heat Transfer Division for publication (without presentation) in the Journal of Heat Transfer. Manuscript received by the Heat Transfer Division April 28, 1972. Paper No. 73-HT-N.

$$\mathrm{PrRe}\delta(\psi_{,y}T_{,x} - \psi_{,x}T_{,y}) = (y^m T_{,y})_{,y};\ m = 0, 1 \qquad (2)$$

$$\mathrm{Pr} = \frac{\nu}{\alpha}, \mathrm{Re} = \frac{u_0'y_0'}{\nu}, \delta = \frac{y_0'}{\lambda}, y = \frac{y'}{y_0'}$$

$$T = \frac{T' - T_w'}{T_0' - T_w'}, \psi = \frac{\psi'}{u_0'y_0'^{m+1}} \qquad (3)$$

where u_0' and ψ' are, respectively, the average longitudinal velocity at the cross-sectional area y_0'. The stream function, which is related to the longitudinal and transverse (or radial) velocity components u' and v', respectively, is given by,

$$u' = \frac{1}{y^m}\psi'_{,y'}, v' = -\frac{1}{y^m}\psi'_{,x'} \qquad (4)$$

The superscripts $m = 0$ and $m = 1$ correspond to plane symmetric and axisymmetric conduits, respectively, and the subscript comma denotes partial differentiation.

The initial and boundary conditions are the conditions specifying the uniform temperature across the conduit at $x = x_0$, the equality of temperature on the wall, and the symmetric condition on the axis of symmetry. These are, respectively,

$$T = 1 \qquad \text{at } x \leq x_0 \qquad (5)$$

$$T = 0 \qquad \text{at } y = \eta, x > x_0 \qquad (6)$$

$$T_{,y} = 0 \qquad \text{at } y = 0, x > x_0 \qquad (7)$$

We have neglected the viscous dissipation terms in equation (2). This is permissible since the order of magnitude of the viscous dissipation term to the conduction term is $4\mu u_0'^2/\kappa(T_0' - T_w')$ and is small for moderate Reynolds number. The symbols μ and κ denote the dynamic viscosity and heat conductivity of the fluid, respectively.

Methods of Solution

The boundary condition, equation (6), can be made independent of the x axis by the following transformation of the independent variables:

$$X = x, Y = \frac{y}{\eta(x)} \qquad (8)$$

In terms of X and Y, the governing equation, equation (2), and the initial and boundary conditions, equations (5), (6), and (7), become, respectively,

$$\psi_{,Y}T_{,X} - \psi_{,X}T_{,Y} = \frac{1}{\mathrm{PrRe}\delta}\eta^{m-1}(Y^m T_{,Y})_{,Y} \qquad (9)$$

$$T = 1 \qquad X \leq X_0 \qquad (10)$$

$$T = 0 \qquad \text{at } Y = 1, X > X_0 \qquad (11)$$

$$T_{,Y} = 0 \qquad \text{at } Y = 0, X > X_0 \qquad (12)$$

The solutions of equation (9) satisfying equations (10)–(12) are first expanded in series in terms of δ, and the asymptotic solutions are sought in the limit of $\delta \to 0$.

$$T(X,Y\!:\ \mathrm{Pr}, \mathrm{Re}, \epsilon, \delta) = \sum_{n=0}^{\infty} \delta^n T_n(X,Y\!:\ \mathrm{Pr}, \mathrm{Re}, \epsilon) \qquad (13)$$

$$\psi(X,Y\!:\ \mathrm{Re}, \epsilon, \delta) = \sum_{n=0}^{\infty} \delta^n \psi_n(X,Y\!:\ \mathrm{Re}, \epsilon) \qquad (14)$$

The substitution of the above series into equation (9) and the subsequent collection of equal powers of δ yield the set of perturbed equations. The equations governing the different orders of the temperature field can be put into the following form:

$$(1 - Y^2)T_{n,X} = \left(\frac{1}{\mathrm{PrRe}\delta}\right)(K_m\eta^{m-1})(Y^m T_{n,Y})_{,Y}$$

$$+ K_m\Phi_n(T_0, T_1, \ldots, T_{n-1}\!:\ \ \psi_0, \psi_1, \ldots, \psi_n)$$

$$n = 0, 1, 2, 3 \ldots \qquad (15)$$

The corresponding initial and boundary conditions are

$$T_0 = 1, T_n = 0 \qquad \text{for } n \geq 1 \text{ at } X \leq X_0 \qquad (16)$$

$$T_n = 0 \qquad \text{at } Y = 1, X > X_0 \qquad (17)$$

$$T_{n,Y} = 0 \qquad \text{at } Y = 0, X > X_0 \qquad (18)$$

In equation (15), the source function Φ_n, the constant K_m, and the explicit forms of the stream function ψ_n up to the second order of δ are [3, 4]

$$\Phi_0 = 0 \qquad (19)$$

$$\Phi_n = \sum_{l=1}^{n} (\psi_{l,X}T_{n-l,Y} - \psi_{l,Y}T_{n-l,X}) \qquad n \geq 1 \qquad (20)$$

for $m = 0$:

$$K_0 = -\frac{1}{3c} \qquad (21)$$

$$\psi_0 = c(Y^3 - 3Y) \qquad (22)$$

$$\psi_1 = c^2\mathrm{Re}\epsilon g_{,X}Y\left(-\frac{3}{70}Y^6 + \frac{3}{10}Y^4 - \frac{33}{70}Y^2 + \frac{3}{14}\right) \qquad (23)$$

$$\psi_2 = -\frac{3cY\epsilon}{10}(4\epsilon g_{,X}{}^2 - \eta g_{,XX})(Y^2 - 1)^2$$

$$+ \mathrm{Re}^2c^3\epsilon^2\eta g_{,XX}F(Y) - \mathrm{Re}^2c^3\epsilon^2 g_{,X}{}^2G(Y) \qquad (24)$$

for $m = 1$:

$$K_1 = -\frac{1}{4c} \qquad (25)$$

$$\psi_0 = c(Y^4 - 2Y^2) \qquad (26)$$

$$\psi_1 = \frac{\mathrm{Re}\epsilon c^2}{9\eta}g_{,X}Y^2(Y^6 - 6Y^4 + 9Y^2 - 4) \qquad (27)$$

$$\psi_2 = -c\epsilon(5\epsilon g_{,X}{}^2 - \eta g_{,XX})H(Y) - \frac{\mathrm{Re}^2\epsilon^2c^3g_{,X}{}^2}{\eta^2}I(Y) \qquad (28)$$

where

$$F(Y) = -\frac{1}{1540}\left(Y^{11} - 11Y^9 + \frac{1518}{35}Y^7 - \frac{462}{5}Y^5 + \frac{3279}{35}Y^3 - \frac{1213}{35}Y\right)$$

$$G(Y) = -\frac{1}{550}\left(Y^{11} - \frac{165}{14}Y^9 + \frac{2244}{49}Y^7 - \frac{627}{7}Y^5 + \frac{4111}{49}Y^3 - \frac{2875}{98}Y\right)$$

$$H(Y) = \frac{(Y^2 - 1)^2Y^2}{3}$$

$$I(Y) = \frac{1}{3600}(32Y^{12} - 305Y^{10} + 750Y^8 - 713Y^6 + 236Y^4)$$

$$c = -\frac{1}{2}$$

The solution of equation (15) satisfying the initial and bound-

Table 1

K	β_{oK}	β_{1K}
0	1.6815953222	2.70436441990
1	5.6698573459	6.66790314493
2	9.6682424625	10.6733795381
3	13.6676614426	14.6710784627
4	17.6673735653	18.6698718645
5	21.6672053243	22.6691433588
6	25.6670964863	26.6686619960
7	29.6670210447	30.6683233409
8	33.6669660687	34.6680738224
9	37.6669244563	38.6678833469

Table 2

K	A_{oK}	A_{1K}
0	0.420876657180	0.0939337679236
1	0.395860429674	0.0375198383265
2	0.393809856830	0.0234421243406
3	0.393256290093	0.0170471104066
4	0.393032212597	0.0133936093750
5	0.392920173537	0.0110298085669
6	0.392856337860	0.00937523183708
7	0.392816582482	0.00815231980450
8	0.392790172160	0.00721163558319
9	0.392771745488	0.00646558481357

ary conditions, equations (16), (17), and (18), are obtained first by solving the homogeneous part of the equation by separation of variables followed by constructing the Green's function to satisfy the inhomogeneous part [5]. The solutions for the different orders of T_n are:

zeroth order:

$$T_0 = \int_0^1 Y'^m(1 - Y'^2)G(X,Y;\ X_0,Y')dY' \qquad (29)$$

nth order:

$$T_n = \int_{X_0}^{X} \int_0^1 \Phi_n{}^m(X',Y')G(X,Y;\ X',Y')dY'dX' \qquad n \geq 1 \quad (30)$$

where Green's function G is given by

$$G(X,Y;\ X',Y') = \sum_{K=0}^{\infty} \frac{1}{A_{mK}} Z_{mK}(X - X')W_{mK}(Y')W_{mK}(Y) \qquad (31)$$

$$A_{mK} = \int_0^1 Y'^m(1 - Y'^2)W_{mK}{}^2(Y')dY' \qquad (32)$$

$$Z_{mK}(X - X') = \exp\left[-\frac{K_m\beta_{mK}{}^2}{\mathrm{PrRe}\delta}\int_{X_0}^{X-X'+X_0} \eta^{m-1}(\zeta)d\zeta\right] \qquad (33)$$

$$W_{mK}(Y) = \sum_{l=0}^{\infty} a_l Y^{2l} \qquad \text{with } a_0 = 1,\ a_1 = -\frac{\beta_{mK}{}^2}{2(1+m)},$$

$$a_l = -\frac{\beta_{mK}{}^2}{2l(2l + m - 1)}(a_{l-1} - a_{l-2}),\ l \geq 2 \qquad (34)$$

β_{mK} is the Kth eigenvalue. The values of β_{mK} and A_{mK} are given in Tables 1 and 2, respectively.

Heat Flux and Nusselt Number

The heat flux at the wall is

$$\left.\frac{\partial T'}{\partial n'}\right|_w = \frac{T_0' - T_w'}{y_0'}\left.\frac{\partial T}{\partial N}\right|_w \qquad (35)$$

where

$$n' = -y'\sqrt{1 + \delta^2\epsilon^2 g_{,x}{}^2},\ N = \frac{n'}{y'} \qquad (36)$$

In terms of (X,Y), equation (35) becomes

$$\left.\frac{\partial T'}{\partial n'}\right|_w = \frac{T_w' - T_0'}{y_0'}\left[\left\{\frac{\partial T}{\partial X} + \left(-\frac{\eta_{,X}}{\eta}Y\right)\frac{\partial T}{\partial Y}\right\}\frac{\partial X}{\partial N} + \left(\frac{1}{\eta}\frac{\partial T}{\partial Y}\right)\eta\frac{\partial Y}{\partial N}\right]_{Y=1} = \frac{T_w' - T_0'}{y_0'}\left(\frac{\sqrt{1 + \epsilon^2\delta^2 g_{,X}{}^2}}{\eta}\right)\left.\frac{\partial T}{\partial Y}\right|_{Y=1} \qquad (37)$$

The Nusselt number based on the mean width (or radius) and the bulk fluid temperature is

$$\mathrm{Nu} = \frac{y_0'}{T_w' - \bar{T}'}\left.\frac{\partial T'}{\partial n'}\right|_w = \left(\frac{\sqrt{1 + \epsilon^2\delta^2 g_{,x}{}^2}}{\eta}\right)\left(\frac{1}{\bar{T}}\left.\frac{\partial T}{\partial Y}\right|_{Y=1}\right) \qquad (38)$$

where

$$\bar{T} = \frac{\int_0^{'} T\psi_{,Y}dY}{\int_0^{'} \psi_{,Y}dY} \qquad (39)$$

Discussion of Results

In the following, we shall present the heat transfer solution in graphical form for the conduits with sinusoidal wall variation (see Fig. 1). First, the effects of the wall constriction upon the

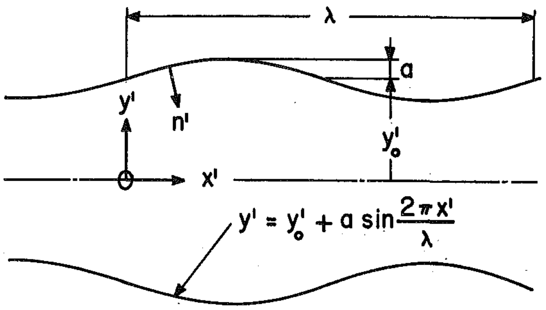

Fig. 1 Conduit with sinusoidal wall variation

flow pattern in a plane symmetric conduit is shown in Fig. 2 for $\delta = 0.1$, $\epsilon = 0.4$, and Re = 25. The figure shows the occurrence of separation and subsequent reattachment in the divergent part of the conduit. The streamline pattern is quite similar to the corresponding axisymmetric flow.

For a small conduit constriction ϵ, the energy dissipation (or average pressure drop) along the conduit is negligible compared with the straight-wall boundary, but it increases rapidly as ϵ increases above 0.1 and approaches infinity as ϵ approaches one, the latter condition corresponding to the complete blockage of the conduit. This is shown in Fig. 3. Any increase in Re or δ also causes a substantial increase in the energy dissipation. It is also found that the pressure drop is higher in the convergent section than in the divergent section due to higher wall shear stresses.

Since the hydrodynamic solutions are obtained up to the second order of δ, the foregoing results are qualitative in nature if the following relations are not strictly satisfied for plane and axisymmetric conduits with sinusoidal wall variation, respectively, $\mathrm{Re}\delta\epsilon \ll 1.39$, $1.35\delta^2 (48\epsilon^2 + 1) + 0.00702 (\mathrm{Re}\delta\epsilon)^2 [(40/\epsilon) + 79] \ll 1$, and $\mathrm{Re}\epsilon\delta/(1 - \epsilon)^{1/2} \ll 1.433$, $(1 + 0.987\epsilon) \epsilon\delta^2 \ll 1.50$. Nevertheless, the asymptotic solution up to the second order of δ gives the essential flow characteristics obtained numerically [6] and experimentally [7] in a tube with local constriction where the parameter δ is of the order one.

The effects of a wavy wall upon the bulk fluid temperature versus the nondimensional axial distance are shown in Figs. 4 and 5 for the plane symmetric and the axisymmetric conduits, respectively. It is readily seen that at a low Reynolds number

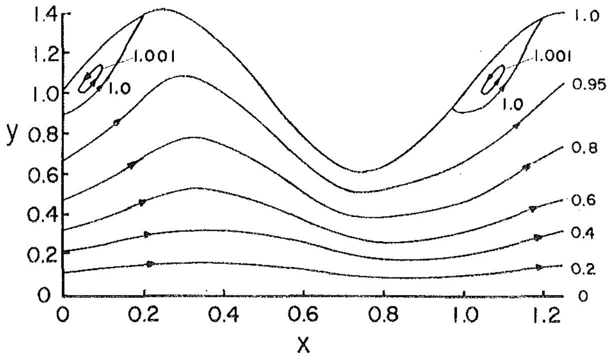

Fig. 2 **Streamlines for $\delta = 0.1$, $\epsilon = 0.4$, and Re = 25 for a plane symmetric channel**

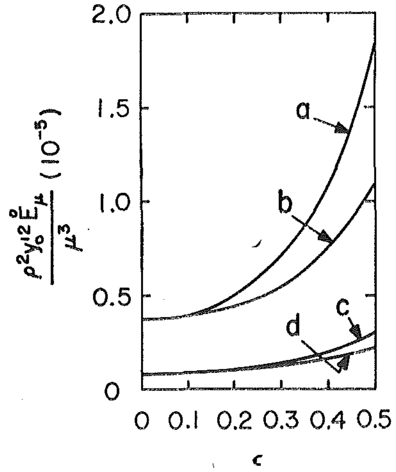

Fig. 3 **Energy dissipation per unit time and per unit length: (*a*) Re = 25 and $\delta = 0.2$; (*b*) Re = 25 and $\delta = 0.1$; (*c*) Re = 12.5 and $\delta = 0.2$; (*d*) Re = 12.5 and $\delta = 0.1$**

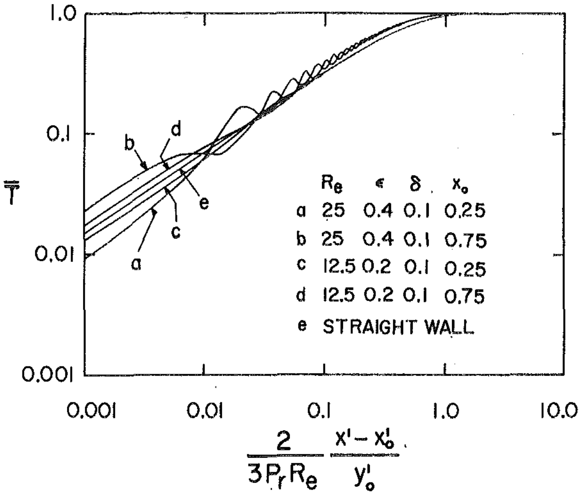

Fig. 4 **Bulk temperature via nondimensional axial distance for plane symmetric channels**

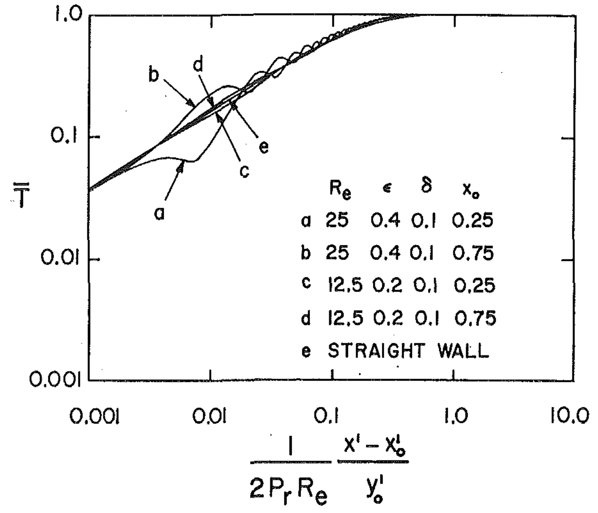

Fig. 5 **Bulk temperature via nondimensional axial distance for axisymmetric tubes**

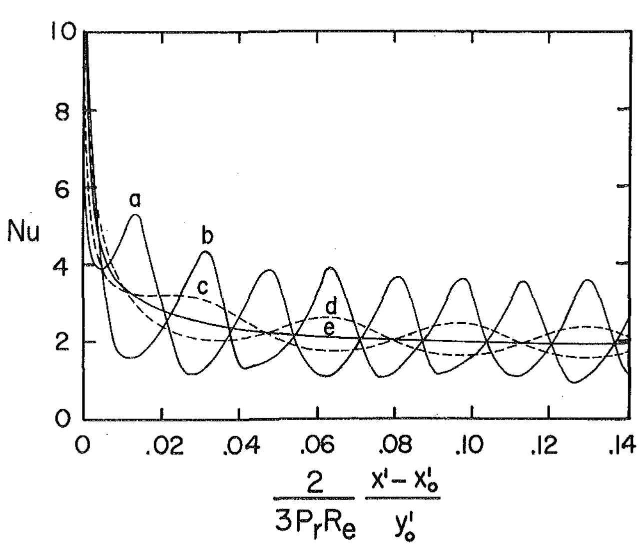

Fig. 6 **Nusselt number via nondimensional axial distance for plane symmetric channels**

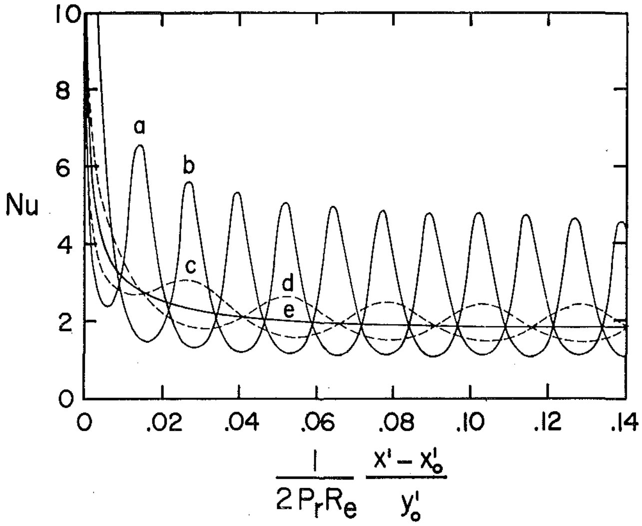

Fig. 7 **Nusselt number via nondimensional axial distance for axisymmetric tubes**

and with a small conduit constriction, the bulk fluid temperatures vary very little from the corresponding straight-wall conduits except that they are oscillatory in nature with decreasing amplitudes as the fluid moves away from the thermal entrance. As one increases both the Reynolds number and the conduit constriction, the behaviors of the bulk temperature stay almost the same as in the previous case, except that the amplitude of the oscillation is much more pronounced.

Again, as in the case of the bulk fluid temperature, the Nusselt number fluctuates markedly with respect to its mean as one increases the Reynolds number and the conduit constriction. But the Nusselt number stays oscillatory in nature throughout due to sinusoidal variation of the wall. At a low Reynolds number and with a small conduit constriction, the mean coincides with its corresponding straight-wall conduit, but as one increases both the Reynolds number and the conduit constriction, the mean becomes considerably high compared with the corresponding straight-wall channel. Due to the oscillatory nature of the local Nusselt number, the thermal entrance length can be defined as the distance from the entrance where the amplitudes of the local Nusselt number become constant. The thermal entry length changes very little from that of the corresponding straight wall conduits. The reason for this is that the concave part of the conduit enhances the heat transfer rate, but the convex part of the conduit decreases the heat transfer; thus the overall effects of the concave and the convex parts upon the heat transfer rate seem to cancel each other out. Also, the overall effect of the position of the thermal entry makes little difference upon the bulk thermal temperature and the Nusselt number, except very close to the thermal entrance.

In conclusion, our analysis of steady laminar flow in conduits with continuous constriction subjected to constant wall temperature shows that there exists a large local temperature and Nusselt number fluctuation as compared with a conduit with a straight wall, with very little change in the thermal entry length. As long as the flow field remains laminar, the foregoing conclusion is valid even if δ is of the order one.

References

1 Graetz, L., "Über die Warmeleitungsfahigkeit von Flussigkeiten," *Annalen der Physik Chem.*, Vol. 25, 1885, p. 337.

2 Shah, R. K., and London, A. L., "Laminar Flow Forced Convection Heat Transfer and Flow Friction in Straight and Curved Duct—A Summary of Analytical Solution," Tech. Rep. No. 75, Department of Mechanical Engineering, Stanford University, Stanford, Calif., Nov. 1971. (to be a special issue in *Advances in Heat Transfer*, J. P. Hartnett and T. F. Irvine, Jr., eds., Academic Press).

3 Chow, J. C. F., Soda, K., and Dean, C., "On Laminar Flow in Wavy Channels," *Proceedings of 12th Midwestern Mechanics Conference*, 1971, p. 247.

4 Chow, J. C. F., and Soda, K., "Laminar Flow in Tubes with Constriction," *The Physics of Fluids*, Vol. 15, 1972, p. 1700.

5 Sneddon, I. N., *Elements of Partial Differential Equations*, McGraw-Hill, New York, 1957.

6 Lee, J. S., and Fung, Y. C., "Flow in Locally Constricted Tubes at Low Reynolds Numbers," *Journal of Applied Mechanics*, Vol. 37, TRANS. ASME, Series E, Vol. 92, No. 1, Mar. 1970, pp. 9–16.

7 Forrester, J. H., and Young, D. F., "Flow Through a Converging–Diverging Tube and Its Implications in Occlusive Vascular Disease—II," *J. Biomechanics*, Vol. 3, 1970, p. 307.

K. C. WESTON
Associate Professor.
Mem. ASME

J. L. HAUTH
Research Associate.
Assoc. Mem. ASME

University of Tulsa,
Tulsa, Okla.

Unsteady, Combined Radiation and Conduction in an Absorbing, Scattering, and Emitting Medium[1]

The transient cooldown of a gray, absorbing, isotropic scattering, emitting, and conducting medium bounded by gray, diffusely emitting and reflecting parallel plates is considered. Numerical solutions are obtained for the initial boundary-value problem with a discontinuous decrease in temperature at one boundary. The quasi-steady equation of radiative transfer is solved using Gaussian quadrature and a matrix eigenvector technique together with explicit numerical solution of the unsteady energy equation. Temperature and energy flux distributions are presented for variations of optical thickness, boundary emissivity, albedo, and conduction–radiation parameter.

Introduction

INTERACTIVE conduction and radiative transfer in materials has been a subject of increasing technical interest in recent years. In part this interest has developed as a natural outgrowth of many studies involving independent convective, conductive, and radiative energy transfer. On the other hand, much activity also is directly attributable to significant technical applications such as heat transfer in fibrous insulations, heating and cooling of glass, radiative behavior of cryodeposits, and volume reflecting heat shields. Undoubtedly, additional applications will follow the enhanced understanding engendered by continuing research in this area.

The classical problem of energy transfer through an intervening medium between two diffusely emitting and reflecting parallel plates is considered here. The plates are assumed to be gray and of uniform temperature. The medium absorbs, scatters, emits, and conducts in accordance with the equations of radiative transfer and energy conservation and Fourier's law. Both the steady-state and unsteady problems are treated, steady-state solutions being obtained as the asymptotic time limit of the transient problem. Such an extensive literature exists in the independent fields of conductive and radiative transfer and in the combined processes for special types of materials that it is inappropriate to attempt here to cite the many pioneering researches in these areas. We will therefore review only those earlier researches having direct bearing on the present problem. Among the early significant papers in one-dimensional combined radiative and conductive transfer was the study of steady-state simultaneous transport in absorbing media between black parallel plates by Viskanta and Grosh [1].[2] The same authors extended their work to include the effect of surface emissivity [2]. Viskanta [3] later considered the same problem but included scattering as well as absorption and emission effects. More recently, Doornink and Hering treated the problem of transient combined radiative and conductive transfer [4]. In the latter work, the authors considered the transient development of temperature and radiation fields in nonscattering media between black parallel plates. The present work extends the problem of Doornink and Hering to consider the effects of isotropic scattering and nonblack boundaries.

The method of idempotents, discussed by Frame [5], was applied by Hsia and Love [6, 7] to the analysis of radiative transfer between parallel plates separated by a nonisothermal medium. In these significant studies the authors made no attempt to couple the temperature field and the radiation field through the energy equation. In the present work the idempotent technique of Hsia and Love has been utilized to study transient interactive radiation and temperature fields in absorbing and scattering media between parallel plates.

Analysis

The simultaneous transport of energy in a gray, absorbing, scattering, emitting, and conducting plane layer may be described in terms of the geometry shown in Fig. 1. The present calculations assume that thermal and radiative properties are temperature-independent, scattering is isotropic, and the index of refrac-

---

[1] This research was performed under NASA-Ames grant NGR 37-008-003.

Contributed by the Heat Transfer Division for publication (without presentation) in the JOURNAL OF HEAT TRANSFER. Manuscript received by the Heat Transfer Division September 21, 1972. Paper No. 73-HT-J.

[2] Numbers in brackets designate References at end of paper.

tion is unity. Recognizing its azimuthal symmetry for the present problem, the intensity field in the layer at a given instant may be considered dependent only on the optical thickness τ and the cosine μ of the elevation angle θ. Thus the dependent variables of the combined radiative and conductive problem may be expressed as $T(\tau, t^*)$ and $I(\tau, \mu, t^*)$ where the dimensionless time t^* has been nondimensionalized using the characteristic conduction time L^2/α.

The analysis of energy transport by radiation and conduction in a plane layer is governed by the quasi-steady equation of radiative transfer

$$\mu \frac{dI}{d\tau}(\tau, \mu, t^*) = -I(\tau, \mu, t^*) + \frac{\omega_0}{2}\int_{-1}^{1} S(\mu, \mu')I(\tau, \mu', t^*)d\mu' + n^2(1 - \omega_0)I_{\mathrm{BB}}(\tau) \quad (1)$$

and the conservation of energy

$$\frac{\partial T}{\partial t^*} = \tau_0^2 \frac{\partial^2 T}{\partial \tau^2} - \frac{\tau_0^2}{\mathcal{K}\beta}\frac{dq_R}{d\tau} \quad (2)$$

where Fourier's law of conduction, the dimensionless time, and the optical depth have been employed in equation (2). These equations are coupled through the radiative-heat-flux divergence term in the energy equation where:

$$q_R(\tau, t^*) = 2\pi \int_{-1}^{1} \mu I(\tau, \mu, t^*)d\mu \quad (3)$$

and through the temperature-dependence of the blackbody intensity function I_{BB}.

Defining the dimensionless temperature Θ and dimensionless radiative flux F_R as

$$\Theta = \frac{T - T_1}{T_2 - T_1} \qquad F_R = \frac{q_R}{\sigma T_2^4}$$

the initial and boundary conditions for diffusely emitting and reflecting boundaries may be stated as

Table 1 Nondimensional parameters for simultaneous conduction and radiation in a plane slab

Equation	Parameter name	Symbol
Equation of radiative transfer	optical thickness	$\tau_0 = (s + k)L$
	albedo of single scattering	$\omega_0 = \frac{s}{s + k} = \frac{s}{\beta}$
Conservation of energy	conduction–radiation parameter	$N = \frac{\mathcal{K}\beta}{4\sigma T_2^3}$
Boundary conditions	surface emissivities	ϵ_1, ϵ_2
	surface temperature ratio	θ_1

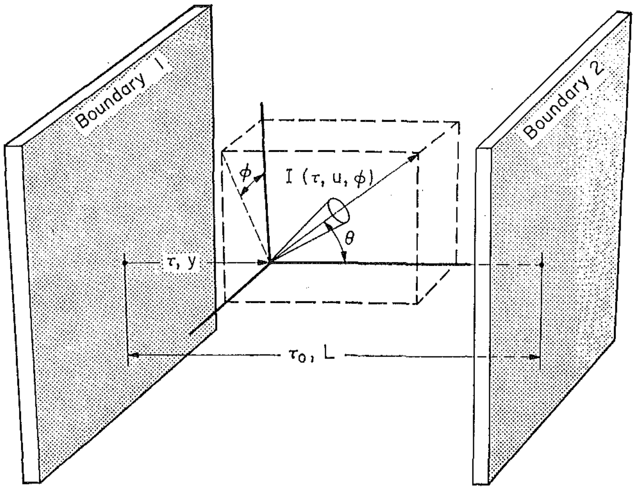

Fig. 1 Geometric nomenclature for radiative transfer between parallel plates

$$\Theta(\tau, 0) = 1, \qquad 0 \le \tau \le \tau_0 \quad (4a)$$

$$\Theta(0, t^*) = 0, \qquad t^* > 0 \quad (4b)$$

$$\Theta(\tau_0, t^*) = 1, \qquad t^* \ge 0 \quad (4c)$$

$$I(0, \mu, t^*) = 2(1 - \epsilon_1)\int_0^{-1} \mu' I(0, \mu', t^*)d\mu' + \epsilon_1 I_{\mathrm{BB}}[\Theta(0, t^*)], \qquad \mu > 0 \quad (4d)$$

$$I(\tau_0, \mu, t^*) = 2(1 - \epsilon_2)\int_0^{1} \mu' I(\tau_0, \mu', t^*)d\mu' + \epsilon_2 I_{\mathrm{BB}}[\Theta(\tau_0, t^*)], \qquad \mu < 0 \quad (4e)$$

The analysis and results of this study can be completely described in nondimensional terms using the independent and dependent variables already discussed and the parameters shown in Table 1. The parameters ω_0 and τ_0 are intrinsic to the analysis of radiative transfer and are determined for a given layer thickness by the characteristics of the media. However, when the interaction of a radiation field and a temperature field is considered, the conservation of energy equation must also be included. Thus the conduction–radiation parameter N enters the problem. In this parameter, both thermal and radiative properties of the medium are involved. The remaining two parameters, the emissivities and temperature ratio of the surfaces, enter through the boundary conditions. Thus we can hope to gain some understanding of the influence of the media through examination of the effects of varying N, ω_0, and τ_0, while variations involving the emissivities and temperature ratio are repre-

Nomenclature

c = heat capacity of medium
F = dimensionless heat flux, $q/\sigma T_2^4$
F_R = dimensionless radiative heat flux, $q_R/\sigma T_2^4$
I = intensity
I_{BB} = blackbody intensity
k = absorption coefficient of medium
$\mathcal{K}$ = thermal conductivity of medium
L = thickness of medium
n = index of refraction of medium
N = conduction–radiation parameter, $\mathcal{K}\beta/4\sigma T_2^3$
q = heat flux
q_R = radiative heat flux
s = scattering coefficient of medium
S = phase function of medium
t = time
t^* = dimensionless time, $\alpha t/L^2$
T = absolute temperature
T_1 = absolute temperature of cold boundary
T_2 = absolute temperature of hot boundary
y = coordinate distance measured from boundary 1
α = thermal diffusivity of medium
β = extinction coefficient of medium, $s + k$
ϵ_1, ϵ_2 = emissivities of bounding surfaces
θ = elevation angle
θ_1 = temperature ratio, T_1/T_2
Θ = dimensionless temperature, $(T - T_1)/(T_2 - T_1)$
μ = $\cos\theta$
ρ = density of medium
τ = optical depth, $\int_0^y \beta dy$
τ_0 = optical thickness of medium, $\int_0^L \beta dy$
ω_0 = albedo for single scattering of medium, s/β

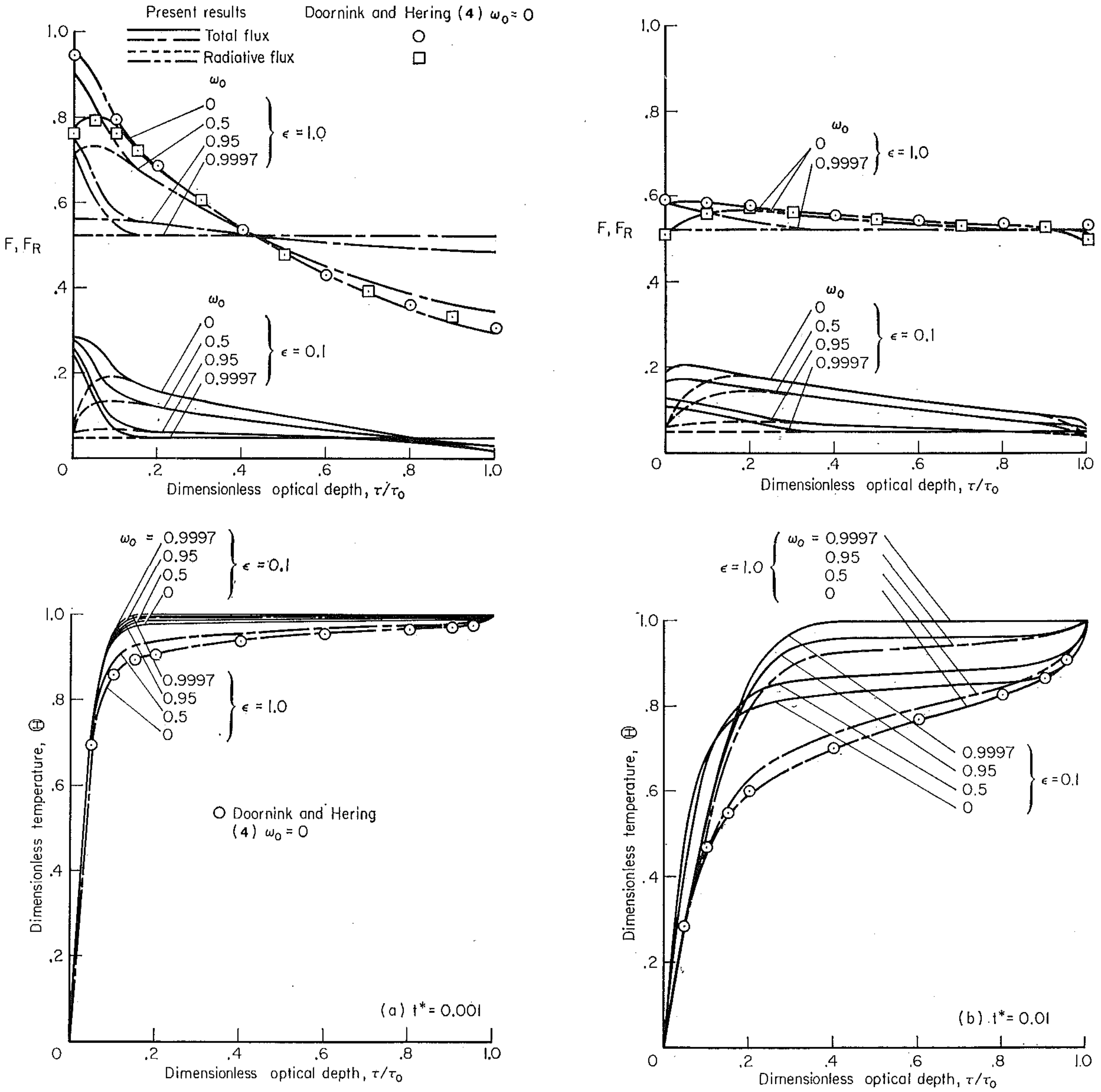

Fig. 2 Effect of albedo and boundary emissivity on the unsteady temperature and energy flux distributions in scattering, absorbing, and emitting media between parallel plates, $N = 0.005$, $\tau_0 = 1.0$, $\theta_1 = 0.5$

sentative of the specific configuration and imposed conditions of the problem formulation.

Six- and eight-point Gaussian quadratures were employed to reduce the differential-integral equation (1) to six or eight differential equations and the integral boundary conditions (4*d*, *e*) to algebraic equations. The differential equations of radiative transfer thus obtained were recast in matrix form. Utilizing the boundary conditions, equations (4*d*, *e*) and a specified instantaneous temperature distribution, the matrix of the six (or eight) intensities describing the radiation field at each point in the medium was determined using the idempotent technique of Hsia and Love [7]. With the radiation field determined, the energy equation was solved for the temperature using the explicit finite-difference technique. Thus with the temperature distribution at the next time interval determined, the new radiation field may be calculated and the cycle continued. In the calculations presented, 7 and 21 nodes were employed in the steady and unsteady solution of the energy equation respectively.

The solutions described here were obtained on the University of Tulsa Sigma VI and the NASA Ames Research Center IBM 360/67 digital computers. Typical run times to steady state were 1 to 2 min for 7 nodes and six-point quadrature on the Sigma VI and 2 to 20 min for 21 nodes and eight-point quadrature on the IBM 360/67. Further details of the analysis and solution technique are discussed in [8].

Results and Discussion

Studies have been made of both steady-state and transient energy transfer between infinite parallel plates. As indicated above, the solutions were obtained by numerical approximation to the energy equation and the equation of radiative transfer. It is estimated that the maximum error in the solutions is about 2 percent. In most cases, the error is believed to be much smaller.

Steady-State Heat Transfer. Extensive comparisons were made with steady-state results reported in the literature to validate computational procedures. All steady-state results discussed here were obtained using six-point quadrature and 7 conduction nodes. Computations of steady-state temperature distribution were made for comparison with the nonscattering results of Vis-

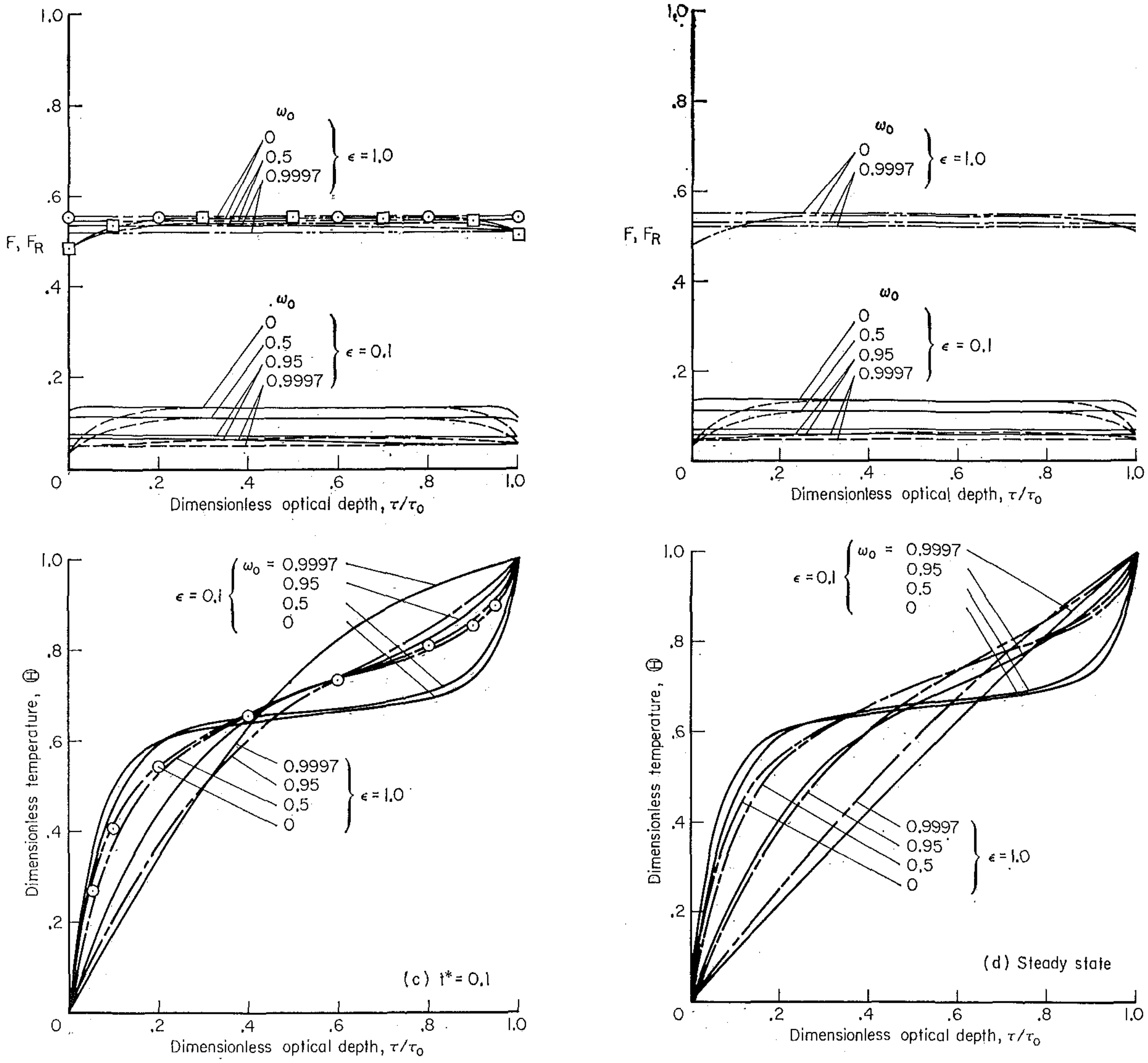

Fig. 2 Effect of albedo and boundary emissivity on the unsteady temperature and energy flux distributions in scattering, absorbing, and emitting media between parallel plates, N = 0.005, τ_0 = 1.0, θ_1 = 0.5

kanta and Grosh [1] for $\tau_0 = 1.0$. Excellent agreement was obtained for $N = 0.01, 0.1$, and 1.0 for $\theta_1 = 0.1$ and 0.5. Additional computations were performed to validate the program for problems including isotropic scattering. Comparison of radiative flux and temperature distributions with those of Viskanta [3] for $\tau_0 = 1.0$, $N = 0.1$, $\theta_1 = 0.1$ and 0.5, and $\omega_0 = 0$, 0.5, and 0.9997 also indicate excellent agreement. Space does not allow the inclusion of these results, but the senior author will be happy to supply them to interested readers. It should be emphasized that the present results were obtained by an entirely different technique than those of Viskanta and Grosh [1] and Viskanta [3]. Thus the present results are both validated by and lend support to these sources.

Unsteady Combined Radiative and Conductive Heat Transfer. Solutions have been obtained for the transient thermal response of a plane layer of a scattering, absorbing, emitting, and conducting medium bounded by diffuse, opaque gray surfaces. Specifically the transient cooldown from a state of thermodynamic equilibrium (Θ = 1) to the steady state developed as a consequence of a discontinuous change at $t^* = 0$ in the temperature at one boundary to $\Theta(0, t^*) = 0$ is considered. Space and resources do not allow an extensive presentation of the effects of varying all the parameters of the problem. Hence results are presented which typify the major dependencies and which allow comparisons to be made with special cases published elsewhere.

Studies of the effects of varying the number of conduction nodes and the order of the Gaussian quadrature revealed that while 7 nodes and sixth-order quadrature were adequate to produce the desired accuracy in the steady-state results discussed above, these selections were clearly inadequate for accurate computation of the unsteady cases considered here. It was found that the steep temperature gradients in the vicinity of the walls, particularly in radiation-dominant cases and at early times, dictated a substantial increase in the number of nodes used. Thus the remaining results presented here were obtained employing 20 spatial increments and eighth-order quadrature.

The effect of variation of albedo on the temperature and flux distributions at several instants of dimensionless time including the steady state are shown in Fig. 2 for $N = 0.005$, $\tau_0 = 1.0$, $\theta_1 = 0.5$, and $\epsilon_1 = \epsilon_2 = 1.0$. In examining these results it is well to recall that variation of albedo here implies variation of at least two quantities—in the simplest case—both the scattering and absorption coefficient. Thus the results presented in Fig. 2 may be viewed as the compound effect of variation of absorption coefficient and scattering coefficient such that their sum—the extinction coefficient—is constant.

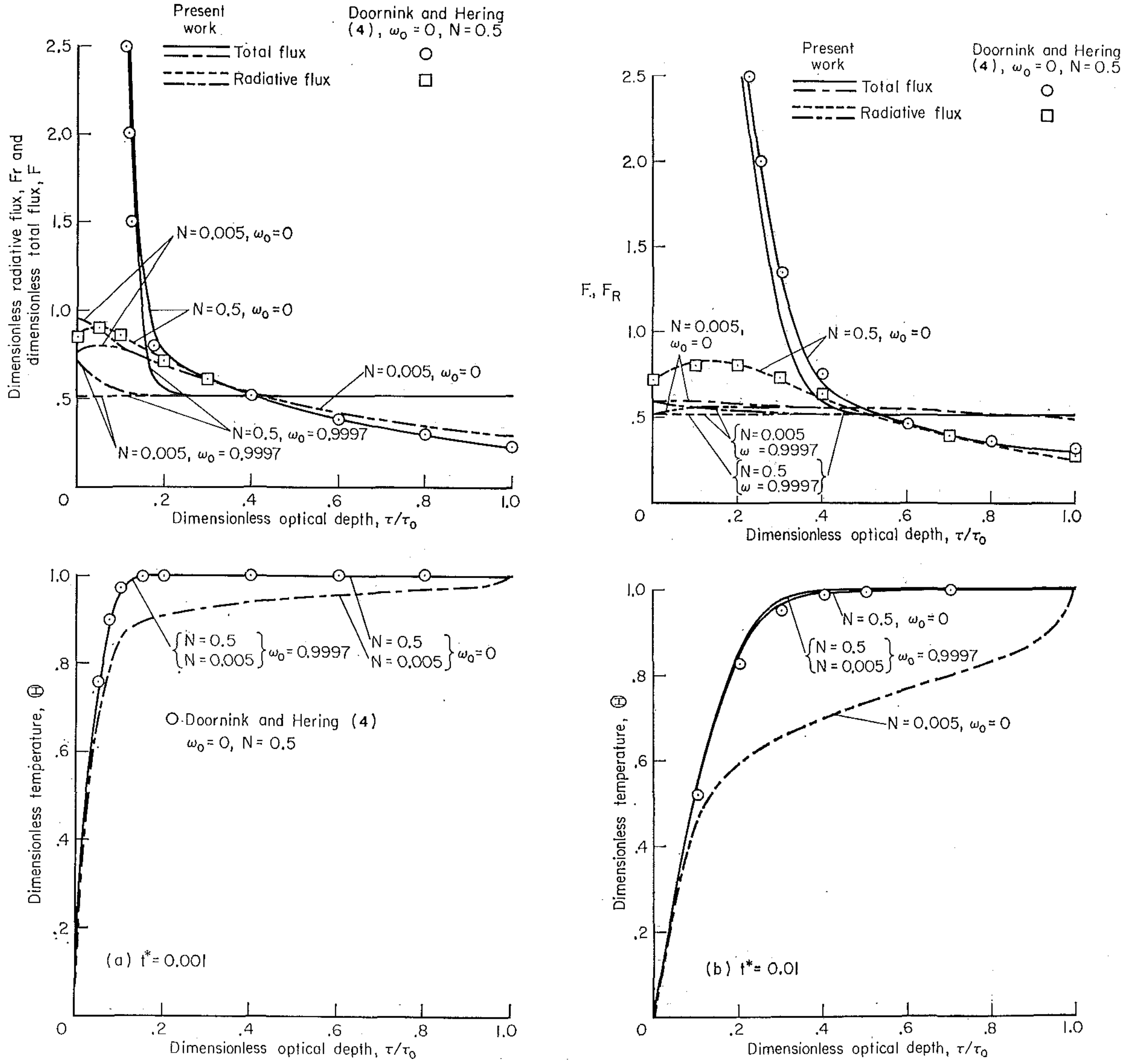

Fig. 3 Effect of albedo and conduction–radiation parameter on the unsteady temperature and energy flux distributions in scattering, absorbing, and emitting media between parallel plates, $\epsilon_1 = \epsilon_2 = 1.0$, $\tau_0 = 1.0$, $\theta_1 = 0.5$

Examination of Fig. 2(*a*) shows clearly the effect of conduction and radiation shortly after the discontinuous temperature change at the left wall. For $\omega_0 = 0.9997$, the temperature and radiation fields are virtually independent, hence the temperature distribution approximates a pure conduction profile. For ω_0 significantly different from unity, a more or less uniform reduction in temperature across the layer is evident except in the region near the left wall where conduction predominates. This is substantiated by examination of the radiative and total flux curve of Fig. 2(*a*). It should be remembered here that the local rate of temperature increase due to radiative interaction is proportional to the local slope of the radiative flux curve. Thus it is apparent that for $\tau/\tau_0 > 0.2$, cooling of the layer due to radiation occurs roughly at a uniform rate. These same effects are evident to a lesser extent at later times in Fig. 2 prior to the attainment of the steady state.

Considering the several parts of Fig. 2 with respect to the temporal evolution of the steady state, it is clear that the steady state is attained most quickly for small albedo due to two effects. First, the increased global cooling effect due to radiative emission throughout the medium together with the conductive flux produces increased overall rates of cooling. Secondly, the steady-state temperature distribution for low albedo exceeds those for higher albedo. Thus not only is the rate of cooling greater for low albedo, but the temperature change needed to achieve the new steady state is also smaller.

Recently, Doornink and Hering [4] have studied extensively the transient cooldown of an absorbing, nonscattering medium bounded by black walls. Fig. 2 and succeeding figures include results taken from [4] for comparison with the present results. Because of the small size of the figures in [4], it is estimated that the reference results presented here may be in error by several percent. Nevertheless, good agreement is evident even though the present computation techniques differ significantly from those of Doornink and Hering.

The effect of reducing the boundary emissivities from 1.0 to 0.1 is also shown in Fig. 2. It is seen that for $\omega_0 < 1$ the early rate of cooling is lower for low emissivity. This may be attributed to the increased boundary reflectances. As the steady state is approached, the temperatures near the cold wall remain higher for low emissivity while they are lower in the vicinity of the hot wall. Evidently the high reflectance at the cold boundary causes increased radiation absorption in this region. Near the hot wall the reduced emitted flux from the wall evidently allows

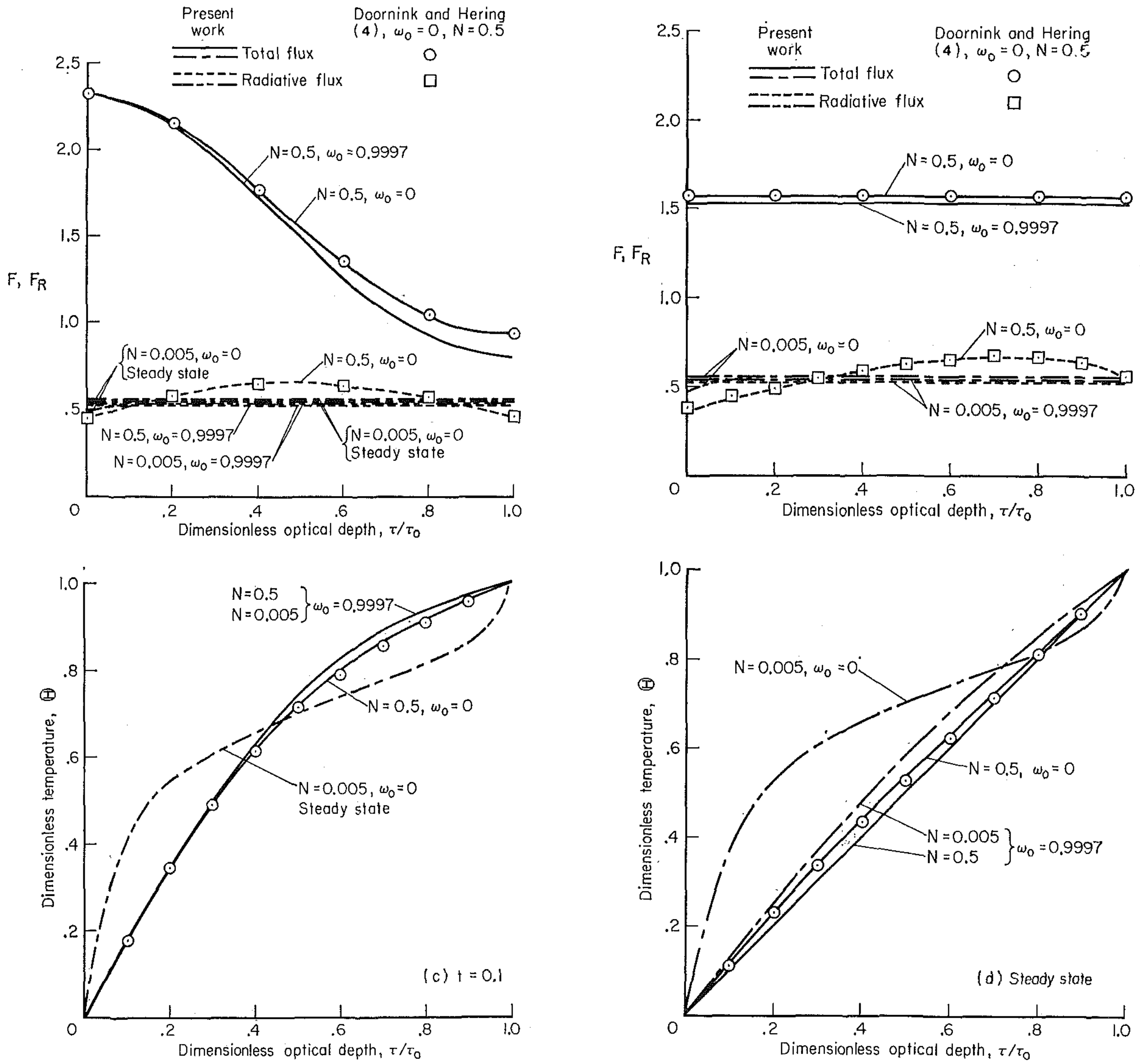

Fig. 3 Effect of albedo and conduction–radiation parameter on the unsteady temperature and energy flux distributions in scattering, absorbing, and emitting media between parallel plates, $\epsilon_1 = \epsilon_2 = 1.0$, $\tau_0 = 1.0$, $\theta_1 = 0.5$

the medium to cool down well below the values associated with the black wall. These emissivity variations are consistent with those discussed by Viskanta and Grosh [2] for steady-state solutions. Substantially reduced radiative and total fluxes are indicated for the reduced-emissivity cases, as expected.

The effect of a change of the conduction–radiation parameter N from 0.005 to 0.5, keeping all the conditions of the preceding figure fixed with $\epsilon_1 = \epsilon_2 = 1.0$, is shown in Fig. 3. Curves from Fig. 2 are repeated here for ease of comparison. It is evident that for $N = 0.5$ the temperature distributions closely resemble pure-conduction temperature distributions and depend only weakly on albedo for a given t^*, indicating clearly that conduction is the dominant mode of energy transfer. Because of this weak dependence on albedo, only the $\omega_0 = 0$ and $\omega_0 = 0.9997$ curves are shown. The reader is warned against interpreting t^* as a measure of absolute time in comparing results for differing values of N. This becomes clear if one considers as an example a fixed medium thickness and volumetric heat capacity. Because $\tau_0 = 1.0$ for Fig. 3, the extinction coefficient must be fixed; thus increasing N by a factor 10^2 implies increasing thermal conductivity by a factor of 10^2. But the absolute time for a given medium thickness is inversely proportional to the thermal conductivity; hence for a given t^* the absolute time for $N = 0.5$ is 10^{-2} times the absolute time for the $N = 0.005$ case. Thus if we wish to compare the temperature and heat flux distributions for $N = 0.005$ and $t^* = 0.001$ with corresponding distributions for $N = 0.5$ at the same absolute time, we should compare these distributions with the corresponding $N = 0.5$ distributions for $t^* = 0.1$, Fig. 3(c). Note also that this relation is not unique for the cases of Fig. 3—other absolute time relations may be obtained by considering examples in which other variables are held fixed.

The interaction between the radiation field and the temperature field as displayed in this figure and the following figure may be best explained by examining the energy equation (2), nondimensionalized:

$$\frac{\partial\Theta}{\partial t^*} = \frac{\partial^2\Theta}{\partial\left(\frac{\tau}{\tau_0}\right)^2} - \frac{\tau_0}{4N(1-\theta_1)}\,\frac{\partial F_R}{\partial\left(\frac{\tau}{\tau_0}\right)} \qquad (5)$$

It is evident that increasing the conduction–radiation parameter reduces the influence of the radiation term on the dimensionless rate of cooling. Thus while Fig. 3(a) shows a slightly steeper slope of the radiative flux for $N = 0.5$, the dimensionless rate of

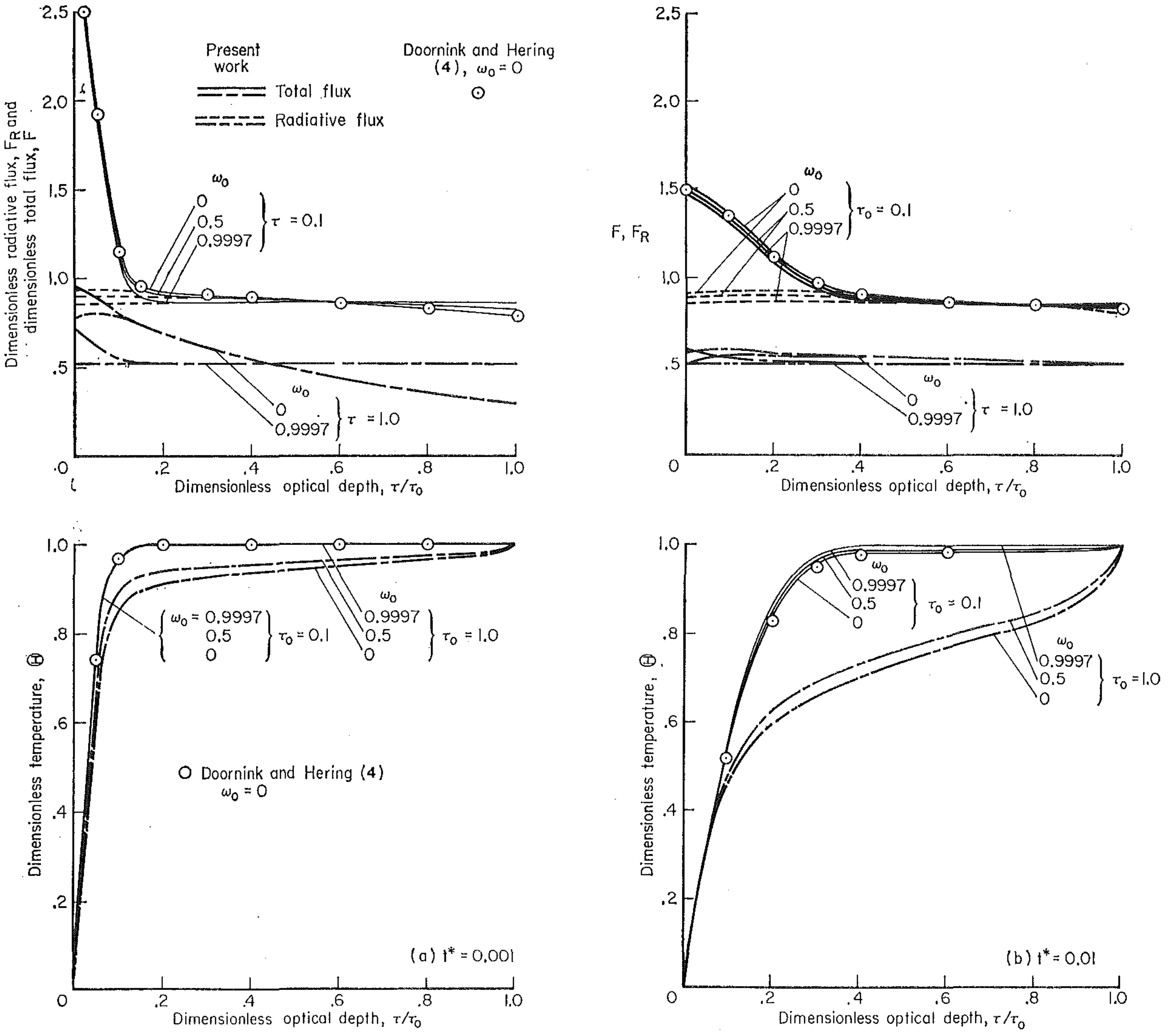

Fig. 4 Effect of albedo and optical thickness on the unsteady temperature and energy flux distributions in scattering, absorbing, and emitting media between parallel plates, $\epsilon_1 = \epsilon_2 = 1.0$, $N = 0.005$, $\theta_1 = 0.5$

cooling $\partial\Theta/\partial t^*$ is governed primarily by its explicit dependence in equation (5) on N. Thus the temperature distribution for $N = 0.5$ shows little influence of the radiation field, in contrast to the $N = 0.005$ temperature distribution.

The effect of reducing τ_0 from 1 to 0.1, holding other parameters at the same values as in Fig. 2 (with $\epsilon_1 = \epsilon_2 = 1.0$), is shown in Fig. 4. It is evident that the effect of varying albedo is much less pronounced at $\tau_0 = 0.1$ than it was for $\tau_0 = 1.0$. This may be attributed to the reduced interaction of the radiation field with the temperature field as the optical thickness is reduced, as indicated by equation (5). The same caution should be observed here as with the preceding figure in comparing results in a temporal vein for different optical thickness. The higher radiative and total fluxes associated with the reduced optical thickness are evident.

For $\tau_0 = 0.1$, the medium offers little opposition to the passage of radiation directly from boundary 2 to boundary 1. The radiative fluxes in fact approximate those for two black plates with no intervening medium. Little radiative cooling is evident; thus the temperature distributions resemble pure-conduction profiles. With little effect of albedo on the temperature distributions, the dimensionless conductive fluxes and hence the total fluxes are almost independent of albedo at a given dimensionless time.

Concluding Remarks

The effect of varying the albedo of single scattering on the transient energy transfer in a semitransparent medium has been explored for several values of the conduction–radiation parameter, optical thickness, wall emissivity, and dimensionless time. Steady-state solutions were also obtained for absorbing and scattering materials. Comparisons with special cases in the literature indicate good agreement for both transient and steady-state solutions. The present work clearly demonstrates the feasibility of computer solution for engineering purposes of transient energy transfer problems in materials in which scattering is significant.

References

1 Viskanta, R., and Grosh, R. J., "Heat Transfer by Simultaneous Conduction and Radiation in an Absorbing Medium," Journal of Heat Transfer, Trans. ASME, Series C, Vol. 84, No. 1, Feb. 1962, pp. 63–72.

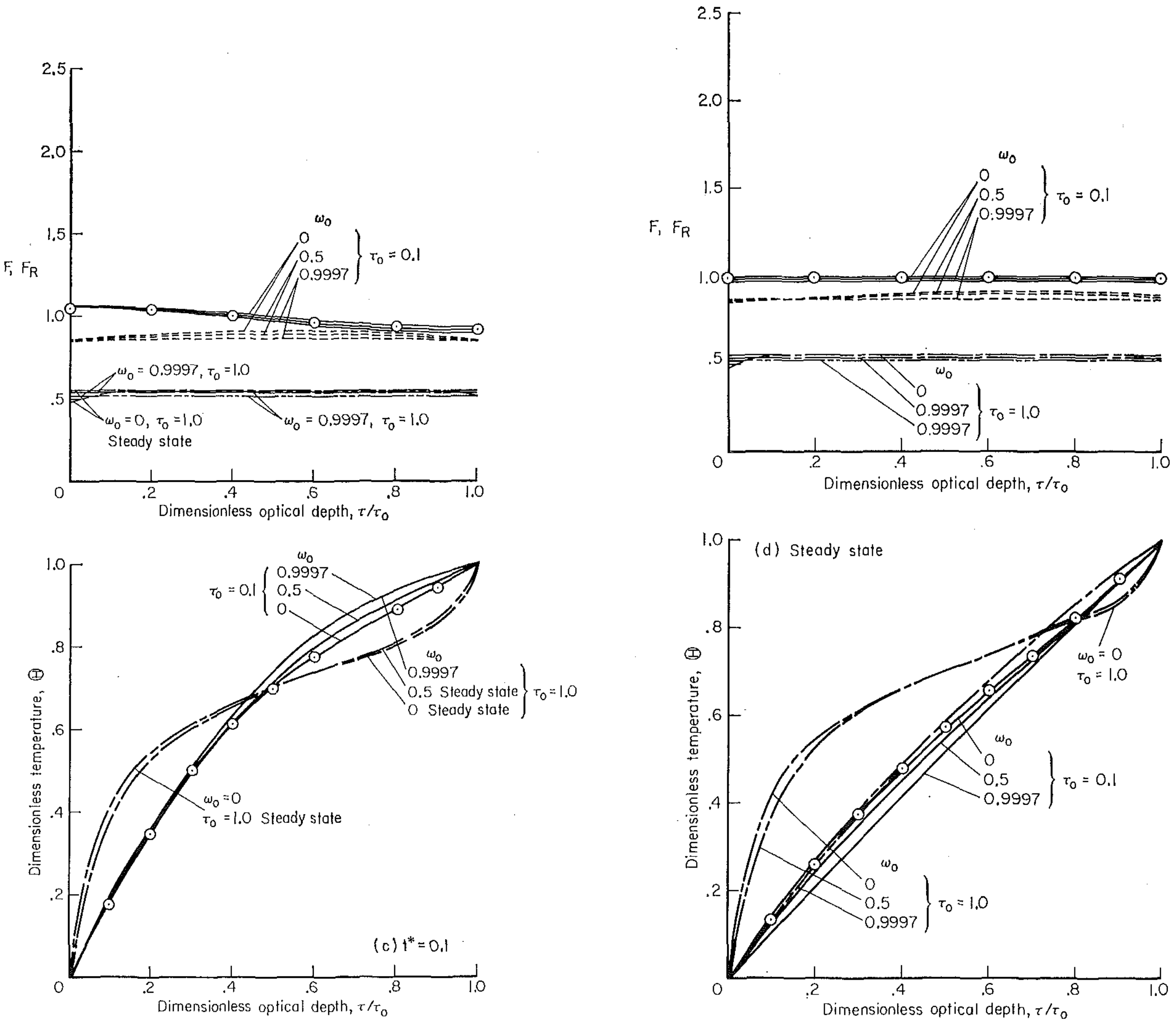

Fig. 4 Effect of albedo and optical thickness on the unsteady temperature and energy flux distributions in scattering, absorbing, and emitting media between parallel plates, $\epsilon_1 = \epsilon_2 = 1.0$, $N = 0.005$, $\theta_1 = 0.5$

2 Viskanta, R., and Grosh, R. J., "Effect of Surface Emissivity on Heat Transfer by Simultaneous Conduction and Radiation," *International Journal of Heat and Mass Transfer*, Vol. 5, 1962, pp. 729–734.

3 Viskanta, R., "Heat Transfer by Conduction and Radiation in Absorbing and Scattering Materials," JOURNAL OF HEAT TRANSFER, TRANS. ASME, Series C, Vol. 87, No. 1, Feb. 1965, pp. 143–150.

4 Doornink, D. G., and Hering, R. G., "Transient Combined Conductive and Radiative Heat Transfer," JOURNAL OF HEAT TRANSFER, TRANS. ASME, Series C, Vol. 94, No. 4, Nov. 1972, pp. 473–478.

5 Frame, J. S., "Matrix Functions and Applications, Part II—Functions of a Matrix," *IEEE Spectrum*, Apr. 1964, pp. 102–108.

6 Hsia, H. M., "Radiative Transfer in an Absorbing, Emitting, Anisotropic Scattering and Nonisothermal Medium between Parallel Plates," PhD thesis, University of Oklahoma, Norman, Okla., June 1965.

7 Hsia, H. M., and Love, T. J., "Radiative Heat Transfer Between Parallel Plates Separated by a Nonisothermal Medium With Anisotropic Scattering," JOURNAL OF HEAT TRANSFER, TRANS. ASME, Series C, Vol. 89, No. 3, Aug. 1967, pp. 197–204.

8 Hauth, J. L., "Transient Simultaneous Conductive and Radiative Heat Transfer in Absorbing, Emitting and Scattering Materials," master's thesis, University of Tulsa, Tulsa, Okla., June 1972.

J. M. DELHAYE
Research Scientist.

R. SEMERIA
Director.

J. C. FLAMAND
Technician.

Heat Transfer Laboratory,
Nuclear Research Center,
Grenoble, France

Void Fraction and Vapor and Liquid Temperatures: Local Measurements in Two-Phase Flow Using a Microthermocouple

A technique is described which enables the detection of the phase (liquid or vapor) in steam-water two-phase flow and the temperature measurement of each phase, using the hot junction of a microthermocouple. The signals are processed with a multichannel analyzer in order to obtain the amplitude histograms of the temperature. Significant results are obtained in pool boiling, forced convection subcooled boiling, and flashing flow of water.

Introduction

THE DEVELOPMENT of nuclear reactor technology has produced an increase in the number of studies of two-phase flow during the last two decades. Many new measurement devices have been invented to give a further insight into the local structure of boiling two-phase flow. The purpose of these investigations has been to understand the complex mechanism of hydrodynamics and heat transfer in such flows, in order to know the normal behavior of the channels in a BWR or the accidental behavior in a PWR. The void formation in a channel drastically changes the pressure drop laws which have to be known accurately to determine the required pumping power or the stability regime of the channels.

A first detailed approach of the "boiling" phenomenon was undertaken in our laboratory with a schlieren method associated with high-speed cinematography [1].[1] This technique showed the destruction and the entrainment of a film of superheated water lying on the heated wall, in the subcooled liquid. It has been thought that this process was connected with some temperature fluctuations produced by the motion of the steam bubbles [2].

The interest in the temperature fluctuations, especially in pool boiling, is not new. A microthermocouple, 50μ in diameter, was used in 1965 by Marcus and Dropkin [3] to evaluate the thickness of the superheated liquid layer in contact with a heated wall. Around the same time, Patten and his co-workers [4, 5] examined the transient aspect of the superheated liquid layer with the same method. In 1966, Bonnet, et al. [6] reported some results obtained with a microthermocouple imbedded in a resin block, in such a way that only a small part (20μ) of the hot junction was in the flow. Unfortunately, the size of the probe (80μ) produced a disturbance in the flow and its thermal inertia led to extra vaporization of the liquid on the sensor so that the significance of the signal was not very clear. In forced convection, the results of similar investigations were published by Treshchov [7] in 1957 and Jiji and Clark [8] in 1964. During our studies, other results on pool boiling were published by Van Stralen and Sluyter [9], Jacobs and Shade [10], and Subbotin and Tsiganok [11], and on forced convection subcooled boiling by Walmet and Staub [12] and Stefanovic, et al. [13]. Although all these works have contributed to a large extent, to the understanding of the local structure of two-phase flow with change of phase, they have not provided any reliable statistical information on the distribution of the temperature between the liquid and the vapor phases.

The originality of our work [14] is based on the possibility of separating the temperature of the liquid phase from the temperature of the vapor phase, and of giving the statistical properties of the temperature of each phase as well as the local void fraction. The basic idea was to use the hot junction, 20μ in diameter, of the microthermocouple, as an electrical probe [15] which indicates the nature of the phase surrounding the sensing element. The temperature signals are then processed in a multichannel analyzer which delivers the amplitude histograms of the liquid and vapor temperatures. Starting from these data, we can easily determine the local void fraction and the time average temperatures of the liquid and of the vapor. This technique requires an electrically conducting liquid, the electrical resistivity of which can be as high as 10 kΩ·cm. In these conditions ordinary water can be considered as an electrically conducting liquid. Nevertheless, the same results can be obtained in a nonequilibrium two-phase flow, without any phase indicator device, after making some assumptions concerning the amplitude histogram of the

---

[1] Numbers in brackets designate References at end of paper.

Contributed by the Heat Transfer Division of THE AMERICAN SOCIETY OF MECHANICAL ENGINEERS and presented at the AIChE-ASME Heat Transfer Conference, Denver, Colo., August 6–9, 1972. Manuscript received by the Heat Transfer Division April 10, 1972; revised manuscript received November 20, 1972. Paper No. 72-HT-13.

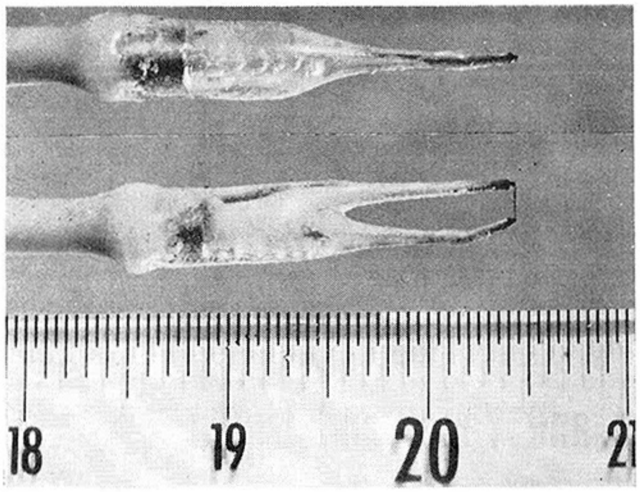

Fig. 1 Microthermocouple used in the first runs

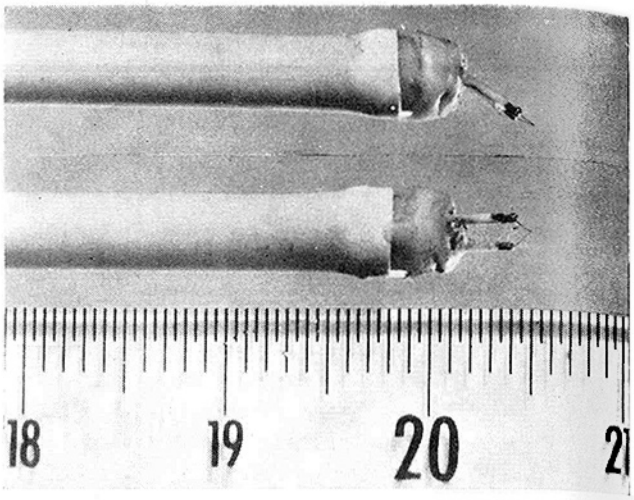

Fig. 2 New microthermocouple

temperature signal given by the microthermocouple without its electrical probe component.

Description of the Microthermocouple

The first runs were carried out with a probe similar to the well-known hot-wire probe. The hot junction connected two chromel-alumel wires, 25μ in diameter, straightened between two quartz supports, Fig. 1. However, this type of probe has two major drawbacks:

1 The steam bubbles tend to avoid the hot junction by rolling around the wire.

2 The quartz supports have poor mechanical resistance and the probe is easily broken.

The microthermocouple that we are now using is made up of the following components (Fig. 2):

1 Two chromel-alumel wires, 150μ in diameter, which support the hot junction.

2 These wires are protected by a stainless steel sheath and insulated by alumina.

3 The sensor, composed of two chromel-alumel wires, 20μ in diameter, 1 mm in length.

The ends of the stainless steel sheath are sealed with an epoxy resin (Araldite) to prevent any infiltration of water. The hot junction is prepared first, then tin-soldered onto the 150μ wires. This method has the advantage of making probe repairs very easy.

Phase Indicator Device

The microthermocouple, except for its hot junction, is electrically insulated from the liquid with a varnish. The insulating resistance between the junction and the ground, which is a function of the phase (vapor or liquid) surrounding the junction, is measured with a Kohlrausch bridge. In order to avoid any disturbances due to stray capacitances, all the sheaths are neutrodyned by the phase indicator signal. Both signals (phase and temperature) are received by a differential amplifier with a high common mode rejection ratio. Only the differential signal (temperature) is processed by the amplifier. The common mode (phase signal) is rejected and directed toward a logical switch circuitry.

Microthermocouple and Electrical Probe Signal Processing

When the microthermocouple is used in a temperature range close to 100 deg C, its cold junction is kept at the saturation temperature corresponding to the atmospheric pressure in an ebullioscope. The e.m.f. difference between the hot and cold junctions is then amplified. In the case of a flashing flow at a subatmospheric pressure, the cold junction is kept at 0 deg C and a known voltage is applied to minimize the e.m.f. difference between the hot and cold junctions.

Both signals (phase and temperature) were observed on a two-beam oscilloscope, and at the same time, the temperature signal was also sent to a multi-channel analyzer, INTERTECHNIQUE DIDAC 4000. This latter device is used as a statistical analyzer so that it delivers the amplitude histogram of the temperature signal. The content N of each channel of this analyzer corresponds to the number of times that the signal reached a given amplitude (Fig. 3). In order to do that, a clock delivers pulses, at a frequency which is chosen according to the power spectrum of the signal which is to be analyzed. At each clock-time, a sample of the signal is picked up and an analog-frequency converter is used to transform this quantity into a pulse-train proportional to the amplitude of the signal. This numerized quantity gives the number of the channel where the sample will be stored. At this time the arithmetic register adds a unit in the selected channel. So, the amplitude histogram $N(e)$ of the signal $e(t)$ is built up. The choice of the scanning rate is given by the Shannon's theorem [16]: the sampling frequency has to be higher than twice the highest frequency occuring in the signal power spectrum. During all our experiments a 1 kHz sampling frequency was chosen. This technique has already been used by Delhaye [17] to process the signal delivered by a hot-film anemometer, in an isothermal air-water flow. The entire signal (air and water) was analyzed, and a hypothesis was made to separate the air histogram from the water histogram, Fig. 4.

In the present work, the phase signal has been used to switch the liquid signal or the vapor signal into a first 1000-channel

Nomenclature

e = signal
N = probability density
S = area

T = temperature
t = time
α = local void fraction

Subscripts

L = liquid
sat = saturation condition
V = vapor

subgroup or into a second 1000-channel subgroup of the 4000-channel analyzer (Fig. 5). We thus obtain separately the histograms of the vapor and of the liquid temperatures.

Signal Processing When the Phase Indication Is Not Available

If it is impossible to detect the phase (liquid or vapor) surrounding the hot junction, only the entire histogram (liquid and vapor) is available. As for the hot-film anemometer signal analysis, we have to make some assumptions to separate the liquid histogram and the vapor histogram. But before making a statement on the entire histogram (liquid and vapor), we have to analyze carefully the temperature signal delivered by the microthermocouple.

Following many runs carried out with high-speed movies, we can visualize the temperature fluctuation, detected by a microthermocouple located on the upward trajectory of a steam bubble very close to a heating wall, in a nucleate pool boiling experiment with subcooled water. These experiments indicated an increase in temperature during the approach of a bubble, Fig. 6. This fact is due to the penetration of the hot junction into a superheated film of water surrounding the bubble. When the microthermocouple enters the bubble, the temperature decreases very rapidly toward the saturation temperature. The high time-rate of change of the temperature level is produced by the vaporization of a small quantity of water remaining on the hot junction after its penetration into the vapor. Then the temperature remains constant and equal to the saturation temperature inside the bubble. Finally, when the hot junction exits from the bubble, it detects a superheated liquid wake and the temperature decreases toward the subcooled liquid temperature.

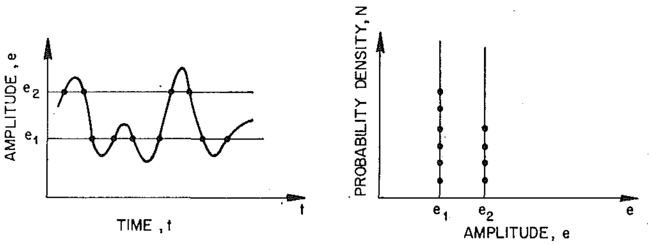

Fig. 3 Amplitude histogram of a given signal

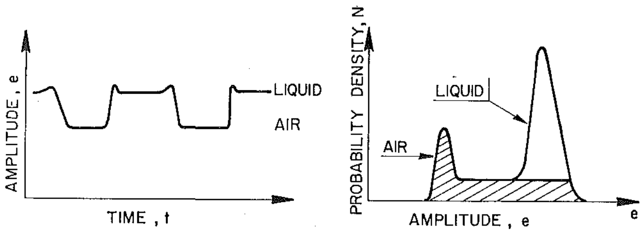

Fig. 4 Amplitude histogram of a hot-film anemometer signal in an air-water flow

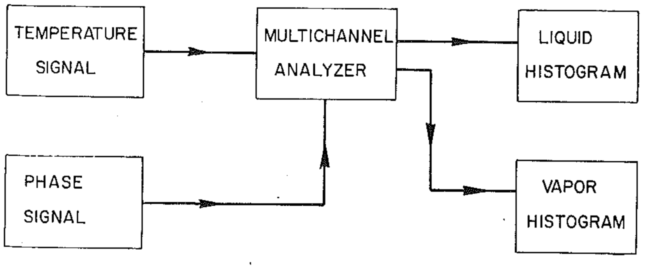

Fig. 5 Diagram for the signal processing

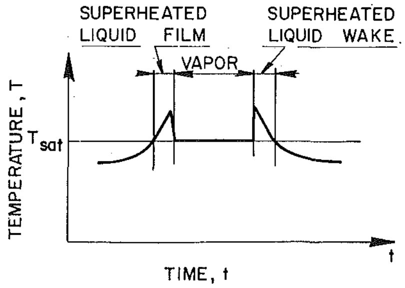

Fig. 6 Temperature signal in local boiling

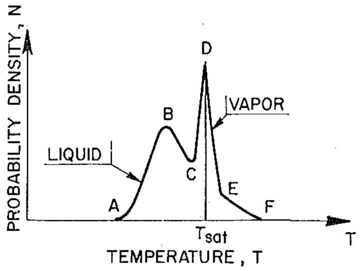

Fig. 7 Temperature histogram in local boiling

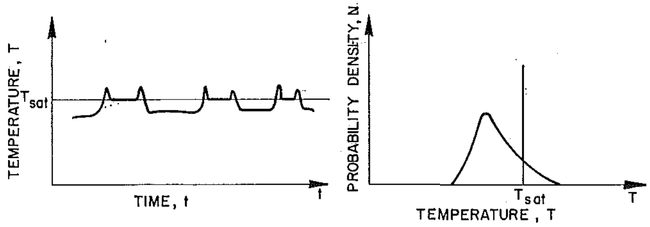

Fig. 8 Temperature amplitude histogram within a system at constant pressure

The histogram corresponding to this sequence is shown in Fig. 7. The main characteristic points on this histogram are:

A = minimum liquid temperature
B = most probable liquid temperature
C = minimum vapor temperature
D = most probable vapor temperature
E = maximum vapor temperature
F = maximum superheated liquid temperature.

If the pressure were constant, the saturation temperature would also be constant, and the temperature amplitude histogram would present a straight vertical line, Fig. 8, corresponding to this constant saturation temperature. However, the pressure is never constant and a distribution of the saturation temperature follows, Fig. 9. Therefore, we have to assume that, between $T_{\text{sat}}^{\min}$ and $T_{\text{sat}}^{\max}$, there exists some liquid. From this statement we derive our main hypothesis to process the temperature histogram in an electrically nonconducting liquid: The vapor temperature histogram is the cross-hatched region CDEC, Fig. 9, and the liquid temperature histogram is the complementary region ABCEFA, Fig. 9. The time average vapor and liquid temperatures are given by the barycenters of these areas, and the local void fraction can be calculated by the formula:

$$\alpha = \frac{S_V}{S_V + S_L}$$

where S_V is the area of the vapor cross-hatched region CDEC, Fig. 9, and S_L the area of the liquid region ABCEFA. The denominator represents the total area of the histogram ABCDEFA.

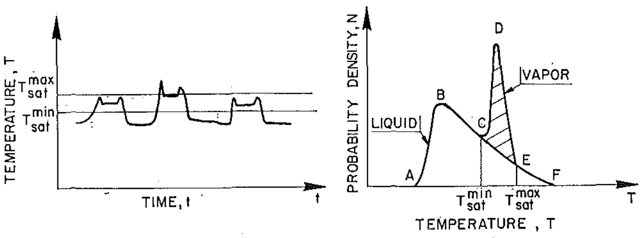

Fig. 9 Actual temperature amplitude histogram in local boiling

Some Experimental Results

The use of a microthermocouple has supplied enough information under different conditions to be considered as a valuable instrumentation device in the study of the local structure of a two-phase flow with change of phase. In the following section, we will investigate the temperature histograms in three types of flow: nucleate pool boiling, forced convection local boiling, and flashing flow.

The study of water nucleate boiling with a microthermocouple was carried out in a test section which is described in reference [14]. In order to understand the physical significance of the temperature signal given by the microthermocouple, we took high-speed movies (20,000 frames per sec) of a bubble pierced by the hot junction simultaneously with the temperature signal. Reference [14] shows the main results of these experiments. The shape of the temperature histogram changes when the hot junction moves away from the wall. In Fig. 10, four histograms are represented with the corresponding temperature signal, as a function of the distance from the wall. The cross-hatched areas are the vapor temperature histograms according to our previous hypothesis. Since the electrical probe function was not yet available in these experiments, we had to process the histograms as in the case of an electrically nonconducting liquid. Near the wall, Fig. 10.1, there is no subcooled water but only vapor and superheated liquid. At 0.5 mm from the wall, Fig. 10.2, water and vapor are practically at the same temperature. At 1 mm above the wall, Fig. 10.3, some superheated water remains but most of the water is already subcooled. Finally when the hot junction is 2 mm above the wall, there is no longer any superheated liquid and the histograms of the vapor and of the subcooled liquid are distinctly separate. A graph of the most probable liquid temperature (point B in Fig. 7) is shown in Fig. 11. The constant local void fraction curves are also represented. These experiments have confirmed the qualitative results which were obtained with a schlieren method by Béhar and Séméria [1]. This technique visualized a destructive process of the superheated liquid layer by the bubble growth, and an entrainment of superheated liquid in the wake of the bubble. The pattern of the temperature profile, Fig. 11, can be explained by a re-supply of

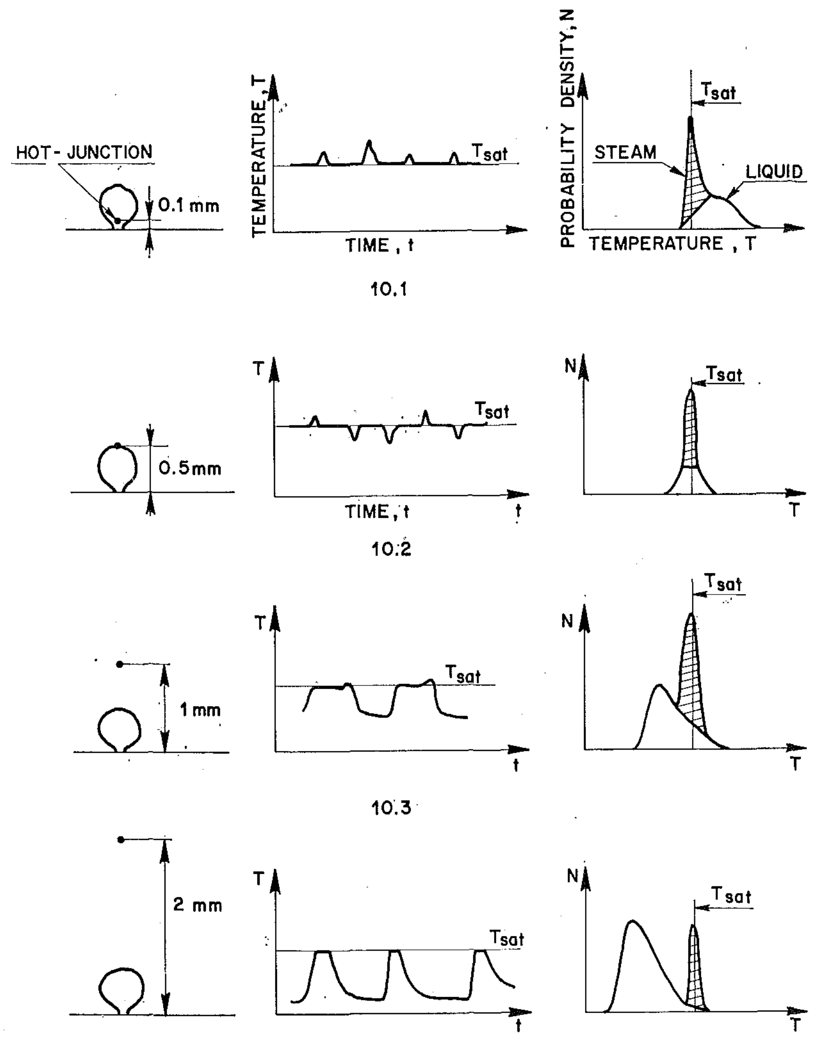

10.1

10.2

10.3

10.4

Fig. 10 Temperature signals and histograms in nucleate pool boiling

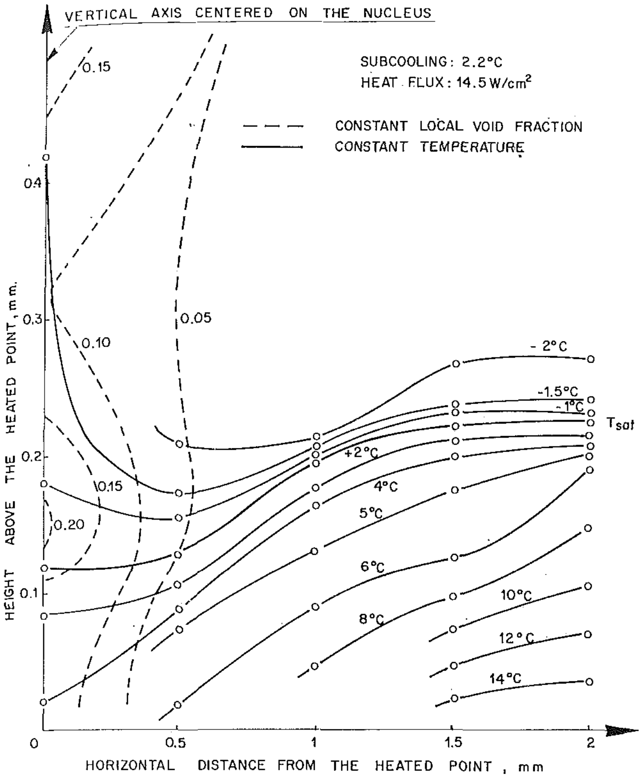

Fig. 11 Most probable liquid temperature and void fraction above a nucleus in nucleate boiling

the wall area by some colder liquid originating from the bulk fluid which leads to an enhancement of the heat transfer coefficient in nucleate pool boiling.

All the tests in forced convection were carried out in a water loop described in reference [14]. The temperature signals and the histograms are identical to those observed in subcooled nucleate boiling.

A graph of the local void fraction distribution across the test section is given in Fig. 12, for a 2.2 deg C subcooling, 1 m/s velocity and with the following heat fluxes: 50, 70, and 80 W/cm². The void fraction was determined with the phase indicator device of the microthermocouple. In reference [14] more detailed results are given on the influence of the subcooling, the heat flux, and the velocity, on the local void fraction profile, and on the temperature profiles.

The more systematic study of flashing flow of water [18] justified the validity of our assumption concerning the processing of the temperature histogram, when the indication of the phase surrounding the hot junction is not available. All the tests were conducted in a subatmospheric loop described in reference [19]. In this work Barois proposed a different hypothesis for the separation of the liquid and vapor histograms. He considers that the vapor histogram has to be symmetrical. This type of assumption, Fig. 13, which was also used afterwards by Stefanovic, et al. [13] in forced convection boiling, gives liquid temperatures which are too high. Our hypothesis, as explained previously, was found to be in better agreement with the direct separation of the histograms made by the phase indicator device. Reference [18] shows various results concerning the evolution of the steam and liquid temperatures, as well as the void fraction along a channel in which a flashing flow of water takes place.

Conclusions and Future Work

1 The microthermocouple has been proved to be a valuable instrumentation device in obtaining information on the local structure of boiling two-phase flow in nonequilibrium conditions.

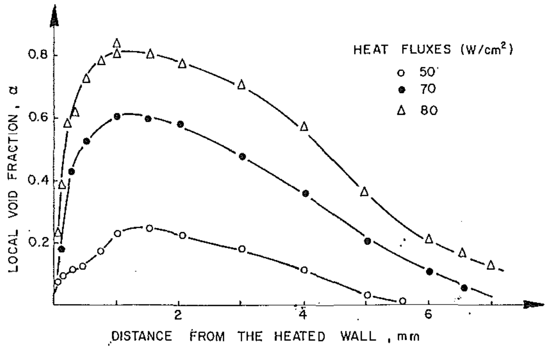

Fig. 12 Local void fraction distribution in forced convection local boiling

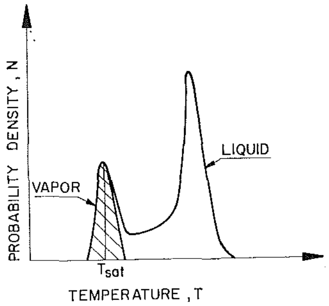

Fig. 13 Barois's hypothesis

2 The microthermocouple, associated with a phase indicator electronic circuit, gives the local void fraction, the time average temperatures of both phases, and their fluctuations.

3 The same results can be obtained with a proper assumption, either when the phase indicator electronic circuitry is not available, or when the fluid is electrically nonconducting. In this case, we have to separate the vapor and liquid histograms according to the hypothesis explained in the text and represented in Fig. 10. As we can see in this figure, this technique cannot be applied when the histogram is symmetric as in Fig. 10.2.

4 The liquid and vapor velocities are expected to be measured by a cross-correlation method, as explained in reference [14], where significant results have already been obtained.

References

1 Béhar, M., and Séméria, R., "La strioscopie appliquée à l'étude de l'ébullition et du dégazage," *La Houille Blanche*, No. 6, Oct., 1963, pp. 687–691.

2 Séméria, R., "Relation entre la structure de la couche diphasique près d'une paroi chauffante et les mécanismes d'échange," Ecole d'Eté Internationale sur les Transferts de chaleur et de masse dans la couche limite turbulente, Herceg Novi, 1968.

3 Marcus, B. D., and Dropkin, D., "Measured Temperature Profiles Within the Superheated Boundary Layer Above a Horizontal Surface in Saturated Nucleate Pool Boiling of Water," JOURNAL OF HEAT TRANSFER, TRANS. ASME, Series C, Vol. 37, Aug. 1965, pp. 333–341.

4 Garg, S. C., and Patten, T. D., "Temperature and Pressure Transients Near the Heating Surface During Nucleate Pool Boiling of Saturated Water," *Proceedings of the Third International Heat Transfer Conference*, Chicago, Vol. 3, Aug. 1966, pp. 204–211.

5 Grant, I. D. R., and Patten, T. D., "Boiling Heat Transfer in Steam-Generating Units and Heat Exchangers," *Proceedings 1965–1966 of the Institution of Mechanical Engineers*, Vol. 180, Par 3C.

6 Bonnet, C., et al., "Fluctuations de température dans la paroi chauffante et dans le liquide au cours de l'ébullition nucléée," EUR 3162.f, 1966.

7 Treshchov, G. G., "Experimental Investigation of the Mechanism of Heat Transfer With Surface Boiling of Water," *Teploenergetika*, Vol. 4, No. 5, 1957, pp. 44–48.

8 Jiji, L. M., and Clark, J. A., "Bubble Boundary Layer and Temperature Profiles for Forced Convection Boiling in Channel Flow," JOURNAL OF HEAT TRANSFER, TRANS. ASME, Series C, Vol. 86, Feb. 1964, pp. 50–58.

9 Van Stralen, S. J. D., and Sluyter, W. M., "Local Temperature Fluctuations in Saturated Pool Boiling of Pure Liquids and Binary Mixtures," *International Journal of Heat and Mass Transfer*, Vol. 12, 1969, pp. 187–199.

10 Jacobs, J. D., and Shade, A. H., "Measurement of Temperatures Associated With Bubbles in Subcooled Pool Boiling," JOURNAL OF HEAT TRANSFER, TRANS. ASME, Series C, Vol. 91, Feb. 1969, pp. 123–128.

11 Subbotin, V. I., Sorokin, D. N., and Tsiganok, A. A., "Some Problems on Pool Boiling Heat Transfer," HEAT TRANSFER *1970*, Vol. 5, Paper No. B1.9, Elsevier, 1970.

12 Walmet, G. E., and Staub, F. W., "Pressure, Temperature, and Void Fraction Measurement in Nonequilibrium Two-Phase Flow," *Two-Phase Flow Instrumentation*, ASME, 1969, pp. 89–101.

13 Stefanovic, M., et al., "Experimental Investigation on the Superheated Boundary Layer in Forced Convection Boiling," *Heat Transfer 1970*, Vol. 5, Paper No. B4.12, Elsevier 1970.

14 Delhaye, J. M., Séméria, R., and Flamand, J. C., "Mesure du taux de vide local et des températures du liquide et de la vapeur en écoulement diphasique avec changement de phase à l'aide d'un microthermocouple," CEA-R-4302, 1972.

15 Bergles, A. E., "Electrical Probes for Study of Two-Phase Flows," *Two-Phase Flow Instrumentation*, ASME, 1969, pp. 70–81.

16 Max, J., *Méthodes et techniques de traitement du signal et applications aux mesures physiques*, 1st ed., Masson, 1972.

17 Delhaye, J. M., "Hot-Film Anemometry in Two-Phase Flow," *Two-Phase Flow Instrumentation*, ASME, 1969, pp. 58–69.

18 Delhaye, J. M., et al., "Etude expérimentale de l'autovaporisation en écoulement vertical ascendant," CENG, S.T.T., Internal Report No. 385, 1971.

19 Barois, G., "Etude expérimentale de l'autovaporisation d'un écoulement ascendant adiabatique d'eau dans un canal de section uniforme," Thèse de docteur-ingénieur, Faculté des Sciences de l'Université de Grenoble, 1969.

C. A. BANKSTON
Staff Member,
University of California,
Los Alamos Scientific Laboratory,
Los Alamos, N. M.

H. J. SMITH
Professor,
University of Michigan,
Ann Arbor, Mich.

Vapor Flow in Cylindrical Heat Pipes[1]

Solutions of the complete axisymmetric Navier–Stokes equations for steady, laminar vapor flow in circular heat pipes with various lengths of evaporator and condenser have been obtained by finite-difference methods. In addition, a new series solution for the slow-motion case was obtained that is valid for arbitrary distributions of evaporation and condensation and that confirms the numerical result in the limit of low Reynolds number. For uniform evaporation and condensation, the motion in the evaporator is found to be described adequately by similar solutions in both limits, and in the transition from low to high Re, the flow is completely determined by the evaporator Reynolds number. The evaporator is very weakly coupled to the condenser. The conditions in the condenser are decidedly more complex, and similar solutions are of value only for small Reynolds numbers and long tubes. Reverse flows occur for condenser Reynolds numbers greater than two and occupy a substantial fraction of the condenser length. Complete flow descriptions for symmetrical and asymmetrical heat pipes were obtained, and practical results for the calculation of pressure losses in low-speed heat-pipe vapor flows are given.

Introduction

The engineering analysis of a heat pipe can often be simplified to the solution of three fluid mechanical problems: (1) the calculation of the capillary pumping action available in the wick structure, (2) the pressure loss associated with the liquid return path, and (3) the pressure loss in the vapor flow between the evaporator and the condenser, and the solution of thermodynamic relations between the phases as shown by Cotter [1].[2] The first two problems can usually be solved readily, but the dynamics of the vapor flow is surprisingly complex, even when the geometry and boundary specifications are simple.

For steady operation within the working range of many heat pipes, the vapor velocity in the evaporator is well below sonic, and to a good approximation the entire process can be considered to take place at constant density. In the regime of creeping flow, the problem is a linear one, and in principle there is no difficulty in obtaining a stream function that can satisfy arbitrary boundary conditions. However, solutions for the transition and inertial flow regimes should satisfy the full Navier–Stokes equation of motion, since viscous effects at the boundaries may have a strong influence on the motion, even in the limit of vanishing viscosity.

Solutions of the Navier–Stokes equations for heat pipes of semi-infinite length with only uniform evaporation or only uniform condensation have been obtained by Knight and McInteer [2], Yuan and Finkelstein [3], Donaldson, et al. [4], and Terrill and Thomas [5]. In each case attention was restricted to a class of similar solutions. The results can be summarized as follows:

(*a*) For positive Re_r (condensation)[3] between 2.30 and 9.11, there are no solutions of the class considered [4, 5].

(*b*) All of the investigators agree that at positive Re_r below 2.30, there is only one solution without reversal of the axial component of velocity (u). The solution also features a single maximum of the axial velocity, which lies on the axis of the pipe. The same is true for all negative Re_r. As Re_r tends to zero, each of these two solutions approaches the Poiseuille form, $u = u_0(1 - r^2/R^2)$, which is the solution for creeping flow in these cases. As Re_r tends to negative infinity, the solution (for negative Re_r) tends to the form $u = u_0 \cos [\pi/2(r/R)^2]$, which is the solution for the inviscid flow appropriate to the boundary conditions [6].

(*c*) At all Re_r less than 2.3, there is a second solution that features flow reversal [4, 5].

(*d*) At Re_r between 9.11 and 20.6, there may be more than

---

[1] This work was performed under the auspices of the U. S. Atomic Energy Commission.

[2] Numbers in brackets designate References at end of paper.

Contributed by the Heat Transfer Division for publication (without presentation) in the Journal of Heat Transfer. Manuscript received by the Heat Transfer Division September 22, 1972. Paper No. 73-HT-P.

[3] It is customary to discuss this class of flows in terms of the radial Reynolds number $\mathrm{Re}_r = \rho \frac{VR}{\mu}$. The axial Reynolds number is related to Re_r by $\mathrm{Re}_A(x) = \frac{4}{R}\int_0^x \mathrm{Re}_r(\xi)d\xi$. For uniform suction or injection, $\mathrm{Re}_A(x) = \frac{4x}{R}\mathrm{Re}_r$. It should be noted that the stability limits for laminar flows of this class have not yet been established. Flows with injection have been found to retain laminar velocity profiles at axial Reynolds numbers greater than 10^5.

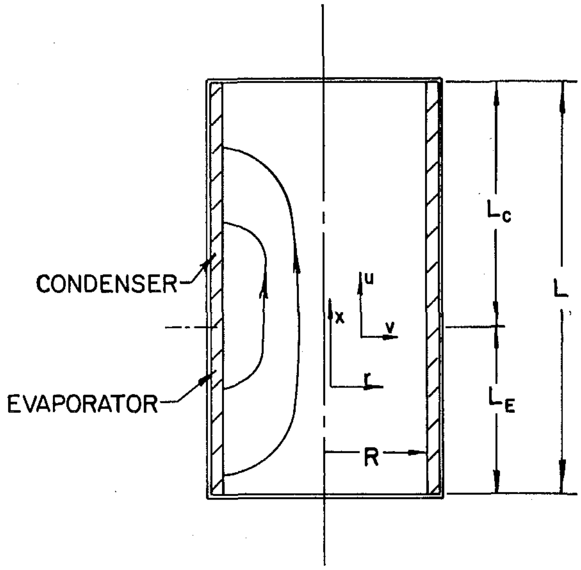

Fig. 1 The cylindrical heat pipe and coordinate system

one solution [5]. One such solution, given in [4], exhibits maxima of the axial velocity off the axis.

(*c*) At Re_r above 20.6, there is a multiplicity of solutions. Four of them, given in [4], exhibit flow reversal or maxima off the axis.

There have been several experimental investigations of laminar flow with uniform injection at the cylindrical wall [7–9], varied initial conditions, and attempts to produce motions with reverse flow. However, only those cases discussed in (*b*) have been observed.

Weissberg [10] used an approximate integral analysis that yields nonsimilar solutions and includes, as a special case, one of the similar solutions of Yuan and Finkelstein [3]. The analysis indicates that reverse flows should occur for $2.4094 < \mathrm{Re} < 7.6344$ and that the explanation of the nonexistence of similar solutions is the onset of velocity reversals near the wall due to the action of an adverse pressure gradient. Results for large Re are not given.

Other investigators have solved equations of the boundary-layer type in which certain gradients in the axial direction are neglected and the pressure is taken to be uniform across the pipe to analyze flow with only injection or only withdrawal at the wall [11–14]. The assumptions limit this type of analysis to small rates of suction or injection and preclude the calculation of reversed flow. They do not require similarity and so at low Re are useful for describing the transitions between components. Busse [14] has applied an approach like that of Weissberg to the case of a slender heat pipe with an evaporator and condenser connected by an adiabatic wall at which no mass transfer occurs.

The effects of compressibility have been studied by Levy [15] and by Deverall, Kemme, and Florshuetz [16] for one-dimensional flows, and very recently by DeMichele for two dimensions [17].

In his original analysis of heat-pipe performance [18], Cotter assumed that the flows in the evaporator and the condenser were nearly uncoupled so that similarity solutions could be applied separately in each. He used solutions of Yuan and Finkelstein for small Re and results of Knight and McInteer for large Re.

Because of the limitations of previous studies as to Reynolds number or geometry, the rational design of real heat pipes has awaited a solution of the full Navier–Stokes equation for a pipe of finite length and with both evaporation and condensation. In this paper such a solution is obtained by a numerical method. A new analytical solution for creeping flow is also given and serves as one of several checks applied to the numerical results.

Mathematical Description

The Differential Equations and Boundary Conditions. We consider the steady, laminar axisymmetric motion of an incompressible vapor in a right-circular-cylindrical cavity as depicted in Fig. 1. The uniform inflow and outflow boundary conditions are referred to here as evaporation and condensation, but no change of phase is actually involved in the calculation. We could just as well describe the processes that occur at the wall as blowing and suction perpendicularly through a porous-walled pipe. Under these conditions, the flow is governed by conservation of mass in the form

$$\frac{\partial u}{\partial x} + \frac{1}{r}\frac{\partial (rv)}{\partial r} = 0 \tag{1}$$

and by conservation of momentum in the form

$$\rho u \frac{\partial u}{\partial x} + \rho v \frac{\partial u}{\partial r} = -\frac{\partial p}{\partial x} + \mu \left[\frac{\partial^2 u}{\partial x^2} + \frac{1}{r}\frac{\partial u}{\partial r} + \frac{\partial^2 u}{\partial r^2}\right] \tag{2}$$

and

$$\rho u \frac{\partial v}{\partial x} + \rho v \frac{\partial v}{\partial r} = -\frac{\partial p}{\partial r} + \mu \left[\frac{\partial^2 v}{\partial x^2} + \frac{1}{r}\frac{\partial v}{\partial r} + \frac{\partial^2 v}{\partial r^2}\right] \tag{3}$$

The boundary conditions are

$$\left.\begin{aligned} u(0, r) &= v(0, r) = 0 \\ u(L, r) &= v(L, r) = 0 \\ v(x, 0) &= 0,\ \partial u(x, 0)/\partial r = 0 \\ u(x, R) &= 0,\ v(x, R) = v_w(x) \\ p(0, 0) &= 0 \end{aligned}\right\} \tag{4}$$

Finite-Difference Solution. The dependent variables are transformed to the stream function and the vorticity, thereby elimi-

Nomenclature

A = constant of integration
a = $\rho v_w/\mu$
B = constant of integration
ba = constant defined by equation (10)
bc = constant defined by equation (10)
I = Bessel function
i = index of axial mesh spacing
J = Bessel function
j = index of radial mesh spacing
K_n = coefficients in equation (14)
L = length of heat pipe or component
p = pressure
R = pipe radius
Re_r = radial Reynolds number, $\rho v_w R/\mu$ (can be $\pm$)
Re = radial Reynolds number, $\rho V_E R/\mu$ = $|\mathrm{Re}_r|$, but is $\rho V_C R/\mu$ where identified as the condenser radial Reynolds number
r = radial coordinate
u = axial velocity component
V = radial speed at wall
v = radial velocity component
x = axial coordinate
y = normal distance from pipe wall, $R - r$
μ = dynamic viscosity
ρ = vapor density
τ = shear stress
ψ = stream function
ω = vorticity, $\partial v/\partial x - \partial u/\partial r$
ω^* = modified vorticity, ω/r

Subscripts

C = condenser
E = evaporator
N = value of mesh index j at $r = R$
0 = condition at $r = 0$
w = condition at pipe wall, $r = R$

nating the unknown pressure and reducing the number of dependent variables to two.

The new variables ψ and ω^* are defined by

$$r\rho u = \frac{\partial \psi}{\partial r}$$
$$r\rho v = -\frac{\partial \psi}{\partial x} \tag{5}$$

and

$$\omega^* = \frac{1}{r}\left(\frac{\partial v}{\partial x} - \frac{\partial u}{\partial r}\right) = \frac{\omega}{r} \tag{6}$$

Then equations (1)–(3) yield the set

$$-\rho\omega^* = \frac{1}{r^2}\frac{\partial^2 \psi}{\partial x^2} + \frac{1}{r^2}\frac{\partial^2 \psi}{\partial r^2} - \frac{1}{r^3}\frac{\partial \psi}{\partial r} \tag{7}$$

and

$$\rho u \frac{\partial \omega^*}{\partial x} + \rho v \frac{\partial \omega^*}{\partial r} = \mu\left[\frac{\partial}{\partial x}\left(\frac{\partial \omega^*}{\partial x}\right) + \frac{1}{r}\frac{\partial}{\partial r} \times \left(r\frac{\partial \omega^*}{\partial r}\right) + \frac{2}{r}\frac{\partial \omega^*}{\partial r}\right] \tag{8}$$

The boundary conditions on ψ in (7) follow readily from (4). Those on ω^* in (8) must be derived from equation (7) in conjunction with (4), noting that the usual finite-difference representations of (7) become inaccurate and may introduce serious errors or instabilities. The procedure used here involves the integration of (8) for the special conditions existing very near the bounding wall and the subsequent integration of (7) to obtain an algebraic relation between ψ and ω^* at the boundaries.

In a region very near a wall, we can neglect the variation of ω^* with x in comparison with the radial variation. Then equation (8) after two integrations reduces to

$$\omega^* = \left(\frac{R}{r}\right)^2 \left\{Be^{-ay} - \frac{A}{\mu a^2} R^2 \left[(1 + aR)e^{-ay} - (1 + ar)\right]\right\} \tag{9}$$

where y is the distance from the wall. Equation (7) can now be integrated twice between the wall and the radius r_{N-1} of the adjacent mesh point to provide a second equation involving the integration constants A and B. An approximation, valid for small values of ay, is

$$\psi_w - \psi = B \cdot bc + A\left[\frac{(1 + aR)bc}{\mu a^2 R^2} - \frac{ba}{\mu a^2}\right] \tag{10}$$

in which

$$bc = R^2 \left\{\left(1 - ar + \frac{(aR)^2}{2}\right)\left(\frac{r}{2}\ln\left(\frac{r}{R}\right) + \frac{R^2 - r^2}{4}\right) + \frac{y^2}{2}\left(aR - \frac{(aR)^2}{2}\right) + \frac{y^3}{3}\left(\frac{a^2R}{4} - a\right) + \frac{y^4a^2}{16}\right\}$$

and

$$ba = \frac{1}{2}r^2 \ln\left(\frac{r}{R}\right) + \frac{R^2 - r^2}{4} + \frac{ay^2R}{2}\left(1 - \frac{2y}{3R}\right)$$

Equations (9) and (10) can be solved for A and B at r_{N-1}, and the value of ω^* at the wall can then be calculated from (10).

When ay is large, the error of (10) can be reduced by decreasing the mesh spacing near the wall or by increasing the number of terms retained in (10), but both measures increase the computational effort required. We note that large values of ay are associated with small viscosities and that at $y > 0$ the viscous forces are small compared to the inertial forces. Then, near a wall along which the radial velocity is constant and to which the streamlines are normal, ω is independent of r. We can write equation (7) in the form

$$-\rho\omega^* r = -\rho\omega = \frac{d}{dr}\left(\frac{1}{r}\frac{d\psi}{dr}\right)$$

integrate, and express the boundary value of ω^* in terms of the value of $d\psi/dr$ at the point adjacent to the wall. Using a central difference scheme, we obtain

$$\rho\omega_w{}^* = \frac{[\psi(x, R) - \psi(x, r_{N-2})]}{2r_{N-2}R(R - r_{N-1})^2} \tag{11}$$

Equation (11) was used for large-Reynolds-number calculations where the approximation of (10) becomes inaccurate.

Similar procedures can be used to derive expressions for the vorticity on the plane impermeable end walls of the heat pipe. At the axis of the pipe the vorticity must vanish, but ω^* remains finite. The simple prescription of a linear variation of ω^* with r was found to produce satisfactory results for heat-pipe flows.

The basic finite-difference solution procedure used in this investigation is that described by Gosman, et al. [19], with special provisions for the calculation of the vorticity at the permeable boundaries and a difference formula that permits the use of nonuniform grid spacing in regions where greater resolution is desired. Pressures were calculated from the integrals of equations (2) and (3), expressed in terms of ω^*. The integration proceeded along the axis of the tube from $x = 0$ to $x - L$, followed by integration from $r = 0$ to $r = R$. A central difference scheme was used for $\partial\omega^*/\partial x$, except at the end walls, where the appropriate forward or backward difference formula was used. Since the ω^* at the corners of the mesh are not required in the solution, and may even be singular points, they are not calculated, and the pressure cannot be obtained accurately near the corners. Further details are given in [20].

Slow-Motion Approximation. Consider the axisymmetric, steady slow motion of a vapor of homogeneous density and viscosity in the cylindrical heat pipe of Fig. 1. In terms of dimensionless variables based on R, V_E, and ρ, equation (1) can be written

$$\frac{\partial(ru)}{\partial x} + \frac{\partial(rv)}{\partial r} = 0 \quad \text{or} \quad u = \frac{1}{r}\frac{\partial \psi}{\partial r}, \qquad v = -\frac{1}{r}\frac{\partial \psi}{\partial x} \tag{12}$$

and for very small Re, equations (2) and (3) with inertial terms neglected yield

$$D^4\psi = 0 \tag{13}$$

in which

$$D^2\psi = r\frac{\partial}{\partial r}\left(\frac{1}{r}\frac{\partial \psi}{\partial r}\right) + \frac{\partial^3 \psi}{\partial x^2} = -r\omega$$

The boundary conditions remain those given in (4).

As shown in [20], separation of variables yields

$$\psi = \sum_n -2(-1)^n K_n \left(\frac{n\pi}{L}\right)^2 I_0\left(\frac{n\pi}{L}\right) \sum_{\lambda_j} \frac{rJ_1(\lambda r)}{\left(\frac{n^2\pi^2}{L^2} + \lambda^2\right)^2 J_1(\lambda)} \times \left[\frac{(-1)^n(L - x)\sinh \lambda x - x \sinh[\lambda(L - x)]}{\sinh \lambda L - (-1)^n \lambda L}\right] + \sum_n \frac{1}{2} K_n \left(\frac{L}{n\pi}\right) \sin\left(\frac{n\pi x}{L}\right) \times \left[r^2 I_2\left(\frac{n\pi r}{L}\right) - \frac{I_1\left(\frac{n\pi}{L}\right)}{I_0\left(\frac{n\pi}{L}\right)} rI_1\left(\frac{n\pi r}{L}\right)\right] \tag{14}$$

in which $\lambda = \lambda_j$ are the zeros of $J_0(\lambda)$, $n = 1, 2, \ldots$, and all requirements are satisfied except the boundary condition $\psi(x, 1) = \psi_w(x)$. The latter was taken as that for a symmetrical pipe with uniform evaporation and condensation, and the roots of the resulting characteristic equation for the coefficients K_n were determined by an iterative procedure. The values of ψ then given by (14) are compared below with the numerical solution of the full Navier-Stokes equations at small Re.

Results

Stability and Accuracy of Numerical Solutions. The method exhibited good numerical stability, and a fairly rapid rate of convergence of the iterative procedure was found so long as the proper relations were used for the vorticity boundary condition. The accuracy of the numerical solution was checked in three ways: (*a*) the mesh spacing was systematically varied and the results for different mesh sizes were compared to the extrapolated results for infinitesimal mesh spacing, (*b*) the results of calculations for large L/R were compared with known similar solutions for both large and small Reynolds numbers, and (*c*) the results for small Reynolds numbers were compared with the slow-motion solution at all mesh points. It appears from this and other work that the condenser results probably converged within 2 percent. A 40 × 20 mesh, which was used for most of the results reported, yielded large L/R results in the evaporator, which agrees with accepted similar solutions within several tenths of a percent. The comparison of the numerical results with the slow-motion solution (14) carried out to 30 terms in both n and λ_j showed agreement better than 0.2 percent at all points; except those lying in the plane separating the evaporator from the condenser where the 30-term slow-motion solution fails to satisfy the boundary condition by about 1.3 percent, and its deviations from the numerical solution are of the same order.

Results for Symmetrical Heat Pipes. A symmetrical heat pipe, in the context of this paper, is one in which the length of the evaporator is the same as the length of the condenser. Because the radial velocity at the wall of the pipe is assumed constant in each section, the stream function at the wall increases linearly from 0 to $L/2$ and then decreases linearly from $L/2$ to L. The calculations were performed in sequence, with the results of each problem serving as initial conditions for the next, in which only a small change of Reynolds number occurred. This procedure allowed the calculation of many cases at a small expense of computer time.

When the Reynolds number is small, and L/R equals 20, Fig. 2(*a*), the axial velocity component (for $r < R$, $0 < x < L$) is everywhere positive. The contours of pressure and the modified vorticity ω^* are nearly straight lines corresponding to a linear

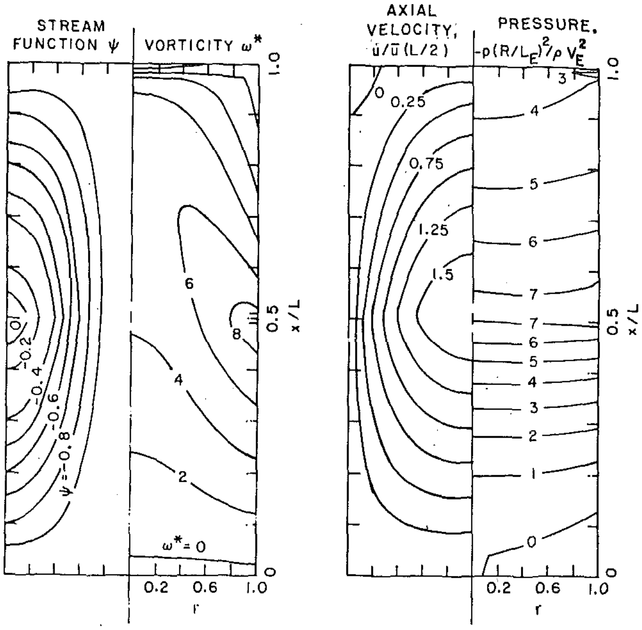

Fig. 2(*b*) Streamlines and contours of the modified vorticity ω^*, the nondimensional axial velocity component, and the nondimensional pressure $-p(R/L_E)^2/\rho V_E^2$ for a symmetrical heat pipe with $L/R = 20$, Re = 4. Note that the axial distance is foreshortened to conserve space.

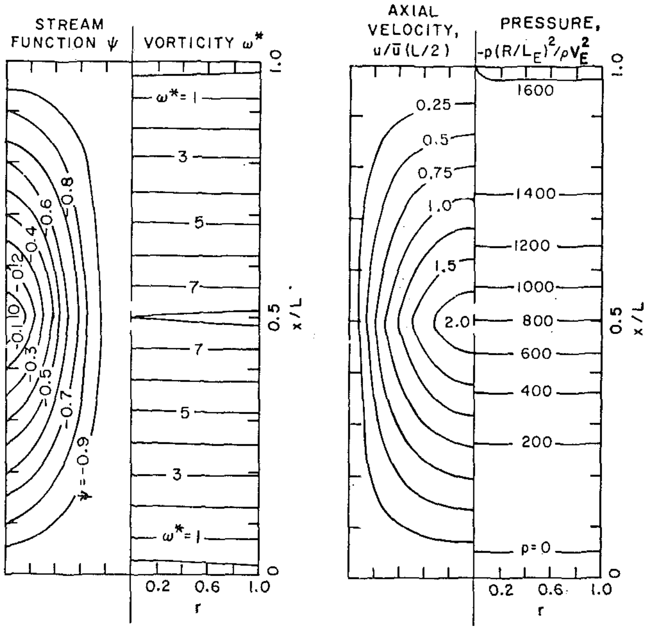

Fig. 2(*a*) Streamlines and contours of the modified vorticity ω^*, the nondimensional axial velocity component, and the nondimensional pressure $-p(R/L_E)^2/\rho V_E^2$ for a symmetrical heat pipe with $L/R = 20$, Re = 0.01. Note that the axial distance is foreshortened to conserve space.

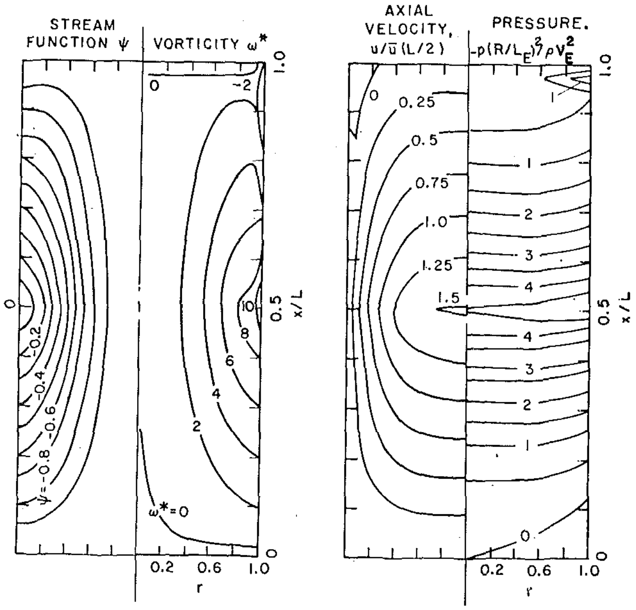

Fig. 2(*c*) Streamlines and contours of the modified vorticity ω^*, the nondimensional axial velocity component, and the nondimensional pressure $-p(R/L_E)^2/\rho V_E^2$ for a symmetrical heat pipe with $L/R = 20$, Re = 1000. Note that the axial distance is foreshortened to conserve space.

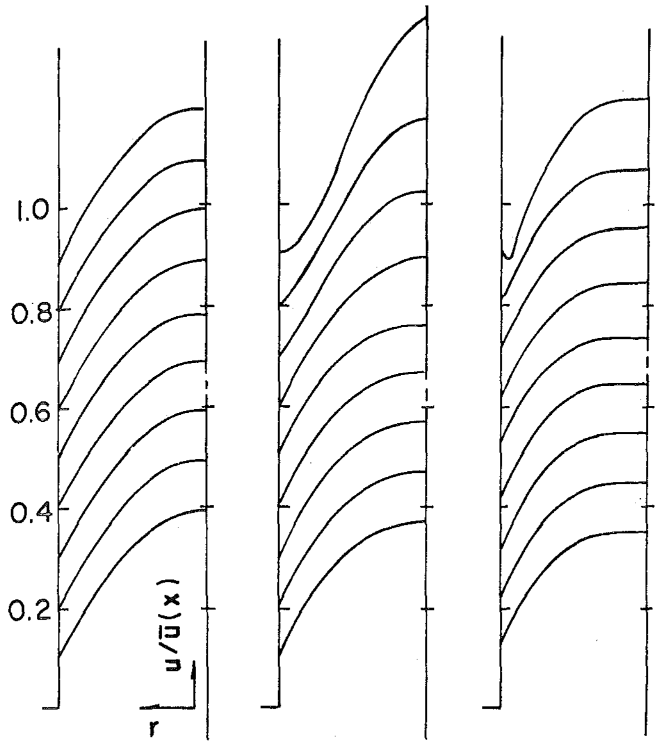

(a) Re = 0.01 (b) Re = 4 (c) Re = 1,000

Fig. 3 Development of the axial velocity profiles $u/\bar{u}(x)$ for $L/R = 20$ and (a) Re = 0.01, (b) Re = 4, and (c) Re = 1000

shear-stress distribution characteristic of a "fully developed" pipe flow.

As the Reynolds number increases, deviations from Poiseuille flow become evident first in the condenser. Reverse flow generally develops in the condenser at Reynolds numbers between two and four, which is consistent with the known disappearance of similar flows. No special attempt was made to narrow the range any further. In Fig. 2(*b*) the Reynolds number is four and reverse flow extends along the wall from $\omega^* = 0$ to the end of the condenser. The vorticity contours are no longer straight but are beginning to be swept downstream. Large vorticity gradients occur close to the end wall of the condenser.

At the highest Reynolds number, Fig. 2(*c*), there is still a small region of reverse flow. The contours of ω^* start to resemble the streamlines, showing that the effective viscosity due to numerical diffusion is not sufficient to prevent the calculations from approaching the expected asymptotic limit. It is apparent even in the distorted maps shown here that the pressure field is truly one-dimensional only in the limit of very small Reynolds numbers.

The development of the axial velocity profile is shown in Fig. 3 for the same conditions. The profiles are each normalized to the local average axial velocity, which varies linearly with x. For the smallest value of Re, the distribution is nearly parabolic over most of the pipe, as expected. For Re = 4, the profiles change very little in the evaporator, but change continuously in the condenser. At $x = 18$ the shear stress is very nearly zero, and at larger x there is flow reversal. In this respect the phenomenon is like the separation of a boundary layer flowing along a solid wall. Reversal persists even when the Reynolds number is increased to 1000, and the entering velocity profile is very nearly the inviscid limit $\cos \pi/2\,(r/R)^2$ of the similar solution for a semi-infinite evaporator. The high-Reynolds-number calculations were repeated with initial distributions of ψ and ω^* appropriate to a uniform axial profile to determine the effect of the initial guesses, but no significant changes in the results were noted. Data for additional values of L/R and other results are given in [20].

Nonsymmetrical Heat Pipes. Calculations were made for nonsymmetrical heat pipes with various lengths of evaporator, condenser, and adiabatic sections. For $L_C > L_E$ such that the condenser Re is in the transitional range from one to two, the frictional pressure losses along the condenser tend to be balanced by the dynamic pressure recovery, and the entire condenser operates at a nearly constant pressure.

Some features of the many possible asymmetrical configurations are disclosed when the characteristics of evaporators and condensers are considered separately. Such a study was conducted. The many interesting results included the extent of the nonreversed flow as a function of Re, L_C/R, and the shape of axial profile entering the condenser. Nonsymmetrical pipe results are given in [20].

Total Pressure Loss in Heat Pipes. Busse's interesting study [14] for uniform evaporation and condensation suggests that at small Re the overall pressure loss in the pipe is just that which would occur if Poiseuille flow prevailed throughout, regardless of the lengths of the evaporator and condenser.

$$\bar{p}(0) - \bar{p}(L) = \frac{8\mu V_E L_E}{R^3}\,[L_E + L_C] \qquad (15)$$

This result was derived by Cotter [18] and greatly simplified his overall analysis of the heat-pipe performance. In Fig. 4 we have plotted the pressure loss for the symmetrical-heat-pipe calculations. In spite of reverse flow, which begins at Reynolds numbers of the order of unity, Busse's result is a good approximation for Reynolds numbers up to 10 in such pipes.

Conclusions

The results of the investigation warrant the following conclusions:

1 For laminar flows in heat pipes of uniform cross section, the flow in the condenser will probably exhibit a region of reversal of the axial velocity when the condenser radial Reynolds number exceeds two. Condensers with entering velocity profiles flatter than those that develop in simple cylindrical evaporators can avoid reversal.

2 Accurate prediction of pressure loss will generally require solution of the complete two-dimensional equations if the radial Reynolds numbers in the condenser are greater than two or if the pipe is short.

3 The pressure loss in the evaporator is often the dominant one in nonsymmetrical pipes, and it can be calculated accurately from results in [20] for all but the shortest evaporators.

4 Estimates of the overall pressure loss may be made using Busse's analysis for Reynolds numbers less than about 10. More accurate estimates can be constructed by using separate results for evaporators and condensers [20].

Acknowledgments

We wish to thank Dr. T. P. Cotter for suggesting the problem and encouraging the completion of the investigation with many helpful discussions, and Mr. James B. Payne, Mrs. Carlotta McInteer, and Mrs. Carmen Shonk for assistance with the numerical work.

References

1 Cotter, T. P., "Status of the Engineering Theory of Heat Pipes," *Proceedings of Joint AEC/Sandia Heat Pipe Conference, Vol. 1*, SC-M-66-623, June 1, 1966, Sandia Corp., Albuquerque, N. M.

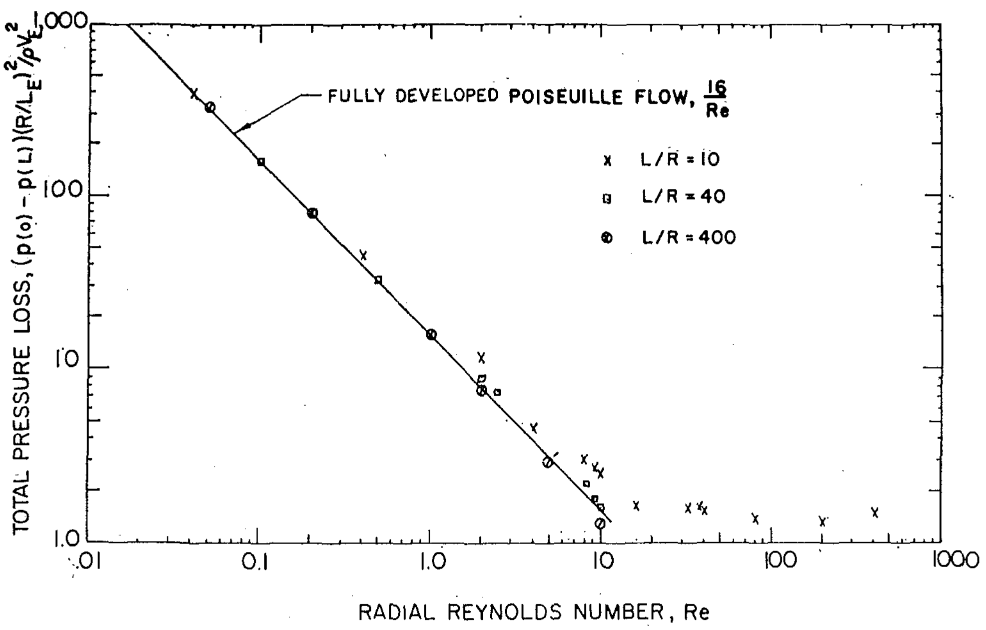

Fig. 4 Pressure loss for symmetrical heat pipes compared with that if the flow were Poiseuille

2 Knight, B. W., and McInteer, B. B., "Laminar Incompressible Flow in Channels With Porous Walls," LADC-5309, 1965, Los Alamos Scientific Laboratory, Los Alamos, N. M.

3 Yuan, S. W., and Finkelstein, A. B., "Laminar Flow With Injection and Suction Through a Porous Wall," *Proceedings of the Heat Transfer and Fluid Mechanics Institute*, Los Angeles, Calif., 1955.

4 Donaldson, C. D., and Sullivan, R. D., "Behavior of the Solutions of the Navier-Stokes Equations for a Complete Class of Three-Dimensional Viscous Vortices," *Proceedings of the Heat Transfer and Fluid Mechanics Institute*, Stanford University Press, 1960, pp. 16–30.

5 Terrill, R. M., and Thomas, P. W., "On Laminar Flow Through a Uniformly Porous Pipe," *Applied Science Research*, Vol. 21, Aug. 1969.

6 Cotter, T. P., private communication.

7 Wageman, W. E., and Guevara, F. A., "Fluid Flow Through a Porous Channel," *Physics of Fluids*, Vol. 3, 1960, p. 878.

8 Bankston, C. A., unreported experiments, 1967.

9 Bundy, R. D., and Weissberg, H. L., "Experimental Study of Fully Developed Laminar Flow in a Porous Pipe With Wall Injection," *Physics of Fluids*, Vol. 13, No. 10, Oct. 1970.

10 Weissberg, H. L., "Laminar Flow in the Entrance Region of a Porous Pipe," *Physics of Fluids*, Vol. 2, No. 5, Sept. 1959.

11 Hornbeck, R. W., Rauleau, W. T., and Osterle, F., "Laminar Entry Problem in Porous Tubes," *Physics of Fluids*, Vol. 6, No. 11, Nov. 1963.

12 Galowin, L. S., and Desantis, M. J., "Theoretical Analysis of Laminar Pipe Flow in a Porous Wall Cylinder," *Journal of Dynamic Systems, Measurement, and Control*, Trans. ASME, Series G, Vol. 93, No. 2, June 1971, pp. 102–108.

13 Galowin, L. S., and Barker, V. A., "Heat Pipe Channel Flow Distribution," ASME Paper No. 69-HT-22,

14 Busse, C. A., "Pressure Drop in the Vapor Phase of Long Heat Pipes," presented at Thermionic Conversion Specialists Conference, Palo Alto, Calif., 1968.

15 Levy, E. K., "Theoretical Investigation of Heat Pipes Operating at Low Vapor Pressures," *Proceedings ASME Aviation and Space Conference*, Beverly Hills, Calif., 1968, pp. 671–676.

16 Deverall, J. E., Kemme, J. E., and Florschuetz, L. N., "Sonic Limitations and Startup Problems of Heat Pipes," LA-4518, Nov. 1970, Los Alamos Scientific Laboratory, Los Alamos, N. M.

17 DeMichele, D. W., "A Numerical Solution to Axial Symmetric Compressible Flow with Mass Injection and Its Application to Heat Pipes," PhD dissertation, Department of Nuclear Engineering, University of Arizona, 1970.

18 Cotter, T. P., "Theory of Heat Pipes," LA-3246-MS, Mar. 1965, Los Alamos Scientific Laboratory, Los Alamos, N. M.

19. Gosman, A. D., Pun, W. M., Runchal, A. K., Spalding, D. B., and Wolfstein, M., *Heat and Mass Transfer in Recirculating Flows*, Academic Press, London and New York, 1969.

20. Bankston, C. A., and Smith, H. J., "Incompressible Laminar Vapor Flow in Cylindrical Heat Pipes," ASME Paper No. 71-WA/HT-15.

A. R. ROHANI
Research Assistant.

C. L. TIEN
Professor.
Mem. ASME

Department of Mechanical Engineering,
University of California,
Berkeley, Calif.

Steady Two-Dimensional Heat and Mass Transfer in the Vapor-Gas Region of a Gas-Loaded Heat Pipe

A numerical analysis is made of the steady two-dimensional heat and mass transfer in the vapor-gas region of a gas-loaded heat pipe. Consideration is given to a cylindrical heat pipe with typical evaporator, condenser, and noncondensible-gas sections and with negligible axial conduction through the wall and the liquid-wick matrix. The elliptical mass, momentum, energy, and species conservation equations have been solved in conjunction with the overall energy and mass conservation constraints and the thermodynamic equilibrium condition for three heat pipe cases with different working fluids and diameters. The results show that in certain gas-loaded heat pipes, such as liquid-metal heat pipes, vapor-gas diffusion and two-dimensionality must be considered in the analysis. Extension of the present numerical framework to more general cases such as including the axial wall conduction is indicated.

Introduction

A MODIFIED version of heat pipes in which the temperature is controlled by having certain amounts of a noncondensible gas inside has found many applications [1-4].[1] In a gas-loaded heat pipe, the gas volume and the condenser area are related to the overall heat transfer rate through the heat pipe. The gas volume varies either by changes in the system pressure [5] or by active or passive control systems [6]. A common assumption made in the consideration of a gas-loaded heat pipe is that the vapor and the gas inside the heat pipe do not mix and there exists a sharp vapor-gas interface between the condenser and the noncondensible gas sections of the heat pipe. The assumption, however, has been questioned recently by several investigators and considerable axial energy conduction and mass transfer between the two sections have been reported [7-9]. Edwards and Marcus [8] made a one-dimensional analysis of the combined energy and mass transfer processes in the vicinity of the vapor-gas front of gas-loaded heat pipes. They considered the case with a relatively small heat pipe diameter and vapor-gas mixtures of relatively low binary mass diffusivity, and found that the axial energy conduction through the heat pipe wall was the dominant factor in determining the temperature variations along the heat pipe.

It is to be demonstrated here that in some gas-loaded heat pipes the energy and mass diffusion between the vapor and the noncondensible gas could have an appreciable effect on heat transfer in the vapor-gas region and the temperature distribution along the gas-loaded heat pipe. In order to achieve a better understanding of the vapor-gas mixing phenomena, a numerical analysis has been made of the two-dimensional heat and mass transfer in the vapor-gas region of a simple cylindrical gas-loaded heat pipe. The solution is based on the elliptic mass, momentum, energy, and species conservation equations with proper boundary conditions. A two-dimensional numerical analysis of heat and mass transfer in the vapor-gas volume of gas-loaded heat pipes was attempted by McDonald [9]. His heat pipe configuration with evaporation and condensation taking place only at the pipe flat ends, however, is not as realistic as the configuration in the present study. A recent paper by Somogyi and Yen [10] presents an approximate two-dimensional analysis of the vapor-gas diffusion effects in cylindrical gas-loaded heat pipes by solving the momentum and species boundary-layer equations. In adopting the boundary-layer approach as well as neglecting the nonisothermal effects and the pressure-temperature thermodynamic relation, their physical model is considerably more restrictive than the present one, but their results concerning the vapor-gas diffusion effects on gas-controlled heat pipe performance are in qualitative agreement with the present findings.

In order to focus on the vapor-gas mixing phenomena in the present analysis, the effects of axial energy conduction through the heat pipe wall and the liquid-wick matrix are neglected, although they can be easily incorporated into the numerical framework (Appendix). The present results show that considerable

---

[1] Numbers in brackets designate References at end of paper.

Contributed by the Heat Transfer Division and presented at the Winter Annual Meeting, New York, N. Y., November 26-30, 1972, of THE AMERICAN SOCIETY OF MECHANICAL ENGINEERS. Manuscript received by the Heat Transfer Division August 14, 1972; revised manuscript received October 12, 1972. Paper No. 72-WA/HT-34.

mass composition and temperature variations in both the axial and radial directions are present in some of the cases considered. The numerical results are also compared with the cross-sectional-area averaged results and those obtained by neglecting heat and mass transfer between the vapor and the gas regions.

General Considerations

The physical model of a sharp vapor-gas front for gas-loaded heat pipes neglects the transfer of energy and mass between the vapor and the gas and the axial energy conduction through the heat pipe wall and the liquid-wick matrix. In this case the energy and mass balance relations can be written as

$$Q = \int_{L_e} PH_e(T_{ae} - T_0)dx = \int_{L_c} PH_c(T_0 - T_{ac})dx \quad (1)$$

$$n_g = \frac{p_g A L_g}{R^0 T_{ac}} \quad (2)$$

where the total length of the condenser section, L_{cg}, is

$$L_{cg} = L_c + L_g \quad (3)$$

Also, a thermodynamic relation exists between the operating temperature of the vapor and the total pressure inside the heat pipe,

$$p = p(T_0) \quad (4)$$

and the noncondensible gas pressure is

$$p_g = p(T_0) - p(T_{ac}) \quad (5)$$

These equations will be employed to obtain initial input values for the iterative numerical solution of the general case to be explained later.

The results of recent experimental studies [7, 11, 12], however, indicated that the axial energy conduction through the heat pipe wall and liquid-wick matrix, as well as the energy and mass transfer between the vapor and the gas inside the heat pipe should be taken into consideration when analyzing the performance of gas-loaded heat pipes. In order to have a better picture of the relative importance of various heat and mass transfer modes present, a simple order-of-magnitude comparison is made. Consider first the relative magnitude of the axial thermal energy transfer rate by the latent heat of the vapor that diffuses into the noncondensible gas region, to the energy transfer rate by axial conduction through the heat pipe wall and liquid-wick matrix

$$R_1 = \frac{A\rho D h_{fg}}{A_w k_w}\left(\frac{dm}{dT}\right) \quad (6)$$

where (dm/dT) can be obtained by averaging the medium slope of the thermodynamic equilibrium curve in the temperature range from T_0 to T_{ac} in each case [13, 14]. In the vapor-gas region, the relative magnitude of energy transfer due to diffusion to that of conduction is

$$R_2 = \frac{\rho D h_{fg}}{k}\left(\frac{dm}{dT}\right) \quad (7)$$

The foregoing two parameters have been calculated for six cases of gas-loaded heat pipe operation. The first three cases are the ones tested by Edwards and Marcus [8] while the other three characterize heat pipes with a typical stainless-steel wall but different working fluids and diameters. Table 1 demonstrates the preliminary information and values of the nondimensional parameters for the foregoing six cases. For all cases, average values of k and D were calculated from the basic thermodynamic relations [13]. It is shown that only the first three cases are wall-conduction-dominated. Hessel and Jankowski [12] reported the results of experiments with sodium-argon over a temperature range close to Case No. 5 in Table 1, but with a stainless steel heat pipe that had a diameter of 5 cm. In their case R_1 would be close to 5 which means a totally diffusion dominated gas-loaded heat pipe. In this and other cases where diffusion energy transport by the vapor and the gas is appreciable as compared to axial conduction through the wall and liquid-wick, a careful analysis of heat and mass transfer in the vapor-gas region is indeed necessary.

Analysis

The physical assumptions employed for the present analysis are as follows:

1 The vapor is at its equilibrium partial pressure corresponding to its temperature only at the vapor-liquid interface. Inside the vapor space, the vapor is either superheated or subcooled depending on its temperature and mass composition. Also, evaporation and condensation take place only at the vapor-liquid interface.

2 The steady vapor-gas flow is laminar and its pressure drop is negligible.

3 The vapor and the gas as well as their mixtures are ideal gases and have constant physical properties.

4 The evaporator and the condenser have constant ambient

Nomenclature

A = vapor-space cross-sectional area
d_0 = vapor-space diameter
D = vapor-gas binary mass diffusivity
D_0 = outside heat pipe diameter
h = enthalpy
h_{fg} = heat of vaporization
H = overall heat transfer coefficient
k = thermal conductivity
L = length of the heat pipe
m = vapor mass composition
n = number of moles
n_1 = distance between the nodes on the boundary and its adjacent node on the normal to the boundary
p = pressure
P = perimeter, πd_0
Pr = Prandtl number, $\mu\Gamma_h$
Q = overall heat transfer rate through the heat pipe
r = radial distance
r_0 = vapor space radius
R^0 = universal gas constant
R_1 = nondimensional parameter, equation (6)
R_2 = nondimensional parameter, equation (7)
Re = radial Reynolds number, $\rho r_0 v_0/\mu$
Sc = Schmidt number, $\mu\Gamma_m$
t_{wi} = wick thickness
T = temperature
T_0 = initial operating vapor temperature
u = axial velocity
v = radial velocity
v_0 = evaporation or condensation velocity
x = axial distance
Γ = exchange coefficient
μ = viscosity
ρ = vapor-gas mixture density
ψ = stream function
ω = vorticity

Subscripts

a = ambient
c = condenser
e = evaporator
g = noncondensible gas
h = enthalpy
m = mass
s = value on the boundary
v = vapor
w = values for the heat pipe wall and liquid-wick matrix

Table 1 Typical values of R_1 and R_2

Case	Vapor-gas mixture	T_0 K	p_0 atm	T_{ac} K	d_0 cm	D_0 cm	t_{wi} cm	A_w cm²	A cm²	R_1	R_2
1	Water-nitrogen	305	0.132	195	1.05	1.45	0.1	0.33	0.867	0.0112	2.76
2	Methanol-nitrogen	305	0.528	195	1.05	1.45	0.1	0.33	0.867	0.0207	0.64
3	Ammonia-nitrogen	305	20.00	195	1.05	1.45	0.1	0.33	0.867	0.0174	3.45
4	Water-air	450	9.530	350	1.72	2.02	0.1	0.30	2.320	0.1920	1.53
5	Sodium-argon	900	0.049	400	1.72	2.02	0.1	0.30	2.320	2.57	115.0
6	Water-air	450	9.530	350	5.16	5.46	0.1	0.84	20.90	0.6170	1.53

temperatures and constant overall heat transfer coefficients between the liquid-vapor interface and the ambient.

Governing Differential Equations. The governing differential equations consist of the mass, momentum, energy, and species conservation equations. For the numerical method of analysis employed in the present study, the mass and momentum conservation equations are expressed in terms of stream function and vorticity as [15]:

$$\frac{\partial}{\partial x}\left[\frac{1}{\rho r}\frac{\partial \psi}{\partial x}\right] + \frac{\partial}{\partial r}\left[\frac{1}{\rho r}\frac{\partial \psi}{\partial r}\right] + \omega = 0 \tag{8}$$

$$r^2\left[\frac{\partial}{\partial x}\left(\frac{\omega}{r}\frac{\partial \psi}{\partial r}\right) - \frac{\partial}{\partial r}\left(\frac{\omega}{r}\frac{\partial \psi}{\partial x}\right)\right] - \frac{\partial}{\partial x}\left[r^3\frac{\partial}{\partial x}\left(\mu\frac{\omega}{r}\right)\right] - \frac{\partial}{\partial r}\left[r^3\frac{\partial}{\partial r}\left(\mu\frac{\omega}{r}\right)\right] - r^2\frac{\partial}{\partial x}\left(\frac{u^2+v^2}{2}\right)\frac{\partial \rho}{\partial r} + r^2\frac{\partial}{\partial r}\left(\frac{u^2+v^2}{2}\right)\frac{\partial \rho}{\partial x} = 0 \tag{9}$$

where

$$\frac{\partial \psi}{\partial r} = \rho u r, \qquad \frac{\partial \psi}{\partial x} = -\rho v r, \qquad \omega = \frac{\partial v}{\partial x} - \frac{\partial u}{\partial r} \tag{10}$$

The energy and species conservation equations are:

$$\left[\frac{\partial}{\partial x}\left(h\frac{\partial \psi}{\partial r}\right) - \frac{\partial}{\partial r}\left(h\frac{\partial \psi}{\partial x}\right)\right] - \frac{\partial}{\partial x}\left[\Gamma_h r\frac{\partial h}{\partial x}\right] - \frac{\partial}{\partial r}\left[\Gamma_h r\frac{\partial h}{\partial r}\right] = 0 \tag{11}$$

$$\left[\frac{\partial}{\partial x}\left(m\frac{\partial \psi}{\partial r}\right) - \frac{\partial}{\partial r}\left(m\frac{\partial}{\partial x}\right)\right] - \frac{\partial}{\partial x}\left[\Gamma_m r\frac{\partial m}{\partial x}\right] - \frac{\partial}{\partial r}\left[\Gamma_m r\frac{\partial m}{\partial r}\right] = 0 \tag{12}$$

Boundary Conditions. For a gas-loaded heat pipe, in order to determine the stream function, vorticity, temperature, and mass composition boundary conditions, the pressure inside the heat pipe must be known beforehand. Initially, the pressure is determined by a simultaneous solution of equations (1)-(5). This value of pressure is corrected during the calculation process by a successive approximation procedure in such a way that the system always satisfies the laws of conservation of energy and mass. Once a value is designated to the total pressure inside the heat pipe, the conditions at the boundary of the vapor-gas volume are determined as follows:

The temperature at the vapor-liquid interface is determined by assuming a parabolic variation for temperature close to the interface. With a uniform grid, T_s is determined from the relation

$$T_s = 3T_1 - 3T_2 + T_3, \tag{13}$$

where T_1, T_2, and T_r are the temperature at nodes one, two, and three steps away from the wall. At the heat pipe flat ends and along the axis, the conditions are

$$\left.\frac{\partial T}{\partial x}\right|_{x=0,L} = 0, \qquad \left.\frac{\partial T}{\partial r}\right|_{r=0} = 0. \tag{14}$$

The vapor mass composition at the liquid-vapor interface is obtained from the equilibrium data for vapor-gas mixtures,

$$m = m(T_0, p) \tag{15}$$

and also

$$\left.\frac{\partial m}{\partial x}\right|_{x=0,L} = 0, \qquad \left.\frac{\partial m}{\partial r}\right|_{r=0} = 0. \tag{16}$$

The velocity components, u and v, at the boundary are determined from the following relations:

$$\begin{gathered} v(0, r) = v(L, r) = v(x, 0) = 0, \\ u(0, r) = u(L, r) = u(x, r_0) = 0, \quad \left.\frac{\partial u}{\partial r}\right|_{r=0} = 0 \end{gathered} \tag{17}$$

The radial component of velocity at the pipe wall is determined by writing the energy balance relation for an axial element of the vapor-liquid interface,

$$v_0 = \left\{H[T_0(x) - T_a] + k\left.\frac{\partial T}{\partial r}\right|_{r_0}\right\} \Big/ m\rho h_{fg} \tag{18}$$

The overall heat transfer coefficient H is usually a function of $T_0(x)$, T_a, and T_w but was taken as constant in the present analysis.

The stream function ψ on the boundary is determined from the integration of equation (10),

$$\psi(0, r) = \psi(L, r) = \psi(x, 0) = 0, \qquad \psi(x, r_0) = -\int_0^x \rho m v_0 r_0 dx \tag{19}$$

The vorticity boundary conditions at the vapor-liquid interface and on the heat pipe flat ends are calculated by a relation based on the assumption that the vorticity is uniform close to the boundary [15]:

$$\omega_s = -2\frac{(\psi_1 - \psi_s)}{r_s n_1 \rho} \tag{20}$$

A more complicated relation for calculation of ω_s, considering blowing and suction at the wall, has been proposed and used by several investigators [15, 16]. For the Reynolds number range of present analysis, the results of various relations for ω_s, when applied to a simple heat pipe, do not differ more than five percent in value. Also, a relation based on the assumption that the vorticity variation close to the axis is parabolic was used for determination of vorticity at the pipe center line.

Numerical Method of Solution. Basically, the finite difference, iterative method of solution based on the upwind method of differencing [15] is used in the present analysis. Considering the previously specified boundary conditions and their interdependency, a special solution procedure is employed as follows:

1 The vapor volume is divided into rows and columns in the radial and axial directions and row and column numbers are assigned to the nodes of the grid that is formed.

Table 2 Three cases of the gas-loaded heat pipe

Case	Re_e, Re_c	M Kg	L cm	L_c, L_g cm	Pr	Sc	H w/cm^2K
4	1	4.373×10^{-4}	60	20	0.825	0.60	4.66×10^{-3}
5	1	1.358×10^{-7}	60	20	0.800	0.15	4.45×10^{-3}
6	1	4.021×10^{-3}	60	20	0.825	0.60	1.55×10^{-3}

2 By solving equations (1), (2), (3), (4), and (5) the length of the condenser and the controlling gas sections, the initial pressure, the initial constant temperature of the vapor and the constant vapor mass composition in noncondensible gas region are determined. The initial gas temperature is assumed to be equal to the condenser ambient temperature and zero initial values of velocity components, stream function, and vorticity are assumed for all the nodes inside the grid.

3 The velocity and stream function boundary conditions are determined from equations (17), (18), and (19) and the sets of algebraic difference equations for the stream function, temperature, and mass composition are solved. This step is repeated 25 times.

4 The new temperature, mass composition, velocity, and stream function boundary conditions are determined and the sets of algebraic difference equations for the stream function, temperature, and mass composition are solved. This step is also repeated 25 times.

5 The vorticity boundary conditions are calculated from equation (20) and the set of algebraic difference equations for the vorticity are solved. Steps 4 and 5 are repeated 25 times as before.

6 After the iteration process is repeated 75 times, the four sets of algebraic difference equations are solved together and the new boundary conditions are calculated each time and the procedure is repeated until a converged solution is obtained. In this step, the pressure inside the system is adjusted after every 5 times of iteration in such a way that the overall energy and mass balance relations are satisfied. This is done by the vapor-gas equilibrium relation and the ideal gas law through equations (1) and (2). Also, the mass balance relation for the vapor is satisfied by adjusting the stream function boundary condition in such a way that the value of stream function, when calculated from equation (19), becomes equal to zero at the end of the noncondensible gas section.

Results and Discussion

The results of the two-dimensional analysis of heat and mass transfer in the vapor-gas region of the gas-loaded heat pipes are presented. The analysis is based on the assumption that axial conduction through the heat pipe wall and liquid-wick can be neglected as compared to the heat transfer due to the latent heat of the vapor diffusing into the noncondensible gas region. Therefore, it was applied only to the last three cases of Table 1, the diffusion dominated situations. Table 2 contains necessary information on the typical cases of gas-loaded heat pipes that were analyzed. A comparison of the Prandtl and Schmidt numbers demonstrates the relative importance of axial heat or mass transfer in the vapor phase in each case. Figs. 1 and 2 demonstrate the axial variations of temperature and vapor mass composition for the three cases along the heat pipe. The radial variations of temperature and vapor mass composition at various locations along the heat pipe are presented in Figs. 3, 4, 5, 6, 7, and 8. Finally, in Figs. 9 and 10, the axial variation of temperature and vapor mass composition at the vapor-liquid interface,

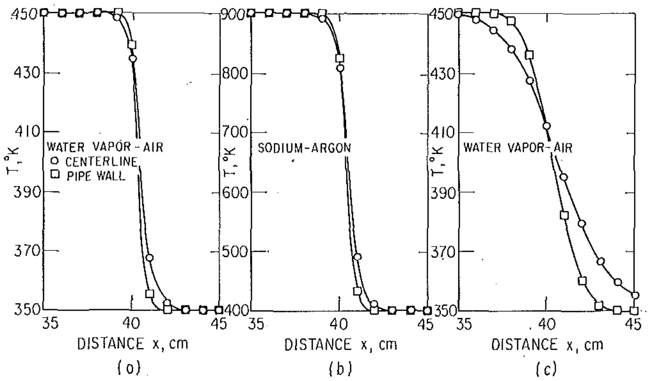

Fig. 1 Axial temperature variation (a, Case 4; b, Case 5; c, Case 6)

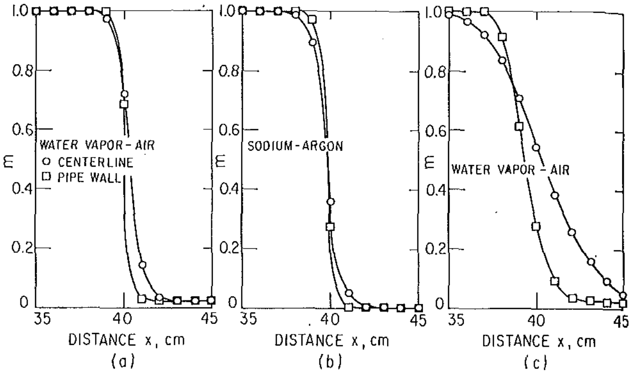

Fig. 2 Axial mass composition variation (a, Case 4; b, Case 5; c, Case 6)

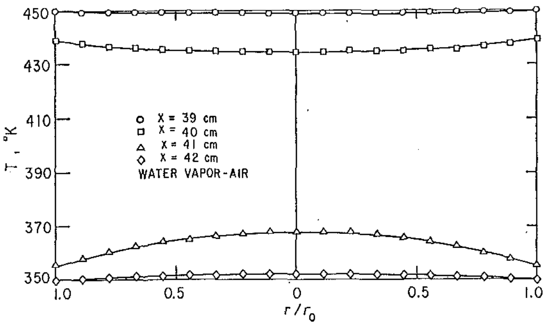

Fig. 3 Radial variation of temperature, Case 4

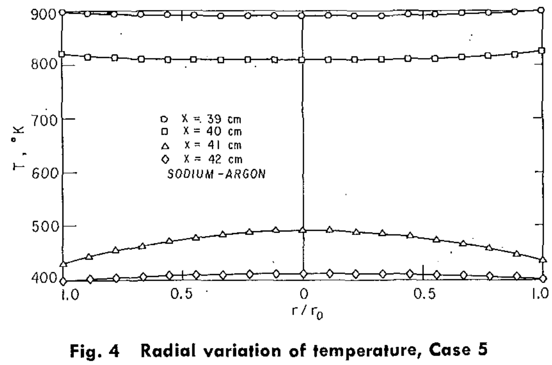

Fig. 4 Radial variation of temperature, Case 5

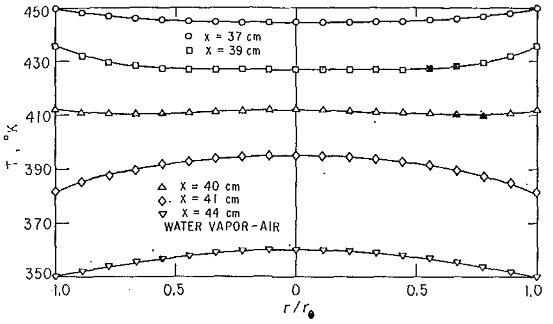

Fig. 5 Radial variation of temperature, Case 6

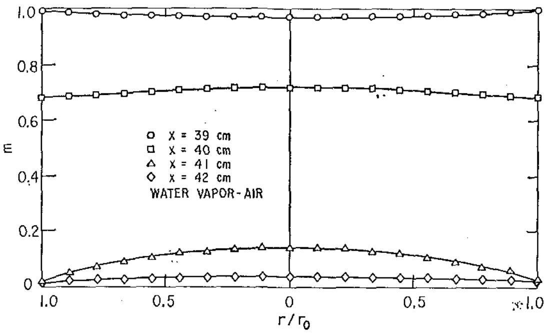

Fig. 6 Radial variation of vapor mass composition, Case 4

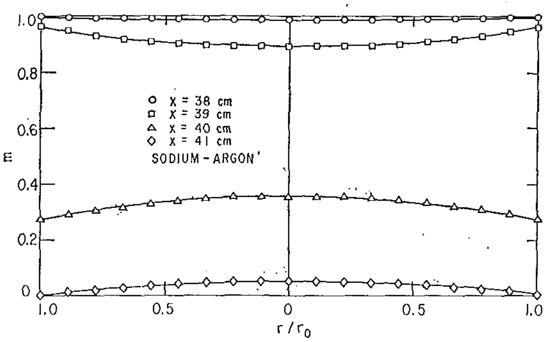

Fig. 7 Radial variation of vapor mass composition, Case 5

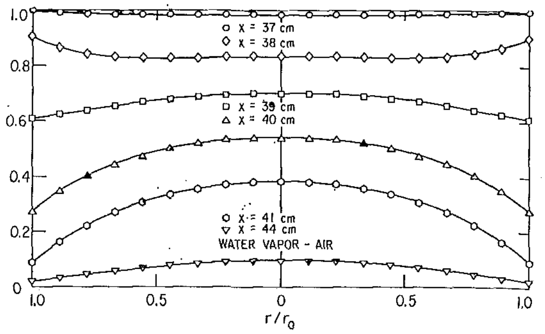

Fig. 8 Radial variation of vapor mass composition, Case 6

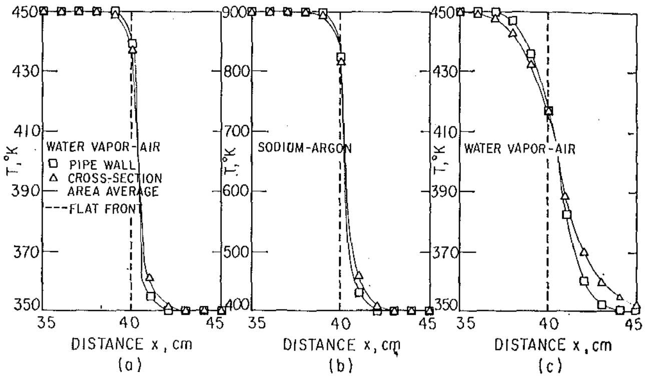

Fig. 9 Comparison of the two-dimensional, cross-sectional-area averaged and flat front results

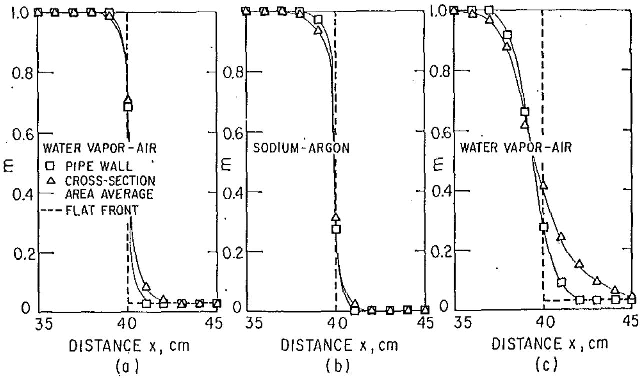

Fig. 10 Comparison of the two-dimensional, cross-sectional-area averaged and flat front results

as obtained from the two-dimensional analysis for the three cases, are compared with the cross-sectional-area averaged results and those from the flat front theory. The flow results are quite similar to those for a simple heat pipe [16] and are omitted here.

In a gas-loaded heat pipe, the vapor velocity components are very much close to zero in the vicinity of the vapor-gas front and transport of energy and mass in that region is essentially by thermal conduction and mass diffusion. The present results confirm the simple dimensional comparison as characterized by R_1 and R_2. In Case 4, Figs. 1(*a*) and 2(*a*), the conductivity and the diffusivity of vapor-gas mixture are relatively low ($R_1 = 0.192$ and $R_2 = 1.530$). Therefore, very little energy and mass transfer take place between the vapor and the gas and there results a sharp vapor-gas front. It is expected from the sharp front that the axial mass composition distribution can be well approximated by the one-dimensional result (Figs. 2(*a*) and 10). It should be mentioned here that in Case 4 the axial energy conduction through the heat pipe wall, if included, would have been the dominant mode of energy transfer across the vapor-gas region.

The vapor-gas mixture mass diffusivity is relatively high in Case 5 (i.e., diffusion dominated case, $R_1 = 2.57$). Thus as it is seen from Fig. 2, the axial mass composition profiles are flatter for sodium-argon heat pipe than for water-air heat pipe in Case 4. Despite the sharp axial temperature profiles between the condenser and the noncondensible gas regions ($R_2 = 115$), Figs. 2(*b*), 7, and 10 show that the axial mass composition distribution can not be approximated with the cross-sectional-area averaged results which may be considered as the results of a one-dimensional analysis.

In Case 6, both the vapor mass diffusion and the energy conduction through the vapor-gas mixture are effective in determination of the temperature and mass composition distribution in the gas-loaded heat pipe ($R_1 = 0.62$ and $R_2 = 1.53$). The two-dimensional nature of the problem is evident in Figs. 1(*c*), 2(*c*), 5, and 8, and the result in Figs. 9 and 10 represents only the average axial temperature and mass composition distribution as compared to the two-dimensional result.

In general the results of the present study demonstrate that energy and mass transfer between the vapor and the gas in a gas-loaded heat pipe, in a variety of cases, such as liquid metal gas-loaded heat pipes, may play a dominant role in determining the system performance. Furthermore, in many cases, the one-dimensional analysis of the energy and mass transfer is not sufficient for a critical study of the operational characteristics of gas-loaded heat pipes. The present study also demonstrates properly the effects and importance of various physical parameters on the performance of gas-loaded heat pipes.

References

1 Bienert, W., "Heat Pipes for Temperature Control," *Proceedings of the Fourth Intersociety Energy Conversion Engineering*, Washington, D. C., Sept. 1969.

2 Turner, R. C., "The Constant Temperature Heat Pipe—A Unique Device for the Thermal Control of Spacecraft Components," AIAA Paper No. 69-632, 1969.

3 Eldstein, F., and Hemback, R. J., "The Design, Fabrication and Testing of a Variable Conductance Heat Pipe for Equipment Thermal Control," AIAA Paper No. 71-422, 1971.

4 Schlosinger, A. P., "Heat Pipes for Space Suit Temperature Control," *Proceedings of the ASME Aviation and Space Conference*, Beverly Hills, Calif., 1968.

5 Hinderman, J. D., and Waters, E. D., "Design and Performance of Non-Condensible Gas-Controlled Heat Pipes," AIAA Paper No. 71-420, 1971.

6 Bienert, W., Brennan, P. J., and Kirkpatrick, J. P., "Feedback Controlled Variable Conductance Heat Pipes," AIAA Paper No. 71-421, 1971.

7 Marcus, B. D., and Fleischman, G. L., "Steady-State and Transient Performance of Hot Reservoir Gas-Controlled Heat Pipes," ASME Paper No. 70-HT/SpT-11, 1970.

8 Edwards, D. K., and Marcus, B. D., "Heat and Mass Transfer in the Vicinity of the Vapor-Gas Front in a Gas-Loaded Heat Pipe," JOURNAL OF HEAT TRANSFER, TRANS. ASME, Series C, Vol. 94, No. 2, May 1972, pp. 155–162.

9 McDonald, J. W., "Numerical Techniques for Analyzing Elliptic Flows With Application to Inlets and Mass Transfer in Gas-Controlled Heat Pipes," PhD thesis, University of California, Los Angeles, Calif., 1971.

10 Somogyi, D., and Yen, H. H., "An Approximate Analysis of the Diffusing Flow in a Self-Controlled Heat Pipe," ASME Paper No. 72-HT-M, 1972.

11 Vidal, C. R., and Cooper, J., "Heat Pipe Oven: A New, Well Defined Metal Vapor Device for Spectroscopic Measurements," *J. Appl. Physics*, Vol. 40, July 1969, pp. 3370–3374.

12 Hessel, M. M., and Jankowski, P., "Two-Metal Heat Pipe Oven: Operation, Dynamics and Use in Spectroscopic Measurements," *J. Appl. Physics, Vol. 43, Jan. 1972, pp. 209–211.*

13 Bird, R. B., Stewart, W. E., and Lightfoot, E. N., *Transport Phenomena*, John Wiley, New York, 1960, pp. 255 and 511.

14 Golden, G. H. and Tokar, J. V., "Thermophysical Properties of Sodium," Argonne National Laboratory Report No. ANL-7323, Argonne, Ill., Aug. 1967.

15 Gosman, A. D., Pun, W. M., Runchal, A. K., Spalding, D. B., and Wolfstein, M., *Heat and Mass Transfer in Recirculating Flows*, Academic Press, New York, 1969.

16 Bankston, C. A., and Smith, H. J., "Incompressible Laminar Flow of Vapor in Cylindrical Heat Pipes," ASME Paper No. 71-WA/HT-15, 1971.

APPENDIX

In this Appendix a method is described to incorporate energy conduction along the heat pipe wall and the liquid-wick matrix into the numerical framework for two-dimensional analysis of heat and mass transfer in the vapor-gas region of cylindrical gas-loaded heat pipes.

The steady-state energy conservation equation is

$$\frac{\partial}{\partial x}\left(k_w \frac{\partial T_w}{\partial x}\right) + \frac{1}{r}\frac{\partial}{\partial r}\left(k_w r \frac{\partial T_w}{\partial r}\right) = 0 \qquad \text{(A-1)}$$

where k_w is the local conductivity of the heat pipe wall or liquid-wick matrix and T_w is the wall or liquid-wick matrix temperature. The boundary conditions for this equation are

$$\text{at } x = 0 \text{ and } L, \qquad \frac{\partial T_w(r)}{\partial x} = 0 \qquad \text{(A-2)}$$

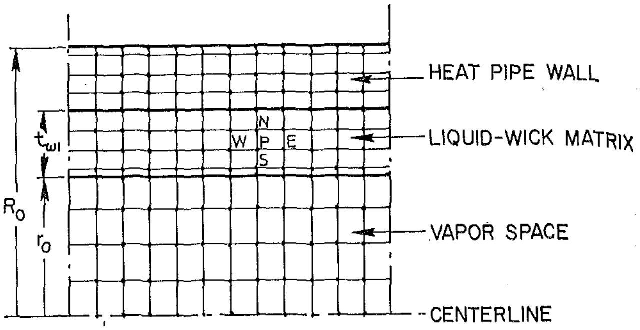

Fig. 11 Axial heat pipe element with grid

$$\text{at } r = r_0, \qquad T_{0w}(x) = T_0(x) \qquad \text{(A-3)}$$

and

$$\text{at } r = R_0, \qquad H(T_a - T_{aw}) = k_w \left.\frac{\partial T_w}{\partial r}\right|_{r=R_0} \qquad \text{(A-4)}$$

where H is the overall heat transfer coefficient between the outside heat pipe wall and the ambient.

By dividing the heat pipe wall and liquid-wick matrix into rows and columns and forming a grid as demonstrated in Fig. 11, temperature distribution in that region can be obtained from a solution of the set of algebraic difference equations written for all the nodes of the grid

$$T_P = A_N T_N + A_S T_S + A_E T_E + A_W T_W + A_P \qquad \text{(A-5)}$$

in which A's for each node P are found from equations (A-1), (A-2), (A-3), or (A-4). The same iterative method of solution can be employed for solving this set of equations along with other sets of equations. For this purpose steps 2 and 3 in the Numerical Method of Solution section should be replaced by the following:

2 By solving equations (1)–(5), L_c, L_g, p_0, P_g, and T_0 are determined. The initial gas temperature is assumed to be equal to the condenser ambient temperature and zero initial values of velocity components, stream function, and vorticity are assumed for all the nodes of the vapor volume grid. The temperatures at the nodes of the wall and liquid-wick matrix grid are assumed equal to the vapor or the gas temperatures depending on their axial position.

3 The set of difference equations for the wall and liquid-wick matrix, equations (A-5), are solved first. The velocity and stream function boundary conditions for the vapor volume are then calculated from equation (17), the following equation

$$v_0 = \frac{-k_w \left.\dfrac{\partial T_w}{\partial r}\right|_{r_0} + k \left.\dfrac{\partial T}{\partial r}\right|_{r=r_0}}{m p h_{fg}} \qquad \text{(A-6)}$$

and equation (19). Next, the sets of difference equations for the stream function, energy and mass in the vapor volume are solved. This step is repeated 25 times.

By following this method, the effects of energy conduction in the heat pipe wall and liquid-wick matrix on heat and mass transfer in gas-loaded heat pipes can be determined in a two-dimensional manner. At the same time, the axial temperature variations in the wall and liquid-wick matrix at the evaporator-condenser or evaporator-adiabatic and adiabatic-condenser sections of both simple and gas-loaded heat pipes can be determined as a result of the analysis. A subroutine must be added to the original program in order to calculate the coefficient A of equations (A-5). Also, in dividing the heat pipe wall and liquid-wick matrix into rows and columns, a nonuniform grid with smaller radial distances in the first and last rows as demonstrated in Fig. 11 would increase the accuracy of the results.

On the Minimum Size of Large Dry Cooling Towers With Combined Mechanical and Natural Draft

F. K. MOORE
Professor,
Department of Mechanical Engineering,
Cornell University,
Ithaca, N. Y.

The gasdynamic performance equation for large-scale dry cooling towers is derived relating size, shape, fan power, and drag and heat-transfer performance of heat exchangers. Induced-, forced-, or natural-draft towers are special cases. The general result consists of a zero-order scaling formula involving a size function having a minimum for a particular combination of temperatures, together with a set of correction terms of first order in temperature rise. Thus systems that are nearly equivalent gasdynamically can be compared. Technical requirements for small tower size or fan power are expressed in terms of heat-exchanger parameters.

Introduction

By the year 2000, it is expected [1][1] that electric power generation will have increased by a factor of more than four within the U. S. alone. By then it will be clear, if it is not so already, that our inland water resources (except the Great Lakes) are inadequate to provide once-through condenser cooling at acceptable levels of thermal pollution and that cooling towers will be used extensively. However, it is by no means clear what the future cooling arrangements will be like.

In the present paper we shall assume that evaporative cooling will not be acceptable in the future, in view of the condensing plumes to be expected in cold weather and in view of the substantial water consumption, amounting to about 30 cfs for a 1000-MW power plant. Rather, some form of dry heat exchange will, we assume, come to dominate the field. Heeren and Holly [2] discuss the present state of large-scale dry cooling methods; Smith and Larinoff [3] discuss in optimistic terms the prospects for dry mechanical-draft cooling; and Christopher and Forster [4] have described the dry natural-draft tower now in service at Rugeley, England, designed to dissipate the $575 \cdot 10^6$ Btu/hr rejected from a 120-MW power plant of quite high efficiency.

Dry cooling towers are considered much more expensive than wet [5], because of the size or fan power required, the cost of heat exchangers, and the poorer cooling potential that characterizes any dry system working toward dry-bulb rather than wet-bulb temperature. However, the technical limitations of these devices are not well understood. In this paper, a theoretical performance equation is developed for a dry tower with combined mechanical and natural draft, expressed, finally, in terms of customary heat-exchanger parameters, tower dimensions, and fan power.

The purpose of this theoretical development is to provide a technical basis for minimizing tower size, power, or cost. One may assume that large tower size is per se objectionable, aesthetically and economically, and we need to know the relevant limits of technical feasibility. Fan power, in mechanical systems, plays the same role as height in the natural ones, and one would wish to minimize fan power because of noise as well as cost.

The study of minimization will not be completed in this paper; subsequent papers will give an application of the present theory to a practical case, extend the theory to questions of heat-exchanger size, and show the derived limits of feasibility under various constraints. Economic analysis, which, taking external costs into account, must finally govern cooling-system design, is beyond the scope of this present study.

In the analysis to follow, tedious but straightforward mathematical details will be omitted; they can be found in [6, 7].

The Gasdynamic Performance Equation

Basic Assumptions and Equations. Fig. 1 is a sketch of the simple flow system we assume, to which we shall apply the laws of inviscid gasdynamics, assuming one-dimensional flow in a vertical duct. That is, we will consider the tower slender enough that gradients of flow quantities transverse to the flow direction are unimportant. At arbitrary locations within this duct we place heat-exchange systems and fan systems (any devices that add momentum to the flow). The geometrical proportions

---

[1] Numbers in brackets designate References at end of paper.

Contributed by the Heat Transfer Division for publication (without presentation) in the JOURNAL OF HEAT TRANSFER. Manuscript received by the Heat Transfer Division October 23, 1972. Paper No. 73-HT-8.

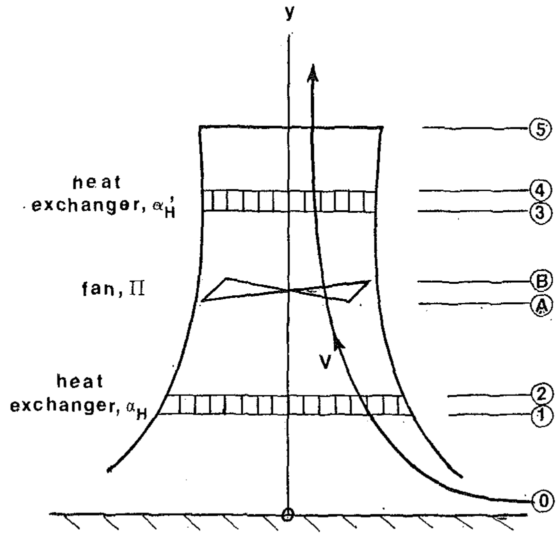

Fig. 1 Sketch of tower geometry

shown are purely schematic; only the sequence of events is made specific. Ambient, stagnant sir (subscript 0) is drawn from the ground-level stratum of the atmosphere. After entering the tower, the air is assumed to accelerate smoothly and isentropically to the first heat-exchanger zone beginning at ①. Any tower entrance losses can usually be assigned to the heat exchanger itself.

The air leaves the heat exchanger at ② after having acquired heat at a rate Q and suffered a momentum loss prescribed by C_D, a drag coefficient. These changes are considered to occur abruptly, across zones negligibly thin in comparison to tower height. The heated air then proceeds isentropically to the fan at location Ⓐ where mechanical power Π is imparted to the flow. The fan zone from Ⓐ to Ⓑ is also considered to be thin—an actuator sheet. The flow proceeds through a second heat exchanger (for which the parameters will be denoted by primes) between ③ and ④. This particular sequence of tower elements is the simplest that can include the special cases of natural draft (one heat exchanger only) and forced- or induced-draft (omitting the first or second heat exchanger, respectively).

The air finally proceeds isentropically to the tower exit at ⑤, where its pressure is matched to that of the ambient atmosphere at the level of ⑤. That is, the entire dynamic head at the top of the tower is assumed to be lost in the mixing processes of the plume above ⑤. Otherwise, total pressure losses are assumed limited to the heat-exchanger zones. Wall friction in the tower is explicitly neglected. These seem reasonable assumptions for such a large, relatively short duct.

This duct flow will be analyzed in terms of small perturbations of state quantities and small Mach number. Leading terms will constitute a simple scaling law, and terms of the next higher order will be retained as corrections. The leading and correction terms together will constitute the desired performance equation.

Except in crossing the three actuator sheets, the air flow proceeds isentropically, subject to the state and Euler equations

$$p \propto \rho^\gamma \qquad p = \rho RT \qquad \frac{dp}{\rho} + VdV + gdy = 0 \tag{1}$$

which may be integrated to yield

$$\frac{\gamma p}{\rho} = (\text{constant}) - \frac{\gamma - 1}{2} V^2 - (\gamma - 1)gy \tag{2}$$

Of course, at each station of Fig. 1, the mass flow

$$\dot m = \rho VA \tag{3}$$

is the same. The area at each station is denoted by A.

Focusing attention on the first heat exchanger, energy in the form of heat (Q) is added to the flow there;

$$T_2 + \frac{1}{2C_p} V_2^2 - T_1 - \frac{1}{2C_p} V_1^2 = \frac{Q}{\dot m C_p} \tag{4}$$

and momentum is extracted by drag, expressed in terms of C_D:

$$p_2 + \frac{\dot m}{A_1} V_2 - p_1 - \frac{\dot m}{A_1} = -\frac{1}{2} \rho_1 V_1^2 C_D \tag{5}$$

We next introduce the following definitions:

$$\alpha_H \equiv \frac{T_2}{T_1} - 1 \qquad \beta_H = 1 - \frac{p_2}{p_1} \qquad M^2 \equiv \frac{V^2}{(\gamma - 1)C_p T} \tag{6}$$

In writing the Mach number M, we recall that for a perfect gas sound speed a is given by

$$a^2 = \gamma RT = \gamma p/\rho = (\gamma - 1)C_p T \tag{7}$$

We then may write the energy and momentum equations (4) and (5) in the forms

$$\alpha_H + \frac{\gamma - 1}{2} [(1 + \alpha_H)M_2^2 - M_1^2] = \frac{Q}{\dot m C_p T_1} \tag{8}$$

Nomenclature

A = area
A_a, A_c = heat-exchange surface and free-flow areas of heat exchanger
a = sound speed, equation (7)
C_D = drag coefficient of heat exchanger, equation (5)
C_p = specific heat of air at constant pressure
E = heat-transfer-resistance coefficient, equation (31)
F = counterflow equivalence, equation (28)
g = acceleration due to gravity
I = initial temperature difference, Fig. 2
K = ratio of friction factor to Stanton number, equation (38)
l = characteristic length, equation (24)
M = Mach number
$\dot m$ = mass flow rate
P = dimensionless approach, Fig. 2
p = pressure
Q = rate of heat exchange
T = temperature
V = flow velocity averaged across duct
Y = generalized height, equation (27)
y = height above tower base
α = dimensionless temperature rise, with subscripts defined in equations (6), (13), and (22)
β = dimensionless pressure rise, with subscripts defined in equations (6) and (13)
γ = ratio of specific heats
δ = dimensionless height, equation (17)
ϵ = small quantity, equation (17)
η = isentropic efficiency of fan
κ = polytropic coefficient for atmosphere
Π = fan mechanical power
π = dimensionless fan power, equation (13)
ρ = density
σ = dimensionless fan thrust, equation (13)
ψ = size function, equation (39)

Subscripts A, B, and 0 through 5 denote positions in the tower according to Fig. 1
Prime denotes upper heat exchanger
Carat denotes division by l
Asterisk denotes the minimum of ψ, Fig. 3

$$\beta_H - \gamma M_1{}^2 \frac{\alpha_H + \beta_H}{1 - \beta_H} = \frac{\gamma}{2} M_1{}^2 C_D \qquad (9)$$

Corresponding expressions apply at the second heat exchanger.

Applying equation (2) between the first heat exchanger and the fan, and introducing equations (1) and (7), yields

$$\left(\frac{p_A}{p_2}\right)^{\frac{\gamma-1}{\gamma}} = \left[1 + \frac{\gamma - 1}{2} M_2{}^2 - (\gamma - 1)\frac{g}{a_2{}^2}(y_A - y_2)\right] \times \left[1 + \frac{\gamma - 1}{2} M_A{}^2\right]^{-1} \qquad (10)$$

From equation (10), the corresponding relations for the other isentropic steps (0–1, B–3, 4–5) can be inferred.

Moving to the fan location, the energy and momentum equations are

$$T_B + \frac{1}{2C_p} V_B{}^2 - T_A - \frac{1}{2C_p} V_A{}^2 = \frac{\Pi}{\dot{m} C_p} \qquad (11)$$

$$p_B + \frac{\dot{m}}{A_A} V_B - p_A - \frac{\dot{m}}{A_A} V_A = \frac{\Sigma}{A_A} \qquad (12)$$

where Π represents the total rate of energy delivery to the air at the fan location, in other words, the power delivered to the fan blades, part of which does useful mechanical work and part of which may be dissipated as heat. The useful work is that done by the thrust force Σ exerted by the fan on the air.

We introduce definitions corresponding to equation (6):

$$\alpha_F = \frac{T_B}{T_A} - 1 \qquad \beta_F \equiv 1 - \frac{p_B}{p_A}$$

$$\pi \equiv \frac{\Pi}{\dot{m} C_p T_A} \qquad \sigma \equiv \frac{\Sigma}{A_A p_A} \qquad (13)$$

which yield, corresponding to equations (8) and (9),

$$\alpha_F + \frac{\gamma - 1}{2}\left[(1 + \alpha_F) M_B{}^2 - M_A{}^2\right] = \pi \qquad (14)$$

$$\beta_F - \gamma M_A{}^2 \frac{\alpha_F + \beta_F}{1 - \beta_F} = -\sigma \qquad (15)$$

in place of equations (11) and (12).

Finally, we assume a quiescent, polytropic atmosphere outside the tower, with the exponent κ replacing γ and $V = 0$ in equation (1). The pressure difference between top and bottom is given by an equation analogous to equation (10):

$$\left(\frac{p_5}{p_0}\right)^{\frac{\kappa-1}{\kappa}} = 1 - \frac{\gamma}{\kappa}(\kappa - 1)\frac{g}{a_0{}^2} y_5 \qquad (16)$$

The final draft equation will be obtained by suitably matching this outside pressure change to the inside one derived from equations (9), (10), and (15), an equation corresponding to equation (9) for the second heat exchanger, and equations comparable to equation (10) for the three remaining isentropic steps. To complete this development, the Mach numbers at the various stations must be related, and further information about performance parameters must be included. Allowing κ to differ from γ permits the atmosphere to be nonadiabatic over the vertical distance of tower height and might also allow the effects of wind to be represented conveniently.

The Perturbation Scheme. We will assume that all changes occurring in the tower are small compared with the corresponding original quantities and that Mach numbers are all small. For convenience, we will write

$$\epsilon \equiv \frac{\gamma - 1}{2} M^2 \qquad \delta \equiv (\gamma - 1) g y / a_0{}^2 \qquad (17)$$

with subscripts being added to denote particular locations. In effect, we will develop a draft equation as a power series in ϵ_1, which is a measure of the tower mass flow:

$$\epsilon_1 = \frac{\gamma - 1}{2} \dot{m}^2 / (\rho_1 a_1 A_1)^2 \qquad (18)$$

We next must assign comparative orders of magnitude to all the small quantities we have introduced. It is simplest to state at this point the relationships that will later prove to be self-consistent, namely,

$$\left.\begin{array}{l} \alpha_H, \qquad \text{all } \delta_m = \mathrm{o}(\epsilon_1)^{1/2} \\ \text{all } \epsilon_m, \beta_H, \pi, \sigma, \alpha_F, \beta_F = \mathrm{o}(\epsilon_1) \end{array}\right\} \qquad (19)$$

We will derive our draft equation only to order $\epsilon_1{}^{3/2}$. Further development would be feasible, but not practically important.

Using equation (1) when appropriate and equations (3), (6), and (13), the various Mach numbers and pressure ratios can be related to the desired order of accuracy. For example, equation (10) becomes

$$\frac{\epsilon_2}{\epsilon_A} = \left(\frac{p_A}{p_2}\right)^{\frac{\gamma+1}{\gamma}} \frac{A_1{}^2}{A_A{}^2} = \left(1 + \frac{\gamma + 1}{\gamma - 1}\delta_{A_1}\right)\frac{A_1{}^2}{A_A{}^2} + \mathrm{o}(\epsilon_1{}^2) \qquad (20)$$

Next, α_F, β_F, and σ should be expressed in terms of π. In [7], it is shown that

$$\left.\begin{array}{l} \alpha_F = \pi + \mathrm{o}(\epsilon_1{}^2) \\ \beta_F = -\dfrac{\gamma}{\gamma - 1}\eta\pi + \mathrm{o}(\epsilon_1{}^2) \\ \sigma = \dfrac{\gamma}{\gamma - 1}\eta\pi + \mathrm{o}(\epsilon_1{}^2) \end{array}\right\} \qquad (21)$$

where η is the isentropic efficiency of the fan, comparing ideal to actual power needed to accomplish given changes of static and total pressure.

The Draft Equation. Now we may chain-multiply the various pressure ratios to carry out the matching of the external pressure drop, equation (16), with the internal one. We omit the tiresome algebraic details of this process; they appear in [7] for a slightly more general case, which includes a second fan between ④ and ⑤.

In carrying out the expansion it becomes clear [7] that convergence is improved by redefining α_H, equation (6), to avoid having to expand the quantity $(1 + \alpha_H)^{-1}$. For each heat exchanger, we define

$$\alpha_E \equiv 1 - T_1/T_2 \qquad \text{or } (1 + \alpha_H)^{-1} = 1 - \alpha_E \qquad (22)$$

The final result, which confirms the ordering of equation (19), is written with the leading terms on the left and corrections of order $\epsilon_1{}^{1/2}$ on the right:

$$\begin{aligned} C_D + \frac{A_1{}^2}{A_3{}^2} C_D{}' + \frac{A_1{}^2}{A_5{}^2} - \left(\frac{\alpha_E \delta_{51}}{\epsilon_1} + \frac{\alpha_E{}' \delta_{53}}{\epsilon_1} + \frac{\eta\pi}{\epsilon_1}\right) \\ + \frac{\gamma - \kappa}{2\kappa(\gamma - 1)} \frac{\delta_{50}{}^2}{\epsilon_1} = \delta_{50}\left(C_D + \frac{A_1{}^2}{A_3{}^2} C_D{}'\right) \\ - \alpha_E\left(\frac{A_1{}^2}{A_5{}^2} + 1\right) - \alpha_E{}'\left(\frac{A_1{}^2}{A_5{}^2} + \frac{A_1{}^2}{A_3{}^2}\right) \\ + \frac{A_1{}^2}{A_5{}^2}\left(\delta_{50} - \frac{\gamma + 1}{\gamma - 1}\delta_{51}\right) - \frac{A_1{}^2}{A_3{}^2} C_D{}' \frac{\gamma + 1}{\gamma - 1}\delta_{31} \\ + \frac{\pi}{\epsilon_1}(\delta_{5A} - \eta\delta_{50}) + \frac{(\gamma - \kappa)[2\gamma - (\gamma + 1)\kappa]}{6\kappa^2(\gamma - 1)^2} \frac{\delta_{50}{}^3}{\epsilon_1} \\ - \alpha_E\left(\frac{\alpha_E{}'}{\epsilon_1} + \frac{A_1{}^2}{A_3{}^2} C_D{}'\right) + \mathrm{o}(\epsilon_1) \qquad (23) \end{aligned}$$

For convenience, we use double subscripts to denote height differences: $\delta_{mn} \equiv \delta_m - \delta_n$.

The meaning of equation (23) is obvious; temperature rise α_E and height above the heat exchanger δ_{51} or δ_{53}, or, alternatively, effective fan power $\eta\pi$, provide the draft to overcome heat-exchanger drag ($\epsilon_1 C_D$) and provide any acceleration in the tower associated with area contraction ($\epsilon_1 A_1^2/A_3^2$). The remaining leading-order term, depending on $\gamma - \kappa$, suggests the possibility of a natural draft augmentation if the atmospheric lapse rate should be greater than adiabatic. However, this term will generally be quite small numerically.

Equation (23) may be simplified by introducing the idea that the tower is of either induced or forced draft; that is, one or the other of the heat exchangers is to be dropped. Actually, of course, the extra heat exchanger could be used to represent heat dissipation and drag of the fan motor. Next, we may introduce a length scale l, recalling that $Q = \dot{m} C_p T_H[\alpha_H + o(\alpha_H \epsilon_1)] \approx \dot{m} C_p T_0(1 - \delta_H)\alpha_H$:

$$l \equiv \left(\frac{Q}{\sqrt{2g}\rho_0 C_p T_0} \right)^{2/5} \qquad \hat{y} \equiv \frac{y}{l} \qquad \hat{A} \equiv \frac{A}{l^2} \tag{24}$$

we will denote by subscript H the parameters of the heat exchanger, whether at ① or ③. With these changes, equation (23) becomes

$$C_D + \frac{\hat{A}_H{}^2}{\hat{A}_5{}^2} - \frac{1 - 2\delta_H}{1 + \alpha_H} \alpha_H{}^3 \left[\hat{y}_{5H} + \frac{a_H{}^2(1 + \alpha_H)}{(\gamma - 1)gl} \frac{\eta\Pi}{Q} \right] \hat{A}_H{}^2$$
$$+ \frac{\gamma - \kappa}{2\kappa(\gamma - 1)} \frac{\delta_{50}{}^2}{\epsilon_1} = \left(\delta_{50} - \frac{\gamma + 1}{\gamma - 1} \delta_{H0} \right) C_D - \alpha_E \left(\frac{\hat{A}_H{}^2}{\hat{A}_5{}^2} + 1 \right)$$
$$- \frac{2}{\gamma - 1} \frac{\hat{A}_H{}^2}{\hat{A}_5{}^2} \delta_{50} + \frac{\pi}{\epsilon_1} [(1 - \eta)\delta_{5A} - \eta \alpha_{E_{\text{lower}}}]$$
$$+ \frac{(\gamma - \kappa)[2\gamma - (\gamma + 1)\kappa]}{6\kappa^2(\gamma - 1)^2} \frac{\delta_{50}{}^3}{\epsilon_1} + o(\epsilon_1) \tag{25}$$

We leave the correction factor $(1 - 2\delta_H)/(1 + \alpha_H)$ unexpanded on the left side of the equation for reasons of convergence explained in [7].

Interpretation and Examples. We now choose a numerical example to gain a feeling for the importance of the various quantities introduced, and then we discuss further the meaning of equation (25). We first consider one of three natural-draft ($\Pi = 0$) towers, each 500 ft in height, above a heat exchanger at ground level, serving a 1000-MW plant of 33 percent thermal efficiency. Thus, $Q = 0.64 \cdot 10^6$ Btu/sec. We suppose further that the air-temperature rise is from 60 to 85 deg F, and thus with $C_p = 0.24$ Btu/lb-deg F, the mass flow $\dot{m}$ must be about 107,000 lb/sec. The value of C_D is taken to be 15, and $A_5/A_H = 0.5$. With $\rho_0 = 0.076$ lb/ft³ and $\gamma = 1.4$, the following derived quantities may be calculated:

$$\alpha_H = 0.048 \qquad l = 37\ \text{ft} \qquad \delta_{50} = 0.0052$$
$$\hat{y}_{50} = 13.5 \qquad A_H = 1.55 \cdot 10^5\ \text{ft}^2 \qquad \epsilon_1 = 1.30 \cdot 10^{-5}$$

The last term on the left of equation (25) is then $2.5[(\gamma/\kappa) - 1]$, which is to be compared with $C_D = 15$. From the atmospheric lapse rate, κ can be inferred; typical values would range between 1.2 and 1.4. The correction term would then range between 0.42 and 0, tending to diminish draft at most by about 2 percent. The error terms on the right of equation (25) depend on the small quantities α_E and δ_3, nominally of the same order:

$$C_D \delta_{50} = 0.08 \qquad -\alpha_E \left(\frac{A_H{}^2}{A_5{}^2} + 1 \right) = -0.23$$
$$-\delta_{50} \frac{A_H{}^2}{A_5{}^2} \frac{2}{\gamma - 1} = -0.10$$

These quantities, which are to be compared with C_D in equation (21), contribute very small corrections totaling -0.25. Of course, the lower the tower drag C_D, the more important these corrections would be. The last term on the right is neglected. The separate correction factor remaining on the left of equation (25), approximately $1 + \alpha_H + 2\delta_H$, gives a correction $(\alpha_H + 2\delta_H)C_D = 0.86$.

Now we consider a mechanical-draft tower of negligible height. Clearly, equation (25) says that the equivalent draft height of a mechanical-draft tower is simply proportional to the ratio of fan power delivered to the air to the heat rejected. Typically, choosing $\gamma = 1.4$, the proportionality factor is about $a_H{}^2/[(\gamma - 1)g] = 97{,}100$ ft. Thus if the draft height is 500 ft, the power/heat ratio is only 0.51 percent. The corrections in this case would include the quantity $-\eta\pi\alpha_E/\epsilon_1 = -(0.87)\eta$, but only if the heat exchanger is below the fan (induced draft).

In the zero-order equation, the fan location is immaterial, and no distinction appears between forced and induced draft. Furthermore, the duct area at the fan location (that is, the fan diameter) is not a parameter, either to zero order or to first order of corrections. So long as the required power is provided, there seems to be no need to have a fan of heroic diameter; cost considerations would presumably favor a compact design, and the present analysis would justify such an approach.

The first appearance of fan location as a parameter is in the correction term $(1 - \eta)(\pi/\epsilon_1)\delta_{5A}$. This expression describes the portion of fan power dissipated as heat, multiplied by height from the fan to the top of the tower. They may be interpreted as representing an additional buoyancy of the heated air column above the fan. However, this effect is very small and is ordinarily negligible.

The only distinction between forced and induced draft appears in the correction term $-(\pi/\epsilon_1)\eta\alpha_{E_{\text{lower}}}$, which includes the temperature rise of only the lower heat exchanger; α_E for induced draft; and 0 for forced draft. This correction, which is a penalty for induced draft equivalent to an increase of about 6 percent in C_D, may be understood by considering that the air entering the fan is warmer in the induced-draft case; hence the fan is somewhat less effective. For the same mass flow and pressure difference, the velocity is a bit larger, and hence a greater power is needed to provide the necessary flow work. Thus one would conclude that for low towers, the forced-draft arrangement would be slightly favored gasdynamically, neglecting natural-draft contributions.

Of course, one might also consider the fact that the air is slightly warmed passing through the fan, equation (21). Thus for the same air temperature leaving the heat exchanger, the value of α_E would be smaller by an amount of order π, which in turn is of order ϵ, equation (19). Accordingly, for the same total heat transfer, the mass flow $\dot{m}$ would need to be larger by an amount also of order ϵ. These corrections would favor the induced-draft arrangement; however, they are much smaller than the term of order α cited in the previous paragraph, and in fact are too small to be included in our draft equation, which we have terminated at order α.

If the natural-draft contribution is substantial, additional differences between induced and forced draft require consideraation. Suppose, for ease of comparison, that the heat-exchanger areas and drags and the fan areas are the same in the two cases. Then the right side of equation (25) for forced draft is less than that for induced draft by the amount $[(\gamma + 1)/(\gamma - 1)](\delta_{30} - \delta_{10})C_D$. The parentheses signify the difference of elevation of the heat exchanger in the two cases. Obviously, this difference between corrections corresponds to a loss of natural draft in the forced case if the heat exchanger is at an elevated height. For this effect, favoring induced draft, to exceed the propulsive-efficiency effect favoring forced draft, the quantity $[(\gamma + 1)/(\gamma - 1)](\delta_{30} - \delta_{10})$ would have to exceed about 5 percent. In that case, difference of exchanger heights would have to exceed about 810 ft, which is not a reasonable possibility. Our conclusion, then, still stands: that the forced-draft arrangement has a propulsive efficiency slightly superior to that of the induced-draft tower by about 5 percent, which is a typical value of α_E.

Other, perhaps more compelling, advantages of the induced-draft arrangements may exist; our consideration is limited to gasdynamics.

Scaling Relationships. Keeping in mind the various correction terms discussed previously we write equation (25) in zero-order form:

$$\hat{Y}\hat{A}_5^2 = \frac{\hat{A}_5^2}{\hat{A}_H^2}\frac{C_D}{\alpha_H^3} + \frac{1}{\alpha_H^3} \tag{26}$$

where Y is a generalized draft height:

$$\hat{Y} \equiv \hat{y}_{5H} + \frac{a_0^2}{(\gamma - 1)gl}\frac{\eta\Pi}{Q} \tag{27}$$

We may consider the expression $\hat{Y}\hat{A}_5^2$ to be a measure of tower size,[2] while the factor α_H^3/C_D expresses the influence of heat-exchanger performance. Clearly, if α is large, the tower need not be so large for a given total heat-exchange rate. If C_D is large, the tower must be large to produce adequate draft. Of course, C_D depends on the heat-transfer rate of the exchanger, and hence upon α. Thus α and C_D are interrelated performance factors that will be studied in subsequent paragraphs.

Clearly, for given drag coefficient and temperature rise, a substantial flow contraction between the heat exchanger and the exit would be desired. In effect, for large C_D, size based on heat-exchanger flow area A_H is fixed. However, visual impact should depend more on A_5, at the top of the tower, and it is that quantity that presumably should be minimized.

It is interesting that gasdynamic size is much less sensitive to height than to lateral dimension. If one is especially anxious to reduce height, it is a happy circumstance that if height is reduced by a factor of two, the lateral dimensions need be increased only by the factor $2^{1/4}$, or 19 percent, to keep gasdynamic equivalence. Of course, this idea must not be applied too enthusiastically, because a tower that is too low and wide will fail to meet our present assumption of one-dimensional flow, and the pressure condition at the exit will not be met, that is, draft will be lost. Study of these practical limitations of tower shape is beyond our present scope.

Minimum Tower Size

Heat-Exchanger Analysis. We must now relate C_D/α^3 more directly to the characteristics of heat exchangers. In doing this, we follow the usual engineering analysis described in the book of Kays and London [9] or that of Kreith [10]. The total heat-transfer rate may be written as

$$Q = UAF\Delta T_E \tag{28}$$

where U is an overall heat-transfer coefficient, A is now the heat-exchanger surface area, and ΔT_E is a suitable average temperature difference between air and water, assuming that the exchanger is of the counterflow type. F is a factor to correct for the exchanger being of a different type, say crossflow.

Fig. 2 sketches our temperature notation in a manner appropriate for counterflow. The initial temperature difference I is that between the hot water entering the cooler (T_{w_2}) and the cooling air entering the exchanger (T_1, very nearly equal to T_0). The water is then cooled through a range RI to a temperature T_{w_1}, which is still above T_1 by the amount of approach PI. The air, meanwhile, is warmed by an amount $\alpha_H T_1$, or, α being redefined, $\alpha_I I$, and it leaves the exchanger at T_2. The usual logarithmic mean temperature difference then may be written

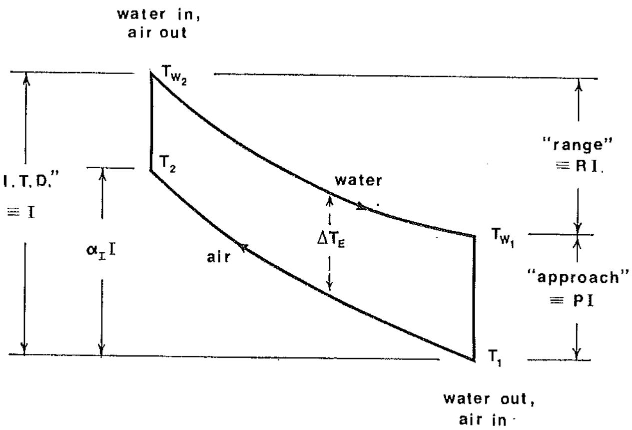

Fig. 2 Temperature diagram of hypothetical counterflow heat exchanger defining terms and notation

$$\Delta T_E = I\,\frac{1 - \alpha_I - P}{\ln|(1 - \alpha_I)/P|} \qquad \alpha_I \equiv \alpha_H \frac{T_1}{I} \tag{29}$$

Turning now to the overall conductance UA, we neglect the wall resistance and write

$$UA = \frac{1}{\dfrac{1}{\eta_0 A_a h_a} + \dfrac{1}{A_w h_w}} = \frac{1}{E}A_a h_a \tag{30}$$

where we have defined

$$E \equiv \frac{1}{\eta_0}\left(1 + \frac{\eta_0 A_a h_a}{A_w h_w}\right) \tag{31}$$

and h_a and h_w are heat-exchange coefficients for the air and water sides of the device. The corresponding exchanger surface areas are A_a and A_w. The area (especially on the air side) may include fins, and a fin efficiency factor η_0 is needed. For air–water heat exchangers, the water-side resistance is usually small. Thus the quantity E might be nearly one, in which case, simply, $UA \simeq \eta_0 A_a h_a$.

We now must plunge into a thicket of definitions having to do with heat-exchanger performance in quest of the quantities h and C_D. First, we shall need to distinguish between four different areas associated with the air side: A_a is the total heat-transfer surface in contact with the air. A_1 is the area of the streamtube entering the exchanger. A_f is the frontal area of the exchanger, across its first row, for example. A_f and A_1 are not necessarily the same. If the exchanger is at an oblique angle to the oncoming flow, A_f would be larger than A_1 by the factor of the secant of the angle. Finally, A_c is the free-flow area, which is some fraction of A_f and represents the minimum flow passage for the particular combination of tube and fin sizes and spacings in question. We will assume that if the heat exchanger is obliquely oriented, its performance is the same as in normal orientation, but with the velocity of approach being that normal to the exchanger face. That is, the air is assumed to turn so as to flow normally through the cooler body. This assumption is appropriate for any high-drag device, and especially for one having high resistance to flow parallel to its face, as would many fin-tube exchangers.

The following equations define a hydraulic radius and the Nusselt, Stanton, Reynolds, and Prandtl numbers:

$$r_h \equiv \frac{A_c L}{A_a} \qquad h_a \equiv \frac{k_1}{4r_h}\,\mathrm{Nu} \qquad \mathrm{St} \equiv \frac{\mathrm{Nu}}{\mathrm{Re}\,\mathrm{Pr}}$$

$$\mathrm{Re} \equiv \frac{\rho_1 V_c 4r_h}{\mu_1} \qquad \mathrm{Pr} \equiv \frac{C_{p1}\mu_1}{k_1} \tag{32}$$

---

[2] In his basic paper on natural-draft evaporative tower design, Chilton [8] finds the relationship height·(area)^2 = constant for a family of towers.

Table 1 Size function ψ and its minimum

α_I	Approach, P								
	0.2	0.3	0.4	0.5	0.6	0.7	0.8	0.9	1.0
0.1	214.9	183.1	162.2	146.9	135.2	125.7	117.8	111.1	105.4
0.2	57.76	49.04	43.32	39.17	35.96	33.38	31.25	29.45	27.89
0.3	27.84	23.54	20.73	18.69	17.13	15.87	14.84	13.96	13.21
0.4	17.17	14.44	12.67	11.40	10.42	9.63	8.99	8.45	7.98
0.5	12.22	10.22	8.93	8.00	7.29	6.73	6.27	5.88	5.54
0.6	9.63	7.99	6.94	6.20	5.63	5.18	4.81	4.50	4.24
0.7	8.28	6.80	5.87	5.21	4.72	4.32	4.00	3.74	3.51
0.8	7.81	6.34	5.42	4.77	4.29	3.92	3.61	3.56	3.14
0.84	7.91	6.36	5.41	4.75	4.26	3.87	3.56	3.31	3.09
0.9	8.56	6.78	5.70	4.97	4.42	4.00	3.67	3.99	3.16
0.95	10.24	7.94	6.58	5.67	5.01	4.50	4.10	3.77	3.49
α_I^*	0.800	0.813	0.822	0.829	0.835	0.840	0.844	0.848	0.851
ψ^*	7.73	6.33	5.40	4.75	4.26	3.88	3.57	3.31	3.07

The exchanger length L is measured normal to A_c. If the exchanger were a single tube, the hydraulic radius r_h would be one-fourth the diameter of the tube. Hence, $4r_h$ appears in the role of a diameter in subsequent definitions. By V_c we mean the normal velocity associated with A_c, that is,

$$\rho_1 V_c A_c = \dot{m} = \rho_1 V_1 A_1 \tag{33}$$

Coefficients of viscosity and heat conduction for air are denoted by μ and k.

Expressions for α_H and C_D. We may anticipate finding h_a via St, given as a function of Re and Pr in the charts of [9] for various configurations and types of heat exchangers. However, our purpose is not to design a heat exchanger. We have a less ambitious goal: to find an expression for α_H to introduce into equation (26). We may write, approximately,

$$Q = \rho_1 V_c A_c C_{p_1} T_1 \alpha_H \tag{34}$$

Combining equations (28), (30), (33), and (34), we obtain

$$\alpha_H = \mathrm{St}\,\frac{L}{r_h}\,\frac{F}{E}\,\frac{\Delta T_E}{T_1} \tag{35}$$

Our gasdynamic definition of C_D is given in equation (5). Conventionally, the pressure drop across a heat exchanger is described by a friction factor f defined on page 33 of [9]. For small Mach numbers,

$$p_2 - p_1 \approx \frac{1}{2}\,\rho_1 V_c^2\,\frac{A_a}{A_c}\,f \tag{36}$$

and equations (5) and (36) give

$$C_D = \frac{L}{r_h}\left(\frac{A_1}{A_c}\right)^2 f \tag{37}$$

The friction factor f is available on the same charts as St, and inspection of these shows that usually f may be taken as proportional to St over an extended range of Re. We adopt such a Reynolds analogy between friction and heat transfer:

$$f = K\,\mathrm{St} \tag{38}$$

Generally, K ranges between two and six.

A Size Function. We are now in a position to express the quantity $C_D/\alpha_H{}^3$ as a function of the cooling-tower parameters. First, we eliminate St between equations (35) and (38). Then we introduce equation (29), first defining a size function $\psi(\alpha_I, P)$

$$\psi \equiv \frac{\ln|(1-\alpha_I)/P|}{\alpha_I{}^2(1-P-\alpha_I)} \tag{39}$$

and equation (26) becomes

$$\left(\frac{I}{T_1}\right)^3 \hat{Y}\hat{A}_5{}^2 = \frac{KE\psi}{F}\left(\frac{A_5}{A_c}\right)^2 + \frac{1}{\alpha_I{}^3} \tag{40}$$

It is interesting that as a function of α_I, ψ has a minimum; this is clear from the fact that ψ is infinite at both $\alpha_I = 0$ and 1. The function ψ is displayed in Table 1 and in Fig. 3.

In general terms, we may understand Fig. 3 as follows: Generally, the closer the approach (the smaller P), the larger the tower, because of the greater heat-transfer area or stronger draft required. Similarly, if $\alpha_I \rightarrow 1$, the air can only approach the entering hot-water temperature in a very large-area tower. On the other hand, if $\alpha_I \rightarrow 0$, the air is only slightly warmed and its buoyancy vanishes, and, more importantly, the mass flow must become infinite to carry away heat at the required rate; both these tendencies imply an infinite flow area. Usually, one would specify a cooling range, and I would be given; thus P would be known. The air warming, α_I, would depend on design, however. From Fig. 3 we see that with P fixed, there is a minimum

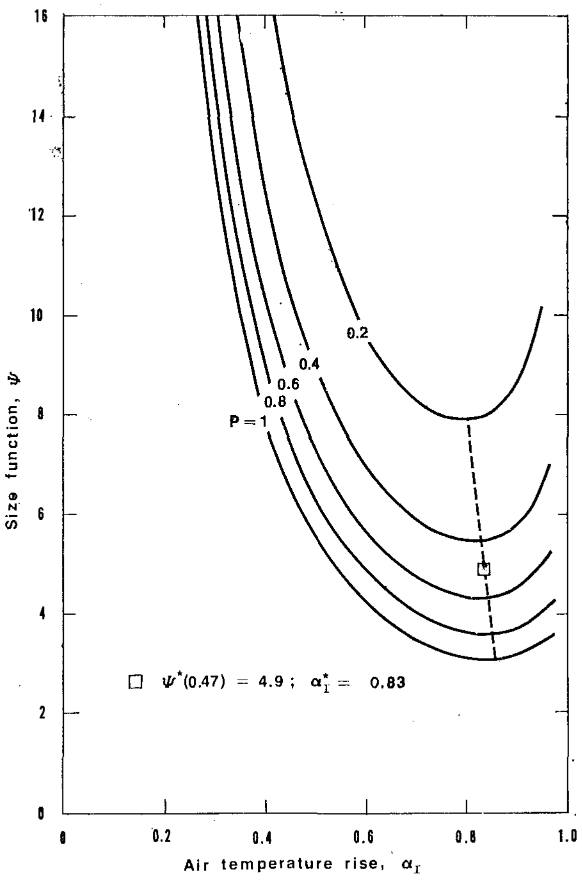

Fig. 3 Size function ψ as a function of air-temperature rise for various values of the approach; dashed line denotes locus of minima

of ψ occurring at an α_I of about 0.8 for all P. Particular minimum values (denoted by an asterisk) are given in Table 1. A log-log plot of these minimum values of ψ versus P shows clearly that

$$\psi^* = 3.2P^{-0.57} \tag{41}$$

is an excellent approximation to the exact function.

The Ideal Minimum-Size Tower. Equation (40) will be applied to various practical situations in a subsequent paper.[3] Here we ask what the ideal goal might be. The more nearly counterflow performance is obtained, the smaller the tower; ideally, $F = 1$. Also ideally, fin ineffectiveness and water-side resistance would both vanish, so that $E = 1$. Since α_I^* ranges between 0.80 and 0.85, $(\alpha_I^*)^{-3}$ ranges between 1.95 and 1.63, depending on P. Choosing an average value, the approximate ideal would be:

$$\left(\frac{I}{T_1}\right)^3 \hat{Y}\hat{A}_5{}^2 = 3.2KP^{-0.57}\left(\frac{A_5}{A_c}\right)^2 + 1.8 \tag{42}$$

The two remaining quantities, K and A_5/A_c, have no best values, but rather should be as small as possible. Of course, a small value of K favors draft, and K might conceivably be as low as three. As an example, if $I = 35$ deg, $T_1 = 520$ deg, approach = 16.5 deg, then $P = 0.47$ and $\psi^* = 4.9$. For a tower dissipating $0.64 \cdot 10^6$ Btu/sec, we found $l = 37$ ft. With these choices and $K = 3$, equation (40) would show that three ideal dry towers for a 1000-MW plant would have to be about 330 ft in scale, if $A_5/A_c = 1$. Now, $(A_3/A_c)^2$ can be considerably less than one, and it is difficult to place a practical lower limit on that quantity. The ratio A_5/A_c can be made small both by choosing a substantial flow contraction and by oblique heat-exchanger arrangements. It is easy to imagine A_5/A_c to be in the vicinity of 0.3, in which case the size scale would be reduced from 330 ft to 235 ft.

Concluding Remarks

In a subsequent paper, the practical implications of equation (40) will be pursued further, especially in regard to heat-exchanger size. For the moment, we may emphasize that the present analysis is intended to provide a technical basis for reducing the overall size (or power) of dry towers, and the result makes clear that heat-exchanger design is crucial in terms of both drag and temperature rise. Accordingly, the scaling law has been expressed in terms of heat-exchanger parameters, and various requirements for minimum tower size are immediately revealed.

However, it is not obvious how such requirements could economically be met in a realistic situation, or what technical compromises would typically be necessary. We will find that the combination of parameters describing the best heat exchanger will vary greatly, according to the particular way in which the system size is to be defined and then minimized. For example, water-side heat transfer and pumping power requirements may be considered important.

In closing, we should recall that this study emphasizes the internal gasdynamics of dry cooling towers; external factors need further study. Specifically, entrance losses and wind effects at the exit should be more closely specified in practical applications.

Acknowledgment

This research has been supported by the National Science Foundation, Division of Advanced Technology Applications (RANN).

References

1 "A Review and Comparison of Selected United States Energy Forecasts," by Battelle Memorial Institute, Pacific Northwest Labs., for Office of Science and Technology, Washington, D. C., Dec. 1969.

2 Heeren, H., and Holly, L., "Air Cooling for Condensation and Exhaust Heat Rejection in Large Generating Stations," *Proc. Am. Power Conf.*, Vol. 32, 1970, pp. 579–594.

3 Smith, E. C., and Larinoff, M. W., "Power Plant Siting, Performance, and Economics With Dry Cooling Tower Systems," *Proc. Am. Power Conf.*, Vol. 32, 1970, pp. 544–572.

4 Christopher, P. J., and Forster, V. T., "Rugeley Dry Cooling Tower System," *Proc. Inst. Mech. Engr.*, Vol. 184, Part 1, No. 11, 1969–1970, pp. 197–222.

5 Parker, F. L., and Krenkel, P. A., *Physical and Engineering Aspects of Thermal Pollution*, C.R.C. Press, Cleveland, Ohio, 1970.

6 Moore, F. K., "On the Minimum Size of Natural-Draft Dry Cooling Towers for Large Power Plants," ASME Paper No. 72-WA/HT-60.

7 Moore, F. K., "Scaling Law for Dry Cooling Towers With Combined Mechanical and Natural Draft," Report No. 72-19, Cornell Energy Project, 304 Olin Hall, Ithaca, N. Y.

8 Chilton, H., "Performance of Natural-Draught Water-Cooling Towers," *Proc. Inst. Mech. Engr.*, Vol. 99, Part 2, No. 71, 1952, pp. 440–456.

9 Kays, W., and London, A. L., *Compact Heat Exchangers*, 1952, 2nd ed., McGraw-Hill, New York, 1964.

10 Kreith, F., *Principles of Heat Transfer*, International, Scranton, Pa., 1958.

---

[3] See [6] for application to the Forgo–Heller type of dry tower at Rugeley, England [4].

W. W. S. CHARTERS
Senior Lecturer.

T. M. LIM
Postgraduate Research Student.

Department of Mechanical Engineering,
University of Melbourne,
Parkville, Victoria, Australia

R. V. DUNKLE
Chief Research Scientist,
Division of Mechanical Engineering,
C.S.I.R.O.,
Highett, Victoria, Australia

Heat and Momentum Transfers: Multiple-Disc Rotor Units

An investigation has been carried out to determine the performance characteristics of a multiple-disc rotor device used as a combined fan/heat exchanger. The advantages of such a system, when applied for example to an air-conditioning system, stem primarily from the simplicity of design and compact nature of the equipment. The assessment of the particular test unit as a fan was done under normal atmospheric conditions using air as the working fluid. A speed range from 550 to 1290 rpm was used in these tests. The maximum efficiency of the momentum transfer from the rotor to the fluid was about 14 percent. The unit capability as a heat exchanger using air flow under normal atmospheric conditions may be judged by the maximum heat transfer effectiveness of about 40 percent. Rotor speeds were varied in the range 700 to 1600 rpm, and at each rotational speed the ratio of the mass flow in the cool stream to that in the hot stream was varied from 0.48 to 1.30. Two different techniques were used in an endeavor to predict the performance of the experimental unit. Of these, the more successful was that based on the assumption that a turbulent boundary layer covered the rotating disc. However, the simpler approach, using calculated friction factors, may well prove acceptable for some engineering applications. The results from each of the prediction techniques are given for comparison with the test results.

Introduction

The first use of a multiple-disc rotor is credited to N. Telsa, who took out a U. S. patent [1][1] on a disc turbine about 1913. No published engineering investigation of the turbine was made, although the semi-technical publications of the time, i.e., *Scientific American* [2] and *Engineering* (London) [3] did report the invention. But it was not until about 1930 that the fundamental research on fluid flow around discs was carried out by Von Karman [4], Cochran [5], and Goldstein [6]. Between the Tesla turbine and the present generation of multi-disc devices came a family of so-called friction disc pumps. These pumps had a single-disc rotor, which was vaned on the periphery. These pumps were widely used in lubrication, control, filtering, and booster systems, as the occurrence of peak efficiencies at low specific speed made them especially suitable for these applications.

There is at present a revival of interest in the use of disc rotors for the conversion of motive shaft power to kinetic energy of the bulk fluid, perhaps because of the inherent simplicity of design and fabrication when compared with the more conventional rotors in standard turbomachinery. In the past, the overriding reasons for not using the multi-disc rotor has been the low efficiency of momentum exchange; but in applications where stability of operation and high reliability are paramount, this class of rotors provides tangible advantages, e.g., development of a disc pump for space-exploration operation is reported by Hasinger and Kehrt [7].

Review of Work Related to Disc Rotors

Analytical solutions of the equation of change are successful only under conditions of laminar flow and with simple boundary assumptions. As, in practice, the bulk of fluid machinery operates in the turbulent range and under geometrical constraints leading to complicated boundary conditions, it is necessary to find other methods of predicting unit performance. One method that has been used successfully involves the formulation and solution of the integral momentum and energy equations written for specific control volumes. An example of this method arises in the theoretical analysis of an "enclosed disc."

Work on the enclosed-disc aspect of the general rotating-disc problem has been concentrated on a smooth disc rotating in a cylindrical housing. Prominent contributors to this body of knowledge are Schultz-Grunow [8], Okaya and Hasegawa [9], Dorfman [10], Soo [11], and Daily and Nece [12]. In particular, Daily and Nece made a lucid review of the available theoretical and experimental information available.

In the field of practical disc rotor machinery research, several

---

[1] Numbers in brackets designate References at end of paper.

Contributed by the Heat Transfer Division for publication (without presentation) in the Journal of Heat Transfer. Manuscript received by the Heat Transfer Division, August 8, 1972. Paper No. 73-HT-Q.

workers have proposed models for the single-vaned rotor disc pump that have met with varying degrees of success in the prediction of system performances. Among these, the earliest models of direct interest were proposed by Iversen [13], Senoo [14], Wilson, et al. [15], and Balje [16].

The works of Rice [17] and Hasinger and Kehrt are directly concerned with smooth disc rotors. The former reported on the use of this shear-force machinery as a water pump and as an air compressor, and the latter workers reported on more sophisticated shear-force pumps to handle fluids in rocket propellant pumps and boiler feed pumps. In both cases the induced flow is through the hub of the rotor, as the pumps are of the radial-flow variety. The method of analysis adopted by Rice involved a solution of the differential equations of motion. No correlation was given between the theoretical and the experimental data in the published paper, although it was stated that numerical and experimental results were obtained. The radial-flow shear-force analysis of Hasinger and Kehrt is restricted to the laminar-flow regime, although the suggestion is made that in the turbulent range the results may be approximately true if adjustment is made to the viscosity term.

Description of Fan Heat Exchanger under Consideration

Details of the fan/heat exchanger rotor and housing are shown in the photographs in Fig. 1. The heart of the unit, the rotor, is made up of 16 smooth aluminum discs fabricated by spinning. The average thickness of the discs is 1.59 mm (0.0625 in.), and the discs sit loosely on a mild-steel shaft. Aluminum ring spacers with a boss diameter of 305 mm (13.75 in.) are placed between every two discs to position the discs on the shaft. The housing itself is made from 20 SWG 0.914-mm (0.036-in.) sheet metal. A geometric constraint on the housing design is that there should be provision for rectangular ducting to be attached to carry both the heated and cooled fluid streams. The ducts leading to and from the test unit are of the same size as the inlet and outlet cross sections on the fan/heat exchanger. The throat sections, however, are of arbitrary design, and it is certain that for any future designs, more attention should be paid to the influence of throat shape on the overall fluid-flow pattern. A geometrical advantage of the unit is that the inlet and outlet cross sections are naturally rectangular. As air-conditioning ducts are usually rectangular in cross section, the need for complex-geometry transition pieces is obviated.

Semi-Theoretical Models

Simple Friction-Factor Model. For air flow through a control volume V under temperatures and pressures close to atmospheric conditions, the energy equation may be written (ignoring potential energy changes) as

$$\dot{Q}_{cv} - \dot{W}_{cv} = \int_A \left(\frac{p}{\rho} + \frac{V^2}{2g}\right) \rho V \cos \alpha dA$$

$$= \int_{A_o} \left(\frac{p}{\rho} + \frac{V^2}{2g}\right) \rho V dA - \int_{A_i} \left(\frac{p}{\rho} + \frac{V^2}{2g}\right) \rho V dA$$

For the operation of the unit as a fan, it is reasonable to assume adiabatic conditions, i.e., $\dot{Q}_{cv} = 0$.

Also, the static pressures in the inlet and the outlet ducts may be assumed to be uniform across the cross section and equal to the pressure measured at a static wall tapping in the duct wall.

These simplifications enable us to write:

$$\int_{A_0} \left(\frac{p}{\rho}\right) \rho V dA - \int_{A_i} \left(\frac{p}{\rho}\right) \rho V dA = \dot{m} \left(\frac{p_0 - p_i}{\rho}\right)$$

The pressure gain across the unit, $\Delta p_{oi} = p_o - p_i$, may be found by considering the entrance loss Δp_{in} and the exit loss Δp_{out} as well as the pressure gain achieved by the smooth disc rotor, Δp_{gain}. The pressure-loss terms may be written in terms of a loss coefficient C as

$$H_L = (\Delta p_{\text{in}} + \Delta p_{\text{out}}) = C \left(\frac{V^2}{2g}\right)$$

where V is the velocity in the inlet duct.

The simple friction-factor model proposed initially by the fan/heat exchanger designer Dunkle [18] relies on the following assumptions: (*a*) uniform pressures and tangential velocity distributions exist at stations 3 and 4, Fig. 2; (*b*) movement of the disc in the fluid stream is at an overall effective velocity based on

Nomenclature

A = area (when used in integral expressions, e.g., $\int_A^X dA$, A represents surface area of the C.V.)
C = coefficient (defined as appropriate)
C_h, C_c = capacity rate of hot and cold fluid streams, respectively
C.V. = control volume
D_h = hydraulic diameter
f = friction factor
g = gravitational-field constant
H = pressure head
H_L = pressure-head losses
M_T = torque on disc
p = pressure
$\dot{Q}_{cv}$ = net rate of thermal energy input to C.V.
Q = flow rate
r = radius
Re = Reynolds number ($r^2\omega/\nu$)
R_{HT} = heat transfer fraction
R_m = ratio of mass flow in cool fluid stream to that in hot stream
T = absolute temperature
T_z = torque
T_s = static temperature
T_t = total (stagnation) temperature
U, V = velocity
$+W_{cv}$ = rate of work done by fluid in control volume
r, θ, z = coordinates of cylindrical-curvi linear system used
v_r, v_θ, v_z = components of a general velocity vector v in the cylindrical curvilinear coordinate system
α = angle between velocity vector of fluid leaving C.V. and the normal to surface of the C.V.
$\propto$ = proportionality sign
β = proportionality constant
γ, ω = angular velocities
δ = boundary-layer thicknesses
ϵ = proportionality factor
ξ = ratio ω/ν
ρ = density
η_m = momentum transfer efficiency of rotor
η_{Tc} = temperature effectiveness for cold fluid in heat exchanger
η_{Th} = temperature effectiveness for hot fluid in heat exchanger
η_{HT} = heat transfer effectiveness of heat exchanger
τ = shear stress
μ = dynamic viscosity
ν = kinematic viscosity
Δ = final − initial
ΔT = difference between disc-surface and bulk-air temperatures

Subscripts

i = inlet
m = mean radius
o = outlet
r = radial
θ = tangential

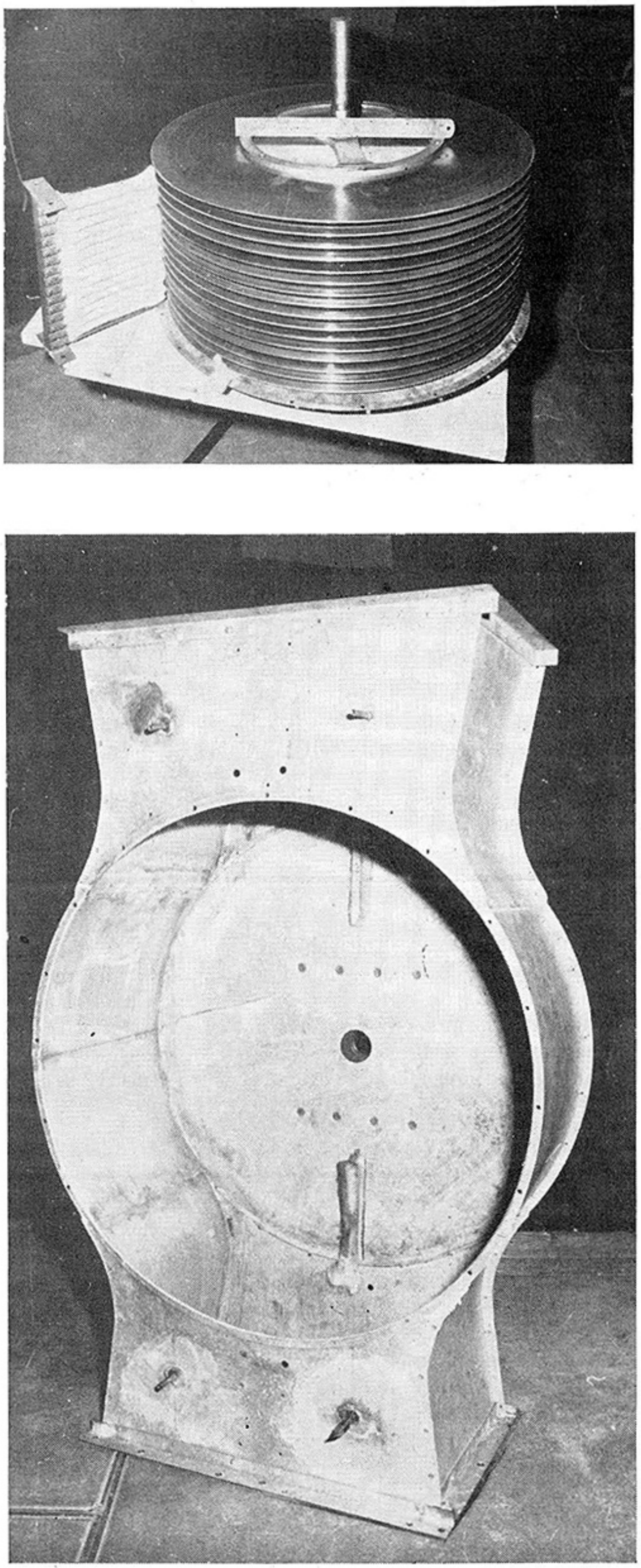

Fig. 1 Photographs of smooth-disc rotor system: (a) rotor and finger seals; (b) rotor housing

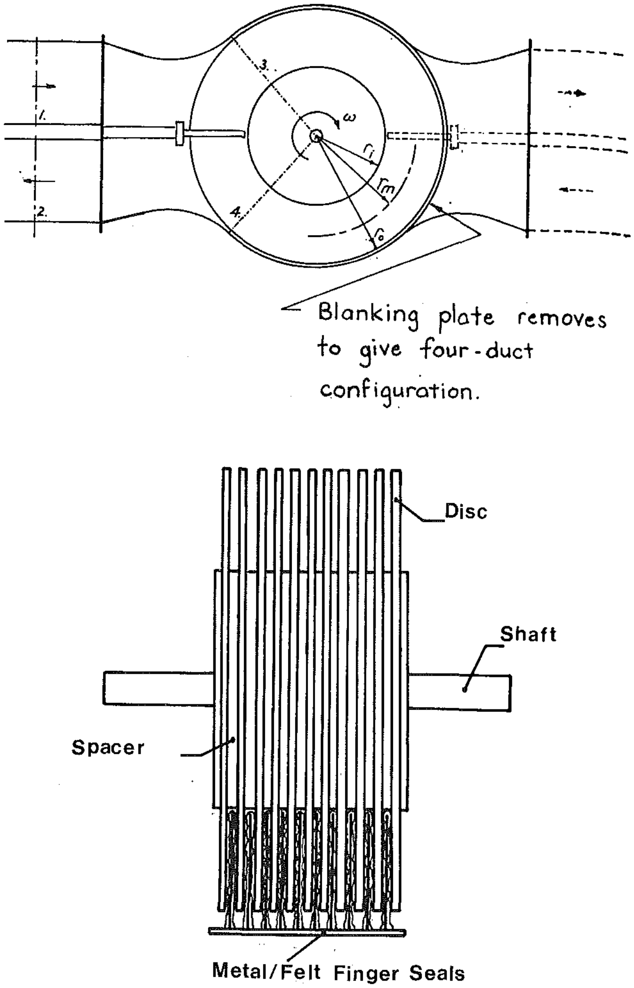

Fig. 2 (a) Two-duct fan configuration and four-duct fan/heat exchanger configuration; (b) schematic side view of rotor and finger seals

the rotational speed of the disc at the radial mid-point of the annular section (outer radius r_o, inner radius r_i); (c) secondary flows are unimportant. The use of these simplifying assumptions is to allow ease of calculation of the overall unit performance without requiring knowledge of the internal flow structure.

A force balance in the axial direction required to find the pressure increase then gives

$$p_4A_4 - p_3A_3 = \tau_mA_m - \tau_oA_o$$

where the subscripts 3 and 4 refer to inlet and outlet conditions at the sections defined in Fig. 2.

To estimate the shear forces τ_m and τ_o, it has been further assumed for ease of analysis that circumferential flow between two rotating discs is equivalent to flow through a high-aspect-ratio rectangular duct, from Dunkle [18]. For a rectangular duct, the shear stresses and the friction factor are related by

$$f = 4\tau/\rho\left(\frac{V^2}{2g}\right)$$

Using an equivalent-diameter concept, the friction factor in the rectangular duct may be found from equations such as that proposed by von Karman to relate friction factor f to the flow Reynolds number Re

$$\frac{1}{\sqrt{f}} = 2.0 \log_{10} (\text{Re}\sqrt{f}) - 0.8$$

Using these steps, the pressure-gain term Δp_{gain} may be calculated.

Boundary-Layer Model. Work on axisymmetric flow around a disc rotating in a cylindrical housing points to an alternative way of evaluating shear forces on the rotating-disc surfaces. This method actually involves the solution of the integral momentum equations written here:

$$r\frac{\tau_r}{\rho} = \int_0^\delta V_\theta^2 dz - \frac{1}{\rho}\int_0^\delta \frac{\partial p}{\partial r} dz - \int_0^\delta rV_r \frac{\partial V_r}{\partial r} dz$$

$$r^2\frac{\tau_\theta}{\rho} = -\int_0^\delta V_r V_\theta dz + \int_0^\delta r^2 V_r \frac{\partial V_\theta}{\partial r} dz$$

For solution of the equations, assumptions regarding the spatial distribution of fluid velocities and wall shear stresses need to be made. Dorfman's assumptions regarding these distributions are used here because of the success of their application to the enclosed-disc problem.

$$V_r = \epsilon r(\omega - \gamma)(z/\delta)^{1/7}(1 - z/\delta)$$

$$V_\theta = r(\omega - \gamma)[1 - (z/\delta)^{1/7}] + r\gamma$$

$$\tau_o = 0.0225\rho V^2 \left(\frac{\nu}{V\delta}\right)^{1/4}$$

By substitution of these expressions and their derivatives into the momentum equations, solutions may be found in the form

$$\epsilon^2 = \frac{115(\xi + 8)}{1799\xi + 1582}$$

$$\delta = \frac{0.0225^{4/5}\,\nu^{1/5}(\omega - \gamma)^{3/5}(1 + \xi^2)^{3/10} r^{3/5}}{A^{4/5}}$$

where

$$A = \frac{\gamma}{720}(119\xi + 469)$$

The torque applied on the fluid by the rotating disc may be written

$$T = \iint_A r\tau_\theta \cdot r d\theta dr$$

Once τ_θ has been evaluated, from the above calculations the torque T may be given quantitative form.

The work done on the fluid by one side of the disc is given by

$$\dot{W} = T(\omega - \gamma)$$

Substitution of this expression into the energy equation then allows the overall pressure rise across the system to be evaluated.

For the present system, while geometric axisymmetry occurs, flow quantities do show circumferential variations. For example, the static pressure rise across the unit points to a circumferential pressure gradient. There would consequently be a boundary-layer-thickness increase in the circumferential direction, which has not been taken into account in the formulation of the solution. In the present model, the boundary-layer thickness is assumed to be substantially constant for any one-flow condition tested in the prediction of fan performance.

Introduction to the Experimental Program

It should be noted that the rotor and the housing of the test system are of the fixed-geometry variety. As Daily and Nece have shown, geometry does influence the flow around enclosed discs, so that the results of the experiments can only be directly extrapolated to systems that are geometrically similar. However, these same results can indicate whether the momentum and heat exchanges between the rotor and the fluid for a smooth disc device are, for example, comparable with the conventional bladed-rotor turbofans and the commonly used shell-and-tube heat exchangers.

To obtain a complete understanding of the momentum and heat transfer around the rotating discs, it would be necessary to map experimentally the temperature, pressure, and velocity fields in the discs, fluid, and housing. As the actual measurement of local velocity, pressure, and temperature distributions would be highly complex, attention has been focused on the bulk momentum and heat exchanges afforded by the unit. The net momentum and thermal energy transfers are obtained by measuring dynamic and thermal quantities at the sections where the fluid enters and leaves the system.

Some understanding of the internal-flow structure has been made possible by carrying out a qualitative study using a flow-visualization technique. This has assisted in gauging the validity of the hypothetical model of internal flow. For reasons of availability and convenience, the fluid medium studied was air under normal atmospheric conditions. As it was possible to test the multi-disc rotor system as a pure fan, or as a fan/heat exchanger, the main experimental program was for convenience subdivided into four sections: (1) measurement of velocity and temperature distributions in the fluid streams at entrance and exit; (2) flow visualization to obtain a qualitative picture of the internal-flow structure; (3) analysis of the system under operation as a fan—flow and pressure measurements taken to obtain fan characteristics; (4) analysis of the system under operation as a fan/heat exchanger—measurements of bulk heat exchange across the fluid streams to obtain heat exchange effectiveness.

Experimental Program

Fan-Mode Operation. To realize the full blowing capacity of the fan, one set of inlet and outlet sections was blanked off, Fig. 2(*a*). In this two-duct configuration the induced air travels almost one complete revolution before being expelled from the rotor. A schematic arrangement of the disc rotor and finger seals is also shown in Fig. 2(*b*). Duct velocity profiles were obtained using a traversing pitot tube connected to a Prandtl micromanometer. It should be noted that the duct equivalent diameter was approximately 25 cm (10 in.) and that consequently fully developed flow conditions would not be expected at the measuring station, which was approximately six diameters from the outlet. A venturi air meter designed and manufactured to standard specification was installed to measure the volume flow rate of the air, and the pressure rise across the unit was monitored by a total pitot tube at the entrance and by a static wall tapping at the exit from the unit. Control of the flow was achieved by a sliding vee baffle plate in the exit duct. Fan characteristics were taken for several rotational speeds.

Heat Exchanger Mode Operation. The full four-duct arrangement was used for these tests by removing the blanking plates and inserting the finger seals and the separation pieces. In addition, a heater-duct section was attached to the top ducting. This heater section was capable of providing up to 12 kw to one air stream. Temperature profiles were obtained using half-shielded copper–constantan thermocouples mounted on a micrometer traversing attachment.

Flow Visualization. Some early flow-visualization tests were made to chart the air-flow pattern between the discs on the rotor. One of the spun aluminum discs was removed and replaced by a clear acrylic disc of the same dimensions. The end cover plate was also replaced by a sheet of clear acrylic. Flow patterns were obtained photographically using a high-speed Polaroid film and a flash-bulb arrangement to illuminate the area between the discs through a slot cut in the housing. Smoke was generated in a conventional way and injected through a small probe at various points around the rotor housing.

Measurement Techniques

Pressure Measurements. All static-pressure measurements were taken using square-edged wall tappings installed normal to the wall, and all dynamic pressures were taken using pitot tubes, as the response time of the instrumentation was relatively unimportant for the steady-state testing carried out.

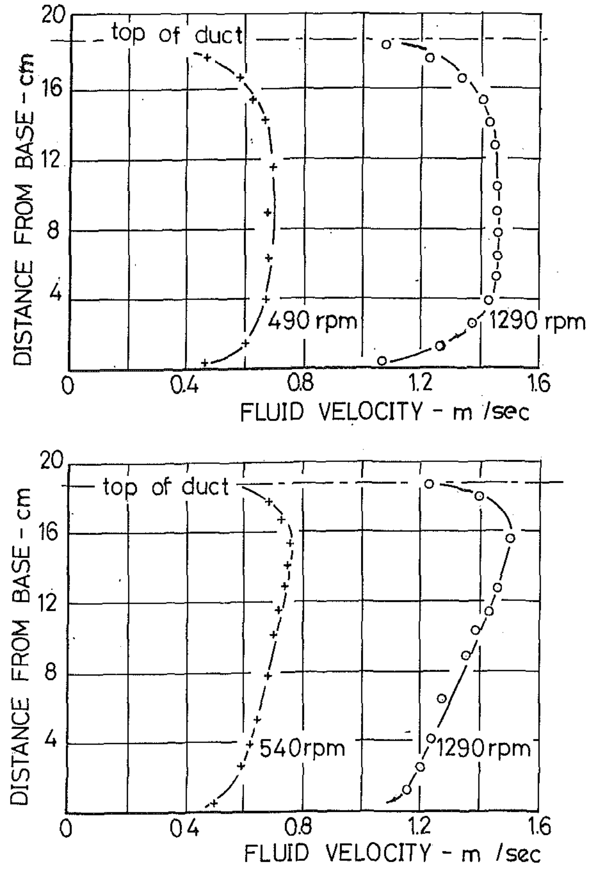

Fig. 3 Velocity profiles: (a) fan inlet; (b) fan outlet

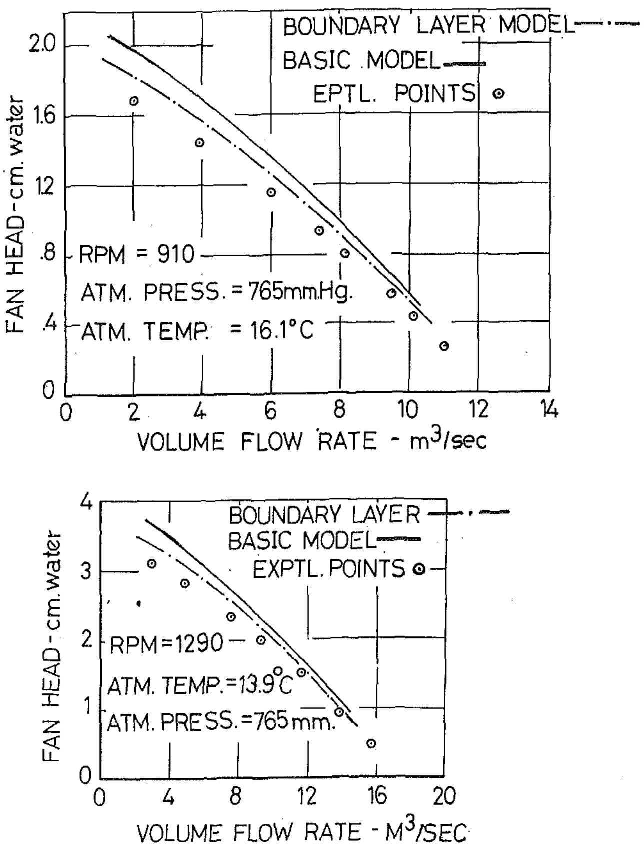

Fig. 4 Theoretical and experimental fan characteristics

Temperature Measurements. Half-shielded thermocouples made from copper–constantan wire 0.127 mm (0.005 in.) in diameter were individually calibrated and used to measure the total fluid temperature at the required stations.

Discussion of Experimental and Theoretical Findings

The velocity profiles at the inlet to and the outlet from the fan/heat exchanger are shown in Fig. 3. These velocities were measured along the vertical medians of the inlet and outlet ducts. The inlet velocity profile exhibits characteristics similar to those in normal duct turbulent air flow. As the measurement station is only approximately three diameters downstream from the air intake point, a fully developed profile would not be expected. The outlet velocity profile contrasts quite radically with the uniform distribution of the inlet one: in the region away from the walls the bulk fluid travels with a velocity that varies linearly with the distance from the horizontal surfaces of the duct. It is known that the dropoff in velocities close to the duct walls is induced by the decelerating effect of the duct boundary on the flow. However, the linear velocity variation in the outlet profile would be a direct result of the rotor. This implicitly ratifies an assumption made in the modeling procedure that the fluid between the discs travels with a tangential velocity component that increases linearly with radial distance from the disc center. The difference in these bulk-velocity profiles also indicates that the rotor unit transfers energy to the fluid by reorientation of the kinetic-energy distribution in the inlet and outlet flows as well as by increasing the pressure of the outgoing fluid.

Flow-Visualization Results

From our point observations of the flow using the smoke probe, a general qualitative picture may be drawn of the flow structure. When operating at low load conditions on the fan characteristics, it may be said that the air at each point between the discs travels in the same direction as the discs. Here a radial distribution of the tangential air velocity in the form $V_\theta = \beta\omega r$ would be an appropriate assumption. At the other extreme, under high loads, considerable backflow occurs near the hub of the rotor. For these loads the distribution of V_θ previously assumed would be erroneous. A further point worth noting is that the turbulent nature of the flow was clearly illustrated, as at a short distance from the probe turbulent diffusion so diluted the injected smoke that the definition of its path became impossible.

Fan Characteristics

The basic fan characteristics obtained at various rotor speeds are presented in Fig. 4. The drop in pressure rise across the unit with increasing volume flow rates is evident. With increase in rotor speed it is possible to extend the operating range of pressure gain and flow rate. The chain dotted line represents the predicted performance based on the turbulent-boundary-layer model, and it is interesting to note the increased divergence of theory and practice in the low-flow-rate range. Because of the radial flow and backflow shown in the flow-visualization tests, the assumption of solid-body flow between the discs would not be valid under the low-flow (high-load) condition. Furthermore, the increased pressure gradients would allow an increasing boundary-layer thickness, which would depend on both the tangential and radial coordinates of the point in question. Under the high-flow (low-load) conditions, on the other hand, the tangential velocity of the fluid with little or no radial component of velocity and the linear outlet velocity profiles lend credibility to the assumption of solid-body rotation of the bulk fluid. In addition, the low pressure rise closely satisfies the assumption of negligible tangential pressure.

In the same figure, the solid line indicates the performance of the unit as predicted by the basic friction-factor model. It can be seen that the correlation of the experimental results is reasonable, especially at the higher volume flow rates.

From the flow-rate efficiency curves, Fig. 5, it is clear that as expected, the efficiency of momentum transfer is low, with the maximum efficiency being of the order of 14 percent (at the maximum speed tested). The torque available at the disc to drive the air through the unit has been calculated from the hypothetical flow model.

Heat Exchanger Characteristics

The results of the experimental work aimed at assessing the heat exchange capability of the unit are tabulated in Fig. 6. The effectiveness is shown in two forms: the standard temperature effectiveness η_T and the heat exchanger effectiveness η_{HT}.

For a perfectly insulated heat exchanger, one may write

$$C_c(T_{c2} - T_{c1}) = C_h(T_{h2} - T_{h1})$$

so that the overall heat transfer effectiveness can be simultaneously evaluated from the equations

$$\eta_{HT} = \frac{C_c}{C_{\min}} \cdot \frac{(T_{c2} - T_{c1})}{(T_{h1} - T_{c1})}$$

or

$$\eta_{HT} = \frac{C_c}{C_{\min}} \cdot \frac{(T_{h1} - T_{h2})}{(T_{h1} - T_{c1})}$$

Because of the heat losses from the present system, the equivalence of the two defining equations is not justified. As the main interest in this series of tests has rested on the thermal energy transfer to the cold stream, the first equation will be used to evaluate η_{HT}.

Although it is realized that leakage of the working fluid through the flexible seals would affect the test results, it is felt that this leakage flow would be negligible because of the small available pressure differential.

It can be seen from the tabulation given in Fig. 6 that the heat exchange effectiveness η_{HT} varies from a minimum of 26 percent for the test run at 1030 rpm (R_m = 120) to a maximum value of 40 percent for the test run at 1030 rpm (R_m = 0.50). The variation of η_{HT} with rotational speed for any fixed value of R_m is slight over the range of speeds tested, but there is a marked decrease of η_{HT} with increasing R_m for all the speeds tested.

As can be seen from the curves plotted in Fig. 6, however, there appears to be a minimum point for each of these curves in the region where R_m varies from 1.0 to 1.2, after which there is a recovery of η_{HT} with increasing R_m.

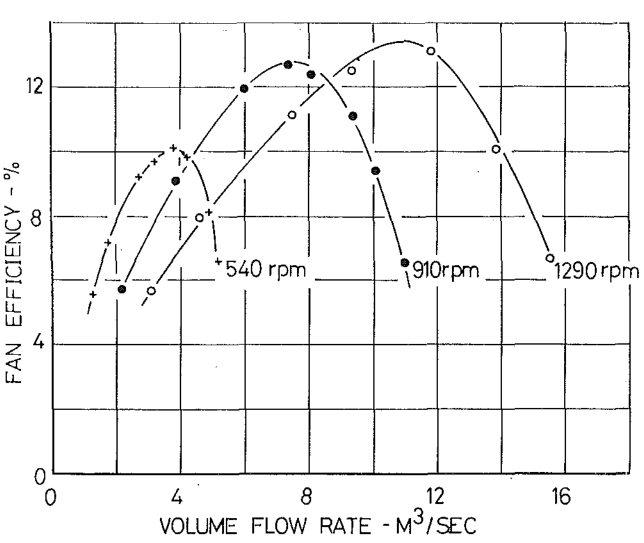

Fig. 5 Flow rate versus efficiency curves

TESTS RESULTS - HEAT EXCHANGE EFFECTIVENESS

Rotor Speed (rpm)	R_m	η_{Tc}	η_{Th}	η_{HT}
700	.77	.33	.33	.33
700	.91	.28	.36	.28
700	1.27	.24	.38	.31
Av. 700				
1020	.50	.40	.32	.40
1020	.80	.29	.35	.29
1050	1.20	.21	.39	.26
1030	1.32	.21	.37	.28
Av. 1030				
1320	.48	.37	.32	.37
1310	.97	.29	.36	.29
1300	1.13	.26	.36	.30
1310	1.28	.25	.33	.32
Av. 1305				
1570	.54	.39	.31	.39
1570	.85	.32	.34	.32
1580	1.13	.27	.33	.31
Av. 1570				

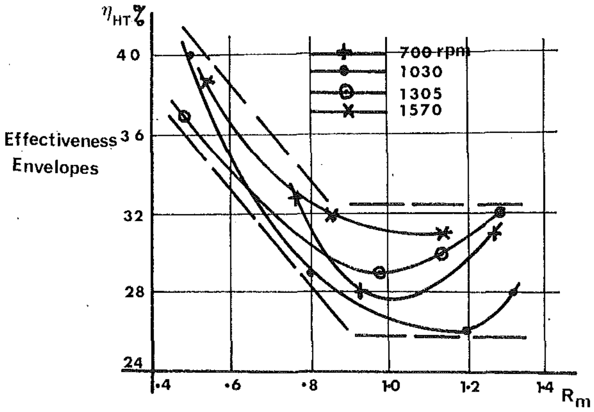

Fig. 6 Heat exchanger test characteristics

Conclusion

The test unit functioned successfully in the dual role of a fan and a heat exchanger. Under the test conditions imposed, the maximum efficiency as a fan was of the order of 14 percent, and the maximum effectiveness as a heat exchanger was of the order of 40 percent. It is clear that in either individual capacity the efficiency figures are relatively low. It should be stressed that the main advantages of the unit lie in the design simplicity and the compact nature of the plant, which is capable of assuming the combined duties of a heat exchanger and two fans (or pumps).

The unit under test was built purely to assess the feasibility of operation and ease of construction of the composite shear fan/heat exchanger. No particular attention was paid to obtaining a high-performance unit. Some possible improvements would include the following: (1) increased hub-to-disc diameter for the rotor to take advantage of the high shear conditions toward the periphery; (2) increased number of discs per unit length of shaft to provide a greater shear area; (3) improved finger seals; (4) consideration of the advantages to be gained by multi-staging near the hub under high-load conditions. This flow phenomenon may well account for some of the discrepancy between the experimental and the predicted results. The best correlation was obtained using a model based on turbulent-boundary-layer theory, although the simpler model developed may well be adequate for most engineering purposes.

Acknowledgments

The authors would like to acknowledge the assistance of C.S.I.R.O., Mechanical Engineering Div., Highett, Victoria, Australia. In addition, thanks are due to Prof. P. W. Whitton and the Mechanical Engineering Department of the University of Melbourne, Victoria, Australia.

References

1 Tesla, N., "Turbine," United States patent No. 1,061,206, May 6, 1913.

2 "The Tesla Turbine," *Scientific American*, Sept. 1911, pp. 296–297.

3 "Bladeless Turbines," *Engineering* (London), Nov. 1911, pp. 637.

4 von Karman, T., "Über Laminare und Turbulente Reibung," *Z. Angew. Math. Mech.*, Vol. 1, 1921, pp. 233–252.

5 Cochran, W. G., "The Flow Due to a Rotating Disc," *Proceedings Cambridge Phil. Soc.*, Vol. 30, 1934, pp. 365–375.

6 Goldstein, S., "On the Resistance to Rotation of a Disc Immersed in a Fluid," *Proceedings Cambridge Phil. Soc.*, Vol. 31, 1935, pp. 232–241.

7 Hasinger, S. H., and Kehrt, L. G., "Investigation of a Shear-Force Pump," *Journal of Engineering for Power*, Trans. ASME, Series A, Vol. 85, No. 3, July 1963, pp. 201–207.

8 Schultz-Grunow, F., "Der Reibungswiederstand rotierender Scheiben in Gehäusen," *Z. Angew. Math. Mech.*, Vol. 15, 1935, pp. 191–204.

9 Okaya, T., and Hasegawa, M., "On the Friction to the Disc Rotating in a Cylinder," *Japanese Jnl. Physics*, Vol. 13, 1939, pp. 29–38.

10 Dorfman, L. A., "Hydrodynamic Resistance and the Heat Loss of Rotating Solids," Oliver & Boyd, 1963.

11 Soo, S. L., "Laminar Flow Over an Enclosed Rotating Disk," Trans. ASME, Vol. 80, 1958, pp. 287–296.

12 Daily, J. W., and Nece, R. E., "Chamber Dimension Effects on Induced Flow and Frictional Resistance of Enclosed Rotating Disks," *Journal of Basic Engineering*, Trans. ASME, Series D, Vol. 82, No. 1, Mar. 1960, pp. 217–232.

13 Iversen, H. W., "Performance of the Periphery Pump," Trans. ASME, Vol. 77, Jan. 1955, pp. 19–28.

14 Senoo, Y., "Theoretical Research on Friction Pumps," *Reports of the Research Institute for Fluid Engineering*, Japan, Vol. 1, 1948.

15 Wilson, W. A., Santalo, M. A., and Oelrich, J. A., "A Theory of the Fluid-Dynamic Mechanism of Regenerative Pumps," Trans. ASME, Vol. 77, Nov. 1955, pp. 1303–1316.

16 Balje, O. E., "Drag-Turbine Performance," Trans. ASME, Vol. 79, Aug. 1957, pp. 1291–1304.

17 Rice, W., "An Analytical and Experimental Investigation of Multiple Disk Pumps and Compressors," *Journal of Engineering for Power*, Trans. ASME, Series A, Vol. 85, No. 3, July 1963, pp. 191–200.

18 Dunkle, R. V., "A Shear Fan Heat Exchanger," unpublished paper presented at 4th A.I.N.S.E. Conference, Lucas Heights, N.S.W., Australia, 1969.

L. H. RUSSELL
Research Engineer.

J. A. CANFIELD
Research Physicist.

Naval Weapons Laboratory,
Dahlgren, Va.

Experimental Measurement of Heat Transfer to a Cylinder Immersed in a Large Aviation-Fuel Fire[1]

Presented are the results of an experimental effort to quantify some of the heat transfer parameters pertaining to the luminous flame that results from the uncontrolled combustion of an 8-ft × 16-ft pool of JP-5 aviation fuel. The temperature and effective total radiant heat flux, both as temporal mean quantities, were measured as functions of position within the quasi-steady burning flame as it existed in a quiescent atmosphere. A grid of infrared radiometers and radiation-shielded thermocouples served as the primary sensing equipment. A determination was made of the perimeter-mean convection coefficient applicable to a horizontally oriented, smooth, 8.530-in-dia circular cylinder immersed at a particular location within the JP-5 flame. The value of this coefficient was the result of a solution to a nonlinear, inverse conduction problem in which the convective heat flux at the cylinder surface was estimated by utilizing a measured temperature history inside the cylinder. An expression relating this coefficient to more general flame/cylinder systems was developed.

Introduction

THE IMMEDIATE GOAL of the research effort was to gain practical information about the heat flow boundary conditions applicable to an object enveloped by a large, luminous aviation-fuel fire. The present investigation dealt specifically with the luminous flame resulting from the uncontrolled combustion of an 8-ft × 16-ft pool of JP-5 jet fuel. This fuel has a kerosene base, and its composition is defined in the military specifications labeled MIL-T-5624G, 25 September 1962, and MIL-T-5624G amendment 1, 21 November 1966. Some of the properties of JP-5 are compiled in [1].[2] All the experimental results of the testing program have application to flames in quiescent atmospheres. The first phase of experimentation included the measurement, on a temporal mean basis, of the temperature and the effective total radiant heat flux, both as functions of position in the flame. The second phase concerned the determination of the perimeter-mean convection coefficient relevant to a smooth 8.530-in-dia circular cylinder immersed at one particular location and orientation within the flame.

The choice of instruments and the configuration of the test vehicles were based upon the premise that for flames in a quiescent environment, quasi-steady burning exists during the relatively long time interval between the end of flame buildup and the beginning of flame exhaustion. As used previously, the term quasi-steady burning implies that from a practical standpoint the temporal means of certain flame properties can be considered essentially invariant with time.

Because of the work of others [2–4], it was also assumed that with an 8-ft × 16-ft fuel pan the regression rate of the fuel surface during the quasi-steady burning interval would approximate the burning rate applicable to a larger fuel pan. Thus the purpose of the testing was to determine some thermal energy transport characteristics that would apply to one particular size of unconfined JP-5 flame. However, it is believed that the results might also be useful in describing larger JP-5 flames.

Mathematical Model

Consider an infinitely long, spatially fixed, circular cylindrical tube that is oriented within a moving fluid medium such that the flow direction is normal to the axis of the cylinder. Both the fluid approach velocity and the fluid free-stream temperature are constant. Diffuse thermal radiation of constant intensity is in-

---

[1] Portions of this paper were based on an MS thesis submitted by the first author to the University of Pittsburgh, Pittsburgh, Pa.

[2] Numbers in brackets designate References at end of paper.

Contributed by the Heat Transfer Division of THE AMERICAN SOCIETY OF MECHANICAL ENGINEERS and presented at the ASME-AIChE Heat Transfer Conference, Atlanta, Ga., August 5–8, 1973. Manuscript received by the Heat Transfer Division April 15, 1971. Paper No. 73-HT-2.

cident on the entire outer tube boundary. During the limited time interval in which the cylinder is immersed, assume that one perimeter-mean surface heat transfer coefficient can be used in quantifying the convective mechanism of heat transfer between the fluid and the outer cylindrical surface. Regard the inner tube surface as being insulated such that no heat flows across this boundary. At some particular time shortly after the initial immersion of the cylinder, the wall temperature distribution of the tube is known. Finally, consider only radial heat conduction as having significance to the problem.

Since the radii of curvature of the inner and outer tube boundaries are relatively large, the partial differential equations describing the foregoing problem can be satisfactorily constructed on the basis of a cartesian coordinate system. Thus a flat-plate analog can represent a section of the cylindrical tube, and the governing equation can be written as

$$\frac{1}{\alpha}\frac{\partial T}{\partial t} = \frac{1}{k}\frac{\partial k}{\partial x}\frac{\partial T}{\partial x} + \frac{\partial^2 T}{\partial x^2} \tag{1}$$

The boundary conditions, with heat flow into the plate defined as positive, are as follows:

$$\text{at} \quad x = 0,\ -k\frac{\partial T}{\partial x} = aq_{ir} - \epsilon\sigma T_s^4 + h(T_\infty - T_s) \tag{2}$$

$$\text{at} \quad x = l,\ \frac{\partial T}{\partial x} = 0 \tag{3}$$

The initial condition is

$$\text{at} \quad t = 0,\ T = T(x); \qquad 0 \le x \le l \tag{4}$$

To facilitate a determination of the transient temperature distribution within the flat-plate analog, equations (1)–(4) can be recast into a simple finite difference system which allows an explicit method of solution. The equations comprising the difference formulation can be found in [5]. In the difference scheme, the width of all interior sub-volumes is Δx, and the time increment is Δt. The initial temperature distribution becomes a set of discrete temperatures, $T_{i,0}$, which represent the temperature of each plate node point at time $t = 0$.

If for a certain situation the parameters $k(T)$, $\alpha(T)$, ϵ, a, q_{ir}, T_∞, and $T_{i,0}$ are all known, and if Δx and Δt are chosen such that a proper stability criterion is maintained, a finite-difference solution for some particular time t^* can be determined once a value for the convection coefficient is established. Of course, such a calculated nodal temperature distribution would be erroneous unless, by the remotest chance, the value chosen for the convection coefficient happened to be that particular one having application to the situation under analysis. However, if at time t^* the temperatures of several node points within the flat-plate analog are exactly known, the degree of disparity between the known and computed temperatures at the specified nodes can be used as the criterion for evaluating the applicability of the estimated value of h.

The degree of disparity, at any specific time t^*, between the mathematically predicted and the known temperatures at four monitor node points can be quantitatively expressed as

$$\eta = \sum_{i=1}^{4} (T_{ci} - T_{mi})^2 \tag{5}$$

At any time t^*, the plate temperature distribution calculated by the finite-difference technique is entirely dependent upon the guessed value of h only after all other system parameters have been specified. For this special case, the degree of disparity η can be thought of as a function of h alone; that is, $\eta = \eta(h)$. Thus, to identify the convection coefficient having application to a specific situation, it is necessary only to determine the value of h that minimizes $\eta(h)$.

In the solution to this optimization problem, the true minimum will not be determined; rather, it will be established that the true minimum lies within an uncertainty interval either to the right or left of the calculated minimum. By using the Fibonacci search technique devised by Kiefer [6], the interval of uncertainty is reduced to less than 1 percent of the original search interval after the placement of only 11 search points.

Experimental Apparatus and Procedures

The construction of the fuel pan that was used in both phases of the testing program is indicated in Fig. 1. Also, the defining coordinate system to which all the experimental results will be related is shown in this figure.

A carriage was constructed to transport the test-instrument packages into and out of the flames. Instrument packages mounted on this carriage included equipment to sense the flame temperature and the radiant heat flux. Flame temperatures were measured by thermocouples constructed from standard-

Nomenclature

a = total hemispherical absorptivity
b = a constant whose value depends on cylinder profile and Reynolds number
h = convection or surface heat transfer coefficient
h_m = perimeter-mean convection coefficient applicable to a cylinder subject to the transverse flow of a fluid
k = thermal conductivity of a solid
k_f = thermal conductivity of a fluid at the film temperature
L = diameter or width of a cylinder taken perpendicular to the flow direction
l = thickness of the flat-plate analog
n = an exponent whose value depends on cylinder profile and Reynolds number
Pr_f = Prandtl number of a fluid at the film temperature
q_c = approximate convective heat flux
q_{ir} = incident total radiant heat flux
q_r = approximate net total radiant heat flux
Re = Reynolds number, $LV_\infty\rho_f/\mu_f$
T = temperature
T_{ci} = any one of the computer-calculated values representing, at a specific time, the temperature of a monitor node point within the central-section wall
$T_{i,0}$ = a set of discrete temperatures representing an initial temperature distribution
T_{mi} = any one of the monitor node temperatures measured within the central-section wall at a specific time
T_s = surface temperature of a solid
T_∞ = free-stream fluid temperature
t = time
t^* = a particular time
V_∞ = free-stream fluid velocity
X = a coordinate defined in Fig. 1
x = depth within the flat-plate analog
Y = a coordinate defined in Fig. 1
Z = a coordinate defined in Fig. 1
α = thermal diffusivity
Δt = time increment
Δx = space increment
ϵ = total hemispherical emissivity
η = degree of disparity, defined in equation (5)
ρ_f = density of a fluid at the film temperature
μ_f = absolute viscosity of a fluid at the film temperature
σ = Stefan-Boltzmann constant
ϕ = a ratio given by L/L_0

Subscripts

0 = actual test situation

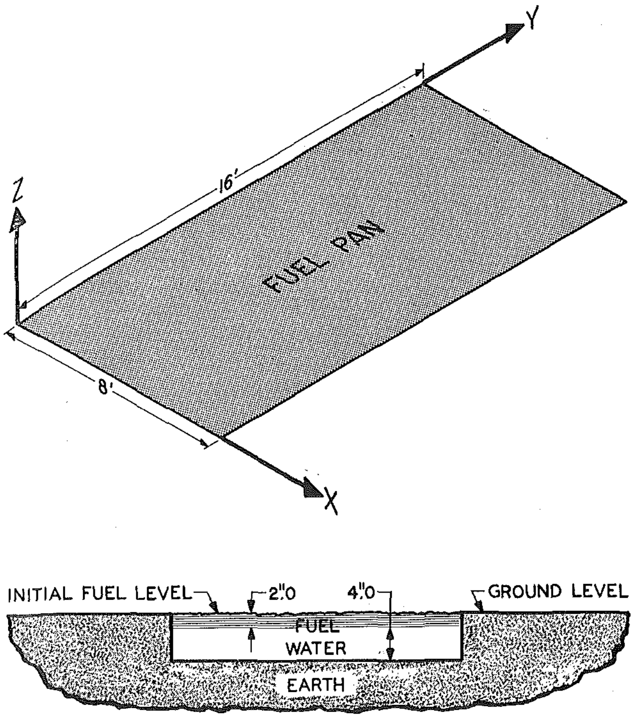

Fig. 1 Coordinate-system definition and fuel-pan construction

grade, 28-gage chromel–alumel wires mounted in $^1/_8$-in-dia stainless-steel sheaths and insulated with magnesium oxide. They were shielded against radiation losses by three concentric, open-ended, circular cylindrical tubes fabricated from 0.003-in-thick stainless-steel foil. The radiant heat flux within the flame was measured by Gardon-type radiometers [7]. The sensing element, a circular constantan foil, was coated with colloidal graphite and was recessed into the copper body so as to give a 20-deg viewing angle. A 1-mm-thick sodium chloride crystal was located directly in front of the foil. This crystal effectively eliminated the response of the sensor to convective heat flux while allowing infrared radiant energy in the 1- to 15-μ wavelength region to pass readily through to the sensor. When a radiometer was used in the flame environment, soot-particle precipitation onto the salt window was prevented by purging the viewing portal with a very low velocity nitrogen gas stream. Each radiometer was calibrated both before and after a field test in order to determine whether or not its sensitivity had been altered by the flame environment. This procedure revealed that no important changes in radiometer sensitivities were caused by immersion in the flame.

The configuration of the radiometers and thermocouples mounted in instrument packages that were used in the first experimental phase is described in [5]. The experimental apparatus used in the second testing phase consisted of an extensively instrumented three-component cylinder.

The specific function of the central section of this cylinder was to respond to the JP-5 flame in a manner analogous to the hypothetical response of the infinite cylindrical tube when that tube is subjected to the moving fluid medium described in the mathematical model. The wall thickness, outside diameter, and length of the type-304 stainless-steel central section were 0.840, 8.530, and 12.0 in. respectively. To provide the central section with a surface having an emissivity and absorptivity each equal to 0.99, it was coated with a layer of JP-5 soot having a thickness of 0.001 to 0.002 in. At each end of the central section there was an insulation plug that thermally isolated the central section from the instrument sections.

To determine temperature–time histories, four sets of monitor thermocouples were embedded within the central-section wall. The thermocouple junctions of each set were located at the outer cylindrical surface and at 0.08, 0.42, and 0.60 in. from the outer boundary. The four thermocouple sets were angularly removed from each other by 90 deg. Premium-grade 30-gage chromel–alumel wires were utilized in the construction of the monitor thermocouples (see [5] for fabrication details).

The instrument sections were designed to perform two specific functions. First, they were to yield the radiant heat flux that could be considered incident on the surface of the central section. Second, they were to indicate the temperature that could be considered to apply to the local flame region about the central-section periphery. Each instrument section contained four radiometers and four flame thermocouples.

When the completely assembled test cylinder was in its correctly deployed position, the cylinder was parallel to the long axis of the 8-ft × 16-ft fuel pan, and its centerline was 4 ft above the initial fuel surface. Also, the axial midpoint of the cylinder was directly above the geometric center of the fuel pan. As were the instrument packages used in the first phase of the experimental program, the test cylinder was introduced into a fire 90 sec after fuel ignition.

Results and Analysis

Some results obtained from the field tests performed in the first phase of the experimental program are presented in Figs. 2 and 3. Flame characteristics in the X–Z plane for Y equal to 8 ft are shown in Fig. 2. In Fig. 3, flame characteristics in the Y–Z plane at X equal to 4 ft are presented. To construct the isotherms in these figures, it was first assumed that the flame temperature varied linearly between those points where the temperature had actually been measured. Then the assumption of symmetry was invoked. In each figure, the temperature and total incident radiant heat flux, both as temporal mean quantities that were determined by a radiometer–thermocouple pair, are indicated for particular spatial locations.

Although it would have been highly desirable to have computed each temporal mean value on the basis of experimental replication, the information associated with any particular spatial location was determined within the quasi-steady burning interval of a single pan burn. The time periods over which the instrument outputs were averaged ranged from a minimum of 20 sec to a maximum of 120 sec. If the flame temperature and incident radiant heat flux relevant to a given point and determined from a 2-min time span were designated R and RR, respectively, then the temperature and flux for the same point but averaged over any 20-sec interval within the 120-sec time period would be within $R \pm 0.02R$ and $RR \pm 0.05RR$, respectively.

Flame characteristics in the X–Z plane for Y equal to 3, 4, 6, and 12 ft are presented in [5]. The weather conditions during the tests were as follows: wind was nonexistent; relative humidity was 100 percent; ambient temperature ranged from 54 to 73 deg F; barometric pressure varied between 29.77 and 30.12 in. of mercury.

Within the 1500 deg F envelope of the test flames, the magnitude of the radiant flux incident on the face of a radiometer was nearly equal to the flux that would be given by a blackbody radiator at the local flame temperature as measured by the thermocouple in the neighborhood of the radiometer. For each of the investigated points that had a temperature 1500 deg F or higher, the ratio of the measured flux to the calculated flux was computed. If perfect correlation between these two quantities had existed, all the ratios would have been unity. However, good correlation did exist and 21 of 24 points had ratios that fell within 1.00 ± 0.27.

Observation of the oscillograph records indicated that within the flame volume bounded by the Z = 3-ft plane and the Z = 9-ft plane the deviations from the means of the measured flame properties were noticeably periodic. The oscillatory aspect of the test flames was also visibly apparent in this region. Here, intensely

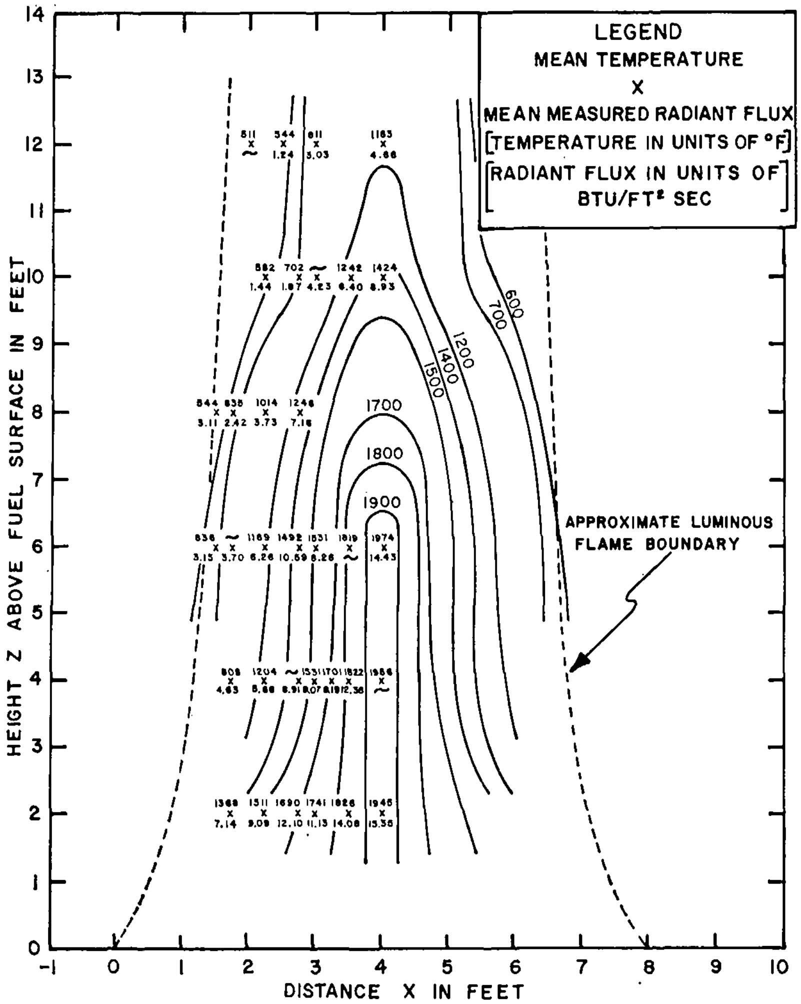

Fig. 2 Flame characteristics at $Y = 8$ ft

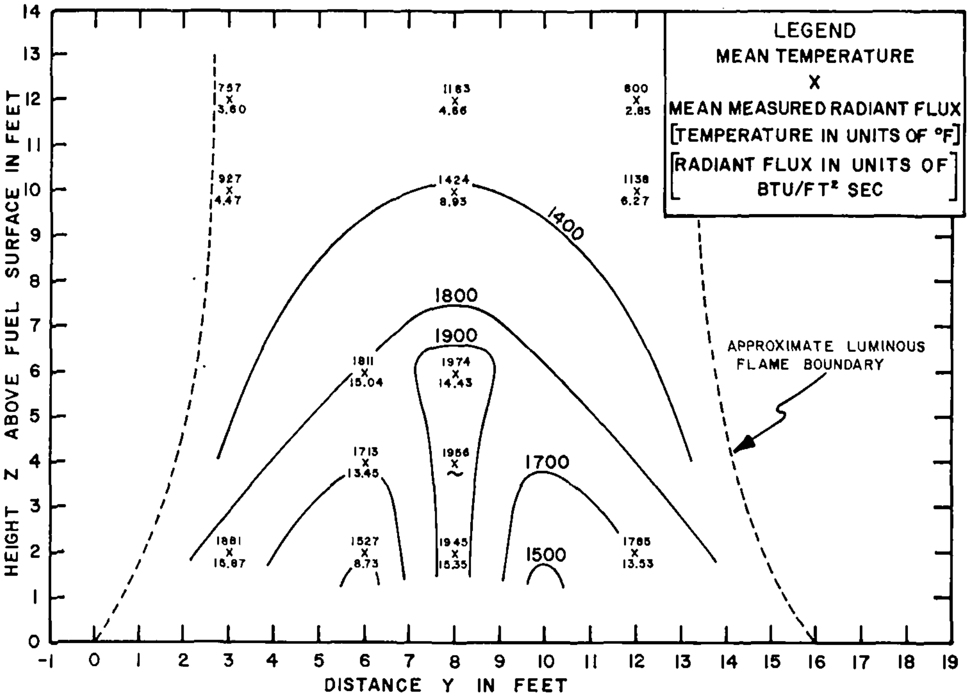

Fig. 3 Flame characteristics at $X = 4$ ft

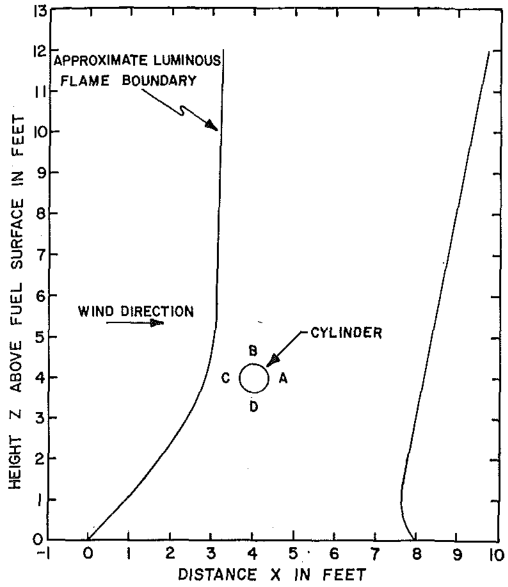

Fig. 4 Position of test cylinder in wind-translated flame

burning balls of fire regularly appeared. A frame-by-frame analysis of the motion-picture records indicated that the gross upward velocity of the fire balls could be estimated as being between 12 and 18 fps.

It is believed that the primary results obtained from the second phase of the experimental program have relevance to flames in a quiescent environment, even though the field test was conducted in a very slight surface wind. In Fig. 4 the position of the test cylinder in the wind-translated flame is schematically shown. The weather conditions at test time were as follows: wind was 1 mph; relative humidity was 100 percent; ambient temperature was 38 deg F; barometric pressure was 30.21 in. of mercury. During flame envelopment, a soot deposit of about 0.001 in. developed on the entire outer surface of the test cylinder. Hence the JP-5 soot layer on the central section had an average final thickness of slightly more than 0.002 in.

The point in time that was considered $t = 0$ actually occurred 20 sec after the test cylinder reached its correct position about the fuel pan. Data from the radiometers and flame thermocouples were analyzed for two specific time intervals, $t = 0$ to $t = 20$ sec and $t = 0$ to $t = 150$ sec. By taking the appropriate averages of the results yielded by the individual flame thermocouples and radiometers, it was possible to determine the flame temperature and incident radiant heat flux that could be considered applicable to each of the four areas on the central section where the wall temperature was being monitored. These four specific areas are indicated in Fig. 4 by the letter symbols A, B, C, and D. For both time periods of interest, Table 1 shows the incident radiant heat flux and flame temperature relevant to each of the four central-section surface areas.

Shown in Fig. 5 is the wall temperature distribution at $t = 0$ for each of the four important central-section locations. The symbols in the figure represent the temperatures given by the central-section monitor thermocouples; the curves represent extrapolations through the symbols. In order to establish the four sets of points through which these curves could be drawn with reasonable ease and confidence, the surface temperature at location B and the four temperatures at the inner cylindrical surface were determined by careful physical–mathematical estimation. A detailed description of this procedure can be found in [5].

It had been anticipated that in a quiescent environment and at any given time the test deployment scheme would have yielded an essentially uniform total heat flux passing through the outer surface of the central section. However, because an unavoidable slight surface wind caused an unsymmetric flame/cylinder system, this expectation was not realized. A single wall temperature distribution could not satisfactorily characterize the thermal response of the central section at a particular time after flame envelopment. Hence, separate convection coefficients applicable to two different time intervals were determined for each of the locations A, B, C, and D that were identified in Fig. 4. These time intervals were from $t = 0$ to $t = 20$ sec and from $t = 0$ to $t = 150$ sec.

The computer-optimized temperature distributions that best fit the monitor node temperatures at $t = 20$ sec are shown in Fig. 6. Adjacent to and responsible for the curves in this figure are the values of the convection coefficients that minimized $\eta(h)$ for each particular central-section location. To determine the two perimeter-mean convection coefficients applicable to the central

Table 1 Incident radiant heat fluxes and flame temperatures pertinent to specific test-cylinder surface areas

Location Reference Letter	Measured Incident Radiant Flux ~ (q_{ir}) [BTU/ft^{2}sec]	Measured Flame Temperature ~ (T_∞) [°F]
Results for the 0 to 20 second time interval		
A	12.71	1658
B	4.20	1281
C	1.56	1097
D	9.08	1474
Results for the 0 to 150 second time interval		
A	11.67	1623
B	4.00	1266
C	1.48	1114
D	8.71	1472

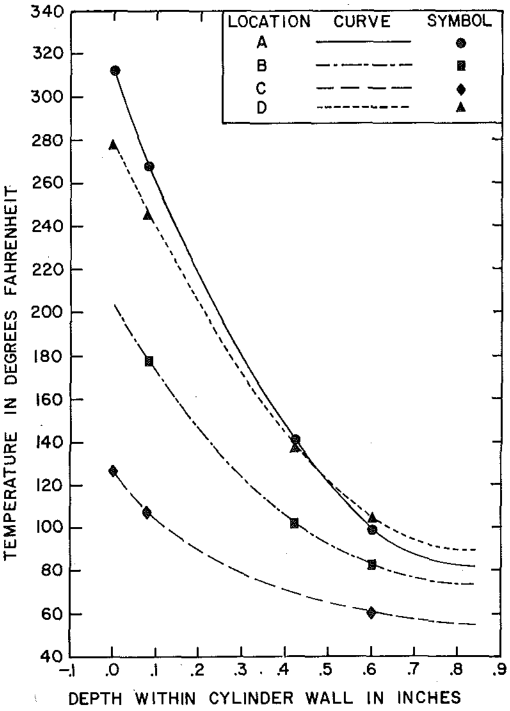

Fig. 5 Initial temperature distribution

section, the values of h relevant to each of the time intervals were averaged together. This operation yielded 9.88 and 8.07 Btu/hr-ft²-deg F for the 20-sec and 150-sec time periods respectively. However, during the small time interval, the actual test circumstance was definitely more like the hypothetical situation described in the mathematical model. Hence the value of 9.88 Btu/hr-ft²-deg F is considered more reliable.

To put the calculated values of the average convection coefficients in proper perspective, an investigation was made of the relationship between these coefficients and other average coefficients determined for an 8.530-in-dia circular cylinder having certain individual gases flowing normal to its axis. Each gas was considered to be undergoing no chemical reactions. The approach velocity of the flowing gases was considered 15 fps. This was the average of the visibly determined gross upward velocity of the previously described fire balls. The general correlation equation (from [8]) that was used to determine the comparative perimeter-mean convection coefficients was

$$\frac{h_m L}{k_f} = 1.12\, b \left(\frac{L\, V_\infty \rho_f}{\mu_f}\right)^n (\mathrm{Pr}_f)^{1/3} \qquad (6)$$

For circular cylinders, b and n are, respectively, 0.174 and 0.618, when Re is between 4000 and 40,000; for Re between 40,000 and 250,000, b and n are 0.0239 and 0.805, respectively.

The gases used for comparative purposes were chosen because they were felt to be representative of the kinds of gases that could have been detected in the local flame volume surrounding the central section of the test cylinder. Each of these gases considered in the comparison had its properties evaluated at a pressure of 1 atm and a temperature of 812 deg F. This temperature was the time-averaged film temperature pertinent to the entire central-section surface during the 20-sec time interval. The computed values of the perimeter-mean convection coefficients associated with the various gases are presented in Table 2.

Table 2

Chemical Formula	Substance	h_m [BTU/hr ft²°F]	Chemical Formula	Substance	h_m [BTU/hr ft²°F]
———	dry air	2.80	C_7H_{16}	2-methylhexane	14.65
N_2	nitrogen	2.75	C_8H_{18}	octane	15.18
CO	carbon monoxide	2.69	C_8H_{18}	isooctane	16.21
H_2O	water vapor	3.48	C_8H_{18}	2-methylheptane	16.05
CH_4	methane	5.59	C_2H_2	acetylene	4.39
C_2H_6	ethane	6.80	C_2H_4	ethylene	5.91
C_3H_8	propane	8.29	C_3H_6	propylene	7.15
C_4H_{10}	butane	10.18	C_6H_6	benzene	9.96
C_4H_{10}	isobutane	10.59	CH_4O	methanol	4.88
C_5H_{12}	pentane	12.24	C_2H_6O	ethanol	6.62
C_5H_{12}	isopentane	12.07	C_3H_8O	propanol	8.30
C_6H_{14}	hexane	13.08	$C_4H_{10}O$	butanol	9.58
C_6H_{14}	isohexane	13.14	C_3H_6O	acetone	7.14
C_7H_{16}	heptane	14.15	C_2H_4O	ethylene oxide	5.28

In order to predict accurately the thermal response of an object immersed in a luminous uncontrolled JP-5 flame, it is advisable to consider that both radiation and convection have significance in the overall mechanism of heat transfer. To emphasize this statement, a comparison was made utilizing the approximate convective and net radiant heat fluxes, q_c and q_r, that passed through the central-section surface at locations A, B, C, and D and acted during the 20-sec time interval. To calculate each q_c and q_r, the following equations were used:

$$q_c = h\left[T_\infty - \left(\frac{T_s\,(t = 0) + T_s\,(t = t_{\mathrm{end}})}{2}\right)\right] \qquad (7)$$

$$q_r = 0.99\left[q_{ir} - \sigma\left(\frac{T_s\,(t = 0) + T_s\,(t = t_{\mathrm{end}})}{2}\right)^4\right] \qquad (8)$$

The term T_s $(t = 0)$ represents the initial surface temperature at one of the central-section locations; the term T_s $(t = t_{\mathrm{end}})$ represents the computer-optimized surface temperature for a given location at $t = 20$ sec. The ratios $q_c/(q_c + q_r)$ applicable to locations A, B, C, and D were found to be 0.173, 0.483, 0.628, and 0.275, respectively. Results similar to these but relevant to cylindrical ordnance enveloped by large JP-5 fires have also been determined by the authors and are available in [9].

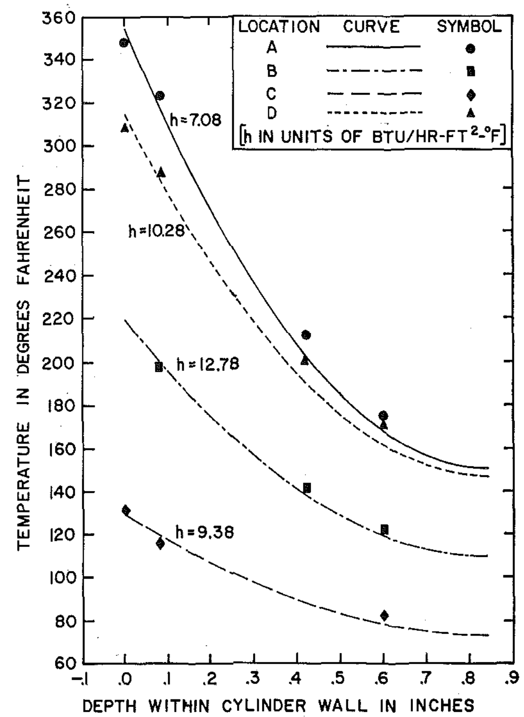

Fig. 6 Temperature distribution at $t = 20$ sec

Discussion of Errors

For each field test performed in the two-phase experimental program, assume that temperature sensors and total incident radiant heat flux indicators, both optimally accurate instruments, had been used in place of the radiation-shielded thermocouples and the Gardon radiometers. It is believed that the "true" temporal mean temperatures and fluxes indicated by such optimal instruments would have been within ±5 percent and ±10 percent respectively of the time-averaged local flame temperatures and total incident radiant heat fluxes indicated by the instruments actually employed. The statement of error about the temporal mean heat-flux measurements is made with the realization that the calibration technique allowed a radiometer to respond accurately only to those test situations where diffuse radiation of constant intensity was uniformly incident on a radiometer face. For all the points within the luminous flame envelope that were investigated during the first testing phase, the average percentage standard deviations associated with the temporal mean temperatures and fluxes were 6 and 30 percent, respectively. In the experiment to determine convection coefficients, the average percentage standard deviations associated with the temporal means yielded by individual flame thermocouples and radiometers were respectively 2 and 37 percent for the 20-sec time interval and 6 and 38 percent for the 150-sec time period.

The finite-difference formulation used in determining the convection coefficients applicable to the four central-section locations did not consider the angular heat conduction within the cylinder wall. Hence some error in the local values of the convection coefficients was introduced by forcing the computer-optimized temperature distributions to be functions of only one space dimension. The net quantity of heat leaving or coming to a given location via angular conduction governed the sign and magnitude of the error associated with the calculated value of h applicable to that locality. However, the errors in the two calculated values of the perimeter-mean convection coefficients were much less dependent upon the neglect of angular heat conduction in the central-section wall. This was because the artificially high and low values of the computer-determined local coefficients tended to compensate one another when they were averaged together to get each perimeter-mean convection coefficient.

In order to establish some type of confidence limit for the best value of the perimeter-mean convection coefficient, a perturbation analysis was conducted. The objective of this analysis was to determine logical high and low values of h applicable, during the 20-sec time interval, to each of the four central-section locations. Pursuant to this goal, the independent variables relevant to a given locality and the 20-sec time period were perturbed from their best experimental or literature values by amounts equal to plus or minus their uncertainty intervals. To be consistent in the analysis, the odds were considered 5 to 1 that the true value of each independent variable would have been within $m \pm w$, where m represents the best value of any particular independent variable and w represents its uncertainty interval.

To determine the limiting values of h for a given location, the appropriate set of perturbed independent-variable values was read into the computer program as data. The computer program then minimized the degree of disparity between the perturbed monitor node temperatures and the geometrically similar mathematically predicted nodal temperatures. The magnitude of h that accomplished this optimization process became a limiting value for the convection coefficient applicable to the given location. Averaging the four low and the four high local coefficients yielded 5.17 Btu/hr-ft²-deg F and 15.80 Btu/hr-ft²-deg F, respectively. Thus the limiting values of the perimeter-mean convection coefficient relevant to the 20-sec time period can be conveniently expressed as $9.88\,^{+5.92}_{-4.73}$ Btu/hr-ft²-deg F.

Possible Generalizations

It would be beneficial to be able to relate the best experimental value of the perimeter-mean convection coefficient to flame/cylinder systems more general than the one investigated. In particular it would be of considerable advantage to relate this coefficient to various sizes of circular and noncircular cylinders that might be immersed within JP-5 flames somewhat larger than the test flame. It will be shown that such extrapolations are indeed possible, but only after certain very restrictive assumptions have been made.

There is some evidence [10–13] that equation (6), with the appropriate sets of n and b values, should adequately correlate the data for the convective heat transfer between an immersed cylinder and a flame region having no substantial dissociation–recombination reactions. Hence, assume that simple convection theory, as represented by equation (6) with b equal to 0.0239 and n equal to 0.805, is applicable to the system composed of the circular test cylinder and the luminous JP-5 test flame. This assumption implies that the Reynolds number for this particular situation is between 40,000 and 250,000. To conclude whether or not it is reasonable to expect that the Reynolds number falls within such a range, this distinctive form of equation (6) was solved for the Reynolds number after h_m, L, Pr_f, and k_f had been numerically designated. The value representing h_m was the experimentally determined perimeter-mean convection coefficient for the 20-sec time interval. The value taken for L was the outside diameter of the circular test cylinder. On the basis of considering the flame gases about the test cylinder as a nonreacting mixture of combustion products, k_f and Pr_f were estimated as having the values 0.0350 Btu/hr-ft-deg F and 0.740, respectively. For these particular system parameters, the Reynolds number was found to be 73,725. Hence, providing that the estimates made for Pr_f and k_f are satisfactory, it seems reasonable to expect that the form of equation (6) applicable to the actual test situation is the correlation pertinent to circular cylinders and a Reynolds number range of 40,000 to 250,000.

Table 3

Flow Direction And Profile	Range Of Re		b	n	h_m [BTU/hr ft^2°F]	Range Of ϕ	
	From	To				From	To
→ ◇	5,000	100,000	0.222	0.588	$8.06\ \phi^{-0.412}$	0.068	1.356
→ ⬭	2,500	15,000	0.224	0.612	$10.65\ \phi^{-0.388}$	0.034	0.203
→ ○	4,000	40,000	0.174	0.618	$8.84\ \phi^{-0.382}$	0.054	0.543
→ ◇	2,500	7,500	0.261	0.624	$14.19\ \phi^{-0.376}$	0.034	0.102
→ ⬣	5,000	100,000	0.138	0.638	$8.78\ \phi^{-0.362}$	0.068	1.356
→ ⬡	5,000	19,500	0.144	0.638	$9.16\ \phi^{-0.362}$	0.068	0.264
→ □	5,000	100,000	0.092	0.675	$8.86\ \phi^{-0.325}$	0.068	1.356
→ □	2,500	8,000	0.160	0.699	$20.16\ \phi^{-0.301}$	0.034	0.109
→ |	4,000	15,000	0.205	0.731	$36.98\ \phi^{-0.269}$	0.054	0.203
→ ⬡	19,500	100,000	0.0347	0.782	$11.08\ \phi^{-0.218}$	0.264	1.356
→ ⬯	3,000	15,000	0.085	0.804	$34.75\ \phi^{-0.196}$	0.041	0.203
→ ○	40,000	250,000	0.0239	0.805	$9.88\ \phi^{-0.195}$	0.543	3.391

In order to extend the use of the perimeter-mean convection coefficient found for the 20-sec time interval, assume further that appropriate forms of equation (6) also apply to noncircular cylinders when they are immersed in a JP-5 flame. The values of b and n for a variety of cylinder profiles and ranges of Reynolds numbers are shown in Table 3 (from [8, 14]). Now take the ratio of two forms of equation (6). Let one form be the correlation that has been shown to be pertinent to the actual test situation. Thus for the actual test situation, the following parameters are specifically defined: $h_{m0} = 9.88$ Btu/hr-ft²-deg F, $L_0 = 8.530$ in. $b_0 = 0.0239$, and $n_0 = 0.805$. Let the other form of equation (6) be a considerably more general one that can be constructed by the use of any set of n and b values found in Table 3. This general form of equation (6) is to apply to the situation where a cylinder of a somewhat arbitrary shape and size is enveloped by a large JP-5 flame. Attach no additional identifying subscripts to the parameters in the general equation. In order to achieve a high degree of similarity between the actual test situation and the general situation, assume that the cylinder of a somewhat arbitrary shape and size is immersed within any region of a large JP-5 flame where $V_\infty = V_{\infty 0}$, $k_f = k_{f0}$, $\rho_f = \rho_{f0}$, $\mu_f = \mu_{f0}$, and $\mathrm{Pr}_f = \mathrm{Pr}_{f0}$. This assumption allows h_m, the perimeter-mean convection coefficient relevant to the arbitrary cylinder, to be written as

$$h_m = h_{m0}\left(\frac{b}{b_0}\right)\left(\frac{L}{L_0}\right)^{n-1}(\mathrm{Re}_0)^{n-n_0} \tag{9}$$

Because of the restrictive assumption about equal free-stream velocities and identical film-temperature-dependent fluid properties, the Reynolds number for the general system, Re, is given by $(L/L_0)\,\mathrm{Re}_0$. Since the values of b and n in equation (9) are valid only for a single cylinder configuration and a specific range of Reynolds numbers, it should be apparent that L for a given cylinder shape can take on only those values that keep Re within the limits for which b and n apply. Hence equation (9) must be subjected to the constraint

$$\frac{\text{Re (lower)}}{\text{Re}_0} \le \frac{L}{L_0} \le \frac{\text{Re (upper)}}{\text{Re}_0} \qquad (10)$$

If equation (9) and inequality (10) are to be useful in providing quantitative estimates, it is necessary to specify a value for Re_0. Hence on the basis of previous estimates, assume that the Reynolds number for the actual test situation was 73,725. For convenience, let L/L_0 be known as ϕ. By utilizing the assumption about Re_0, equation (9) and inequality (10) can be evaluated for each cylinder configuration and Reynolds-number range indicated in Table 3. Expressions for h_m as a function of ϕ are shown in the sixth column of Table 3, while the allowable range of ϕ is given in columns seven and eight.

References

1 Barnett, H. C., and Hibbard, R. R., "Properties of Aircraft Fuels," NACA-TN-3276, 1956.

2 Blinov, V. I., and Khudiakov, G. N., "Certain Laws Governing the Diffusive Burning of Liquids," *Dokl. Akad. Nauk, SSSR*, Vol. 113, 1957, pp. 1094–1098.

3 Hottel, H. C., a review of reference [1], in: *Fire Research Abstracts and Reviews*, Vol. 1, 1959, pp. 41–44.

4 Burgess, D. S., Grumer, J., and Wolfhard, H. G., "Burning Rates of Liquid Fuels in Large and Small Open Trays," in: *International Symposium on the Use of Models in Fire Research*, NAS-NRC Publication 786, Washington, D. C., 1961, pp. 68–75.

5 Russell, L. H., *Quantification of the Heat Transfer Parameters Relevant to a Cylinder Immersed in a Large Aviation Fuel Fire*, MS thesis, University of Pittsburgh, Pittsburgh, Pa., 1970.

6 Kiefer, J., "Sequential Minimax Search for a Maximum," *Proceedings of the American Mathematical Society*, Vol. 4, 1953, pp. 502–506.

7 Gardon, R., "An Instrument for the Direct Measurement of Intense Thermal Radiation," *Review of Scientific Instruments*, Vol. 24, No. 5, 1953, pp. 366–370.

8 Gebhart, B., *Heat Transfer*, McGraw-Hill, New York, 1961, pp. 209–213.

9 Russell, L. H., and Canfield, J. A., "Simulation of the Thermal Response of Ordnance Immersed in Large Aviation Fuel Fires," NWL Technical Report TR-2661, Naval Weapons Laboratory, Dahlgren, Va., 1972, pp. 24–25.

10 Kilham, J. K., "Energy Transfer From Flame Gases to Solids," *Third Symposium on Combustion, Flame, and Explosion Phenomena*, Williams and Wilkins, Baltimore, Md., 1949, pp. 733–740.

11 Davies, R. M., "Heat Transfer Measurements on Electrically Boosted Flames," *Tenth Symposium (International) on Combustion*, The Combustion Institute, 1964, pp. 755–766.

12 Cookson, R. A., and Kilham, J. K., "Energy Transfer From Hydrogen-Air Flames," *Ninth Symposium (International) on Combustion*, Academic Press, New York, 1963, pp. 257–263.

13 Kilham, J. K., and Dunham, P. G., "Energy Transfer From Carbon Monoxide Flames," *Eleventh Symposium (International) on Combustion*, The Combustion Institute, 1967, pp. 899–905.

14 Jakob, M., *Heat Transfer*, Vol. 1, Wiley, New York, 1957, p. 562.

journal of heat transfer

technical briefs

This section consists of contributions of 1500 words or less (about 5 double-spaced typewritten pages, including figures). Technical briefs will be reviewed and approved by the specific division's reviewing committee prior to publication. After approval such contributions will be published as soon as possible, normally in the next issue of the journal.

Wave Instability of Natural Convection on Inclined Surfaces Accounting for Nonparallelism of the Basic Flow

S. E. HAALAND[1] **and E. M. SPARROW**[2]

Neutral stability results for Prandtl numbers of 6.7 and 0.733 were obtained by solving disturbance equations that take account of the nonparallelism of the basic flow. Compared with the results for the conventional parallel-flow model, the neutral curves are shifted to higher Grashof numbers and higher wave numbers but maintain their characteristic shapes. The effect of varying the plate inclination from downward-facing to upward-facing is to increase the susceptibility of the flow to instability. The critical Grashof numbers are substantially lower than the Grashof numbers of experiments where instability was due to natural disturbances.

Introduction

NATURAL CONVECTION on vertical and inclined surfaces belongs to a class of flows where (*a*) the streamwise velocity component vanishes in the free stream and (*b*) the transverse velocity component is directed toward the surface and has a finite value in the free stream. The linear stability of this class of flows was examined in general by Haaland [1],[3] and the governing equations for plane-wave instability of buoyant boundary layers were formulated. This formulation is reproduced in [2], where it was applied to the stability of a buoyant plume.

It has been demonstrated that for the stability problem the convection of disturbance quantities by the transverse velocity of the basic flow cannot be neglected; that is, the conventional parallel-flow model is not uniformly valid in the entire domain in which the stability problem is defined. The transverse velocity terms cause the disturbance vorticity and temperature to be contained within the boundary layer of the basic flow. This containment has been termed the bottling effect. The formulation given in [1] for buoyant boundary layers includes the just-mentioned transverse convection terms as well as all other terms arising from the x-dependence of the basic flow.

The objective of the present note is to report on neutral stability results obtained by applying the formulation of [1] to natural convection on isothermal vertical and inclined surfaces. Owing to space limitations, only a very brief outline of the analysis will be given here.

In [1], the formulation of the stability problem was carried out for plane-wave disturbances that were represented as an amplitude function times $\exp[i(\alpha x - \beta t)]$, where the wave number α is complex and the frequency β is real. The disturbance amplitudes (stream function ϕ, vorticity ω, temperature τ) are governed by equations (15)–(17) of [2], which are specialized to the present problem by taking

$$a_1 = 0 \qquad a_2 = -1 \qquad g_x/g = -\cos\theta \qquad g_y/g = -\sin\theta \qquad (1)$$

where $\theta = 0$ corresponds to the vertical plate, and $\theta > 0$ and <0, respectively, denote upward-facing and downward-facing inclined plates. The boundary conditions are that $\phi = \phi' = \tau = 0$ at $\eta = 0$ (plate surface) and $\eta = \infty$.

The basic flow solution that was used as input to the disturbance equations is described in detail in [1]. There it was shown that the buoyancy force normal to the plate surface induces a streamwise pressure gradient that is of order $(\tan\theta)/\mathrm{R}$ relative to the streamwise buoyancy force (R is a characteristic Reynolds number). Therefore, for $|\theta| \leq 45$ deg and for the range of R values encountered in the solutions ($\mathrm{R} \geq 22$), the induced streamwise pressure gradient was neglected.

The solution of the disturbance equations made use of analytical solutions at large η in conjunction with numerical integration for intermediate and small η. Numerical values from the large η solutions served as starting values for the numerical integration, which proceeded toward the wall.

Numerical results were obtained for θ between -45 and 45 deg for $\mathrm{Pr} = 6.7$ and for $\theta = 0$ and 30 deg for $\mathrm{Pr} = 0.733$. Some results were also obtained for the conventional parallel-flow model whereby the transverse velocity and the other terms connected with the x-dependence of the basic flow are omitted.

Results and Discussion

Figs. 1 and 2 contain a comparison of neutral stability results from the present, more complete formulation (solid lines) and from the conventional parallel-flow model (dashed lines). The Prandtl numbers for the figures are 6.7 (Fig. 1) and 0.733 (Fig. 2). The ordinate variable α_r is dimensionless and represents the real part of the wave number. The abscissa variable is a characteristic Reynolds number R that is related to the Grashof number Gr as follows

$$\mathrm{Gr} = \mathrm{R}^4/64 = \beta g \cos\theta (T_w - T_\infty)x^3/\nu^2 \qquad (2)$$

The relation between the dimensionless quantity α_r and its di-

---

[1] Fluid Mechanics Program, University of Minnesota, Minneapolis, Minn.

[2] Fluid Mechanics Program, University of Minnesota, Minneapolis, Minn. Mem. ASME.

[3] Numbers in brackets designate References at end of technical brief.

Contributed by the Heat Transfer Division of THE AMERICAN SOCIETY OF MECHANICAL ENGINEERS. Manuscript received by the Heat Transfer Division January 12, 1973.

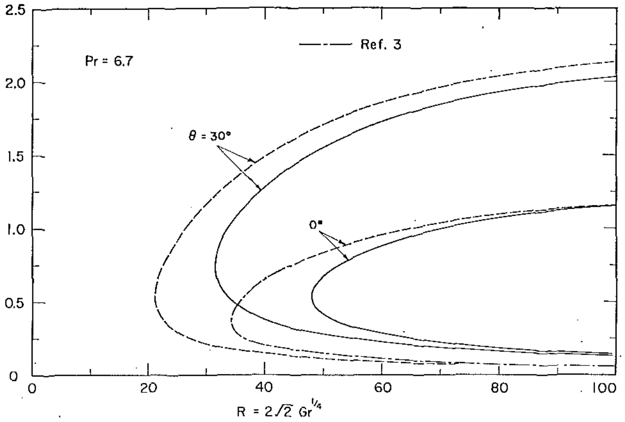

Fig. 1 Neutral stability results from nonparallel and parallel flow models, Pr = 6.7

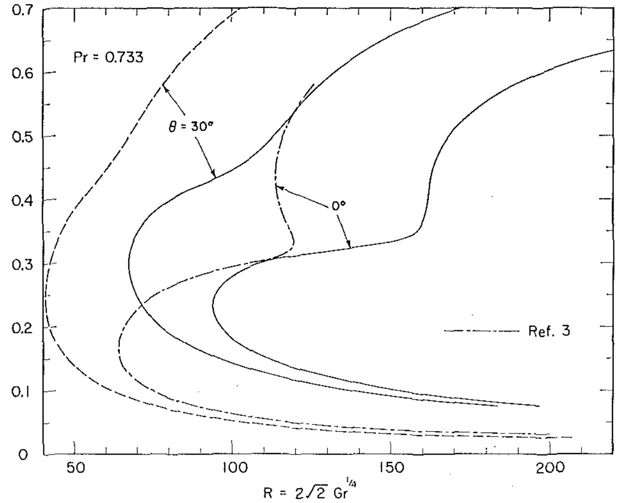

Fig. 2 Neutral stability results from nonparallel flow models, Pr = 0.733

mensional counterpart α_r' also involves the Grashof number, that is,

$$\alpha_r = (\sqrt{2}x/\mathrm{Gr}^{1/4})\alpha_r' \qquad (3)$$

The uniformly dashed curves of Figs. 1 and 2 were computed by the present authors, whereas the short–long dashed curves are from Nachtsheim [3].

Examination of the figures shows that accounting for the nonparallelism of the basic flow causes a shifting of the neutral curves to higher Grashof numbers and higher wave numbers. At a fixed wave number, the largest changes in Grashof number are encountered on the lower branch of the neutral curve. The critical Grashof numbers increase by about a factor of five owing to the nonparallelism of the basic flow. It is interesting to note that in spite of the shifting, the neutral curves retain their characteristic shapes. Thus the multi-lobe nature of the curves for Pr = 0.733 is preserved as is the simple form of the curves for Pr = 6.7.

The authors have also examined neutral curves in which a dimensionless counterpart of the frequency β is plotted against α_r. These neutral curves are substantially less affected by the accounting of the nonparallelism of the basic flow than are those of Figs. 1 and 2. At a given wave number, the maximum change in the dimensionless frequency was found to be on the order of 10 percent.

A presentation of neutral stability results for Pr = 6.7 encompassing the range of plate inclinations from −45 to 45 deg

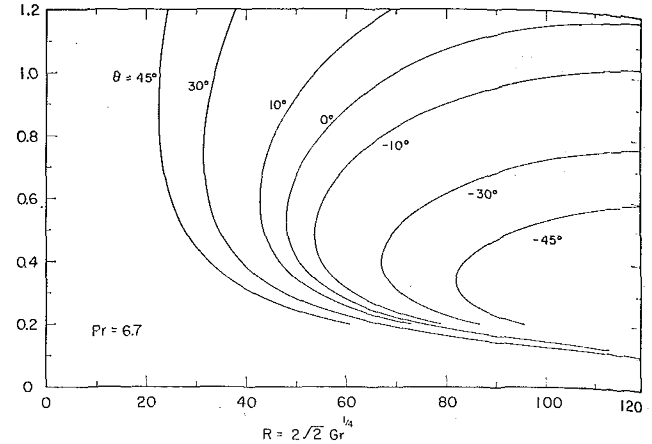

Fig. 3 Neutral stability results for various plate inclinations, Pr = 6.7

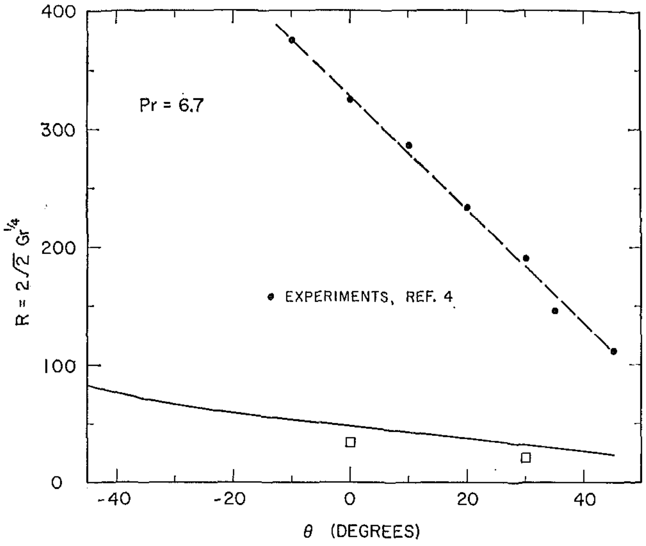

Fig. 4 Critical Grashof numbers for Pr = 6.7 and instability Grashof numbers from experiments with water

is made in Fig. 3. The curves are displaced toward lower Grashof numbers as one proceeds from downward-facing inclined plates ($\theta < 0$) to upward-facing inclined plates ($\theta > 0$). Furthermore, for the upward-facing plates, the range of unstable wave numbers is substantially greater than for downward-facing plates. Taken together, these findings indicate that the flow adjacent to upward-facing plates is more susceptible to instability owing to small disturbances.

In Fig. 4, the critical Grashof numbers for Pr = 6.7 (solid line for nonparallel-flow model; square symbols for parallel-flow model) are compared with instability Grashof numbers of experiment [4] (blackened points). The experiments were performed using a heated plate situated in water, and instability was identified by visual observations made feasible by an electrochemical reaction. Instability was due to natural disturbances.

It is seen from the figure that the critical Grashof numbers lie well below the experimental results. This is in accord with all known results for natural disturbances in boundary-layer flows, where appreciable amplification is necessary before any disturbance can be detected.

For inclination angles of 17 deg and greater, longitudinal vortices were observed in [4]. The existence of these vortices does not preclude the possibility that the initial instability was due to plane-wave disturbances. Also, one cannot rule out the possibility that both forms of instability coexisted.

References

1 Haaland, S. E., "Contributions to Linear Stability Theory of Nearly Parallel Flows," PhD thesis, Fluid Mechanics Program, University of Minnesota, Minneapolis, Minn., 1972.

2 Haaland, S. E., and Sparrow, E. M., "Stability of Buoyant Boundary Layers and Plumes, Taking Account of Nonparallelism of the Basic Flows," Journal of Heat Transfer, Trans. ASME, Series C, Vol. 95, No. 3, Aug. 1973, pp. 295–301.

3 Nachtsheim, P. R., "Stability of Free Convection Boundary Layer Flows," NASA TN D-2089, 1963.

4 Lloyd, J. R., and Sparrow, E. M., "On the Instability of Natural Convection Flow on Inclined Plates," *Journal of Fluid Mechanics*, Vol. 42, 1970, pp. 465–470.

Finite Amplitude Longitudal Convection Rolls in an Inclined Layer

R. M. CLEVER[1]

For the case of a large Prandtl number, buoyancy driven flow in an inclined fluid layer, it is shown that all longitudinal-coordinate-independent solutions of the governing equations are obtainable from a knowledge of the existing results for two-dimensional convection in a horizontal layer, heated from below. The rescaling here yields results which compare favorably with those of existing experimental heat transport values.

Introduction

The instability of the basic state in an inclined layer of a large Prandtl number fluid flow is known to manifest itself in the form of longitudinal rolls (see De Graff and van der Held [1],[2] Kurzweg [2] and Hart [3]). Also, the linear stability equations governing such a tilted flow are essentially the same as those for the Benard problem, and linear stability results for the general problem can therefore be obtained by a mere rescaling (see reference [2]). While such a rescaling of the three-dimensional stability equations is not possible for a finite amplitude flow, it is demonstrated here that any two-dimensional solution of the stability or base flow equations governing a horizontal fluid layer, heated from below, also governs the corresponding longitudinal-independent solutions for an inclined layer.

For a horizontal layer Busse [4, 5] has shown that stationary, finite amplitude, two-dimensional solutions of the equations of motion are stable in a small part of the wavenumber range up to a Rayleigh number R of 22,600. Above this Rayleigh number all two-dimensional solutions become unstable. It will be shown that these, and any other two-dimensional solutions of the equations of motion for the horizontal case, correspond to an x-independent solution (see Fig. 1) of the equations of motion for an inclined fluid layer.

Analysis

The Basic Equations. The Navier-Stokes equations in the Boussinesq approximation are used for a description of the convective motion in an inclined layer. Using the layer thickness, d, as length scale, d^2/κ as time scale, and $R/\Delta T$ as temperature scale, the equations governing the velocity vector $\mathbf{v}$ and the deviation of temperature, θ, from the conductive state become (see Fig. 1):

$$\nabla \cdot \mathbf{v} = 0 \tag{1}$$

$$\nabla^2 \mathbf{v} + \boldsymbol{\lambda}(\theta + \mathrm{R}z) - \nabla\Gamma = \frac{1}{P}\frac{D\mathbf{v}}{Dt} \tag{2}$$

and

$$\nabla^2\theta - (\mathbf{k}\cdot\mathbf{v})R = \frac{D\theta}{Dt} \tag{3}$$

where $\mathrm{R} = \dfrac{\alpha g \Delta T d^3}{\nu\kappa}$ is the Rayleigh number and $P = \nu/\kappa$ is the Prandtl number. $\nabla\Gamma$ includes all terms that can be expressed as gradients.

A general description of a velocity field satisfying (1) can be written as:

$$\mathbf{v} = \boldsymbol{\delta}\phi + \boldsymbol{\varepsilon}\psi \tag{4}$$

where the vector differential operators $\boldsymbol{\delta}$ and $\boldsymbol{\varepsilon}$ are defined by

$$\boldsymbol{\delta}\phi = \nabla \times (\nabla \times \mathbf{k}\phi) \tag{5}$$

and

$$\boldsymbol{\varepsilon}\psi = \nabla \times (\mathbf{k}\psi) \tag{6}$$

For large Prandtl number fluid the stationary x-independent equations of motion become:

$$\partial_{yy}(\nabla^4\phi - \tilde{\theta}) = 0 \tag{7}$$

$$\partial_y\{\partial_y\nabla^2\tilde{\psi} + \tilde{\theta}\} = 0 \tag{8}$$

$$\nabla^2\tilde{\theta} - \tilde{\mathrm{R}}\partial_{yy}\phi = \partial_{yz}\phi\partial_y\tilde{\theta} - \partial_{yy}\phi\partial_z\tilde{\theta} \tag{9}$$

where $\tilde{\theta} = \theta\cos\gamma$, $\tilde{\mathrm{R}} = \mathrm{R}\cos\gamma$, and $\tilde{\psi} = \psi/\tan\gamma$.

In these equations the nonlinearity associated with $\tilde{\psi}$ in equation (9) is absent. The temperature deviation, $\tilde{\theta}$, from conduction is governed by equations (7) and (9) only, which are independent of γ and equivalent to the Benard equations. The boundary conditions are also equivalent for the infinite layer.

Discussion

For a large Prandtl number, buoyancy driven system it has been demonstrated that all stationary x-independent solutions of

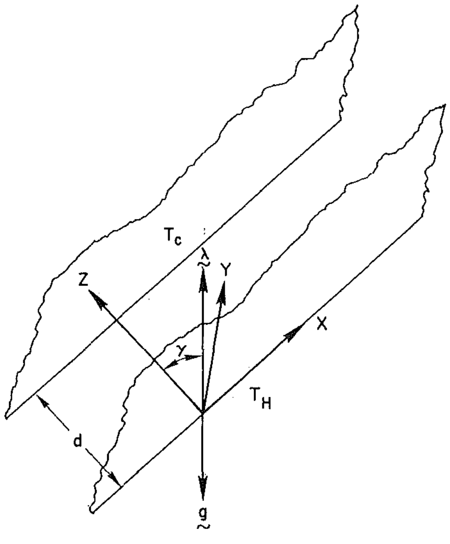

$\underset{\sim}{\lambda}$ = (Sin γ, O, Cos γ) IS IN THE X, Z PLANE

Fig. 1 Geometry and coordinate system

---

[1] Postgraduate Research Engineer, Energy and Kinetics Department, School of Engineering and Applied Science, University of California, Los Angeles, Calif.

[2] Numbers in brackets designate References at end of technical brief.

Contributed by the Heat Transfer Division of The American Society of Mechanical Engineers. Manuscript received by the Heat Transfer Division, March 26, 1973.

References

1 Haaland, S. E., "Contributions to Linear Stability Theory of Nearly Parallel Flows," PhD thesis, Fluid Mechanics Program, University of Minnesota, Minneapolis, Minn., 1972.

2 Haaland, S. E., and Sparrow, E. M., "Stability of Buoyant Boundary Layers and Plumes, Taking Account of Nonparallelism of the Basic Flows," Journal of Heat Transfer, Trans. ASME, Series C, Vol. 95, No. 3, Aug. 1973, pp. 295–301.

3 Nachtsheim, P. R., "Stability of Free Convection Boundary Layer Flows," NASA TN D-2089, 1963.

4 Lloyd, J. R., and Sparrow, E. M., "On the Instability of Natural Convection Flow on Inclined Plates," *Journal of Fluid Mechanics*, Vol. 42, 1970, pp. 465–470.

Finite Amplitude Longitudal Convection Rolls in an Inclined Layer

R. M. CLEVER[1]

For the case of a large Prandtl number, buoyancy driven flow in an inclined fluid layer, it is shown that all longitudinal-coordinate-independent solutions of the governing equations are obtainable from a knowledge of the existing results for two-dimensional convection in a horizontal layer, heated from below. The rescaling here yields results which compare favorably with those of existing experimental heat transport values.

Introduction

The instability of the basic state in an inclined layer of a large Prandtl number fluid flow is known to manifest itself in the form of longitudinal rolls (see De Graff and van der Held [1],[2] Kurzweg [2] and Hart [3]). Also, the linear stability equations governing such a tilted flow are essentially the same as those for the Benard problem, and linear stability results for the general problem can therefore be obtained by a mere rescaling (see reference [2]). While such a rescaling of the three-dimensional stability equations is not possible for a finite amplitude flow, it is demonstrated here that any two-dimensional solution of the stability or base flow equations governing a horizontal fluid layer, heated from below, also governs the corresponding longitudinal-independent solutions for an inclined layer.

For a horizontal layer Busse [4, 5] has shown that stationary, finite amplitude, two-dimensional solutions of the equations of motion are stable in a small part of the wavenumber range up to a Rayleigh number R of 22,600. Above this Rayleigh number all two-dimensional solutions become unstable. It will be shown that these, and any other two-dimensional solutions of the equations of motion for the horizontal case, correspond to an x-independent solution (see Fig. 1) of the equations of motion for an inclined fluid layer.

Analysis

The Basic Equations. The Navier-Stokes equations in the Boussinesq approximation are used for a description of the convective motion in an inclined layer. Using the layer thickness, d, as length scale, d^2/κ as time scale, and $R/\Delta T$ as temperature scale, the equations governing the velocity vector $\mathbf{v}$ and the deviation of temperature, θ, from the conductive state become (see Fig. 1):

$$\nabla \cdot \mathbf{v} = 0 \tag{1}$$

$$\nabla^2 \mathbf{v} + \boldsymbol{\lambda}(\theta + \mathrm{R}z) - \nabla\Gamma = \frac{1}{P}\frac{D\mathbf{v}}{Dt} \tag{2}$$

and

$$\nabla^2\theta - (\mathbf{k}\cdot\mathbf{v})R = \frac{D\theta}{Dt} \tag{3}$$

where $\mathrm{R} = \dfrac{\alpha g \Delta T d^3}{\nu\kappa}$ is the Rayleigh number and $P = \nu/\kappa$ is the Prandtl number. $\nabla\Gamma$ includes all terms that can be expressed as gradients.

A general description of a velocity field satisfying (1) can be written as:

$$\mathbf{v} = \boldsymbol{\delta}\phi + \boldsymbol{\varepsilon}\psi \tag{4}$$

where the vector differential operators $\boldsymbol{\delta}$ and $\boldsymbol{\varepsilon}$ are defined by

$$\boldsymbol{\delta}\phi = \nabla \times (\nabla \times \mathbf{k}\phi) \tag{5}$$

and

$$\boldsymbol{\varepsilon}\psi = \nabla \times (\mathbf{k}\psi) \tag{6}$$

For large Prandtl number fluid the stationary x-independent equations of motion become:

$$\partial_{yy}(\nabla^4\phi - \tilde{\theta}) = 0 \tag{7}$$

$$\partial_y\{\partial_y \nabla^2 \tilde{\psi} + \tilde{\theta}\} = 0 \tag{8}$$

$$\nabla^2\tilde{\theta} - \tilde{\mathrm{R}}\partial_{yy}\phi = \partial_{yz}\phi\partial_y\tilde{\theta} - \partial_{yy}\phi\partial_z\tilde{\theta} \tag{9}$$

where $\tilde{\theta} = \theta\cos\gamma$, $\tilde{\mathrm{R}} = \mathrm{R}\cos\gamma$, and $\tilde{\psi} = \psi/\tan\gamma$.

In these equations the nonlinearity associated with $\tilde{\psi}$ in equation (9) is absent. The temperature deviation, $\tilde{\theta}$, from conduction is governed by equations (7) and (9) only, which are independent of γ and equivalent to the Benard equations. The boundary conditions are also equivalent for the infinite layer.

Discussion

For a large Prandtl number, buoyancy driven system it has been demonstrated that all stationary x-independent solutions of

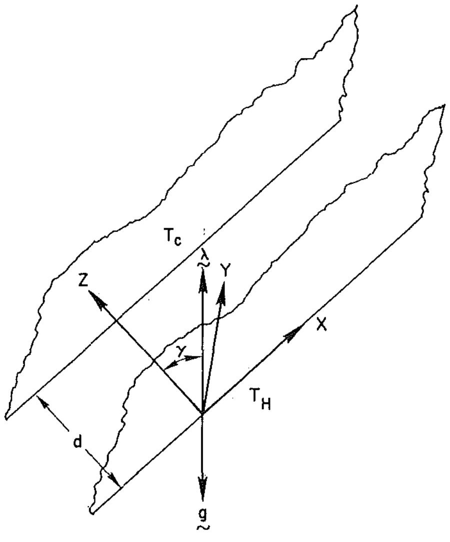

λ = (Sin γ, O, Cos γ) IS IN THE X, Z PLANE

Fig. 1 Geometry and coordinate system

---

[1] Postgraduate Research Engineer, Energy and Kinetics Department, School of Engineering and Applied Science, University of California, Los Angeles, Calif.

[2] Numbers in brackets designate References at end of technical brief.

Contributed by the Heat Transfer Division of The American Society of Mechanical Engineers. Manuscript received by the Heat Transfer Division, March 26, 1973.

the equations governing finite amplitude convection in a horizontal layer, heated from below, correspond to an equivalent set of solutions (in terms of the transverse convective mechanism) when the layer is inclined. The additional velocity component present in the inclined case, due to nonvanishing solutions to equation (8) for $\tilde{\psi}$, does not alter the basic transverse heat transport mechanism as expressed by solutions to equations (7) and (9) for ϕ and $\tilde{\theta}$. Although differences in the equations governing stability of such finite amplitude flows in inclined layers do not allow this rescaling, there is experimental evidence that such x-independent flows are physically realizable solutions of the equations of motion.

De Graff and Van der Held [1] and Hart [3] have experimentally observed longitudinal convection rolls for Rayleigh numbers of the order 10^4. Transition to other forms of convection occurs, depending on the angle of inclination, at Rayleigh numbers of this order. For angles of inclination near vertical, the transition to longitudinal rolls is inhibited by the appearance of a steady y-independent circulation. Although Hart [3] has observed a transverse instability for angles of inclination near vertical, the theoretical investigation of Gershuni and Zhukhovitskii [7] has shown that instability in the form of longitudinal rolls will predominate even for angles of inclination near vertical in the case of a large Prandtl number fluid. Since aforementioned experiments were carried out with air and water as the contained fluid, the observation of hydrodynamic instabilities for angles of inclination near vertical do not allow any definite conclusions as to the preferred mode for a large Prandtl number fluid.

In Fig. 2 the heat transport measurements of De Graff and Van der Held [1] and Dropkin and Somerscales [6], for a variety of tilt angles, are shown in the rescaled variables. Here the Nusselt number should appear as a function of $\tilde{R}$ only, when the flow is in the form of longitudinal rolls. The results indicate that, within experimental error, the heat transport results do lie on a single line, in agreement with the assumption that the transport mechanism is x-independent. Although the results of the former authors are for air with a Prandtl number of 0.74, the heat transport measurements of others have not revealed a large Prandtl number effect at these rather low Rayleigh numbers. Additionally, the rescaling seems to be valid beyond Rayleigh numbers at which transition to other forms of convection has been observed. Although Busse [5] has shown, in the horizontal case, that for $R > 22{,}600$ transition to bimodal convection must take place, the dominant heat transport mechanisms seem to be due to the primary x-independent convection as discussed by Busse and Whitehead [8] and Malkus [9]. This dominance would lead to the universality shown in Fig. 2, if it continued in the inclined layer.

Acknowledgments

The author wishes to thank Prof. D. K. Edwards and Dr. P. Ayyaswamy for helpful discussions during the course of this work. Grateful acknowledgment is also made for support by the National Science Foundation Grant GK35892.

References

1 De Graff, J. G. A., and van der Held, E. F. M., "The Relation Between the Heat Transfer and the Convection Phenomena in Enclosed Plane Air Layers," *Appl. Sci. Res.*, Vol. 3, 1953, pp. 393–409.

2 Kurzweg, U. H., "Stability of Natural Convection Within an Inclined Channel," JOURNAL OF HEAT TRANSFER, TRANS. ASME, Series C, Vol. 92, No. 1, 1970, pp. 190–191.

3 Hart, J. E., "Stability of the Flow in a Differentially Heated Inclined Box," *J. Fl. Mech.*, Vol. 47, 1971, pp. 547–576.

4 Busse, F. H., "Stability Regions of Cellular Fluid Flow," *IUTAM Symposium Herrenalb 1969*, Springer-Verlag, Berlin, Heidelberg, New York, 1971.

5 Busse, F. H., "On the Stability of Two-Dimensional Convection in a Layer Heated From Below," *J. Math. Phyi.*, Vol. 46, 1967, pp. 140–150.

6 Dropkin, D., and Somerscales, E., "Heat Transfer by Natural Convection in Liquids Confined by Two Parallel Plates Which are Inclined at Various Angles With Respect to the Horizontal," JOURNAL OF HEAT TRANSFER, TRANS. ASME, Series C, Vol. 87, 1965, pp. 77–84.

7 Gershuni, G. Z., and Zhukhovitskii, E. M., "Stability of Plane-Parallel Convective Motion With Respect to Spatial Perturbations," *PMM*, Vol. 33, 1969, pp. 830–835.

8 Busse, F. H., and Whitehead, J. A., "Instabilities of Convection Rolls in a High Prandtl Number Fluid," *J. Fl. Mech.*, Vol. 47, 1971, pp. 305–320.

9 Malkus, W. V. R., "Discrete Transitions in Turbulent Convection," *Proceedings Royal Soc.*, Vol. 225, 1954, pp. 185–195.

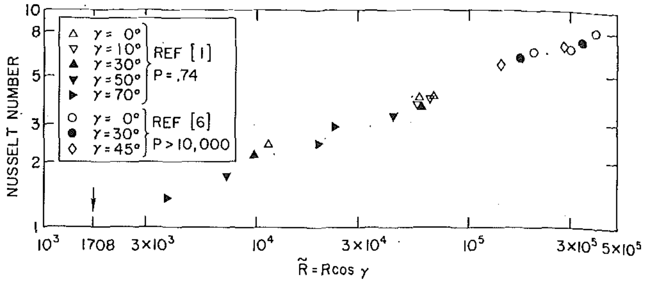

Fig. 2 Experimental heat transport measurements

A Technique For Visualization of the Very Slow Motion of Water in Enclosed Spaces

R. E. POWE,[1] S. H. YIN,[2] J. A. SCANLAN,[3] and E. H. BISHOP[4]

DURING THE COURSE of a study of buoyancy driven flow due to natural convection between a body and its finite enclosure, it became desirable to visualize the flow patterns which were occurring. This presented no great difficulties for air as the gap working fluid since cigar smoke has been used successfully on a number of previous occasions [1, 2].[5] However, no suitable visualization techniques were found to be available when water was utilized as the test fluid. In order to be useable, tracer particles must possess at least the following minimum characteristics:

1 they must be neutrally buoyant over a wide temperature range, and this characteristic must not be highly time dependent;

2 they must have a high apparent reflectivity in order to be visible and photographable;

3 they must not adhere to solid surfaces; and

4 they must follow and indicate the actual physical flow phenomena.

Several types of tracer particles which are commonly used in the forced flow of water were evaluated for the current study, but none of these proved suitable for the low velocities, and the particular problems, encountered in natural convective flows. These tracers included hydrogen bubbles, aluminum powders, poly-

---

[1] Assistant Professor, Mechanical Engineering Department, Montana State University, Bozeman, Mont. Mem. ASME.

[2] Assistant Professor, Chung Yuan Christian College of Science and Engineering, Chung Li, Taiwan, Republic of China.

[3] Professor, Mechanical Engineering Department, Montana State University, Bozeman, Mont. Mem. ASME.

[4] Professor and Head, Mechanical Engineering Department, Montana State University, Bozeman, Mont. Mem. ASME.

[5] Numbers in brackets designate References at end of technical brief.

Contributed by the Heat Transfer Division of THE AMERICAN SOCIETY OF MECHANICAL ENGINEERS. Manuscript received by the Heat Transfer Division March 12, 1973.

the equations governing finite amplitude convection in a horizontal layer, heated from below, correspond to an equivalent set of solutions (in terms of the transverse convective mechanism) when the layer is inclined. The additional velocity component present in the inclined case, due to nonvanishing solutions to equation (8) for $\tilde{\psi}$, does not alter the basic transverse heat transport mechanism as expressed by solutions to equations (7) and (9) for ϕ and $\tilde{\theta}$. Although differences in the equations governing stability of such finite amplitude flows in inclined layers do not allow this rescaling, there is experimental evidence that such x-independent flows are physically realizable solutions of the equations of motion.

De Graff and Van der Held [1] and Hart [3] have experimentally observed longitudinal convection rolls for Rayleigh numbers of the order 10^4. Transition to other forms of convection occurs, depending on the angle of inclination, at Rayleigh numbers of this order. For angles of inclination near vertical, the transition to longitudinal rolls is inhibited by the appearance of a steady y-independent circulation. Although Hart [3] has observed a transverse instability for angles of inclination near vertical, the theoretical investigation of Gershuni and Zhukhovitskii [7] has shown that instability in the form of longitudinal rolls will predominate even for angles of inclination near vertical in the case of a large Prandtl number fluid. Since aforementioned experiments were carried out with air and water as the contained fluid, the observation of hydrodynamic instabilities for angles of inclination near vertical do not allow any definite conclusions as to the preferred mode for a large Prandtl number fluid.

In Fig. 2 the heat transport measurements of De Graff and Van der Held [1] and Dropkin and Somerscales [6], for a variety of tilt angles, are shown in the rescaled variables. Here the Nusselt number should appear as a function of $\tilde{R}$ only, when the flow is in the form of longitudinal rolls. The results indicate that, within experimental error, the heat transport results do lie on a single line, in agreement with the assumption that the transport mechanism is x-independent. Although the results of the former authors are for air with a Prandtl number of 0.74, the heat transport measurements of others have not revealed a large Prandtl number effect at these rather low Rayleigh numbers. Additionally, the rescaling seems to be valid beyond Rayleigh numbers at which transition to other forms of convection has been observed. Although Busse [5] has shown, in the horizontal case, that for $R > 22{,}600$ transition to bimodal convection must take place, the dominant heat transport mechanisms seem to be due to the primary x-independent convection as discussed by Busse and Whitehead [8] and Malkus [9]. This dominance would lead to the universality shown in Fig. 2, if it continued in the inclined layer.

Acknowledgments

The author wishes to thank Prof. D. K. Edwards and Dr. P. Ayyaswamy for helpful discussions during the course of this work. Grateful acknowledgment is made for support by the National Science Foundation Grant GK35892.

References

1 De Graff, J. G. A., and van der Held, E. F. M., "The Relation Between the Heat Transfer and the Convection Phenomena in Enclosed Plane Air Layers," *Appl. Sci. Res.*, Vol. 3, 1953, pp. 393–409.

2 Kurzweg, U. H., "Stability of Natural Convection Within an Inclined Channel," JOURNAL OF HEAT TRANSFER, TRANS. ASME, Series C, Vol. 92, No. 1, 1970, pp. 190–191.

3 Hart, J. E., "Stability of the Flow in a Differentially Heated Inclined Box," *J. Fl. Mech.*, Vol. 47, 1971, pp. 547–576.

4 Busse, F. H., "Stability Regions of Cellular Fluid Flow," *IUTAM Symposium Herrenalb 1969*, Springer-Verlag, Berlin, Heidelberg, New York, 1971.

5 Busse, F. H., "On the Stability of Two-Dimensional Convection in a Layer Heated From Below," *J. Math. Phyi.*, Vol. 46, 1967, pp. 140–150.

6 Dropkin, D., and Somerscales, E., "Heat Transfer by Natural Convection in Liquids Confined by Two Parallel Plates Which are Inclined at Various Angles With Respect to the Horizontal," JOURNAL OF HEAT TRANSFER, TRANS. ASME, Series C, Vol. 87, 1965, pp. 77–84.

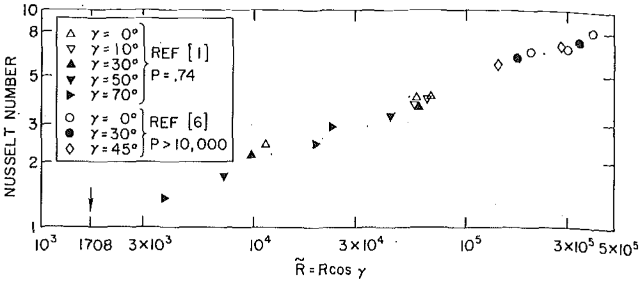

Fig. 2 Experimental heat transport measurements

7 Gershuni, G. Z., and Zhukhovitskii, E. M., "Stability of Plane-Parallel Convective Motion With Respect to Spatial Perturbations," *PMM*, Vol. 33, 1969, pp. 830–835.

8 Busse, F. H., and Whitehead, J. A., "Instabilities of Convection Rolls in a High Prandtl Number Fluid," *J. Fl. Mech.*, Vol. 47, 1971, pp. 305–320.

9 Malkus, W. V. R., "Discrete Transitions in Turbulent Convection," *Proceedings Royal Soc.*, Vol. 225, 1954, pp. 185–195.

A Technique For Visualization of the Very Slow Motion of Water in Enclosed Spaces

R. E. POWE,[1] S. H. YIN,[2] J. A. SCANLAN,[3] and E. H. BISHOP[4]

DURING THE COURSE of a study of buoyancy driven flow due to natural convection between a body and its finite enclosure, it became desirable to visualize the flow patterns which were occurring. This presented no great difficulties for air as the gap working fluid since cigar smoke has been used successfully on a number of previous occasions [1, 2].[5] However, no suitable visualization techniques were found to be available when water was utilized as the test fluid. In order to be useable, tracer particles must possess at least the following minimum characteristics:

1 they must be neutrally buoyant over a wide temperature range, and this characteristic must not be highly time dependent;

2 they must have a high apparent reflectivity in order to be visible and photographable;

3 they must not adhere to solid surfaces; and

4 they must follow and indicate the actual physical flow phenomena.

Several types of tracer particles which are commonly used in the forced flow of water were evaluated for the current study, but none of these proved suitable for the low velocities, and the particular problems, encountered in natural convective flows. These tracers included hydrogen bubbles, aluminum powders, poly-

---

[1] Assistant Professor, Mechanical Engineering Department, Montana State University, Bozeman, Mont. Mem. ASME.

[2] Assistant Professor, Chung Yuan Christian College of Science and Engineering, Chung Li, Taiwan, Republic of China.

[3] Professor, Mechanical Engineering Department, Montana State University, Bozeman, Mont. Mem. ASME.

[4] Professor and Head, Mechanical Engineering Department, Montana State University, Bozeman, Mont. Mem. ASME.

[5] Numbers in brackets designate References at end of technical brief.

Contributed by the Heat Transfer Division of THE AMERICAN SOCIETY OF MECHANICAL ENGINEERS. Manuscript received by the Heat Transfer Division March 12, 1973.

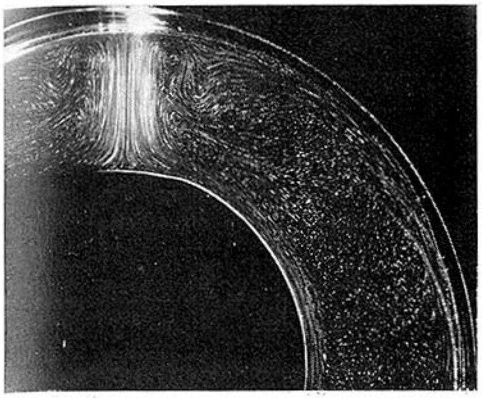

Fig. 1 Particles in spherical annulus with Rayleigh number of 4×10^6 and Prandtl number of 10

ethylene particles, polystyrene particles, small hollow glass spheres (commercially called Eccospheres, which have previously been used by Brooks [3]), and a dye formed by passing an electric current through a thymol blue pH indicator solution as suggested by Baker [4].

In view of the foregoing, it became necessary to develop a visualization technique which would be specificially applicable to the very slow motion of water in confined spaces. This was accomplished in the following manner. First, the desired quantity of distilled water was boiled for deaeration purposes in order to minimize undesirable bubble collection on the solid boundaries of the flow system, as such bubbles would partially obstruct the view of the flow pattern. Next, the boiled water was cooled to approximately 80 deg F, and about five drops of "Ajax" liquid detergent were added per gallon of water. Gentle stirring of the container was then necessary to form a homogeneous mixture, but care had to be taken to avoid introducing air bubbles into the system during this process. Finally, after the mixture had remained stationary for several hours, numerous small, neutrally buoyant particles could be observed in a lighted plane through the mixture. The ability of these particles to follow the flow in a spherical annulus, operating under steady-state conditions, is indicated in Fig. 1 where the two spheres are held at different temperatures. The exposure time used in obtaining the photograph in this figure was approximately 10 sec.

In using the foregoing method it was found that several problems could be encountered if care were not taken. The concentration of particles was affected by the quantity of detergent added. Too little detergent resulted in so few particles that the complete flow pattern could not be determined; too much detergent caused the water to appear milky gray in color, and this reduced the contrast significantly, thereby yielding poor photographic results. Also, it was discovered that when the temperature of the mixture which was finally used exceeded approximately 120 deg F, the number of particles was considerably reduced, thereby greatly reducing the usefulness of this technique for flow visualization at elevated temperatures. Although several additional brands of detergents were tested, only one, in addition to Ajax, was found which yielded any particles, and it was of a much poorer quality for flow visualization purposes.

In an attempt to learn more of the exact nature of the tracer particles, samples of the mixture were passed through filters of various sizes, and the particles remaining on these filters were studied microscopically. It was determined that those particles had primary dimensions on the order of 5 to 15 microns and were highly angular in nature, which accounts for their excellent optical reflectivity. It is hypothesized that these particles result from one of two sources: they may be an abrasive material which is purposely added to the detergent to aid in cleaning, or they may be impurities encountered in the manufacturing process. In either case they are excellent tracers for the current application.

In summary, this paper has described a technique developed for the visualization of relatively slow motion of water in confined spaces. The specific example given was the buoyancy-driven convection of water in spherical annuli, but the technique should be applicable to any situation where the velocities are relatively low, and the temperatures do not exceed approximately 120 deg F.

Acknowledgment

The work described in this paper was supported by the Atomic Energy Commission under contract AT(45-1)-2214 and the National Science Foundation under Grant GK-31908.

References

1 Bishop, E. H., Kolflat, R. S., Mack, L. R., and Scanlan, J. A., "Convective Heat Transfer Between Concentric Spheres," *Proceedings of the 1964 Heat Transfer and Fluid Mechanics Institute*, Stanford University Press, 1964, pp. 69–80.

2 Powe, R. E., Carley, C. T., and Bishop, E. H., "Free Convective Flow Patterns in Cylindrical Annuli," Journal of Heat Transfer, Trans. ASME, Series C, Vol. 91, No. 3, 1969, p. 310.

3 Brooks, R. V., "Free Convection Velocity Measurements by the Use of Neutral Density Particles," unpublished MS thesis, Georgia Institute of Technology, 1965.

4 Baker, D. J., "A Technique for the Precise Measurement of Small Fluid Velocities," *Journal of Fluid Mechanics*, Vol. 26, No. 3, 1966, p. 573.

Free Convective Heat Transfer From Horizontal Cones

P. H. OOSTHUIZEN[1]

Introduction

While extensive analytical and experimental studies of free convective heat transfer rates from bodies of other shape are available, relatively little attention has been given to such heat transfer from cones. Several analytical studies of free convective flow from vertical cones are available, e.g., see references [1 and 2],[2] and some experimental measurements of mean heat transfer rates from vertical cones are presented in reference [3]. However, no analytical or experimental studies of mean heat transfer rates from horizontal cones appear to be available. The present study was, therefore, undertaken since practical situations involving heat transfer by free convection from bodies that are essentially horizontal cones do arise. The apparatus and method of measuring the heat transfer rate are similar to those used in reference [3].

Apparatus and Method

Mean heat transfer rates have been measured from a series of eight cones, the dimensions of these cones being given in Table 1. D is the diameter of the base of the cone, L is its vertical height and ϕ is its included angle. The diameters of the tips of the cones were small compared to their other dimensions and the effect of this finite tip size was, therefore, assumed to be negligible.

The cones were made of solid aluminum with caps made of fiberboard insulating material fitted to their bases. Small

---

[1] Department of Mechanical Engineering, Queen's University, Kingston, Ontario, Canada.

[2] Numbers in brackets designate References at end of technical brief.

Contributed by the Heat Transfer Division of The American Society of Mechanical Engineers. Manuscript received by the Heat Transfer Division May 9, 1973.

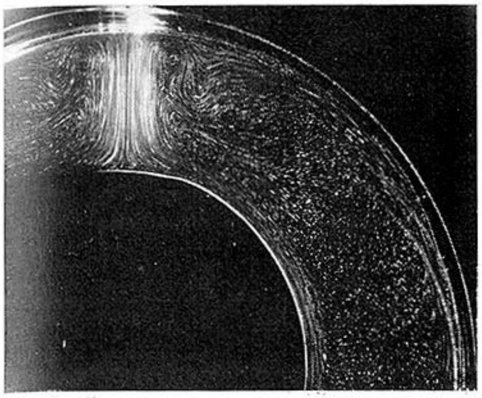

Fig. 1 Particles in spherical annulus with Rayleigh number of 4 × 10^6 and Prandtl number of 10

ethylene particles, polystyrene particles, small hollow glass spheres (commercially called Eccospheres, which have previously been used by Brooks [3]), and a dye formed by passing an electric current through a thymol blue pH indicator solution as suggested by Baker [4].

In view of the foregoing, it became necessary to develop a visualization technique which would be specificially applicable to the very slow motion of water in confined spaces. This was accomplished in the following manner. First, the desired quantity of distilled water was boiled for deaeration purposes in order to minimize undesirable bubble collection on the solid boundaries of the flow system, as such bubbles would partially obstruct the view of the flow pattern. Next, the boiled water was cooled to approximately 80 deg F, and about five drops of "Ajax" liquid detergent were added per gallon of water. Gentle stirring of the container was then necessary to form a homogeneous mixture, but care had to be taken to avoid introducing air bubbles into the system during this process. Finally, after the mixture had remained stationary for several hours, numerous small, neutrally buoyant particles could be observed in a lighted plane through the mixture. The ability of these particles to follow the flow in a spherical annulus, operating under steady-state conditions, is indicated in Fig. 1 where the two spheres are held at different temperatures. The exposure time used in obtaining the photograph in this figure was approximately 10 sec.

In using the foregoing method it was found that several problems could be encountered if care were not taken. The concentration of particles was affected by the quantity of detergent added. Too little detergent resulted in so few particles that the complete flow pattern could not be determined; too much detergent caused the water to appear milky gray in color, and this reduced the contrast significantly, thereby yielding poor photographic results. Also, it was discovered that when the temperature of the mixture which was finally used exceeded approximately 120 deg F, the number of particles was considerably reduced, thereby greatly reducing the usefulness of this technique for flow visualization at elevated temperatures. Although several additional brands of detergents were tested, only one, in addition to Ajax, was found which yielded any particles, and it was of a much poorer quality for flow visualization purposes.

In an attempt to learn more of the exact nature of the tracer particles, samples of the mixture were passed through filters of various sizes, and the particles remaining on these filters were studied microscopically. It was determined that those particles had primary dimensions on the order of 5 to 15 microns and were highly angular in nature, which accounts for their excellent optical reflectivity. It is hypothesized that these particles result from one of two sources: they may be an abrasive material which is purposely added to the detergent to aid in cleaning, or they may be impurities encountered in the manufacturing process. In either case they are excellent tracers for the current application.

In summary, this paper has described a technique developed for the visualization of relatively slow motion of water in confined spaces. The specific example given was the buoyancy-driven convection of water in spherical annuli, but the technique should be applicable to any situation where the velocities are relatively low, and the temperatures do not exceed approximately 120 deg F.

Acknowledgment

The work described in this paper was supported by the Atomic Energy Commission under contract AT(45-1)-2214 and the National Science Foundation under Grant GK-31908.

References

1 Bishop, E. H., Kolflat, R. S., Mack, L. R., and Scanlan, J. A., "Convective Heat Transfer Between Concentric Spheres," *Proceedings of the 1964 Heat Transfer and Fluid Mechanics Institute*, Stanford University Press, 1964, pp. 69–80.

2 Powe, R. E., Carley, C. T., and Bishop, E. H., "Free Convective Flow Patterns in Cylindrical Annuli," JOURNAL OF HEAT TRANSFER, TRANS. ASME, Series C, Vol. 91, No. 3, 1969, p. 310.

3 Brooks, R. V., "Free Convection Velocity Measurements by the Use of Neutral Density Particles," unpublished MS thesis, Georgia Institute of Technology, 1965.

4 Baker, D. J., "A Technique for the Precise Measurement of Small Fluid Velocities," *Journal of Fluid Mechanics*, Vol. 26, No. 3, 1966, p. 573.

Free Convective Heat Transfer From Horizontal Cones

P. H. OOSTHUIZEN[1]

Introduction

WHILE extensive analytical and experimental studies of free convective heat transfer rates from bodies of other shape are available, relatively little attention has been given to such heat transfer from cones. Several analytical studies of free convective flow from vertical cones are available, e.g., see references [1 and 2],[2] and some experimental measurements of mean heat transfer rates from vertical cones are presented in reference [3]. However, no analytical or experimental studies of mean heat transfer rates from horizontal cones appear to be available. The present study was, therefore, undertaken since practical situations involving heat transfer by free convection from bodies that are essentially horizontal cones do arise. The apparatus and method of measuring the heat transfer rate are similar to those used in reference [3].

Apparatus and Method

Mean heat transfer rates have been measured from a series of eight cones, the dimensions of these cones being given in Table 1. D is the diameter of the base of the cone, L is its vertical height and ϕ is its included angle. The diameters of the tips of the cones were small compared to their other dimensions and the effect of this finite tip size was, therefore, assumed to be negligible.

The cones were made of solid aluminum with caps made of fiberboard insulating material fitted to their bases. Small

---

[1] Department of Mechanical Engineering, Queen's University, Kingston, Ontario, Canada.

[2] Numbers in brackets designate References at end of technical brief.

Contributed by the Heat Transfer Division of THE AMERICAN SOCIETY OF MECHANICAL ENGINEERS. Manuscript received by the Heat Transfer Division May 9, 1973.

Table 1

Cone number	D in.	L in.	ϕ deg
1	0.58	8.0	3.8
2	1.22	8.0	8.9
3	1.67	8.0	11.5
4	1.87	12.0	8.9
5	2.50	16.0	8.9
6	0.90	7.9	6.6
7	0.50	8.0	3.5
8	0.70	4.7	8.6

holes were drilled longitudinally into the cones at various locations and thermocouples inserted into these holes were used to measure the temperature during the tests. These tests were carried out with the cones mounted horizontally, one at a time, in an enclosure which was open at the top and bottom and was large compared to the dimensions of the cones.

The mean heat transfer rates from the cones were determined by heating them to a temperature of just over 300 deg F and then measuring the rate at which they cooled, these measurements being continued until the temperature had dropped to about 130 deg F. The thermocouples indicated that, for all the cones, the temperature remained effectively uniform during the cooling, the temperature variation between the points at which it was measured being less than 1 deg F. Therefore, the total mean heat transfer coefficient at any time could be calculated in the usual way from the measured variation of temperature with time. The mean convective heat transfer rate could then be found by making an allowance for radiant heat transfer. This allowance was found to be small in all cases. In this way, then, the variation of the convective heat transfer coefficient over a range of temperatures was derived for each cone. Since the cooling took at least 15 min, the maximum cooling rate varying from about 20 deg F per min at the higher temperatures to about 5 deg F per min at the lower temperatures, it seems unlikely that unsteady effects had any influence on this variation.

Results

The convective heat transfer rates from horizontal cones can, of course, be correlated in the following way.

$$\mathrm{N}_D = \text{function}\ (\mathrm{G}_D, \mathrm{P}_r, \phi) \tag{1}$$

where

N_D = Nusselt number, hD/k
h = mean heat transfer coefficient
D = base diameter of cone
G_D = Grashof number, $\beta g(T_w - T_1)D^3/\nu^2$
$(T_w - T_1)$ = temperature difference between cone and surrounding air
P_r = Prandtl number
ϕ = included angle of cone.

The remaining symbols k, β, g, and ν have their conventional meaning.

Now, for the range of temperatures covered by the present tests, the Prandtl number of air remains almost constant. For the present tests, therefore, equation (1) reduces, effectively, to

$$\mathrm{N}_D = \text{function}\ (\mathrm{G}_D, \phi) \tag{2}$$

The variation of N_D with G_D for all the cones tested is shown in Fig. 1. It will be seen from these results that, at least for the range of values of ϕ covered by the tests, the variation of N_D with G_D is independent of ϕ. This result suggests that the flow over every cross section of the cone is effectively two-dimensional, i.e., there is effectively no flow in the axial direction along the cone surface. If this is so, then the flow over each cross section of the cone is the same as the flow over a cylinder of the same diameter and, therefore, a correlation equation for the heat transfer rate from a cone can be deduced from known correlations equations for free-convective heat transfer from cylinders in the following way. If $\bar{h}$ is the average value of the heat transfer coefficient for a section of the cone of diameter d, this section being a distance x from the vertex of the cone, then the average heat transfer coefficient, h, for the whole cone is, of course, given by

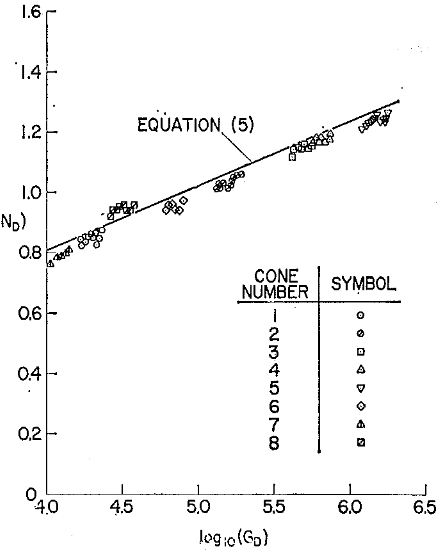

Fig. 1 Variation of Nusselt number with Grashof number

$$h = \frac{2}{\pi D L}\int_0^L \pi d\bar{h}\,dx \tag{3}$$

If it is assumed, therefore, that $\bar{h}$ is given by the correlation equation for a cylinder e.g., if the correlation proposed in reference [4] is used, $\bar{h}$ will be given by

$$\mathrm{N}_d = 0.35 + 0.25(\mathrm{G}_d\mathrm{P}_r)^{0.125} + 0.45(\mathrm{G}_d\mathrm{P}_r)^{0.25} \tag{4}$$

where N_d and G_d are the Nusselt and Grashof numbers respectively based on the local diameter d, then equation (3) gives the following equation for the mean heat transfer rate

$$\mathrm{N}_d = 0.7 + 0.35(\mathrm{G}_D\mathrm{P}_r)^{0.125} + 0.51(\mathrm{G}_D\mathrm{P}_r)^{0.25} \tag{5}$$

The variation of N_D with G_D for air given by this equation is shown in Fig. 1. It will be seen that it agrees with the experimental results for the cones to a similar degree of accuracy to that with which equation (4) agrees with the range of experimental results available for cylinders.

Acknowledgments

This work was supported by the National Research Council of Canada under Grant Number A5573.

References

1 Herring, R. G., and Gosh, R. J., "Laminar Free Convection From a Non-Isothermal Cone," *International Journal of Heat and Mass Transfer*, Vol. 5, 1962, pp. 1059–1068.

2 Kuiken, H. K., "Axisymmetric Free Convection Boundary Layer Flow Past Slender Bodies," *International Journal of Heat and Mass Transfer*, Vol. 11, 1968, pp. 1141–1153.

3 Oosthuizen, P. H., and Donaldson, E., "Free Convective Heat Transfer From Vertical Cones," JOURNAL OF HEAT TRANSFER, TRANS. ASME, Series C, Vol. 94, No. 3, 1972, pp. 330–331.

4 Van Der Hegge Zijnen, B. G., "Modified Correlation Formulae for the Heat Transfers by Natural and by Forced Convection From Horizontal Cylinders," *Applied Scientific Research*, Vol. A6, 1957, pp. 129–140.

The Effect of Thermal Contact Resistance on Heat Transfer Between Periodically Contacting Surfaces

J. R. HOWARD[1] **and A. E. SUTTON**[2]

An analog-computer study is made of one-dimensional heat conduction through two bars whose axes are in line and whose adjacent ends make and break contact periodically. The work extends a previous study to take account of imperfect thermal contact at the contact interface. The effect of frequency and duration of contact are also discussed.

Nomenclature

f = frequency
$g(\ )$ = function of ( )
l = length of bar
l_i = length of bar material representing thermal resistance due to periodic interruptions of heat flow
Q = heat transfer rate (energy per unit time) under periodic contact conditions
Q_c = heat transfer rate (energy per unit time) under permanent contact conditions
t = time
T = temperature
x = distance
α = thermal diffusivity
λ = length of bar representing thermal contact resistance
τ_c = time surfaces are in contact per cycle
τ_0 = time surfaces are separated per cycle

Introduction

HEAT TRANSFER across the interface between two solids held permanently in contact has been the subject of much study. Various surveys of literature have been made [1–4],[3] and the subject continues to be studied.

The work in [5] described a one-dimensional heat transfer study along two identical bars whose axes are in line. The remote ends of the bars were at different, but fixed, temperatures and the adjacent ends were brought into contact and separated according to a continuous regular cycle. When the adjacent ends of the bars made contact, it was assumed that the thermal contact resistance was zero, and when they were separated there was no heat flow across the gap between the ends of the bars.

The foregoing work has been extended to examine the effect of finite thermal contact resistance at the interface when the bars make contact.

Formulation

An exact solution to the three-dimensional heat diffusion equation

$$\nabla^2 T = \frac{1}{\alpha}\frac{\partial T}{\partial t} \tag{1}$$

is not practical, due to the physical shape of the boundary at the contact interface and the numerous boundary conditions to be satisfied. Even when the surfaces are permanently in contact and the right-hand side of equation (1) is zero, e.g., see [6, 7], approximations had to be made.

An approximate representation is possible using the one-dimensional heat diffusion equation

$$\frac{\partial^2 T}{\partial t^2} = \frac{1}{\alpha}\frac{\partial T}{\partial t} \tag{2}$$

by assuming that during the period of contact the thermal contact resistance between the contact surfaces is due to a thin film whose thermal resistance is equal to the steady-state thermal contact resistance of the real surfaces. For simplicity, the heat capacity of the film is assumed to be negligible. A solution in the quasi-steady state is to be obtained.

Boundary and Initial Conditions. Since the bars are identical, events in only one bar, the hotter one, need be considered. The origin is taken at the hottest end of the bar, where the temperature is fixed at T_A. The temperature at the midpoint of the film is taken as zero, the length of bar as l, and half the thermal contact resistance equivalent to length λ of the bar material. The boundary conditions are then

1 at $x = 0$

$$T = T_A, \text{ at all times}$$

2(a) at $x = l$ during the contact period $0 < t < \tau_c$

$$\frac{\partial T}{\partial x} = -\frac{T}{\lambda}$$

2(b) at $x = l$ when the surfaces are separated $\tau_c < t < (\tau_0 + \tau_c)$

$$\frac{\partial T}{\partial x} = 0$$

Dimensional Analysis. The existence of an additional variable, namely thermal contact resistance characterised by a length λ of bar material, gives rise to a dimensionless group additional to the two quoted in [5]. If l_i is the length of bar material equivalent to the thermal resistance due to the periodic interruption of the heat flow, the groups become

$$\left(\frac{f l_i^2}{\alpha}\right) = g\left[(f\tau_c), \left(\frac{f\lambda^2}{\alpha}\right)\right] \tag{3}$$

for sufficiently large values of bar length l such that

$$\left(\frac{f l^2}{\alpha}\right) > 2.56\pi \tag{4}$$

see [5].

The inset at the top of Fig. 1 shows the time-average temperature distribution in the hotter bar when the surfaces are permanently in contact and when in the quasi steady state.

Simulation. Finite-difference approximations to the heat diffusion equation (2) and the boundary conditions were made, the mesh being identical to that used in [5]. The diagram of the circuit used will not be shown here as it differed from that described in [5] only at the section used to simulate the boundary condition at the contact interface.

Results and Discussion

The relationship between the dimensionless groups is shown plotted in Fig. 1, demonstrating the validity of equation (3).

Heat flow through the system may conveniently be expressed by the ratio Q/Q_c, where Q is the heat transfer rate under *periodic* contact conditions and Q_c is the heat transfer rate under *permanent* contact conditions with zero thermal contact resistance.

$$\frac{Q}{Q_c} = \frac{l}{l + \lambda + l_i} \tag{5}$$

Fig. 2, which is derived from equation (5) and Fig. 1 at a fixed frequency f and given diffusivity α, illustrates by example the importance of thermal contact resistance under periodic contact conditions.

---

[1] Department of Mechanical Engineering, University of Aston, Birmingham, England.

[2] Department of Mathematics, University of Aston, Birmingham, England.

[3] Numbers in brackets designate References at end of technical brief.

Contributed by the Heat Transfer Division of THE AMERICAN SOCIETY OF MECHANICAL ENGINEERS. Manuscript received by the Heat Transfer Division July 28, 1972.

A numerical method of solution shows extremely good agreement with these analog-computer results, showing that any errors due to the use of a nonuniform mesh for the finite-difference equations are small.

Conclusion

Thermal contact resistance between two periodically contacting surfaces can be the most significant factor in controlling the heat flow, particularly when the ratio of contact time/periodic time, $f\tau_c$, is high.

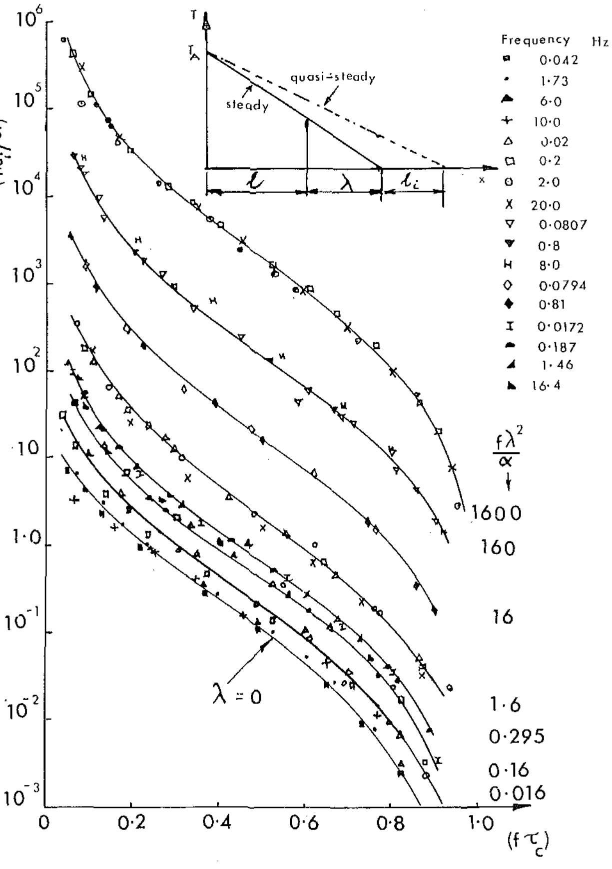

Fig. 1 Dimensionless plot of fl_i^2/α versus $f\tau_c$

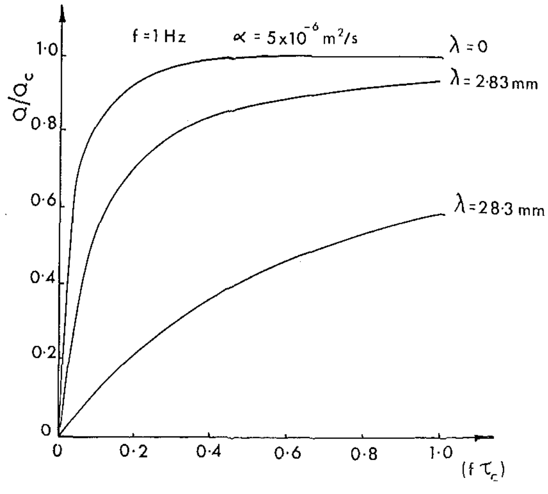

Fig. 2 Effect of contact time/periodic time on heat flow with various thermal contact resistances

Acknowledgments

We are grateful to our colleagues Prof. D. E. Elliott, N. Kerruish, and D. C. Hickson for their criticism and comments on this work.

References

1 Wong, H. Y., "A Survey of Thermal Conductance of Metallic Contacts," Ministry of Technology, Aeronautical Research Council Current Papers CP No. 973 HMSO, 1968.

2 Atkins, H., "Bibliography on Thermal Metallic Contact Conductance," NASA Technical Memorandum TMX-53227, Apr. 15, 1965.

3 Hseih, C. K., and Davis, F. E., "Bibliography on Thermal Contact Conductance," Purdue University Thermophysical Properties Research, AFML-TR-69-24, 1969.

4 Moore, C. J., Jr., Atkins, H., and Blum, H. A., "Subject Classification Bibliography for Thermal Contact Resistance Studies," ASME Paper No. 68-WA/HT-18.

5 Howard, J. R., and Sutton, A. E., "An Analogue Study of Heat Transfer Through Periodically Contacting Surfaces," *International Journal of Heat and Mass Transfer*, Vol. 13, 1970, pp. 173–183.

6 Fenech, H., and Rohsenow, W. M., "Prediction of Thermal Conductance of Metallic Surfaces in Contact," Journal of Heat Transfer, Trans. ASME, Series C, Vol. 85, No. 1, Feb. 1963, pp. 15–24.

7 Cetinkale, T. N., and Fishenden, M., "Thermal Conductance of Metallic Surfaces in Contact," General Discussion on Heat Transfer, *Proc. Inst. Mech. Engrs.*, London, Sept. 1951, pp. 271–275.

Transient Heat Flow in Half-Space Due to an Isothermal Disk on the Surface[1]

NED R. KELTNER[2]

Nomenclature

a = interfocal distance in oblate spheroidal coordinates
R = radius of disk
t = time
t^* = dimensionless time, $\alpha t/R^2$
T = temperature
T_0 = disk temperature
α = thermal diffusivity
δ = penetration depth
η = angle coordinate in oblate spheroidal coordinates
ξ = radial coordinate in oblate spheroidal coordinates
ϕ = polar coordinate in oblate spheroidal coordinates

Solutions of the transient heat diffusion equation for the case of a uniform step temperature change over a disk on the surface of a half-space are obtained by applying the heat balance integral technique [1, 2][3] in oblate spheroidal coordinates. These solutions are compared to an existing late time, asymptotic solution [3] and to a finite difference solution [4].

Oblate spheroidal coordinates are used to eliminate the mixed boundary conditions which occur on the surface if the problem is

---

[1] This work was supported by the United States Atomic Energy Commission.

[2] Staff Member Thermal and Centrifuge Division, Sandia Laboratories, Albuquerque, New Mexico 87115.

[3] Numbers in brackets designate References at end of technical brief.

Contributed by the Heat Transfer Division of The American Society of Mechanical Engineers. Manuscript received by the Heat Transfer Division February 20, 1973.

A numerical method of solution shows extremely good agreement with these analog-computer results, showing that any errors due to the use of a nonuniform mesh for the finite-difference equations are small.

Conclusion

Thermal contact resistance between two periodically contacting surfaces can be the most significant factor in controlling the heat flow, particularly when the ratio of contact time/periodic time, $f\tau_c$, is high.

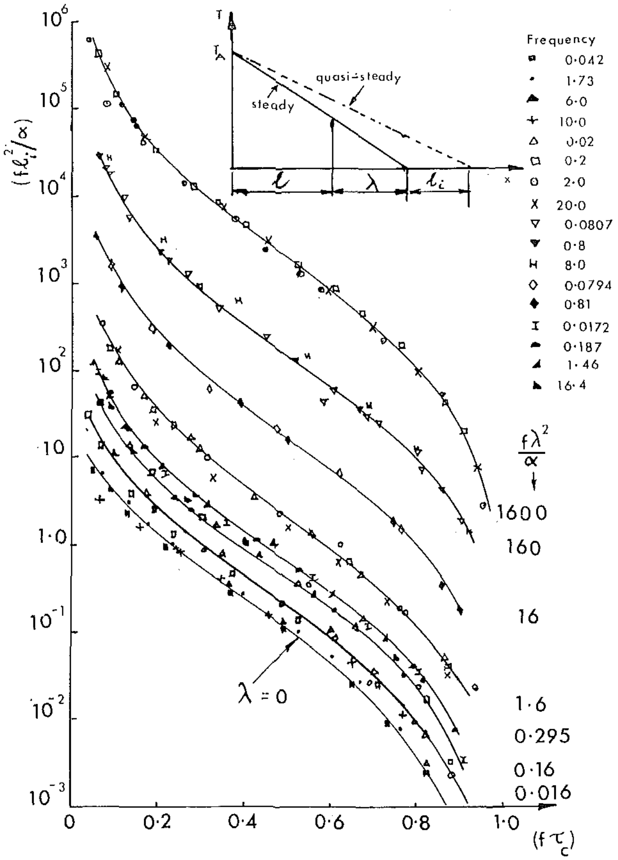

Fig. 1 Dimensionless plot of fl_i^2/α versus $f\tau_c$

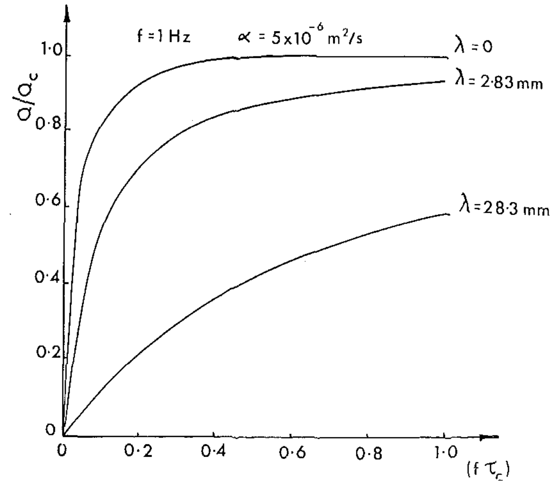

Fig. 2 Effect of contact time/periodic time on heat flow with various thermal contact resistances

Acknowledgments

We are grateful to our colleagues Prof. D. E. Elliott, N. Kerruish, and D. C. Hickson for their criticism and comments on this work.

References

1 Wong, H. Y., "A Survey of Thermal Conductance of Metallic Contacts," Ministry of Technology, Aeronautical Research Council Current Papers CP No. 973 HMSO, 1968.

2 Atkins, H., "Bibliography on Thermal Metallic Contact Conductance," NASA Technical Memorandum TMX-53227, Apr. 15, 1965.

3 Hseih, C. K., and Davis, F. E., "Bibliography on Thermal Contact Conductance," Purdue University Thermophysical Properties Research, AFML-TR-69-24, 1969.

4 Moore, C. J., Jr., Atkins, H., and Blum, H. A., "Subject Classification Bibliography for Thermal Contact Resistance Studies," ASME Paper No. 68-WA/HT-18.

5 Howard, J. R., and Sutton, A. E., "An Analogue Study of Heat Transfer Through Periodically Contacting Surfaces," *International Journal of Heat and Mass Transfer*, Vol. 13, 1970, pp. 173–183.

6 Fenech, H., and Rohsenow, W. M., "Prediction of Thermal Conductance of Metallic Surfaces in Contact," JOURNAL OF HEAT TRANSFER, TRANS. ASME, Series C, Vol. 85, No. 1, Feb. 1963, pp. 15–24.

7 Cetinkale, T. N., and Fishenden, M., "Thermal Conductance of Metallic Surfaces in Contact," General Discussion on Heat Transfer, *Proc. Inst. Mech. Engrs.*, London, Sept. 1951, pp. 271–275.

Transient Heat Flow in Half-Space Due to an Isothermal Disk on the Surface[1]

NED R. KELTNER[2]

Nomenclature

a = interfocal distance in oblate spheroidal coordinates
R = radius of disk
t = time
t^* = dimensionless time, $\alpha t/R^2$
T = temperature
T_0 = disk temperature
α = thermal diffusivity
δ = penetration depth
η = angle coordinate in oblate spheroidal coordinates
ξ = radial coordinate in oblate spheroidal coordinates
ϕ = polar coordinate in oblate spheroidal coordinates

SOLUTIONS of the transient heat diffusion equation for the case of a uniform step temperature change over a disk on the surface of a half-space are obtained by applying the heat balance integral technique [1, 2][3] in oblate spheroidal coordinates. These solutions are compared to an existing late time, asymptotic solution [3] and to a finite difference solution [4].

Oblate spheroidal coordinates are used to eliminate the mixed boundary conditions which occur on the surface if the problem is

---

[1] This work was supported by the United States Atomic Energy Commission.

[2] Staff Member Thermal and Centrifuge Division, Sandia Laboratories, Albuquerque, New Mexico 87115.

[3] Numbers in brackets designate References at end of technical brief.

Contributed by the Heat Transfer Division of THE AMERICAN SOCIETY OF MECHANICAL ENGINEERS. Manuscript received by the Heat Transfer Division February 20, 1973.

set up in cylindrical coordinates. The range of coordinates pertinent to a half-space is $0 \le \xi \le \infty$, $0 \le \eta \le 1$, and $0 \le \phi \le 2\pi$. The surface, $\xi = 0$, is a disk on the surface of the half-space of radius $a/2$, where a is the interfocal distance of the ellipsoids and hyperboloids. The surface, $\eta = 0$, is the remainder of the half-space surface.

If the axial symmetry of the temperature field is assumed, the diffusion equation in oblate spheroidal coordinates is [4, 5]

$$\frac{4}{a^2(\eta^2+\xi^2)}\left\{\frac{\partial}{\partial\eta}\left[(1-\eta^2)\frac{\partial T}{\partial\eta}\right]+\frac{\partial}{\partial\xi}\left[(1+\xi^2)\frac{\partial T}{\partial\xi}\right]\right\} = \frac{1}{\alpha}\frac{\partial T}{\partial t} \quad (1)$$

To obtain the heat balance integral solution, it was further assumed that T was a function of ξ and t^* only; i.e., the isotherms are oblate spheroids. Under the assumption that $T = T(\xi, t^*)$, equation (1) becomes

$$\frac{1}{(\eta^2+\xi^2)}\left\{\frac{\partial}{\partial\xi}\left[(1+\xi^2)\frac{\partial T}{\partial\xi}\right]\right\} = \frac{\partial T}{\partial t^*}. \quad (2)$$

To remove the η dependence, equation (2) is integrated with respect to η over $0 \le \eta \le 1$. This gives[4]

$$\frac{\partial}{\partial\xi}\left[(1+\xi^2)\frac{\partial T}{\partial\xi}\right] = \frac{(1+3\xi^2)}{3}\frac{\partial T}{\partial t^*}. \quad (3)$$

The heat balance integral equation is obtained from equation (3) by integrating once with respect to ξ over $(0, \delta)$. When the limits are applied to the left side of the integrated equation, and the integral on the right-hand side is rearranged by Leibniz' rule for the differentiation of an integral, the equation becomes

$$\left[(1+\xi^2)\frac{\partial T}{\partial\xi}\right]_{\xi=\delta} - \left[(1+\xi^2)\frac{\partial T}{\partial\xi}\right]_{\xi=0} = \frac{d}{dt^*}\left[\int_0^\delta\left(\frac{1+3\xi^2}{3}\right)Td\xi\right] - \left[\frac{1+3\xi^2}{3}T\right]_{\xi=\delta}\frac{d\delta}{dt^*}. \quad (4)$$

From the definition of the penetration layer and the initial condition, both T and $\partial T/\partial\xi$ evaluated at $\xi = \delta$ are zero; thus equation (4) becomes

$$-\left.\frac{\partial T}{\partial\xi}\right|_{\xi=0} = \frac{d}{dt^*}\left[\int_0^\delta\left(\frac{1+3\xi^2}{3}\right)Td\xi\right]. \quad (5)$$

Next, a suitable form for the temperature distribution must be assumed. To obtain a suitable approximation in nonplanar geometries, references [1, 2] suggest that a product of a polynomial and some form of the steady-state temperature distribution be used. The steady-state solution is [6]

$$T(\xi, \eta) = \frac{2T_0}{\pi}\cot^{-1}\xi. \quad (6)$$

This form is used with second and third-degree polynomials to obtain expressions for the step responses.

Second-Degree Approximation

The assumed temperature distribution in this case is

$$T = (a + b\xi + c\xi^2)\cot^{-1}\xi \quad (7)$$

The coefficients in equation (7) are evaluated from the following conditions:

$$T(0) = T_0,\ T(\delta) = 0,\ (\partial T/\partial\xi)_{\xi=\delta} = 0. \quad (8a), (8b), (8c)$$

By using these conditions with equation (7),

$$T(\xi, t^*) = \frac{2T_0}{\pi}\left(1 - \frac{2\xi}{\delta} + \frac{\xi^2}{\delta^2}\right)\cot^{-1}\xi. \quad (9)$$

By using equation (9), equation (5) becomes

$$3\left(\frac{\pi}{\delta}+1\right) = \frac{d}{dt^*}\left[\int_0^\delta(1+3\xi^2)\left(1-\frac{2\xi}{\delta}+\frac{\xi^2}{\delta^2}\right)\cot^{-1}\xi d\xi\right]. \quad (10)$$

After carrying out the integration and then performing the differentiation, all the terms containing δ are collected on the right-hand side; this gives the separated differential equation relating δ and t^*;

$$3dt^* = \left[\left(\frac{3\delta^3}{10}+\frac{\delta}{3}\right)\cot^{-1}\delta + \frac{\tan^{-1}\delta}{2\delta} + \frac{1}{(1+\delta^2)} \times\left(-\frac{7}{30}-\frac{\delta^2}{3}-\frac{\delta^4}{10}\right) + \frac{3\delta^2}{10} - \frac{4\log(1+\delta^2)}{15\,\delta^2}\right]\frac{d\delta}{(\delta+\pi)}. \quad (11)$$

The solution of equation (11) to obtain δ as a function of t^* will be discussed later.

Third-Degree Modified Polynomial Approximations

If the temperature distribution is assumed to have the form

$$T = (a + b\xi + c\xi^2 + d\xi^3)\cot^{-1}\xi, \quad (12)$$

two third-degree approximations can be developed on the basis of the conditions employed to evaluate the coefficients. The third-degree approximation requires the use of four boundary conditions to evaluate the coefficients in equation (12). The first three conditions used are the same as for the second-degree approximations (equations [8]). For the fourth condition, either of the following equations, which are obtained from equation (3), can be used:

$$(\partial^2T/\partial\xi^2)_{\xi=\delta} = 0 \text{ or } (\partial^2T/\partial\xi^2)_{\xi=0} = 0. \quad (13a), (13b)$$

The third-degree approximation developed here will use equation (13*b*) for the fourth condition. Equation (13*a*) was used in reference [4] to develop another third-degree solution; however, it provides a poorer approximate solution to the problem than the two solutions presented here.

If equations (8) and (13*b*) are used in equation (12) to evaluate the coefficients, the expression for $T(\xi, t^*)$ takes the form

$$T(\xi, t^*) = T_0\left[\frac{2}{\pi} - \frac{3\xi}{\delta(\pi+\delta)} - \frac{6\xi^2}{\pi\delta(\pi+\delta)} + \frac{(\pi+4\delta)\xi^3}{\pi\delta^3(\pi+\delta)}\right]\cot^{-1}\xi. \quad (14)$$

Following the procedure used in the second-degree solution, the separated differential equation is

$$3dt^* = \left\{\left[\frac{3\pi^2}{4} + 2\pi\delta + \left(1+\frac{3\pi^2}{4}\right)\delta^2 + \frac{21\pi\delta^3}{10} + \frac{6\delta^4}{5}\right]\delta\cot^{-1}\delta + \frac{4(\pi+2\delta)}{5\delta}\log(1+\delta^2) + \left[\frac{3\pi^2}{4\delta^3} + \frac{3\pi}{\delta^2} + \left(3+\frac{3\pi^2}{4}\right)\frac{1}{\delta} + \frac{3\pi}{2}\right]\tan^{-1}\delta + \left(-\frac{\pi}{4\delta^3} - \frac{1}{\delta^2} - \frac{3\pi}{4\delta} - \frac{3\pi\delta}{4} - \delta^2 - \frac{\pi\delta^3}{4} - \frac{2\delta^4}{5}\right)\frac{\pi\delta}{(1+\delta^2)} + \left(-\frac{\pi^2}{2\delta^2} - \frac{7\pi}{4\delta} - 2 + \frac{\pi\delta}{15} + \frac{7\pi^2\delta^2}{10} + \frac{37\pi\delta^3}{20} + \delta^4\right)\right\} \times \frac{2d\delta}{(\pi+\delta)[3\pi^2+4\delta(\pi+\delta)]}. \quad (15)$$

Equations (11) and (15), which relate δ to t^*, were integrated

---

[4] This equation can also be developed by performing a heat balance on an oblate spheroidal shell and then letting the thickness go to zero.

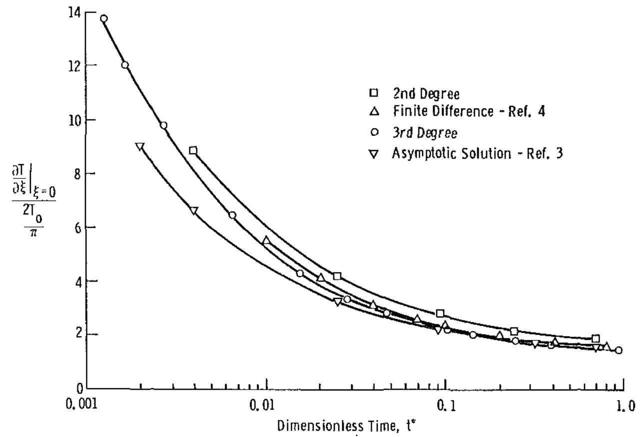

Fig. 1 Values of $(\partial T/\partial \xi)_{\xi=0}$ versus t^*

Table 1 Values of T/T_0 from equation (9) (No. 1), equation (14) (No. 2), the late time, asymptotic solution of reference [3] (No. 3), and the finite difference solution of reference [4] (No. 4)

		ξ						
t^*	No.	0.05	0.15	0.25	0.50	1.0	2.0	5.0
0.01	1	0.822	0.528	0.310	0.032	...	...	...
	2	0.836	0.527	0.272	...	...	...	...
	3	0.895	(a)	(a)	(a)	...	...	...
	4	0.824	0.505	0.264	0.027	...	...	...
0.10	1	0.917	0.764	0.631	0.375	0.106	...	...
	2	0.931	0.794	0.664	0.386	0.064	...	...
	3	0.933	0.809	0.695	(a)	(a)	...	...
	4	0.929	0.789	0.655	0.373	0.057	...	...
1.00	1	0.948	0.850	0.759	0.567	0.315	0.102	...
	2	0.958	0.875	0.795	0.613	0.349	0.094	...
	3	0.957	0.872	0.789	0.602	0.332	0.098	...
	4	0.956	0.870	0.786	0.598	0.304	0.083	...
10.0	1	0.961	0.884	0.812	0.652	0.426	0.211	0.048
	2	0.966	0.899	0.834	0.686	0.467	0.244	0.049
	3	0.965	0.894	0.826	0.671	0.444	0.217	(a)
	4	0.965	0.894	0.826	0.670	0.443	0.218	0.041

(a) Solution unreliable for $t^*/\xi^2 > 1$[3].

numerically by using an adaptive Simpson's rule algorithm [7]. The integration was performed over successive small ranges of the δ variable; for both equations, power series expansions of certain terms were required to evaluate the integrands in the region near $\delta = 0$ and to show that they behave properly [4].

Results and Discussion

The values of δ versus t^* were used in equations (9) and (14) to evaluate $T(\xi)$ at several values of t^* and also to evaluate $(\partial T/\partial \xi)_{\xi=0}$ which is related to the heat flux across the disk. For comparison, T and $(\partial T/\partial \xi)_{\xi=0}$ were also evaluated by using the asymptotic solution of reference [3] and a one-dimensional, finite-difference model developed in reference [4].

The results in Table 1 show that both heat balance integral solutions provide good agreement with the temperatures predicted by the other methods. The results in Fig. 1 show that the value of $(\partial T/\partial \xi)_{\xi=0}$ obtained from equation (14) provides the best agreement with the values predicted by other methods, particularly for $t^* > 0.1$. At earlier times, the asymptotic solution falls well below the third degree, and finite difference results; however, this probably results from the asymptotic solution being a "late-time" solution [3].

Acknowledgments

This note represents a portion of the work done by the author to partially fulfill the requirements for the doctor of philosophy degree at the University of New Mexico.

References

1 Goodman, T. R., "Application of Integral Methods of Transient Nonlinear Heat Transfer," in *Advances in Heat Transfer*, Vol. 1, Academic Press, New York, 1964.

2 Ozisik, M. N., "Approximate Methods in the Solution of Heat Conduction Problems," *Boundary Value Problems of Heat Conduction*, International Textbook, Scranton, Pa., 1968.

3 Norminton, E. J., and Blackwell, J. H., "Transient Heat Flow From Constant Temperature Spheroids and the Thin Circular Disk," *Quarterly Journal of Mechanics and Applied Mathematics*, Vol. 17, Part 1, 1964.

4 Keltner, N. R., "Heat Transfer in Intrinsic Thermocouples—Application to Transient Temperature Measurement Errors," PhD dissertation, University of New Mexico, Albuquerque, N. Mex., 1973.

5 Hanish, S., et al., "Tables of Radial Spheroidal Wave Function," Vols. 1–6, Naval Research Laboratory, Washington, D. C., NRL-Reports 7088 to 7093, 1970.

6 Tranter, C. J., *Integral Transforms in Mathematical Physics*, Second ed., Wiley, New York, 1962.

7 Bailey, C. B., and Jones, R. E., *MATHLIB, A Brief User's Guide to the Sandia Mathematical Program Library*, Sandia Laboratories, Albuquerque, N. Mex. SC-M-720142, Apr., 1972.

Transient Heat Conduction in an Infinite Plate With a Transverse Circular Cylindrical Hole

C. D. MICHALOPOULOS[1] **and J. J. SECO**[2]

The flow of heat in an infinite plate with a transverse circular cylindrical hole is considered. The boundary conditions are zero temperature on the cylindrical surface and arbitrary but axisymmetric temperature distributions on the plane surfaces. The solution is obtained by means of Laplace and an unconventional Hankel transforms. Numerical results are given in graphical form for a plate with a step temperature distribution on one face and zero temperature on the other.

Introduction

PROBLEMS of heat conduction in regions bounded internally by a circular cylinder have been considered by several investigators through the years. Nicholson [1][3] applied the Weber expansion [2] to the solution of a heat conduction problem for an infinite medium with a circular cylindrical hole. Goldstein [3] and Carslaw and Jaeger [4] considered two-dimensional problems in diffusion and heat conduction with circular symmetry. Blackwell [5] analyzed the radial-axial heat flow in an infinite solid bounded internally by a circular cylinder and in an infinite plate with a transverse circular cylindrical hole.

In the studies of [1, 3, 4, and 5] the results are given in integral form or as series. No numerical results are presented. The purpose of this study is to obtain transient and steady-state axisymmetric solutions (with numerical results) of the heat conduction equation for an infinite plate with a transverse cylindrical hole.

The solution herein utilizes an unconventional Hankel transform which is based on an expansion formula discovered by Weber [2] in 1873. Orr [6] rediscovered Weber's formula in 1909 by a method of contour integration. The formal proof of the

---

[1] Associate Professor, Department of Mechanical Engineering, University of Houston, Houston, Texas.

[2] Assistant Professor of Mechanical Engineering, University of Costa Rica, Costa Rica, Central America.

[3] Numbers in brackets designate References at end of technical brief.

Contributed by the Heat Transfer Division of THE AMERICAN SOCIETY OF MECHANICAL ENGINEERS. Manuscript received by the Heat Transfer Division, December 11, 1972.

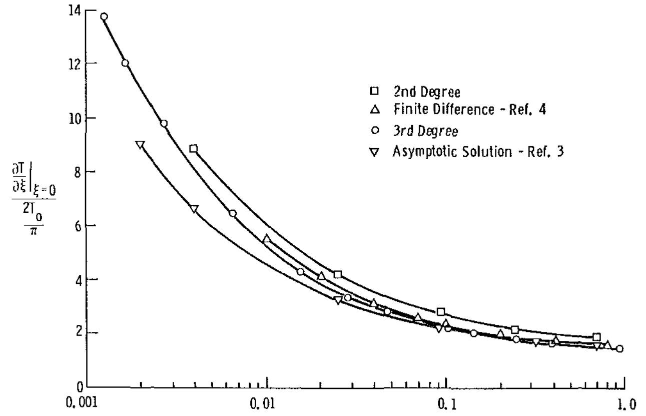

Fig. 1 Values of $(\partial T/\partial \xi)_{\xi=0}$ versus t^*

Table 1 Values of T/T_0 from equation (9) (No. 1), equation (14) (No. 2), the late time, asymptotic solution of reference [3] (No. 3), and the finite difference solution of reference [4] (No. 4)

		ξ						
t^*	No.	0.05	0.15	0.25	0.50	1.0	2.0	5.0
0.01	1	0.822	0.528	0.310	0.032	...	...	...
	2	0.836	0.527	0.272	...	...	...	...
	3	0.895	(a)	(a)	(a)	...	...	...
	4	0.824	0.505	0.264	0.027	...	...	...
0.10	1	0.917	0.764	0.631	0.375	0.106	...	...
	2	0.931	0.794	0.664	0.386	0.064	...	...
	3	0.933	0.809	0.695	(a)	(a)	...	...
	4	0.929	0.789	0.655	0.373	0.057	...	...
1.00	1	0.948	0.850	0.759	0.567	0.315	0.102	...
	2	0.958	0.875	0.795	0.613	0.349	0.094	...
	3	0.957	0.872	0.789	0.602	0.332	0.098	...
	4	0.956	0.870	0.786	0.598	0.304	0.083	...
10.0	1	0.961	0.884	0.812	0.652	0.426	0.211	0.048
	2	0.966	0.899	0.834	0.686	0.467	0.244	0.049
	3	0.965	0.894	0.826	0.671	0.444	0.217	(a)
	4	0.965	0.894	0.826	0.670	0.443	0.218	0.041

(a) Solution unreliable for $t^*/\xi^2 > 1$[3].

numerically by using an adaptive Simpson's rule algorithm [7]. The integration was performed over successive small ranges of the δ variable; for both equations, power series expansions of certain terms were required to evaluate the integrands in the region near $\delta = 0$ and to show that they behave properly [4].

Results and Discussion

The values of δ versus t^* were used in equations (9) and (14) to evaluate $T(\xi)$ at several values of t^* and also to evaluate $(\partial T/\partial \xi)_{\xi=0}$ which is related to the heat flux across the disk. For comparison, T and $(\partial T/\partial \xi)_{\xi=0}$ were also evaluated by using the asymptotic solution of reference [3] and a one-dimensional, finite-difference model developed in reference [4].

The results in Table 1 show that both heat balance integral solutions provide good agreement with the temperatures predicted by the other methods. The results in Fig. 1 show that the value of $(\partial T/\partial \xi)_{\xi=0}$ obtained from equation (14) provides the best agreement with the values predicted by other methods, particularly for $t^* > 0.1$. At earlier times, the asymptotic solution falls well below the third degree, and finite difference results; however, this probably results from the asymptotic solution being a "late-time" solution [3].

Acknowledgments

This note represents a portion of the work done by the author to partially fulfill the requirements for the doctor of philosophy degree at the University of New Mexico.

References

1 Goodman, T. R., "Application of Integral Methods of Transient Nonlinear Heat Transfer," in *Advances in Heat Transfer*, Vol. 1, Academic Press, New York, 1964.

2 Ozisik, M. N., "Approximate Methods in the Solution of Heat Conduction Problems," *Boundary Value Problems of Heat Conduction*, International Textbook, Scranton, Pa., 1968.

3 Norminton, E. J., and Blackwell, J. H., "Transient Heat Flow From Constant Temperature Spheroids and the Thin Circular Disk," *Quarterly Journal of Mechanics and Applied Mathematics*, Vol. 17, Part 1, 1964.

4 Keltner, N. R., "Heat Transfer in Intrinsic Thermocouples—Application to Transient Temperature Measurement Errors," PhD dissertation, University of New Mexico, Albuquerque, N. Mex., 1973.

5 Hanish, S., et al., "Tables of Radial Spheroidal Wave Function," Vols. 1–6, Naval Research Laboratory, Washington, D. C., NRL-Reports 7088 to 7093, 1970.

6 Tranter, C. J., *Integral Transforms in Mathematical Physics*, Second ed., Wiley, New York, 1962.

7 Bailey, C. B., and Jones, R. E., *MATHLIB, A Brief User's Guide to the Sandia Mathematical Program Library*, Sandia Laboratories, Albuquerque, N. Mex. SC-M-720142, Apr., 1972.

Transient Heat Conduction in an Infinite Plate With a Transverse Circular Cylindrical Hole

C. D. MICHALOPOULOS[1] **and J. J. SECO**[2]

The flow of heat in an infinite plate with a transverse circular cylindrical hole is considered. The boundary conditions are zero temperature on the cylindrical surface and arbitrary but axisymmetric temperature distributions on the plane surfaces. The solution is obtained by means of Laplace and an unconventional Hankel transforms. Numerical results are given in graphical form for a plate with a step temperature distribution on one face and zero temperature on the other.

Introduction

PROBLEMS of heat conduction in regions bounded internally by a circular cylinder have been considered by several investigators through the years. Nicholson [1][3] applied the Weber expansion [2] to the solution of a heat conduction problem for an infinite medium with a circular cylindrical hole. Goldstein [3] and Carslaw and Jaeger [4] considered two-dimensional problems in diffusion and heat conduction with circular symmetry. Blackwell [5] analyzed the radial-axial heat flow in an infinite solid bounded internally by a circular cylinder and in an infinite plate with a transverse circular cylindrical hole.

In the studies of [1, 3, 4, and 5] the results are given in integral form or as series. No numerical results are presented. The purpose of this study is to obtain transient and steady-state axisymmetric solutions (with numerical results) of the heat conduction equation for an infinite plate with a transverse cylindrical hole.

The solution herein utilizes an unconventional Hankel transform which is based on an expansion formula discovered by Weber [2] in 1873. Orr [6] rediscovered Weber's formula in 1909 by a method of contour integration. The formal proof of the

---

[1] Associate Professor, Department of Mechanical Engineering, University of Houston, Houston, Texas.

[2] Assistant Professor of Mechanical Engineering, University of Costa Rica, Costa Rica, Central America.

[3] Numbers in brackets designate References at end of technical brief.

Contributed by the Heat Transfer Division of THE AMERICAN SOCIETY OF MECHANICAL ENGINEERS. Manuscript received by the Heat Transfer Division, December 11, 1972.

Weber-Orr expansion was established in 1922 by Titchmarch [7] who, in his book [8], broadened its use. The transform of an arbitrary function $f(r)$ and its inverse employed here are defined by

$$\mathcal{W}\{f(r)\} \equiv \bar{f}(s) = \int_a^\infty tW_0(s, t, a)f(t)dt, \tag{1}$$

$$\mathcal{W}^{-1}\{\bar{f}(s)\} \equiv f(r) = \int_0^\infty \frac{s\bar{f}(s)W_0(s, r, a)ds}{J_0^2(sa) + Y_0^2(sa)}, \tag{2}$$

where $W_0(s, r, a) = J_0(sr)Y_0(sa) - J_0(sa)Y_0(sr)$, J_0 and Y_0 being zero-order Bessel functions of the first and the second kind, respectively. The conditions that the function $f(r)$ must satisfy for the existence of the transform are stated by Titchmarsh [7]. The properties of the transform are given in [9, pp. 3–9].

Solution of the Heat Conduction Equation

Consider an infinite plate of thickness L with a transverse circular cylindrical hole of radius a and define a cylindrical coordinate system (r, θ, z) such that z is coincident with the axis of the hole, as shown in Fig. 1 and 2.

For axial symmetry, the flow of heat is governed by the differential equation

$$\frac{\partial^2 T}{\partial r^2} + \frac{1}{r}\frac{\partial T}{\partial r} + \frac{\partial^2 T}{\partial z^2} = \frac{1}{\alpha}\frac{\partial T}{\partial t} \tag{3}$$

where $T = T(r, z, t)$ is the temperature, α is the diffusivity, and t is the time. The boundary conditions considered herein are:

$$T(r, 0, t) = F_1(r); \quad T(r, L, t) = F_2(r); \tag{4}$$

$$T(a, z, t) = 0. \tag{5}$$

It should be noted that

$$\lim_{r \to \infty} T(r, z, t) = 0 \tag{6}$$

As shown in reference [9, pp. 9–17], the solution of equation (3) subject to conditions (4), (5), and (6) is

$$T(r, z, t) = \int_0^\infty \frac{2\pi}{L^2} \sum_{n=1}^\infty \left\{ \left[(-1)^{n-1} n \frac{1 - e^{-\left(s^2 + \frac{n^2\pi^2}{L^2}\right)\alpha t}}{s^2 + \frac{n^2\pi^2}{L^2}} \right] \cdot \left[\bar{F}_1(s) \sin \frac{n\pi(L - z)}{L} + \bar{F}_2(s) \sin \frac{n\pi z}{L} \right] \right\} \frac{W_0(s, r, a)sds}{J_0^2(sa) + Y_0^2(sa)}. \tag{7}$$

The steady-state temperature distribution can be obtained from equation (7) by taking the limit as time tends to infinity and using the following relation (see, for example, reference [10, p. 40, number 1.445–4]):

$$\frac{\sinh sz}{\sinh sL} = \frac{2\pi}{L^2} \sum_{n=1}^\infty \frac{(-1)^{n-1} n \sin \frac{n\pi z}{L}}{s^2 + \frac{n^2\pi^2}{L^2}}. \tag{8}$$

Thus, the steady-state temperature distribution $T(r, z)$ is given by

$$T(r, z) = \int_0^\infty \frac{W_0(s, r, a)s}{J_0^2(sa) + Y_0^2(sa)} \cdot \left[\bar{F}_1(s) \frac{\sinh s(L - z)}{\sinh sL} + \bar{F}_2(s) \frac{\sinh sz}{\sinh sL} \right] ds. \tag{9}$$

A Numerical Example

Numerical results are given here for an infinite plate with the following boundary conditions on z:

$$T(r, 0, t) = F_1(r) = \begin{cases} T_0, & a \le r \le b \\ 0, & b < r \end{cases} \tag{10}$$

$$T(r, L, t) = F_2(r) = 0. \tag{11}$$

The $\mathcal{W}$ transform of boundary condition (10) is

$$\bar{F}_1(s) = \int_a^b rW_0(s, r, a)T_0 dr.$$

Introduce now the function $W_1(s, r, a) = J_1(sr)Y_0(sa) - J_0(sa)Y_1(sr)$. Noting that $\frac{\partial}{\partial r}[W_1(s, r, a)] = srW_0(s, r, a)$ and $W_1(s, a, a) = 2/\pi$ as one obtains for $\bar{F}_1(s)$

$$\bar{F}_1(s) = T_0 \left[\frac{bW_1(s, b, a)}{s} - \frac{2}{\pi s^2} \right]. \tag{12}$$

Numerical result were obtained by numerical evaluation of the infinite integrals of equations (7) and (9) with $\bar{F}_2(s) = 0$ and $\bar{F}_1(s)$ as given by (12). In all computations, the following values for the parameters were used: $a = 1$ in., $b = 3a$, $L = a$, $\alpha = 0.01$ in.^{2}/sec.

The approximate evaluation of the inversion integrals was effected by the trapezoidal rule together with Romberg's extrapolation scheme. Due to the nature of the integrands, it was observed that no significant improvement in the answer was found for an upper limit greater than about 20.

The results of this section are presented in graphical form in Figs. 1 and 2. In Fig. 1, graphs of T/T_0 versus r/a are shown with time as a parameter for z/L equal to 0.8. Fig. 2 gives the steady-state dimensionless temperature T/T_0 as a function of r/a

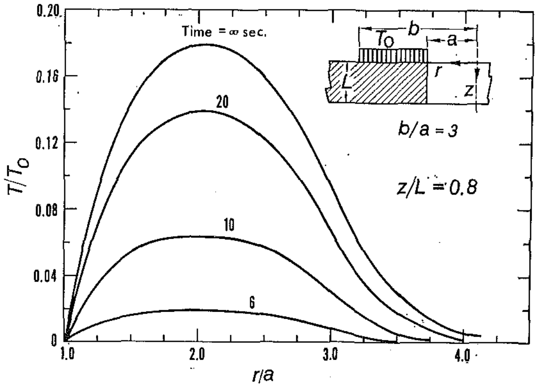

Fig. 1 Transient temperature distribution

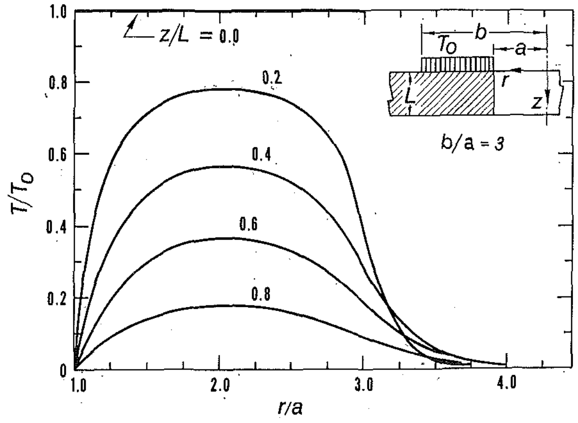

Fig. 2 Steady-state temperatures at $z/L = 0.8$

with z/L as a parameter. Transient temperatures at other ratios of z/L as well as the steady-state isotherms are given in [9].

Discussion

The solution derived here could have also been obtained by changing the nonhomogeneous boundary conditions, equations (4), to homogeneous through the introduction of a new variable $U(r, z, t)$ defined by

$$U(r, z, t) = T(r, z, t) + \left(\frac{z}{L} - 1\right)F_1(r) - \frac{z}{L} F_2(r)$$

However, the differential equation satisfied by U is nonhomogeneous. This equation can be solved by taking a Laplace transform in t and then a Fourier finite transform in z. The resulting ordinary differential equation in r is a nonhomogeneous Bessel equation of order zero. The solution of such an equation is considerably more involved than that of the present study which is a simple ordinary homogeneous differential equation in z resulting after the application of the unconventional Hankel transform employed herein.

Apparently, no solutions (transient or steady state) have appeared in the literature for heat conduction problems involving an infinite plate with a transverse cylindrical hole subject to nonhomogeneous boundary conditions on the plane surfaces. The present study illustrates a convenient analytical approach to heat conduction problems for regions bounded internally by circular cylinders. Other Hankel transforms similar to the one used here (given in [9]) can be employed to obtain solutions of the heat conduction equation for boundary conditions other than that of zero temperature on the cylindrical surface considered in this article.

References

1 Nicholson, J. W., "A Problem in the Theory of Heat Conduction," *Proceedings Royal Soc.*, Vol. A, Series C, 1921, p. 226.

2 Weber, H., "Veber eine Darstellung will Kurlicher Functionen durch Bessel'sche Functionen," *Math. Annelen*, Vol. 6, 1873, p. 154.

3 Goldstein, S., "Some Two-Dimensional Problems With Circular Symmetry," *Proceedings London Math. Soc.*, Vol. 34, Series 2, 1932, p. 51.

4 Carslaw, H. S., and Jaeger, J. C., "Some Two-Dimensional Problems in Conduction of Heat With Circular Symmetry," *Proceedings London Math. Soc.*, Vol. 46, Series 2, 1940, p. 361.

5 Blackwell, J. H., "Radial-Axial Heat Flow in Regions Bounded Internally by Circular Cylinders," *Canadian J. Phys.*, Vol. 31, 1953, p. 472.

6 Orr, W. M., "Extensions of Fourier's and the Bessel-Fourier Theorems," *Proceedings Royal Irish Acad.*, Vol. 27, No. A 11, 1909, p. 222.

7 Titchmarsh, E. C., "Weber's Integral Theorems," *Proceedings London Math. Soc.*, Vol. 22, Series 2, 1923, p. 15.

8 Titschmarsh, E. C., *Eigenfunction Expansion*, Part 1, Second ed., Oxford University Press, London, 1962.

9 Seco, J. J., "Use of Generalized Hankel Transforms in the Solution of Some Axially-Symmetric Problems in Heat Conduction," MS thesis, University of Houston, Houston, Texas, May 1969.

10 Gradshteyn, I. S., and Ryzhik, I. M., *Table of Integrals, Series and Products*, Fourth ed., Academic Press, New York, 1965.

Correlations for Laminar Forced Convection in Flow Over an Isothermal Flat Plate and in Developing and Fully Developed Flow in an Isothermal Tube

STUART W. CHURCHILL[1] and HIROYUKI OZOE[2]

Nomenclature

D = tube diameter, ft
$f(\mathrm{Pr})$ = a computed function, see equation (9)
$\mathrm{Gz} = \pi D^2 u_m / 4\alpha x$ = local Graetz number
j = local heat flux density at wall, Btu/hr ft^2
k = thermal conductivity, Btu/hr ft deg F
n = arbitrary exponent
$\mathrm{Nu}_D = jD/k(T_w - T_m)$ = local Nusselt number of tube
$Nu_x = jx/k(T_w - T_0)$ = local Nusselt number for flat plate
$\mathrm{Pe} = Du_m/\alpha$ = Peclet number
$\mathrm{Pr} = \nu/\alpha$ = Prandtl number
$\mathrm{Re}_D = Du_m/\nu$ = Reynolds number for tube
$\mathrm{Re}_x = xu_0/\nu$ = Reynolds number for flat plate
T = temperature, deg F
u = velocity component in x-direction, ft/hr
x = independent variable or distance along flat plate or tube, ft
y = dependent variable or distance normal to flat plate or wall of tube, ft
$y(x)$ = dependent variable
$y_0(x)$ = asymptotic solution for $x \to 0$
$y_\infty(x)$ = asymptotic solution for $x \to \infty$
α = thermal diffusivity, ft^2/hr
$\eta = y(u_0/x\nu)^{1/2}/2$
ν = kinematic viscosity, ft^2/hr
$\phi(\eta) = 2u/u_0$ = velocity distribution function in Blasius solution.

Subscripts

m = mixed mean value
0 = free stream or inlet value
w = value at wall

Churchill and Ozoe [1][3] used the procedure proposed by Churchill and Usagi [2] to derive an empirical expression for the effect of Pr on laminar forced convection in flow over a uniformly heated flat plate. Simple, empirical expressions were similarly derived for plug, fully developed and developing flow in a uniformly heated tube. The process of correlation indicated that the various computed values for a flat plate were very precise and consistent but revealed inconsistencies in the asymptotic solutions and computed values for a tube. Accordingly the various solutions for laminar forced convection in flow over an isothermal flat plate and in developing and fully developed flow in an isothermal tube are herein subjected to the same process of analysis and correlation.

Limitations of space have forced deletion of details of the development and evaluation of the correlating equations presented herein. An expanded version of the manuscript is available from S. W. Churchill.

Correlations for Fully Developed and Plug Flow in a Tube

The Graetz [3] solution for a step change in wall temperature in fully developed, laminar (parabolic) flow in a tube is in the form of a ratio of infinite series. The series converges very slowly for large Gz creating a role for a convenient and accurate approximation. The expression proposed for such purposes by Churchill and Usagi [2] has the form

$$y^n(x) = y_0{}^n(x) + y_\infty{}^n(x) \tag{1}$$

---

[1] Carl V. S. Patterson Professor, School of Chemical Engineering University of Pennsylvania, Philadelphia, Pa.

[2] Assistant Professor, Department of Industrial and Mechanical Engineering, Okayama University, Okayama Japan.

Contributed by the Heat Transfer Division, of THE AMERICAN SOCIETY OF MECHANICAL ENGINEERS. Revised manuscript received by the Heat Transfer Division, August 25, 1972.

[3] Numbers in brackets designate References at end of technical brief.

with z/L as a parameter. Transient temperatures at other ratios of z/L as well as the steady-state isotherms are given in [9].

Discussion

The solution derived here could have also been obtained by changing the nonhomogeneous boundary conditions, equations (4), to homogeneous through the introduction of a new variable $U(r, z, t)$ defined by

$$U(r, z, t) = T(r, z, t) + \left(\frac{z}{L} - 1\right)F_1(r) - \frac{z}{L} F_2(r)$$

However, the differential equation satisfied by U is nonhomogeneous. This equation can be solved by taking a Laplace transform in t and then a Fourier finite transform in z. The resulting ordinary differential equation in r is a nonhomogeneous Bessel equation of order zero. The solution of such an equation is considerably more involved than that of the present study which is a simple ordinary homogeneous differential equation in z resulting after the application of the unconventional Hankel transform employed herein.

Apparently, no solutions (transient or steady state) have appeared in the literature for heat conduction problems involving an infinite plate with a transverse cylindrical hole subject to nonhomogeneous boundary conditions on the plane surfaces. The present study illustrates a convenient analytical approach to heat conduction problems for regions bounded internally by circular cylinders. Other Hankel transforms similar to the one used here (given in [9]) can be employed to obtain solutions of the heat conduction equation for boundary conditions other than that of zero temperature on the cylindrical surface considered in this article.

References

1 Nicholson, J. W., "A Problem in the Theory of Heat Conduction," *Proceedings Royal Soc.*, Vol. A, Series C, 1921, p. 226.

2 Weber, H., "Veber eine Darstellung will Kurlicher Functionen durch Bessel'sche Functionen," *Math. Annelen*, Vol. 6, 1873, p. 154.

3 Goldstein, S., "Some Two-Dimensional Problems With Circular Symmetry," *Proceedings London Math. Soc.*, Vol. 34, Series 2, 1932, p. 51.

4 Carslaw, H. S., and Jaeger, J. C., "Some Two-Dimensional Problems in Conduction of Heat With Circular Symmetry," *Proceedings London Math. Soc.*, Vol. 46, Series 2, 1940, p. 361.

5 Blackwell, J. H., "Radial-Axial Heat Flow in Regions Bounded Internally by Circular Cylinders," *Canadian J. Phys.*, Vol. 31, 1953, p. 472.

6 Orr, W. M., "Extensions of Fourier's and the Bessel-Fourier Theorems," *Proceedings Royal Irish Acad.*, Vol. 27, No. A 11, 1909, p. 222.

7 Titchmarsh, E. C., "Weber's Integral Theorems," *Proceedings London Math. Soc.*, Vol. 22, Series 2, 1923, p. 15.

8 Titschmarsh, E. C., *Eigenfunction Expansion*, Part 1, Second ed., Oxford University Press, London, 1962.

9 Seco, J. J., "Use of Generalized Hankel Transforms in the Solution of Some Axially-Symmetric Problems in Heat Conduction," MS thesis, University of Houston, Houston, Texas, May 1969.

10 Gradshteyn, I. S., and Ryzhik, I. M., *Table of Integrals, Series and Products*, Fourth ed., Academic Press, New York, 1965.

Correlations for Laminar Forced Convection in Flow Over an Isothermal Flat Plate and in Developing and Fully Developed Flow in an Isothermal Tube

STUART W. CHURCHILL[1] **and HIROYUKI OZOE**[2]

Nomenclature

D = tube diameter, ft

$f(\mathrm{Pr})$ = a computed function, see equation (9)

$\mathrm{Gz} = \pi D^2 u_m / 4\alpha x$ = local Graetz number

j = local heat flux density at wall, Btu/hr ft^2

k = thermal conductivity, Btu/hr ft deg F

n = arbitrary exponent

$\mathrm{Nu}_D = jD/k(T_w - T_m)$ = local Nusselt number of tube

$Nu_x = jx/k(T_w - T_0)$ = local Nusselt number for flat plate

$\mathrm{Pe} = Du_m/\alpha$ = Peclet number

$\mathrm{Pr} = \nu/\alpha$ = Prandtl number

$\mathrm{Re}_D = Du_m/\nu$ = Reynolds number for tube

$\mathrm{Re}_x = xu_0/\nu$ = Reynolds number for flat plate

T = temperature, deg F

u = velocity component in x-direction, ft/hr

x = independent variable or distance along flat plate or tube, ft

y = dependent variable or distance normal to flat plate or wall of tube, ft

$y(x)$ = dependent variable

$y_0(x)$ = asymptotic solution for $x \to 0$

$y_\infty(x)$ = asymptotic solution for $x \to \infty$

α = thermal diffusivity, ft^2/hr

$\eta = y(u_0/x\nu)^{1/2}/2$

ν = kinematic viscosity, ft^2/hr

$\phi(\eta) = 2u/u_0$ = velocity distribution function in Blasius solution.

Subscripts

m = mixed mean value

0 = free stream or inlet value

w = value at wall

Churchill and Ozoe [1][3] used the procedure proposed by Churchill and Usagi [2] to derive an empirical expression for the effect of Pr on laminar forced convection in flow over a uniformly heated flat plate. Simple, empirical expressions were similarly derived for plug, fully developed and developing flow in a uniformly heated tube. The process of correlation indicated that the various computed values for a flat plate were very precise and consistent but revealed inconsistencies in the asymptotic solutions and computed values for a tube. Accordingly the various solutions for laminar forced convection in flow over an isothermal flat plate and in developing and fully developed flow in an isothermal tube are herein subjected to the same process of analysis and correlation.

Limitations of space have forced deletion of details of the development and evaluation of the correlating equations presented herein. An expanded version of the manuscript is available from S. W. Churchill.

Correlations for Fully Developed and Plug Flow in a Tube

The Graetz [3] solution for a step change in wall temperature in fully developed, laminar (parabolic) flow in a tube is in the form of a ratio of infinite series. The series converges very slowly for large Gz creating a role for a convenient and accurate approximation. The expression proposed for such purposes by Churchill and Usagi [2] has the form

$$y^n(x) = y_0{}^n(x) + y_\infty{}^n(x) \qquad (1)$$

---

[1] Carl V. S. Patterson Professor, School of Chemical Engineering University of Pennsylvania, Philadelphia, Pa.

[2] Assistant Professor, Department of Industrial and Mechanical Engineering, Okayama University, Okayama Japan.

Contributed by the Heat Transfer Division, of The American Society of Mechanical Engineers. Revised manuscript received by the Heat Transfer Division, August 25, 1972.

[3] Numbers in brackets designate References at end of technical brief.

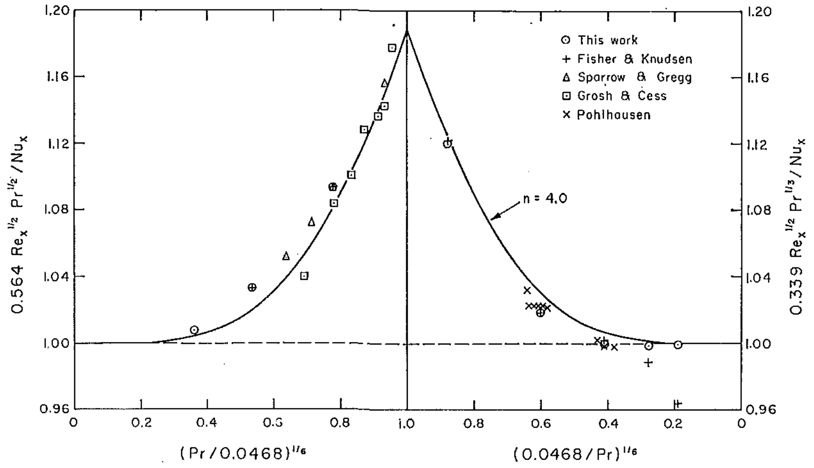

Fig. 1

This expression requires asymptotic solutions for large and small values of the independent variable and one or more intermediate values of $y(z)$ from which the aribtrary coefficient n can be evaluated.

The Lévêque [4] solution is not a lower bound for Gz → ∞ owing to the neglect of curvature. The empirical expression

$$\mathrm{Nu}_D = 1.167\ \mathrm{Gz}^{1/3} - 1.7 \tag{2}$$

proposed by Lipkis [5] was therefore combined with the asymptotic value of 3.657 for Nu_D for Gz → 0 yield the trial expression

$$[(\mathrm{Nu}_D + 1.7)/5.357]^n = 1 + (\mathrm{Gz}/97)^{n/3} \tag{3}$$

Equation (3) with $n = 8/3$ agrees within 6 percent for all Gz with the Graetz solution as computed by Munakata [6].

A solution for plug flow in a tube is of interest for fluids primarily because it constitutes an upper bound for developing flow. The asymptotic solution for plug flow for Gz → ∞ corresponding to the Lévêque solution for parabolic flow is

$$\mathrm{Nu}_D = 0.6366\ \mathrm{Gz}^{1/2} \tag{4}$$

The neglect of curvature is less serious in this case [7]. Combining equation (4) with the asymptotic value of 5.784 for Gz → 0 yields the trial expression

$$(\mathrm{Nu}_D/5.784)^n = 1 + (\mathrm{Gz}/82.5)^{n/2} \tag{5}$$

The five coefficients computed by Drew [8] for the Graetz [3] series solution for this case are sufficient only for $\mathrm{Gz} < 130$. Equation (5) with $n = 9/4$ agrees within 6 percent. The values obtained by Rosenberg [9] for higher Gz by numerical integration of the differential energy balance fall as much as 10 percent above equation (5) with $n = 9/4$ but may be in error by this much or more.

Solutions and Correlation for the Flat Plate

Pohlhausen [10] derived a solution for laminar forced convection from an isothermal flat plate using the velocity field of Blasius [11] and making the usual assumptions of boundary layer theory. He evaluated the integral in his solution numerically for Pr from 0.6 to 15. Fisher and Knudsen [12] used the more precise values obtained by Howarth [13] for the Blasius solution and evaluated the integral for $\mathrm{Pr} = 10^{-3}(10)10^{3}$. Additional results for low Pr have been obtained by Grosh and Cess [14] and by Gregg and Sparrow [15]. The asymptotic solutions given by Schlichting and Kestin [16] can be expressed as

$$\mathrm{Nu}_x = 0.5642\ \mathrm{Re}_x^{1/2}\,\mathrm{Pr}^{1/2} \text{ for } \mathrm{Pr} \to 0 \tag{6}$$

and

$$\mathrm{Nu}_x = 0.3387\ \mathrm{Re}_x^{1/2}\,\mathrm{Pr}^{1/3} \text{ for } \mathrm{Pr} \to \infty \tag{7}$$

A preliminary examination indicated that none of the computed values were for effectively small Pr. Hence a set of consistent values was calculated for the entire range of Pr using the boundary layer model which has the solution:

$$\mathrm{Nu}_x = 0.3387\ \mathrm{Re}_x^{1/2}\,\mathrm{Pr}^{1/3} f(\mathrm{Pr}) \tag{8}$$

where

$$f(\mathrm{Pr}) = 1.476/\mathrm{Pr}^{1/3} \int_0^\infty e^{-\mathrm{Pr}\int \phi(\eta)d\eta} d\eta \tag{9}$$

Values of $f(\mathrm{Pr})$ obtained by numerical integration are given in the expanded version.

Nu_x has a decreasing dependence on Pr as Pr increases. Therefore to avoid a negative value of n in equation (1) $1/\mathrm{Nu}_x$ is taken as the dependent variable. The trial expression resulting from the combination of equations (6) and (7) is then

$$0.5642\ \mathrm{Re}_x^{1/2}\,\mathrm{Pr}^{1/2}/\mathrm{Nu}_x = [1 + (\mathrm{Pr}/0.0468)^{n/6}]^{1/n} \tag{10}$$

The various numerical solutions for the flat plate are compared in Fig. 1 in the form suggested by Churchill and Usagi [2]. Some of the values of Pohlhausen [10] and of Fisher and Knudsen [12] for high Pr fall slightly below unity which is the lower bound provided by equation (6) but otherwise the computed values reveal only trivial discrepancies. Some dissymmetry is apparent about the central value of $\mathrm{Pr} = 0.0468$ but all of the values are represented within about 1 percent by $n = 4$.

Acrivos [17] proposed the equivalent of equation (10) with $n = 3$ for the representation of all wedge flows including the flat plate. Analysis of the computed values which he graciously supplied indicates that $n = 3$ provides an excellent fit for flow normal to a plate but confirms that the best value of n increases to 4 with decreasing wedge angles.

Re-expression of equation (10) with $n = 4$ in terms of Nu_D and Gz, and neglecting the difference between T_m and T_0, yields

$$\mathrm{Nu}_D = 0.6366\ \mathrm{Gz}^{1/2}/[1 + (\mathrm{Pr}/0.0468)^{2/3}]^{1/4} \tag{11}$$

as an asymptotic solution for the inlet of a tube. For Pr → 0 equation (11) reduces to equation (4) which was previously utilized for Gz → ∞ in plug flow.

Correlations for Developing Flow in a Tube

Prior Work. Kays [18] obtained results for developing flow by numerical integration. He used the theoretical solution of Langhaar [19] for the longitudinal velocity field and neglected radial convection.

Ulrichson and Schmitz [20] carried out numerical calculations for developing flow for $\mathrm{Pr} = 0.7$ using the Langhaar solution for the longitudinal velocity but also the radial component obtained

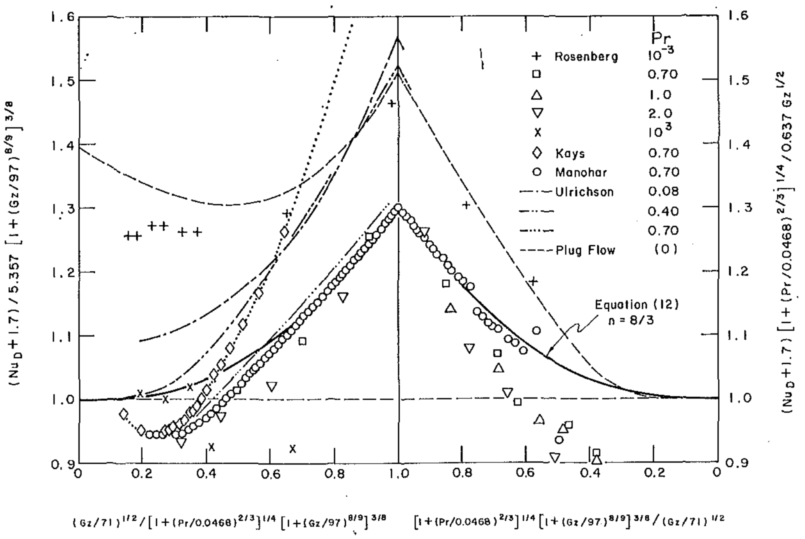

Fig. 2

from the continuity equation. They plotted but did not tabulate values for $4 < Gz < 786$. Additional results for Pr = 0.4 and 0.08 are given graphically by Ulrichson [21]. (Note: the abscissa of the plots in Ulrichson and Schmitz should be labeled $X/4Re_rPr$ which is equivalent to x/DRe_DPr in the Nomenclature of this paper rather than $4X/Re_rPr$.)

Rosenberg and Hellums [22] solved the momentum and continuity equations as well as the energy equation numerically for developing flow in the inlet of an isothermal tube. The test calculations of Rosenberg [9] for plug and fully developed flow were found to be in reasonable agreement with other solutions except at high Gz. The computed values for developing flow for Pr = 0.001, 0.70, 2.0, and 1000 and Gz as high as 7×10^8 were tabulated by Rosenberg. They note that Kays' values for Pr = 0.7 erroneously approach the limiting solution for plug flow as Gz increases and hence conclude that his results are in serious error due to the neglect of radial convection. However they concede that their results for Pr = 1000 are as much as 20 percent below the Graetz solution for parabolic flow which should be a lower bound.

Manohar [23] also solved this same set of equations by a finite-difference method for Pr = 0.7. He asserts that his results are an improvement over those of Ulrichson and Schmitz in the inlet region. In response to an inquiry he confirms that his Curve 2, representing the values of Ulrichson and Schmitz in Fig. 1 of his article, is misplotted and should be only slightly above Curve 3. His Curve 1 representing the computed values of Kays is similarly plotted too high. He graciously supplied a print-out of his computed values for use in this investigation.

All of the solutions above neglect the effect of longitudinal conduction. Based on the computations of Munakata [6] this assumption is probably reasonable for Pr Re >10. Rosenberg and Hellums [22] included in their study the effect of physical property variations and conclude that these variations may have a significant effect.

Development. The following correlating equation for all Gz and Pr was constructed by combining equation (3) with $n = 8/3$ as an asymptotic solution for Gz → 0 and equation (11) with 1.7 arbitrarily added to the left side as an asymptotic solution for Gz → ∞

$$\frac{\mathrm{Nu} + 1.7}{5.357[1 + (\mathrm{Gz}/97)^{8/9})^{3/8}} = \left[1 + \left(\frac{\mathrm{Gz}/71}{[1 + (\mathrm{Pr}/0.0468)^{2/3}]^{1/2}[1 + (\mathrm{Gz}/97)^{8/9}]^{3/4}}\right)^{n/2}\right]^{1/n} \tag{12}$$

The various computed values are plotted in the suggested form in Fig. 2. A curve representing the Graetz solution for plug flow is included by setting Pr = 0 in the coordinates. This curve is presumably an upper bound for all Pr and Gz in developing flow. It appears to be a useful bound for large Gz but not for small Gz since Nu_D approaches 5.784 rather than 3.657 leading to the high values in Fig. 2.

At first glance the various computed values appear to scatter bewilderingly. However it should be noted that the very small range of this plot as opposed to the conventional plot of log Nu_D versus log Gz tends to exaggerate the deviations. Actually, the computed values of Rosenberg for Pr = 0.7, 1.0, and 2.0 and Manohar for Pr = 0.7 and the curve representing values read from the plot of Ulrichson for Pr = 0.7 are in reasonable agreement over the central range of Gz. The values of Kays are obviously in increasing error as Gz increases as noted by all of the other investigators. This error must be primarily due to failure to achieve convergence in the numerical calculations. Either the effect of Pr as introduced by equation (11) or the values of Rosenberg for Pr = 0.001 and 1000 and of Ulrichson for Pr = 0.08 and 0.40 are in serious error. Comparison of these values with the curve representing plug flow suggests that the numerical integrations for small Pr may not take the velocity distribution into account properly. The values of Rosenberg for Pr = 1000 generally fall below unity in Fig. 2 and for large Gz even below the scale of the figure. Since these computed values do not show a consistent pattern and do not appear to converge to the limiting solutions they are tentatively presumed to be in error. The values of Rosenberg for Pr = 0.7, 1.0 and 2.0 are self-consistent but fall below unity for large Gz. Unfortunately the calculated values of Ulrichson do not extend into this region and the calculated values of Manohar become erratic for Gz >15000.

Equation (12) with $n = 8/3$ appears to provide a reasonable representation for all Gz for those computed values in which the most confidence can be placed. This expression appears to be somewhat ungainly but is probably the simplest possible expression which converges to the chosen limiting conditions for both large and small Pr and Gz.

References

1 Churchill, S. W., and Ozoe, H., "Correlations for Laminar Forced Convection With Uniform Heating in Flow Over a Plate and in Developing and Fully Developed Flow in a Tube," JOURNAL OF HEAT TRANSFER, TRANS. ASME, Ser. C, Vol. 95, 1973, pp. 78–84.

2 Churchill, S. W., and Usagi, R., "A General Expression for the Correlation of Rates of Transfer and Other Phenomena," *AIChE Journal*, Vol. 18, 1972, pp. 1121–1128.

3 Graetz, L., "Uber die Wärmeleitungsfahigkeit von Flüssigkeiten," *Annalen der Physik Chem.*, Vol. 18, 1883, pp. 79–94; Vol. 25, 1885, pp. 337–357.

4 Lévêque, M. A., "Les lois de la transmission de la chaleur par convection," *Ann. Mines*, Series 12, Vol. 13, 1928, pp. 201, 301, 381.

5 Lipkis, R., Discussion of reference [18], TRANS. ASME, Vol. 77, 1955, pp. 1272–1273.

6 Munakata, T., "A Calculation on Laminar Heat Transfer in Tube," *Chem. Eng.*, Tokyo, Vol. 26, 1962, pp. 1085–1088.

7 Churchill, S. W., and Balzhiser, R. E., "The Radial Heat Flux," *Chemical Engineering Progress Symposium*, Series No. 29, Vol. 55, 1955, pp. 127–135.

8 Drew, T. B., "Mathematical Attacks on Forced Convection Problems: A Review," *Trans. AIChE*, Vol. 26, 1931, pp. 26–80.

9 Rosenberg, D. E., "Numerical Solutions for Flow Development and Heat Transfer of Variable Viscosity Fluids," MS thesis, Rice University, Houston, Texas, 1963.

10 Pohlhausen, E., "Der Wärmaustausch zwischen festen Körpern und Flüssigkeiten mit kleiner Reibung und Wärmeleitung," *Z. angew. Math. Mech.*, Vol. 1, 1921, pp. 115–121.

11 Blasius, H., "Grenzschichten in Flüssigkeiten mit kleiner Reibung," *Z. Math. Phys.*, Vol. 56, 1908, pp. 1–37.

12 Fisher, F. D., and Knudsen, J. G., "Heat Transfer During Laminar Flow Past Flat Plates: An Extension of Pohlhausen's Solution to Low and High-Prandtl-Number Fluids," *Chemical Engineering Progress Symposium*, Series No. 29, Vol. 55, 1959, pp. 209–213.

13 Howarth, L., "On the Solution of the Laminar Boundary Layer Equations," *Proceedings of the Royal Society* (London), Series A, Vol. 164, 1938, pp. 547–579.

14 Grosh, R. J., and Cess, R. D., "Heat Transfer to Fluids With Low Prandtl Numbers for Flow Across Plates and Cylinders of Various Cross-Sections," TRANS. ASME, Vol. 80, 1958, pp. 667–676.

15 Sparrow, E. M., and Gregg, J. L., "Details of Exact Low Prandtl Number Boundary-Layer Solutions for Forced and for Free Convection," N.A.S.A., Memo 2-27-59E., Washington, D. C., 1959.

16 Schlichting, H., and Kestin, J., *Boundary Layer Theory*, Sixth ed., McGraw-Hill, New York, 1968, pp. 281.

17 Acrivos, A., "On the Solution of the Convection Equation in Laminar Boundary Layer Flows," *Chem. Eng. Sci.*, Vol. 17, 1962, pp. 457–465.

18 Kays, W. M., "Numerical Solutions for Laminar-Flow Heat Transfer in Circular Tubes," TRANS. ASME, Vol. 77, 1955, pp. 1265–1274.

19 Langhaar, H. L., "Steady Flow in the Transition Length of a Straight Tube," *Journal of Applied Mechanics*, Vol. 9, TRANS. ASME, Vol. 64, 1942, pp. A-55–58.

20 Ulrichson, D. L., and Schmitz, R. A., "Laminar Flow Heat Transfer in the Entrance Region of Circular Tubes," *International Journal of Heat and Mass Transfer*, Vol. 8, 1965, pp. 253–258.

21 Ulrichson, D. L., MS thesis, University of Illinois, Urbana, 1963.

22 Rosenberg, D. E., and Hellums, J. D., "Flow Development and Heat Transfer in Variable Viscosity Fluids," *Industrial and Engineering Chemistry Fundamentals*, Vol. 4, 1965, pp. 417–421.

23 Manohar, R., "Analysis of Laminar-Flow Heat Transfer in the Entrance Region of Circular Tubes," *International Journal of Heat Mass Transfer*, Vol. 12, 1969, pp. 15–22.

Unsteady Stagnation Point Heat Transfer due to Unsteady Free Stream Temperature

D. R. JENG[1] **and R. S. REDDY GORLA**[2]

THE UNSTEADY heat transfer processes in steady flow caused by time dependent surface temperature and surface heat flux have been studied extensively (see [1][3] for literature citation). A more realistic but more complicated problem is to investigate the transient heat transfer when a solid body initially at an uniform temperature is placed in a stream having a time-varying temperature or heat flux. In 1963, Lyman [2] reported a Kerman-Pohlhausen type analysis for unsteady heat transfer in the neighborhood of a two-dimensional stagnation point of an air stream impinging at right angles to the solid wall, when the free-steam temperature of the air has a step change. His results show a physically unlikely behavior that the time required for the heat to penetrate thermal boundary layer goes to infinity as the thermal boundary layer thickness tends to zero. This difficulty was attributed to the integral method of solution and the assumption that heat is added to the boundary layer by convection alone. The main objective of the present paper is to re-investigate the problem considered in [2] but for wide range of Prandtl number Pr.

Assuming steady, incompressible flow with constant properties and negligible dissipation, the velocity at the edge of the boundary layer near a two-dimensional stagnation is Kx where K is a constant and x is measured along the surface from the stagnation point. Let y represent the distance normal the surface. The velocity components u and v in x and y directions, respectively, may be written as $u = Kxf'(\eta)$ and $v = -(\nu K)^{1/2}f(\eta)$ where $\eta = y(K/\nu)^{1/2}$ and ν denotes the kinematic viscosity. The function $f(\eta)$ satisfies Falkner and Skan equation with $\beta = 1$ and its solution is well known [3]. Thus, no further consideration is necessary for the velocity field. For the temperature field, our analysis will center at the case when the free stream temperature initially at T_i is subjected to a step change to T_∞. The linearity of the energy equation permits the use of a superposition technique to generalize the step function results obtained previously to any arbitrary free stream temperature variation with time, $T_\infty(t)$ for $t > 0$. The governing energy equation for the problem considered shall be formulated for the fluid (with the subscript f) and the solid (with the subscript s). Introducing the dimensionless temperature $\theta = (T - T_i)/(T_\infty - T_i)$ and the dimensionless time $\tau = Kt/\mathrm{Pr}$ into the energy equations near the stagnation point, we have,

for fluid $\eta > 0$

$$\frac{\partial\theta_f}{\partial\tau} = \frac{\partial^2\theta_f}{\partial\eta^2} + \mathrm{Pr}f\frac{\partial\theta_f}{\partial\eta} \tag{1}$$

for solid $\eta < 0$

$$\frac{\partial\theta_s}{\partial\tau} = \frac{\alpha_s}{\alpha_f}\left(\frac{\partial^2\theta_s}{\partial\eta^2}\right) \tag{2}$$

and the initial and boundary conditions then become,

for $\tau < \tau_{tr}$

$$\theta_f(\eta, 0) = 0 \tag{3a}$$

$$\theta_f(\eta_\infty, \tau) = 1 \tag{3b}$$

$$\theta_f(0, \tau) = \frac{\partial\theta_f(0, \tau)}{\partial\eta} = 0 \tag{3c}$$

for $\tau \geq \tau_{tr}$

$$\theta_f(\eta, \tau_{tr}) = \theta_{fi}(\eta) \tag{4a}$$

$$\theta_f(\eta_\infty, \tau) = 1 \tag{4b}$$

$$\theta_s(\eta, \tau_{tr}) = 0 \tag{4c}$$

$$\theta_s(-\infty, \tau) = 0 \tag{4d}$$

and at the interface,

---

[1] Associate Professor of Mechanical Engineering, The University of Toledo, Toledo, Ohio. Mem. ASME.

[2] Research and Development Engineer, Associate Turbine Aerodynamics and Heat Transfer Division, Teledyne CAE, Toledo, Ohio. Mem. ASME.

[3] Numbers in brackets designate References at end of technical brief.

Contributed by the Heat Transfer Division of THE AMERICAN SOCIETY OF MECHANICAL ENGINEERS. Manuscript received by the Heat Transfer Division December 6, 1972.

3 Graetz, L., "Uber die Wärmeleitungsfahigkeit von Flüssigkeiten," *Annalen der Physik Chem.*, Vol. 18, 1883, pp. 79–94; Vol. 25, 1885, pp. 337–357.

4 Lévêque, M. A., "Les lois de la transmission de la chaleur par convection," *Ann. Mines*, Series 12, Vol. 13, 1928, pp. 201, 301, 381.

5 Lipkis, R., Discussion of reference [18], Trans. ASME, Vol. 77, 1955, pp. 1272–1273.

6 Munakata, T., "A Calculation on Laminar Heat Transfer in Tube," *Chem. Eng.*, Tokyo, Vol. 26, 1962, pp. 1085–1088.

7 Churchill, S. W., and Balzhiser, R. E., "The Radial Heat Flux," *Chemical Engineering Progress Symposium*, Series No. 29, Vol. 55, 1955, pp. 127–135.

8 Drew, T. B., "Mathematical Attacks on Forced Convection Problems: A Review," *Trans. AIChE*, Vol. 26, 1931, pp. 26–80.

9 Rosenberg, D. E., "Numerical Solutions for Flow Development and Heat Transfer of Variable Viscosity Fluids," MS thesis, Rice University, Houston, Texas, 1963.

10 Pohlhausen, E., "Der Wärmaustausch zwischen festen Körpern und Flüssigkeiten mit kleiner Reibung und Wärmeleitung," *Z. angew. Math. Mech.*, Vol. 1, 1921, pp. 115–121.

11 Blasius, H., "Grenzschichten in Flüssigkeiten mit kleiner Reibung," *Z. Math. Phys.*, Vol. 56, 1908, pp. 1–37.

12 Fisher, F. D., and Knudsen, J. G., "Heat Transfer During Laminar Flow Past Flat Plates: An Extension of Pohlhausen's Solution to Low and High-Prandtl-Number Fluids," *Chemical Engineering Progress Symposium*, Series No. 29, Vol. 55, 1959, pp. 209–213.

13 Howarth, L., "On the Solution of the Laminar Boundary Layer Equations," *Proceedings of the Royal Society* (London), Series A, Vol. 164, 1938, pp. 547–579.

14 Grosh, R. J., and Cess, R. D., "Heat Transfer to Fluids With Low Prandtl Numbers for Flow Across Plates and Cylinders of Various Cross-Sections," Trans. ASME, Vol. 80, 1958, pp. 667–676.

15 Sparrow, E. M., and Gregg, J. L., "Details of Exact Low Prandtl Number Boundary-Layer Solutions for Forced and for Free Convection," N.A.S.A., Memo 2-27-59E., Washington, D. C., 1959.

16 Schlichting, H., and Kestin, J., *Boundary Layer Theory*, Sixth ed., McGraw-Hill, New York, 1968, pp. 281.

17 Acrivos, A., "On the Solution of the Convection Equation in Laminar Boundary Layer Flows," *Chem. Eng. Sci.*, Vol. 17, 1962, pp. 457–465.

18 Kays, W. M., "Numerical Solutions for Laminar-Flow Heat Transfer in Circular Tubes," Trans. ASME, Vol. 77, 1955, pp. 1265–1274.

19 Langhaar, H. L., "Steady Flow in the Transition Length of a Straight Tube," *Journal of Applied Mechanics*, Vol. 9, Trans. ASME, Vol. 64, 1942, pp. A-55–58.

20 Ulrichson, D. L., and Schmitz, R. A., "Laminar Flow Heat Transfer in the Entrance Region of Circular Tubes," *International Journal of Heat and Mass Transfer*, Vol. 8, 1965, pp. 253–258.

21 Ulrichson, D. L., MS thesis, University of Illinois, Urbana, 1963.

22 Rosenberg, D. E., and Hellums, J. D., "Flow Development and Heat Transfer in Variable Viscosity Fluids," *Industrial and Engineering Chemistry Fundamentals*, Vol. 4, 1965, pp. 417–421.

23 Manohar, R., "Analysis of Laminar-Flow Heat Transfer in the Entrance Region of Circular Tubes," *International Journal of Heat Mass Transfer*, Vol. 12, 1969, pp. 15–22.

Unsteady Stagnation Point Heat Transfer due to Unsteady Free Stream Temperature

D. R. JENG[1] **and R. S. REDDY GORLA**[2]

The unsteady heat transfer processes in steady flow caused by time dependent surface temperature and surface heat flux have been studied extensively (see [1][3] for literature citation). A more realistic but more complicated problem is to investigate the transient heat transfer when a solid body initially at an uniform temperature is placed in a stream having a time-varying temperature or heat flux. In 1963, Lyman [2] reported a Kerman-Pohlhausen type analysis for unsteady heat transfer in the neighborhood of a two-dimensional stagnation point of an air stream impinging at right angles to the solid wall, when the free-steam temperature of the air has a step change. His results show a physically unlikely behavior that the time required for the heat to penetrate thermal boundary layer goes to infinity as the thermal boundary layer thickness tends to zero. This difficulty was attributed to the integral method of solution and the assumption that heat is added to the boundary layer by convection alone. The main objective of the present paper is to re-investigate the problem considered in [2] but for wide range of Prandtl number Pr.

Assuming steady, incompressible flow with constant properties and negligible dissipation, the velocity at the edge of the boundary layer near a two-dimensional stagnation is Kx where K is a constant and x is measured along the surface from the stagnation point. Let y represent the distance normal the surface. The velocity components u and v in x and y directions, respectively, may be written as $u = Kxf'(\eta)$ and $v = -(\nu K)^{1/2}f(\eta)$ where $\eta = y(K/\nu)^{1/2}$ and ν denotes the kinematic viscosity. The function $f(\eta)$ satisfies Falkner and Skan equation with $\beta = 1$ and its solution is well known [3]. Thus, no further consideration is necessary for the velocity field. For the temperature field, our analysis will center at the case when the free stream temperature initially at T_i is subjected to a step change to T_∞. The linearity of the energy equation permits the use of a superposition technique to generalize the step function results obtained previously to any arbitrary free stream temperature variation with time, $T_\infty(t)$ for $t > 0$. The governing energy equation for the problem considered shall be formulated for the fluid (with the subscript f) and the solid (with the subscript s). Introducing the dimensionless temperature $\theta = (T - T_i)/(T_\infty - T_i)$ and the dimensionless time $\tau = Kt/\mathrm{Pr}$ into the energy equations near the stagnation point, we have,

for fluid $\eta > 0$

$$\frac{\partial\theta_f}{\partial\tau} = \frac{\partial^2\theta_f}{\partial\eta^2} + \mathrm{Pr} f\frac{\partial\theta_f}{\partial\eta} \qquad (1)$$

for solid $\eta < 0$

$$\frac{\partial\theta_s}{\partial\tau} = \frac{\alpha_s}{\alpha_f}\left(\frac{\partial^2\theta_s}{\partial\eta^2}\right) \qquad (2)$$

and the initial and boundary conditions then become,

for $\tau < \tau_{tr}$

$$\theta_f(\eta, 0) = 0 \qquad (3a)$$

$$\theta_f(\eta_\infty, \tau) = 1 \qquad (3b)$$

$$\theta_f(0, \tau) = \frac{\partial\theta_f(0, \tau)}{\partial\eta} = 0 \qquad (3c)$$

for $\tau \geq \tau_{tr}$

$$\theta_f(\eta, \tau_{tr}) = \theta_{fi}(\eta) \qquad (4a)$$

$$\theta_f(\eta_\infty, \tau) = 1 \qquad (4b)$$

$$\theta_s(\eta, \tau_{tr}) = 0 \qquad (4c)$$

$$\theta_s(-\infty, \tau) = 0 \qquad (4d)$$

and at the interface,

---

[1] Associate Professor of Mechanical Engineering, The University of Toledo, Toledo, Ohio. Mem. ASME.

[2] Research and Development Engineer, Associate Turbine Aerodynamics and Heat Transfer Division, Teledyne CAE, Toledo, Ohio. Mem. ASME.

[3] Numbers in brackets designate References at end of technical brief.

Contributed by the Heat Transfer Division of The American Society of Mechanical Engineers. Manuscript received by the Heat Transfer Division December 6, 1972.

Table 1 Values of dimensionless penetration thickness and transit time for a range of Prandtl numbers

Pr	0.01	0.1	0.7	1.0	7.0	10.0	50.0
η_∞	35.72	11.44	4.25	3.76	1.79	1.64	0.98
τ_{tr}	50.122	6.224	1.089	0.809	0.149	0.112	0.0305
Pr	100.0	200.0	300.0	400.0	500.0	1000.0	
η_∞	0.82	0.66	0.58	0.54	0.50	0.39	
τ_{tr}	0.0178	0.0112	0.0087	0.0070	0.00605	0.00382	

$$\theta_f(0, \tau) = \theta_s(0, \tau) \tag{5a}$$

$$k_f \frac{\partial \theta_f(0, \tau)}{\partial \eta} = k_s \frac{\partial \theta_s(0, \tau)}{\partial \eta} \tag{5b}$$

In the foregoing, U_∞ denotes the free stream velocity, α the thermal diffusivity, and k the thermal conductivity. Before proceeding further, the boundary conditions (3b) and (4b) require some explanation. Mathematically, η_∞ should be replaced by ∞, however, we have introduced a fictitious distance,[4] y_∞ (the corresponding dimensionless coordinate will be η_∞). This means that the step change in free stream temperature will be transmitted instantly to the fluid immediately outside the region $y = y_\infty$, however, the redistribution of the temperature in the region $y < y_\infty$ will not be instantaneous. The dimensionless transit time τ_{tr} is defined such that it corresponds to the time required for the thermal front to penetrate the distance η_∞. Thus, for certain interval of time following a step change in the free stream temperature, there is no change in the temperature in the solid so that the energy equation in the boundary layer may be decoupled from that of solid and treated separately.

Applying the Laplace transformation to (1) and (3) with respect to τ and assuming small τ_{tr}, since $\tau \leq \tau_{tr}$, we now seek the asymptotic solution with respect to large Laplace transform variable p. The result is

$$\theta_f(\eta, \tau) = \exp\left\{\frac{\Pr}{2}\int_\eta^{\eta_\infty} f d\eta\right\} \sum_{n=0}^{\infty} \times U_n(\eta)(4\tau)^{n/2} i^n erfc\left(\frac{\eta_\infty - \eta}{2\sqrt{\tau}}\right) \tag{6}$$

where U_n's satisfy $U_0(\eta) = 1$ and

$$2\, U_n'(\eta) + U_{n-1}''(\eta) - \left(\frac{\Pr f'}{2} + \frac{\Pr^2 f^2}{4}\right) U_{n-1}(\eta) = 0 \text{ for } \eta \geq 1 \tag{7}$$

with

$$U_1(\eta_\infty) = U_2(\eta_\infty) = - - - = U_n(\eta_\infty) = 0$$

Using the appropriate boundary conditions, a set of differential equations generated by (7) for $n = 1$ to 5 are solved successively on an IBM 360 computer by making use of the fourth order Runge-Kutta method of numerical integration procedure. A value has to be assigned for η_∞ such that the obtained solution shows little further change for η larger than η_∞. The values of the dimensionless penetration thicknesses η_∞ were determined for Prandtl numbers ranging from 0.01 to 1000, using the data obtained for $U_n(\eta)$ where n varies from 1 to 5. This was accomplished by choosing the value of η at which all the values of $U_n(\eta)$ for n varying from 1 to 5 become less than or equal to 0.01. The numerical values of the dimensionless penetration thickness have been listed in Table 1. The complete data of $U_n(\eta)$ are compiled in reference [1] and will not be given here. The transit times are then obtained by (6) using the condition that θ_f assumes a value of 0.01 at $\eta = 0.01$. These results are also included in Table 1.

For all times greater than the transit time τ_{tr}, heat will be transferred from the fluid to the solid. It is now required to consider the interaction of fluid and solid. In order to facilitate the analysis, we further introduce $\tau^* = \tau - \tau_{tr}$ into equations (1) to (5). The solution of (2) to satisfy (4c) and (4d) is given by [4] as

$$\theta_s(\eta, \tau^*) = \frac{\eta}{2\left(\frac{\alpha_s}{\alpha_f}\pi\right)^{1/2}} \int_0^{\tau^*} \theta_w(\zeta)(\tau^* - \zeta)^{-3/2} \times \exp\left\{-\frac{\eta^2}{4\frac{\alpha_s}{\alpha_f}(\tau^* - \zeta)}\right\} d\zeta \tag{8}$$

and

$$\frac{\partial \theta_s(0, \tau^*)}{\partial \eta} = \left(\frac{\alpha_f}{\alpha_s}\right)^{1/2} \frac{\theta_w(\tau^*)}{(\pi\tau^*)^{1/2}} \tag{9}$$

where $\theta_w(\tau^*)$ is an unknown interface temperature to be determined. Using (9), the boundary condition (5) may be rephrased as

$$\frac{\partial \theta_f(0, \tau^*)}{\partial \eta} = \frac{\Omega \theta_f(0, \tau^*)}{(\pi\tau^*)^{1/2}} \tag{10}$$

where

$$\Omega = \frac{k_s}{k_f}\left(\frac{\alpha_f}{\alpha_s}\right)^{1/2}$$

The solution of (1) with (6) as an initial condition and (10) as boundary condition is then obtained by a finite-difference numerical method. A detailed description is given in reference [1].

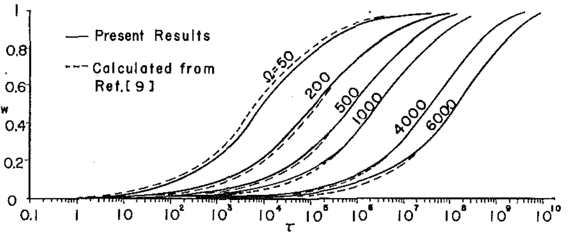

Fig. 1 Comparison of transient interface temperature for Pr = 0.7

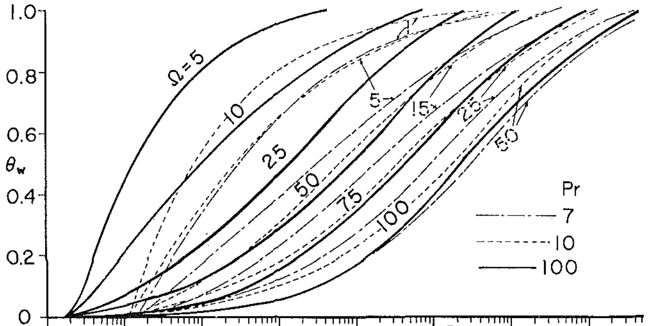

Fig. 2 Transient interface temperature for Pr = 7.0, 10, and 100

---

[4] In this paper, we defined y_∞ as a thermal boundary layer thickness which has a different physical meaning from an ordinary thermal boundary layer thickness.

A sequence of numerical results for transient interface temperature was obtained with the property ratio Ω and Prandtl number as parameters. They are presented graphically in Figs. 1 and 2. For a given Prandtl number, time required to attain steady state increases with increasing values of Ω. For example, let us consider air ($\Pr = 0.7$) with a free stream velocity of 200 ft/sec impinging normal to the axis of a cylindrical asbestos rod of one foot radius. For this condition, the parameter $K = \frac{2U_\infty}{R} = 400 \text{ sec}^{-1}$ and $\Omega = 51$ (the properties of air and asbestos have been obtained at a reference temperature of 145 deg F). From Fig. 1 we find that the dimensionless time required for the interface temperature θ_w to attain one-half of its steady state value is 1.1×10^4 or the time is about 19 sec. If one replaces the asbestos rod by an aluminum rod with other conditions unchanged, the time is 962 sec. (This case corresponds to $\Omega = 4034$.) On the other hand, if Ω is fixed, the dimensionless time required for θ_w to attain steady state decreases with increasing Prandtl numbers. Lyman [2] reported an equation for transient interface temperature obtained by the integral approach. The numerical values have been calculated by the authors using his equation for air and have been shown in Fig. 1 for the sake of comparison. The agreement is good for very large values of τ but some deviation is noticed for $\tau \leq 10^5$.

The heat flux at the interface is

$$q_w = -k_f \left.\frac{\partial T_f}{\partial y}\right|_{y=0} = -k_f(T_\infty - T_i)\left(\frac{K}{\nu}\right)^{1/2} \theta_f'(0, \tau) \qquad (11)$$

and the corresponding Nusselt number is

$$\mathrm{Nu} = \frac{q_w \left(\frac{LU_\infty}{K}\right)^{1/2}}{(T_\infty - T_i)k_f} = -(\mathrm{Re}_L)^{1/2}\theta_f'(0, \tau) \qquad (12)$$

where L is a characteristic length.

By virtue of (5*b*) and (9), (12) may be written as

$$\mathrm{Nu}(\mathrm{Re}_L)^{-1/2}\Omega^{-1} = -\frac{\theta_w(\tau^*)}{(\pi\tau^*)^{1/2}} \text{ for } \tau^* > 0 \qquad (13)$$

and with the known values of $\theta_w(\tau^*)$ presented in figures, the value of $\mathrm{Nu}(\mathrm{Re}_L)^{-1/2}\,\Omega^{-1}$ may be obtained numerically. Calculation of (13) for a Prandtl number of 0.7 are made and it is of interest to note that the dimensionless group $\mathrm{Nu}(\mathrm{Re}_L)^{-1/2}\,\Omega^{-1}$ is independent of Ω until τ^* assumes a value of 10^2. It is expected when $\tau^* \to \infty$, the Nusselt number approaches zero value.

References

1 Gorla, R. S., Reddy, "Unsteady Stagnation Point Heat Transfer Due to Time Dependent Free Stream Temperature," PhD dissertation, The University of Toledo, 1972.

2 Lyman, F. A., "Heat Transfer at a Stagnation Point When the Free-Stream Temperature is Suddenly Increased," *Applied Scientific Research*, Vol. 13, 1963, pp. 65–80.

3 Hartree, D. R., "On an Equation Occurring in Falkner and Skan's Approximation Treatment of the Equations of the Boundary Layer," *Proceedings Camb. Phil. Society*, Vol. 33, 1937, pp. 223–239.

4 Carslaw, H. S., and Jaeger, J. C., *Conduction of Heat in Solids*, Clarendon Press, Oxford, 1959, pp. 87.

Lateral Heat Transfer by Conduction and Radiation Along Two Parallel Plates—an Analogy Between Surface and Gaseous Radiation

P. S. JAGANNATHAN[1] and S. H. CHAN[1]

Introduction

LATERAL HEAT TRANFER along two long parallel plates plays an important role in several engineering problems such as thermal performance of multilayer insulation systems, effectiveness of fins, etc. [1, 2, 3].[2] Since earlier investigators have analyzed this problem only for the case of specularly reflecting side walls [4, 5] the present study will extend the problem to the case of diffusely reflecting side walls. It is found that the present problem of conduction and radiation along two long parallel diffuse surfaces spaced by nonparticipating medium is similar to the Viskanta's model of conduction and radiation [6] in an absorbing, emitting, and scattering medium and that the Viskanta's numerical solution can be used as a good approximate solution to the present problem. Also found is an analogy between the diffusing surfaces and a radiating gas.

Analysis

The physical system under investigation is shown in Fig. 1(*a*) where the two plates are separated by a nonabsorbing dielectric of refractive index n. All boundaries are gray and diffuse and the side walls 3 and 4 are externally insulated to represent, for example, one layer of an evacuated multilayer insulation system Since the length $L \gg$ the spacing h and end temperatures uniform, the end surface radiosities are assumed to be uniform. This approximation makes the problem one-dimensional.

The governing equation for the dimensionless temperature distribution can be readily shown as [3, 7]

$$d^2\theta/d\tau^2 = N(1 - \rho)(\theta^4 - H^*) \qquad (1)$$

where

$$H^* = \frac{B_1^*}{2}\left[1 - \tau/\sqrt{\tau^2 + 0.25}\right] + \frac{B_2^*}{2}\left[1 - (\tau_0 - \tau)/\sqrt{(\tau_0 - \tau)^2 + 0.25}\right]$$
$$+ \int_0^{\tau_0} \{[(1 - \rho)\theta^4 + \rho H^*](0.25/2)/[0.25 + (\tau - \tau')^2]^{3/2}\} d\tau' \qquad (2)$$

$$B_1^* = (1 - \rho_1) + 2\rho_1\{B_2^*(\sqrt{\tau_0^2 + 0.25} - \tau_0) + \int_0^{\tau_0} [(1 - \rho)\theta^4 + \rho H^*](1 - \tau/\sqrt{\tau^2 + 0.25})\, d\tau\} \qquad (3)$$

$$B_2^* = (1 - \rho_2)\theta_2^4 + 2\rho_2\{B_1^*(\sqrt{\tau_0^2 + 0.25} - \tau_0) + \int_0^{\tau_0} [(1 - \rho)\theta^4 + \rho H^*](1 - (\tau_0 - \tau)/ \times \sqrt{(\tau_0 - \tau)^2 + 0.25})\, d\tau\} \qquad (4)$$

$$\tau = 0,\ \theta = 1;\ \tau = \tau_0,\ \theta = \theta_2 \qquad (5)$$

The nondimensional heat flux is given by

$$\Phi = -\left.\frac{d\theta}{d\tau}\right|_0 + \frac{N}{4}\Psi(0) \qquad (6)$$

where

---

[1] Post doctoral fellow, Associate Professor, Department of Mechanical Engineering, New York University, New York, N. Y. 10453. Assoc. Mem. ASME.

[2] Number in brackets designate References at end of technical brief.

Contributed by the Heat Transfer Division of THE AMERICAN SOCIETY OF MECHANICAL ENGINEERS. Manuscript received by the Heat Transfer Division, January 5, 1973.

A sequence of numerical results for transient interface temperature was obtained with the property ratio Ω and Prandtl number as parameters. They are presented graphically in Figs. 1 and 2. For a given Prandtl number, time required to attain steady state increases with increasing values of Ω. For example, let us consider air ($\Pr = 0.7$) with a free stream velocity of 200 ft/sec impinging normal to the axis of a cylindrical asbestos rod of one foot radius. For this condition, the parameter $K = \frac{2U_\infty}{R} = 400\ \text{sec}^{-1}$ and $\Omega = 51$ (the properties of air and asbestos have been obtained at a reference temperature of 145 deg F). From Fig. 1 we find that the dimensionless time required for the interface temperature θ_w to attain one-half of its steady state value is 1.1×10^4 or the time is about 19 sec. If one replaces the asbestos rod by an aluminum rod with other conditions unchanged, the time is 962 sec. (This case corresponds to $\Omega = 4034$.) On the other hand, if Ω is fixed, the dimensionless time required for θ_w to attain steady state decreases with increasing Prandtl numbers. Lyman [2] reported an equation for transient interface temperature obtained by the integral approach. The numerical values have been calculated by the authors using his equation for air and have been shown in Fig. 1 for the sake of comparison. The agreement is good for very large values of τ but some deviation is noticed for $\tau \leq 10^5$.

The heat flux at the interface is

$$q_w = -k_f \left.\frac{\partial T_f}{\partial y}\right|_{y=0} = -k_f(T_\infty - T_i)\left(\frac{K}{\nu}\right)^{1/2} \theta_f'(0, \tau) \qquad (11)$$

and the corresponding Nusselt number is

$$\mathrm{Nu} = \frac{q_w \left(\dfrac{LU_\infty}{K}\right)^{1/2}}{(T_\infty - T_i)k_f} = -(\mathrm{Re}_L)^{1/2}\theta_f'(0, \tau) \qquad (12)$$

where L is a characteristic length.

By virtue of (5*b*) and (9), (12) may be written as

$$\mathrm{Nu}(\mathrm{Re}_L)^{-1/2}\Omega^{-1} = -\frac{\theta_w(\tau^*)}{(\pi\tau^*)^{1/2}} \text{ for } \tau^* > 0 \qquad (13)$$

and with the known values of $\theta_w(\tau^*)$ presented in figures, the value of $\mathrm{Nu}(\mathrm{Re}_L)^{-1/2}\,\Omega^{-1}$ may be obtained numerically. Calculation of (13) for a Prandtl number of 0.7 are made and it is of interest to note that the dimensionless group $\mathrm{Nu}(\mathrm{Re}_L)^{-1/2}\,\Omega^{-1}$ is independent of Ω until τ^* assumes a value of 10^2. It is expected when $\tau^* \to \infty$, the Nusselt number approaches zero value.

References

1 Gorla, R. S., Reddy, "Unsteady Stagnation Point Heat Transfer Due to Time Dependent Free Stream Temperature," PhD dissertation, The University of Toledo, 1972.

2 Lyman, F. A., "Heat Transfer at a Stagnation Point When the Free-Stream Temperature is Suddenly Increased," *Applied Scientific Research*, Vol. 13, 1963, pp. 65–80.

3 Hartree, D. R., "On an Equation Occurring in Falkner and Skan's Approximation Treatment of the Equations of the Boundary Layer," *Proceedings Camb. Phil. Society*, Vol. 33, 1937, pp. 223–239.

4 Carslaw, H. S., and Jaeger, J. C., *Conduction of Heat in Solids*, Clarendon Press, Oxford, 1959, pp. 87.

Lateral Heat Transfer by Conduction and Radiation Along Two Parallel Plates—an Analogy Between Surface and Gaseous Radiation

P. S. JAGANNATHAN[1] and S. H. CHAN[1]

Introduction

LATERAL HEAT TRANFER along two long parallel plates plays an important role in several engineering problems such as thermal performance of multilayer insulation systems, effectiveness of fins, etc. [1, 2, 3].[2] Since earlier investigators have analyzed this problem only for the case of specularly reflecting side walls [4, 5] the present study will extend the problem to the case of diffusely reflecting side walls. It is found that the present problem of conduction and radiation along two long parallel diffuse surfaces spaced by nonparticipating medium is similar to the Viskanta's model of conduction and radiation [6] in an absorbing, emitting, and scattering medium and that the Viskanta's numerical solution can be used as a good approximate solution to the present problem. Also found is an analogy between the diffusing surfaces and a radiating gas.

Analysis

The physical system under investigation is shown in Fig. 1(*a*) where the two plates are separated by a nonabsorbing dielectric of refractive index n. All boundaries are gray and diffuse and the side walls 3 and 4 are externally insulated to represent, for example, one layer of an evacuated multilayer insulation system Since the length $L \gg$ the spacing h and end temperatures uniform, the end surface radiosities are assumed to be uniform. This approximation makes the problem one-dimensional.

The governing equation for the dimensionless temperature distribution can be readily shown as [3, 7]

$$d^2\theta/d\tau^2 = N(1 - \rho)(\theta^4 - H^*) \qquad (1)$$

where

$$\begin{aligned} H^* = {} & \frac{B_1^*}{2}\left[1 - \tau/\sqrt{\tau^2 + 0.25}\right] \\ & + \frac{B_2^*}{2}\left[1 - (\tau_0 - \tau)/\sqrt{(\tau_0 - \tau)^2 + 0.25}\right] \\ & + \int_0^{\tau_0} \{[(1 - \rho)\theta^4 + \rho H^*](0.25/2)/[0.25 + (\tau - \tau')^2]^{3/2}\} d\tau' \end{aligned} \qquad (2)$$

$$\begin{aligned} B_1^* = {} & (1 - \rho_1) + 2\rho_1\{B_2^*(\sqrt{\tau_0^2 + 0.25} - \tau_0) \\ & + \int_0^{\tau_0} [(1 - \rho)\theta^4 + \rho H^*](1 - \tau/\sqrt{\tau^2 + 0.25})\, d\tau\} \end{aligned} \qquad (3)$$

$$\begin{aligned} B_2^* = {} & (1 - \rho_2)\theta_2^4 + 2\rho_2\{B_1^*(\sqrt{\tau_0^2 + 0.25} - \tau_0) \\ & + \int_0^{\tau_0} [(1 - \rho)\theta^4 + \rho H^*](1 - (\tau_0 - \tau)/ \\ & \times \sqrt{(\tau_0 - \tau)^2 + 0.25})\, d\tau\} \end{aligned} \qquad (4)$$

$$\tau = 0,\ \theta = 1;\ \tau = \tau_0,\ \theta = \theta_2 \qquad (5)$$

The nondimensional heat flux is given by

$$\Phi = -\left.\frac{d\theta}{d\tau}\right|_0 + \frac{N}{4}\Psi(0) \qquad (6)$$

where

---

[1] Post doctoral fellow, Associate Professor, Department of Mechanical Engineering, New York University, New York, N. Y. 10453. Assoc. Mem. ASME.

[2] Number in brackets designate References at end of technical brief.

Contributed by the Heat Transfer Division of THE AMERICAN SOCIETY OF MECHANICAL ENGINEERS. Manuscript received by the Heat Transfer Division, January 5, 1973.

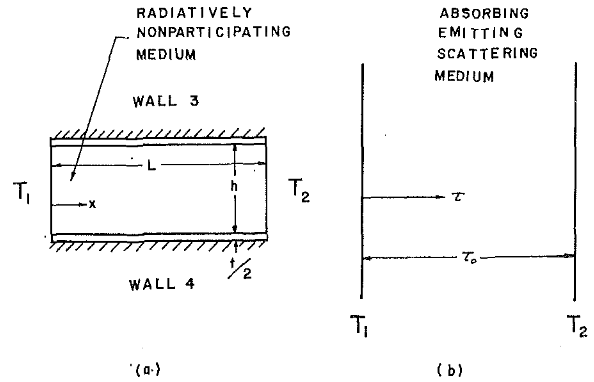

(a) (b)

Fig. 1 System configuration

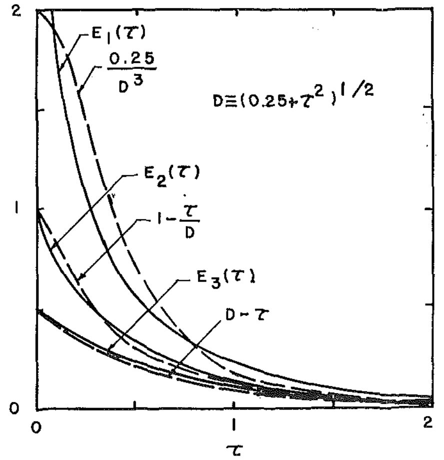

Fig. 2 Comparison between exponential integrals and their approximations

$$
\begin{aligned}
\Psi(\tau) &= 2B_1^*(\sqrt{\tau^2 + 0.25} - \tau) \\
&\quad - 2B_2^*(\sqrt{(\tau_0 - \tau)^2 + 0.25} - \tau_0 + \tau) \\
&\quad + 2\int_0^{\tau} [(1-\rho)\theta^4 + \rho H^*][1 - (\tau - \tau')/ \\
&\qquad \times \sqrt{(\tau - \tau')^2 + 0.25}]\, d\tau' \\
&\quad - 2\int_{\tau}^{\tau_0} [(1-\rho)\theta^4 + \rho H^*][1 - (\tau' - \tau)/ \\
&\qquad \times \sqrt{(\tau' - \tau)^2 + 0.25}]\, d\tau' \qquad (7)
\end{aligned}
$$

In the above equations, ρ, ρ_1, and ρ_2 are the reflectivities of side walls, walls 1 and 2, respectively. The other dimensionless quantities are defined as

$$
\theta = T/T_1,\ \theta_2 = T_2/T_1,\ \tau = x/2h,\ \tau_0 = L/2h,\ N = \frac{8n^2\sigma T_1^3 h}{k_e},\ k_e = k_w \frac{t}{h} + k_s
$$

$$
\Phi = \frac{Q/h}{\frac{k_e t}{h} \cdot \frac{1}{2h} \cdot T_1},\ \Psi = \frac{Q_R/2h}{n^2\sigma T_1^4},\ B_1^* = B_1/n^2\sigma T_1^4,\ B_2^* = B_2/n^2\sigma T_1^4,\ H^* = H/n^2\sigma T_1^4
$$

where B is the radiosity, H the incident radiation, k_w and k_s the thermal conductivities of the side walls and the spacer, respectively, and Q and Q_R the total and radiant heat fluxes, respectively. The equivalent length τ_0 which depends on the system geometry is similar to the optical path length in gaseous radiation, and radiation conduction parameter N determines the relative magnitude of the two modes of heat transfer.

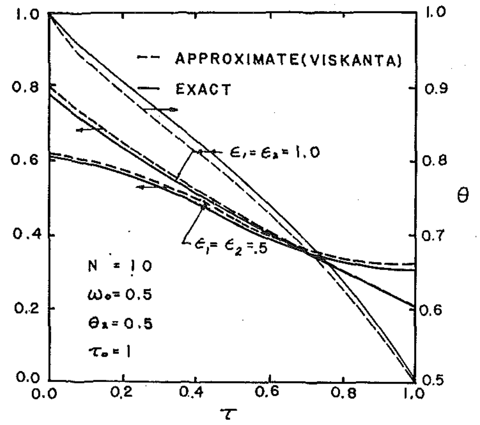

Fig. 3 Comparison between exact and approxfmate results for temperature distribution and incident radiation

Now, consider the problem of combined conduction and radiation heat transfer through an absorbing, emitting and scattering gas bounded by two isothermal walls maintained at two different temperatures T_1 and T_2 (see Fig. 1(b)). On the assumption of a gray medium, the temperature distribution in the gas was obtained by solving the following equation [6]

$$
\frac{d^2\theta}{d\tau^2} = \frac{4n^2\sigma T_1^3}{k_g\beta}(1 - \omega_0)(\theta^4 - \eta) \qquad (8)
$$

where

$$
\eta(\tau) = B_1^* E_2(\tau)/2 + B_2^* E_2(\tau_0 - \tau)/2 + \int_0^{\tau_0} \{[(1-\omega_0)\theta^4 + \omega_0\eta]E_1(|\tau - \tau'|)/2\}\, d\tau' \qquad (9)
$$

$$
B_1^* = (1 - \rho_1) + 2\rho_1\{B_2^* E_3(\tau_0) + \int_0^{\tau_0} [(1-\omega_0)\theta^4 + \omega_0\eta]E_2(\tau)d\tau\} \qquad (10)
$$

$$
B_2^* = (1 - \rho_2)\theta_2^4 + 2\rho_2\{B_1^* E_3(\tau_0 - \tau) + \int_0^{\tau_0} [(1-\omega_0)\theta^4 + \omega_0\eta]E_2(\tau_0 - \tau)d\tau\} \qquad (11)
$$

with the boundary condition given by equation (5) and the radiant flux given by

$$
\begin{aligned}
\psi(\tau) &= 2B_1^* E_3(\tau) - 2B_2^* E_3(\tau_0 - \tau) \\
&\quad + 2\int_0^{\tau} [(1-\omega_0)\theta^4 + \omega_0\eta]E_2(\tau - \tau')\, d\tau' \\
&\quad - 2\int_{\tau}^{\tau_0} [(1-\omega_0)\theta^4 + \omega_0\eta]E_2(\tau' - \tau)\, d\tau' \qquad (12)
\end{aligned}
$$

The total heat flux through such a gas is given by

$$
q = -k_g\beta T_1 \left.\frac{d\theta}{d\tau}\right|_{\tau=\tau_0} + n^2\sigma T_1^4\psi(0) \qquad (13)
$$

Complete analogy between the two sets of governing equations, i.e., equations (1)-(7) and equations (8)-(13), can be readily shown. First consider the governing equation (1). By choosing

$$
\rho = \omega_0,\ k_e = k_g,\ {}^1\!/_2 h = \beta,\ \text{and } H^* = \eta \qquad (14)
$$

equation (1) becomes identical to equation (8). Furthermore if the shape factors can be approximated by the respective exponential integrals $E_1(\tau)$, $E_2(\tau)$, and $E_3(\tau)$ as

$$0.25/[0.25 + \tau^2]^{3/2} \simeq E_1(\tau)$$

$$1 - \tau/\sqrt{\tau^2 + 0.25} \simeq E_2(\tau)$$

$$\sqrt{\tau^2 + 0.25} - \tau \simeq E_3(\tau)$$

and if Q/t is set to be equal to q, then equations (2)–(7) are identical to equations (9)–(13). The foregoing approximations are good as illustrated in Fig. 2, especially since such approximations are better than the well established exponential kernel approximation which approximates exponential integrals by exponential functions [7]. Because the use of the exponential kernel approximation generally yields an excellent temperature distribution or heat flux etc., one can expect the same by using the above approximations as can be seen in Fig. 3. Consequently the existing solution obtained by Viskanta [6] can be used directly as an approximate solution to the present problem involving lateral, combined conduction and radiation heat transfer along diffusely reflecting side walls.

In order to show that the Viskanta's solution can serve as a good approximate solution to the present problem, this approximate solution must be compared with exact solution of equations (1)–(7). Because it involves a system of complicated, nonlinear integro-differential equations, no analytical solution of these equations is possible. The solutions, therefore, are obtained by numerical procedures.

Before applying the numerical technique, equation (1) is integrated twice to obtain an equivalent integral equation including the boundary condition as

$$\theta(\tau) = 1 - (1 - \theta_2)\tau/\tau_0 - N(1 - \rho) \times \left\{ \int_0^{\tau} \tau'(1 - \tau/\tau_0)(\theta^4 - H^*)\, d\tau + \int_{\tau}^{\tau_0} \tau(1 - \tau'/\tau_0)(\theta^4 - H^*) d\tau' \right\} \quad (15)$$

The governing integral equations (2), (3), (4), and (15) are converted into a set of algebraic equations by discretizing the definite and indefinite integrals by using the Simpson's quadrature formulas. The resulting set of equations have two sets of unknown H^* and θ. The relations are linear in H^* and highly nonlinear in θ. Guessing values of θ, the equations are solved for H^* by Gaussian Matrix inversion. Next, the equations are solved for θ by using direct iteration technique. The entire process is repeated until convergence is obtained in the value of θ as well as H.* However, even if such an elaborate procedure is used, it is found that the numerical solution still does not converge for all possible values of the six governing parameters, N, θ_2, τ_0, ρ, ρ_1, and ρ_2. Generally speaking the larger the N or τ_0, the less stable is the solution. For example, if N is chosen as large as 10 to emphasize the radiation effect and other parameters are taken as those shown in Fig. 3, the solution converges for $\tau_0 = 1$ or less. Fig. 3 shows the case of $\tau_0 = 1$ and the agreement between the approximate and exact numerical solutions is remarkably good. For larger values of τ_0, the agreement could be expected to be even better because the approximation of the shape factors by the exponential integrals as shown in Fig. 2 works better for larger values of τ_0, just like the case of replacing the exponential integrals by the exponential kernal approximation. Therefore the existing Viskant'a solution for a radiation participating medium can be used as a good approximate solution to the present problem of nonparticipating medium.

In conclusion, the present study shows an analogy between surface and gaseous radiations. The two long parallel diffuse surfaces with an reflectivity ρ and a spacing h are equivalent to an absorbing, emitting and scattering medium with a scattering albedo $\omega_0 = \rho$ and an extinction coefficient $\beta = {}^1/_2h$.

References

1 Coston, R. M., and Vliet, G. C., "Thermal Energy Transport Parallel to the Lamination in Multilayer Insulation," *Advances in Cryogenic Engineering*, Vol. 13, 1968, p. 671.

2 Androulakis, J. G., and Kosson, R. M., "Effective Thermal Conductivity Parallel to the Lamination and Total Conductance for Combined Parallel and Normal Heat Flow in Multilayer Insulation," AIAA Paper No. 68-765, Los Angeles, Calif., 1968.

3 Donovan, R. C., and Rohrer, W. M., "Radiative Conducting Fins on a Plane Wall, Including Mutual Irradiation," ASME paper 69 WA/HT-22, Los Angeles, Calif., 1969.

4 Tien, C. L., Jagannathan, P. S., and Armaly, B. F., "Analysis of Lateral Conduction and Radiation Along Two Parallel Long Plates," *AIAA Journal*, Vol. 7, 1969, p. 1806.

5 Jagannathan, P. S., and Tien, C. L., "Spacer Effects on Lateral Heat Transfer in Multilayer Insulation," *Journal of Spacecraft and Rockets*, Vol. 8, 1971, p. 416.

6 Viskanta, R., "Heat Transfer by Conduction and Radiation in Absorbing and Scattering Materials," JOURNAL OF HEAT TRANSFER, TRANS. ASME, Series C, Vol. 1, 87, 1965, p. 143.

7 Sparrow, E. M., and Cess, R. D., "Radiation Heat Transfer," Brooks/Cole, Belmont, Calif., 1967, pp. 96–98.

The Effect of Changes in Sphere Coating Reflectance on the Performance of Integrating Spheres

C. K. HSIEH[1]

Nomenclature

A = area
H = irradiation flux
R = reflected flux of radiation
λ = wavelength
ρ = reflectance

Subscripts

B = bright spot
D = dark shadow
E = apertures
0 = total sphere ($A_0 = A_B + A_D + A_E$)
S = externally originated incoming radiation

Introduction

THE INTEGRATING SPHERE has been indispensable in measurements of hemispherical-directional reflectance of substances [1, 2].[2] Recently, it has also been used as a flux averaging device in optical systems [3, 4]. In both applications, chopped incoming radiation passes through one aperture of the sphere and strikes on the interior of the sphere wall. Because of the highly reflective and diffuse coating on the wall, this incoming radiation can undergo a process of diffuse multi-reflections. As a result, there are only two zones inside the sphere. The zone which is directly illuminated by the external irradiation appears bright to the eye, as contrasted to the dark shadow zone where illumination is solely a result of multi-reflections.

An examination of literature reveals that the previous theories on integrating spheres [5, 6, 7, 8] used only total properties which offer no perspective as to the performance of the sphere on a spectral basis. Edwards, et al. [9] derived equations for per-

---

[1] Assistant Professor, Department of Mechanical Engineering, University of Florida, Gainesville, Fla. Assoc. Mem. ASME.

[2] Numbers in brackets designate References at end of technical brief.

Contributed by the Heat Transfer Division of THE AMERICAN SOCIETY OF MECHANICAL ENGINEERS. Manuscript received by the Heat Transfer Division, February 13, 1973.

the shape factors can be approximated by the respective exponential integrals $E_1(\tau)$, $E_2(\tau)$, and $E_3(\tau)$ as

$$0.25/[0.25 + \tau^2]^{3/2} \simeq E_1(\tau)$$

$$1 - \tau/\sqrt{\tau^2 + 0.25} \simeq E_2(\tau)$$

$$\sqrt{\tau^2 + 0.25} - \tau \simeq E_3(\tau)$$

and if Q/l is set to be equal to q, then equations (2)–(7) are identical to equations (9)–(13). The foregoing approximations are good as illustrated in Fig. 2, especially since such approximations are better than the well established exponential kernel approximation which approximates exponential integrals by exponential functions [7]. Because the use of the exponential kernel approximation generally yields an excellent temperature distribution or heat flux etc., one can expect the same by using the above approximations as can be seen in Fig. 3. Consequently the existing solution obtained by Viskanta [6] can be used directly as an approximate solution to the present problem involving lateral, combined conduction and radiation heat transfer along diffusely reflecting side walls.

In order to show that the Viskanta's solution can serve as a good approximate solution to the present problem, this approximate solution must be compared with exact solution of equations (1)–(7). Because it involves a system of complicated, nonlinear integro-differential equations, no analytical solution of these equations is possible. The solutions, therefore, are obtained by numerical procedures.

Before applying the numerical technique, equation (1) is integrated twice to obtain an equivalent integral equation including the boundary condition as

$$\theta(\tau) = 1 - (1 - \theta_2)\tau/\tau_0 - N(1 - \rho) \times \left\{\int_0^\tau \tau'(1 - \tau/\tau_0)(\theta^4 - H^*)\, d\tau + \int_\tau^{\tau_0} \tau(1 - \tau'/\tau_0)(\theta^4 - H^*) d\tau'\right\} \quad (15)$$

The governing integral equations (2), (3), (4), and (15) are converted into a set of algebraic equations by discretizing the definite and indefinite integrals by using the Simpson's quadrature formulas. The resulting set of equations have two sets of unknown H^* and θ. The relations are linear in H^* and highly nonlinear in θ. Guessing values of θ, the equations are solved for H^* by Gaussian Matrix inversion. Next, the equations are solved for θ by using direct iteration technique. The entire process is repeated until convergence is obtained in the value of θ as well as H^*. However, even if such an elaborate procedure is used, it is found that the numerical solution still does not converge for all possible values of the six governing parameters, N, θ_2, τ_0, ρ, ρ_1, and ρ_2. Generally speaking the larger the N or τ_0, the less stable is the solution. For example, if N is chosen as large as 10 to emphasize the radiation effect and other parameters are taken as those shown in Fig. 3, the solution converges for $\tau_0 = 1$ or less. Fig. 3 shows the case of $\tau_0 = 1$ and the agreement between the approximate and exact numerical solutions is remarkably good. For larger values of τ_0, the agreement could be expected to be even better because the approximation of the shape factors by the exponential integrals as shown in Fig. 2 works better for larger values of τ_0, just like the case of replacing the exponential integrals by the exponential kernal approximation. Therefore the existing Viskant'a solution for a radiation participating medium can be used as a good approximate solution to the present problem of nonparticipating medium.

In conclusion, the present study shows an analogy between surface and gaseous radiations. The two long parallel diffuse surfaces with an reflectivity ρ and a spacing h are equivalent to an absorbing, emitting and scattering medium with a scattering albedo $\omega_0 = \rho$ and an extinction coefficient $\beta = 1/2h$.

References

1 Coston, R. M., and Vliet, G. C., "Thermal Energy Transport Parallel to the Lamination in Multilayer Insulation," *Advances in Cryogenic Engineering*, Vol. 13, 1968, p. 671.

2 Androulakis, J. G., and Kosson, R. M., "Effective Thermal Conductivity Parallel to the Lamination and Total Conductance for Combined Parallel and Normal Heat Flow in Multilayer Insulation," AIAA Paper No. 68-765, Los Angeles, Calif., 1968.

3 Donovan, R. C., and Rohrer, W. M., "Radiative Conducting Fins on a Plane Wall, Including Mutual Irradiation," ASME paper 69 WA/HT-22, Los Angeles, Calif., 1969.

4 Tien, C. L., Jagannathan, P. S., and Armaly, B. F., "Analysis of Lateral Conduction and Radiation Along Two Parallel Long Plates," *AIAA Journal*, Vol. 7, 1969, p. 1806.

5 Jagannathan, P. S., and Tien, C. L., "Spacer Effects on Lateral Heat Transfer in Multilayer Insulation," *Journal of Spacecraft and Rockets*, Vol. 8, 1971, p. 416.

6 Viskanta, R., "Heat Transfer by Conduction and Radiation in Absorbing and Scattering Materials," JOURNAL OF HEAT TRANSFER, TRANS. ASME, Series C, Vol. 1, 87, 1965, p. 143.

7 Sparrow, E. M., and Cess, R. D., "Radiation Heat Transfer," Brooks/Cole, Belmont, Calif., 1967, pp. 96–98.

The Effect of Changes in Sphere Coating Reflectance on the Performance of Integrating Spheres

C. K. HSIEH[1]

Nomenclature

A = area
H = irradiation flux
R = reflected flux of radiation
λ = wavelength
ρ = reflectance

Subscripts

B = bright spot
D = dark shadow
E = apertures
0 = total sphere ($A_0 = A_B + A_D + A_E$)
S = externally originated incoming radiation

Introduction

THE INTEGRATING SPHERE has been indispensable in measurements of hemispherical-directional reflectance of substances [1, 2].[2] Recently, it has also been used as a flux averaging device in optical systems [3, 4]. In both applications, chopped incoming radiation passes through one aperture of the sphere and strikes on the interior of the sphere wall. Because of the highly reflective and diffuse coating on the wall, this incoming radiation can undergo a process of diffuse multi-reflections. As a result, there are only two zones inside the sphere. The zone which is directly illuminated by the external irradiation appears bright to the eye, as contrasted to the dark shadow zone where illumination is solely a result of multi-reflections.

An examination of literature reveals that the previous theories on integrating spheres [5, 6, 7, 8] used only total properties which offer no perspective as to the performance of the sphere on a spectral basis. Edwards, et al. [9] derived equations for per-

---

[1] Assistant Professor, Department of Mechanical Engineering, University of Florida, Gainesville, Fla. Assoc. Mem. ASME.

[2] Numbers in brackets designate References at end of technical brief.

Contributed by the Heat Transfer Division of THE AMERICAN SOCIETY OF MECHANICAL ENGINEERS. Manuscript received by the Heat Transfer Division, February 13, 1973.

formance analysis of their designed integrating sphere reflectometer. Errors were calculated for both specular and perfectly diffuse samples. This technical brief attempts to follow a different approach by studying the effects of changing of coating reflectance on the performance of integrating spheres.

Analysis

The analysis is considerably simplified in view of the fact that the incoming radiation is chopped. This eliminates the effect of the emitted energy that is received by a detector and reflected energy becomes the only concern. A model is considered that consists of a sphere with two circular apertures, one for incoming pencil of ray to pass through and the other for detection; both are considered black for reflected energies. The interior wall of the sphere is opaque, nongray, and a diffuse emitter and reflector of radiation. The gas medium inside the sphere is radiatively nonparticipating; and diffraction, interference, and polarization effects are ignored.

For any surface element $dA(\theta', \phi')$ on a sphere wall, see Fig. 1, the radiant flux reflected from the surface can be expressed as

$$R_\lambda(\theta', \phi', \lambda) = \rho_\lambda(\theta', \phi', \lambda)\left[H_{S\lambda}(\theta', \phi', \lambda)\sin\frac{\theta'}{2} + H_\lambda'(\theta', \phi', \lambda)\right] \quad (1)$$

where $\sin\frac{\theta'}{2}$ in the first term on the right emerges as a result of the cosine of the incident ray, $\cos\frac{1}{2}(\pi - \theta')$. By invoking use of the configuration factor and recognizing that, for a spherical geometry, this factor is independent of the area from which radiant flux leaves a surface [10], equation (1) can be rewritten as

$$R_\lambda(\theta', \phi', \lambda) = \rho_\lambda(\theta', \phi', \lambda)\left[H_{S\lambda}(\theta', \phi', \lambda)\sin\frac{\theta'}{2} + \frac{1}{A_0}\int\int_A R_\lambda(\theta'', \phi'', \lambda)dA(\theta'', \phi'')\right] \quad (2)$$

As noted earlier, there are two zones inside the sphere, a bright spot (B) and a dark shadow zone (D). Equation (2) can be used to write, for these two regions,

$$R_{\lambda B} = \rho_\lambda H_{S\lambda}\sin\frac{\theta'}{2} + \rho_\lambda\left(\frac{A_D}{A_0}\right)R_{\lambda D} + \rho_\lambda\left(\frac{A_B}{A_0}\right)R_{\lambda B} \quad (3a)$$

and

$$R_{\lambda D} = \rho_\lambda\left(\frac{A_D}{A_0}\right)R_{\lambda D} + \rho_\lambda\left(\frac{A_B}{A_0}\right)R_{\lambda B} \quad (3b)$$

where position dependency has been omitted for simplicity in expressions. Both equations (3*a*) and (3*b*) should be solved simultaneously for $R_{\lambda B}$ and $R_{\lambda D}$. Yet, in practical applications, they can be used to derive two equations:

$$R_{\lambda D} = \left[\left(\frac{A_B}{A_0}\right)\rho_\lambda^2 H_{S\lambda}\sin(1/2)\theta'\right]\left[1 - \rho_\lambda + \rho_\lambda\left(\frac{A_E}{A_0}\right)\right]^{-1} \quad (4)$$

$$\frac{R_{\lambda B}}{R_{\lambda D}} = \left[1 - \rho_\lambda\left(\frac{A_D}{A_0}\right)\right]\left[\rho_\lambda\left(\frac{A_B}{A_0}\right)\right]^{-1} \quad (5)$$

which are more useful in analysis. Equation (4) is indispensable in evaluating the signal level and, therefore, the signal-to-noise ratio for the energy that reaches a detector in the optical system. Equation (5) is useful to estimate the error that might be involved if the bright spot on the sphere wall comes into the field of view of a detector. The latter is particularly meaningful in view of the fact that, in the case of an integrating sphere reflectometer, $R_{\lambda B}/R_{\lambda D}$ ratio provides a means for checking the condition of uniform irradiation on a specimen. This uniform irradiation is a prerequisite for directional-hemispherical reflectance to be equal to hemispherical-directional reflectance according to theory [11].

Results and Discussion

It is noted that A_B in equations (4) and (5) is independent of the area of the aperture for incident radiation $H_{S\lambda}$. The sum of the two areas of the apertures is A_E. To facilitate comparison of the performance of the integrating sphere over a broad spectrum, a MgO coated sphere is considered. An attempt is made to study the deterioration of the sphere performance due to aging of the coating. The reflectance of MgO is taken from a paper by Edwards, et al. [9] in which a 3 hour old coating and a 1 month old coating are respectively identified as "fresh" and "aged." The reflectance values are used to evaluate ratios $R_{\lambda D(\text{fresh})}/R_{\lambda D(\text{aged})}$ versus wavelengths, see Fig. 2. The ratio of reflectances $\rho_{\lambda(\text{fresh})}/\rho_{\lambda(\text{aged})}$ is also plotted along the right ordinate. A_E/A_0, being fixed for a given sphere, is suitably chosen as a parameter. The A_E in the numerator has also been used to compute a total equivalent field angle for apertures, θ_E defined as the angle subtended by $A_E = A_{E_1} + A_{E_2}$ at the center of the sphere, see Fig. 1. The values of θ_E are given along with the parameter A_E/A_0 in Fig. 2 to facilitate comparison and visualization.

Fig. 2 shows clearly that the performance of the integrating sphere is strongly dependent on the surface property variation. From 0.6 to 1μm, where aging does not lower reflectance appreciably (less that 0.5 percent), reflected flux ratios do not show marked increase. Even for small apertures ($A_E/A_0 = 0.00759$),

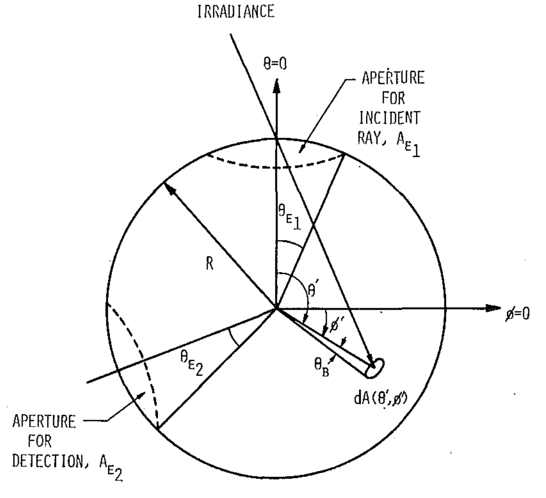

Fig. 1 Spherical coordinate system for the integrating sphere

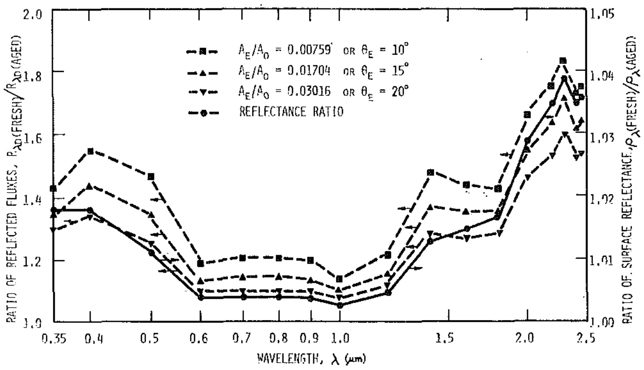

Fig. 2 Curves for ratios of reflected fluxes from shadow zones versus wavelengths

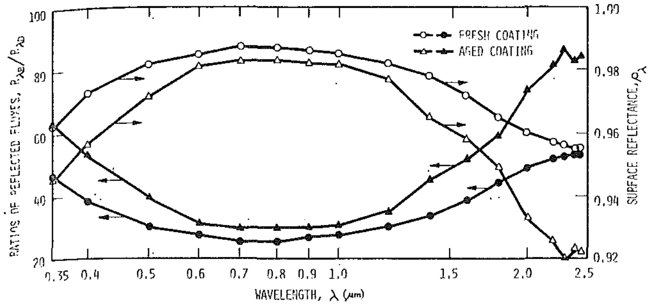

Fig. 3 Curves for ratios of raidiant flux reflected from bright spot to that dark zone versus wavelengths

the value of this ratio remains low at about 1.2, which implies that using a fresh coating does not offer great advantage. Toward either shorter or longer wavelengths, using a fresh coating becomes highly desirable. For instance, at 2.3μm the reflectance of a fresh MgO coating is only 3.8 percent higher than that of an aged one. Yet, the reflected energy in the shadow zone from the former is 83 percent higher than that from the latter for these apertures. While increasing A_E/A_0 decreases the flux ratio slightly, it still reaches a high value of 1.6 for $A_E/A_0 = 0.03016$.

An examination of equation (5) shows that the ratio $R_{\lambda B}/R_{\lambda D}$ can be decreased by either increasing ρ_λ or decreasing A_E if the area of the bright spot is kept unchanged. Unlike $R_{\lambda D}$, this ratio is independent of the incoming radiation $H_{S\lambda}$. A plot representative of a typical sphere in working condition with $A_E/A_0 = 0.01704$ and the field angle of the bright spot $\theta_B = 4$ deg is given in Fig. 3. The ratios of the flux reflected from the bright spot to that from the shadow zone can be seen to be high for both fresh and aged coatings over the entire spectrum. Toward the two ends of the spectrum this ratio reaches extremely high values. These are the wavelengths where excessive error might result if one equates the directional-hemispherical reflectance to the hemispherical-directional reflectance provided that the latter is measured by an integrating sphere reflectometer with the bright spot exposed toward the specimen. This ratio is nevertheless higher for aged coating rather than for fresh in contrast with what one might normally expect.

The analysis can also be extended to cases when upper and lower spheres have different reflectance values. Hsieh and Lee's work [12] can be referred to for further information on such analysis.

Acknowledgment

The material presented in this paper consists of a portion of a research project supported jointly by the National Science Foundation (grant number GK 28865) and the American Society of Heating, Refrigerating, and Air-Conditioning Engineers (grant number RP-114). Mr. K. H. Lee assisted in computing numerical data.

References

1 Clayton, W. A., "Comment on Measurement Techniques," Symposium on Thermal Radiation of Solids, NASA SP-55, 1964, pp. 213–215.

2 Touloukian, Y. S., and DeWitt, D. P., *Thermal Radiative Properties, Metallic Elements and Alloys*, IFI/Plenum, New York, 1970.

3 Dunn, S. T., Richmond, J. C., and Wiebelt, J. A., "Ellipsoidal Mirror Reflectometer," *Journal of Research*, National Bureau of Standards, Section C, Engineering and Instrumentation, Vol. 70C, No. 2, 1966, pp. 75–88.

4 Bennett, H. E., and Koehler, W. F., "Precision Measurement of Absolute Specular Reflectance With Minimized Systematic Errors," *Journal of the Optical Society of America*, Vol. 50, No. 1, 1960, pp. 1–6.

5 Jacquez, J. A., and Kuppenheim, H. F., "Theory of the Integrating Sphere," *Journal of the Optical Society of America*, Vol. 45, 1955, pp. 460–470.

6 Hisdal, B. J., "Reflectance of Perfect Diffuse and Specular Samples in the Integrating Sphere," *Journal of the Optical Society of America*, Vol. 55, No. 9, 1965, pp. 1122–1128.

7 Hisdal, B. J., "Reflectance of Nonperfect Surfaces in the Integrating Sphere," *Journal of the Optical Society of America*, Vol. 55, No. 10, 1965, pp. 1255–1260.

8 Goebel, D. G., "Generalized Integrating-Sphere Theory," *Applied Optics*, Vol. 6, No. 1, 1967, pp. 125–128.

9 Edwards, D. K., et al., "Integrating Sphere for Imperfectly Diffuse Samples," *Applied Optics*, Vol. 51, 1961, pp. 1279–1288.

10 Jakob, M., *Heat Transfer*, Vol. II, Wiley, New York, 1957, pp. 28–29.

11 Siegel, R., and Howell, J. R., "Thermal Radiation Heat Transfer," Vol. 1, The Blackbody, Electromagnetic Theory, and Material Properties, NASA SP-164, 1968, pp. 76.

12 Hsieh, C. K., Lee, K. H., "An Analytical Approach to a Performance Study of Integrating Spheres," a trl Report, TRL-72-B1, Thermal Radiation Laboratory, Department of Mechanical Engineering, University of Florida, 1972.

Local Liquid Film Thickness Around Taylor Bubbles[1]

MUSTAFA R. ÖZGÜ,[2] JOHN C. CHEN,[3] and ALAN H. STENNING[4]

Nomenclature

g = gravitational acceleration
$\dot{m}$ = mass flow rate in film per unit depth
R_0 = tube radius
u = axial velocity in film
u_δ = velocity at liquid-vapor interface
u_p = potential flow velocity at liquid-vapor interface
x = axial distance below bubble nose
y = normal distance measured from tube wall
δ = film thickness
δ_p = potential flow film thickness
μ = absolute viscosity of liquid
η = nondimensional film thickness, δ/R_0
η_p = nondimensional potential flow film thickness, δ_p/R_0
δ = liquid density
ξ = nondimensional axial distance, x/R_0

Introduction

THE STEADY-STATE rise of long bullet-shaped bubbles of gas (referred to as Taylor bubbles) in large circular tubes filled with a liquid of low viscosity was first studied by Dumitrescu [1],[5] and Davies and Taylor [2]. Their work served as the starting point for the studies of Griffith and Wallis [3], Moissis and Griffith [4], Stanley [5], Nicklin, et al. [6], Brown [7], Collins [8], Hsu and Simon [9], and others. These studies were mainly concentrated on the bubble rise velocity, bubble stability, pressure drop, shear stress, and entrance effects in flows in which Taylor bubbles are separated by slugs of liquid, i.e., two-phase slug flow. Little information, however, has been obtained on the local liquid-film thickness around the bubbles. In some heat transfer problems involving slug flow or single-bubble flow (e.g., reactor coolant

---

[1] This work was supported by an NSF Departmental Scientific Development Grant.

[2] Assistant Professor, Department of Mechanical Engineering and Mechanics, Lehigh University, Bethlehem, Pa. Assoc. Mem. ASME.

[3] Professor, Department of Mechanical Engineering and Mechanics, Lehigh University, Bethlehem, Pa. Mem. ASME.

[4] Professor, Department of Mechanical Engineering and Mechanics, Lehigh University, Bethlehem, Pa. Mem. ASME.

[5] Numbers in brackets designate References at end of technical brief.

Contributed by the Heat Transfer Division of THE AMERICAN SOCIETY OF MECHANICAL ENGINEERS. Manuscript received by the Heat Transfer Division, March 26, 1973.

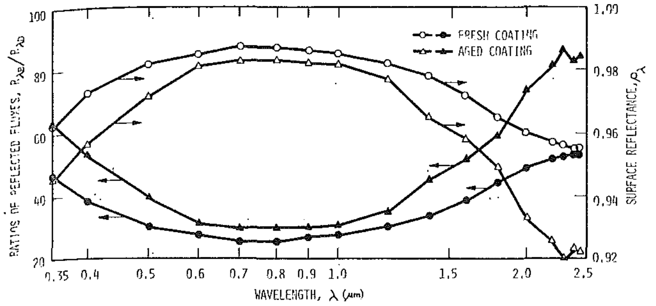

Fig. 3 Curves for ratios of raidiant flux reflected from bright spot to that dark zone versus wavelengths

the value of this ratio remains low at about 1.2, which implies that using a fresh coating does not offer great advantage. Toward either shorter or longer wavelengths, using a fresh coating becomes highly desirable. For instance, at 2.3μm the reflectance of a fresh MgO coating is only 3.8 percent higher than that of an aged one. Yet, the reflected energy in the shadow zone from the former is 83 percent higher than that from the latter for these apertures. While increasing A_E/A_0 decreases the flux ratio slightly, it still reaches a high value of 1.6 for $A_E/A_0 = 0.03016$.

An examination of equation (5) shows that the ratio $R_{\lambda B}/R_{\lambda D}$ can be decreased by either increasing ρ_λ or decreasing A_E if the area of the bright spot is kept unchanged. Unlike $R_{\lambda D}$, this ratio is independent of the incoming radiation $H_{S\lambda}$. A plot representative of a typical sphere in working condition with $A_E/A_0 = 0.01704$ and the field angle of the bright spot $\theta_B = 4$ deg is given in Fig. 3. The ratios of the flux reflected from the bright spot to that from the shadow zone can be seen to be high for both fresh and aged coatings over the entire spectrum. Toward the two ends of the spectrum this ratio reaches extremely high values. These are the wavelengths where excessive error might result if one equates the directional-hemispherical reflectance to the hemispherical-directional reflectance provided that the latter is measured by an integrating sphere reflectometer with the bright spot exposed toward the specimen. This ratio is nevertheless higher for aged coating rather than for fresh in contrast with what one might normally expect.

The analysis can also be extended to cases when upper and lower spheres have different reflectance values. Hsieh and Lee's work [12] can be referred to for further information on such analysis.

Acknowledgment

The material presented in this paper consists of a portion of a research project supported jointly by the National Science Foundation (grant number GK 28865) and the American Society of Heating, Refrigerating, and Air-Conditioning Engineers (grant number RP-114). Mr. K. H. Lee assisted in computing numerical data.

References

1 Clayton, W. A., "Comment on Measurement Techniques," Symposium on Thermal Radiation of Solids, NASA SP-55, 1964, pp. 213–215.

2 Touloukian, Y. S., and DeWitt, D. P., *Thermal Radiative Properties, Metallic Elements and Alloys*, IFI/Plenum, New York, 1970.

3 Dunn, S. T., Richmond, J. C., and Wiebelt, J. A., "Ellipsoidal Mirror Reflectometer," *Journal of Research*, National Bureau of Standards, Section C, Engineering and Instrumentation, Vol. 70C, No. 2, 1966, pp. 75–88.

4 Bennett, H. E., and Koehler, W. F., "Precision Measurement of Absolute Specular Reflectance With Minimized Systematic Errors," *Journal of the Optical Society of America*, Vol. 50, No. 1, 1960, pp. 1–6.

5 Jacquez, J. A., and Kuppenheim, H. F., "Theory of the Integrating Sphere," *Journal of the Optical Society of America*, Vol. 45, 1955, pp. 460–470.

6 Hisdal, B. J., "Reflectance of Perfect Diffuse and Specular Samples in the Integrating Sphere," *Journal of the Optical Society of America*, Vol. 55, No. 9, 1965, pp. 1122–1128.

7 Hisdal, B. J., "Reflectance of Nonperfect Surfaces in the Integrating Sphere," *Journal of the Optical Society of America*, Vol. 55, No. 10, 1965, pp. 1255–1260.

8 Goebel, D. G., "Generalized Integrating-Sphere Theory," *Applied Optics*, Vol. 6, No. 1, 1967, pp. 125–128.

9 Edwards, D. K., et al., "Integrating Sphere for Imperfectly Diffuse Samples," *Applied Optics*, Vol. 51, 1961, pp. 1279–1288.

10 Jakob, M., *Heat Transfer*, Vol. II, Wiley, New York, 1957, pp. 28–29.

11 Siegel, R., and Howell, J. R., "Thermal Radiation Heat Transfer," Vol. 1, The Blackbody, Electromagnetic Theory, and Material Properties, NASA SP-164, 1968, pp. 76.

12 Hsieh, C. K., Lee, K. H., "An Analytical Approach to a Performance Study of Integrating Spheres," a trl Report, TRL-72-B1, Thermal Radiation Laboratory, Department of Mechanical Engineering, University of Florida, 1972.

Local Liquid Film Thickness Around Taylor Bubbles[1]

MUSTAFA R. ÖZGÜ,[2] JOHN C. CHEN,[3] and ALAN H. STENNING[4]

Nomenclature

g = gravitational acceleration
$\dot{m}$ = mass flow rate in film per unit depth
R_0 = tube radius
u = axial velocity in film
u_δ = velocity at liquid-vapor interface
u_p = potential flow velocity at liquid-vapor interface
x = axial distance below bubble nose
y = normal distance measured from tube wall
δ = film thickness
δ_p = potential flow film thickness
μ = absolute viscosity of liquid
η = nondimensional film thickness, δ/R_0
η_p = nondimensional potential flow film thickness, δ_p/R_0
δ = liquid density
ξ = nondimensional axial distance, x/R_0

Introduction

THE STEADY-STATE rise of long bullet-shaped bubbles of gas (referred to as Taylor bubbles) in large circular tubes filled with a liquid of low viscosity was first studied by Dumitrescu [1],[5] and Davies and Taylor [2]. Their work served as the starting point for the studies of Griffith and Wallis [3], Moissis and Griffith [4], Stanley [5], Nicklin, et al. [6], Brown [7], Collins [8], Hsu and Simon [9], and others. These studies were mainly concentrated on the bubble rise velocity, bubble stability, pressure drop, shear stress, and entrance effects in flows in which Taylor bubbles are separated by slugs of liquid, i.e., two-phase slug flow. Little information, however, has been obtained on the local liquid-film thickness around the bubbles. In some heat transfer problems involving slug flow or single-bubble flow (e.g., reactor coolant

---

[1] This work was supported by an NSF Departmental Scientific Development Grant.

[2] Assistant Professor, Department of Mechanical Engineering and Mechanics, Lehigh University, Bethlehem, Pa. Assoc. Mem. ASME.

[3] Professor, Department of Mechanical Engineering and Mechanics, Lehigh University, Bethlehem, Pa. Mem. ASME.

[4] Professor, Department of Mechanical Engineering and Mechanics, Lehigh University, Bethlehem, Pa. Mem. ASME.

[5] Numbers in brackets designate References at end of technical brief.

Contributed by the Heat Transfer Division of THE AMERICAN SOCIETY OF MECHANICAL ENGINEERS. Manuscript received by the Heat Transfer Division, March 26, 1973.

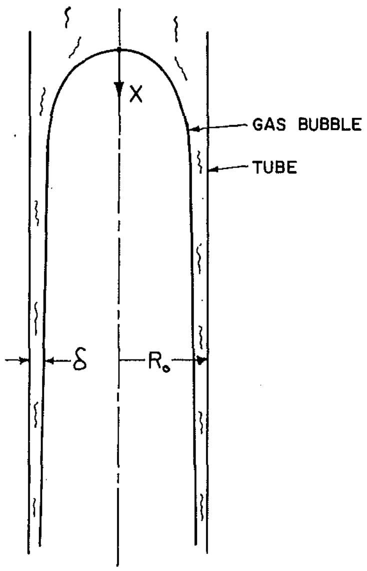

Fig. 1 Bubble profile and coordinates

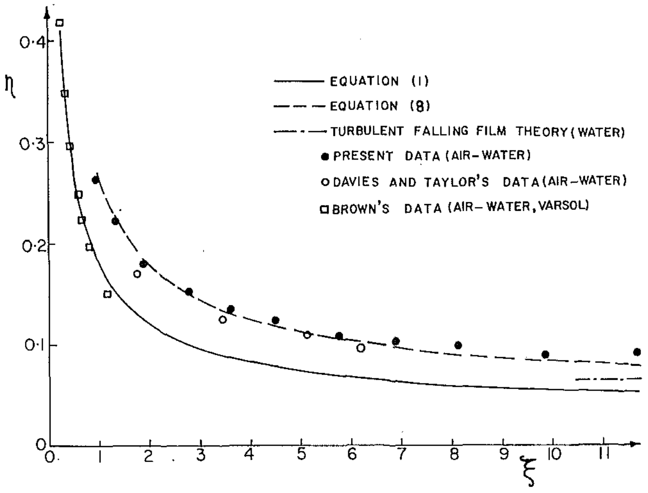

Fig. 2 Normalized liquid film thickness

expulsion), the local film thickness is an important governing parameter. It was the objective of this work to study the variation of the liquid-film thickness around Taylor bubbles of different lengths.

Previous Work

By assuming potential flow conditions at the bubble nose and in the film, and by assuming that the nose of the bubble was a portion of a spherical surface, Davies and Taylor [2] determined the following expression for the local film thickness around Taylor bubbles:

$$\eta_p - \frac{\eta_p^2}{2} = 0.165\ \xi^{-1/2}. \tag{1}$$

$\eta_p^2/2$ can be neglected at large values of ξ where the film is thin. The coordinate system is shown in Fig. 1. Equation (1) is represented by the solid line in Fig. 2. Davies and Taylor also obtained experimental values for the film thickness in the region of $2 < \xi < 6$ using a photographic technique. Their results were 30 percent higher than the predictions of equation (1) and are shown as circles in Fig. 2. They attributed the discrepancy to the neglect of the viscous boundary layer effects in the film and also to the errors involved in their photographic measurements. Brown [7] made experimental measurements of the local film thickness in regions close to the bubble nose ($\xi < 1.2$) using photography. His results are shown as rectangles in Fig. 2.

As seen from Fig. 2, these available results were insufficient to describe local film thicknesses over a wide range of axial position (ξ). The potential flow theory, which neglects viscous effects, can be expected to apply only at small values of ξ (i.e., $\xi < 1$). The two previously published sets of experimental data together cover values of ξ only up to 6, and also exhibit some disagreement. The present study was undertaken to obtain additional information on local film thicknesses, with emphasis on the range $1 \leq \xi \leq 12$, where viscous effects become important.

Present Study

(*a*) Theoretical Considerations. The liquid ahead of the bubble can be assumed to have a uniform velocity profile relative to the bubble. The flat velocity profile is deformed at the bubble nose, and laminar boundary layer formation starts at the tube wall. The effect of this boundary layer is small and can be neglected for *short* distances below the nose of the bubble. At the other limit of large distances below the nose, the acceleration of the film under gravity ceases and the film is supported by wall shear stress. Hence, the film thickness reaches an asymptotic value which should approach the value predicted by falling film theory if wave motion is disregarded. In between the nose region and the asymptotic region there should exist a transition region where potential flow aspects and boundary layer flow aspects are both important.

For this transition region, an approximate model for the velocity distribution in the liquid film can be formulated by:

(*a*) neglecting curvature effects in view of small film thickness compared with the tube radius;

(*b*) assuming that the laminar viscous wall-shear force and gravity force balance each other, as in falling film theory;

(*c*) equating the velocity at the liquid-vapor interface to that obtained from potential flow theory.

In (*b*) it is assumed that the axial convective term is small compared with wall-shear and gravity forces. Neglecting the density of the vapor in the bubble compared with the density of the liquid, the laminar film velocity profile is:

$$u = \frac{\rho g}{\mu}\,[\delta y - {}^1\!/_2\, y^2] \tag{2}$$

The mass flow rate in the film can be obtained by integrating equation (2) as

$$\dot{m} = \frac{\rho^2 g \delta^3}{3\mu} \tag{3}$$

From equation (2), the velocity at the liquid-vapor interface is obtained as:

$$u_\delta = \frac{\rho g \delta^2}{2\mu} \tag{4}$$

Using assumption (*c*)

$$u_\delta = u_p = \frac{\rho g \delta^2}{2\mu} \tag{5}$$

But,

$$\dot{m} = u_p \delta_p \tag{6}$$

Combining (4) and (6)

$$\dot{m} = \frac{\rho g \delta^2 \delta_p}{2\mu} \tag{7}$$

Equating (3) and (7)

$$\frac{\delta_p}{\delta} = {}^2/_3 = 0.667 \tag{8}$$

or

$$\frac{\eta_p}{\eta} = 0.667$$

Alternately, if the Blasius velocity profile were used in place of equation (2), the ratio η_p/η would be 0.656—a difference of only 1.5 percent.

Equation (8) is represented by the broken line in Fig. 2.

Experiments were performed to complement the analysis described in the foregoing. The experimental program and results are presented in the following.

(b) Experimental Work and Results. Air bubbles of different lengths were introduced into a 1 in. ID tube filled with water. Local film thickness measurements were made along the bubble using a new capacitance measurement technique. The details of the experimental setup and capacitance technique are given in reference [10]. In normalized coordinates of η versus ξ, the experimentally determined bubble shapes were found to be independent of bubble length, as expected. Due to the steep variation of film thickness with axial position in the nose region and the particular design of the capacitance gauge, no accurate measurements of film thickness could be made in the region of $\xi < 1.0$. Fortunately, for application to heat transfer problems, major interest is in the region of thin film ($\xi > 1$). Thus, data are presented as solid circles in Fig. 2 only for values of $\xi > 1.0$.

The agreement between equation (8), the present experimental data and the data of Davies and Taylor is very good in the region of $1 < \xi < 10$. It is seen that for $\xi > 1$, all data lie noticeably higher than the theoretical curve for potential flow. This confirms our expectation that viscous thickening of the liquid film becomes significant within a short distance below the nose of the bubble. In the region $\xi > 1$, these data are seen to agree with the earlier results of Davies and Taylor, but do indicate a thicker film than the results of Brown. Aside from possible uncertainties due to different experimental techniques (photographic versus capacitance measurement) no explanation was found for this discrepancy.

In the region of high ξ, one would not expect equation (8) to be applicable due to onset of turbulent flow and wave formation. For the experimental conditions for this work, the measured film thicknesses appeared to agree with equation (8) up to $\xi \sim 10$.

Conclusion

The results of this study indicate that liquid films around Taylor bubbles are significantly thicker than predicted by potential flow theory. In the region $1 < \xi < 10$, the experimentally measured film thickness agreed well with the approximate analysis proposed.

References

1 Dumitrescu, D. T., "Flow Past an Air Bubble in a Vertical Pipe," *Zeitschrift fuer Angewandte Mathematek und Mechanik*, Vol. 23, 1943, pp. 139–148.

2 Davies, R. M., and Taylor, G. I., "The Mechanics of Large Bubbles Rising Through Extended Liquids and Through Liquids in Tubes," *Proceedings of the Royal Society*, London, Vol. 200, Series A, 1950, pp. 375–390.

3 Griffith, P., and Wallis, G. B., "Two-Phase Slug Flow," JOURNAL OF HEAT TRANSFER, TRANS. ASME, Series C, Vol. 83, No. 3, Aug. 1961, pp. 307–320.

4 Moissis, R., and Griffith, P., "Entrance Effects in a Two-Phase Slug Flow," JOURNAL OF HEAT TRANSFER, TRANS. ASME, Series C, Vol. 84, No. 1, Feb. 1962, pp. 29–39.

5 Stanley, D. W., "Wall Shear Stress in Two-Phase Slug Flow," MS thesis, Mechanical Engineering Department, Massachusetts Institute of Technology, June 1962.

6 Nicklin, D. J., Wilkes, J. O., and Davidson, J. F., "Two-Phase Flow in Vertical Tubes," *Transactions* of the Institute of Chemical Engineers, Vol. 40, 1962, pp. 61–68.

7 Brown, R. A. S., "The Mechanics of Large Gas Bubbles in Tubes. I. Bubble Velocities in Stagnant Liquids," *Canadian Journal of Chemical Engineering*, Vol. 43, Oct. 1965, pp. 217–223.

8 Collins, R., "The Effect of a Containing Cylindrical Boundary on the Velocity of a Large Gas Bubble in a Liquid," *Journal of Fluid Mechanics*, Vol. 28, Part I, 1967, pp. 97–112.

9 Hsu, Y. Y., and Simon, F. F., "Stability of Cylindrical Bubbles in a Vertical Pipe," ASME Paper No. 69-HT-28.

10 Özgü, M. R., Chen, J. C., and Eberhardt, N., "A Capacitance Method for Measurement of Film Thickness in Two-Phase Flow," accepted for publication in *The Review of Scientific Instruments*.

11 Tailby, S. R., and Portalski, S., "The Hydrodynamics of Liquid Films Flowing on a Vertical Surface," *Trans.* Instn. Chem. Engrs., Vol. 38, 1960, pp. 324–330.

12 Dukler, A. E., and Bergelin, O. P., "Characteristics of Flow in Falling Liquid Films," *Chemical Engineering Progress*, Vol. 48, No 11, 1952, pp. 557–563.

Dependence of Friction Factor Upon Liquid Level in Two-Phase One-Component Stratified Flow

M. A. VAN DROMME and L. J. HELLINCKX[1]

Nomenclature

a = half-width of interface
b = wetted perimeter
d = tube diameter
f = friction factor
h = height of arc of wetted perimeter
x, y = cartesian coordinates
E_k = specific kinetic energy
F = frictional force acting on liquid at wall
P = force acting on unit volume of liquid
Q = rate of discharge, volumetric
Re = Reynolds number ($4\rho Q/b\mu$)
α = form factor
β = one-half arc of wetted perimeter
γ = wetted area
ξ, η = polar coordinates
λ = integration variable
μ = dynamic viscosity
Ω = liquid-section area
ρ = density of liquid

Subscripts

L = liquid
V = vapor

Introduction

IN A STUDY on condensation of pure substances in horizontal tubes, Rufer and Kezios [1][2] proposed a model describing the case of stratified two-phase flow of vapor and condensate with annular condensation superimposed. This model resulted in an equation giving the slope of the vapor–bulk liquid interface along the tube, which was derived using the principles of conservation of mass, energy, and momentum. Within this equation coefficients appear that take into account the variation of friction factors with liquid level for both vapor and liquid phase. Values, or an expression for these so-called form factors, were not given.

In another work, Sarma and co-workers [2] studied the dependence of liquid level on void fraction in the same model. Therein the value of the ratio of the form factors for vapor and

---

[1] Instituut voor Chemie-Ingenieurstechniek, Katholieke Universiteit, Leuven de Croylaan 2, Heverlee-Leuven, Belgium.

[2] Numbers in brackets designate References at end of technical brief.

Contributed by the Heat Transfer Division of THE AMERICAN SOCIETY OF MECHANICAL ENGINEERS. Manuscript received by the Heat Transfer Division October 19, 1972.

$$\frac{\delta_p}{\delta} = {}^2/_3 = 0.667 \tag{8}$$

or

$$\frac{\eta_p}{\eta} = 0.667$$

Alternately, if the Blasius velocity profile were used in place of equation (2), the ratio η_p/η would be 0.656—a difference of only 1.5 percent.

Equation (8) is represented by the broken line in Fig. 2.

Experiments were performed to complement the analysis described in the foregoing. The experimental program and results are presented in the following.

(b) Experimental Work and Results. Air bubbles of different lengths were introduced into a 1 in. ID tube filled with water. Local film thickness measurements were made along the bubble using a new capacitance measurement technique. The details of the experimental setup and capacitance technique are given in reference [10]. In normalized coordinates of η versus ξ, the experimentally determined bubble shapes were found to be independent of bubble length, as expected. Due to the steep variation of film thickness with axial position in the nose region and the particular design of the capacitance gauge, no accurate measurements of film thickness could be made in the region of $\xi < 1.0$. Fortunately, for application to heat transfer problems, major interest is in the region of thin film ($\xi > 1$). Thus, data are presented as solid circles in Fig. 2 only for values of $\xi > 1.0$.

The agreement between equation (8), the present experimental data and the data of Davies and Taylor is very good in the region of $1 < \xi < 10$. It is seen that for $\xi > 1$, all data lie noticeably higher than the theoretical curve for potential flow. This confirms our expectation that viscous thickening of the liquid film becomes significant within a short distance below the nose of the bubble. In the region $\xi > 1$, these data are seen to agree with the earlier results of Davies and Taylor, but do indicate a thicker film than the results of Brown. Aside from possible uncertainties due to different experimental techniques (photographic versus capacitance measurement) no explanation was found for this discrepancy.

In the region of high ξ, one would not expect equation (8) to be applicable due to onset of turbulent flow and wave formation. For the experimental conditions for this work, the measured film thicknesses appeared to agree with equation (8) up to $\xi \sim 10$.

Conclusion

The results of this study indicate that liquid films around Taylor bubbles are significantly thicker than predicted by potential flow theory. In the region $1 < \xi < 10$, the experimentally measured film thickness agreed well with the approximate analysis proposed.

References

1 Dumitrescu, D. T., "Flow Past an Air Bubble in a Vertical Pipe," *Zeitschrift fuer Angewandte Mathematek und Mechanik*, Vol. 23, 1943, pp. 139–148.

2 Davies, R. M., and Taylor, G. I., "The Mechanics of Large Bubbles Rising Through Extended Liquids and Through Liquids in Tubes," *Proceedings of the Royal Society*, London, Vol. 200, Series A, 1950, pp. 375–390.

3 Griffith, P., and Wallis, G. B., "Two-Phase Slug Flow," JOURNAL OF HEAT TRANSFER, TRANS. ASME, Series C, Vol. 83, No. 3, Aug. 1961, pp. 307–320.

4 Moissis, R., and Griffith, P., "Entrance Effects in a Two-Phase Slug Flow," JOURNAL OF HEAT TRANSFER, TRANS. ASME, Series C, Vol. 84, No. 1, Feb. 1962, pp. 29–39.

5 Stanley, D. W., "Wall Shear Stress in Two-Phase Slug Flow," MS thesis, Mechanical Engineering Department, Massachusetts Institute of Technology, June 1962.

6 Nicklin, D. J., Wilkes, J. O., and Davidson, J. F., "Two-Phase Flow in Vertical Tubes," *Transactions* of the Institute of Chemical Engineers, Vol. 40, 1962, pp. 61–68.

7 Brown, R. A. S., "The Mechanics of Large Gas Bubbles in Tubes. I. Bubble Velocities in Stagnant Liquids," *Canadian Journal of Chemical Engineering*, Vol. 43, Oct. 1965, pp. 217–223.

8 Collins, R., "The Effect of a Containing Cylindrical Boundary on the Velocity of a Large Gas Bubble in a Liquid," *Journal of Fluid Mechanics*, Vol. 28, Part I, 1967, pp. 97–112.

9 Hsu, Y. Y., and Simon, F. F., "Stability of Cylindrical Bubbles in a Vertical Pipe," ASME Paper No. 69-HT-28.

10 Özgü, M. R., Chen, J. C., and Eberhardt, N., "A Capacitance Method for Measurement of Film Thickness in Two-Phase Flow," accepted for publication in *The Review of Scientific Instruments*.

11 Tailby, S. R., and Portalski, S., "The Hydrodynamics of Liquid Films Flowing on a Vertical Surface," *Trans.* Instn. Chem. Engrs., Vol. 38, 1960, pp. 324–330.

12 Dukler, A. E., and Bergelin, O. P., "Characteristics of Flow in Falling Liquid Films," *Chemical Engineering Progress*, Vol. 48, No 11, 1952, pp. 557–563.

Dependence of Friction Factor Upon Liquid Level in Two-Phase One-Component Stratified Flow

M. A. VAN DROMME and L. J. HELLINCKX[1]

Nomenclature

a = half-width of interface
b = wetted perimeter
d = tube diameter
f = friction factor
h = height of arc of wetted perimeter
x, y = cartesian coordinates
E_k = specific kinetic energy
F = frictional force acting on liquid at wall
P = force acting on unit volume of liquid
Q = rate of discharge, volumetric
Re = Reynolds number ($4\rho Q/b\mu$)
α = form factor
β = one-half arc of wetted perimeter
γ = wetted area
ξ, η = polar coordinates
λ = integration variable
μ = dynamic viscosity
Ω = liquid-section area
ρ = density of liquid

Subscripts

L = liquid
V = vapor

Introduction

IN A STUDY on condensation of pure substances in horizontal tubes, Rufer and Kezios [1][2] proposed a model describing the case of stratified two-phase flow of vapor and condensate with annular condensation superimposed. This model resulted in an equation giving the slope of the vapor–bulk liquid interface along the tube, which was derived using the principles of conservation of mass, energy, and momentum. Within this equation coefficients appear that take into account the variation of friction factors with liquid level for both vapor and liquid phase. Values, or an expression for these so-called form factors, were not given.

In another work, Sarma and co-workers [2] studied the dependence of liquid level on void fraction in the same model. Therein the value of the ratio of the form factors for vapor and

---

[1] Instituut voor Chemie-Ingenieurstechniek, Katholieke Universiteit, Leuven de Croylaan 2, Heverlee-Leuven, Belgium.

[2] Numbers in brackets designate References at end of technical brief.

Contributed by the Heat Transfer Division of THE AMERICAN SOCIETY OF MECHANICAL ENGINEERS. Manuscript received by the Heat Transfer Division October 19, 1972.

liquid phases was supposed, without justification, to lie between 0.8 and 1.2.

It is the aim of this note to provide information about the variation of these form factors with liquid level and to fix the limits of their ratio.

Analysis

In stratified two-phase flow in circular tubes, each phase flows in a space of segmental section. If the shear stress at the interface is supposed to be zero [1, 2] this interface can be seen as a free surface and the flow in one phase can be considered as open-channel flow, whether laminar or turbulent.

Laminar Flow in Open Circular Channels. The same expression for the local velocity applies for laminar flow in open circular channels as well as for flow in symmetrical lenticular tubes, for by symmetry the velocity gradient at the plane dividing the lenticular tube into two segments is zero, and identical conditions exist at the free surface in open-channel flow.

The expressions for local velocity and for rate of discharge for laminar flow in symmetrical lenticular tubes have been derived by Chaudhury [3] using a bipolar coordinate system defined by the equation

$$x + iy = a \tanh\left(\frac{\xi + \eta}{2}\right) \tag{1}$$

The two poles of the system are either at the intersection of the two arcs or at the intersection of one arc and the straight line representing the free surface. In this system the Navier-Stokes equation of motion takes the form

$$\frac{\partial^2 v}{\partial \xi^2} + \frac{\partial^2 v}{\partial \eta^2} = \frac{-Pa^2}{\mu(\cosh \xi + \cos \eta)^2} \tag{2}$$

with the boundary condition $v = 0$ for $\eta = \pm\beta$. The solution of this equation is

$$v = \frac{Pa^2}{2\mu}\left[\frac{\cos \eta}{(\cosh \xi + \cos \eta)} - 2 \cot \beta \int_0^\infty \frac{\tanh \lambda\beta \cosh \lambda\eta}{\sinh \lambda\pi} \cos \lambda\xi d\lambda\right] \tag{3}$$

By integrating this expression over the flow-section area, one obtains for the rate of discharge for flow in an open circular channel

$$Q = \frac{Pa^4}{8\mu}\left[(\beta + \cot \beta - 2\beta \cot^2 \beta + 3 \cot^3 \beta - 3\beta \cot^4 \beta) - 4\pi \cot \beta \operatorname{cosec}^2 \beta \int_0^\infty \frac{\tanh \beta\lambda(\sinh 2\beta\lambda - \lambda \sin 2\beta)}{\sinh^2 \lambda\pi} d\lambda\right] \tag{4}$$

or

$$Q = \frac{Pa^4}{8\mu} F(\beta)$$

From the definition of the friction factor [4]

$$F = f\gamma E_k \tag{5}$$

one obtains

$$f = \frac{2P\Omega^3}{bQ^2\rho} \tag{6}$$

Substituting the expression for Q in this formula gives

$$f = \frac{64\Omega^3}{b^2a^4 \operatorname{Re} F(\beta)} \tag{7}$$

or

$$f = \frac{16}{\operatorname{Re}} \alpha \tag{8}$$

where

$$\alpha = \frac{4\Omega^3}{b^2a^4} F^{-1}(\beta) \tag{9}$$

Substituting for Ω, a, and b, which are geometrical functions of β only, gives

$$\alpha = \left[\frac{\beta - \sin \beta \cos \beta}{\sin^2 \beta}\right]^3 \left[\frac{\sin \beta}{\beta}\right]^2 F^{-1}(\beta) \tag{10}$$

This latter shows that the form factor is really independent of flow properties and only depends on the geometry of the channel, characterized by the value of β or by an equivalent parameter such as the relative flow depth h/d.

We have calculated this factor α for different values of β. The integral in the denominator has been integrated through a combination of analytical and numerical methods. From $\lambda = 0$ to $\lambda = 6$ the integration has been performed by means of the trapezium rule with a step length of 0.1. For $\lambda > 6$ the expression to be integrated can, without loss of accuracy, be replaced by the following:

$$\frac{\tanh \beta\lambda(\sinh 2\beta\lambda - \lambda \sin 2\beta)}{\sinh^2 \lambda\pi} = 2 \exp\left[2\lambda(\beta - \pi)\right] - 4\lambda \sin 2\beta \exp(-2\lambda\pi) \tag{11}$$

The difference between the expressions has always been less than 10^{-13} for values of β up to 179 deg. The analytical integration of this expression gives

$$\int_6^\infty 2 \exp\left[2\lambda(\beta - \pi)\right] - 4\lambda \sin 2\beta \exp(-2\lambda)d\lambda = \exp(-12\pi)\left[\frac{\exp(12\beta)}{\pi - \beta} - \frac{\sin 2\beta}{\pi^2}(12\pi + 1)\right] \tag{12}$$

The results of these calculations are represented in Fig. 1, where the values of α have been plotted as the ordinate versus the relative flow depth h/d as abscissa.

From this figure one can see that for h/d smaller than 0.5, the difference between completely and partly filled tube-section flow is rather small, while the difference is much larger for $h/d > 0.5$. Here α reaches the maximum value of 1.1099 for $h/d = 0.97$. The curve attains the value $\alpha = 1$ for values of h/d equal to 0.26, 0.5, and 1.0.

Whereas the last two points, which were predicted by the

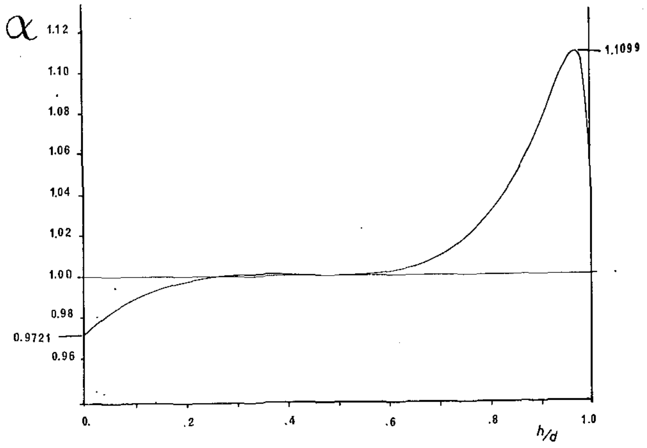

Fig. 1

Hagen–Poiseuille equation [4], could be fixed a priori, the limit for h/d going to zero was more difficult to determine. Indeed, for β going to zero, equation (9) takes the undefined form 0/0. The uncertainty at this point could be solved by making use of a simplified formula for the rate of discharge derived by Buffham [5], which is only applicable for very shallow channels:

$$Q = \frac{P}{\mu} \frac{d^4}{2} \frac{64}{105} \left(\frac{h}{d}\right)^{3.5} \tag{13}$$

The assumptions made when deriving this formula entail that the lower the value of h/d, the more reliable the calculated value for the rate of discharge. Putting this expression in equation (5) and substituting Ω, b, and h as functions of β, the following expression is obtained:

$$f = \frac{1}{\mathrm{Re}} \frac{105}{64} \frac{1}{32} \frac{(2\beta - \sin 2\beta)^3}{\beta^2 \sin^7 \dfrac{\beta}{2}} \tag{14}$$

The last quotient in this equation also takes the undefined value 0/0 for β going to zero, but by means of l'Hôpital's rule the limit for f can be calculated. Therefore we calculated the ninth-order derivative of numerator and denominator, giving 1680×2^9 and $9! \times 2^{-7}$, respectively. Finally, the limit of f for h/d going to zero was found to be 15.5555 . . . /Re, giving a limiting value for α of 0.9721. It is evident that the figure also applies for the determination of friction factors for laminar flow in symmetrical lenticular tubes, as was explained earlier.

Turbulent Flow in Open Circular Channels. As reported by several authors, the friction factor for turbulent flow in closed [6] and in open [7] channels does not depend upon the geometric form of the section, provided the hydraulic radius has the same value. This entails that for turbulent flow

$$\alpha = 1$$

and one can use one of the known relations expressing the friction factor as a function of the Reynolds number, for instance the Blasius equation

$$f = 0.0791\ \mathrm{Re}^{-1/4} \tag{15}$$

Conclusion

While the form factor for turbulent flow is always close to unity, for laminar flow a variation between 0.9721 and 1.1099 is possible. This results in the following extreme values for the ratio of the form factors of each phase:

laminar–laminar:

$$0.88 < \frac{\alpha_L}{\alpha_V} < 1.14$$

liquid laminar–vapor turbulent:

$$0.97 < \frac{\alpha_L}{\alpha_V} < 1.11$$

liquid turbulent–vapor laminar:

$$0.90 < \frac{\alpha_L}{\alpha_V} < 1.03$$

The first and the third cases, with laminar vapor flow, are very rarely encountered. In the second case the deviation from unity of the ratio α_L/α_V is considerable only when $h/d > 0.75$, a condition in which the flow can hardly persist to be stratified. This leads us to the conclusion that the assumption of

$$\frac{\alpha_L}{\alpha_V} = 1$$

can be justified in most cases.

References

1 Rufer, C. E., and Kezios, S. P., "Analysis of Two-Phase, One-Component Stratified Flow With Condensation," JOURNAL OF HEAT TRANSFER, TRANS. ASME, Series C, Vol. 88, No. 3, Aug. 1966, pp. 265–275.

2 Sarma, P. K., Sarma, A. S. P., and K. Venkata Apparao, "Predictions of Flow-Level Angles in Two-Phase One-Component Stratified Flow," JOURNAL OF HEAT TRANSFER, TRANS. ASME, Series C, Vol. 93, No. 2, May 1971, pp. 254–256.

3 Chaudhury, T. K., "On the Steady Flow of Viscous Liquid under Constant Pressure Gradient in a Cylinder of Lenticular Section," *Rev. Roum-Sci. Techn. -Méc. Appl.*, Vol. 9, 1964, pp. 759–766.

4 Bird, R. B., Stewart, W. E., and Lightfoot, E. N., *Transport Phenomena*, Wiley, New York, 1960.

5 Buffham, B. A., "Laminar Flow in Open Circular Channels and Symmetrical Lenticular Tubes," *Trans. Instn. Chem. Engrs.*, Vol. 46, 1968, pp. T152–T157.

6 Knudsen, J. G., and Katz, D. L., *Fluid Dynamics and Heat Transfer*, McGraw-Hill, New York, 1958.

7 Whitaker, S., *Introduction to Fluid Mechanics*, Prentice-Hall, Englewood Cliffs, N. J.

A Generalized King's Law of a Conical Hot-Film Anemometer Sensor

C. H. GOODMAN[1] **and H. H. SOGIN**[2]

Introduction

THE CONSTANT-TEMPERATURE quartz-coated hot-film anemometer sensor is one of the few instruments available to measure local and instantaneous velocity of a liquid over a wide speed range. In practice each sensor is calibrated to establish the bridge voltage versus velocity (E versus V) relation. Since the sensor performance depends upon both the sensor and the ambient temperatures (T_s and T_∞, respectively), as well as the velocity, the calibration and its utilization are parametrically complex. In order to reduce the calibrating time and to provide an interpolating scheme, the calibrations are sometimes generalized in terms of a dimensionless heat transfer correlation, or a generalized King's law. This paper provides a fairly rational correlation representing the heat transfer on a conical hot-film sensor in axisymmetrical flow (Fig. 1).

Heat transfer correlations have been presented in quasi-dimensionless form or in dimensionless form over limited range of Reynolds number and overheat. A major difference between the present and earlier works [1-6][3] is coverage of a broad Reynolds number range which includes a low-speed portion where buoyancy is manifest. By juxtaposing a few elementary guidelines, the heat transfer correlation on the small conical surface is cast in a conventional dimensionless form.

Global Unit Surface Conductance

In a statistically steady calibration the bridge voltage $E = E(V, T_s, T_\infty;\ q, \psi)$; q denotes the heat transfer, and ψ the angle between the velocity and gravitational fields. A global unit surface conductance denoted by h is arbitrarily based on the

---

[1] Southern Services, Inc., Birmingham, Ala.

[2] Department of Mechanical Engineering, Tulane University, New Orleans, La.

[3] Numbers in brackets designate References at end of technical brief.

Contributed by the Heat Transfer Division of THE AMERICAN SOCIETY OF MECHANICAL ENGINEERS. Manuscript received by the Heat Transfer Division March 22, 1973.

Hagen–Poiseuille equation [4], could be fixed a priori, the limit for h/d going to zero was more difficult to determine. Indeed, for β going to zero, equation (9) takes the undefined form 0/0. The uncertainty at this point could be solved by making use of a simplified formula for the rate of discharge derived by Buffham [5], which is only applicable for very shallow channels:

$$Q = \frac{P}{\mu}\,\frac{d^4}{2}\,\frac{64}{105}\left(\frac{h}{d}\right)^{3.5} \tag{13}$$

The assumptions made when deriving this formula entail that the lower the value of h/d, the more reliable the calculated value for the rate of discharge. Putting this expression in equation (5) and substituting Ω, b, and h as functions of β, the following expression is obtained:

$$f = \frac{1}{\mathrm{Re}}\,\frac{105}{64}\,\frac{1}{32}\,\frac{(2\beta - \sin 2\beta)^3}{\beta^2 \sin^7 \dfrac{\beta}{2}} \tag{14}$$

The last quotient in this equation also takes the undefined value 0/0 for β going to zero, but by means of l'Hôpital's rule the limit for f can be calculated. Therefore we calculated the ninth-order derivative of numerator and denominator, giving 1680×2^9 and $9! \times 2^{-7}$, respectively. Finally, the limit of f for h/d going to zero was found to be 15.5555 . . . /Re, giving a limiting value for α of 0.9721. It is evident that the figure also applies for the determination of friction factors for laminar flow in symmetrical lenticular tubes, as was explained earlier.

Turbulent Flow in Open Circular Channels. As reported by several authors, the friction factor for turbulent flow in closed [6] and in open [7] channels does not depend upon the geometric form of the section, provided the hydraulic radius has the same value. This entails that for turbulent flow

$$\alpha = 1$$

and one can use one of the known relations expressing the friction factor as a function of the Reynolds number, for instance the Blasius equation

$$f = 0.0791\ \mathrm{Re}^{-1/4} \tag{15}$$

Conclusion

While the form factor for turbulent flow is always close to unity, for laminar flow a variation between 0.9721 and 1.1099 is possible. This results in the following extreme values for the ratio of the form factors of each phase:

laminar–laminar:

$$0.88 < \frac{\alpha_L}{\alpha_V} < 1.14$$

liquid laminar–vapor turbulent:

$$0.97 < \frac{\alpha_L}{\alpha_V} < 1.11$$

liquid turbulent–vapor laminar:

$$0.90 < \frac{\alpha_L}{\alpha_V} < 1.03$$

The first and the third cases, with laminar vapor flow, are very rarely encountered. In the second case the deviation from unity of the ratio α_L/α_V is considerable only when $h/d > 0.75$, a condition in which the flow can hardly persist to be stratified. This leads us to the conclusion that the assumption of

$$\frac{\alpha_L}{\alpha_V} = 1$$

can be justified in most cases.

References

1 Rufer, C. E., and Kezios, S. P., "Analysis of Two-Phase, One-Component Stratified Flow With Condensation," Journal of Heat Transfer, Trans. ASME, Series C, Vol. 88, No. 3, Aug. 1966, pp. 265–275.

2 Sarma, P. K., Sarma, A. S. P., and K. Venkata Apparao, "Predictions of Flow-Level Angles in Two-Phase One-Component Stratified Flow," Journal of Heat Transfer, Trans. ASME, Series C, Vol. 93, No. 2, May 1971, pp. 254–256.

3 Chaudhury, T. K., "On the Steady Flow of Viscous Liquid under Constant Pressure Gradient in a Cylinder of Lenticular Section," *Rev. Roum-Sci. Techn. -Méc. Appl.*, Vol. 9, 1964, pp. 759–766.

4 Bird, R. B., Stewart, W. E., and Lightfoot, E. N., *Transport Phenomena*, Wiley, New York, 1960.

5 Buffham, B. A., "Laminar Flow in Open Circular Channels and Symmetrical Lenticular Tubes," *Trans. Instn. Chem. Engrs.*, Vol. 46, 1968, pp. T152–T157.

6 Knudsen, J. G., and Katz, D. L., *Fluid Dynamics and Heat Transfer*, McGraw-Hill, New York, 1958.

7 Whitaker, S., *Introduction to Fluid Mechanics*, Prentice-Hall, Englewood Cliffs, N. J.

A Generalized King's Law of a Conical Hot-Film Anemometer Sensor

C. H. GOODMAN[1] **and H. H. SOGIN**[2]

Introduction

The constant-temperature quartz-coated hot-film anemometer sensor is one of the few instruments available to measure local and instantaneous velocity of a liquid over a wide speed range. In practice each sensor is calibrated to establish the bridge voltage versus velocity (E versus V) relation. Since the sensor performance depends upon both the sensor and the ambient temperatures (T_s and T_∞, respectively), as well as the velocity, the calibration and its utilization are parametrically complex. In order to reduce the calibrating time and to provide an interpolating scheme, the calibrations are sometimes generalized in terms of a dimensionless heat transfer correlation, or a generalized King's law. This paper provides a fairly rational correlation representing the heat transfer on a conical hot-film sensor in axisymmetrical flow (Fig. 1).

Heat transfer correlations have been presented in quasi-dimensionless form or in dimensionless form over limited range of Reynolds number and overheat. A major difference between the present and earlier works [1-6][3] is coverage of a broad Reynolds number range which includes a low-speed portion where buoyancy is manifest. By juxtaposing a few elementary guidelines, the heat transfer correlation on the small conical surface is cast in a conventional dimensionless form.

Global Unit Surface Conductance

In a statistically steady calibration the bridge voltage $E = E(V, T_s, T_\infty;\ q, \psi)$; q denotes the heat transfer, and ψ the angle between the velocity and gravitational fields. A global unit surface conductance denoted by h is arbitrarily based on the

---

[1] Southern Services, Inc., Birmingham, Ala.

[2] Department of Mechanical Engineering, Tulane University, New Orleans, La.

[3] Numbers in brackets designate References at end of technical brief.

Contributed by the Heat Transfer Division of The American Society of Mechanical Engineers. Manuscript received by the Heat Transfer Division March 22, 1973.

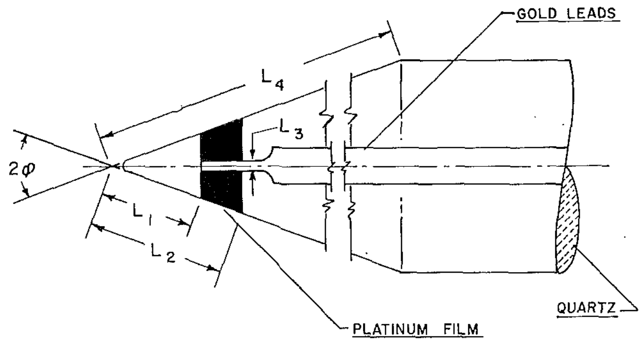

Fig. 1 Conical sensor structure and nomenclature. Dimensions of present sample: ϕ = 23.9 deg, L_1 = 0.34_6, L_2 = 0.45_7, L_3 = 0.08_5, L_4 = 3.0 mm

surface area S of one face of the film. The steady heat balance takes the form:

$$\frac{E^2[R_s/(R_s + R')]^2}{R_s} = hS(T_s - T_\infty) \qquad (1)$$

The numerator is the square of the sensor (net) voltage, R' being a constant bridge resistance. In the range of utilization reported in the following, the R_s versus T_s relation is found experimentally to be linear:

$$R_s/R_0 = 1 + \beta_0(T_s - T_0) \qquad (2)$$

The limiting conduction is approximated by supposing that the hot film forms the surface of a spherical cavity of radius r_s centered at the virtual vertex of the cone in an infinite domain. The conduction through the water is assumed to "parallel" the conduction through the quartz. If ϕ is the cone half angle (Fig. 1) and a geometric factor C is defined by

$$2\pi C = (1 - L_1/L_2)[\pi(1 + L_1/L_2)\sin\phi - 2L_3/L_2] \qquad (3)$$

then the film surface area $S = 2\pi CL_2^2$, and $r_s = L_2\sqrt{C/2}$. The limiting conduction Nusselt number

$$\mathrm{Nu}_k = q_kL_2/[Sk_\infty(T_s - T_\infty)]$$
$$= (2/C)^{1/2}\left[\frac{1 - \cos\phi}{2}\frac{k_q}{k_\infty} + \frac{1 + \cos\phi}{4}\left(1 + \frac{k_s}{k_\infty}\right)\right] \qquad (4)$$

The first term in brackets represents the fraction conducted through the quartz, and the second term the fraction through the liquid; their ratio for water is about 1:10. The characteristic length L_2, the slant height from the vertex to the trailing edge of the hot film, is the hydrodynamic length of the boundary layer presumed to develop at high sensor Reynolds number.

If the fluid properties were independent of temperature, the convective part would be proportional to $\mathrm{Pr}^m\mathrm{Re}^n$. To allow for the variation of fluid properties, a power of the viscosity ratio $(\mu_\infty/\mu_s)^\gamma$ is suffixed, as for liquids through tubes [7].

In order to reduce the number of degrees of freedom in the correlation, values of m and γ are fixed. Similarity solutions show that m is practically $^1/_3$, and since the conjugate boundary condition cannot alter the influence of the Prandtl number, $m = 2n/3$. As for γ, prior experiences, particularly with water, suggest that it equals 0.14.

Accordingly, the generalized form of the heat transfer correlation under zero gravity is

$$\mathrm{Nu}_\infty = A\mathrm{Nu}_k + B(\mathrm{Pr}_\infty^{2/3}\mathrm{Re}_\infty)^n(\mu_\infty/\mu_s)^{0.14} \qquad (5)$$

Here, $\mathrm{Nu}_\infty = hL_2/k_\infty$, $\mathrm{Re}_\infty = VL_2/\nu_\infty$ and the quantities A, B, and n remain to be determined by experimentation.

A correction is now required to account for the buoyant effects observed when the sensor orientation relative to the gravity field is altered at low velocity. If the velocity and the gravity fields are parallel (sensor pointing upward) the buoyancy effectively retards the on-coming fluid, reducing the heat transfer, and vice versa if they are anti-parallel. When the velocity and the gravity fields are perpendicular, the thermal plume induces a vertical velocity component which is observed to increase the heat transfer.

An approximate perturbation analysis based on point-source laminar plume theory has been used [8] to investigate the effect of the free convection at the heated sensor. The result is that the magnitude of the change in the velocity of approach is $w = \beta gq/(2\pi V\ \mu c_p)$. Here, β is the volume expansivity, μ the viscosity, and c_p the specific heat of the liquid. Thus, when the speeds are not too low, the thermal probe is presumed to sense the velocity $V \pm w$ as though it were in a zero-gravity field, the minus or plus sign corresponding to the case that the velocity and gravity fields are parallel or anti-parallel, respectively.

In order to incorporate the buoyant effect into (5) it is convenient to introduce K_∞ defined by

$$\frac{w}{V} = \frac{\beta gq}{2\pi V^2\mu c_p} = C\frac{\mathrm{Nu}_\infty\mathrm{Gr}_\infty}{\mathrm{Pt}_\infty\mathrm{Re}_\infty^2} \equiv CK_\infty \qquad (6)$$

where the Grashof number $\mathrm{Gr}_\infty = L_2^3\beta g\rho_\infty^2(T_s - T_\infty)/\mu_\infty^2$ and C is given by (3).

Experimental Results

A detailed description of the calibration apparatus and its performance has been reported elsewhere [5, 8]. All the anemometric data were obtained on a Thermo-Systems, Inc., Model 1050 constant temperature anemometer system. The sensor was of their Model 1230.

Low speed data (V < 7cm/sec) at the several sensor temperatures are depicted in Figs. 2 and 3. The ordinate in Fig. 2

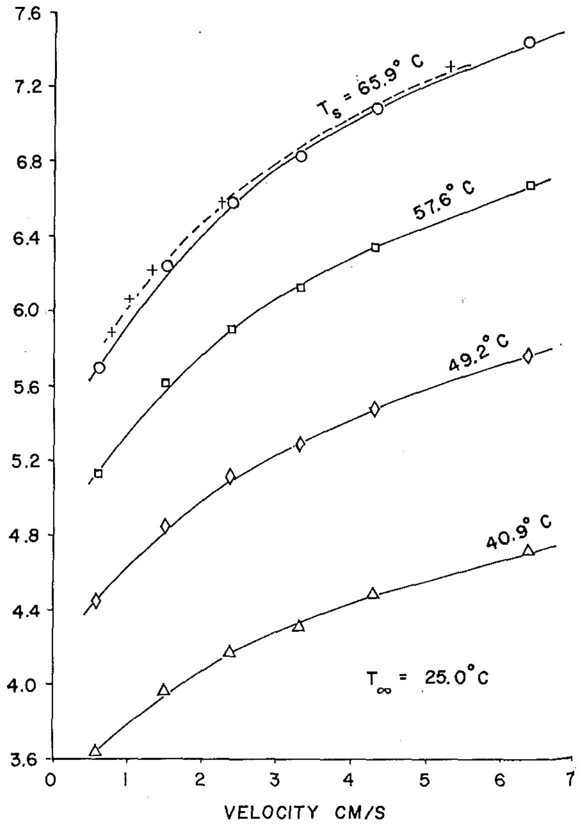

Fig. 2 Calibration data in the mixed convection regime reduced to zero-gravity conditions. T_∞ = 25.0 deg C, four sensor temperatures

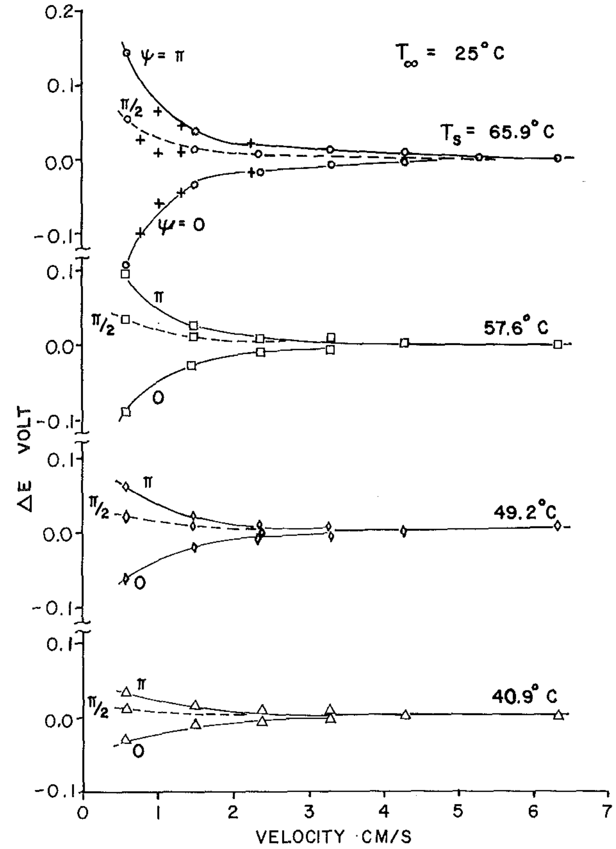

Fig. 3 Gravitational effects in the mixed convection regime

represents the arithmetic mean value of E measured when the laminar flow pipe was in the two vertical positions. The dotted curve represents data reported earlier [5], and the solid lines show recent data. Fig. 3 shows the departures from mean E which are ascribed to buoyancy, the three curves at each sensor temperature corresponding to the three orientations. The ordinates represent the amounts of voltage that must be added to the corresponding average curve in Fig. 2 in order to recover the original calibration data; iteration converges rapidly. Note that the horizontal position ($\psi = \pi/2$) favors the anti-parallel orientation ($\psi = \pi$).

A zero-gravity correlation was established by averaging $E^2 \sim q$ at $\psi = 0$ and $\psi = \pi$. There were 192 data points throughout the experimentation, including [5]. Constants A, B, and n were determined on basis of a least square fit accomplished with a program developed by Law [9]. The buoyant effects were then accounted for in the manner previously suggested.

Expressed at length, the correlation of the global unit surface conductance on the quartz-coated conical hot-film sensor at arbitrary orientation in the gravitational field is

$$\mathrm{Nu}_\infty = 1.1\sqrt{\frac{2}{C}}\left[\frac{1-\cos\phi}{2}\,\frac{k_q}{k_\infty} + \frac{1+\cos\phi}{4}\left(1+\frac{k_s}{k_\infty}\right)\right] + 5.5[\mathrm{Pr}_\infty{}^{2/3}\mathrm{Re}_\infty(1+0.7C_\psi K_\infty)]^{0.309} \times \left(\frac{\mu_\infty}{\mu_s}\right)^{0.14},\ 3 < \mathrm{Re} < 1000 \quad (7)$$

where $C_\pi = -C_0 = C\,0.072$, and $C_{\pi/2} = +0.043$. The standard deviation of the deviation parameter $(\mathrm{Nu}_{\infty,\mathrm{exp.}} - \mathrm{Nu}_{\infty,\mathrm{calc.}})/\mathrm{Nu}_{\infty,\mathrm{calc.}}$ was 1.6 percent.

The result might be further generalized to include a correction for the unheated hydrodynamic starting length L_1, which varies from sensor to sensor. An estimate based on laminar boundary-layer heat transfer on slender cones suggests that the coefficient 5.5 ought be replaced by the factor $6.0[1 - (L_1/L_2)^{0.46}]^{2/3}$.

References

1 Fabula, A. G., "Operating Characteristics of Some Hot Film Velocity Sensors in Water," *Advances in Hot-Wire Anemometry*, W. L. Melnik and J. R. Weske, eds., AFOSR No. 68-1492, Univ. of Maryland, 1968, pp. 167–193.

2 Resch, F. J., "Etudes sur le fil chaud et le film chaud dans l'eau," Thesis, Docteur Ingenieur, Marseille, 1968.

3 Resch, F. J., and Coantic, M., "Etude sur le fil chaud et le film chaud dans l'eau," *La Houille Blanche*, No. 2, 1969, pp. 151–161.

4 Resch, F. J., and Leutheusser, H. J., "Mesures de turbulence dans le ressaut hydraulique," *La Houille Blanche*, No. 1, 1971, pp. 17–31.

5 Goodman, C. H., and Sogin, H. H., "Calibration of a Hot-Film Anemometer in Water Over the Velocity Range 0.5 to 200 Cm/sec," Paper No. 2-2-62 presented at the Symposium on Flow—Its Measurement and Control in Science and Industry, Pittsburgh, Pa., May, 1971. Jointly sponsored by AIP, ASME, ISA, and NBS.

6 Morrow, T. B., and Kline, S. J., "The Evaluation and Use of Hot-Wire and Hot-Film Anemometers in Liquids," Report MD-25, Stanford University, Aug. 1971.

7 Kays, W. M., *Convective Heat and Mass Transfer*, McGraw-Hill, New York, 1966, pp. 214–222, 258, 260.

8 Goodman, C. H., "Calibration of a Hot-Film Anemometer in Water Over the Velocity Range 0.5 to 200 Cm/sec," PhD dissertation, Tulane University, Apr. 1971.

9 Law, V. J., "Solution of Systems of Nonlinear Equations," Final Report, NASA Contract NAS8-21484, Dept. of Chemical Engineering, Tulane University, 1971.